



HAL
open science

Fluid-structure interaction on yacht sails: from full-scale approach to wind tunnel unsteady study

Nicolas Aubin

► **To cite this version:**

Nicolas Aubin. Fluid-structure interaction on yacht sails: from full-scale approach to wind tunnel unsteady study. Mechanical engineering [physics.class-ph]. Université de Bretagne occidentale - Brest, 2017. English. NNT: 2017BRES0012 . tel-01779521

HAL Id: tel-01779521

<https://theses.hal.science/tel-01779521>

Submitted on 26 Apr 2018

HAL is a multi-disciplinary open access archive for the deposit and dissemination of scientific research documents, whether they are published or not. The documents may come from teaching and research institutions in France or abroad, or from public or private research centers.

L'archive ouverte pluridisciplinaire **HAL**, est destinée au dépôt et à la diffusion de documents scientifiques de niveau recherche, publiés ou non, émanant des établissements d'enseignement et de recherche français ou étrangers, des laboratoires publics ou privés.



université de bretagne
occidentale

UNIVERSITE
BRETAGNE
LOIRE



THÈSE / UNIVERSITÉ DE BRETAGNE OCCIDENTALE

sous le sceau de l'Université Bretagne Loire

pour obtenir le titre de

DOCTEUR DE L'UNIVERSITÉ DE BRETAGNE OCCIDENTALE

Mention : Génie mécanique, mécanique des fluides et énergétique
École Doctorale des Sciences de la Mer (EDSM)

présentée par

Nicolas AUBIN

Préparée à l'Institut de Recherche de l'Ecole Navale (IRENav), département Mécanique et Energétique en Environnement Naval (M2EN)

Fluid-structure interaction on yacht sails: from full-scale approach to wind tunnel unsteady study.

Thèse soutenue le 25 janvier 2017
devant le jury composé de :

Jacques-André ASTOLFI
HDR, IRENav / *co-directeur*

Patrick BOT
Maître de Conférences, IRENav / *encadrant*

Christophe CLANET
Directeur de recherche CNRS HDR, LadHyX / *examineur*

Richard G.J. FLAY
Professor, University of Auckland / *co-director*

Grégory GERMAIN
HDR, IFREMER / *rapporteur*

Guilhem MICHON
HDR, ISAE / *rapporteur*

Marc RABAUD
Professeur des Universités, Université Paris-Sud FAST / *examineur*

Bernard SIMON
Professeur des Universités, UBO / *examineur*

Année : 2017

THÈSE

présentée à

L'UNIVERSITÉ DE BRETAGNE OCCIDENTALE

pour obtenir le titre de

DOCTEUR DE L'UNIVERSITÉ DE BRETAGNE OCCIDENTALE

Mention *Génie mécanique, mécanique des fluides et énergétique*

par

Nicolas Aubin

**Fluid-structure interaction on yacht sails: from
full-scale approach to wind tunnel unsteady study**

soutenue le 25 janvier 2017 devant la commission d'examen :

J.A. Astolfi	Co-directeur
P. Bot	Encadrant
C. Clanet	Président du jury, examinateur
R.G.J. Flay	Co-directeur
G. Germain	Rapporteur
G. Michon	Rapporteur
M. Rabaud	Examineur
B. Simon	Examineur

Acknowledgement

Being involved in an international collaboration, I have chosen to write this thesis in English. However I prefer to make the traditional acknowledgement in the native tongue of those who deserve it.

Je tiens à profondément remercier mes encadrants Patrick Bot et Frédéric Hauville. Merci de m'avoir fait confiance pour tant de choses, de m'avoir embarqué sur Téthys, de m'avoir supporté sur les hauts et creux de vagues. Patrick, merci pour tes cours passionnants sur la transition, la sensibilité aux conditions initiales, ta disponibilité et tes relectures parfois bien tardives. Frédéric merci pour ta patience lors des formations initiales sur les codes numériques, de ta bonne humeur continuelle et de tes histoires de moutons. Bien que quelques éléments vous opposent, notamment la méthode de conservation du beurre, vous insufflez une telle dynamique de recherche dans le projet Voilenav que c'est un véritable plaisir de travailler à vos côtés. Merci encore à vous deux.

Remerciement profond également à mon co-directeur français Jacques-André Astolfi ayant toujours le sage conseil et, pour avoir soutenu et surtout modéré les démarches de mes différents projets. Merci d'avoir été là, apportant du recul, n'étant toi même pas un expert de ce domaine spécifique et mystérieux qu'est la voile. Je retiendrai notamment ton "Small is beautiful" et pardonne moi si j'ai oublié quelques blagues corses. Thanks to Richard G.J. Flay, my new zealander co-director. Thank you Richard for your overseas and accurate advices and guidance. Many thanks also to Peter Richards and Ignazio M. Viola -who kindly accepted this meeting in Edinburgh- for their precious help. I felt very lucky for having such a great thesis board.

Je tiens aussi à chaleureusement remercier l'ensemble des membres du jury. Tout d'abord mes rapporteurs messieurs Grégory Germain et Guilhem Michon pour leurs relectures attentives et leurs retours précis et constructifs. Messieurs Marc Rabaud et Bernad Simon pour leurs interrogations pertinentes, en compléments de leur savoir de naviguant. Enfin monsieur le président Christophe Clanet, qui m'a permis de découvrir d'autres horizons dans la physique du sport. L'ensemble de vos questions, remarques et commentaires ont à la fois permis d'améliorer grandement le manuscrit, mais aussi ouverts d'autres perspectives.

Ces travaux de thèse s'inscrivent dans de nombreuses collaborations. Pour les collaborations industrielles, merci à Yann Roux de K-Epsilon, société fournissant le code ARAVANTI, à Ronan Floch de la voilerie Incidence Sails pour le dessin et la réalisation de voiles maquettes. Merci à BSG Developements et à Laurent Guillon pour ses conseils, et à son maintenant magnifique Sail Pack qui toujours à la pointe, n'arrête pas de s'améliorer en fonctions des retours et des besoins des utilisateurs.

For the academic collaborations thanks to the Sailing Fluids program (see

<http://www.sailingfluids.org/>), many thanks to my Kiwi supervisors and colleagues. A great thanks to David Le Pelley, former YRU wind tunnel manager and VSPARS support. Thanks again for providing such a user-friendly and great tool as VSPARS. Thank you also to my former colleagues there. Alex, best wingman ever in Auckland, thank you so much for your always warm welcome. I would like to thank my favourite Italian team (not the soccer one), Dario Motta, for his interesting FEPV and the invention of the perfectly burned Italian coffee smell and Stefano for the numerical simulation discussions. Great thanks also to you Filippo for your help. Thank you so much Ben for all the DMCs, your highly-skilled sailing comments back and really good moments in NZ. Without your help guys, it would not have been possible.

Merci à Brest métropole océane pour le financement de cette thèse, au LabexMER pour les aides de financement à la mobilité, à l'Ecole Navale et la Marine Nationale pour leur support continu.

Merci à mes prédécesseurs, maintenant docteurs, pour avoir su ouvrir la voie VOILENav et d'être toujours réactifs, moteurs et intéressés par nos problématiques. Merci à toi Benoît pour le west coast support au départ, à l'initiation aux astuces Inkscape ainsi que ton humour légendaire. Merci aussi pour ton renfort au labo et au YRU et merci à Fanny pour l'atelier gomette. Bon vent à votre petit Noé. Merci à Mathieu Durand qui a su trouver le temps de réaliser nos lettres au Père Noël en terme de besoin pour nos études au laboratoire. Bien le meilleur pour tes futurs projets.

Merci amical à l'équipage VOILENav junior: Dr Julien Deparday, pour son accueil, ses conseils, sa complémentarité, sa sagesse, ses blagues et le beau modèle d'illustration 3D du J80. Gros bisou à ta petite famille Gaëlle et Émilie et rétablis toi vite. Merci à Matthieu Sacher pour toutes les petites formations aux outils numériques, ainsi que ses trucs et astuces dont il a toujours le secret. Merci à toi Matthieu d'avoir fait le traducteur de Mathieu, pour toute l'optimisation, ton renfort à Auckland. Bien le meilleur avec Aurélie et Lilwenn. Merci à Hugo pour les nombreux échanges sur le vent, pour son support NKE, sa télévision pour ping-ponger les lignes de départ proprement (enfin quand le viseur ne dérape pas), et le soutien dans la dernière ligne droite de la fin de thèse. Bon vent à Goulven pour la relève.

Merci au SEFER, Didier Munck, Alain Boulch et aussi au support informatique de Venec et Yannick. Tous ont su me sauver la vie un bon millier de fois pour pouvoir toujours être pleinement opérationnel. Merci à Tina et Denis, côté Caparmor. Merci chaleureux à celles et ceux à l'IRENav qui au jour le jour nous permettent de rendre l'ordinaire parfois complexe ou obscur en formalités transparentes pour le bord: grand merci à Marie (ou plutôt super Marie) notre deuxième maman (et parfois maman canard) à tous les doctorants, Magalie et Christine, Luc, Jacques et aux Stéphane. Bon courage avec les transitions à venir.

Merci à Phillippe, Mickael et à Alain Daoulas du club voile ailée (un jour peut être Téthys refera une régates sans BFD ou protest). Merci à Fabrice pour ses leçons de matelotage et tous tes bons petits plats préparés avec humour et amour pour que nous soyons toujours bien lesté sur l'eau le lendemain. Merci à Ludo et ses divers équipiers de m'avoir permis de continuer à naviguer, pour l'ensemble des régates, que ce soit sous le soleil de Camaret à domicile, ou pour cet inoubliable et magnifique GPEN 2016 (pourtant mal engagé) achevé en beauté!

Un grand merci à l'équipe de doctorants du laboratoire: Georges alias Mr Bubble, Emery, Dieudonné, Christophe, Pierre-Luc ex agent 00 et initiateur à OpenFOAM, Alexandra best foilwoman ever in Lanvéoc, Joseph (méfie toi des vélos à l'avenir). Merci à Oussman, Ines, les presqu'iliens

Nico et Mathieu, jean-JB et Clément de la KGB, Bruno, Wissam, Meihan. Merci à Alexandre pour les quelques soirées presqu'île et à Loïc le roi des trajectoire mobiles. Merci à Charlotte pour ses pièces de théâtre et à Camille pour les discussion dont elle a le secret à la pause déjeuner. Merci à Arnaud, cobureau de choc, à ta musique flamenco, tes problèmes (dé)ontologiques. Merci pour les innombrables échanges constructifs que ce soit à propos de RDP, de pdftex, de marées, de cartes ou même tout simplement de vie. Merci à Jishen de m'avoir supporté aussi dans la même pièce sur la fin de thèse. Merci particulier à Lamia et son chien Galactus.

Merci aux stagiaires ayant apporté des briques à l'édifice Voile/Kitenav: Sophie, Jessica, Nicolas pour ses formes de spi et surtout William: tâche d'éviter les parpaing dans ta voiture même si tu te défends pas mal à Halo 3 et n'abuse pas trop du lait pour remplir le volume interchocapical dès le matin. Merci aux masters ayant eux aussi apporté de l'eau au moulin: Charles, Antoine et un grand mecricri à toi Ulysse pour l'analyse vidéo. Merci respectueux aux bordaches ayant participé au projet et apporté une briquette à l'édifice. Si lors d'une SURMAR ou d'un SAR vous croisez un voilier, ne soyez pas nerveux et vérifiez juste que son CPA est supérieure à la Dmp avant d'alerter le pacha.

Thanks to my flatmates during my visits to Auckland, which are now my friends. Thanks to them and also my always welcoming friends in New Zealand: Amaury & Viviane (such a beautiful wedding), Andrea, Shank, Stephanie, Brandon, Jamie (really appreciate your "majestical" Verve magazine articles and thank you for letting me join you during the working weekends to complete my final manuscript), Heather, David and Karina. Muchas gracias a ti Verónika por tus gustos musicales, tus discusiones profundas y tu hermosa sonrisa. Thanks to John, Crocodile and her crew members, Bruce for letting me racing and sailing on the Pacific ocean. I will never forget the "road 26" stopover weekend, and the hundreds of dolphins in the proper road 66.

Merci à tous ceux qui rendent la presqu'île tous les jours bien vivante: au club de judo Renshinkan de Crozon, Stéphane, Manu, Cécile, Mireille, Thierry, les autres et surtout Nico, joyeux compagnon des épiques soirées camarétoises. Merci à Yvon pour les délices de camembert, à JP pour son maxi planteur et à Lolo pour les discussions palmes et saucissons avec un ptit cidre... Merci aux volleyeuses brestoises de venir se perdre au bout du monde pour partager quelques moments. Merci à Robin Foster pour ses albums instru d'inspirations locales qui sont la bande son de la rédaction du présent manuscrit.

Remerciement aux officiers, marins, équipages et unités de la Marine Nationale que j'ai pu servir lors de mon VOA: vous avez tous changé ma vie. Votre exemple et vos souvenirs m'inspirent tout les jours. La mer est grande mais le monde est petit. BZ à tous, content d'en avoir revu certains (Thomas, PH, Chloé) et merci à Maxime de me faire encore vivre ses aventures. Merci aussi à mes camarades et profs de promo océan du côté de Nantes, aux Marie (et son mini) et Marie.

Remerciement final à mes proches amis toujours présents, même si je me suis embarqué pour le bout du monde, que ce soit à Camaret ou à Auckland: Alexandre, Fabien, Maxime, Jean-Phi, Charlotte, Yaël.

A mes parents, mes sœurs, Caro pour son courage et son exemple quotidien, et Juju, pour sa dévotion auprès des autres. Merci à Matthieu et à vous deux (maintenant trois) pour ce bien beau mariage (j'en ai encore mal aux pieds mais je ne suis pas contre goûter du vin du mariage, avec modération bien sûr, pour rester lucide lors du dooble). Merci à ma famille.

Funding

This thesis has received many financial support:

- this work was supported by Brest Métropole Océane,
- this work was supported by the French Naval academy,
- the wind tunnel experimental campaigns project in 2015 and 2016 took part of the Sailing Fluids collaboration. This project has received funding from the European Union's Seventh Programme for research, technological development and demonstration under grant agreement n°PIRSES-GA-2012-318924 (SAILING FLUIDS) and from the Royal Society of New Zealand.
- the wind tunnel experimental campaign in 2015 and 2016 were supported by the "Laboratoire d'Excellence" LabexMER (ANR-10-LABX-19) and co-funded by a grant from the French government under the program "Investissements d'Avenir",
- the participation and precious help of Dr Benoit Augier for his secondment during the 2016 experimental campaign was supported by the European Union's Seventh Framework Programme (FP7/2007-2013) under REA grant agreement n°PCOFUND-GA-2013-609102 (PRESTIGE-Campus France).

Citations

Les études habituelles, pratiquées dans les bureaux d'études d'architecture navale et par quelques constructeurs de mâts, utilisent des formules de résistance des matériaux associées à un coefficient de sécurité qui dépend de l'âge du calculateur (expérience professionnelle) et du nombre de départs au lof vécus (expérience nautique).

Franck de Rivoyre, ingénieur

Smith: Why, Mr. Anderson, why? Why? Why do you do it? Why? Why get up? Why keep fighting? Do you believe you're fighting for something, for more than your survival? Can you tell me what it is? Do you even know? Is it freedom, or truth, perhaps peace? Could it be for love? Illusions, Mr. Anderson, vagaries of perception, temporary constructs of a feeble human intellect trying desperately to justify an existence that is without meaning or purpose. And all of them as artificial as the Matrix itself. Although... Only a human mind can invent something as insipid as love. You must be able to see it, Mr. Anderson, you must know it by now. You can't win, it is pointless to keep fighting. Why, Mr. Anderson, why, why you persist?

Neo: Because I choose to.

Extracted from Matrix Revolution

Je dédie cette thèse au futur, à ma nièce Manon.

Contents

Acknowledgement	iii
List of Figures	v
List of Tables	xi
Acronyms	xiii
Notation	xiv
Introduction	1
Context	1
The calm before the storm	3
The methods and tools for sailing yacht study	9
Fluid-structure interaction on yacht sails	15
PhD project objectives	17
I Numerical-experimental comparison and applications	19
1 Full-scale approach of sailing and numerical-experimental comparison	21
1.1 Introduction	21
1.1.1 Sailing yacht physics: point of sail and wind	21
1.1.2 Information and elements that can be measured then compared	29
1.2 Article [Aubin et al., 2016a]: Inviscid approach for upwind sails aerodynamics. How far can we go?	33
1.3 Conclusions	42

II	Wind tunnel experimental campaigns	45
2	Wind tunnel experimental set-up	49
2.1	Wind tunnel description	50
2.1.1	Twisted Flow Wind Tunnel description	50
2.1.2	Model presentation	55
2.1.3	Model windage	58
2.2	Wind tunnel flow mapping	60
2.2.1	Wind tunnel flow mapping	60
2.2.2	Wind profile	63
3	Upwind wind tunnel results	67
3.1	Upwind sail presentation	68
3.2	Static trim, reference case and two-parameter optimisation	69
3.2.1	Static trim geometry	69
3.2.2	Reference case $\beta_{AW} = 40^\circ$	72
3.2.3	Two-parameter optimisation results	77
3.2.4	Optimum location at close-hauled $\beta_{AW} = 25^\circ$	80
3.2.5	Optimum location on a close reach $\beta_{AW} = 40^\circ$	86
3.2.6	Optimum location on a beam reach $\beta_{AW} = 60^\circ$	92
3.2.7	Effect of AWA (apparent wind angle) on the optimum and general conclusions	97
3.3	Pumping: effect of dynamic trimming on respective optimum	98
3.3.1	Dynamic trimming	98
3.3.2	Pumping in the reference case $\beta_{AW} = 40^\circ$	102
3.3.3	Pumping at beam reach $\beta_{AW} = 60^\circ$	106
3.3.4	Results discussion	115
3.3.5	Conclusions, limitations and perspectives	117
4	Downwind wind tunnel results	119
4.1	Downwind sail presentation	120
4.1.1	Spinnakers presentation	120
4.1.2	Curling phenomena presentation	121
4.2	Natural curling effect: free mast, partially-rigged mast and additional twisted flow .	127
4.2.1	Free mast situation	127
4.2.2	Partially-rigged mast situation	139

4.2.3	Partially-rigged mast situation with twisted flow	144
4.2.4	Comparison of the different mast configurations	146
4.2.5	Unfolding dynamics of the folding hysteresis: usual recovering and extreme events	147
4.3	Natural curling effect: fully rigged mast	151
4.3.1	$\beta_{AW} = 80^\circ$	153
4.3.2	$\beta_{AW} = 100^\circ$	156
4.3.3	$\beta_{AW} = 120^\circ$	159
4.3.4	General conclusions about curling apparition	162
4.4	Curling frequency measurement and evolution	165
4.4.1	How to measure the curling frequency?	165
4.4.2	Curling frequency evolution	166
4.4.3	Why measuring the curling frequency?	171
4.5	Curling temporal evolution	172
4.6	Discussions, conclusions and perspectives	178
	Conclusions	181
	Appendices	185
	A Yacht vocabulary	187
	B Frames and coordinate system	189
	C Complementary information on the wind tunnel experimental campaign	193
C.1	Uncertainty evaluation	193
C.1.1	Uncertainty on force coefficients	193
C.2	Recording architecture	194
C.2.1	Signal post-processing	194
C.3	Blockage effect on aero-forces coefficient measurements	195
	D Complementary information on the load sensor	197
D.1	Load sensor calibration	197
D.2	Load sensor complementary information	199
D.2.1	Zeroing of the load sensor	199
D.2.2	Load sensor positioning	199

E	Wind tunnel upwind configuration	201
E.1	Geometry of upwind configuration	201
E.1.1	Measured geometry of upwind elements	201
E.2	Mast alignment	203
E.3	Upwind static command law: presentation of static trim	204
E.3.1	Experimental static sheet length application	206
E.3.2	Uncertainty estimation	208
E.3.3	Numerical static sheet length equivalent	211
E.4	Dynamic command law	212
F	Wind tunnel downwind configuration	227
G	Sail cloth properties	229
H	Masts and battens properties	233
I	Directionnal Load Cells (DLC) applications	235
J	Résumé étendu en français	237
J.1	Introduction	237
J.2	Approche in situ et comparaison numérique-expérimentale	243
J.3	Expérience en soufflerie: présentation de l'installation expérimentale	248
J.4	Expérience en soufflerie: essais sur grand voile. De l'optimisation statique à l'étude du pumping	250
J.5	Expérience en soufflerie: essais au portant. Etude de l'effet du curling: repliement périodique du guindant	263
J.6	Conclusion	279
	Bibliography	281

List of Figures

1	Type of coupling in numerical methods applied to Fluid-Structure Interaction (FSI) problems.	11
1.1	Point of sail.	22
1.2	Representation of the apparent wind.	26
1.3	Wind information processing.	28
1.4	TFWT during 2016 experimental campaign.	47
2.1	Side view cross-section scheme of the Twisted Flow Wind Tunnel (TFWT).	50
2.2	TFWT vanes.	51
2.3	Geometry of the TFWT.	52
2.4	TFWT force balance.	53
2.5	Platform configuration.	57
2.6	Windage measurement.	59
2.7	System for measuring the velocity profile and flow mapping.	61
2.8	Empty TFWT velocity field.	62
2.9	Wind profile comparison.	63
2.10	Central wind tunnel velocity profile.	64
2.11	Evolution of the Pitot measurement for different fan frequencies.	64
3.1	Illustration of camber for the model mainsails used for upwind experimental campaign.	68
3.2	Upwind geometric configuration of stepper motors and trim adjustment.	70
3.3	L_{sheet} - $L_{sheet\ 0}$ map as a function of L_{car} and L_{ord}	70
3.4	Illustration of set up in the two-parameter optimisation configuration.	71
3.5	Reference upwind case.	72
3.6	Reference upwind case, drive vs side and lift vs drag.	73
3.7	Effect of sheet length on the flying shape for upwind cases.	74
3.8	Upwind configuration TFWT velocity field.	75

3.9	Central wind profile compare to outlet section wind profile data with upwind sails. . .	76
3.10	Mainsail sheet load coefficient for the maximum camber mainsail $\beta_{AW}= 25^\circ$	81
3.11	Mainsail sheet load coefficient for the flat mainsail $\beta_{AW}= 25^\circ$	81
3.12	Two-parameter optimisation for the standard mainsail $\beta_{AW}= 25^\circ$	82
3.13	Two-parameter optimisation for the maximum camber mainsail $\beta_{AW}= 25^\circ$	83
3.14	Two-parameter optimisation for the flat mainsail $\beta_{AW}= 25^\circ$	84
3.15	Effect of design shape on the optimum at $\beta_{AW}= 25^\circ$	85
3.16	Mainsail sheet load coefficient for the different design shapes $\beta_{AW}= 40^\circ$	87
3.17	Two-parameter optimisation for the standard mainsail $\beta_{AW}= 40^\circ$	88
3.18	Two-parameter optimisation for the maximum camber mainsail $\beta_{AW}= 40^\circ$	89
3.19	Two-parameter optimisation for the flat mainsail $\beta_{AW}= 40^\circ$	90
3.20	Effect of design shape on the optimum at $\beta_{AW}= 40^\circ$	91
3.21	Effect of mast alignment on the optimum for the standard mainsail at $\beta_{AW}= 40^\circ$. . .	92
3.22	Mainsail sheet load coefficient for the maximum camber mainsail $\beta_{AW}= 60^\circ$	93
3.23	Mainsail sheet load coefficient for the flat mainsail $\beta_{AW}= 60^\circ$	93
3.24	Two-parameter optimisation for the standard mainsail $\beta_{AW}= 60^\circ$	94
3.25	Two-parameter optimisation for the maximum camber mainsail $\beta_{AW}= 60^\circ$	95
3.26	Two-parameter optimisation for the flat mainsail $\beta_{AW}= 60^\circ$	96
3.27	Effect of design shape on the optimum at $\beta_{AW}= 60^\circ$	97
3.28	Dynamic trimming device in upwind configuration.	99
3.29	Drive force coefficient with dynamic trimming for the reference case at $\beta_{AW}= 40^\circ$. .	103
3.30	Side force coefficient with dynamic trimming for the reference case at $\beta_{AW}= 40^\circ$. . .	104
3.31	Optimisation target function coefficient with dynamic trimming for the reference case at $\beta_{AW}= 40^\circ$	105
3.32	Mean drive and side force coefficient with dynamic trimming for $\beta_{AW}= 60^\circ$	107
3.33	Mean optimisation target function and sheet load coefficient with dynamic trimming for $\beta_{AW}= 60^\circ$	108
3.34	Time series evolution representation for the standard mainsail with $A = 20$ mm at $f_r = 0.127$	109
3.35	Time series evolution for standard mainsail, $A = 20$ mm, $AWA = 60^\circ$, lower frequencies.	110
3.36	Time series evolution for standard mainsail, $A = 20$ mm, $AWA = 60^\circ$, higher frequencies.	111
3.37	Power calculation for the amplitude $A = 20$ mm, $\beta_{AW}= 60^\circ$	113
3.38	Lissajou representation of drive and sheet load coefficients, standard mainsail $A =$ 20 mm, $\beta_{AW}= 60^\circ$	114

4.1	Model spinnakers photographs.	120
4.2	Curling sequence at full-scale.	122
4.3	Curling sequence in the wind tunnel.	123
4.4	Rig downwind configuration.	126
4.5	Effect of curling with static trim on force coefficients with a free mast at $\beta_{AW} = 80^\circ$	129
4.6	Effect of curling with static trim on sheet load coefficient at $\beta_{AW} = 80^\circ$	130
4.7	Centreline wind profile compared to outlet section wind profile data with downwind sails.	131
4.8	Downwind configuration TFWT velocity field.	132
4.9	Fold maintained while trimming.	134
4.10	Effect of curling with static trim on force coefficients with a free mast at $\beta_{AW} = 110^\circ$	134
4.11	Effect of curling with static trim on sheet load coefficient at $\beta_{AW} = 110^\circ$	135
4.12	Effect of curling with static trim on force coefficients at $\beta_{AW} = 140^\circ$	136
4.13	Effect of curling with static trim on sheet load coefficient at $\beta_{AW} = 140^\circ$	137
4.14	Folding hysteresis description.	138
4.15	Effect of curling with static trim on sheet load coefficient at $\beta_{AW} = 80^\circ$ with a partially-rigged mast.	139
4.16	Effect of curling with static trim on force coefficients at $\beta_{AW} = 80^\circ$ with a partially-rigged mast.	140
4.17	Effect of curling with static trim on sheet load coefficient at $\beta_{AW} = 140^\circ$ with a partially-rigged mast.	141
4.18	Effect of curling with static trim on force coefficients at $\beta_{AW} = 140^\circ$ with a partially-rigged mast.	142
4.19	Detached flow hysteresis description.	143
4.20	Measured twisted flow wind profile vs the theoretical wind profile.	145
4.21	Effect of curling with static trim on sheet load coefficient at $\beta_{AW} = 80^\circ$ with a partially-rigged mast and twisted flow.	145
4.22	Effect of curling with static trim on force coefficients at $\beta_{AW} = 80^\circ$ with a partially-rigged last and twisted flow.	146
4.23	Spinnaker extreme event while unfolding.	149
4.24	Flying shape evolution during a spinnaker unfolding collapse.	149
4.25	C_{F_x} vs L_{sheet} at $\beta_{AW} = 80^\circ$	154
4.26	C_{F_y} vs L_{sheet} at $\beta_{AW} = 80^\circ$	155
4.27	$C_{F_{sheet}}$ vs L_{sheet} at $\beta_{AW} = 80^\circ$	156
4.28	C_{F_x} vs L_{sheet} at $\beta_{AW} = 100^\circ$	157

4.29	C_{F_y} vs L_{sheet} at $\beta_{AW} = 100^\circ$.	158
4.30	$C_{F_{sheet}}$ vs L_{sheet} at $\beta_{AW} = 100^\circ$.	159
4.31	C_{F_x} vs L_{sheet} at $\beta_{AW} = 120^\circ$.	160
4.32	C_{F_y} vs L_{sheet} at $\beta_{AW} = 120^\circ$.	161
4.33	$C_{F_{sheet}}$ vs L_{sheet} at $\beta_{AW} = 120^\circ$.	162
4.34	Optimum and verge of curling C_{F_x} and L_{sheet} evolution with the AWA.	163
4.35	Time folded fraction for different AWA.	167
4.36	Curling frequency and reduced frequency for the different AWA tested.	168
4.37	Curling frequency for the different spinnaker with a variation of AWA.	169
4.38	Curling reduced frequency for the different spinnaker with a variation of AWA.	170
4.39	Drive force coefficient fluctuations in a curling and a not curling cases.	172
4.40	Time series of force coefficients of a curling situation.	174
4.41	Drive vs side force coefficient evolution during one curling cycle.	175
4.42	Not filtered time series of force coefficients of a curling situation focused on two curling cycle.	176
4.43	Filtered time series of force coefficients of a curling situation focused on two curling cycle.	176
4.44	Curling sequence in the wind tunnel.	177
A.1	Yacht vocabulary.	187
B.1	Angular positioning of the ship and the different frames.	191
D.1	Comparison of load sensor calibration.	198
D.2	Load sensor dimensions and positioning.	200
E.1	Mast alignment.	203
E.2	Low friction ring geometry.	205
E.3	Geometry configuration of the dynamic trimming device in upwind configuration.	214
E.4	Error computation of dynamic sheet length model law.	219
E.5	Reorientation of the dynamic trimming configuration.	222
G.1	Weaven orientation and photographs of cloths.	229
H.1	Bending experiments.	233
J.1	Allures de navigations pour un voilier.	243
J.2	Représentation du vent apparent.	244

J.3	Illustration de profil de la soufflerie TFWT.	248
J.4	Balance de la soufflerie TFWT.	249
J.5	Profil de vitesse d'écoulement de la soufflerie.	249
J.6	Illustration des creux de grand-voiles testées en soufflerie.	250
J.7	Géométrie du réglage à deux paramètres par moteur pas à pas pour les essais statique de grand-voile.	251
J.8	Réglage de grand-voile vue par le cockpit.	252
J.9	Effet de la forme de dessin sur l'optimum à $\beta_{AW}=60^\circ$	253
J.10	Optimisation à 2 paramètres pour la grand-voile standard à $\beta_{AW}=60^\circ$	254
J.11	Système de réglage dynamique.	256
J.12	Coefficient d'effort de propulsion et de dérive moyen en réglage dynamique pour $\beta_{AW}=60^\circ$	257
J.13	Fonction objectif et coefficient d'effort dans l'écoute moyen sous réglage dynamique pour $\beta_{AW}=60^\circ$	258
J.14	Evolution des séries temporelles de coefficient pour la grand-voile standard pour $A = 20 \text{ mm}$ à $f_r = 0.127$	259
J.15	Evolution des séries temporelles de coefficient pour la grand-voile standard pour $A = 20 \text{ mm}$ à $AWA = 60^\circ$, pour les basses fréquences réduites.	260
J.16	Evolution des séries temporelles de coefficient pour la grand-voile standard pour $A = 20 \text{ mm}$ à $AWA = 60^\circ$, pour les hautes fréquences réduites.	261
J.17	Photographies des spinnakers.	265
J.18	Séquence de repliement de guindant de spinnaker en soufflerie.	266
J.19	C_{F_x} vs L_{sheet} à $\beta_{AW}=80^\circ$	268
J.20	C_{F_y} vs L_{sheet} à $\beta_{AW}=80^\circ$	269
J.21	$C_{F_{sheet}}$ vs L_{sheet} à $\beta_{AW}=80^\circ$	270
J.22	C_{F_x} vs L_{sheet} à $\beta_{AW}=100^\circ$	271
J.23	C_{F_y} vs L_{sheet} à $\beta_{AW}=100^\circ$	272
J.24	$C_{F_{sheet}}$ vs L_{sheet} à $\beta_{AW}=100^\circ$	273
J.25	Fréquence et fréquence réduite de curling pour différents AWA.	275
J.26	Fluctuations du coefficient de la force propulsive dans un cas avec et sans curling.	278
J.27	Séries temporelles filtrées sur un cas de curling sur deux cycles représentatifs.	278

List of Tables

3	State of the art method upwind.	13
4	State of the art method downwind.	14
5	Dimensionless number for FSI study of yacht sails.	16
2.1	Model configurations for windage measurements.	55
2.2	Summary of the sail tested on the model.	56
2.3	Windage correction table.	59
3.1	Description of model scale mainsails used during the upwind wind tunnel campaign.	68
3.2	Optimum results for the standard mainsail $\beta_{AW}=40^\circ$, reference case.	73
3.3	Optimum results for $\beta_{AW}=25^\circ$	81
3.4	Optimum results for $\beta_{AW}=40^\circ$	86
3.5	Optimum results for $\beta_{AW}=60^\circ$	93
3.6	Tested dynamic frequencies and the associated reduced frequencies.	100
4.1	Description of spinnakers models tested for the downwind wind tunnel campaign.	121
4.2	Horizontal stripes and curling apparition for free mast at $\beta_{AW}=80^\circ$	127
4.3	Horizontal stripes and curling apparition for free mast at $\beta_{AW}=110^\circ$	133
4.4	Curling apparition for free mast at $\beta_{AW}=140^\circ$	135
4.5	Curling apparition for partially-rigged mast at $\beta_{AW}=80^\circ$	139
4.6	Horizontal stripes and curling apparition for free mast at $\beta_{AW}=140^\circ$, partially-rigged.	141
4.7	Curling apparition for partially-rigged mast at $\beta_{AW}=80^\circ$ with twisted flow.	144
4.8	Flow velocity for the different fans frequencies for the 2016 experimental campaign.	151
4.9	Sheet length when curling appears for $\beta_{AW}=80^\circ$	153
4.10	Sheet length when curling appears for $\beta_{AW}=100^\circ$	156
4.11	Sheet length when curling appears for $\beta_{AW}=120^\circ$	159
4.12	Curling vs non curling case.	172

A.1	Sailing vocabulary.	188
B.1	Frames definition for full-scale, numerical experiments and wind tunnel testing.	190
C.1	Pressure factor correction table.	196
D.1	Calibration of Garos load sensor for 2015.	198
D.2	Calibration of Garos load sensor for 2016.	199
E.1	Model reference points coordinates.	202
E.2	Measured element coordinates in the model frame.	202
E.3	Dimension for the low ring friction used for the upwind wind tunnel experiments.	205
E.4	Element positioning on low friction ring in upwind configuration.	206
E.5	Mark measurement for κ_0 calculation.	216
F.1	Coordinate of points in the model frame for the 2015 experimental campaign.	227
F.2	Coordinate of points in the model frame for the 2016 experimental campaign.	227
G.1	Data for AirX 500 cloth.	230
G.2	Data for SuperKote 0.75 cloth.	230
G.3	Cauchy number C_Y for the cloth in wind tunnel conditions.	231
H.1	Value of EI modulus and structural values for the different rig elements used in the wind tunnel experiments.	234
J.1	Nombres adimensionnels d'interaction fluid-structure pour l'étude des voiles.	241
J.2	Informations sur les voiles testées.	249
J.3	Résultats d'optimisation pour $\beta_{AW} = 60^\circ$	253
J.4	Fréquences dynamiques testées et fréquences réduites associées.	255
J.5	Vitesse d'écoulement en fonction des fréquences ventilateurs pour la campagne 2016.	263
J.6	Description des spinnakers utilisés pendant la campagne expérimentale en soufflerie.	265
J.7	Cas avec et sans curling.	276

Acronyms

Term	Units	Description
AoA	°	Angle of Attack
AW		Apparent wind
AWA	°	Apparent Wind Angle
AWS	m s^{-1}	Apparent Wind Speed
CFD		Computational Fluid Dynamic
CPU		Central Processing Unit
D-VPP		Dynamic Velocity Prediction Program
DLC		Directional Load Cells
EMD		Empirical Mode Decomposition
FEM		Finite Element Method
FEPV		Force Evaluation via Pressures and VSPARS
fps		Frame per Second
FSI		Fluid-Structure Interaction
GPS		Global Positioning System
IMOCA		International Monohull Open Class Association
IMU		Inertial Measurement Unit
IRENav		Institut de recherche de l'Ecole Navale
LES		Large Eddy Simulation
MR		Measuring Range
PoV		Point of View
PS		Port Side or port tack
RANS		Reynolds-Averaged Navier-Stokes
SB		Starboard or starboard sidetack
TFWT		Twisted Flow Wind Tunnel
UoA		University of Auckland
VLM		Vortex Lattice Method
VPP		Velocity Prediction Program
VSPARS		Visualisation of Sail Position And Rig Shape
YRU		Yacht Research Unit

Notation

Term	Units	Description
A	mm	Amplitude of sheet length trimming oscillation
AoA	°	Angle of attack
c	m	Representative chord length
C_{F_i}	-	Force coefficient along axis i : $i = x$ drive force, $i = y$ side force. $C_{F_i} = \frac{F_i}{q_{Pitot}S}$
$C_{F_{obj}}$	-	Optimisation target function for upwind cases. $C_{F_{obj}} = C_{F_x} + 0.1C_{F_y}$
$C_{F_{sheet}}$	-	Sheet load coefficient $C_{F_{sheet}} = \frac{F_{sheet}}{q_{Pitot}S}$
c_q	-	Pressure factor
C_Y	-	Cauchy number $C_Y = \frac{\rho_f U^2}{E}$
D	-	Displacement number $D = \frac{\xi_0}{L}$
d_{AB}	-	Distance between the two points A and B
E	MPa	Young modulus
E_{acc}	% MR	accuracy error
E_{hys}	% MR	hysteresis error
E_{tru}	% MR	trueness or linearity error
f	Hz	Dimensional frequency of oscillating trimming
f_c	Hz	Curling natural frequency
f_{fans}	Hz	Wind tunnel fans frequency
F_i	N	Force along axis i : $i = x$ drive force, $i = y$ side force
f_r	-	Dimensionless reduced frequency of dynamic trimming $f_r = \frac{f_c}{U_{Pitot}}$
f_{rc}	-	Dimensionless natural curling reduced frequency $f_{rc} = \frac{f_c \sqrt{S}}{U_{Pitot}}$
F_{sheet}	N	Sheet load force
I_{uvw}	-	Turbulent level intensity
L	m	Representative length scale
L_{car}	mm	Position of car traveller along the model rail
l_{fr}	mm	Length of low friction ring inner radius
L_{ord}	mm	Ordered sheet length modification from the main stepper motor reference position
$L_{ord C}$	mm	L_{ord} where curling appear for downwind sail
$L_{ord H}$	mm	L_{ord} where visualisation stripes are estimated to be horizontal
l_P	m	Length of mainsail luff
L_{sheet}	mm	Sheet length
$L_{sheet 0}$	mm	Initial reference sheet length
$L_{sheet C}$	mm	Sheet length where curling appears for downwind sail
$L_{sheet H}$	mm	Sheet length where visualisation stripes are estimated to be horizontal

Term	Units	Description
L_{tot}	mm	Total length from winch point to sail sheeting point
P	W	Power
p	Pa	Pressure
q_{Pitot}	Pa	Dynamic pressure measured by the Pitot tube
Re	-	Reynolds number $Re = \frac{\rho_f UL}{\nu}$
S	m ²	area of a surface, usually sail area
sC_{F_i}	-	Variance of force coefficient or optimisation target function or sheet load coefficient
$stdC_{F_i}$	-	Standard deviation of force, optimisation target function or sheet load coefficients
th	mm	Thickness
T	s	Dynamic trimming period
T_c	s	Curling natural period
t_{c1}	-	Fraction duration of unfolded (full spinnaker shape) stage $t_{c1} = \frac{T_{c1}}{T_c}$
T_{c1}	s	Duration of unfolded (full spinnaker shape) stage
t_{c2}	-	Fraction duration of folded (luff spinnaker curled) stage $t_{c2} = \frac{T_{c2}}{T_c}$
T_{c2}	s	Duration of folded (luff spinnaker curled) stage
T_f	s	Representative time scale of fluid
T_s	s	Representative time scale of structure
U	m s ⁻¹	Representative flow velocity
U_R	-	Reduced velocity $U_R = \frac{T_s}{T_f}$
U_{ref}	m s ⁻¹	Reference wind velocity
$\overrightarrow{U_{Pitot}}$	m s ⁻¹	Wind velocity in the wind tunnel measured by the ceiling Pitot tube <i>i.e.</i> at its location
$\overrightarrow{V_{AW}}$	m s ⁻¹	Apparent wind velocity vector
$\overrightarrow{V_{BS}}$	m s ⁻¹	Boat speed velocity vector
$\overrightarrow{V_{TW}}$	m s ⁻¹	True wind velocity vector
W	J	Mechanical energy defined for a work of a force
β_{AW}	°	Apparent wind angle relative to the yacht centreline
β_{TW}	°	True wind angle relative to the yacht centreline
γ_i	-	Constant used in the dynamic sheet length command law demonstration
ϵ_{ri}	mm	Uncertainty number i evaluation on the sheet length
κ	°	Angular position of main sheet stepper motor compared to its initial position
κ_0	°	Initial angular position of main sheet stepper motor in model frame
κ_a	°	Angular position of eccentric P when it belongs to $[O_{rotating\ disk}C]$ in model frame
κ_T	°	Angular position of main sheet stepper motor in model frame
ν	m s ⁻²	Kinematic viscosity of the fluid
ρ_f	kg m ⁻³	Density of the fluid
ρ_s	kg m ⁻³	Density of the structure
ξ_0	m	Order of magnitude of displacement of the structure

Other complementary notations are defined in appendixes while been used.

Introduction

The work achieved during this thesis takes part in the VOILENav project described first in this introduction. It includes many fruitful collaborations with academic and industrial partners. The different methods used in the yacht research field are then introduced followed by the presentation of the different aspects that a study can take, focusing on results from a static to a dynamic analysis. The properties of the Fluid-Structure Interaction (FSI) phenomena applying to sails are provided, highlighting the challenging aspects of this specific research topic. The thesis objectives section ends this introduction.

Context

This thesis is part of the VOILENav project carried out in the Mechanics and Energy in Naval Environment Group at the Institut de recherche de l'Ecole Navale (IRENav). It has been developed along different works in the past 10 years which improved the understanding of FSI phenomena occurring on sails with innovative results. The development of an instrumentation system onboard the 8-meter J80 one design keel boat by [Augier, 2012] was the first milestone that brought to the project the first steady and unsteady full-scale experimental results in upwind situations. Parallel works carried out by [Durand, 2012] -as a collaboration between the k-Epsilon company, Ecole Centrale de Nantes and IRENav- have developed numerical tools that are able to model unsteady FSI situations. This work has first developed the Finite Element Method (FEM) code ARA, the Vortex Lattice Method (VLM) code AVANTI, dedicated to attached flow, which is relevant for upwind sailing situations, and the coupling FSI scheme. Comparison between unsteady upwind full-scale test [Augier et al., 2013] and upwind wind tunnel situation with rigid sails [Durand, 2012] have shown good agreement in the results. Comparison on an oscillating soft cloth was performed with the second FSI coupling between ARA and ISIS-CFD developed by the Ecole Centrale de Nantes (Reynolds-Averaged Navier-Stokes (RANS) code commercialised as FINETM/Marine) relevant for detached flow conditions. Downwind experimental data were nevertheless required to also validate this coupling on representative downwind situations.

The VOILENav project has been successfully extended by [Deparday, 2016] to the downwind situations where the recording of the flying shape -*i.e.* the actual shape of the sail while sailing- is more challenging than in the upwind sailing case. The instrumented system has been adapted for downwind navigation. Photogrammetry techniques [Deparday, 2010] combined with pressure measurement and the use of Directional Load Cells (DLC) [Le Pelley et al., 2015] provided by

a collaboration work with [Motta et al., 2014, Motta, 2015] enabled to improve the analysis of downwind sail behaviour. The photogrammetry technique is more adapted for fuller shoulder shapes like the J80 spinnaker compared to flying shape reconstructed with stripes interpolation as used in FEPV (Force Evaluation via Pressures and VSPARS) techniques. The natural flapping or curling phenomenon has been experimentally investigated. Innovative results show the effect of curling on the instantaneous pressure distribution providing a first explanation on the efficiency of the so called “on the verge of curling” trim used while racing. A curling model is then suggested justifying such a pressure variation. Numerical simulation on curling spinnaker were performed by [Durand et al., 2014] and was used to predict stability of the spinnaker during the design process. However, so far no successful numerical-experimental comparison in downwind situation has been achieved in this project yet. The true wind information required as an input of the simulation is difficult to measure at sea, especially with an information provided by an onboard sensor in unsteady conditions. Major improvements have been brought by the PhD candidate Hugo Kerhascoët working with the NKE company and IRENav on the wind information measurement. His work provides a better design of the wind measuring tool [Kerhascoët et al., 2016a] and also a new method to detect error of boat speed information [Kerhascoët et al., 2016b]. Despite these recent progress, study of aeroelastic of a sail at full-scale remains complex. The use of a wind tunnel facility to record unsteady FSI sailing situations with more controlled conditions was therefore one logical further step.

Wind tunnel testing has been possible thanks to the Sailing Fluids collaboration. This EU - New Zealand research collaboration develops synergies and makes cutting edge breakthroughs in yacht engineering. It gathers three major academic research centres on the yacht research field: the IRENav at Ecole Navale, France, the University of Newcastle and the University of Edinburgh, United Kingdom, and the University of Auckland (UoA), New Zealand. The work presented in this thesis took part in two of the program topics: the aerodynamic of sails, and the fluid-structure interaction on sails. The well-known Twisted Flow Wind Tunnel (TFWT) of the Yacht Research Unit (YRU) of the UoA is probably one of the most famous wind tunnel facilities dedicated to yacht engineering. Two 3-month secondments (in 2015 and in 2016) carried out by the author have provided most of the experimental data presented in this thesis. The author has been in charge of the design of the experiments (apart from the model sails tested and rig elements) including the coordination or achievement of the logistic and manufacturing. He carried out the two experimental campaigns and the post processing and analysis of the collected data. During wind tunnel experimental campaigns, wind flow and trimming conditions can be controlled and measured more accurately compared to full-scale situations. The unsteadiness of the wind tunnel situation can either be natural, such as the curling of a spinnaker with a constant static trim length, or either generated by an active dynamic trimming system in the case of the mainsail pumping. The wind tunnel tests are first a complementary method for the investigation of FSI phenomenon applied to yacht sails and their understanding. The wind speed is controlled and models quasi-steady situations compared to full-scale conditions. The test of model sails manufactured by industrial partners and designed with dedicated FSI tools is also a second perspective, probably more adapted for hopefully successful future numerical-experimental comparison in the project.

This project has also benefited from many collaborations with other academic institutions and major industrial partners in the sail engineering environment. For example, the Visualisation

of Sail Position And Rig Shape (VSPARS) system [Le Pelley and Modral, 2008] was provided by the VSPARS company. This system gives key information on the upwind full-scale flying-shape measurement. For the full-scale tests, NKE wind sensors or Inertial Measurement Unit (IMU) sensors and network equipment have also been used on-board the J80. Incidence Sails nowadays uses the SailPack-Aravanti tool to design and manufacture their sails. This tool is the combination of the two softwares, Sail Pack provided by BSG Developements, and the FSI code ARAVANTI provided by the k-Epsilon company. Nowadays the FSI ability is used by the sail designers in the design loop to predict the sail behaviour in upwind situations. Some phenomena such as wrinkles or batten deformations have been both observed while sailing and predicted by the tool. The fast computation is also a key asset in the design process and sail designers now rely on this tool, however, some limitations may still exist due to the model itself. This thesis intends to provide some indicators to detect the model limit in the design stage. The k-Epsilon and Ecole Centrale de Nantes collaboration provided both ARAVANTI and ARA-ISIS codes. Some numerical results have been compared with upwind wind tunnel experimental cases. For instance the numerical tools results were compared to the wind tunnel ones in a trimming optimisation problem by [Sacher et al., 2016]. The optimisation methods and code developed at IRENav by the PhD candidate Matthieu Sacher were used experimentally for the first time during the 2015 wind tunnel testing campaign. This optimisation code is still under developments for various applications in the yachting industry (sail and foil optimisations).

Along all this studies, the VOILENav project has been constantly highlighting the necessity of using unsteady analysis to correctly model sailing FSI phenomenon. The different definitions related to the time evolution of physics phenomena are presented next, completed with a more general review about methods and results in the FSI research field with their application to sailing yachts.

The calm before the storm

Phenomena in physics can be characterized by their evolution over time. FSI phenomena occurring between the air and the sail and rig in yacht engineering can present many kinds of evolution type. Here are presented some characteristics over time that can qualify those FSI phenomena. These definitions follow the chronology of the scientific approach along the yacht research history, starting from a steady static stationary state and reaching the unsteady dynamic non-stationary state, going from easier to more challenging situations to handle, such as sailors experiencing the calm before the storm.

Steady vs unsteady

A steady phenomenon applied to a system (fluid and/or solid) is a phenomenon where all properties on any point location in the system do not change over time. On the contrary an unsteady phenomenon is a phenomenon where at least one physical property changes over time in an arbitrary location of the system. The unsteadiness can be either associated to a transient phenomenon or an oscillatory pattern. Steadiness of a phenomenon implies that the local time derivatives are zero in the entire domain. Turbulent flow are by definition unsteady but can be stationary from statistical

consideration as explained later like for instance the vortex wake around cylinder. Some flows, can be steady in a certain frame of reference and are called pseudosteady.

A quasi-steady state can also be used to characterize a system when the temporal variations at a spatial location are much smaller compared to spatial variations for any quantity. The time scale of evolution is long. This is usually the case for attached air flow on upwind sails.

Static vs dynamic

The static or dynamic qualification can be applied to two things: the type of approach and the kind of conditions.

The approach

Static approaches study the system at rest. Quasi-static approaches decompose the system evolution by time discretisation. Each time step focuses on an evolution that happens slowly enough to be able to be considered as a static situation. This approach is not affected by the time direction. It would give identical results with reversed time evolution. On the contrary the dynamic approach resolves the entire dynamic aspect contained in the equations describing the system. It takes into account the past evolution of the system. Quasi-static and dynamic methods should give close results if the evolution of the system is slow enough. However, for yacht engineering, typical evolution is fast enough to make the quasi-static approach no longer accurate. Dynamic analysis applied on dynamic situations show usual results which deviate from a quasi-static approach.

The conditions

Static and dynamic qualification can also refer to the conditions applied to the system. For example, the wind and sea state unsteadiness generating pitching motion corresponds to dynamic environmental conditions. When the dynamic aspect is generated by the environment, literature works may also use the term steady, quasi-steady or unsteady conditions. For this thesis work, the words steady, quasi steady and unsteady are used only to describe the physical properties of the system as defined in the previous section. A run where the crew changes the sheet length also corresponds to a dynamic condition but this time it is created by a specific action. For this thesis, static or dynamic are linked to the change of conditions. Dynamic conditions necessarily lead to unsteady situation. In the FSI field some static conditions can lead to unsteady behaviour (airfoil fluttering, bluff body galloping). One of the unsteady phenomena studied in this thesis known as curling also corresponds to a static situation with a constant sheet length.

In both cases where they apply -either the method or the conditions- the change from a static to a dynamic approach generally both increases the study complexity, but improves the analysis accuracy. For instance the dynamic approach certainly gives more refined prediction, but might require larger computation times than a first quasi-static approach.

Stationary vs non-stationary

The stationary aspect is often used to qualify a process. The word process can also refer to two notions. It can refer to the phenomenon acting on a system generating the variables or signals associated with the phenomenon. It can also refer to the properties of the signals themselves.

Stationarity is associated with the statistical properties of a process. [Challis and Kitney, 1990] define a stationary process as a process in which all statistics (such as mean or standard deviation values) are invariant under a shift in time. In other words, the statistical parameters of the process do not change with time. A stationary process implies another prerequisite: the autocorrelation function of the process must depend only on the lag and must not change with the time at which the function is calculated.

A weak stationary condition is considered if the mean value, the autocorrelation function and therefore the variance (and covariance) of the process are constant. In fluid mechanics, turbulence clearly implies unsteadiness but nevertheless it can also be considered as stationary. Stationary fluid properties can show fluctuations but do not show any trend in time.

Using all these definitions we can make several comments about sailing situations:

1. static conditions can cause an unsteady response (spinnaker curling)
2. dynamic conditions can be generated by natural unsteadiness of the environment or crew dynamic actions
3. dynamic conditions generate unsteady responses and require a dynamic approach. Typical dynamic sailing conditions make the quasi-static approach no longer relevant.

Sailing yachts: the ultimate unsteady machine

This section describes the usual unsteady phenomena that can be observed while sailing and is organized as follows: a first part shows that these phenomena can either occur naturally or be initiated by crew actions. Then the particular case of mainsail pumping is examined. The debate about downwind sail curling is presented last.

The different source of unsteadiness: from nature to crew actions

Rigs and sails can be submitted to unsteady effects due to environmental reasons or dynamic actions of the crew. The true wind speed and direction can change and the sea state with waves and swell can affect the yacht motion. For instance [Fossati, 2009, Fossati and Muggiasca, 2011, Fossati and Muggiasca, 2012a] investigated with wind tunnel experiments the pitching effect due to waves. Failure of the structure can also generate an unsteady and in general transient response of the rig which can result in dismasting through a dramatic cascade effect. For instance [Menotti et al., 2013] numerically investigated the Volvo 70 Groupama 4 dismasting during the

2011-2012 edition of the Volvo Ocean Race.

Dynamic sailing techniques are already well known by sailors. However different crew actions are forbidden by [International sailing Federation, 2013] while racing and are defined in the article 42.2 :

- (a) pumping defined as *“repeated fanning of any sail either by pulling in and releasing the sail or by vertical or athwartship body movement”*.
- (b) rocking defined by *“repeated rolling of the boat induced by (1) body movement, (2) repeated adjustments of the sails or centreboard, or (3) steering”*
- (c) ooching by a *“sudden forward body movement, stopped abruptly”*
- (d) sculling by a *“a repeated movement of the helm that is either forceful or that propels the boat forward or prevent here from moving astern”*
- (e) *“repeated tacks or gybes unrelated to changes in the wind or to tactical considerations”*.

These official definitions give an exhaustive list of possible dynamic crew actions. Those actions can be used once or can be repeated to improve the yacht performance. Several effects can be taken into account in these techniques. For instance in a rolling motion, both aerodynamic and hydrodynamic parts play a role in the performance evolution. The change in the heel angle may generate propulsion through the appendages which can generate hydrodynamic vortex patterns. [Schutt and Williamson, 2016] presents flicking techniques and measured the performance of a laser dinghy. During those full-scale test, aerodynamic and hydrodynamic parts are acting. In this thesis we are interested in the aerodynamic part only like [Schutt and Williamson, 2016] who use a 3D printed rigid and flexible profile moving in a water tank to focus on the modelled sail wake evolution.

The periodicity of the dynamic condition or unsteady phenomena is also a key characteristic. Does it happen once, like in roll-tacking when sailor voluntary exaggerates the rolling motion of the boat while tacking? Is it repeated with a given frequency like the pitching motion of the boat linked to the apparent wave frequency?

Effects of tacking ([Gerhardt, 2010]) and gybing ([Banks et al., 2010]) have also been studied because those two main manoeuvres are extensively used while racing. A lack of published data about dynamic sailing configuration due to other crew actions defined in the article 42.2 of [International sailing Federation, 2013] can be observed in the sailing literature. This lack of information could be justified by the fact that most of these techniques are still forbidden generally.

Pumping being authorized under certain conditions, it has been studied as a first typical dynamic and forced unsteady phenomena while sailing and is presented in the chapter 3. Curling or spinnaker flapping was then studied as another typical unsteady phenomenon occurring naturally either under static or dynamic conditions and is presented in chapter 4.

Pumping: unsteadiness generated by crew action

The dynamic technique called pumping may look like as a first approach as a pitching motion applied on lifting bodies previously studied in aeronautics [Katzmayr, 1922, Kramer, 1932] or in biology fields. The repeated fanning either by pulling in and releasing the sail can be seen first as a repeated change of the AoA (Angle of Attack) on the sail. However, this sailing action results in quite unique and complex FSI phenomena acting on a system composed of a rig and a sail. [Marchaj, 1964, Marchaj, 1996] has already provided a first explanation of the pumping effect in the sailing case, by comparing this situation to a rigid body airfoil submitted to the Kramer effect [Kramer, 1932]. He explained that “*the phenomenon is not confined to the reaching case considered, but can be exploited at most points of sailing other than close hauled on a run*”. He also explained that these kinds of techniques were prohibited because they are considered as not being the “*natural action of the wind on the sails*” according to former sailing federation authorities. Similarity may exist but the sail motion under crew action cannot be compared directly to rigid body reaction, or to a bird flight [Dhawan, 1991, Viieru et al., 2006, Hubel et al., 2009, Spedding and Hedenström, 2010, Lua et al., 2016], insect wing flapping [Rival et al., 2010, Nakata and Liu, 2012] or fish swimming [Combes and Daniel, 2001, Schouveiler et al., 2005, Egan et al., 2016]. Most of animal wing flappings are initiated from the leading edge of the wing, contrary to sail pumping where the motion comes from the clew part attached to the boom. Effect of pumping will be investigated in this PhD project. Parallel work carried out by [Brummer, 2016] presents numerical simulation results of pumping on a *Finn*, a 4.5 m Olympic dinghy. His research project presents the computation of the effort provided by the athlete while pumping, the results from rocking only, pumping only and the combination of the two actions which leads to a significant increase of 70% in the drive force. The pumping techniques is also widely used by windsurfers.

Curling: natural unsteadiness

Another unsteady FSI phenomenon occurring on downwind sails is the alternative oscillation of the luff (leading edge) of downwind sails known as curling. This phenomenon can also be called flapping in past studies [Deparday, 2016], insisting on the alternative motion of the luff, however this term can also be associated to pitching and heaving motion of wing in fluid mechanics which is close to the pumping action introduced above. Therefore the word curling is chosen in this thesis to describe this phenomenon. Curling can be observed for a fixed sheet length associated to static conditions. Sailors often acknowledge the fact that the best trim for downwind sails to set is on the “verge of curling”. Discussions with many trimmers rapidly provided a large set of different recommendations and explanations about the “verge of curling” limit. However, this definition might contain different meanings which can be classified within three major types of recommendation:

1. a first group of the sailing community admits that permanent trimming adjustment at full-scale (*i.e.* the dynamic trim adjustment) is only used to keep the sail on the verge of the curling limit due to the changing apparent wind. The curling condition is in this case an indication of a good trimming location. In this recommendation the optimum is considered to be located just before curling and once the spinnaker is curling, the sail must be trimmed in slightly.
2. a second group estimates that curling must be maintained, and therefore the sail sheet length

must be adjusted to seek and maintain the natural curling of the sail.

3. a last group explains that the dynamic trimming adjustment by itself is the major part of the improvement of the performance rather than keeping the sheet length fixed. In other words, the sail get extra drive force by periodically pulling on the sheet, *i.e.* pumping.

In this PhD project, static optimum search phase therefore addresses the question about the best trim to reach under static conditions to discuss the two first group recommendations. Highly innovative results has been provided to the sailing yacht research community thanks the experimental campaign carried out during this thesis. If better performance has been measured at some point on the verge of curling limit, the sailing community once again disagrees about the origin of this improvement. The possible origin of the improvement admitted so far are linked to the three previous trim recommendations:

1. the first group generally estimates that the best flying shape providing better performance is located just before curling.
2. the second group recommends maintaining the unsteady aspect of curling can also provide different explanations of this improvements:
 - some of them will estimate that the curling phenomenon once again corresponds to a better flying shape using two different reasons. The aero force is more oriented forward because the sheeting angle is maximum and the projected area of the sail in the crossflow direction is increased.
 - others may explain that the dynamic behaviour when curling benefits on the aerodynamic part as suggested by previous recent full-scale studies [Motta, 2015, Deparday, 2016]. The local and temporary high suction peaks associated to curling when the spinnaker recover its full flying shape increase the average generated drive force.
3. the last group considers that the dynamic trimming adjustment play a role like in the upwind pumping cases where the modification of the flow pattern may occur increasing the thrust.

From these provided explanations, the kind of origin presented here can be classified as either a better average flying shape explanation or either the dynamic aspect one. Measured data in this PhD project will provide indications on the probable origin of the improvement of performance associated to curling in order to enhance its understanding at model scale first. Comparison with past full-scale downwind studies will hopefully suggest a general model of curling that can be validated at any scale.

Different methods with different approaches can be used to discuss the issues related to the two FSI phenomena presented in this section (mainsail pumping and spinnaker curling). The next section presents the classical different methods used for yacht research field.

The methods and tools for sailing yacht study

The hydrodynamic study of yacht physics is not presented in this thesis which focuses only on the aerodynamic part. Three different methods can be used to study the sail aerodynamics or aero-elastic behaviour, each of them with advantages and drawbacks. Tab. 3 and Tab. 4 sum up different yacht sail studies. Specific aspects of static and dynamic approaches are presented for each methods.

Full-scale testing

This method has been first performed by the sailors themselves using qualitative observations or quantitative measurements. Instrumentation systems providing onboard real time data are nowadays possible thanks to the improvement of the robustness and miniaturization of computers and electronic sensors. This progress has given access to more sophisticated data, measuring time series with higher frequencies adapted to dynamic studies. Many projects have developed full-scale instrumented sailing yachts, from dinghies [Williamson and Schutt, 2016], sportboats in the VOILENav project [Augier, 2012], to cruiser size. Some instrumentations are limited and focuses onto some kinds of data such as the flying shape of the sail, the pressure on sails [Graves et al., 2008, Viola et al., 2010, Viola and Flay, 2010a], or the rig loads. To measure the total aerodynamic forces generated by the sails, a balance frame is nevertheless required inside the yacht hull as presented in [Hochkirch and Brandt, 1999, Masuyama, 2014, Fossati et al., 2015a]. This special manufacturing of the boat is quite expensive and can only be applied to an experimental dedicated boat. Full-scale instrumentation is used intensively by the competition world where the sailing syndicates develop dedicated systems for their racing boats. However this data is rarely available due to confidentiality. Some projects carried out by the Sailing Yacht Research Foundation (SYRF) tend to provide telemetry data recorded during races [AC34th, 2017] but this is more dedicated to Velocity Prediction Program (VPP) studies and not dedicated to physics of sails study.

Full-scale static approach is difficult to justify. The unsteadiness of the environment tends to oppose the scientist's secret wish to record a run under perfect static conditions. A large first part of the full-scale post processing is the location of periods within runs that can be considered as static enough. In fact during these periods the parameters changes may exist but are lower than a fixed limit given by the observer, like in [Deparday, 2016]. The evolution within these limitations are considered to be small enough compared to the global evolution of the system. On the J80 situations, one can typically only hope to get 10s to 20s of considered static conditions with large criteria on wind (10% on the apparent wind speed and 4° on the apparent wind direction as defined in [Deparday, 2016]) about the measured evolution over a recording period of several minutes.

Moreover full-scale testing still suffers from important logistic considerations and are subject to weather conditions. The unsteadiness of the sailing conditions can also make it more difficult to interpret some results and the true wind or leeway measurements remain challenging ([Dougnet, 2014]).

Wind tunnel testing

Wind tunnel testing can provide a quasi-steady environment with flow controlled conditions to test model sails. A model yacht or sail is set up onto a balance which is nowadays equipped with electronic instrumentation contrary to past mechanical ones. The first information available is therefore lift, drag, drive and side forces. Measurement of dynamic pressure then enables one to compute the associated aerodynamic coefficients [Flay and Jackson, 1992, Flay, 1996, Hansen, 2006]. However the natural boat velocity is not achieved in the wind tunnel, therefore to accurately reproduce the apparent wind applied to the full-scale sail, the flow must be twisted especially for downwind conditions. The TFWT developed by [Flay and Vuletich, 1995, Flay, 1996] was the first one to ever perform the twisting profile thanks the use of twisting vanes. This facility was mainly dedicated to the America's Cup downwind sail development. However the use of twisted flow is more time consuming as it requires to obtain a particular twist angle profile for a given sailing condition (boat speed and wind speed and angle). Numerical simulation of the twist is also more difficult to perform therefore twisted flow results are only presented for one case of the experimental campaign shown in this thesis. Other sensors such as pressure measurement on semi-rigid core flute sails [McQuoid, 2010, Viola and Flay, 2011c, Bot et al., 2013] or soft sails [Viola and Flay, 2015], load sensors, flow visualisation [Serres, 2004], rigid and semi rigid sails [Richards et al., 2006], flying-shape recording devices [Graf and Müller, 2009, Fossati et al., 2015b] or actuator such as electronic motors [Fossati and Muggiasca, 2011, Aubin et al., 2016b] provide results in a static or dynamic controlled testing condition.

Real time VPP is used to directly measure the aerodynamic forces with a realistic heel angle while testing in the wind tunnel [Le Pelley and Hansen, 2003, Hansen et al., 2003, Hansen et al., 2005]. This method determines the angle where the heeling moment is balanced by the yacht righting moment. Some tests can be carried out in a water tunnel to represent the sail behaviour such as [Schutt and Williamson, 2016]. Wind tunnel techniques nevertheless suffer from some limitations. They can be affected by the blockage effect [Mompó Laborda, 2009] and cannot match all dimensionless parameters such as the Reynolds number or structural parameters of sails as described in the next section presenting the sailing FSI aspects.

Wind tunnel testing used to be mainly focused on the static approach. Each run is recorded when all input variables are set up to a constant value. Nowadays improvements in recording hardware and miniaturisation of model controls enable a large possibility of dynamic testing in wind tunnel. Pitching motion are imposed in [Fossati and Muggiasca, 2011, Fossati and Muggiasca, 2012a] and some manoeuvres such as gybing are presented in [Banks et al., 2010]. Wind tunnel testing is chosen in this PhD project to study pumping and curling. Contrary to full-scale, the controlled flow and sheeting conditions are likely to achieve more easily successful numerical experimental comparison for downwind sails.

Numerical simulation

The evolution from simple 2D models on rigid bodies using potential flow theory [Gentry, 1971] to 3D FSI strongly coupled code modelling the sail cloth deformations and displacements [Durand et al., 2014] has been possible with the large improvements of computing methods and resources. The different models developed in fluid mechanics are adapted to the kind of flow being

studied. For instance with attached flow in upwind situation, the potential theory can be applied coupled with an ideally flexible sail structural model [Le Maître et al., 1996, Le Maître, 1998, Le Maître et al., 1998, Le Maître et al., 1999]. This model is faster than models taking into account separation and turbulent aspects of the flow such as RANS or Detached Eddy Simulation [Viola et al., 2014]. Simulations can be performed with rigid bodies, or with FSI computations [Mounoury et al., 2005b, Mounoury et al., 2005a].

When the FSI ability of a numerical tool is developed, computations can also be carried out using different types of coupling as shown in Fig. 1. As described in [Sigrist, 2011, Sigrist, 2015], the use of a direct fluid-structure code (monolithic solver) is possible only if a mathematical model of the coupled problem is established in a suitable form for numerical discretisation.

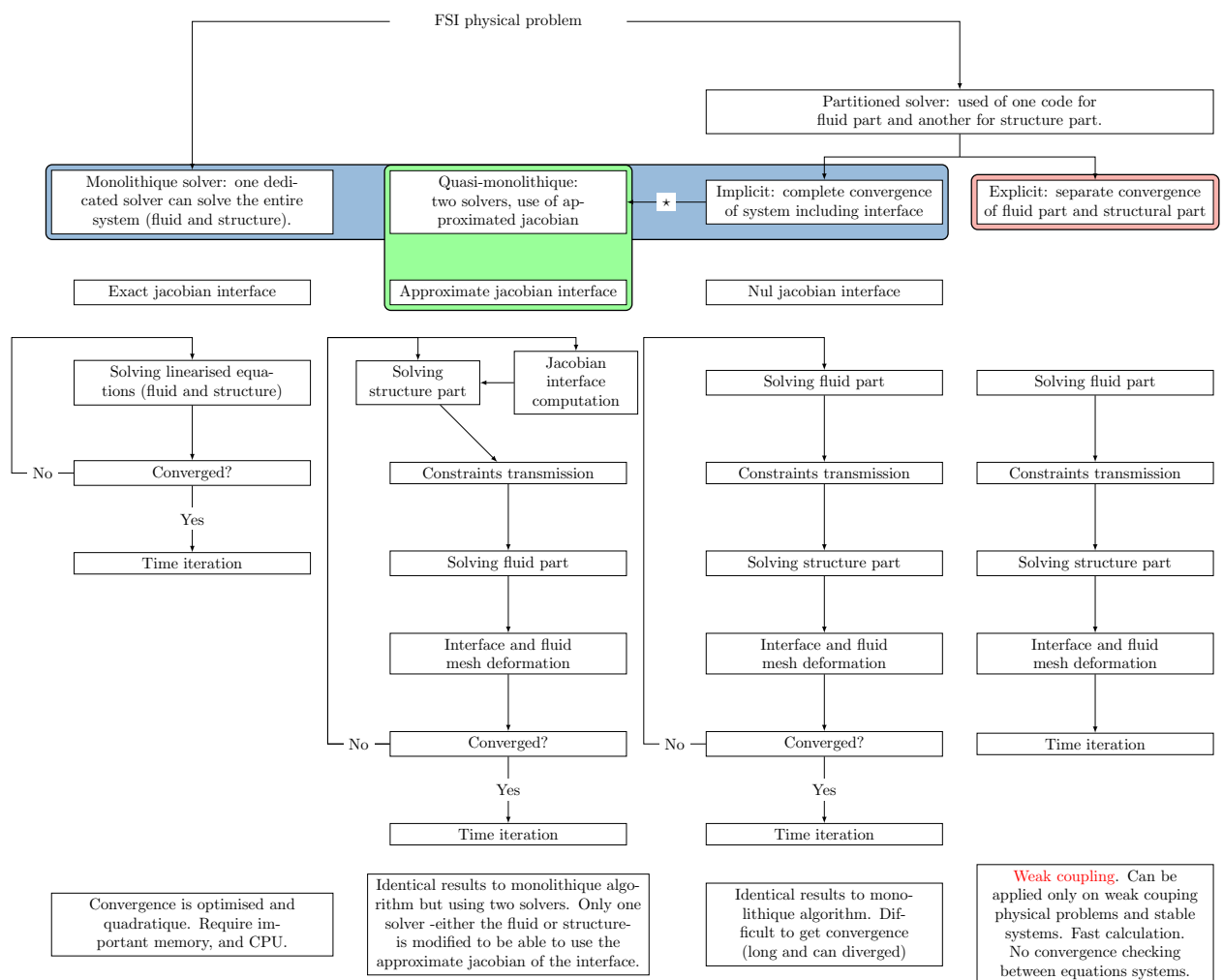


Figure 1 – Type of coupling in numerical methods applied to FSI problems as described in [Durand, 2012] who has been developing (*) a quasi monolithic coupling method with approximate jacobian of the interface of the structure.

The coupling of a fluid and a structure code (partitioned solver) has largely been developed for different applications with the Arbitrary Lagrangian Eulerian (ALE) formulation like in [Michalski et al., 2015]. The scheme in the partitioned solver can be implicit where the system is

designed for a complete convergence of the system and interface, however the convergence can be harder to obtain due to coupling instabilities. The scheme can also be explicit where the convergence of the fluid and structural parts are separated. This scheme is faster but can only be applied to weakly coupled problems. [Durand, 2012] developed a quasi-monolithic coupling with the use of an approximation of the interface jacobian compared to monolithic coupling which has an exact interface jacobian and usual implicit scheme in a partitioned solver which has a zero interface jacobian. Eventually the dynamic approach can be considered in the coupling scheme for representative sailing situations. If the evolution of the phenomenon is slow enough, a quasi-static approach could also provide relevant information as a first approach. A dynamic method can be applied to a static case and should give close results to the static method applied on the same case. However, especially if the FSI part is modelled with structural deformation of the sail in downwind situations, the computation cost becomes rapidly significant with the mesh deformation or the re-meshing step of the fluid domain. Computations carried out for innovative industrial or racing projects are rarely immediately published or available, however the Sailing Yacht Research Foundation (SYRF) also provides aerodynamic studies achieved by acknowledged industrials: [Braun, 2016]. Other sail makers also present and advertise some simulation capabilities [WB-sails, 2017, NorthSails, 2017, Incidence sails, 2017, Ranzenbach and Armitage, 2013]. Some FSI characteristics are presented for the sailing case in the next section.

Upwind

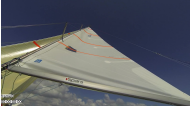

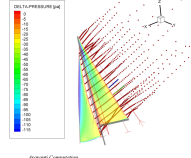
Method	Static approach	Dynamic approach
Full-scale  (1)	<ul style="list-style-type: none"> • [Van Hemmen, 1986], rig load measurement on a 12-meter yacht • [Herman, 1989], MIT dynamometer sailboat • [Hochkirch and Brandt, 1999] dynamometer sailboat <i>Dyna</i> • [Flay and Millar, 2006], pressure system • [Puddu et al., 2006], full-scale catamaran • [Masuyama, 2014], sailboat dynamometer <i>Fujin</i> * [Aubin et al., 2016a], traveller, car position and backstay adjustment effect on flying shape 	<ul style="list-style-type: none"> • [Masuyama and Fukasawa, 2011], tacking measurement • [Augier et al., 2012], rig loads and flying shape on J80 • [Brummer, 2012], Finn mast dynamics • [Lozej et al., 2012], pressure distribution spectra • [Bergsma et al., 2012], pressure and flying shape • [Schutt and Williamson, 2016], body weight motion on laser
Wind tunnel (or water tunnel)  (2)	<ul style="list-style-type: none"> • [Marchaj, 1991], wind tunnel testing • [Campbell and Claughton, 1994], wind tunnel testing • [Flay, 1996], development of TFWT • [Fossati et al., 2006], wind tunnel techniques • [Fluck et al., 2010, Viola and Flay, 2011a], rigid fiber glass sail providing pressure distribution 	<ul style="list-style-type: none"> • [Gerhardt et al., 2009, Gerhardt, 2010, Gerhardt et al., 2011] tacking, pitching, measurement • [Fossati and Muggiasca, 2011], harmonic pitching * [Aubin et al., 2016b], pumping: dynamic trimming on mainsail • [Schutt and Williamson, 2016], oscillating 3D printed rigid and soft sail profile
Numerical  (3)	<ul style="list-style-type: none"> • [Gentry, 1971] sail interaction using analogy between potential flow and electric potential • [Milgram and Frimm, 1993], sail forces ACC • [Clauss and Heisen, 2005], RANS numerical-experimental comparison • [Braun and Imas, 2008], RANS upwind • [Chapin et al., 2011], FSI • [Viola et al., 2013], comparison with wind tunnel pressure • [Ranzenbach and Armitage, 2013], FSI on TP52 * [Aubin et al., 2016a], numerical-experimental comparison and criteria to detect inviscid flow hypothesis limit • [Nava et al., 2016], RANS-Large Eddy Simulation (LES) 	<ul style="list-style-type: none"> • [Masuyama and Fukasawa, 2011], tacking measurement • [Schoop and Bessert, 2001], VLM with instantaneous flow • [Fossati and Muggiasca, 2010] pitching • [Augier et al., 2013], numerical-experimental FSI comparison • [Augier et al., 2014], FSI pitching

Table 3 – Non exhaustive state of the art for **upwind** sails based on [Deparday, 2016]. * **symbols indicate articles or conference papers using results obtained during this PhD project.** (1) flying shape footage of upwind J80 mainsail, (2) mainsail tested in the TFWT of the UoA, (3) ARAVANTI (a k-Epsilon FSI tool) computation providing the pressure distribution on the J80 numerical model sailing upwind.

Downwind



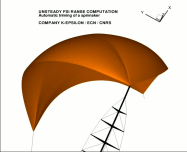
Method	Static approach	Dynamic approach
Full-scale  (4)	<ul style="list-style-type: none"> • [Viola and Flay, 2010b], pressures • [Mausolf et al., 2011], photogrammetry flying shape • [Motta et al., 2014], FEPV pressure + flying shape • [Campbell, 2014b], comparison wind tunnel/full-scale • [Deparday et al., 2016a], photogrammetry flying shape on J80 	<ul style="list-style-type: none"> • [Deparday et al., 2014], curling analysis • [Motta et al., 2015, Motta, 2015], pressure fluctuation pattern • [Deparday et al., 2016b, Deparday, 2016], modal analysis on pressure fluctuation
Wind tunnel (or water tunnel)  (5)	<ul style="list-style-type: none"> • [Ranzenbach and Kleene, 2002], flying shapes • [Hansen et al., 2002, Hansen, 2006], wind tunnel and full-scale comparison of sail force • [Richards et al., 2006], semi rigid sails • [Graf and Müller, 2009], photogrammetry techniques for flying shape measurement • [Viola and Flay, 2009], force and pressure soft sails • [Renzsch and Graf, 2013], force and flying shape, numerical experimental comparison • [Campbell, 2014a] comparison of results from different wind tunnels 	<ul style="list-style-type: none"> • [Banks et al., 2010], gybing in wind tunnel • [Bot et al., 2014], time series pressure on semi-rigid sail * To curl or not to curl: wind tunnel investigations of spinnaker performance, submitted for INNOV'SAIL 2017 (28th, 29th, 30th of June 2017, Lorient, France).
Numerical  (6)	<ul style="list-style-type: none"> • [Hedges et al., 1996], Computational Fluid Dynamic (CFD) on downwind sail • [Lasher and Sonnenmeier, 2008], RANS on downwind sail • [Renzsch and Graf, 2010], FSI with RANS on downwind sail • [Viola, 2009], high grid resolution • [Viola and Flay, 2011b], pressure comparison for full-scale, wind tunnel and numerical • [Trimarchi et al., 2009, Trimarchi, 2012, Trimarchi et al., 2013], FSI with shell • [Viola et al., 2014], Dettached Eddy Simulation 	<ul style="list-style-type: none"> • [Lombardi et al., 2012], dynamic FSI • [Durand et al., 2013, Durand et al., 2014], automatic dynamic trimming FSI

Table 4 – Non exhaustive state of the art for **downwind** sails based on [Deparday, 2016]. * **symbols indicate articles or conference papers using results obtained during this PhD project.** (4) full scale downwind test on J80, (5) model J80 spinnaker tested in the TFWT of the UoA, (6) ARA-ISIS-CFD (a k-Epsilon FSI tool) computation from [Durand, 2012].

Fluid-structure interaction on yacht sails

General FSI literature such as [de Langre, 2009] can be used to classify the kind of problem modelling the air interaction with sails and rig. [Deparday, 2016] already applied this kind of analysis to yacht sails as presented in Tab. 5 and this section provides the general conclusions of this characterisation:

- the dimensionless reduced velocity defined as the ratio of the structure time evolution over the fluid time evolution is the same order of magnitude as the displacement number. Therefore strong assumption such as quasi-static aeroelasticity (problem depends mostly on the structure position) or pseudo-static aero-elasticity (problem depends mostly on structure position and velocity) cannot be used.
- the Cauchy number, defining the ratio of the inertia forces over the structural stiffness, is quite small, which indicates the order of magnitude of structure deformation due to fluid loading. Here the structure deformation is small, however the sail displacement can be important.
- the Reynolds number R_e indicates if the flow is laminar or turbulent.
- [Durand, 2012] illustrates how important the added mass effect from the fluid is.

These different elements make the air and sail interaction a strongly coupled FSI phenomenon. Moreover the flying shape of a sail corresponds to the different shapes that the sail will present once used on the boat. It is strongly dependent on the sailing conditions and different trimming adjustments. The sail designer draws a design shape that is supposed to reach the best flying shape providing highest aerodynamic performance for given conditions. The shape of upwind sails can nowadays be literally moulded onto a design shape, using materials which will insure low stretching and deformation. The flying shape in this case is supposed to remain even closer to the design shape. On the contrary for downwind sails, the flying shape prediction is still challenging because the light sail cloth structure has no proper shape at rest. This property makes the FSI study of downwind sails even more challenging.

Dimensionless number	Representation of	Full-scale	Wind tunnel
Reduced velocity $U_R = \frac{T_s}{T_f}$	comparison of fluid and structure dynamic	0.6	0.4 to 0.7
Displacement number $D = \frac{\xi_0}{L}$	comparison of structure deformation over its representative scale	0.125	0.112
Mass number $M = \frac{\rho_f}{\rho_s}$	ratio of the mass of the fluid over the mass of the structure as a first indicator of the added mass magnitude effect	1.2×10^{-3}	1.5×10^{-3} (SuperKote 0.75) 1.7×10^{-3} (AirX 500)
Cauchy $C_Y = \frac{\rho_f U^2}{E}$	Ratio of fluid loads over material stiffness indicating the magnitude of deformation due to fluid loading	1.9×10^{-8}	3.1×10^{-9} to 1.5×10^{-8}
Reynolds $Re = \frac{\rho_f U L}{\nu}$	Representation of inertia over viscous effect within the flow, indicating the laminar or turbulent state	2.7×10^6	3.0×10^5 to 6.5×10^5

Table 5 – Dimensionless number for FSI study of yacht sails. Order of magnitude are provided for downwind sails, either at full-scale as given in [Deparday, 2016] or for the wind tunnel testing as presented in Chap. 4

Motivations of this PhD project

This PhD project tends to address some remaining questions on sailing yacht FSI field of knowledge:

1. improve FSI understanding in controlled environment (wind tunnel) about classical sailing situations:
 - (a) What are the effects of pumping? Does pumping improve the aerodynamic performance? If so in which conditions (better dynamic trimming amplitude and reduced frequency)?
 - (b) What are the effects of curling on downwind sails? Using dynamic approach to be compared with full-scale and numerical results, what are the characteristics of curling?
2. improve FSI understanding of full-scale sailing modelling: is there a simple criteria which detects the inviscid flow modelling limitation comparing numerical simulations with known full-scale results?

The thesis objectives to address those questions are presented in the next section.

PhD project objectives

The thesis is divided into two parts which fulfils three objectives presented here and which will be addressed along different chapters.

Assessing the validity of the inviscid assumption as provided by modern tools used in sail design: numerical-experimental comparison.

The yacht hydrodynamic part has been extensively studied and nowadays the remaining challenge in the yacht design and sailing race industry is to be able to fully and correctly model FSI dynamic phenomena occurring onto sails. Sail makers are largely advertising the numerical tools they are using. Some advanced America's cup syndicate even claim the choice to go with fully numerical campaign for their design process without any wind tunnel experiments.

The first part of this thesis presents comparisons between full-scale measurements and numerical simulations on a J80 sailing upwind with potential flow model. General definitions about sailing are presented first with the different data that could be measured onboard then compared with or used for numerical simulation. Several usual static trim adjustments are shown such as change in the backstay tension or jib roller and mainsail car traveller positions. Comparisons on two backstay adjustments give an example where the righting-heeling moment balance indicates if the numerical model is over-predicting the aerodynamic forces. This simple criterion can be used by a sailmakers to estimate if the potential and attached flow hypothesis is valid for the studied case. This comparison process is not strictly a verification and validation work about the numerical model but already shows reliable agreement in upwind configurations as previously demonstrated in [Augier, 2012]. Results are presented in chapter 1 based on the publication [Aubin et al., 2016a].

Better understanding of the sail aero-elastic behaviour from steady to unsteady situations

The main goal of this thesis work is to study upwind and downwind sails in classical unsteady situations. Facing the existing limitations associated to the actual inviscid model, experimental data are therefore still required to better understand the unsteady phenomenon effects occurring on sails. Nevertheless gathering experimental data about unsteady phenomenon at full-scale also remains challenging as the wind fluctuations cannot be controlled. Therefore measurements in a more controlled environment -such as a wind tunnel- have been carried out. The twisted flow wind tunnel facility used extensively to provide the experimental results is presented in chapter 2.

Chapter 3 is dedicated to pumping on upwind sails studied in a wind tunnel. A first step using static trim was required before studying the dynamic trimming. This initial step gathers data from the sails in static conditions: a static optimum is determined for different AWA (apparent wind angle), mast alignment and design shape configurations using a specific optimisation algorithm. This optimisation process is used to determine better trim adjustments in a two-parameter space. Then different reduced frequencies and amplitudes trimming are tested on the different design shapes around the optimal trim. The dynamic aerodynamic forces are studied with the evolution of the

sheet length.

Chapter 4 presents the curling of spinnaker results in static (constant sheet length) conditions. Curling phenomenon presents a significant effect on aerodynamic forces generated by the sail. The evolution of the curling frequency with the wind flow velocity is also investigated. The evolution of aerodynamic forces is presented in a representative curling case.

Effect of design shape, cut, materials and sailing parameters on performance

The second goal of this PhD project is to present some elements to discuss normal sailor trimming behaviour.

The upwind configuration presented in chapter 3, discussing the effect of pumping on the mainsail sheet, is presented to measure any possible improvement in the yacht performance from an aerodynamic point of view compared to the optimum static case. If the sail performance is increased under these conditions, the study would also present the energy required to improve the performance. The effects in the design shape under static and dynamic conditions are presented. In chapter 4, the downwind sail configuration is tested to get the static optimum which seems to be related to the edge of curling. Testing different spinnakers and several configurations provides the AWA effect, the effect of mast rig configurations, the effect of twisted flow, the effect of spinnaker cut and materials on the optimum value and location. In this thesis the trimming recommendations in the yacht performance are discussed. The origin of this improvement is however not investigated because it requires other kind of measurement such as pressure measurements or high quality flow visualisation. The measurements achieved in wind tunnel conditions nevertheless provides some insight into mechanisms involved in the performance improvement.

All these tests provide a better understanding about pumping in upwind and curling in downwind situations. They therefore give experimental elements to discuss some of the sailing community interrogations. The experimental work of this project also provides information to eventually improve numerical modelling in both static and dynamic conditions for upwind and downwind sails.

This manuscript has consequently been divided into two parts, reflecting the chronological development of this thesis work. The first part highlights the accuracy as a first approach and the limitations of the model used nowadays for upwind sail design. It compares full-scale experimental results to numerical simulations in chapter 1. The experimental measurements have also shown that the study of unsteady phenomenon still remains challenging due to high uncertainty on the flow measurement while sailing. Therefore the second part focuses on the wind tunnel experimental campaigns where the wind tunnel facility, presented in chapter 2, ensures a better controlled environment compared to full-scale testing. The effect of upwind sail pumping is then presented in chapter 3 and the effect of downwind sail curling is presented in chapter 4. Those results provides a large dataset of experimental cases to first better understand unsteady effects and sail and would possibly be compared in future work with dynamic FSI modelling.

Part I

Numerical-experimental comparison and applications

Full-scale approach of sailing and numerical-experimental comparison

Contents

1.1	Introduction	21
1.1.1	Sailing yacht physics: point of sail and wind	21
1.1.2	Information and elements that can be measured then compared	29
1.2	Article [Aubin et al., 2016a]: Inviscid approach for upwind sails aerodynamics. How far can we go?	33
1.3	Conclusions	42

This chapter presents full-scale experimental data compared with numerical model results in upwind quasi-steady conditions. The first section introduces general sailing notions -such as the points of sail and wind definitions- and the different data that can be used to achieve numerical-experimental comparison on sails. This comparison is then used and presented in the article provided in the second section. Results show that numerical-experimental comparison on inviscid model enables to validate a criterion indicating if the inviscid flow hypothesis overestimates the generated aero forces.

1.1 Introduction

1.1.1 Sailing yacht physics: point of sail and wind

This section presents general notions useful for the physics of yachts analysis.

1.1.1.1 Point of sail

The first notion to be defined when sailing is the point of sail. It corresponds to the different usual orientations that the yacht heading can take compared to the true wind direction as described in Fig. 1.1. The true wind notion is described further. When the yacht is going towards a point which is located to windward (*i.e.* upstream) compared to her location, she is sailing upwind. In this case the true wind angle $|\beta_{TW}| < 90^\circ$. When she is going towards a point which is located to leeward (*i.e.* downstream) of her position, she is sailing downwind. In this case the true wind angle $|\beta_{TW}| > 90^\circ$. When she receives the wind from her port side, she is on port tack. On the contrary when she receives the wind from starboard side, she is on starboard tack. The limit between the portside and starboard tack is given by the blue dashed line in Fig. 1.1 representing the true wind direction.

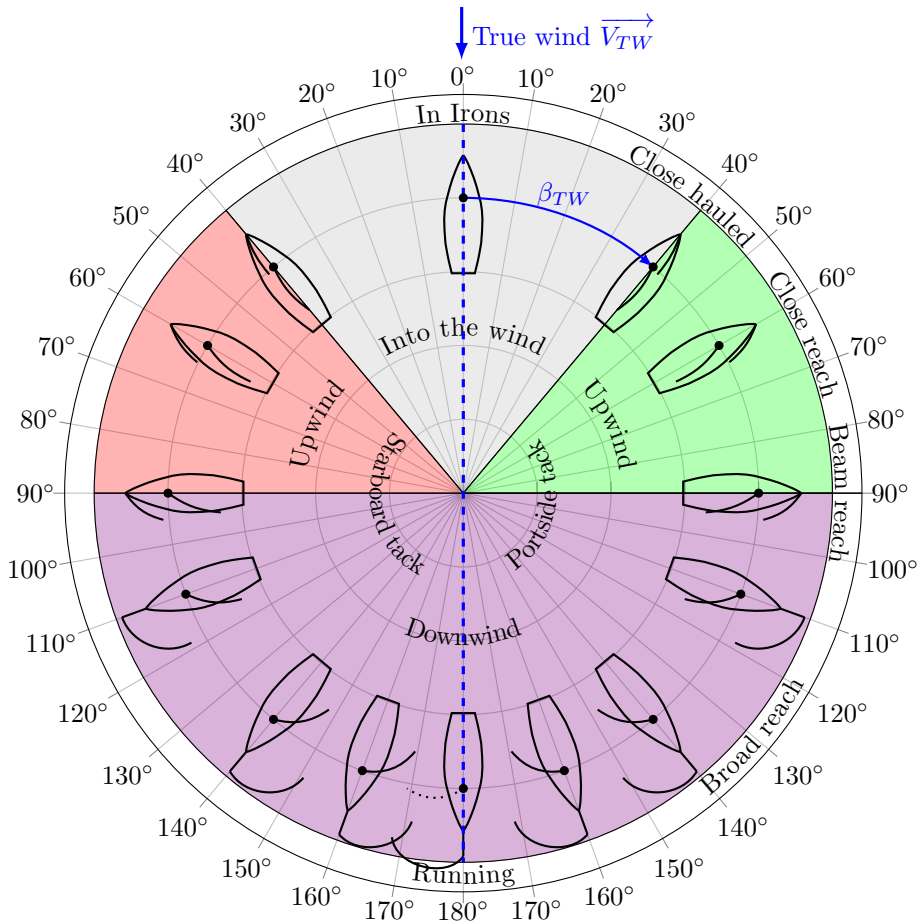


Figure 1.1 – Point of sail.

The first sailing boats using the wind as propulsion may have been limited to downwind sailing (purple angle in Fig. 1.1) probably using only windage (drag). Navigation was submitted in this case to the fate of the weather conditions even if alternative propulsion remained possible (rowing). Sailing has benefited from many development for both the hydrodynamic and aerodynamic parts [Whitewright, 2011] until nowadays when sailing yachts still cannot go directly forward into the true wind direction, but are able to easily sail upwind. Successive manoeuvring known as tacks are

required to evolve to a point located into the true wind direction. In practice, the upwind phase has for a long time remained more challenging to achieve compared to the downwind phase. However the intense development of aeronautics in the XXth century with the extensive study of lifting bodies such as wings have provided modern scientific approaches, methods and tools for the upwind sail studies. The relevant comparison of an upwind sail acting as a vertical wing has now led to interesting wing developments such as high performance devices in racing (America's cup) and cruising yacht history.

Upwind and downwind phases used to be associated to one type of flow behaviour around sails. The flow for sailing upwind was supposed to remain attached, generating smooth path-lines along the sails. On the contrary, downwind sails used to be associated with strong detached flow, generating vortices and natural unsteadiness. Each type of flow has been studied with dedicated tools or methods. This attached-detached distinction type of flow in the sailing literature is generally still associated with the type of sail for upwind or downwind. The restricted use of a sail to one type of flow is, however, no longer relevant, especially for modern downwind sails used at high speeds [Richards et al., 2001] or new reaching sails, whose shapes are in between the design of upwind or deep downwind sails. Moreover the mainsails are used in all the point of sail. The fully attached flow hypothesis can also be discussed for upwind sails where detached flow can occur before the sail leech (trailing edge).

The flow acting on sails can therefore be attached, partially detached or massively detached. The mean flow characteristic applied to sails (velocity and direction) results in a combination of the true wind, and the flow velocity generated by the yacht velocity and motion. The different wind definitions are presented next in order to provide the key elements that are required for the different yacht study methods.

1.1.1.2 The wind: from true to apparent

This subsection provides information about the wind definition in the sailing yacht research field.

The true wind is defined as the outdoor fluid flow generated by either a global atmospheric circulation system or a local weather phenomenon or a combination of both. The true wind can be experienced by a non-moving observer or instrument in the terrestrial frame. In that case we assume that the observer does not affect the flow velocity or direction. The true wind is generally defined by a wind profile corresponding to the mean flow velocity and turbulence level defined as a function of the height above the surface.

Wind profile $U(Z)$ are generally given for the mean flow velocity U as a function of the height Z over the surface (land or sea). One of the highest sailing yachts, *Mirabella V* is about 88.5 m high, so we will restrict our study to the limit of the lower 100 m of the atmosphere which corresponds to the minimum size of the atmospheric boundary layer also called the planetary boundary layer. This atmospheric boundary layer corresponds to the lowest part of the troposphere (0 km to 11 km) and its depth varies with the diurnal variation (*i.e.* time changes) over the surface.

We consider here a neutral or neutrally stratified boundary layer which occurs in the absence of significant thermal processes. For this part the usual wind profile model is given for the mean velocity of the wind flow. The true wind direction information β_{TW} defines the point of sail shown on Fig. 1.1.

The log law wind profile is described by the following equation 1.1:

$$\frac{U(Z)}{U_*} = \frac{1}{k} \ln \left(\frac{Z}{z_0} \right) \quad (1.1)$$

where

1. $U(Z)$ is true wind mean velocity as a function of height Z above the sea level
2. U_* is the friction velocity defined by $U_* = \frac{0.4V_T}{\ln(\frac{10}{z_0})}$ with V_T the wind velocity at 10 m height above the sea level in m s^{-1} . This variable is a representation of the flow surface stress.
3. k is the von Kármán constant $k = 0.4$
4. z_0 is the aerodynamic roughness length. Over land, it is not equal to the roughness element size on the ground but it is only dependent on these roughness elements. The aerodynamic roughness length over land does not change with wind speed, stability or stress, just on the size of the surface texture. However for sailing application, the aerodynamic roughness length does depend on the sea state and therefore on the wind velocity. The aerodynamic roughness is described as a function of the wind speed using Cook's formula ([Cook, 1985, Hansen, 2006]): $z_0 \approx 5 \cdot 10^{-5} \frac{V_T^2}{g}$ which provides a roughness length about 0.2 mm. Another formula can be used to define the aerodynamic roughness length due to the gravity-capillarity waves forced by the wind ([Charnock, 1955, Chamberlain, 1983, Wiernga, 1993]) $z_0 \approx 0.016 \frac{U_*^2}{g}$. Another formulation of the log law can be found in [Hémon, 2006].

From these relationships, we can determine the wind speed at any height from the wind speed V_{ref} measured at a given altitude Z_{ref} .

$$U(Z) = U_* \frac{1}{k} \ln \left(\frac{Z}{z_0} \right) \quad (1.2)$$

$$U_* = \frac{V_{ref}}{\frac{1}{k} \ln \left(\frac{Z_{ref}}{z_0} \right)} \quad (1.3)$$

$$U(Z) = \frac{V_{ref}}{\frac{1}{k} \ln \left(\frac{Z_{ref}}{z_0} \right)} \frac{1}{k} \ln \left(\frac{Z}{z_0} \right) \quad (1.4)$$

$$\boxed{U(Z) = V_{ref} \frac{\ln(Z) - \ln(z_0)}{\ln(Z_{ref}) - \ln(z_0)}} \quad (1.5)$$

The true wind is generally defined at a reference height or altitude Z_{ref} of 10 m. We assume here that the true wind is also not affected by any manufactured object such as a yacht or a facility on

land or at sea. The shore effect for a natural wind coming from the shore can be used to adjust this wind profile model.

Turbulence intensity I_{uvw} of true wind can be defined by $I_{uvw} = \frac{\sqrt{\frac{1}{3}(\overline{u^2} + \overline{v^2} + \overline{w^2})}}{\|\vec{V}\|}$ (provided in [TFI, 2015]). As described in [Flay and Jackson, 1992, Flay and Millar, 2006] for full scale situations, it goes from 8% in the higher part of the sail to 11% for the lower part for a wind speed of 8 m s^{-1} . [Flay and Vuletic, 1995] suggested to use the fact that the standard deviation of the velocity fluctuation is about 2.5 times the friction velocity [Flay et al., 1982]. In this case, turbulence intensity profile follows the relation:

$$I_{uvw}(Z) = \frac{1}{\ln\left(\frac{Z}{z_0}\right)} \quad (1.6)$$

More information about experimental wind measurement analysis as used for sailing competition can be found in [Herlédant, 2011].

Additional wind shear phenomenon can occur when the wind direction or velocity deviates from the log law profile. It can be caused by a true wind affected by the sea state surface, like the swell and/or the tidal current direction. This kind of situations is not considered in this thesis but possible modifications of wind velocity profile by interaction with sea state have been investigated in recent studies ([Cathelain, 2017]).

The apparent wind has to be taken into account for relevant modelling of the flow around a sail. When a sailing yacht is moving on the sea surface, she generates her own wind due to :

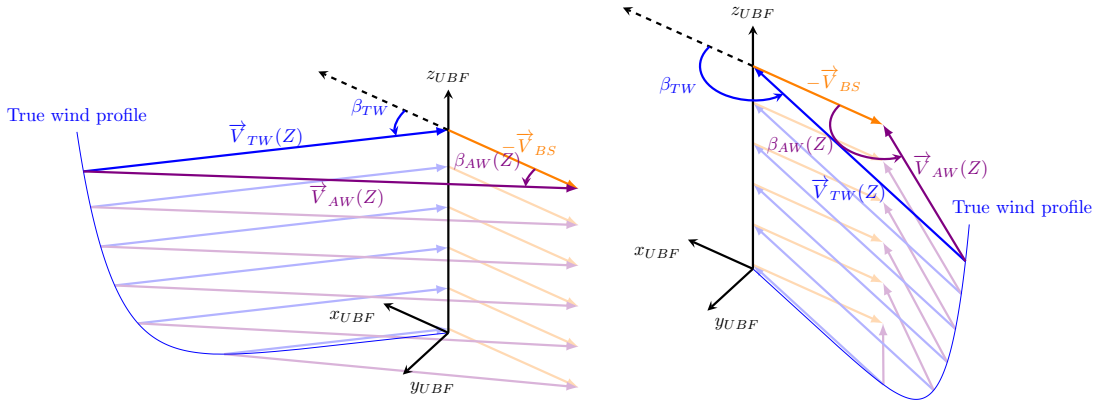
- her boat speed \vec{V}_{BS} , defined as the velocity of her reference point on the yacht in the terrestrial frame. This reference point is generally located close to a yacht representative rotation center. From an hydrodynamic point of view, its longitudinal position is commonly located at a third along the chord of the keel. From an aerodynamic point of view, it can generally be defined as the mast step in the J80 case which corresponds to the point O described in App. B.
- her motion, defined in this thesis, as a transient change in her angular position (also called attitude for aircrafts) defined by a combination of a yaw, pitch and roll motion in the terrestrial frame mostly generated by the waves, crew position and wind conditions. The angular position definition is provided in App. B.

Apparent wind definition is generally provided when boat has no angular velocity compared to the terrestrial frame. In this case the apparent wind \vec{V}_{AW} is defined as the sum of the true wind vector at the studied location and the opposite of the boat speed vector \vec{V}_{BS} . In this conditions we can observe that the composition of those vectors will generate:

- an apparent wind with a magnitude depending on the altitude

- an apparent wind direction β_{AW} which also depends on the altitude. This twist effect is quite small for upwind sailing conditions and more pronounced for downwind sailing conditions as shown in the 3D illustration in Fig. 1.2b. It justifies the use of twisting vanes in wind tunnel downwind testing.

The twist effect is presented in Fig. 1.2 where the *UBF* designation stands for *UBF* Upright Boat Frame as defined in App. B.



(a) Apparent wind profile in upwind condition. J80 twist value between the apparent wind direction at reference height and sea surface is about 5° , for a true wind speed of 16knots at $Z = 10$ m with $\beta_{TW} = 45^\circ$.

(b) Apparent wind profile in downwind condition. The twist evolution is more pronounced compared to upwind situation. J80 twist value between the apparent wind direction at reference height and sea surface is about 35° , for a true wind speed of 16 knots at $Z = 10$ m with $\beta_{TW} = 135^\circ$.

Figure 1.2 – Representation of the apparent wind. *UBF* stand for upright boat frame.

The apparent wind definition requires a correction when considering a yacht with angular velocity compared to the terrestrial frame. In this case the rotation of the boat also generates a flow which takes part in the apparent wind. Complementary works have been carried out in a collaboration with Hugo Kerhascoët PhD candidate ([Kerhascoët, 2017]), on a more precise definition on wind in order to improve the wind information post-processing, but is not presented in this thesis.

Turbulence of apparent wind is affected by the yacht itself and the yacht motion. [Larsson, 2005, Horel, 2011] gives some measurements at full-scale which are required to select and manufacture the pressure sensors used on sails [Flay and Millar, 2006].

The measured wind is the wind measured by an on-board instrument or felt by an observer located on the yacht. It corresponds to the apparent wind affected by the possible motion of the instrument or observer in the boat frame and by the deviation of the flow due to sails, boat and rig, called upwash effect. The motion of the instrument in the boat frame can be due to structural deformations of the yacht herself. A yacht is first modelled by a rigid body, however it remains

strongly affected by rig deformations. For instance a wind sensor located on the top of the mast is affected by the mast vibrations, by the mast deformation due to the sail loads or by rig adjustments and the mast head orientation if the mast is twisted or rotated. To collect information about the sensor motion in the boat frame, a motion sensor can be set up as close as possible to the wind sensor as described in [Gerster, 2016].

The second effect due to upwash is mainly due to the presence of the sails which affect the flow velocity and direction. For usual sensors used in the sailing industry, a small part of the upwash effect is generated by the sensor itself. Only non-intrusive techniques such as LIDAR (light detection and ranging) or PIV (particle image velocimetry) may provides information about the flow without affecting it, but are reserved for in laboratory conditions.

For high performance sailing requiring precise instantaneous wind information, or for research application (numerical-experimental comparison), it is therefore required to take into account the mast deformation, the boat motion and the upwash effect.

Wind information post-processing is one of the most challenging step while doing full-scale analysis. The wind information is processed in the following way described in Fig. 1.3. During full-scale experimental campaigns the raw information provided by the sensor is the measured wind. Then possible post-processing based on upwash corrections and taking into account the motion of the wind sensor in the boat frame enables the apparent wind to be determined. Then the angular motion component of the yacht measured by an onboard IMU can be subtracted from the apparent wind to provide the corrected apparent wind. Then the boat speed measured by a speedometer (either mechanical or ultrasonic) can provide the boat velocity which subtracted from the corrected apparent wind gives the true wind at the wind sensor location. The measurement of the wind sensor altitude using the measured yacht angular position can then provide the true wind information. This method might work well in theory providing the true wind information required for numerical simulation, however it still suffers from large uncertainties.

The wind properties provided in this sections underline that:

1. the apparent wind acting onto the sails is twisted, even in upwind conditions. The apparent wind angle β_{AW} depends on the altitude.
2. the usual wind triangle is defined by the true wind vector \vec{V}_{TW} , the boat speed vector \vec{V}_{BS} and the apparent wind vector \vec{V}_{AW} . Those quantities are generally defined for a static angular position of the yacht. Some studies take into account the dynamic part of the boat motion and its effect in the apparent wind [Fossati and Muggiasca, 2010, Fossati and Muggiasca, 2011, Fossati and Muggiasca, 2012b, Augier et al., 2014]. In this thesis, only static boat position is presented either in wind tunnel or full-scale situations.
3. true wind computation remains challenging and presents large uncertainty in the full-scale results for numerical-experimental comparison.

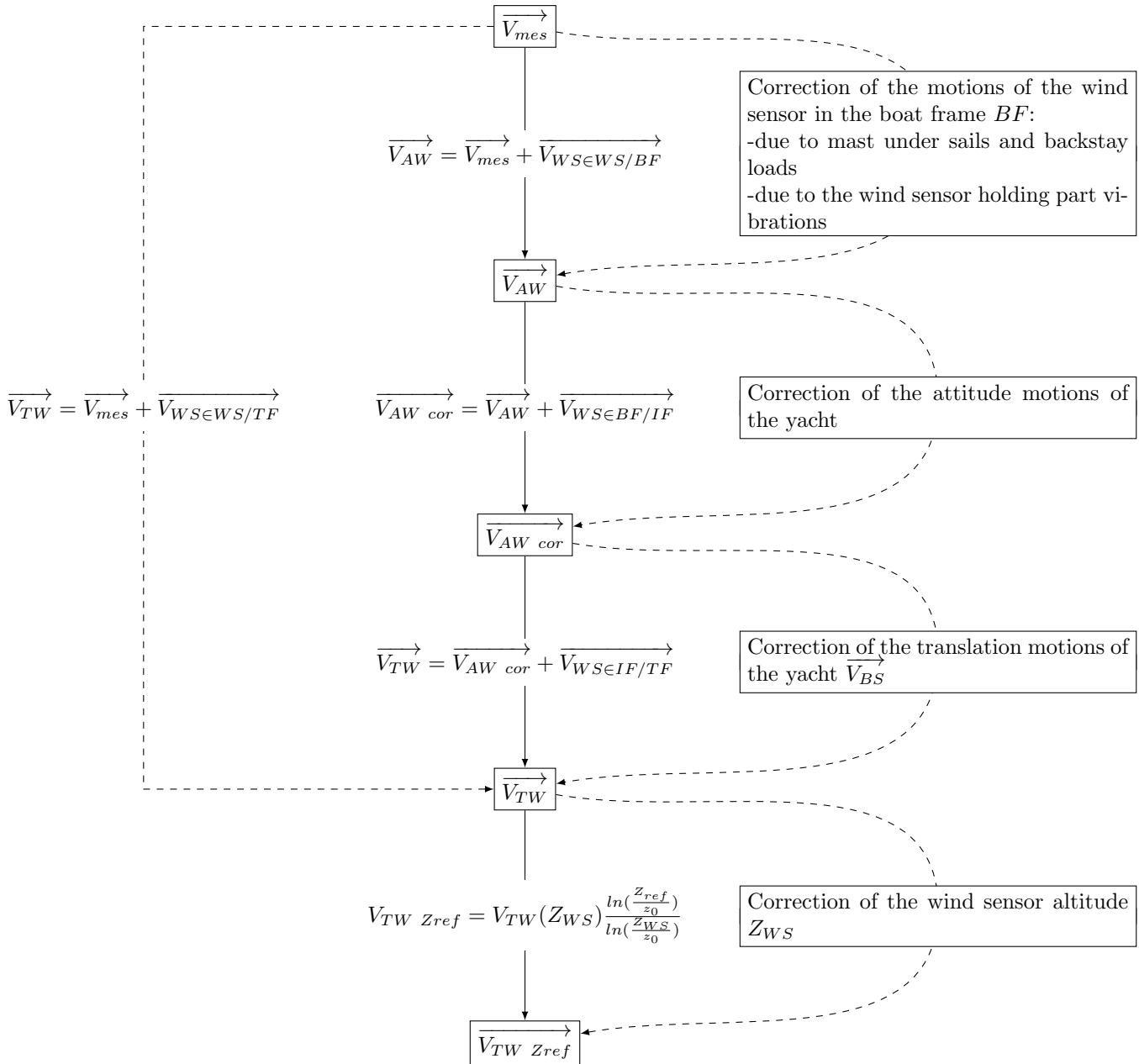


Figure 1.3 – Wind information processing. WS stands for Wind Sensor, either the measurement point or the associated frame. Frames are defined in App. B. Upwash corrections can be applied on different stage of the process.

1.1.1.3 The new tools of modern sail designers

Computational methods are required nowadays to develop efficient and competitive sail products. During the 5th High Performance Yacht Design conference held in Auckland in 2015, Burns Fallow -head sail designer and director of North Sails New Zealand- has indicated that *“from the past thirty years sail design has definitely comes from art to real science”*. Advanced sail and rig makers intensively use these different numerical tools for their design however the fully coupled simulation of the FSI phenomena taking into account the dynamic aspect in viscous flow remains still challenging and expensive in time and requires many Central Processing Unit (CPU). For codes using much faster simple models for the flow part such as VLM based method, some limitations still exist. The flow detachment which can also appear in upwind sailing conditions remains challenging to predict on a changing flying shape and under unsteady conditions.

K-Epsilon company FSI tools ARAVANTI, coupling the FEM code ARA and the inviscid VLM model AVANTI, have been developed by [Durand, 2012]. [Augier et al., 2012] provided some experimental situations to achieve numerical-experimental comparison with good agreement. This tool is now part of the SailPack-Aravanti, Fluid-Structure Interaction product available from BSG developements. The inviscid flow approach is reasonable as long as no flow detachment occurs. The goal of this chapter is to investigate the use of an indicator that can warn the sail designer that this hypothesis is no longer respected. In that case, the sail designer will either adjust the sail trim to get a reattached flow in an early design stage, or investigate viscous flow models.

Experimental full-scale or model wind tunnel data have been collected along this PhD work. The experimental data are first used to get a better understanding about unsteady FSI phenomena occurring on sails. Full-scale experimental data presented in this chapter are compared with ARAVANTI numerical code results. Comparison can be applied on several data of very different types. A list about the usual data that can be compared is presented next. The reader is referred to [Deparday, 2016] for details about the new recording system and its architecture developed on the J80 instrumented boat.

1.1.2 Information and elements that can be measured then compared

Verification and validation or comparison use output quantities available both in the numerical computation and in the experimental data. Most of these quantities can be computed in a FSI simulation therefore the useful various outputs depend essentially on what measurements are recorded during the experiments. This subsection presents the different kind of data that can be compared. Their numerical equivalent is also described when it requires additional relevant information.

1.1.2.1 Yacht and navigation information

The first elements to be recorded are the ones associated to the navigation such as the boat speed provided by mechanical or ultrasonic loch sensor under the yacht hull. Angular positions (heading, trim and heel angles), velocities and accelerations are provided by an inboard IMU. Positioning is provided by a Global Positioning System (GPS) which also gives the speed over

ground and course over ground affected by the tide and leeway. This data is used as input parameters for the numerical simulation providing the boat speed and the angular positions the numerical model should be set up to. The boat speed is also required to reconstruct the wind velocity triangle.

1.1.2.2 Loads

Rig loads can be measured using instrumented shackles and turnbuckles in different points of the J80 rig as developed by [Augier, 2012]. These elements are a key output for the structural designers such as rig makers who are interested in unsteady loads in the rig in order to adjust their safety coefficients. Moreover literature suffer a lack of open data due to potential confidentiality associated to them. For example during the 2015 Volvo Ocean race, yachts mast were instrumented and loads of mast sections have been measured in order to give live information to the crew. This information was used on-board with an indicator about the mast loading from normal load to overloaded but none of it was publicly released.

On the J80 instrumented system a zeroing step is required before leaving the harbour where the entire rig is totally eased. This operation also requires to warm up the system until all the measuring bridge reach their working temperature. Calibration of these instruments is done on laboratory environment were calibrated weight are lifted.

On the numerical model, the loads are essentially an output element of the computation, using the length of the different wire elements as an input data. However it can also be used to adjust the length of a given element where its length adjustment cannot be measured. For example, in the presented article the length adjustment of the backstay cannot be achieved and therefore, the measured load is applied through the backstay cable element for the two presented situations: backstay on (trimmed in) and off (released) cases.

1.1.2.3 Aerodynamic forces

The aerodynamic forces can be measured using a balance providing the total aerodynamic forces. This method can be used at full-scale like in [Masuyama, 2014, Fossati et al., 2015a] but requires the development of a full-scale steel frame manufactured at the hull size of the boat and used as a balance structure. On a model yacht, the wind tunnel balance directly provides these informations ([Hansen, 2006]). Gathering the aerodynamic data is the first essential part to evaluate the boat performance and provide data that can be used for a VPP.

Other methods using DLC developed by [Le Pelley et al., 2015] can also compute the total aerodynamic forces generated by a sail but the sail has to be only attached with DLC which is achieved only with a spinnaker or gennaker. The DLC provides the force transmitted by the sail to the boat rig but also their direction. The direction in the boat frame is measured comparing the relative rotation between the base unit set up fixed on the hull frame, and each individual DLC local frame. An algorithm has been developed during Julien Deparday thesis ([Deparday, 2016]) to calibrate the DLC direction. However the angular calibration checking can be difficult to achieve considering a specific frame. The alternative numeric method shown on App. I suggests a process where no specific frame alignment is required to compute coupled rotations. The local direction

provided by a DLC can be an additional relevant information as it is supposed to tangent the local sail cloth surface attached to this point. Another application of DLC would be to get the hydrodynamic matrix of a full-scale yacht hull using quasi-steady situations where hydrodynamic forces are balanced by the measured aerodynamic ones.

Another method used by [Motta et al., 2014] called FEPV is based on the synchronised measurement of pressure distribution and the sail flying shape. In this method, the measured pressure field is interpolated and extrapolated on the measured flying shape which provides the instantaneous aero forces acting on the sail. [Motta et al., 2014] used this system with a VSPARS system to compute the flying shape compared to [Deparday, 2016] who used a photogrammetry technique. Differences have been observed between DLC and FEPV results. DLC compute smaller forces than FEPV techniques. Next are presented the pressure distribution and flying shape measurement techniques.

1.1.2.4 Pressure distribution

The sails pressure distribution can be measured using pressure tapes of either differential or absolute type. The differential technology measures directly the difference of pressure between both sides of the sails. The sensor is taped onto one side and a tiny hole is made in the sail cloth to make the piezoelectric membrane in the sensor sensible to differential pressure. It has been used in wind tunnel with a lighter configuration of the measuring system compared to the full-scale one ([Viola and Flay, 2009]). Absolute type can also be used with a semi rigid sails ([Bot et al., 2014]) in wind tunnel conditions. Other methods can be developed such as the pressure sensitive paint described in [Abbitt et al., 1996]. The pressure can be used as an input of the FEM code ARA. It can provide a realistic initial flying shape that can be used as a first state of a full FSI computation.

1.1.2.5 Flying shape

The flying shape of a sail is a key element because it might be the only output that sailors can directly use without any other onboard sensor. For a given sailing condition they target a flying shape known as efficient adjusting different trim. This flying shape comparison can be either on 2D parameters focused onto several stripes (2D sections of the sail at different height) or in 3D.

This is probably the type of information which has benefited from many early developments from different racing teams (*e.g.* ISIS then Sail Vision by Virginie and François Nivellean) and industrials ([Le Pelley and Modral, 2008] for VSPARS used in this chapter). It is also a way for sail makers to measure how far from the design shape is an actual flying shape. Some sail makers develop their own product (ASA for North sails Japan, Accumeasure for UK-sailmaker, SailVision for BSG). Photograph based methods have to take into account the fish-eye effects and the rolling shutter effect for unsteady situations. Time of flight methods using laser scanning can also be used to record a sail shape [Lindbom, 2006, Fossati et al., 2015b]. However the scanning rate has to be fast enough compared to the dynamic motion of the sail. New method using strain measurements can also be suggested as shown in [Ferreira et al., 2017].

Once the flying shape has been recorded and measured, it can be interpreted in two ways.

It can correspond to a collection of 2D stripes at different sail span position with their usual sail stripes information (camber, draft, entry and exit angles). This representation is well adapted for upwind sails. A 3D representation will provide more detailed information but will require more space to store the information. [Deparday, 2016] suggests a new way to interpret a 3D cloud point measured using Bezier surface method.

The numerical-experimental flying shape comparison can be generally done using three methods as shown in this chapter article. The experimental-numerical point of view superposition either gives a qualitative comparison. The second method corresponds to the quantitative computation of geometric parameters such as the draft and camber of a stripe. The third one is the numerical superimposition of the measured and computed flying shape.

1.1.2.6 Flow information and measurement

Wind information is a major element for the comparison and true wind information is required as an input of the numerical simulation. The true wind measurement remains challenging as it suffers many perturbations. The wind sensor frame can be affected by the yacht parts deformation (volunteer or not mast twist, high frequency vibration in structural parts of the boat). Adding to yacht mean speed, the yacht motion itself induces an additional instantaneous wind that has to be taken into account, either with an IMU located on the boat or directly on the wind sensor generally set up on mast head. [Gerster, 2016] shows that these motions can be cancelled out and [Kerhascoët et al., 2016a] designed an optimised wind vane tail to minimize the wind sensor response time. The wind information suffers also from the upwash effect, where sails strongly affect the flow direction and velocity at the sensor location compared to the upstream flow. This can be taken into account using upwash correction tables. These correction tables can be based on numerical simulations. Once the wind information has been obtained, it can be used as an input of the numerical simulation. However full-scale tests still suffer of a larger uncertainty due to the unsteady wind conditions. That is why a wind tunnel comparison with a quasi steady known wind but dynamic conditions might be preferable as a first approach to validate the numerical model under dynamic conditions.

Flow information can also be measured on others part, such as the sails themselves. Traditional tell-tale taped onto a sail are used by sailors to have indication about the nature of the flow (attached or detached). Recently an electronic tell-tale [Voisin et al., 2013] has been developed to be able to integrate this information on an inboard pilot. These data providing the location of detached flow can be compared to what is given by a RANS solver.

1.1.2.7 Element tracking

Some elements of the rig can be visually tracked in order to record their trajectory. It is essential in dynamic situation to check that the structural parts are affected by the same deformation as a result of similar loads. Trajectory can be compared giving the instantaneous deformation or adjustment of different elements such as the boom end or mast head. [Augier, 2012, Durand, 2012] make comparison of batten ends trajectory on a simple oscillating cloth.

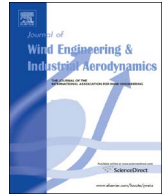
Some of the elements presented above are used for this chapter article where comparison is done under quasi-steady upwind situations carried out in 2014 full-scale experimental campaign. The first idea of this chapter is to be able to numerically detect when the inviscid approach can no longer be used to simulate a design case in quasi-steady conditions with a simple criterion using the righting-heeling moment equilibrium. In this case the sail designer can choose either to do a full RANS simulation and to compare the two models results such as in [Sacher et al., 2015] or either to adjust the trim.

1.2 Article [Aubin et al., 2016a]: Inviscid approach for upwind sails aerodynamics. How far can we go?



Contents lists available at ScienceDirect

Journal of Wind Engineering and Industrial Aerodynamics

journal homepage: www.elsevier.com/locate/indaer

Inviscid approach for upwind sails aerodynamics. How far can we go?

N. Aubin^a, B. Augier^{a,*}, P. Bot^a, F. Hauville^a, R. Floch^b^a Institut de Recherche de l'Ecole Navale, IRENav, BCRM de Brest, Ecole navale, CC 600 - Lanveoc, F-29240 BREST Cedex 9, France^b Incidence Sails, 520 rue Alain Colas, 29200 Brest, France

ARTICLE INFO

Article history:

Received 19 November 2015

Received in revised form

6 June 2016

Accepted 6 June 2016

Keywords:

Fluid–structure interaction

Numerical simulation

Yacht sails

Full scale measurements

Instrumented boat

Inviscid flow

Aerodynamic forces

Sails flying shape

ABSTRACT

This work presents a full-scale experimental study of a yacht rig and sails in real upwind sailing conditions and a comparison with Fluid Structure Interaction (FSI) simulations with the ARAVANTI model (Finite Element Method for the structure and Vortex Lattice Method for the fluid). A specific on-board instrumentation system simultaneously measures loads in the rig and sails, sailing data (wind, boat attitude and speed) and the shape of sails in real navigation conditions (flying shape). Flying shape parameters are extracted using the camera-based VSPARS system to characterize the effects of sail trims and to be compared with the results of the simulation. The potential flow solver gives fast and accurate predictions of both the flying shape and the loads in the rig in most conditions. The inviscid approach, commonly used in the early stage of design, must be checked, as in particular cases where the sails are heavily loaded, flow separation is significant and results from a potential flow solver are inaccurate. A new version of the model including the heel angle as an additional degree of freedom in the structural solver enables to detect when the inviscid flow approach overestimates the aerodynamic load. This upgrade improves the utility and reliability of the inviscid flow approach which remains relevant at the early stages of design as it is much more cost-effective than RANS models.

© 2016 Elsevier Ltd. All rights reserved.

1. Introduction

The prediction of the aerodynamic performance of yacht sails has improved greatly due to different approaches followed by the research community. Direct measurements based on full-scale experiments in real sailing conditions give data for the design and analysis of the performance. Several previous research programs have developed instrumented yachts to obtain full-scale experimental data via sailing dynamometers like Fujin (Masuyama, 2014), MIT Sailing Dynamometer (Milgram et al., 1993), DYNA (Hochkirch and Brandt, 1999), and LECCO (Fossati et al., 2015a). Other full scale specific instrumented yachts have been developed to measure simultaneously the loads in all the tension points of the rig, the flying shape, the wind data and attitude of the boat (Augier, 2012) or the pressure on sails (Viola and Flay, 2010; Motta et al., 2014). Wind tunnel studies (Flay, 1996a,b; Lasher et al., 2005) have proven to be a great tool to study the aero-elastic problem of sails in wind. More recently, wind tunnel has been also used to study the Fluid Structure Interaction (FSI) phenomena that occur with sails in dynamic conditions in pitching (Fossati and Muggiasca, 2009) or with a dynamic trimming (Aubin et al., 2016). The recent increase in computation capabilities has allowed the

development of accurate CFD tools to model the FSI of sails (Braun and Imas, 2008; Lasher and Sonnenmeir, 2008). However, both results from wind tunnel and particularly CFD need to be validated by full-scale observation. For instance Yoo and Kim (2006) compared CFD results and experimental measurements on yacht sails. IRENav has validated a numerical FSI model with full-scale results achieved on an instrumented J80-class yacht (Augier, 2012; Augier et al., 2012) in both steady and unsteady situations. The model was then used to predict the aerodynamic forces and rig loads of a sailing yacht in dynamic conditions (Augier et al., 2014) and can be used for performance studies. Using an FSI tool can be interesting to predict the effect of trimming the sails and the rig to adapt to the sailing conditions. The FSI tool ARAVANTI (Roux et al., 2008) developed by the K-EPSILON Company and IRENav has already been validated in such situations and has proven to be an accurate prediction tool, even in highly unsteady cases (Augier et al., 2012). The model, based on a potential flow approach is limited to cases where the flow is assumed to be fully attached, i.e. upwind conditions. It is now well known that flow separation may be non-negligible also in upwind sailing (e.g. Fluck et al., 2010; Fossati and Muggiasca, 2012; Viola et al., 2013). Some studies have already compared the inviscid flow FSI model ARAVANTI to the viscous flow FSI model ARA-ISIS, coupling the same structural code ARA to the RANS solver ISIS-CFD (commercialized as FINE™/Marine), and have highlighted situations where the potential flow approach is

* Corresponding author.

E-mail address: augier.ben@gmail.com (B. Augier).

Nomenclature

Δ	boat displacement (kg)	M_x	heeling moment (N m)
ϕ	heel angle ($^\circ$)	R_m	righting moment (N m)
F_x	driving force (N)	ARAVANTI	FSI coupling between the structure model ARA and the inviscid fluid model AVANTI
g	acceleration of gravity (m s^{-2})	FSI	Fluid Structure Interaction
GZ	hydrostatic righting arm (m)	NMEA	National Marine Electronics Association
L	moment arm of crew weight (m)	VSPARS	Visual Sail Position And Rig Shape (Le Pelley and Modral, 2008)
m	crew weight (kg)		

incorrect (Sacher et al., 2015). However, as viscous flow simulations require a large amount of CPU time (Löhner et al., 2015; Michalski et al., 2015), the potential flow approach is still largely used at early design stages.

The goals of this paper are to measure the effects of sail and rig trims on the sails shape, and to assess the ability of the potential flow FSI tool ARAVANTI to predict aerodynamic loads and sails flying shape. An improved model is also presented, including heel as an additional degree of freedom in the structural model. A simple criterion based on the balance of righting and heeling moments allows the relevance of the potential flow approach to be easily checked. Sections 2 and 3 introduce the experimental and numerical tools used for this study. Section 4 shows the effects of different trims (sheeting car position) on the sails shape. In Section 5, experimental results are compared to FSI simulations for two different cases of backstay tension: one where the simulation is correct and one where the inviscid flow assumption is violated. The latter case is better analyzed in Section 6 thanks to the upgraded model. A few concluding remarks are made in the last section.

2. Measurements

2.1. System apparatus

Full-scale measurements are performed on a J80-class yacht, an 8 m one-design cruiser-racer boat. A specific instrumentation described in Augier et al. (2012) is used to measure the loads in 16 points of the rig, the yacht motion and attitudes, the sails flying shape and navigation parameters. Mainsail and jib luffs are hanked on, foots and leeches are loose. The instrumented boat is presented in Fig. 1. In the present setup, the on-board acquisition system is divided into two parts: one is in charge of recording all the navigation and load data (rig loads, wind information, boat speed and attitude, etc.) and the other one is in charge of the flying shape acquisition (based on deck-mounted GoPro cameras filming stripes taped on the sails). A triggered laser pulse is used to synchronize the video with the recorded data. Motions and attitudes are recorded using an SBG Systems motion sensor. Wind data are recorded using a 3D ultrasonic anemometer and Nke wind vane and cup anemometer placed at the top of the mast. Loads are measured with specific instrumented shackles and turnbuckles fitted with strain gauges that replace the classical fittings. The precision error on the loads is less than 2% over a 10 000 N range for the rig and 5000 N for the sails' lines. The upwind experiments presented herein were carried out in the bay of Brest in June 2014 with a North Westerly wind of 12.5 kn in average and calm water.

2.2. Data post-processing

Special care was taken in data post-processing to cope with the high number and heterogeneity of the recorded data. Navigation

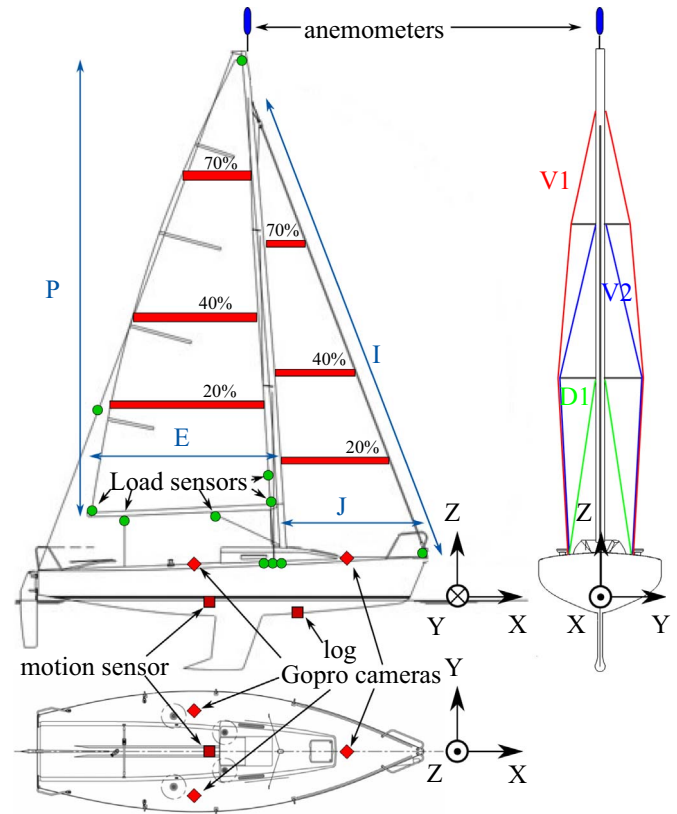


Fig. 1. Yacht system apparatus.

data such as boat speed from the loch, GPS data, Nke company wind sensors and motion sensor are gathered and recorded by the Nke company system using the NMEA protocol. That information is sent and time-stamped at reception by a Compact Rio acquisition unit, which also directly receives the analog signals from the load sensors (25 Hz), the 3D anemometer (10 Hz) and another motion sensor (free IMU). Each sensor records the corresponding signal with its own sampling frequency, therefore re-sampling is applied to obtain synchronous data.

2.3. Flying shape analysis

Several techniques can be used to measure the 3D flying shape of sails such as laser scanning (Fossati et al., 2015b) or photogrammetry (Mausolf et al., 2011). In this study, sails fitted with taped stripes are visualized by 3 deck-mounted GoPro cameras and the VSPARS system is used to provide the 3D stripe coordinates in the boat frame (Le Pelley and Modral, 2008). Three stripes per sail were used: stripe 1 at 20% (lower stripe), stripe 2 at 40% (middle stripe) and stripe 3 at 70% (upper stripe) of the luff length (Fig. 1). After synchronizing the video with the other recordings using the

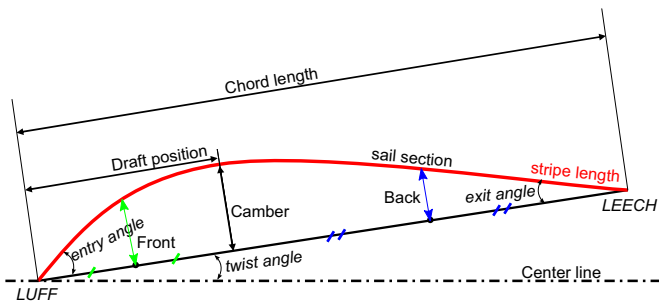


Fig. 2. Stripe parameters of the sail.

laser pulses, each video frame is extracted as an image and time-stamped. A calibration is applied to correct the so-called 'fish-eye' lens distortion. Flying shape of the sails is characterized with stripe parameters (defined in Fig. 2) commonly used to define sails aerodynamic sections. This allows quantitatively analyzing the sails shape and the effects of trimming.

3. Numerical simulation

3.1. Numerical model

Inviscid models have been used for a long time in sail aerodynamics (e.g. Fiddes and Gaydon, 1996; Gerhardt et al., 2011). Despite the development of more advanced models, the inviscid approach is still commonly used in the early design stage because it is very fast. The FSI model ARAVANTI from K-EPSILON Company is used for the numerical simulations in upwind situations presented here. The structural solver ARA is a Finite Element Method model. Sails are described with constant strain triangle membrane elements, the mast, boom, spreaders and battens use beam elements, while shrouds and running rigging use wire elements. The rig's structural properties have been measured (Augier et al., 2012) and the sails' materials and structural properties were provided by Incidences Sailmaker. The AVANTI flow solver is a Vortex Lattice Method modelling an inviscid flow. The sails' surface is described using rectangular panels and the wake is modelled with particles. More details about the coupling scheme can be found in Roux et al. (2008). The ability of ARAVANTI to accurately predict aerodynamic loads and the flying shape of the sails in both steady and unsteady situations has been shown in Augier et al. (2012).

3.2. Simulation and experimental comparison process

The method for numerical simulation based on experimentally recorded inputs is illustrated in Fig. 3. As this work deals with steady-state simulations, only experimental runs with near-steady situations are considered and data are time-averaged over a 10 s run. The following parameters are determined from the selected experimental run and given as inputs to the numerical simulation:

- true wind: determined from the measured Apparent Wind Speed (AWS), Apparent Wind Angle (AWA) and boat speed, assuming a logarithmic profile over the sea surface, with a roughness length $z_0 = 0.2$ mm (Flay, 1996a);
- length of shrouds, and trimming lines from the running rigging manually measured for each run; concerning the backstay, the measured tension is used as input;
- structural mechanical properties either given by the sail maker or measured for each rig item (Augier et al., 2012);
- boat attitudes and speed: in the first approach, trim, heading and heel angles are set to the measured values and fixed in the

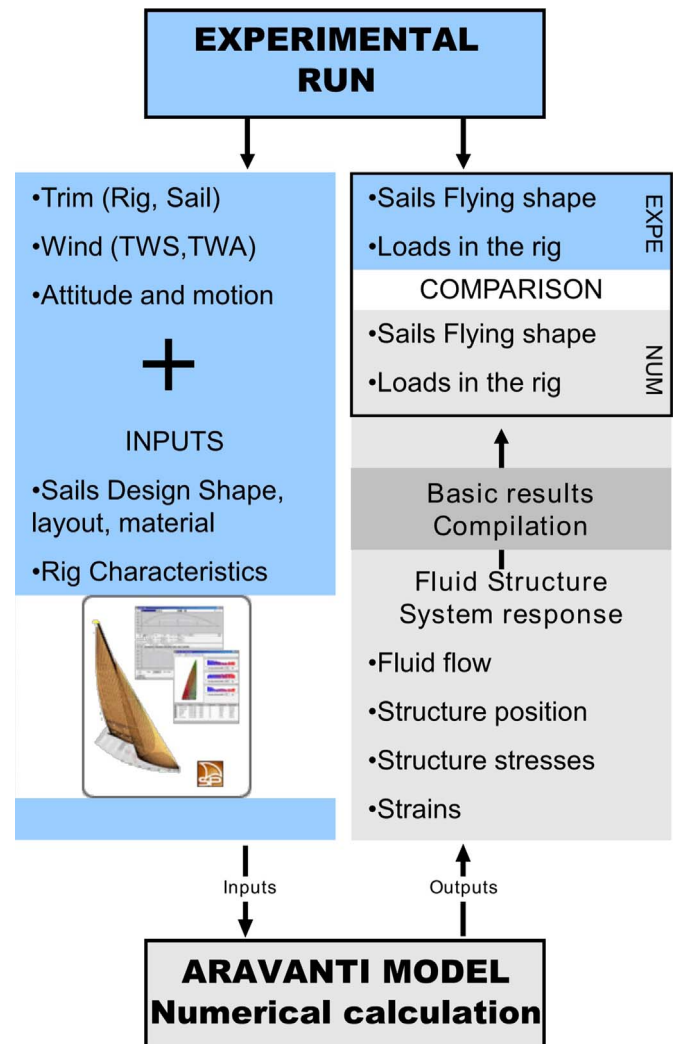


Fig. 3. Method for numerical calculation representing an experimental situation and experimental validation.

simulation; in the second approach described in Section 6, the heel angle is not fixed but is an additional degree of freedom in the structural solver, and the FSI iteration loop converges to balance heeling and righting moments.

The comparison of experimental and simulation results is made on the flying shape of the sails and the loads in the rig (and the heel angle in the second approach).

4. Effects of trimming on flying shape of the sail

The flying shapes of the sails are recorded for different cases of trim consisting in changing the jib and mainsail sheeting car position on the travellers, in constant sailing conditions.

4.1. Jib car position

Three different jib car positions on the longitudinal traveller were tested (illustrated in Fig. 4): the position #9, 5 cm aft from the reference position #10, positions #11 and #12, respectively 5 cm and 10 cm in front of the reference position #10. Position #9 is used to flatten the jib in case of stronger breeze. Positions #11 and #12 are used to increase the camber in order to get more power in the jib in case of light winds or waves. When the car

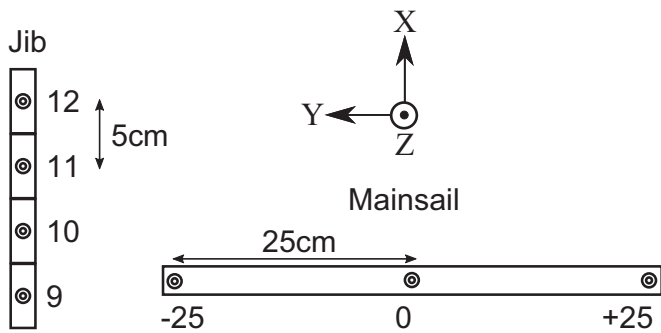


Fig. 4. Positions of the jib and mainsail traveller.

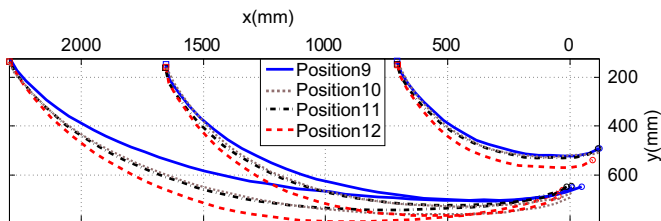


Fig. 5. Jib stripes for different jib car positions, from #9 (aft) to #12 (forward).

position was changed, the jib sheet was adjusted for the best trim.

Fig. 5 shows the jib shape for each case. When the car is moved forward, the camber is higher especially for the lower part of the sail where the camber increases from 11% at position #9 to 17% at position #12. The measured effects on the volume of the sail correspond to the evolution desired by sailors described previously. Note that the twist is not much affected, but this is because the main reference used by the trimmer during these runs is to align the jib leech with the same mark on the first spreader, resulting in a constant twist between stripes 2 and 3. The higher sail camber is related to the observed increase in heel (from 22° to 25°) and in forestay load (by 300 N).

4.2. Mainsail car position

The mainsail flying shape is presented for three positions of the main car on the transverse traveler: position 0 on the yacht centerline, position +0.25 at 0.25 m to leeward, position -0.25 at 0.25 m to windward (Fig. 6). Contrarily to what was done during the jib car tests presented in the previous subsection, the main sheet was not changed during these 3 cases. The position of the main car is used to alter the sheeting angle, in order to point to an angle closer to the wind when the car is moved to windward, or to increase boat speed when the car is moved to leeward. As can be seen on the measured mainsail shapes, the camber and draft are not affected by adjusting the car's position, but only the sheeting angle and twist vary. Hence, trimming the main car results in rotating aerodynamic sections around the mast. However, when the

car is moved 0.5 m to windward (from position +0.25 to position -0.25), the sail's trailing edge is moved to windward by only 0.19 m on stripe 1, by 0.05 m on stripe 2, and to leeward by 0.05 m on stripe 3. This reveals that the sail is more twisted even if the sheet length remains the same, due to higher aerodynamic loading stretching the leech. As the main car is moved to windward (from position -0.25 up to +0.25), the measured boat speed decreases from 6.1 kn down to 5.9 kn, the AWA decreases from 26° to 23° and heel angle increases from 18° to 21°. The recorded sailing data confirms the expected trends desired by sailors.

The information on the flying shape of the sails measured as a function of trim not only corresponds to the common observations done by sailors when trimming but also enables a real quantitative analysis of the evolution of the aerodynamic profiles resulting from these adjustments and the FSI behavior. Sail makers and trimmers could use the measured values in their optimization process.

5. Backstay trimming – experimental numerical comparison

The effect on sails shape of the backstay tension is now studied and a numerical–experimental comparative analysis is performed. The cases presented here correspond to two upwind port side tack runs of 7 s duration. During the first run, the backstay is trimmed for sailing upwind in the prevailing wind according to an experienced sailor (backstay ON). For the second run, the backstay is released (backstay OFF) when other parameters are fixed, thus the main sheet length remains the same. Table 1 gives the averaged measured parameters used as inputs to the simulation for each case.

5.1. Flying shape

Fig. 7 shows the superposition of photographs from the experimental test with the computed sails shape after convergence of the FSI simulation. The rig and flying shape of the sails from experiments and simulation are in very good agreement. The numerical stripes are defined as cross sections of the predicted sails shape with planes at constant heights in the boat frame (heeled plane). These numerical stripes do not exactly match the physical experimental stripes taped on the sails as the latter are not exactly at constant height in the boat frame. Hence, numerical and experimental stripes are not exactly superimposed in Fig. 7 even if the 3D sails' shapes are the same. More quantitative assessment can be made thanks to the stripe parameters.

Figs. 8 and 9 give the evolution of geometrical parameters of the stripes for the jib and the mainsail with the backstay tension ON. Concerning the jib, tightening the backstay increases the draft for an almost constant camber, increases the twist and decreases the entry angle. Effects on the mainsail are to decrease camber and increase the twist, particularly in the higher sections. These observations are consistent with the common knowledge of sailors

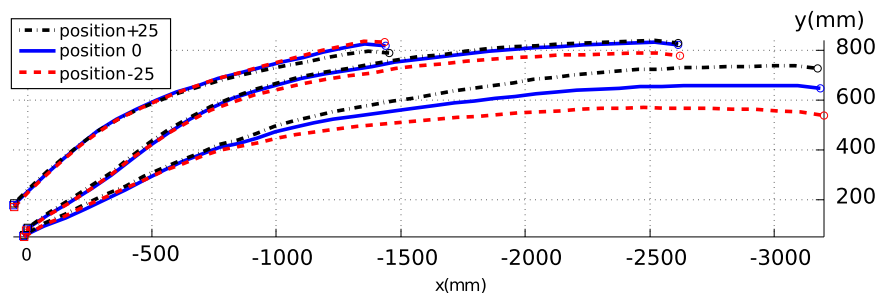


Fig. 6. Mainsail stripes for different mainsail car positions (-0.25 cm is for the leeward position and +0.25 cm for the windward position).

Table 1

Numerical input parameters for backstay cases, corresponding to experimental conditions.

Backstay case	ON	OFF
Heel angle ϕ ($^\circ$)	20.7	25.3
Boat speed (kn)	6.02	5.85
AWS (kn)	17	17.5
AWA ($^\circ$)	27	30
Backstay load (N)	1957	770

and related to increasing the mast bend and decreasing the forestay sag, resulting in flattening the sails and twisting them more to allow pointing to a higher wind angle and reducing heel. These trends are well resolved by the FSI simulations. The experimental setup used in this work allows the effects of backstay tension to be quantitatively measured, and the simulation tool enables one to predict them along with the associated flying shape of the sails. Furthermore, the superposition of simulation results on recorded pictures shown in Fig. 7 allows a display in augmented reality, as in this example showing the strains in the sails, a very useful piece of information for sail designers.

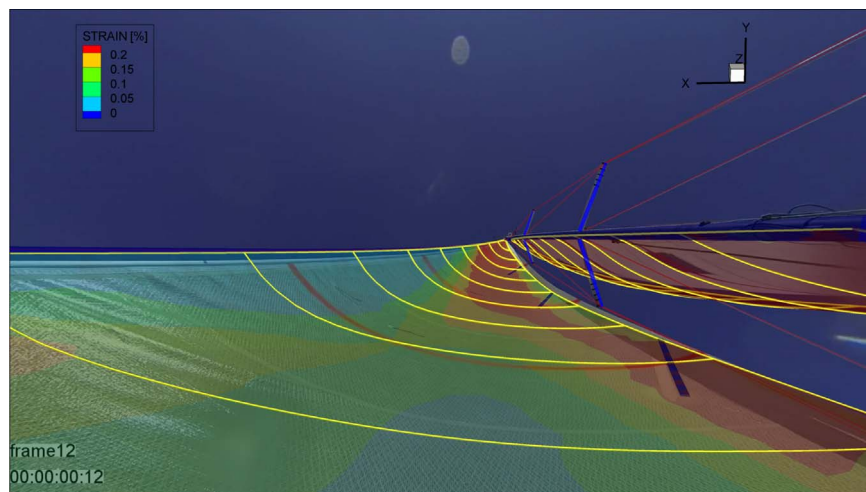
5.2. Load comparison

The loads in the rig are shown in Fig. 10 from the experimental tests and the simulation, in both cases with backstay ON and OFF. Good overall agreement is found between the measured and predicted loads, and their variation with the backstay tension is well resolved. In general, loads are increased when the backstay is released – except for the case of the forestay – showing higher aerodynamic loads due to fuller sails.

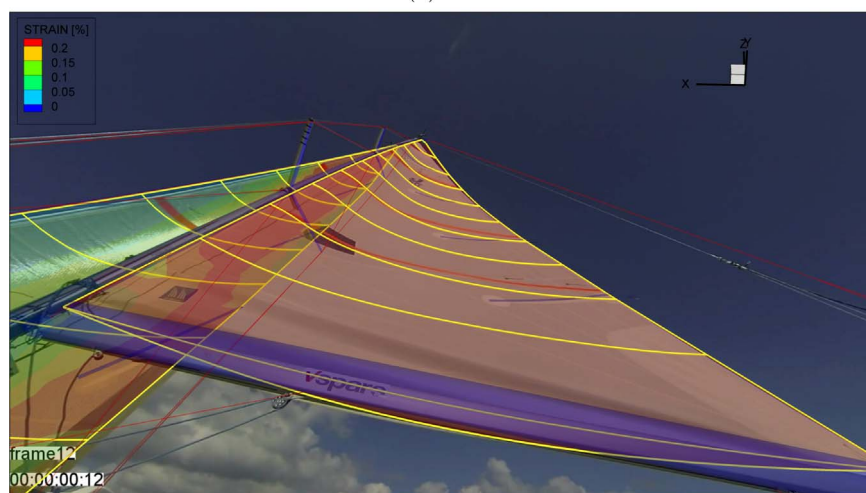
When the backstay is eased, the loads in the rig, and particularly in the V1 shroud, are overestimated in the simulation (Fig. 10). This indicates that aerodynamic forces are overestimated by the model – excess of 800 N on all measured loads for backstay OFF, default of only 7 N for backstay ON – and particularly on the upper part of the sail. Indeed, due to lack of twist, the upper part of the sail has a greater angle of attack and may be subjected to a separated flow. This flow separation is not modelled by the inviscid flow solver and induces an overestimation of the load transferred to the shrouds.

5.3. Limit of the inviscid approach

The inviscid fluid approach used in this study gives accurate



(a) Jib



(b) Mainsail

Fig. 7. Position of rig and sails from FSI simulation (in bright colors) superimposed on the experimental pictures, in the case backstay ON. The color field on the sails surface represents the strain in the fabric. (For interpretation of the references to color in this figure caption, the reader is referred to the web version of this paper.)

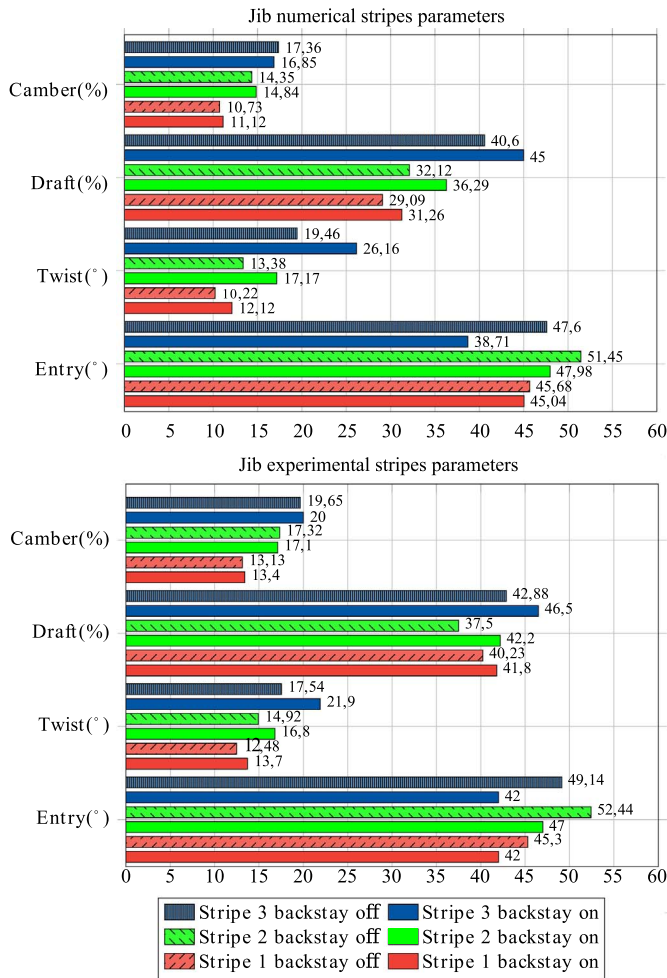


Fig. 8. Jib experimental and numerical stripe parameters.

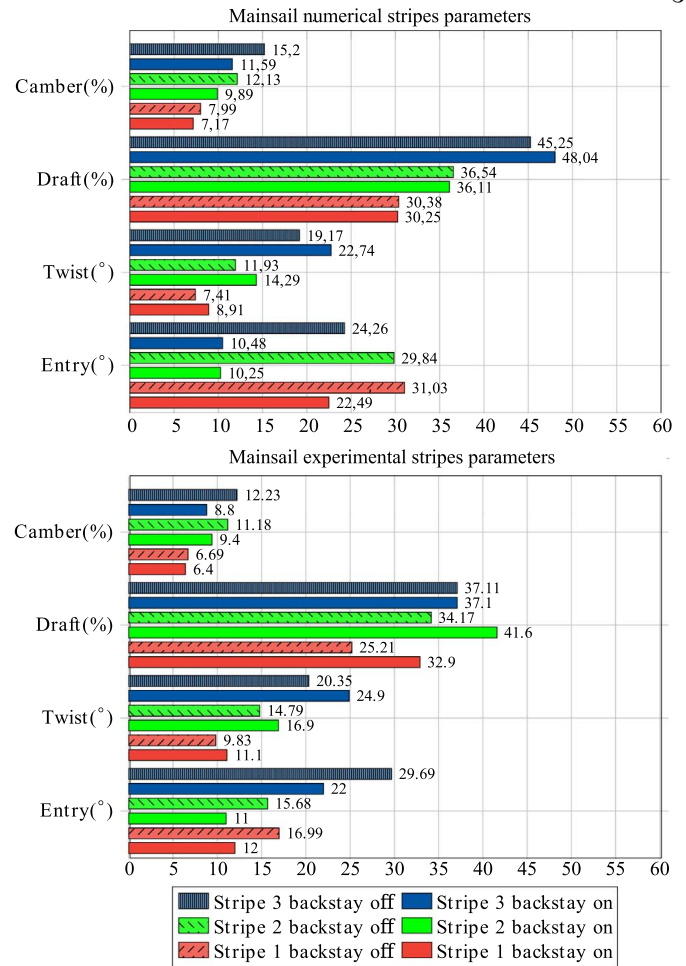


Fig. 9. Mainsail experimental and numerical stripe parameters.

numerical results with a considerably shorter simulation time compared to RANS models. This potential flow approach is proven here to be very useful and adapted to the described condition backstay ON. Nevertheless, the inviscid approach is limited to cases where the flow can be considered fully attached, a consequential hypothesis that needs to be checked. In upwind sailing with flat and twisted sails such as the presented backstay ON case, this is mostly the case, but it is known that there are situations where flow separation is significant even in upwind sailing, particularly in light wind conditions when the sails are fuller and not twisted much (Sacher et al., 2015; Viola et al., 2013). The sails top sections are particularly prone to flow separation. In the second case backstay OFF, sails are fuller and much less twisted. One may wonder whether the flow remains attached to the suction side of the sails, particularly on the highest sections, and consequently whether the potential flow approach is still valid. If the real flow is significantly detached, a potential flow simulation would overestimate the aerodynamic lift by considering a fully attached flow. The next section presents a simple testing process to assess whether the potential flow aerodynamic forces are realistic by checking the heeling balance.

6. Free heel simulation

While previously presented simulation results were obtained with a fixed heel angle (measured in the experiments), an

upgraded version of the model is now applied with the heel angle as an extra degree of freedom in the structural solver. Indeed, the whole deformable structure resolved in the FSI loop is now free to rotate around a given axis defined by the yacht's center of gravity and its centerline. The righting moment as a function of the heel angle is an input to the FSI model, given by a hydrostatic analysis of the hull, and the FSI loop converges to the heeling balance between heeling (M_x) and righting (R_m) moments. The static righting moment table is computed with the in-house hydrostatic solver Grinnaert (2010), based on the geometry of the J80 yacht hull, previously measured by photogrammetry. The hydrostatic model gives the righting arm GZ as a function of the heel angle, and the righting moment R_m of the yacht including the crew's weight $m = 300$ kg can be calculated as:

$$R_m = (GZ(\phi) \times \Delta + L \times m \times \cos \phi)g$$

with $L = 1.2$ m for the moment arm of the crew's weight and $\Delta = 1400$ kg for the boat's displacement. Fig. 11 shows the computed heeling moment compared to the balance curve $R_m = M_x$. While the fixed-heel simulation result is very close to the balance curve in the backstay ON case, the backstay OFF case is relatively far from the heel balance. When the simulation is run with free heel, balance is reached at an angle $\phi = 31.8^\circ$, which is much higher than the experimental one ($\phi = 25.3^\circ$, see Table 1). It is clear from this result that the heeling moment, and thus the whole aerodynamic force are overestimated by the potential flow solver, and one can infer that the inviscid assumption is not verified in the backstay OFF case. Moments and angles for the free heel

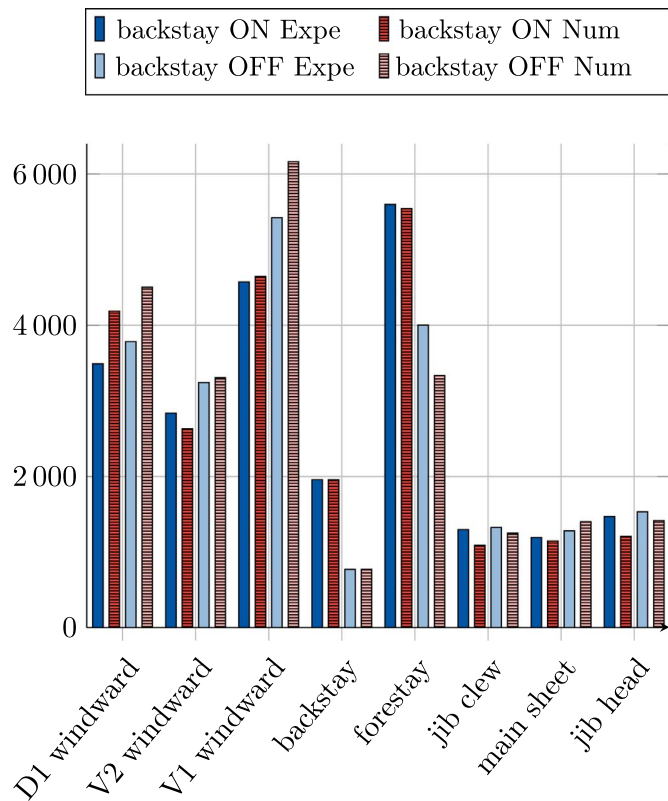


Fig. 10. Numerical and experimental comparison of the loads in the rig for backstay ON and OFF.

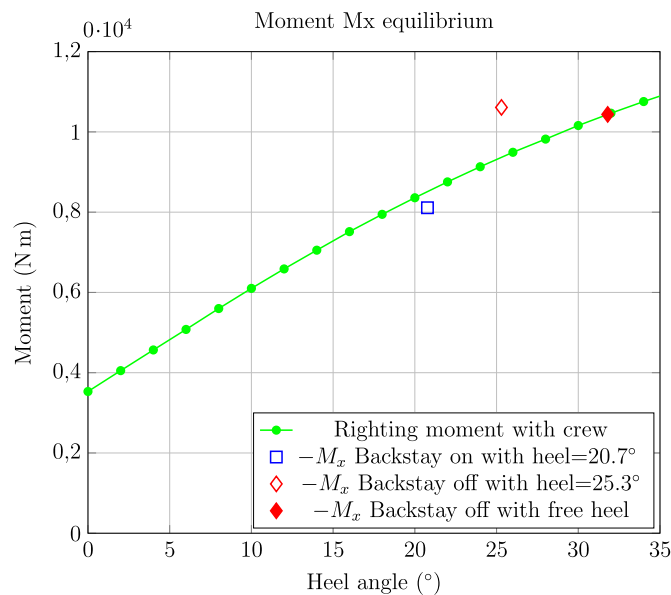


Fig. 11. Heeling moment and balance with righting moment.

Table 2
Output parameters for free heel calculation.

Backstay case, free heel	ON	OFF
F_x driving force (N)	529	632
M_x heeling moment (N m)	8512	10436
Heel angle at equilibrium (°)	20.8	31.8
Heel difference with the imposed heel model (%)	0.6	25.7

simulations are summarized in Table 2.

Considering the balance of the boat in heel is a significant improvement in the simulations to spot cases where the inviscid approach is invalid. Indeed, the user must check the values of righting and heeling moments as they will underline if the computed aerodynamic force is realistic or not. In this particular case backstay OFF, the fact that $R_m \neq M_x$ would warn the user that the simulations are not realistic and that the results from the potential flow solver are inaccurate. In addition, from a trimming optimization point of view, the simulation result shows that the yacht is overpowered and that sails should be flattened and further twisted. More generally, the free heel simulation is a very useful option which allows the user to input the yacht's heel into a Velocity Prediction Program (VPP), which fits closer to the classical design process.

7. Conclusions

This study presents full-scale tests of a yacht sailing upwind with investigation of the flying shape of the sails resulting from different trims. Effects of different trims are quantitatively characterized using the on-board instrumentation system and VSPARS for measuring the flying shape for different trims of the jib and main sheet (adjusting the car position on travelers) and for different values of the backstay tension. The aeroelastic deformation of the sail, i.e. the resulting flying shape of the sails, is accurately predicted in the simulations with the FSI model ARAVANTI – Finite Element structural solver coupled to a potential flow solver. The flying shape of the sails and aerodynamic loads measured at full-scale in real sailing conditions and their prediction with fast FSI simulations are interesting inputs for sail or rig designers, naval architects and sailors (e.g. Shankaram et al., 2002). Inviscid fluid solvers are convenient and commonly used for upwind sailing in the early design stages because they allow a very fast investigation compared to viscous models. However, even in upwind situations, flow separation on the sails may be non-negligible and the challenge for the designer is to determine when the results from potential flow models are no longer reliable. Running a RANS model to check this is very time consuming (Graf et al., 2014). A new feature in the ARAVANTI model with the heel angle as an extra degree of freedom enables the reliability of the potential flow assumption to be rapidly assessed by checking the balance of heeling and righting moments. Indeed, for a separated flow, a potential flow solver would overestimate the aerodynamic forces. It would in particular predict an excessive heeling moment. This simple criterion allows us to detect when significant flow separation occurs without running a full RANS calculation. Moreover, when the fully attached flow assumption is valid, accurately predicting the heel angle is very useful for performance prediction. Future work will be devoted to developing models to account for flow separation as a correction to the inviscid fluid model, based on investigations with RANS CFD.

Acknowledgments

The authors are grateful to Nke, VSPARS and K-EPSILON Company for continuous collaboration. The authors would like to warmly thank Alcino Ferreira for his review and remarks. This work was supported by Brest Métropole Océane, Région Bretagne (SAD-V1-2014) and the European Union's Seventh Framework Programme (FP7/2007-2013) under REA grant agreement no. PCOFUND-GA-2013-609102 (PRESTIGE-Campus France).

References

- Aubin, N., Augier, B., Bot, P., Hauville, F., Sacher, M., 2016. Wind tunnel investigation of dynamic trimming on upwind sail aerodynamics. In: Proceedings of the 22th Chesapeake Sailing Yacht Symposium. Annapolis, USA.
- Augier, B., 2012. Experimental Studies of FSI on Soft Membrane. Application to Yacht Sails (Ph.D. thesis). Université de Bretagne Occidentale.
- Augier, B., Bot, P., Hauville, F., Durand, M., 2012. Experimental validation of unsteady models for fluid structure interaction: application to yacht sails and rigs. *J. Wind Eng. Ind. Aerodyn.* 101, 53–66.
- Augier, B., Hauville, F., Bot, P., Aubin, N., Durand, M., 2014. Numerical study of a flexible sail plan submitted to pitching: hysteresis phenomenon and effect of rig adjustments. *Ocean Eng.* 90, 119–128.
- Braun, J.B., Imas, L., 2008. High fidelity CFD simulations in racing yacht aerodynamic analysis. In: Proceedings of the 3rd High Performance Yacht Design Conference. Auckland, New-Zealand.
- Fiddes, S.P., Gaydon, J.H., 1996. A new vortex lattice method for calculating the flow past yacht sails. *J. Wind Eng. Ind. Aerodyn.* 63, 35–59.
- Flay, R.G.J., 1996a. A twisted flow wind tunnel for testing yacht sails. *J. Wind Eng. Ind. Aerodyn.* 63, 171–182.
- Flay, R.G.J., 1996b. *J. Wind Eng. Ind. Aerodyn.* (Special issue on sail 63(1)), vii–ix.
- Fluck, M., Gerhardt, F.C., Pilate, J., Flay, R.G.J., 2010. Comparison of potential flow-based and measured pressure distributions over upwind sails. *J. Aircr.* 47 (6), 2174–2177.
- Fossati, F., Bayati, I., Orlandini, F., Muggiasca, S., Vandone, A., Mainetti, G., Sala, R., Bertorello, C., Begovic, E., 2015a. A novel full scale laboratory for yacht engineering research. *Ocean Eng.* 104, 219–237.
- Fossati, F., Mainetti, G., Malandra, M., Sala, R., Schito, P., Vandone, A., 2015b. Offwind sail flying shapes detection. In: Proceedings of 5th High Performance Yacht Design Conference. Auckland, New-Zealand.
- Fossati, F., Muggiasca, S., 2009. Sails aerodynamic behavior in dynamic condition. In: Proceedings of the 19th Chesapeake Sailing Yacht Symposium. Annapolis, USA.
- Fossati, F., Muggiasca, S., 2012. An experimental investigation of unsteady sail aerodynamics including sail flexibility. In: Proceedings of 4th High Performance Yacht Design Conference. Auckland, New-Zealand.
- Gerhardt, F.C., Flay, R.G.J., Richards, P., 2011. Unsteady aerodynamics of two interacting yacht sails in two dimensional potential flow. *J. Fluid Mech.* 668, 551–581.
- Graf, K., Hoeve, A.v., Watin, S., 2014. Comparison of full 3D-RANS simulations with 2D-RANS/lifting line method calculations for the flow analysis of rigid wings for high performance multihulls. *Ocean Eng.* 90, 49–61.
- Grinnaert, F., 2010. Calcoque: Hydrostatic Calculation Software. URL (<http://www.calcoque.fr/>).
- Hochkirch, K., Brandt, H., 1999. Fullscale hydrodynamic force measurement on the Berlin sailing dynamometer. In: 14th Chesapeake Sailing Yacht Symposium. Annapolis, pp. 33–44.
- Lasher, William C., Sonnenmeir, James R., 2008. An analysis of practical RANS simulations for spinnaker aerodynamics. *J. Wind Eng. Ind. Aerodyn.* 96, 143–165. <http://dx.doi.org/10.1016/j.jweia.2007.04.001>.
- Lasher, William C., Sonnenmeir, James R., Forsman, David R., Tomcho, Jason, 2005. The aerodynamics of symmetric spinnakers. *J. Wind Eng. Ind. Aerodyn.* 93, 311–337. <http://dx.doi.org/10.1016/j.jweia.2005.02.001>.
- Le Pelley, D.J., Modral, O., 2008. V-SPARS: a combined sail and rig shape recognition system using imaging techniques. In: 3rd High Performance Yacht Design Conference. Auckland, New-Zealand, pp. 57–66.
- Löhner, R., Haug, E., Michalski, A., Muhammad, B., Drego, A., Nanjundaiah, R., Zarfam, R., 2015. Recent advances in computational wind engineering and fluid structure interaction. *J. Wind Eng. Ind. Aerodyn.* 144, 14–23. <http://dx.doi.org/10.1016/j.jweia.2007.04.001>.
- Masuyama, Y., 2014. The work achieved with the sail dynamometer boat “Fujin”, and the role of full scale tests as the bridge between model tests and CFD. *Ocean Eng.* 90, 72–83.
- Mausolf, J., Deparday, J., Graf, K., Renzsh, H., Böhm, C., 2011. Photogrammetry based flying shape investigation of downwind sails in the wind tunnel and at full scale on a sailing yacht. In: 20th Chesapeake Sailing Yacht Symposium. Annapolis, USA.
- Michalski, A., Gawanat, B., Gelenne, P., Haug, E., 2015. Computational wind engineering of large umbrella structures. *J. Wind Eng. Ind. Aerodyn.* 144, 96–107.
- Milgram, J.H., Peters, D.B., Eckhouse, N., 1993. Modelling IACC sail forces by combining measurements with CFD. In: Proceedings of the 11th Chesapeake Sailing Yacht Symposium. Annapolis, USA.
- Motta, D., Flay, R.G.J., Richards, P.J., Le Pelley, D.J., Deparday, J., Bot, P., 2014. Experimental investigation of asymmetric spinnaker aerodynamics using pressure and sail shape measurements. *Ocean Eng.* 90, 104–118.
- Roux, Y., Durand, M., Leroyer, A., Queutey, P., Visonneau, M., Raymond, J., Finot, J., Hauville, F., Purwanto, A., 2008. Strongly coupled VPP and CFD RANSE code for sailing yacht performance prediction. In: Proceedings of the 3rd High Performance Yacht Design Conference. Auckland, New-Zealand.
- Sacher, M., Hauville, F., Bot, P., Durand, M., 2015. Sail trimming FSI simulation – comparison of viscous and inviscid flow models to optimise upwind sail trim. In: Proceedings of 5th High Performance Yacht Design Conference. Auckland, New-Zealand.
- Shankaram, S., Doyle, T., Gerritsen, M., Gianluca, I., Jameson, A., 2002. Improving the design of sails using CFD and optimization algorithms. In: Proceedings of High Performance Yacht Design Conference. Auckland, New-Zealand.
- Viola, I.M., Bot, P., Riotte, M., 2013. Upwind sail aerodynamics: a RANS numerical investigation validated with wind tunnel pressure measurements. *Int. J. Heat Fluid Flow* 39, 90–101. <http://dx.doi.org/10.1016/j.ijheatfluidflow.2012.10.004>.
- Viola, I.M., Flay, Richard G., 2010. Full-scale pressure measurements on a Sparkman and Stephens 24-foot sailing yacht. *J. Wind Eng. Ind. Aerodyn.* 98, 800–807. <http://dx.doi.org/10.1016/j.jweia.2010.07.004>.
- Yoo, J., Kim, H.T., 2006. Computational and experimental study on performance of sails of a yacht. *Ocean Eng.* 33, 1322–1342. <http://dx.doi.org/10.1016/j.oceaneng.2005.08.008>.

1.3 Conclusions

In this chapter general definition used in the sailing field and different elements that can be compared between numerical and experimental results have been presented. Some of these elements were used in the numerical-experimental comparison achieved in the article previously shown. It indicates several aspects to take into account in the sail design process:

- the righting moment equilibrium is essential to ensure that the simulation corresponds to a realistic case. It requires the hydrodynamic information on the yacht or at least its hull hydrostatic curve. In the design process the numerical free heel model is therefore a great improvement.
- potential flow theory as used in ARAVANTI tends to over-estimate the aero-forces generated when the camber increases considering that the flow stays attached till the sail leech. In such a situation, detachment is not predicted by the numerical model used.
- evolution of running rigging adjustments such as the position of jib roller of mainsail traveller have been recorded in experimental cases. Flying shape evolution trends have been provided and can be used as references for future numerical simulations.

From this study, several perspectives and development aspects for the sail design process can be drawn:

- the prediction of detached flow would be an important information in order to determine if a viscous fluid model is required or not to model the situation. As suggested by the article, the fact that the righting moment (obtained thanks hydrodynamic computation) and heeling moment (which aerodynamic part is provided by the code) equilibrium is not achieved for a known quasi-steady given sailing condition (heel, boat speed, wind conditions, trim adjustments) is a relevant indicator. In this case the heeling moment is certainly overestimated and the attached flow hypothesis is no longer accurate.
- new developments directly on ARAVANTI or the use of different tools applied on a computed stripe flying shape could give first an indication about detachment. For example, a computed stripe shape can be tested under a code such as XFoil ([Drela, 1989]) to predict if its shape for the considered wind flow conditions (speed and direction) might be submitted to detached flow. The prediction could also be based on extracted 2D stripes which shape can be compared to experimental database where detachment is related to the Reynolds, the AoA and the camber.
- if detached flow is indicated, sail designer should either investigate a viscous model or adapt the sail trim

This chapter has shown that the comparison between numerical and experimental data improves the use of the numerical design tools for sail designers. It provides a simple analysis criterion which indicates when the non-viscous flow hypothesis is not any more relevant for upwind sailing situations. For downwind sailing situation where significant detached flow occurs, the use of a FSI tool with a viscous model is required but it still requires validation especially under unsteady situations.

However unsteady situations measured at full-scale -mostly generated by wind variation in force and direction- remain challenging to model accurately as the wind information suffers a large uncertainty in those conditions. Furthermore the differences between the cause and the effect among the data variations remain sometimes complex. Therefore a generated and controlled unsteadiness applied to a sail system in a more steady flow condition might be a more relevant approach to study FSI unsteady phenomenon on sails. This is the topic of the part II of this thesis presenting unsteady situations measured during wind tunnel experimental campaigns.

Part II

Wind tunnel experimental campaigns

This part presents experimental campaigns carried out in the Twisted Flow Wind Tunnel of the Yacht Research Unit at the University of Auckland in both upwind and downwind configurations. The first campaign carried out in 2015 includes both upwind and preliminary downwind tests in static and dynamic trimming situations. Three mainsails and two spinnakers were tested. This campaign was achieved during a three month secondment with seven testing weeks for a total of 103 hours of running wind tunnel tests. The second campaign carried out in 2016 is focused on downwind situations where four spinnakers were studied. It was achieved during a three month secondments, with five testing weeks representing 83 hours and 42 minutes of running wind tunnel tests. As part of this thesis work, the author has been in charge of the design and logistic coordination, of the tests achievement, participating to all tests along the two campaigns and has been carrying on the post-processing and analysis of the results. The goals of these experimental campaigns are:

- to improve knowledge and understanding of some dynamic and unsteady behaviour in sails aerodynamics.
 - study of pumping: forced unsteady effects of dynamic trimming on upwind conditions
 - study of curling: natural unsteady effects on downwind conditions
- to provide results on sail performance according to their design shapes for upwind sails and panelling or materials for downwind sails
- to provide a database of steady and unsteady wind tunnel experimental results that can be used for numerical-experimental comparisons in steady and unsteady conditions

Chapter 2 as a first chapter of this part presents the wind tunnel facility and the system apparatus. The second chapter (chapter 3) presents results on upwind sails in static conditions where a two-parameter optimisation is carried out. Then a dynamic trimming oscillation, known as pumping, is tested around a reference situation or around the optimum point found previously, to measure possible improvements in the yacht performance. The last chapter of this part -chapter 4- presents results for downwind configurations. First the effects of the natural curling unsteadiness of a spinnaker is studied. Then the effects of different parameters on the curling frequency are presented. Lastly the effects of curling on the time series of forces are presented in a representative case.

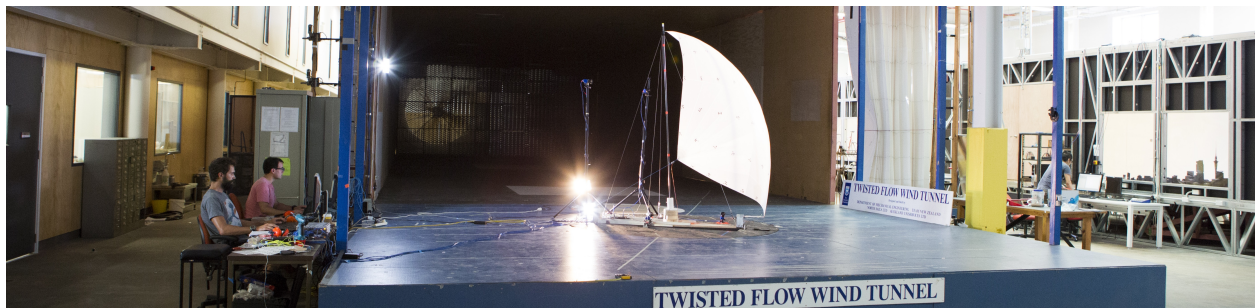


Figure 1.4 – TFWT during 2016 experimental campaign. Credit: the UoA, YRU of the Faculty of Engineering, TFWT.

Wind tunnel experimental set-up

Contents

2.1	Wind tunnel description	50
2.1.1	Twisted Flow Wind Tunnel description	50
2.1.2	Model presentation	55
2.1.3	Model windage	58
2.2	Wind tunnel flow mapping	60
2.2.1	Wind tunnel flow mapping	60
2.2.2	Wind profile	63

This chapter describes the Twisted Flow Wind Tunnel (TFWT) facility initially developed by [Flay and Vuletich, 1995, Flay, 1996]. Its geometry and different equipment used to carry out the two experimental campaigns in 2015 and 2016 are introduced. Some general measurements about the flow field and wind profile are also presented.

2.1 Wind tunnel description

This section describes the TFWT facility and its different elements used to accomplish the experimental campaign.

2.1.1 Twisted Flow Wind Tunnel description

The TFWT designed by [Flay and Vuletich, 1995, Flay, 1996] presented in Fig. 2.1 is an open circuit wind tunnel powered by two three-meter diameter four-bladed fans. Each of them is powered by a 45 kW electric motor. First the different elements shown in Fig. 2.1 are introduced. Then the geometry of the testing area downstream of the twisting vanes section location is described.

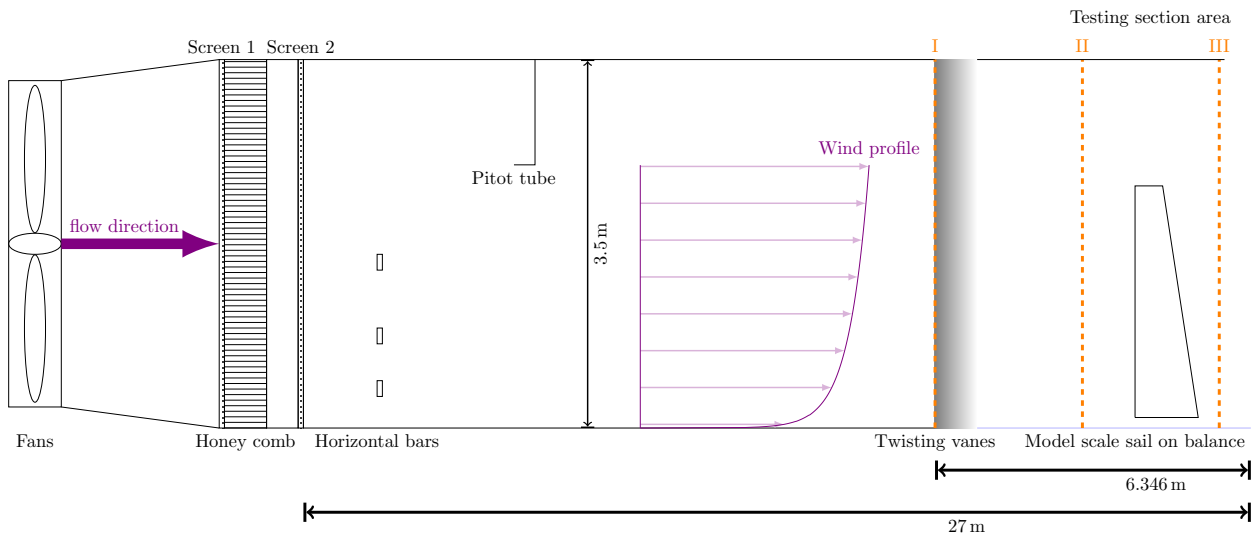


Figure 2.1 – Side view cross-section of the TFWT. The test section geometry is further described in Fig. 2.3a. Sections I, II and III indicate the flow mapping sections: I for the outlet section of the enclosed part of the wind tunnel, II for the close upstream flow conditions, III for the close downstream flow conditions (wake). The horizontal length is not scaled to the actual length of the TFWT.

2.1.1.1 Twisted Flow Wind Tunnel components

The different elements used to generate and adjust the flow are presented in their respective relative position from the fans to the testing section (as shown in Fig. 2.1). For more details on the different components the reader is referred to [Hansen, 2006].

Fans generate the flow speed. The 2 fans are turning in clockwise direction when facing the flow. Flow properties and speed are detailed in the flow measurement section. A honey comb and screens are used to straighten the flow and to get relevant level of turbulence in appropriate flow directions. Additional wood structures (cube on the floor, triangular spikes) can be added to adjust this turbulence intensity level but they were not used during the experimental campaigns presented in this studies.

Bars can be used to adjust the velocity profile. Up to six rectangular bars with different

projected areas can be used, and their respective vertical positions can be changed in order to adjust the wind tunnel velocity profile. For every different AWA the vertical positions of the bars are supposed to be adjusted to accurately reproduce the full scale wind profile. No bars were used in this study. The natural wind tunnel velocity profile was measured for future numerical experimental comparisons and can be directly used as an input parameter for such simulations.

The TFWT was the first wind tunnel to ever reproduce the twist phenomenon required to accurately model the twisted flow in downwind situations. The twist due to the combined effect of yacht velocity on the natural wind gradient is shown in Fig. 1.2. Vanes powered by electronic winches along the vanes span can be used to adjust the twist angle along the altitude above the floor. Because twisted flow might be harder to achieve on a FSI CFD simulation than a straight flow, initially it was decided not to use the vanes. Vanes were used only in very few tests in the 2015 wind tunnel campaign to observe the difference between twisted and untwisted downwind configurations. In these cases the twisted velocity profiles were measured, providing data for future numerical experimental comparison. No vanes have been used for the 2016 experimental campaign.

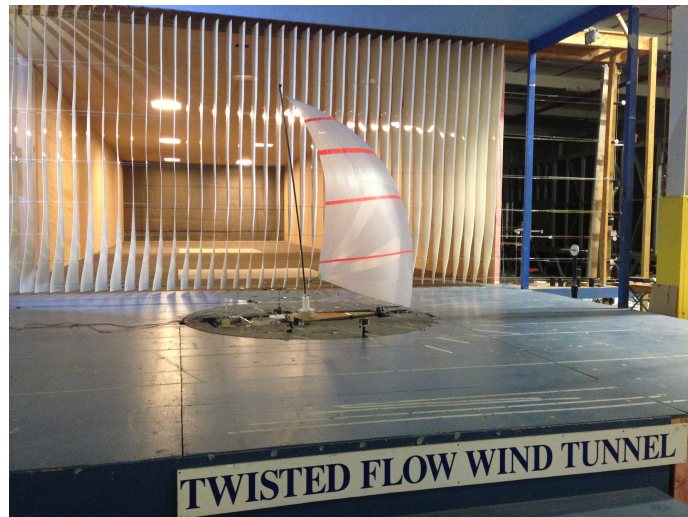
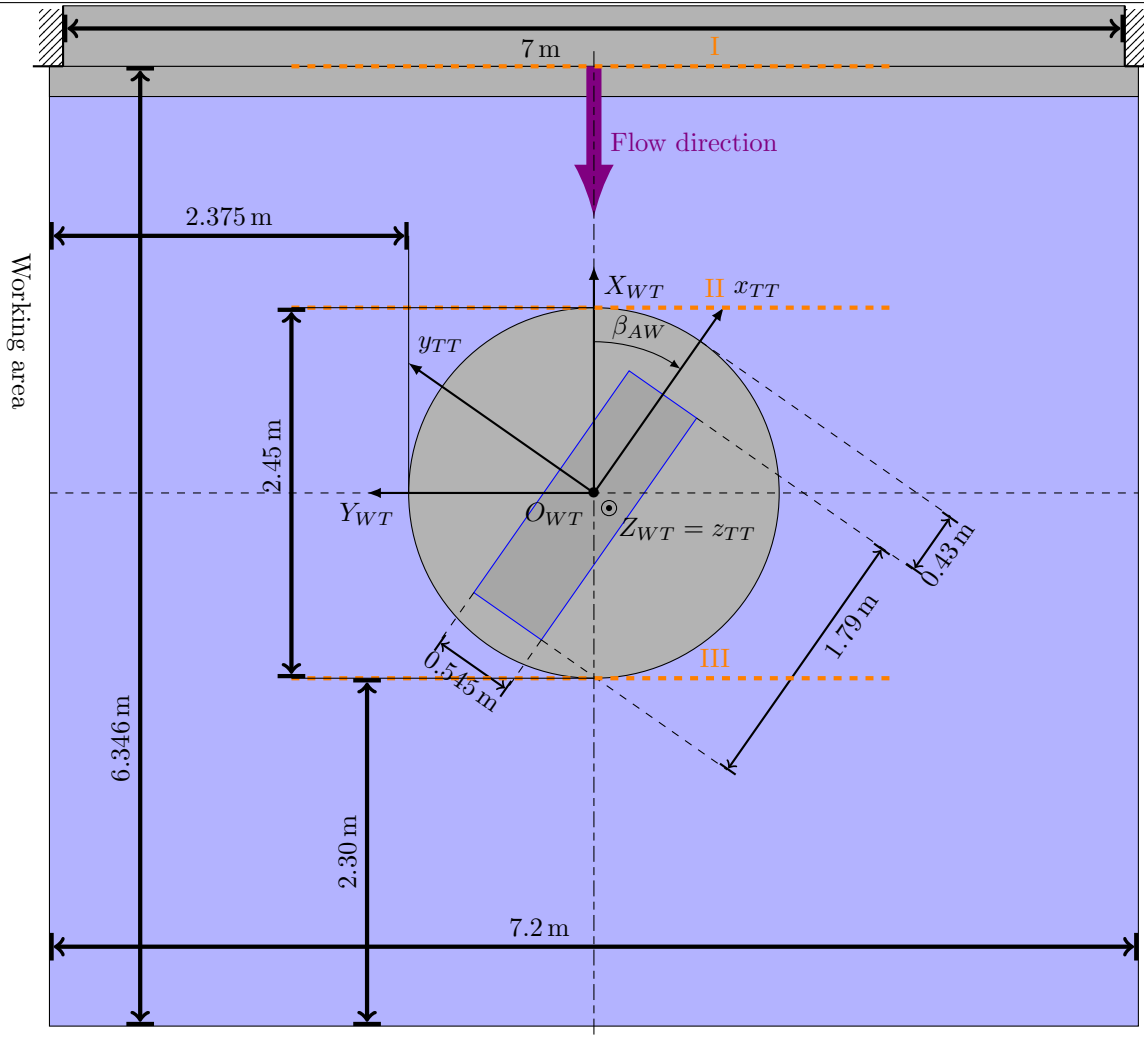


Figure 2.2 – TFWT vanes upstream of the test section, shown here with a downwind sail.

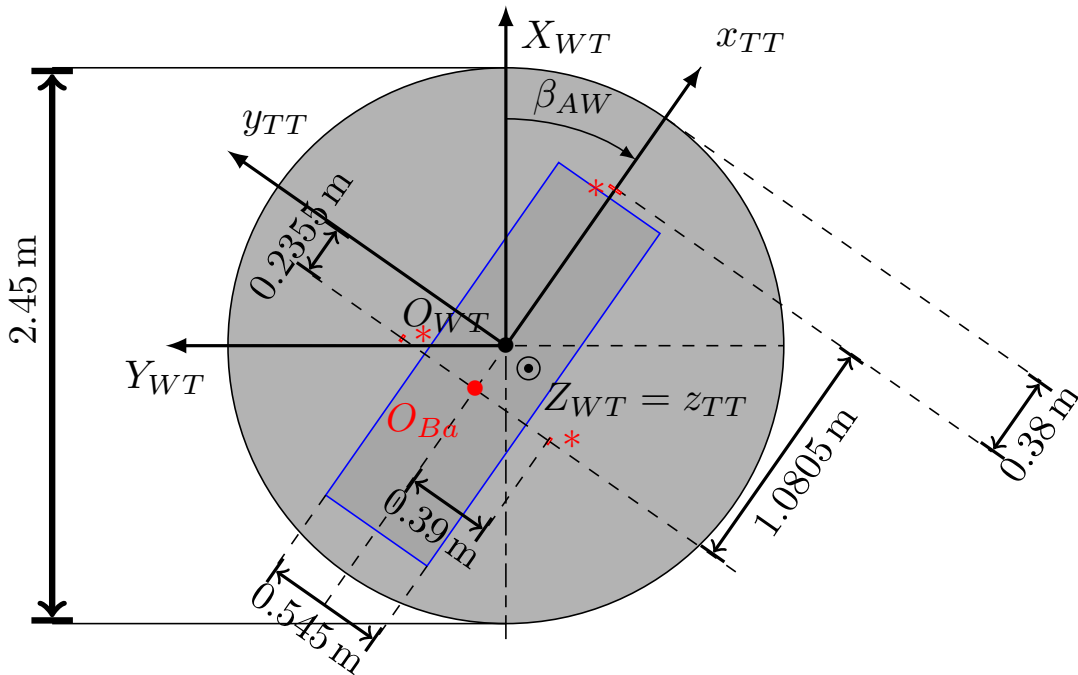
2.1.1.2 Facility geometry

A detailed description of the wind tunnel can be found in [Flay and Vuletich, 1995, Flay, 1996, Hansen, 2006]. Since then the enclosed section originally about 24-meter long has been extended, but the open testing section has been kept identical. The 7.2 m wide 3.5 m high open section geometry is described in Fig. 2.3a. The model yacht is put onto the force balance located on the turn table corresponding to the dark circle shown in Fig. 2.3a). The turn table is used to adjust the AWA applied to the model (β_{AW}). Here the tested model is always on portside tack.

The reference point of the geometry of the wind tunnel frame is the point O_{WT} defined as the centre of the circular turn table. The center of the balance frame O_{Ba} is defined as the intersection of the centreline of the model and the line joining the two back holding points of the balance.



(a) Top view of the geometry of the testing open section area of the TFWT (right part on Fig. 2.1). I, II and III correspond to the location of the flow mapping sections.



(b) Geometry of the turn table area of the TFWT. Stared * red rectangles represent the balance arms holding the model frame. Blue rectangle represents cavity where usually the model hull is located, which can be filled with water to make the flow around model more representative of actual sailing conditions.

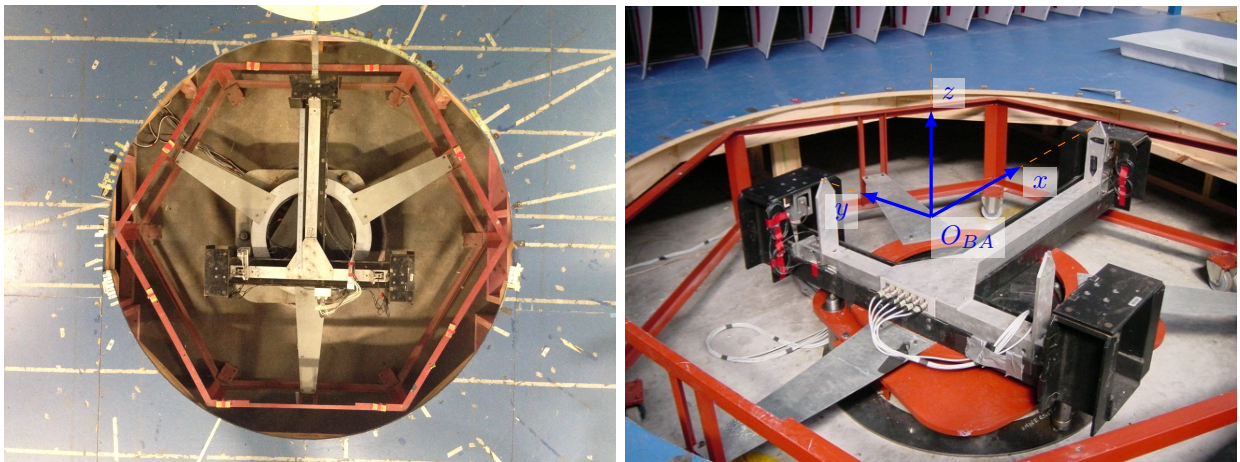
Figure 2.3 – Geometry of the TFWT.

2.1.1.3 Measuring the aerodynamic coefficients: force balance, dynamic pressure and load sensor

All data presented here are recorded with a sampling frequency of 200 Hz. Synchronized recording of force balance and Pitot tube measurements is achieved by the native wind tunnel acquiring system architecture. Synchronization of additional data such as the the motor position, the sheet load sensor, the camera timing was evaluated thanks calibration experiments and did not show significant delay.

The force balance holds the triangular steel frame through three points. Their location is described in Fig. 2.3b. The model is built around this triangular frame. The deformation of the balance three holding parts are measured by six linear variable differential transducers which provide the six voltage signals $[X1 Y1 Y2 Z1 Z2 Z3]$ used to compute the different forces and moments applied on the model using the equation given by Eq. 2.1. In this equation the calibration matrix is obtained after a calibration procedure based on the use of a dedicated pyramidal frame with known loads applied in known directions.

$$\begin{aligned}
 [X1 Y1 Y2 Z1 Z2 Z3] \times & \begin{bmatrix} -0.04 & 6.187 & 17.469 & 0.032 & 0.067 & 0.483 \\ -6.533 & 0.161 & -0.729 & -0.121 & -0.184 & 0.05 \\ -0.077 & 0.017 & -0.492 & -5.547 & -14.529 & -15.557 \\ -1.007 & 0.017 & -0.716 & -6.861 & 1.514 & 0.641 \\ 0.013 & 0.946 & 2.96 & -0.06 & -8.605 & 8.464 \\ -3.103 & -0.414 & 21.129 & 0.008 & -0.084 & 0.105 \end{bmatrix} \\
 & = [F_y F_x F_z M_y M_x M_z] \quad (2.1)
 \end{aligned}$$



(a) Balance view from the ceiling without the turn table surface (b) Balance from wind tunnel area without the turn table surface, adapted from [Hansen, 2006]

Figure 2.4 – TFWT force balance.

Because the TFWT was recently moved before starting the 2015 experimental campaign, which was the first tests to use the balance in this new location, a verification of the calibration of the balance was performed in order to check the accuracy of the calibration matrix provided. More details are provided in App. C.

A Pitot tube is positioned near the ceiling in the enclosed section to measure the dynamic pressure q_{Pitot} . Its position is 12.14 m upstream of the section II shown in Fig. 2.3a along the wind tunnel central axis. Its height is about 2.545 m high above the floor. The distance to the ceiling is 0.935 m. Its external diameter about 8 mm. A zeroing step is first required measuring the signal without flow velocity. For this thesis, the Pitot dynamic pressure is used to compute dimensionless force coefficients as described above. Some corrections for possible relevant comparison are discussed and can be found on App. C.

Force coefficients can be computed to get dimensionless results. In the wind tunnel configuration the instantaneous force and load coefficients are computed using Eqs. (2.2), (2.3) where $\overline{q_{Pitot}}$ is the time averaged dynamic pressure during a run, S the associated sail area and i stand for x, y, z, obj .

$$C_{F_i}(t) = \frac{F_i(t)}{\overline{q_{Pitot}}S} \quad (2.2)$$

$$C_{F_{sheet}}(t) = \frac{F_{sheet}(t)}{\overline{q_{Pitot}}S} \quad (2.3)$$

The averaged values of these quantities are defined using Eqs. 2.4 and 2.5

$$C_{F_i} = \overline{C_{F_i}(t)} = \frac{\overline{F_i(t)}}{\overline{q_{Pitot}}S} \quad (2.4)$$

$$C_{F_{sheet}} = \overline{C_{F_{sheet}}(t)} = \frac{\overline{F_{sheet}(t)}}{\overline{q_{Pitot}}S} \quad (2.5)$$

Every run was recorded over 30 s with a sampling frequency of 200 Hz. Another recording duration is stated when different. When the dynamic trimming device was used with a given frequency, the averaged value is determined over an entire number of oscillation periods of the force coefficient signals. Uncertainty in the force coefficient measurements are ± 0.05 on C_{F_x} , ± 0.06 on C_{F_y} and ± 0.08 on C_{F_z} . The $F_{sheet}(t)$ signal was measured using a load sensor described below.

A load sensor was used to record the load through the mainsail or spinnaker sheet. Its measuring range is 50 N. The static accuracy of the load sensor was checked several times and is described in Tabs. D.1 and D.2 given in App. D. Its uncertainty is about $\pm 0.36\%$ of the measured value. However, its signal when recording time series was quite noisy, even in the best connection conditions.

2.1.2 Model presentation

The model is based on a wood platform screwed to a triangular steel frame directly attached to the balance arms. Remotely controlled winches are screwed on the wood platform. Several elements were recorded:

- the force balance signals sampled at 200 Hz
- the sheet load signal sampled at 200 Hz
- stepper motors angular positions in both static and dynamic configurations. This information can be used to compute the sheet length in the different situations. The sample frequency was not constant but about 100 Hz which was enough to compute maximum dynamic trimming oscillations of 5 Hz
- a laser and LED signals was used to synchronise the measured data and videos.
- dedicated cameras recorded the flying shape using either the VSPARS system ([Le Pelley and Modral, 2008]) for upwind tests or photogrammetry techniques for the downwind tests. For the 2015 experimental campaign, Gopro cameras were used to record the videos. The Frame per Second (fps) rate was not constant and videos were recorded on each camera individually. Synchronisation was achieved during post processing using the laser signal. For the 2016 experimental campaign, four HD triggered cameras were used providing time stamped pictures. The recording architecture still required synchronisation with the data using the laser signal.
- some other cameras were also used to provide data about rig tracking. These cameras suffered a low fps rate and quality. This information can be used to compute mast head or boom end trajectory.
- the water tank represented by a rectangle in the turning table in Fig. 2.3b, which can be seen in Fig. 2.5, was not filled with water for the experimental campaigns presented in this thesis.

Tab. 2.1 summarizes the main differences between the different model configurations for the mast geometry and the platform location. These differences are shown in Fig. 2.5.

Configuration name	Mast description	Platform position	Windage measurement	
			without mast	with mast
2015	14 mm diameter carbon fibre mast with rear rail	Low	Yes	Yes
2016	20 mm diameter circular carbon fibre mast	High	No	Yes

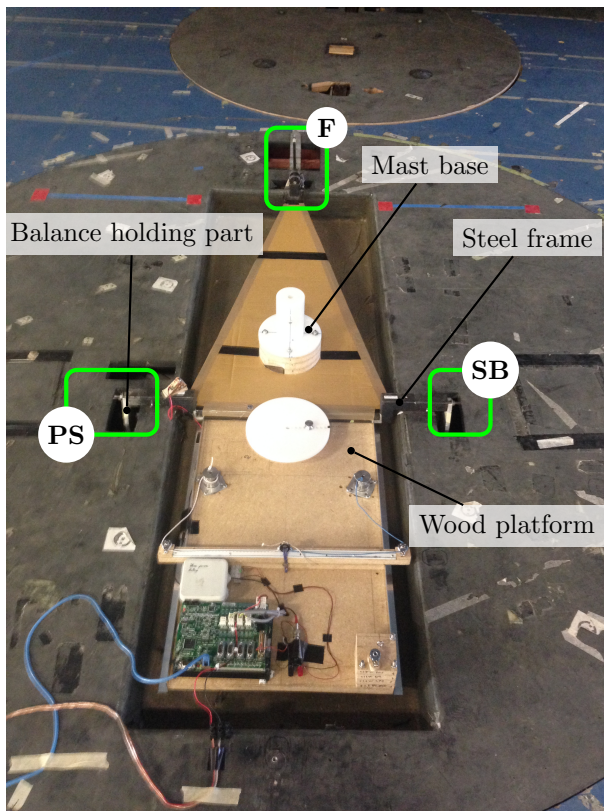
Table 2.1 – Model configuration for windage measurements.

Tab. 2.2 provides first elements of presentation of the sails used on the model.

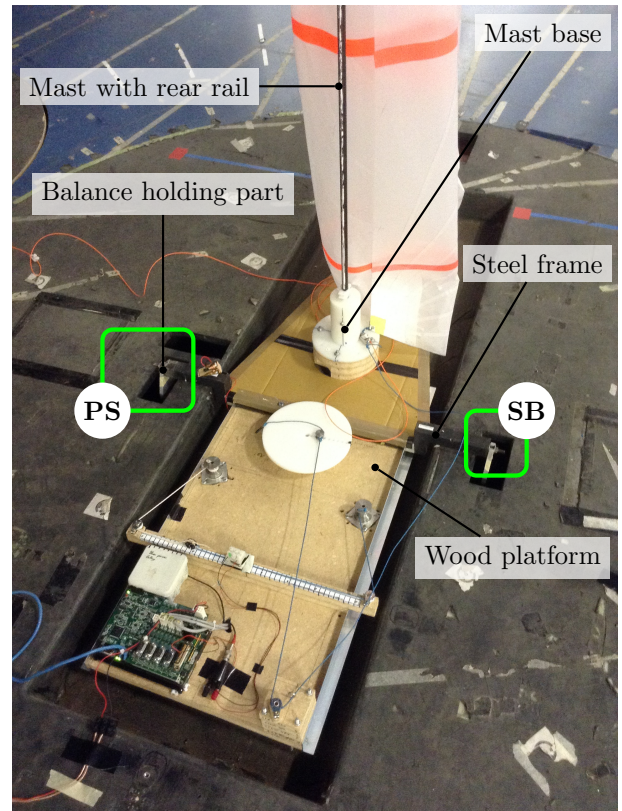
Sail	Scale	Area S (m ²)	Flow velocity range (m s ⁻¹)	Representative chord (m)	Reynolds range (10 ⁵)
Upwind mainsail	1:13	0.959	3.5	S/h : 0.475	1.07
Downwind spinaker	1:4.6	3.187	2.49 to 4.36	\sqrt{S} : 1.79	2.85 to 4.99

Table 2.2 – Summary of the sails tested on the model. More information on upwind sails can be found in Chap. 3, more information on downwind sails can be found in Chap. 4. Complementary information about cloth are provided in App. G.

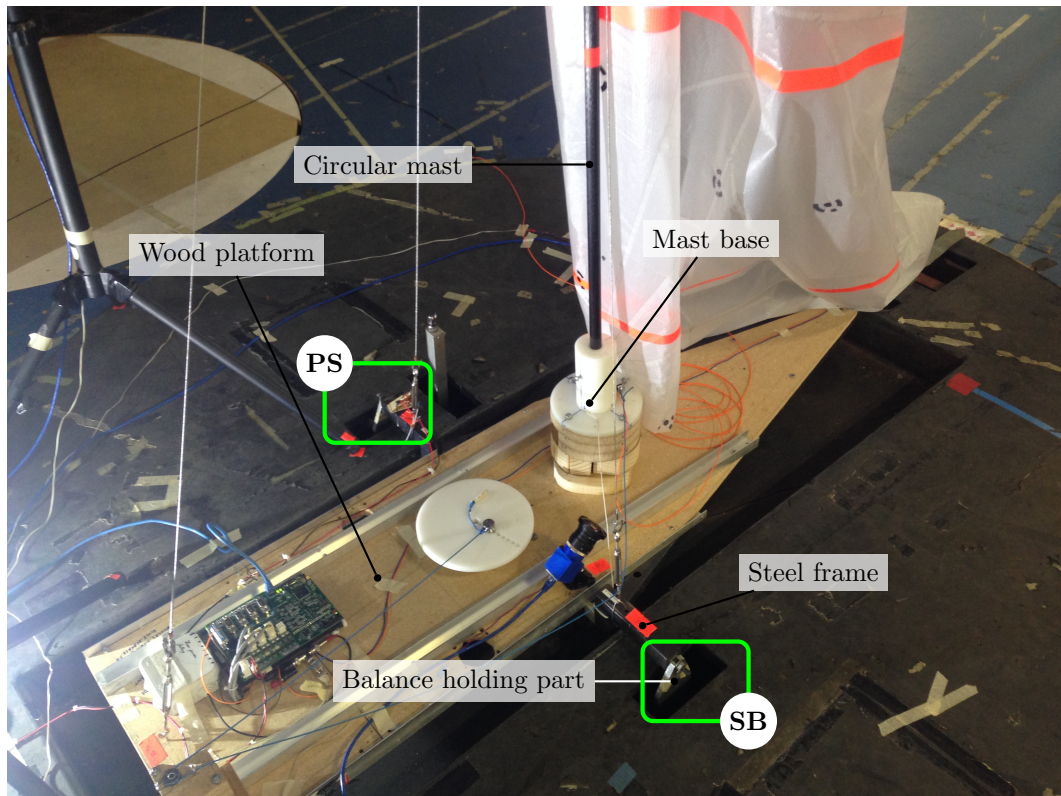
Wind tunnel experiments can however suffer from different effects such as blockage effect for large model sails as measured in [Mompó Laborda, 2009] or scale effect as described in [Hansen, 2006]. For instance the Reynolds number most of the time cannot be identical between full-scale and wind tunnel testing. Wind tunnel testing nevertheless remains a relevant modelling tool to study what can occur at full-scale, especially if it is strengthened by good quality flow measurements and experimental conditions.



(a) Model frame without mast during 2015 experimental campaign.



(b) Model frame with mast during 2015 experimental campaign.



(c) Model frame with mast during 2016 experimental campaign.

Figure 2.5 – Platform configuration. (**PS**) for balance portside holding arm, (**SB**) for balance starboard side holding arm and (**F**) for balance front holding arm location. Figs. 2.5b and 2.5c are presented in downwind configurations with the dynamic trimming system.

2.1.3 Model windage

In most cases, studies focus on the aerodynamic forces generated by the sails only. However, the balance system also measures the model windage due to the rig and the platform. To achieve relevant comparisons between different cases it is required to also measure this windage under the same conditions than the sail testing. Moreover, some numerical simulation models do not take into account the part due to the rig in the model flow. For instance, ARAVANTI FSI model does not take into account the mast in the flow calculation and ARA-FINETM/Marine can either model the rig in the fluid or not. Windage measurement is also important in order to evaluate its contribution to the aerodynamic forces measured in the tests. Windage is evaluated separately from any sail test results. Some results are presented here on the measured windage without a sail. These windage results can be then subtracted from the aerodynamic coefficients presented in this thesis to provide information without the rig and platform.

Fig. 2.6 describes the windage results for the different configurations as presented in Tab. 2.1 and shown in Fig 2.5. It is interesting to notice that in the 2015 configuration with a mast (shown on Fig. 2.5b), there is a range where the drive force is positive for an AWA lower than 90° which was not expected as the drag force is supposed to generate only negative component on the drive force projection direction. This is probably due to the lift force from the mast which is not circular (a rail for the mainsail luff is located on the rear part of the mast as shown in Fig. E.1 in App. E). For windage measurements without mast or with a circular mast, the change of sign of the drive force windage component is given as expected for an AWA of 90°. The mast represent about half of the windage in the 2015 configuration projected on the drive force component for the two extremum AWA tested. The side force increases with the surface area configuration, which is more important in the 2016 tests. In 2016, the model was set up with a higher platform which was located in the flow stream. In 2016 (shown on Fig. 2.5c) the circular mast diameter was thicker (20 mm against 14 mm in 2015). The drive force sign changes at 90° as expected in the 2016 configuration with a circular mast section. The mast represents also the major effect of the windage. The platform shown in Fig. 2.5a is located in the lower part of the boundary layer, and is partly in the cavity of the water tank represented by a rectangle in Fig. 2.3b located in the turning table that can be seen in Fig. 2.5. The sail was removed during the windage measurements.

Eq.2.6 uses the dimensional quantities and is based on a linearity assumption for the summation of the aerodynamic forces generated by the sail and the windage (rig and platform or platform alone). In Eq. 2.7, S corresponds to the sail area (projected area of the rig and deck are considered as negligible). $q_{Pitot\ run}$ is the dynamic pressure measured with a sail and $q_{Pitot\ windage}$ is the dynamic pressure measured during windage measurement in the same configuration. Eq. 2.7 provides the windage correction to be applied to experimental measurement.

$$F_i\ without\ windage = F_i\ with\ windage - q_{Pitot\ run} \frac{F_i\ windage}{q_{Pitot\ windage}} \quad (2.6)$$

$$C_{F_i\ without\ windage} = C_{F_i\ with\ windage} - \frac{F_i\ windage}{q_{Pitot\ windage} S} = C_{F_i\ with\ windage} - C_{F_i\ windage} \quad (2.7)$$

The windage correction measurement is estimated directly in Tab. 2.3 defined by $C_{F_i\ windage} = \frac{F_i\ windage}{q_{Pitot\ windage} S}$ using S as the standard mainsail or spinnaker area for the appropriate AWA. Corrections without the mast are lower than those values, and are indicated in Fig. 2.6. Values given

in Tab. 2.3 can be used as an indicator, however they are based on a linearity assumption that is discussed. The windage is small, compared to the aerodynamic forces generated by the sail. However, the total forces with rig and sails are not exactly equal to the sum of the rig windage and the sail contribution, especially in the upwind configuration where the mast-sail interaction modifies the flow near the sail luff. This interference effect is very difficult to determine.

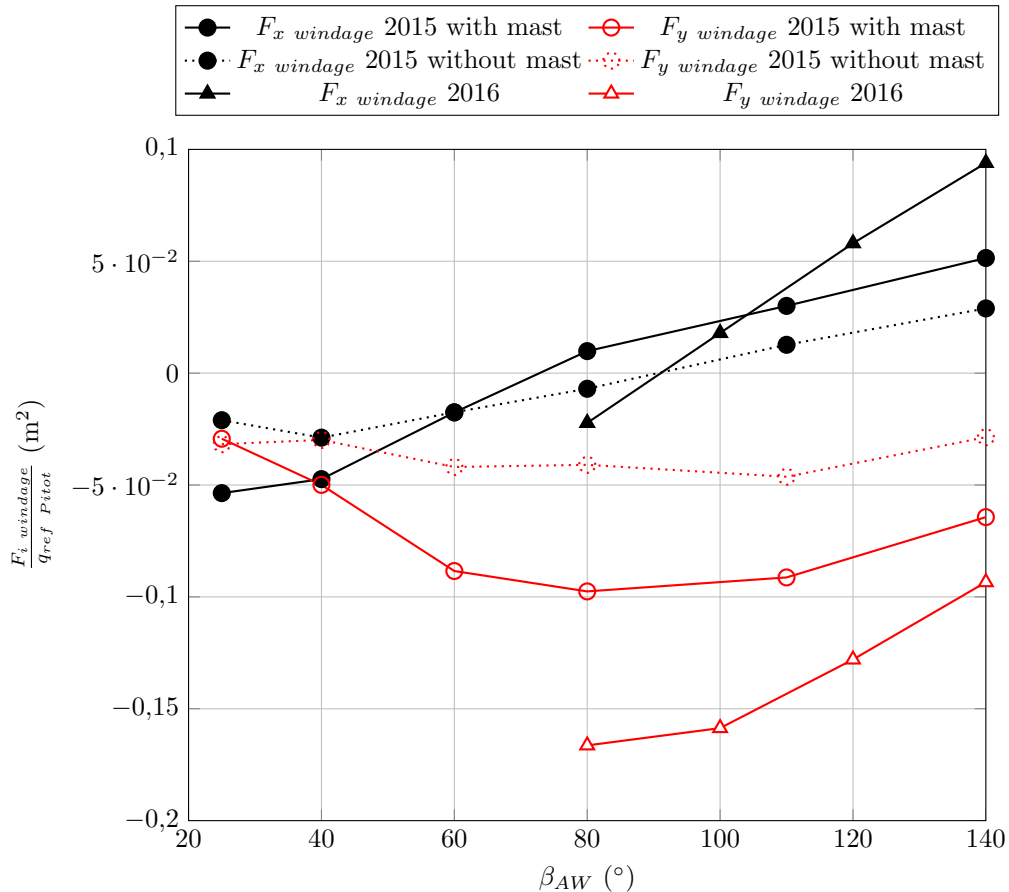


Figure 2.6 – Windage measurement for the different tested apparent wind angles. The 2015 windage measurement was done with and without the mast (windage of the platform and mast base only). The 2016 windage was measured with the mast. For windage measurement, mast was aligned with model centreline when set up.

β_{AW} (°)	$C_{F_x \text{ windage}} 2015$	$C_{F_y \text{ windage}} 2015$	$C_{F_x \text{ windage}} 2016$	$C_{F_y \text{ windage}} 2016$
25	-0.05	-0.03		
40	-0.04	-0.05		
60	-0.01	-0.09		
80	0.09	-0.1	-0.01	-0.05
100			0.01	-0.05
110	0.02	-0.1		
120			0.02	-0.04
140	0.04	-0.07	0.03	-0.03

Table 2.3 – Force coefficient correction due to windage for the different configurations with the mast. These values correspond to the values shown in Fig. 2.6 divided by the corresponding sail area for each situation.

The next section presents the wind flow measurement techniques and results.

2.2 Wind tunnel flow mapping

This section describes the different measurements done in the TFWT without the yacht model set up on the turntable. Flow information is important to firstly be able to reproduce the same experimental conditions. It is secondly required for numerical experimental comparisons where upstream measurements at the outlet section of the enclosed part can define an input to the simulation ([Fossati et al., 2008, Sacher et al., 2016]). Upstream and downstream flow measurements in sections close to the model can be compared. The instrument used for the measurement is first presented. Then three measured section results without any models are shown. Flow information with the model in the upwind and downwind configurations are presented in their associated chapters (3, 4). The last part of this section presents the central velocity profile at the exit section of the enclosed part of the TFWT for different fan frequencies, and the relationship between the fans frequency and the reference wind speed at the Pitot tube location.

2.2.1 Wind tunnel flow mapping

Flow mapping was done in three different cross flow sections of the wind tunnel:

- the first section corresponds to the outlet (exit) of the wind tunnel enclosed section represented by I in Fig. 2.3a.
- the second section is the upstream flow of the model, 1.59 m downstream of the outlet of the TFWT closed section represented by II in Fig. 2.3a. It can be used for comparisons with numerical results (this section is quite close to the model and therefore is not appropriate for being used as an inlet condition). Flow direction in this section is already affected by the upwash effect. This cross flow section is located on the windward limit of the turntable.
- the third section is the leeward flow behind the model represented by III in Fig. 2.3a, 4.04 m downstream of the outlet of the TFWT closed section and can be used for comparison with numerical results. This section corresponds to the cross section on the leeward limit of the turning table.

Refined wind tunnel flow mapping was done under three configurations:

- empty wind tunnel configuration at a reference wind speed close to 3.5 m s^{-1} measured at the Pitot tube location ($f_{fans} = 23.8 \text{ Hz}$) presented in this section
- wind tunnel with the model in the upwind configuration ($\beta_{AW} = 40^\circ$) with the standard mainsail at a reference wind speed of 3.5 m s^{-1} measured at the Pitot tube location ($f_{fans} = 23.8 \text{ Hz}$) presented further in chapter 3
- wind tunnel with the model in the downwind configuration at a reference wind speed of 3 m s^{-1} measured at the Pitot tube location ($f_{fans} = 20 \text{ Hz}$) presented further in chapter 4

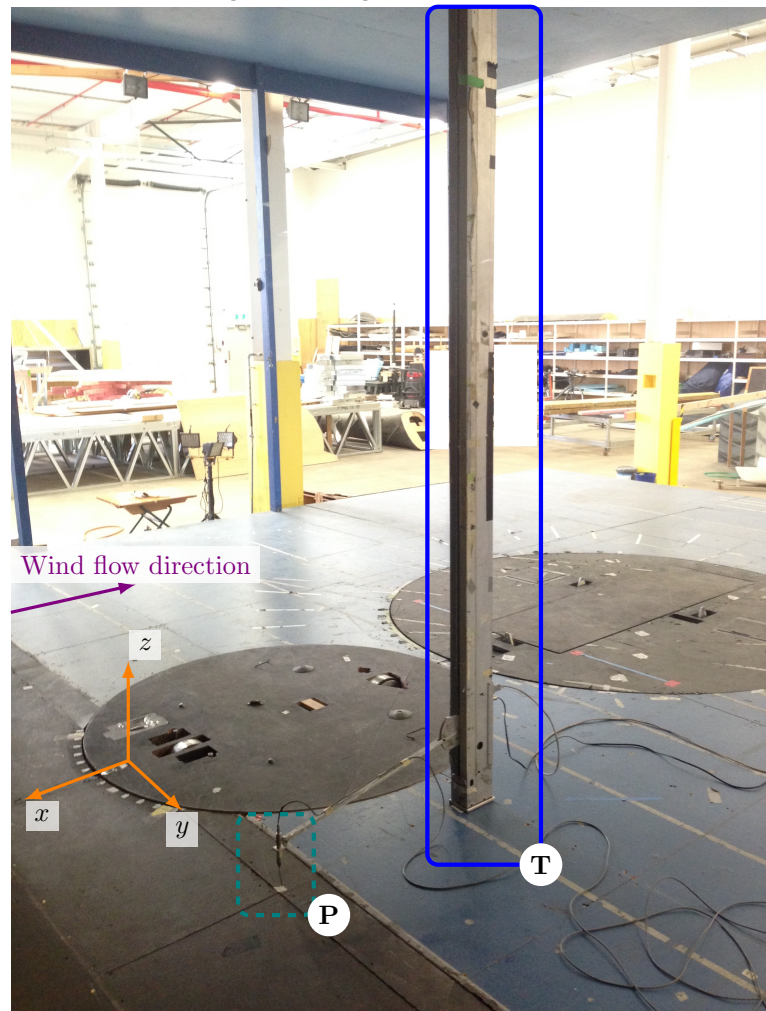
2.2.1.1 Flow measurement system

A four-hole pressure probe called a Cobra probe shown in Fig. 2.7a developed by Turbulent Flow Instrumentation company, was used to measure the velocity field in the wind tunnel (device

ID n°129). This instrument was mounted onto a vertical traverse rig with remotely controlled Z_{WT} positions, as shown in Fig. 2.7b. Its (X_{WT}, Y_{WT}) position was manually changed to different locations above the wind tunnel floor. For the empty wind tunnel configuration, one vertical profile of 12 measurements -refined within the boundary layer close to the floor- is achieved every meter along the measurement sections I, II or III. The recording time for each measurement is 30 s. Each measurement is represented by a circle in Fig. 2.8. The Cobra probe's typical accuracy given by the user's guide is $\pm 0.3 \text{ m s}^{-1}$ and $\pm 1^\circ$ for flow between 2 m s^{-1} and 100 m s^{-1} . The testing speed is at the lower part of this measuring range, which is why for low velocities the recorded data can have a lower goodness value (indication provided by the instrument representing the quality of the measured flow) especially behind a bluff body such as the spinnaker. This Cobra probe is supposed to be placed on a $\pm 45^\circ$ acceptance cone compared to the local flow direction to provide good data. Again this condition might not be achieved in the direct wake flow behind the model scale spinnaker. For more technical details the reader is referred to [TFI, 2015].



(a) Cobra probe. Magnification shows the holes where pressure is measured.



(b) Cobra probe (**P**) mounted on traverse rig (**T**) arm. The flow measurement frame is represented here on central position ($Y_{WT} = 0 \text{ m}$) of the wind tunnel at the outlet section of the enclosed part ($X_{WT} = 2.821 \text{ m}$).

Figure 2.7 – System for measuring the velocity profile and flow mapping.

2.2.1.2 Empty wind tunnel configuration

The flow mapping presented here is done without any model. A blackboard was used to cover the water tank cavity on the turntable. Fig. 2.8a shows that the flow is not perfectly symmetric and presents a small area where the velocity is slightly higher on the right side facing the flow ($Y_{WT} < 0$). This side corresponds to the flow trajectory where there is more space available for the stream to circulate in the TFWT hall. The turbulence intensity I_{uvw} in the wind tunnel above the boundary layer is mainly about 2%.

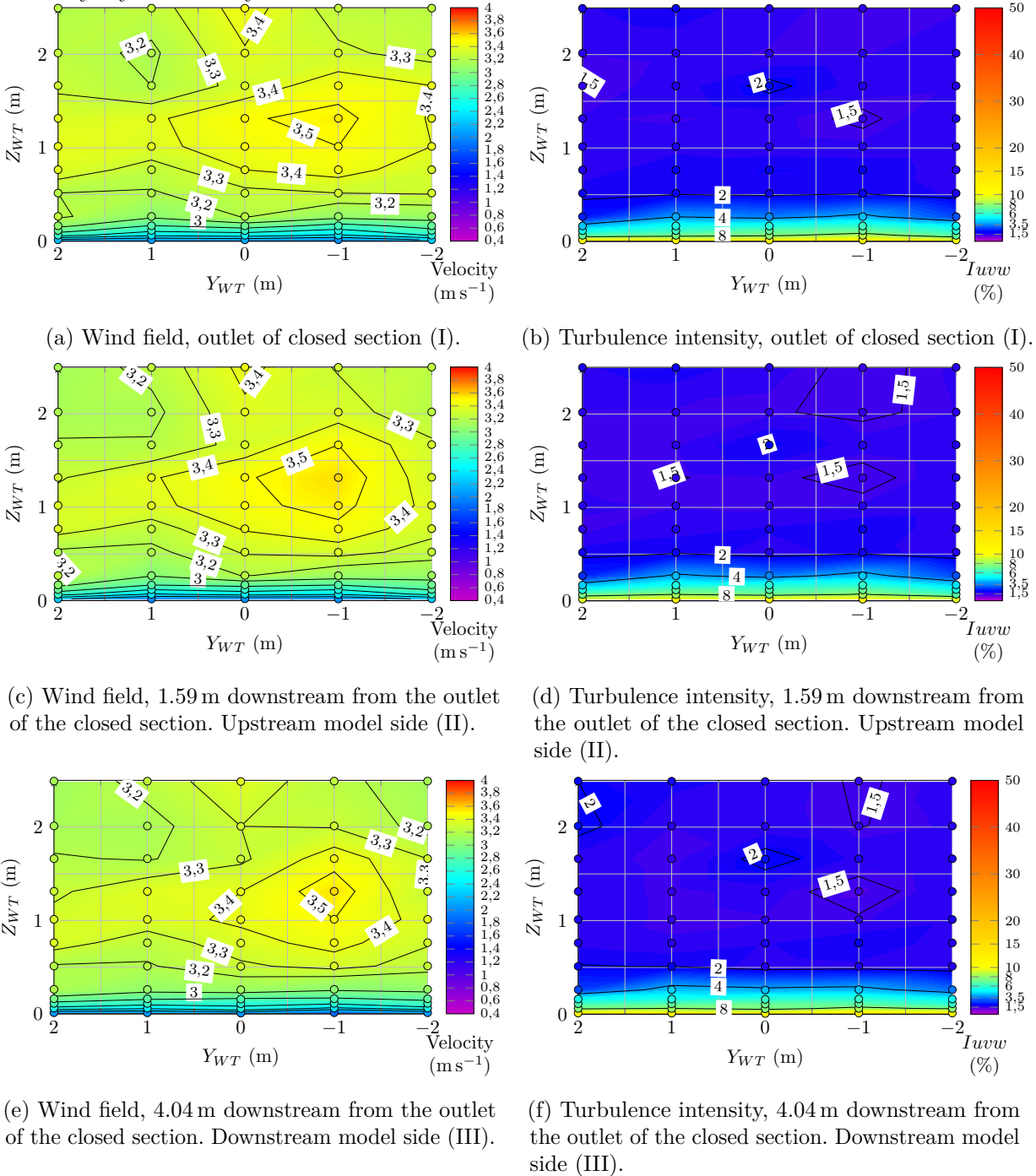


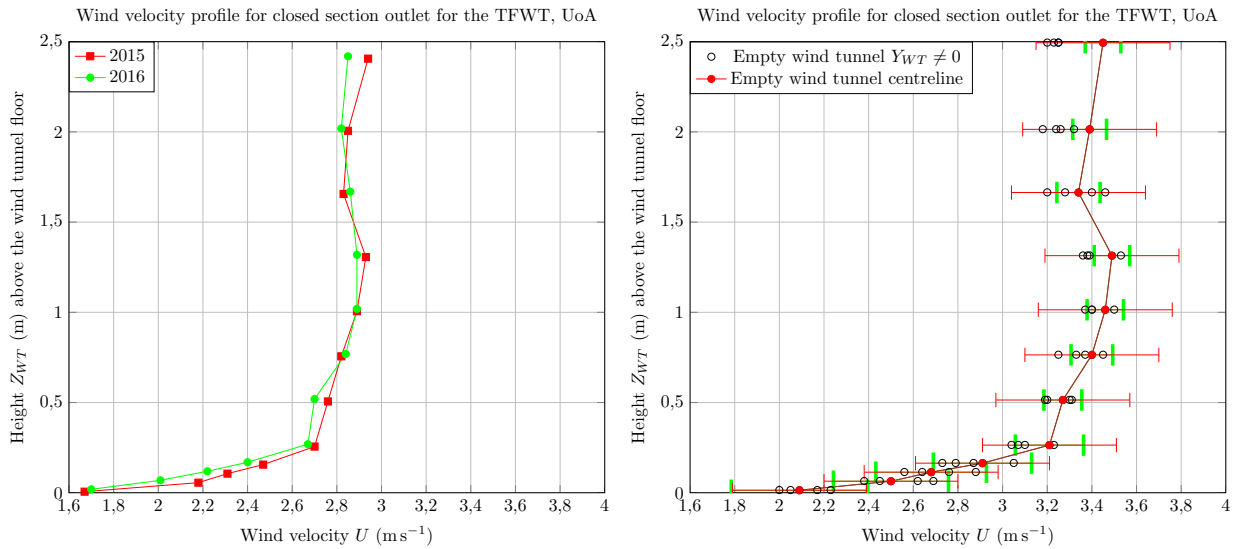
Figure 2.8 – Empty TFWT velocity field. \circ indicates location of measurement points. I, II, III sections are presented on Fig. 2.1.

2.2.2 Wind profile

Wind profile measurements at the central location of the wind tunnel floor are presented here. The first part compares this central wind profile to the other wind profiles measured at this same section in order to ensure that the central wind profile is a good representation of the entire flow mapping of this section. The second part presents more detail about the central velocity profile.

2.2.2.1 Wind profile comparison at the central location at the outlet section

Wind velocity profiles are usually measured at the central location ($Y_{WT} = 0$) of the outlet section of the enclosed part of the wind tunnel. Here are first presented the velocity profiles of the two experimental campaigns in Fig. 2.9a. In both cases the fan frequency was set up to 20 Hz. Results show a good general repeatability of the wind profile over the two experimental campaigns in 2015 and in 2016 considering that the measurement in 2015 was done with the model with spinnaker, and without any sail in 2016. Other parameters may explain the differences such as the cleaning state of the screens close to the fans, the changing environment affecting the recirculation through the wind tunnel hall (the new boundary layer wind tunnel that can be seen on right side background in Fig. 1.4 was not completed in 2015).



(a) Wind profile comparison for 2015 and 2016 for $f_{fans} = 20$ Hz. Wind profiles remain fairly close showing reasonable repeatability along time.

(b) Centreline wind profile compared to outlet section wind profile data $f_{fans} = 23.8$ Hz in empty configuration.

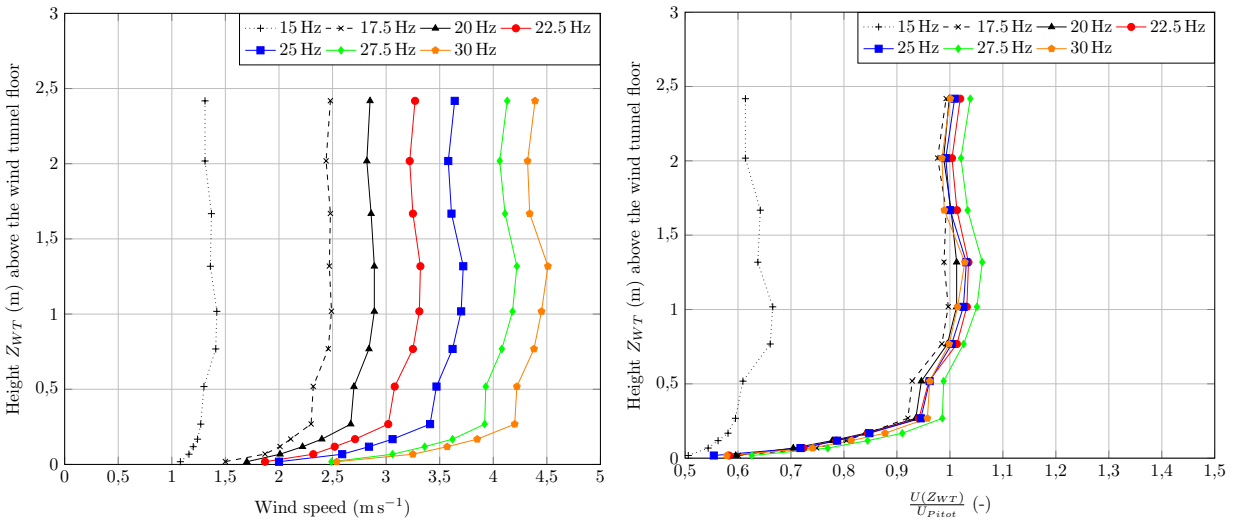
Figure 2.9 – Wind profile comparison between 2015 and 2016 and comparison between the profile on the TFWT outlet section centre and the other profiles in the outlet section. Red error bars represent the uncertainty provided by the instrument manufacturer. Green errors bars indicate the standard deviation measured on time series on the centreline wind tunnel profile. All measurement done in empty configuration.

At the outlet of the closed part of the TFWT, the central wind profile is compared to the measurement done in the same section in Fig. 2.9b. Measurements are in the error bar range of $\pm 0.3 \text{ m s}^{-1}$ of measurement of the central wind profile. Therefore the central profile is considered as sufficient to get a good representation of wind profiles information on different Y_{WT} position on the outlet section. That is why no flow mapping has been done in 2016 but only the central wind profile was measured at the outlet of the closed section.

2.2.2.2 Wind profile vs fan frequency evolution

During the 2015 experimental campaign two wind velocities were used (one for the upwind configuration and one for the downwind configuration). For the 2016 experimental campaign where wind speed effect on curling of spinnaker was studied, several wind velocities were used (up to seven different levels). Fig 2.10a shows the change in the velocity profile for different fan frequencies.

For the Pitot tube measurement, an expected linear trend was observed in Fig. 2.11 between the measured reference velocity and the fan frequency: $U_{Pitot} = 0.1496 f_{fans} - 0.1281$ for the experimental used frequency domain (15 Hz to 30 Hz), with a maximum standard deviation of 0.16 m s^{-1} . Fig. 2.10b shows that the lower frequency initially tested, 15 Hz, is not on the expected trend of evolution of the wind tunnel functioning curve. Therefore results of 15 Hz are not presented in this thesis because the difference with the other frequencies might come from this wind profile difference.



(a) Wind profile at the center of the outlet section of the closed part for different fan frequencies f_{fans} .

(b) Evolution of the dimensionless wind profile $\frac{U}{U_{Pitot}}$ for different fan frequencies f_{fans} at the centre of the outlet section.

Figure 2.10 – Central wind tunnel velocity profile.

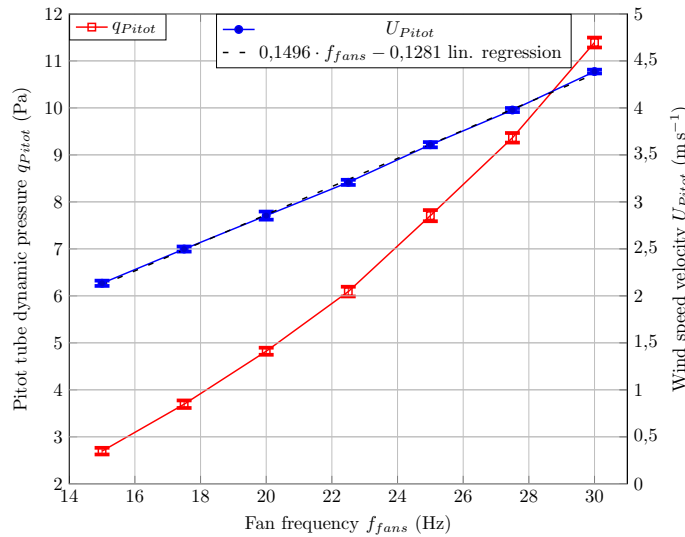


Figure 2.11 – Evolution of the Pitot measurement for different fan frequencies. Error bars represent the standard deviation of the measured time series.

A general presentation of the TFWT facility has been given in this chapter. Elements measured for the study are defined and general flow information is provided. The next chapter is dedicated to upwind tests where different mainsails were first tested under static and then under dynamic conditions.

Contents

3.1	Upwind sail presentation	68
3.2	Static trim, reference case and two-parameter optimisation	69
3.2.1	Static trim geometry	69
3.2.2	Reference case $\beta_{AW} = 40^\circ$	72
3.2.3	Two-parameter optimisation results	77
3.2.4	Optimum location at close-hauled $\beta_{AW} = 25^\circ$	80
3.2.5	Optimum location on a close reach $\beta_{AW} = 40^\circ$	86
3.2.6	Optimum location on a beam reach $\beta_{AW} = 60^\circ$	92
3.2.7	Effect of AWA on the optimum and general conclusions	97
3.3	Pumping: effect of dynamic trimming on respective optimum	98
3.3.1	Dynamic trimming	98
3.3.2	Pumping in the reference case $\beta_{AW} = 40^\circ$	102
3.3.3	Pumping at beam reach $\beta_{AW} = 60^\circ$	106
3.3.4	Results discussion	115
3.3.5	Conclusions, limitations and perspectives	117

This chapter presents the results for the upwind configuration tests carried out during the 2015 wind tunnel experimental campaign. A study of dynamic effect on yacht upwind performance is the goal of this chapter which starts with the upwind mainsails presentation. No head sail has been used in order to restrict the study on a simplified cantilevered mast, without forestay or head sail luff which would have restricted the mast motion. This simplification make the situation similar to one mainsail dinghies which more elastic rig compared to keel boats is more likely to facilitate pumping when authorized or used at full-scale. This absence of head sail also tends to make easier numerical-experimental comparison for future work. In order to make relevant comparison about performance between a static case and a dynamic one, it is first necessary to get the optimum static trim configuration. This is the topic of the second section of this chapter which presents the static trim geometry and the two-parameter optimisation results for different configurations. Eventually dynamic trimming configurations and the effects of dynamic trimming on the mainsail, known as pumping, is presented.

3.1 Upwind sail presentation

Three different mainsails, inspired by a 60 foot International Monohull Open Class Association (IMOCA) model were designed and manufactured by Incidence sails, using SailPack software produced by BSG Developements. This design tool provides the structural description such as the cloth panels and batten geometries and the way they are assembled. This provided description can be adapted and used for FSI numerical simulation. The three mainsails were built using AirX 500 cloth material and hoisted on a mast without any shroud, backstay or forestay. Cloth description can be found in App. G. The different sails were striped using orange fluorescent coloured tape. The standard mainsail corresponds to the standard design of the IMOCA 60 mainsail scaled down by a factor 1 : 13. The two other design shapes were based on the same design shape but their cambers are different. For the flat mainsail, there is no camber and the sail corresponds to one flat panel. For the maximum camber mainsail the camber is slightly increased as illustrated in Fig. 3.1.

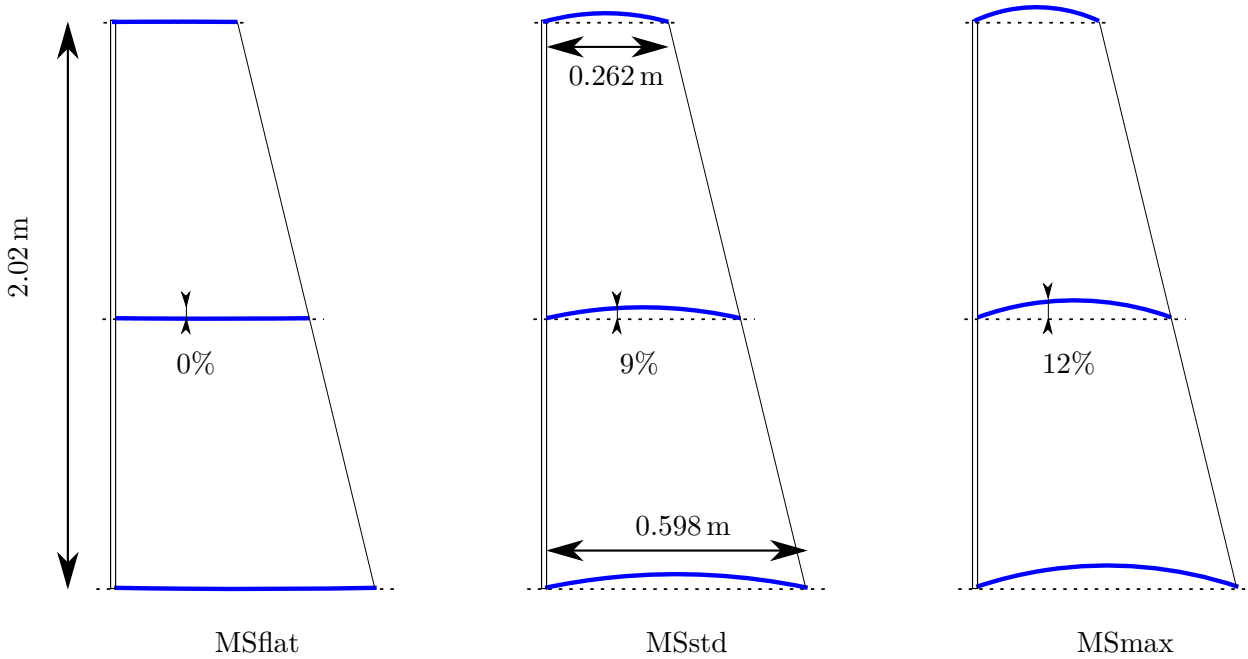


Figure 3.1 – Illustration of camber for the model mainsails used for upwind experimental campaign. Camber is given for an identical reference stripe.

Mainsail type	Area S (m ²)	Mass during 2015 testing (g)	Abbreviations
Mainsail flat	0.959	68.58	MS flat
Mainsail standard	0.959	70.44	MS std
Mainsail maximum camber	0.970	73.56	MS max

Table 3.1 – Description of mainsails tested during the upwind 2015 experimental campaign. The design shape depends of the type of mainsail.

The sails were hoisted along a rail on the aft part of the cantilevered carbon fibre mast. Its mechanical properties are presented in App. H. The 14 mm diameter mast had a rake of 3.5° aft.

3.2 Static trim, reference case and two-parameter optimisation

This section presents the upwind configuration results with a static trim *i.e.* with a fixed and constant trim during each run. This corresponds to the usual method applied during wind tunnel testing: the trimmer operator remotely adjusts the different running rig length available until reaching the configuration he/she wants to test. Two parameters are used during this experiment to trim the mainsail. The two parameters correspond to classical running rig adjustments. A reference case was first tested by fixing one of those two parameters. An optimisation algorithm was then tested for the first time in experimental conditions using the two available possible trim adjustments.

3.2.1 Static trim geometry

Three stepper motors attached to their winch cylinders shown in Fig. 3.2 were used to trim the mainsail. The motors can be seen on the photographs presented on Fig. 3.4. Their purposes are different:

- the main stepper motor is dedicated to the mainsail sheet trimming. This stepper motor directly changes the L_{ord} quantity affecting the sheet length L_{sheet} . L_{ord} corresponds to the ordered sheet length to be rolled (trimmed) or unrolled (eased) by the main stepper motor compared to its reference initial position. The reference is set up during the motor zeroing phase where the remote control card consider the actual motor position as the reference one. This adjustment is mostly used by sailors to change the sail leech tension which mainly affects the twist.
- two smaller stepper motors adjust the car traveller position along the rail. Those two motors have to work together, one trimming and one easing the exact same quantity at the same time to maintain tension on the car traveller positioning line along the rail. This adjustment is mostly used by sailors to change the AoA of the lower part of the sail. Those two motors directly act on the position of the car, *i.e.* on the quantity L_{car} . Because the rail is not circular, a change in the L_{car} quantity affects L_{sheet} .

The relationship to compute the actual sheet length L_{sheet} in mm for the upwind configuration is given by equation 3.1. The reader can refer to App. E for the derivation. Its representation is given in Fig. 3.3 :

$$L_{sheet} = 333.43 - \sqrt{111073.81 + (10 + L_{car})^2} + L_{sheet\ 0} + L_{ord} \quad (3.1)$$

To prevent any structural damage to the mast or to the sail, strong over trimming must be avoided. This corresponds to a lower limit of L_{sheet} . Its limit is illustrated in Fig. 3.3 (upper limit of the hatched area). Trim was stopped by operators during experimental campaign based on their live observations of sail stretch and mast bending which must not take an unrealistic shape. Mast alignment can be either set up on the boat centreline or on the TFWT flow direction (more details are given on App. E).

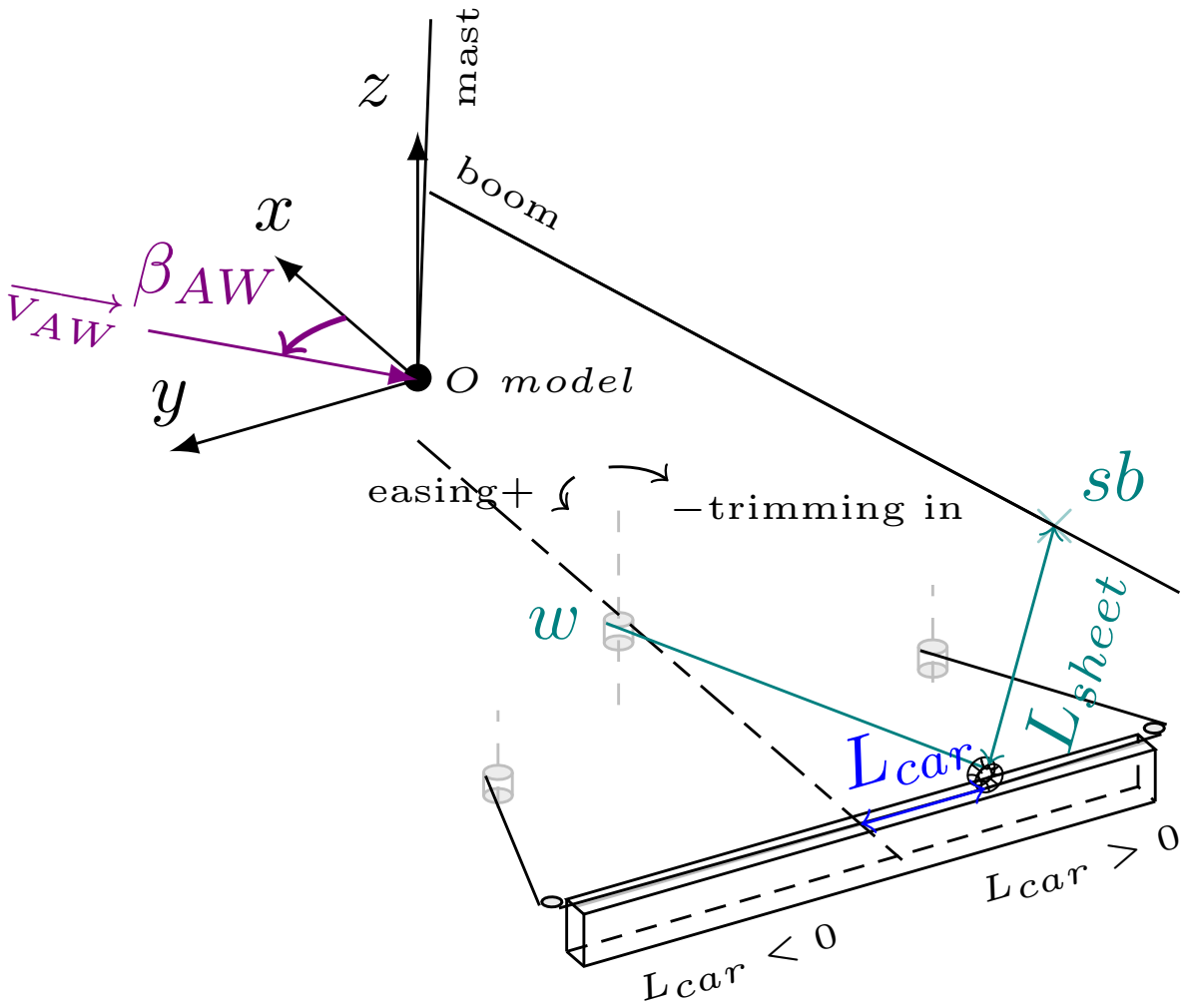
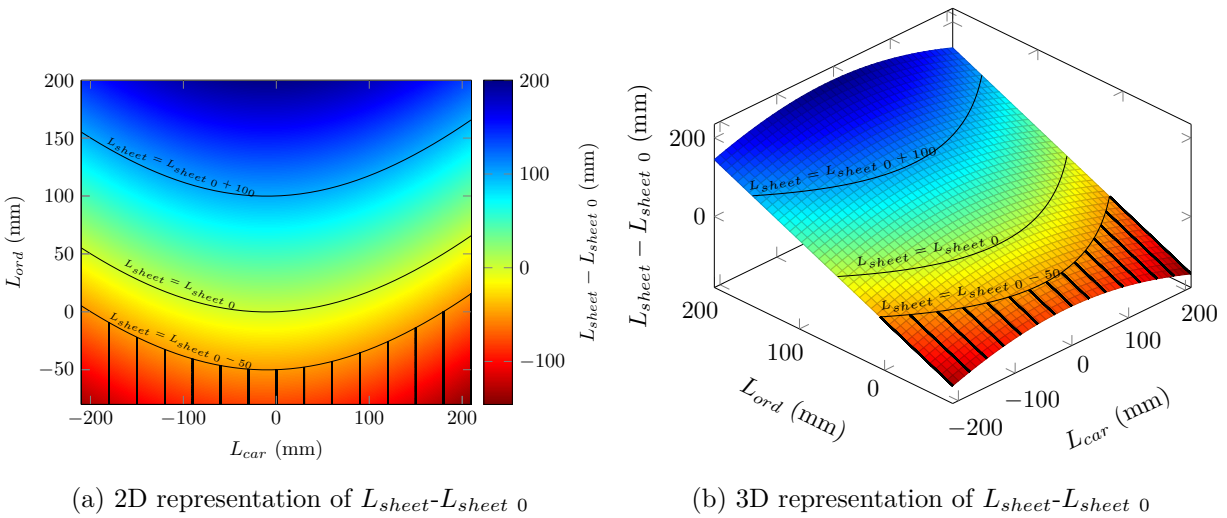


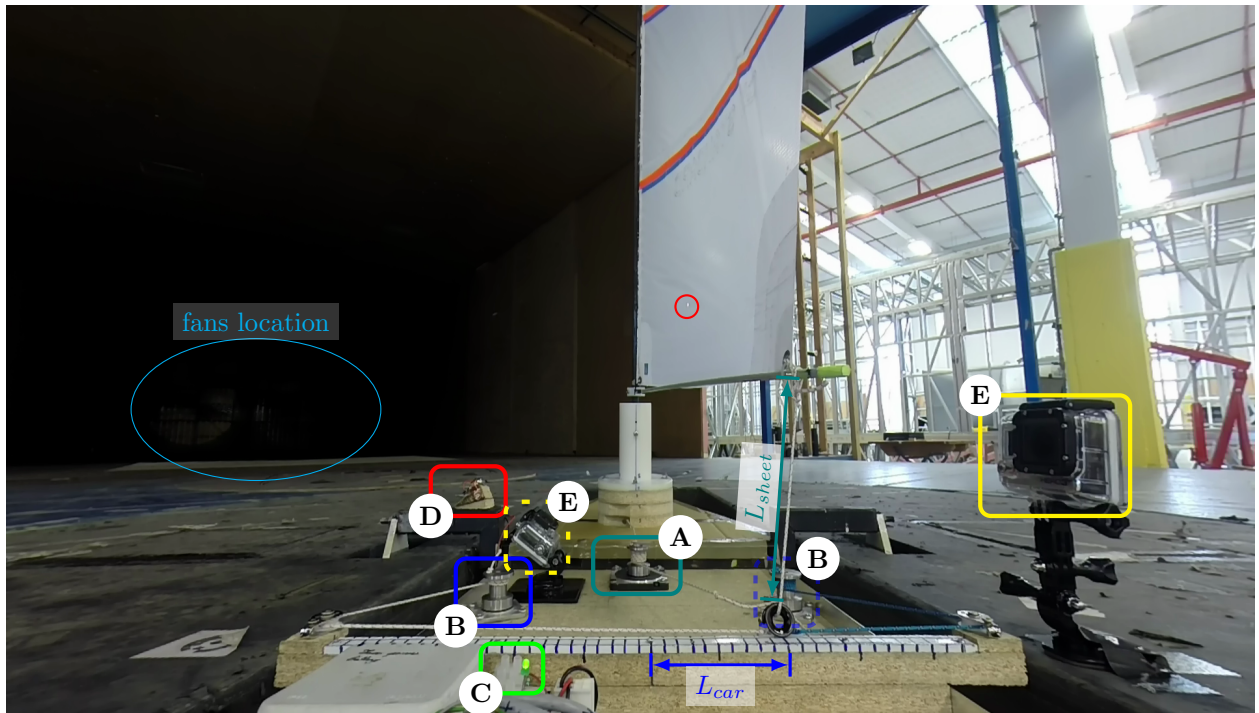
Figure 3.2 – Upwind geometric configuration of stepper motors and static trim adjustment.



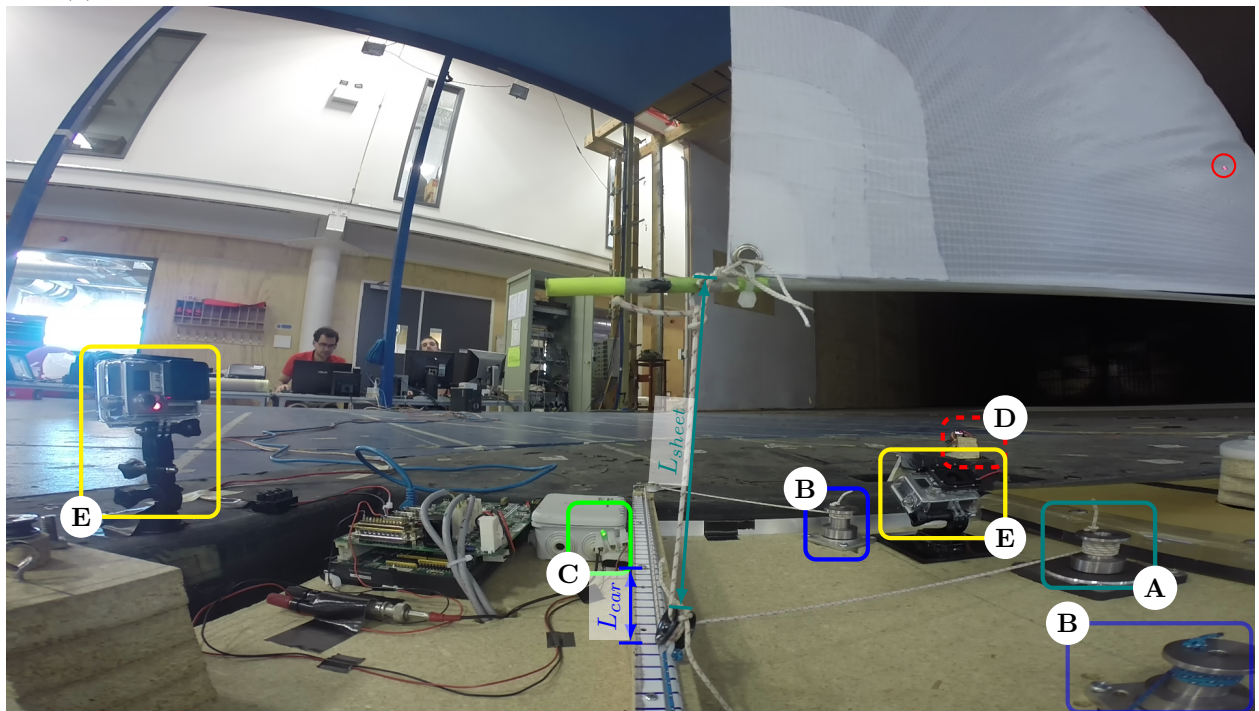
(a) 2D representation of $L_{sheet} - L_{sheet_0}$

(b) 3D representation of $L_{sheet} - L_{sheet_0}$

Figure 3.3 – $L_{sheet} - L_{sheet_0}$ map as a function of L_{car} and L_{ord} .



(a) Upwind trimming configuration view from cockpit camera. Fish eye effect has been corrected.



(b) Upwind trimming configuration view from starboard camera. Fish eye effect has not been corrected.

Figure 3.4 – Illustration of set up in the two-parameter optimisation configuration. (A) mainsail sheet winch, (B) car traveller winches, (C) synchronisation LED, (D) synchronisation laser (red circle represents the location of the laser impact point on the sail), (E) cameras. The load sensor is not mounted on those photographs. The mast is aligned in this case with the wind tunnel streamwise direction.

3.2.2 Reference case $\beta_{AW} = 40^\circ$

One reference case was tested with the car traveller fixed on the centreline of the model with the standard mainsail. In this configuration L_{car} remains constant and equal to 0 mm and only L_{sheet} is modified to measure the evolution of the aerodynamic forces coefficients. The reference wind speed measured by the upstream Pitot tube was $U_{Pitot} = 3.5 \text{ m s}^{-1}$. The measured force coefficients are presented in Fig. 3.5. For this configuration the mast is aligned with the wind tunnel streamwise direction. The optimisation target function $C_{F_{obj}}$ in Fig. 3.5c defined as $C_{F_x} + 0.1C_{F_y}$ follows the trend of the drive force coefficient C_{F_x} . More details about the optimisation target function are provided in the next subsection 3.2.3.

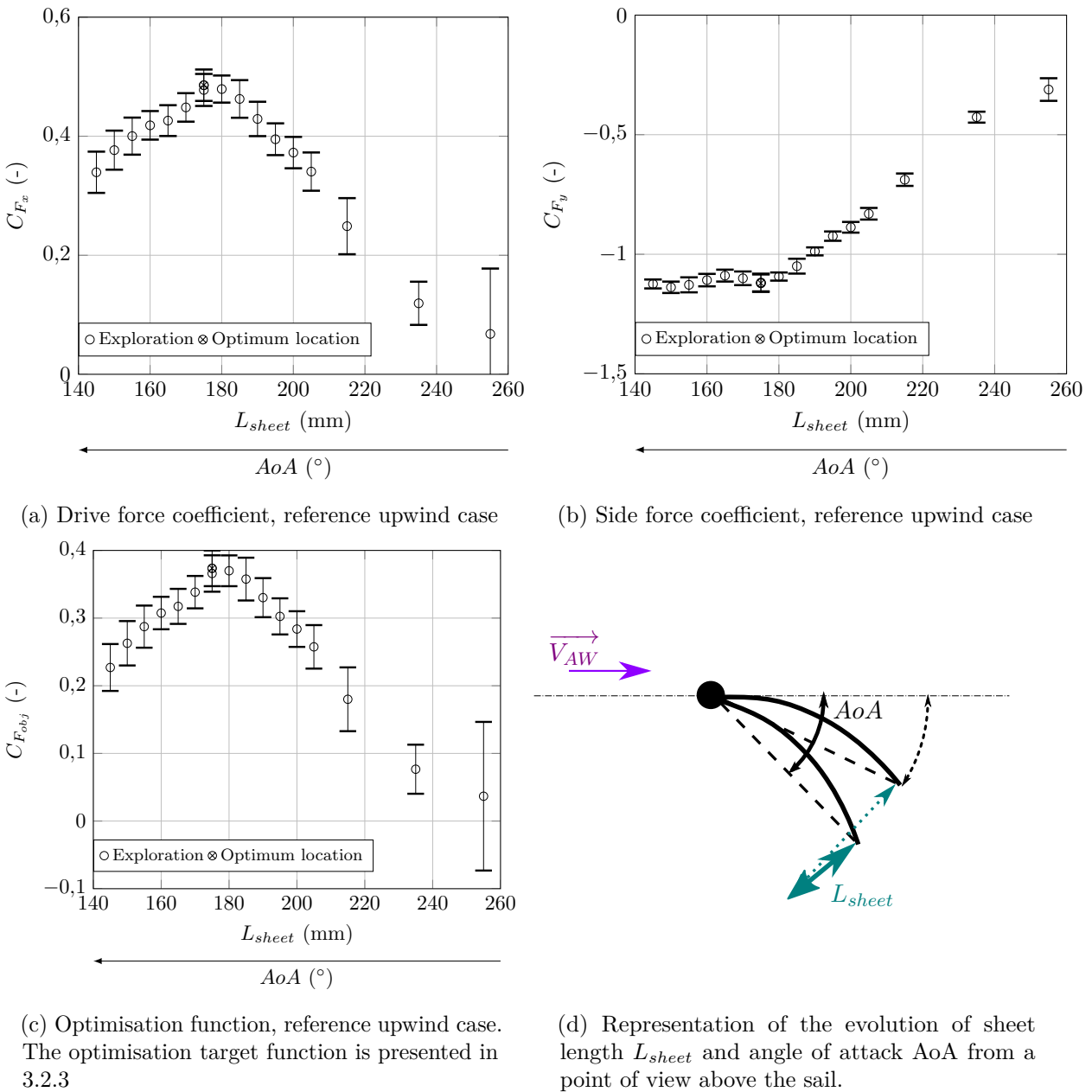


Figure 3.5 – Reference upwind case. Error bars represent the measured standard deviation in the 30 s runs.

3.2.2.1 Effect of the sheet length on the angle of attack

When the sheet length increases, corresponding to easing the sail, the sheeting angle increases and the AoA decreases. On the contrary, when the sheet length L_{sheet} decreases, corresponding to trimming the sail in, the sheeting angle decreases and the AoA increases as shown in Fig. 3.5d. However there is no simple relation between L_{sheet} and AoA . Those trends are indicated by arrows under the x coordinate axis in Fig. 3.5. Flying shape analysis is required to compute the sheeting angle and AoA value. Therefore, only L_{sheet} which can be directly computed according to the stepper motor information is used from now to describe the evolution of the input parameter. AoA is no longer indicated under graphs. The reader is referred to this part to keep in mind the evolution trends of the sheeting angle and AoA with L_{sheet} evolution.

Once the mainsail starts to be significantly trimmed (lower L_{sheet} value), the evolution of AoA slows down. Any added trim will mainly tend to pull down the boom end, stretching more the sail leech, closing the mainsail twist and bending the mast in the aft direction. When the mainsail sheet is really eased (higher L_{sheet} value) the standard deviation of time series increases. It corresponds to the sail luffing (sail front part shape oscillates like as shown on Fig. 3.7c). On Fig. 3.7, three situations are presented to visualize the sheet length effect on the sail flying shape.

The drive vs side force coefficient and lift vs drag coefficient representation are given in Fig. 3.6. Arrows indicate the increasing evolution of AoA and L_{sheet} . The optimum location seems to closely match the stall (lift decreases while drag increases). The fact that for low L_{sheet} values the AoA does not change more when the sail is trimmed *i.e.* is indicated by the plateau seen in Fig. 3.6b. The experimental optimum measurement is presented in Tab. 3.2.

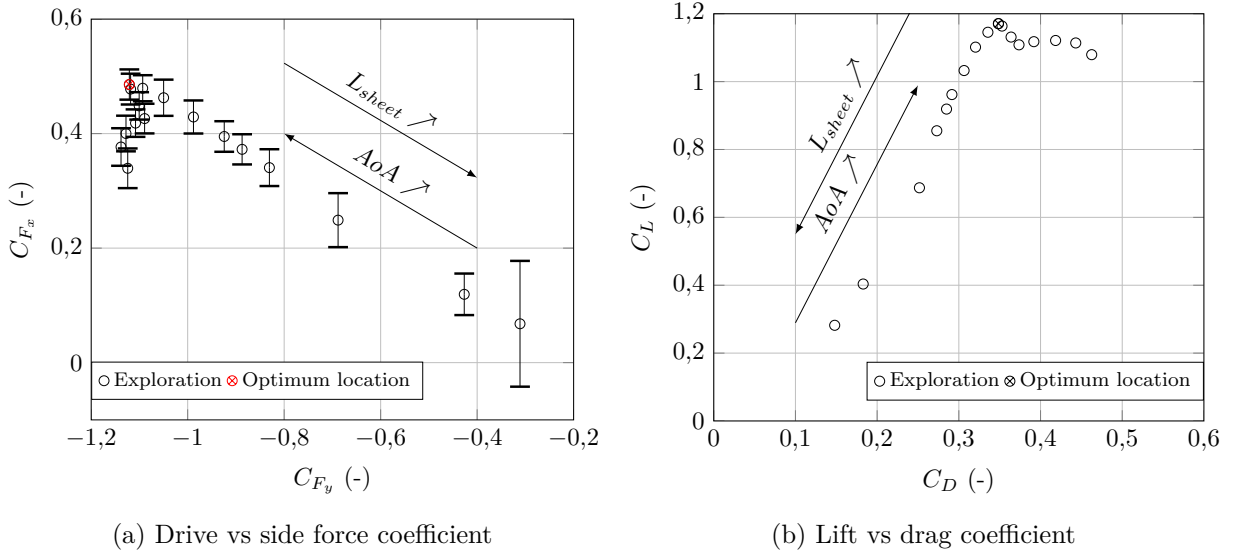


Figure 3.6 – Reference upwind case, drive vs side and lift vs drag.

L_{car} (mm)	L_{sheet} (mm)	C_{F_x} ([-])	C_{F_y} ([-])	$C_{F_{obj}}$ ([-])
0	175	0.486	-1.121	0.374

Table 3.2 – Optimum results for the standard mainsail $\beta_{AW} = 40^\circ$, reference case.

Fig. 3.7 shows that for an identical length of sheet adjustment, trimmed in for $L_{sheet} 0 - 30$ mm or eased for $L_{sheet} 0 + 30$ mm, the evolution of the boom position does not take the same direction.

Fig. 3.7g shows that the boom is more vertically moved than horizontally opened. Fig 3.7i shows a large opening both in the horizontal and vertical directions.

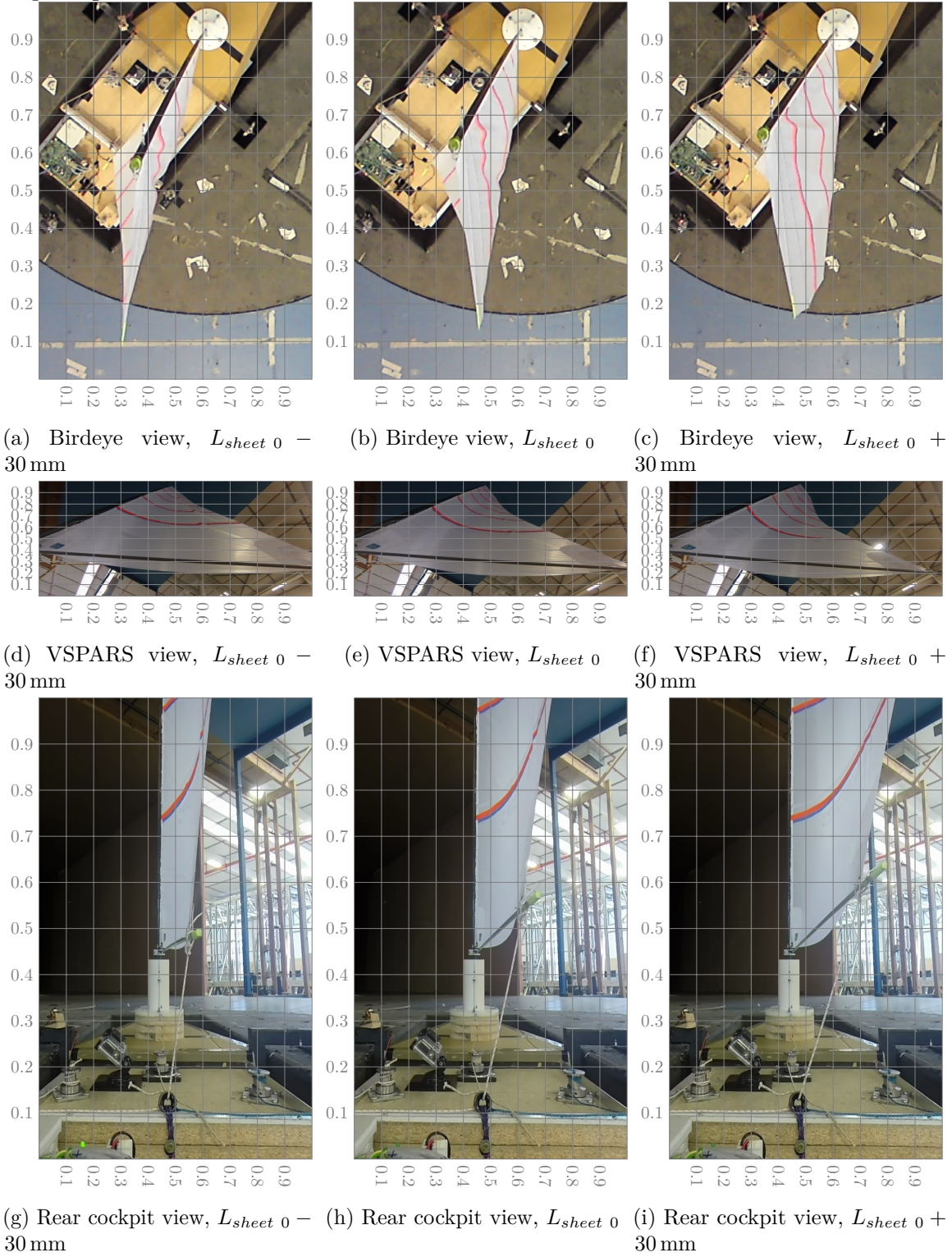


Figure 3.7 – Effect of sheet length on the flying shape for upwind cases. Fish-eye effect has been removed from Gopro camera footage. Reference case $\beta_{AW} = 40^\circ$, $L_{sheet\ 0} = 175\text{ mm}$.

Once the optimum has been located, flow velocity field was measured using the Cobra probe and is shown next.

3.2.2.2 Flow mapping for upwind reference case

Flow mapping in this reference case was measured using the Cobra probe. The reference wind speed was $U_{P_{itot}} = 3.5 \text{ m s}^{-1}$. Wind speed and turbulent intensity results are presented on Fig. 3.8.

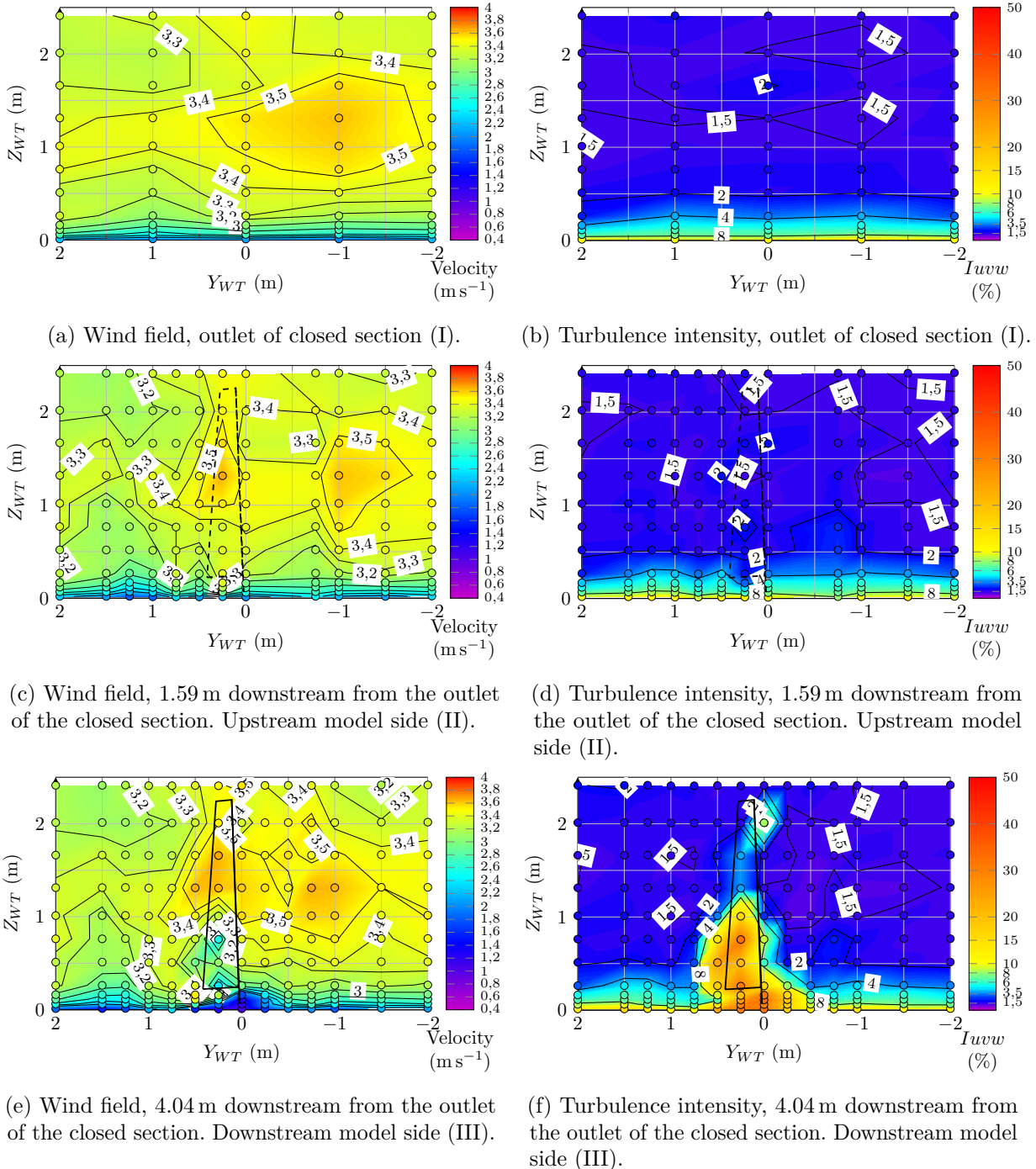


Figure 3.8 – Upwind configuration TFWT velocity field. \circ indicates location of measurement points. The configuration corresponds to the reference case at static optimum AWA of 40° $L_{sheet} = 175 \text{ mm}$. I, II, III sections are presented on Fig. 2.1.

In Fig. 3.8 the thick line represents the mainsail and mast shape projected on the measuring

plane when the model is upstream of the measurement plane. Results shown in Fig. 3.8a are similar to the empty wind tunnel results on Fig. 2.8a. Both present an over speed area on the right part when facing the flow on the outlet section of the enclosed part. Differences exist between the empty wind tunnel configuration in Fig. 2.8c and the configuration with a model mainsail in Fig. 3.8c. Dashed thick line represents the mainsail and mast shape projected on the measuring plane when the model is downstream of measurement plane. These representations correspond to the estimate position of the mainsail considering the sail as rigid and the mast aligned with the model centreline. On the downstream part of the flow mapping in Fig. 3.8e the mainsail wake can be observed. These measurements may indicate that the mainsail is more twisted than the solid representation due to the sail deformation in the flow. It can be noticed that above one meter height the decrease of the wind velocity in the sail wake is negligible. The effect of the mainsail can be observed on the upstream measurement plane on Fig. 3.8c where a second over speed area occurs in front of the sail. The wake measurements can also be used to compute the lift and drag span-wise distribution like in [Jackson et al., 1996].

Fig. 3.9 presents the measurement on the outlet section of enclosed part of the TFWT mapped on 3.8a. It compares the central profile ($Y_{WT} = 0$ m) and the other profiles measured on this section. All profiles do not match exactly the central profile but they are all contained on the measuring range of the central profile and remain close to its standard deviation range. The upwind sail seems to accelerate slightly the reference velocity profile measured with an empty wind tunnel at the centre of the outlet of the closed part.

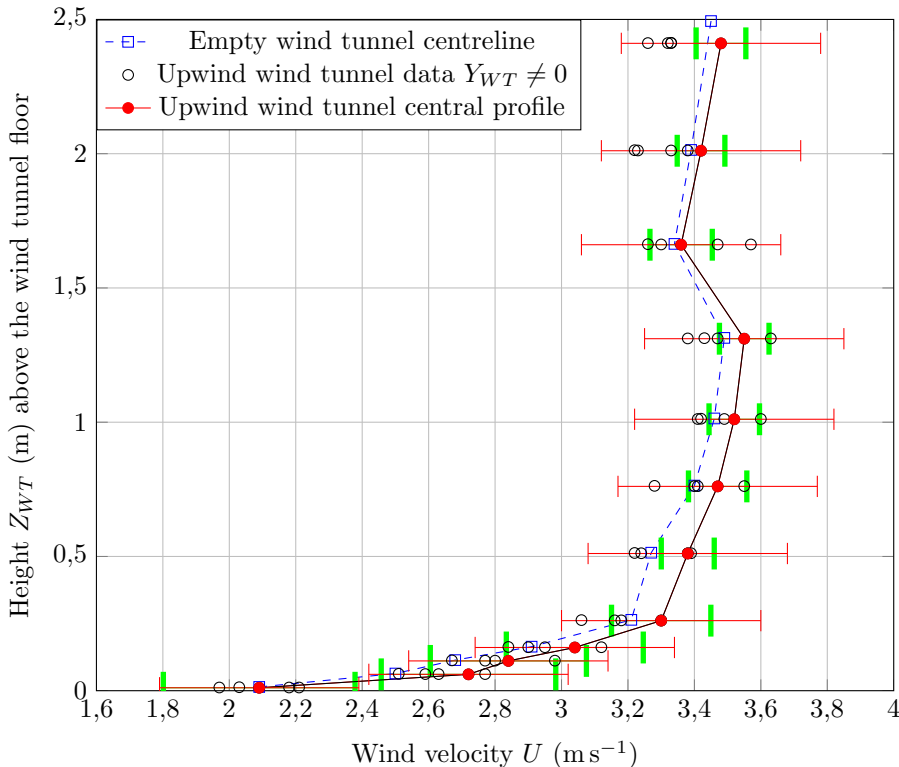


Figure 3.9 – Central wind profile compare to outlet section wind profile data $f_{fans} = 23.8$ Hz with upwind sails. Blue square dashed curve data corresponds to the empty wind tunnel configuration. Red error bars represent the uncertainty provided by the instrument manufacturer. Green errors bars indicate the standard deviation measured on time series on the centreline wind tunnel profile. The configuration corresponds to the reference case at static optimum AWA of 40° , $L_{sheet} = 175$ mm.

A reference case has been studied in order to provide static data information of the wind tunnel experiments with flow information. This flow information is quite important to be able to reproduce the experimental conditions and for numerical-experimental comparison, where the central profile can be used as an input of the computation. In this case the traveller position is fixed on the model centreline which reduces the uncertainty about the sheet length. Flow measurement is done around the one parameter (L_{sheet}) optimum.

Optimisation with two parameters is presented next but no flow measurements are done for these experiments.

3.2.3 Two-parameter optimisation results

As seen previously, two running rig adjustments can usually be applied on a mainsail yacht: the car traveller position and the mainsail sheet length. The experimental setup described in Fig. 3.2 enables one to adjust these two settings in order to represent a classical sailing situation. Moreover this experimental setup is a way to test for the first time the optimisation code developed at IRENav under experimental representative sailing conditions. This algorithm development is part of Matthieu Sacher's PhD project focused on optimisation tools dedicated to yacht engineering (sail design, trim adjustment, foil design). The algorithm is based on Gaussian process which approximate the measured performance. As shown in [Sacher et al., 2017], this algorithm is well adapted for situations where full FSI simulations with RANS computation cost can be significant and a full exploration of parameter space is not reasonable. It has already been used with numerical simulation methods in [Sacher et al., 2015]. It is expected to benefit from further developments and improvements. Thanks to the wind tunnel data recorded, experimental and numerical optimisation results are compared in [Sacher et al., 2016].

Before presenting any dynamic situations, several static scenarii were tested with the static trimming device with different parameters:

- three different AWA were tested to represent different points of sail.
- three different sails were tested to study the effect of the design shape on the trim adjustments.
- different configurations of mast alignment were performed in order to better represent the IMOCA rotating mast and to facilitate numerical-experimental comparison.

For each of these configurations, between 20 to 50 values of parameters (L_{car} , L_{sheet}) were tested. One of the challenging part of this work is to summarize such a large amount of information. Results presented here are focused on:

- drive and side force coefficients, representing the major part of the aerodynamic forces generated.
- the optimisation target function $C_{F_{obj}}$ as a simple indicator of the boat performance.
- the load sheet tension coefficient $C_{F_{sheet}}$.

Results are represented in the variable space (L_{car}, L_{sheet}) for a given AWA, design shape and mast alignment. At each step of the optimisation process, the next point to be tested is indicated by the algorithm, therefore the variable space is not explored entirely and neither equally. The algorithm tends to explore only areas of interest where the performance potential is higher than other areas briefly tested. By the end of the optimisation process, the point to be tested tends to remain in the same area. As a direct result of this experimental campaign, raw data coefficients can be provided for the different points explored in the variable space but not for the entire domain. An interpolation-extrapolation step is required to provide information over the considered domain of (L_{car}, L_{sheet}) . The optimisation process already provides the computation of the expected value and the uncertainty on those values on the domain. Therefore the interpolation chosen to represent the information is based on the same method used by the optimisation process but uses the data at the final stage of the optimisation process.

This part introduces first the optimisation context and process used. Then optimum results are presented for the different cases.

3.2.3.1 Short optimisation context: two parameters, target function, forbidden areas and procedure

A summary of the key notions of the algorithm used and develop by Matthieu Sacher is presented here. More details can be found in [Sacher et al., 2016, Sacher et al., 2017] which present the results of the optimisation process applied in the wind-tunnel experimental conditions and their comparison to numerical simulations.

Optimisation is based on a meta-model approach which aims to evaluate the researched performance function in order to get its optimum with the lowest number of evaluations. A Gaussian process is used to approximate the measured performance providing error and noise evaluation about the performance over the parameter space. The optimisation algorithm is based on iteration steps which select a next parameter point to be tested based on the evaluation of the merit function thanks to the observed data. Augmented expected improvement merit function is used, evaluating the expected increase in the performance taking into account the noise in the measured values and penalizing areas where performance knowledge is important (*i.e.* where the variance is small).

The noise can be set up to the experimental level one or computed by the Gaussian process. Results show that computed noise matches the experimental one. Here the computed noise is used by the Gaussian process.

The space parameter is defined by (L_{car}, L_{sheet}) variables as shown in Fig. 3.2.

The performance function is a representative function of the performance of the boat. In the upwind cases, it is a linear combination of the drive and side force as described in [Sacher et al., 2015, Sacher et al., 2016]. This optimisation target function takes into account a penalty due to the added hydrodynamic drag generated by side force which creates heeling moment. The coefficient of penalisation can be evaluated using hydrodynamic study on the model hull comparing the heeling

and leeway effect on speed equilibrium ([Sacher et al., 2015]). Its value remains close to 0.1 for typical upwind sailing conditions even for yacht with different hull shapes. The performance function or optimisation target function $C_{F_{obj}}$ associated to the performance is defined with the time series of drive and side forces. Its formula can change according to the yacht tack and the orientation of the measuring frame. Here on port side tack with a direct orthonormal frame, side force being usually negative in quasi-static state, *i.e.* $C_{F_y} < 0$, the formula reads:

$$C_{F_{obj}} = \overline{C_{F_{obj}}(t)} = \overline{C_{F_x}(t) + 0.1C_{F_y}(t)} \quad (3.2)$$

$$C_{F_{obj}} = C_{F_x} + 0.1C_{F_y} \quad (3.3)$$

This kind of linear combination is generally used only for upwind situations. For downwind cases, most of the time, the target function is directly the drive force (side force being no longer strongly opposed to the boat motion).

Forbidden areas can exist when adjusting the sail trim. Over trimming can be a major risk for the structural part (mast breaking or sail tearing). There are two extreme values of L_{car} depending on the rail length. The L_{sheet} parameter lower value is limited by the visual observations of the load that can be applied on the mast and sail. Optimisation in experimental sail trimming situation taking into account the forbidden areas location is an interesting issue to address. Some configurations may present an optimum location inside the variables space or on the forbidden area limit. For a deeper upwind AWA the optimum can be located on the border of a forbidden area.

The optimisation procedure is done following several steps of the algorithm. The first step is the initialisation step where 10 cases are tested. In this study the initialisation cases were chosen identical in order to be able to be compared for the different sails. The second step is an exploration phase where the algorithm indicates the next point to be tested depending on the results of previous points using the merit function.

A convergence criteria can be based on the distance of two successive input parameters given by the process. Here the convergence is reached when the algorithm proposed two successive points at a distance less than 1 mm, which is the order of magnitude of the sheet length measurement uncertainty. During the process, the measured optimum point might be tested before reaching the convergence. In general, no more than 40 points were required to reach the optimum.

Results corresponds to both the raw data measured during the algorithm process (scatter representation in the two-parameter space) and the Gaussian process evaluation map of these experimental data (coloured surface and contour representation in the two-parameter space). Gaussian process variance information is also provided in order to be able to do relevant comparison using this interpolation. Its notation is sC_{F_i} for the variance of the aerodynamic coefficient C_{F_i} .

For each situations, only the measured experimental optimum will be indicated. This optimum can be slightly different from the one computed through the interpolation process but remains close in general.

3.2.4 Optimum location at close-hauled $\beta_{AW} = 25^\circ$

For this AWA, the mast was aligned with the model centreline.

3.2.4.1 Respective optimum location

Here are presented the different results for the different design shapes for $\beta_{AW} = 25^\circ$.

Results for the standard mainsail are presented in Fig. 3.12. The experimental optimum is located with a traveller on the windward part of the rail. Being trimmed with L_{sheet} close to its minimum possible limit in this situation does not correspond to the optimum. A large part of the presented domain for large L_{car} and L_{sheet} presents a negative drive force coefficient and target function. The situation with large L_{sheet} and large L_{car} corresponds to sail luffing which significantly decreases the absolute value of side force and decreases the drive force coefficient close to 0 or even down to negative values. The other situation where L_{sheet} is small and the car traveller on the windward side corresponds to an overtrimmed car situations. The drive force coefficient tends to be smaller and the side force coefficient absolute value tends to be greater. This is due to the aerodynamic force being oriented more sideways. Moreover, flow separation is probably large on the leeward surface of the sail.

Results for the maximum camber mainsail are presented in Fig. 3.13. Results are quite similar to the standard mainsail design however the optimum configuration of the maximum camber mainsail is slightly different. The optimum car traveller position is located on the leeward side and presents worst performance than the standard one.

Results for the flat mainsail are presented in Fig. 3.14. The optimum corresponds to a centred car position with a more eased sheet length compared to the two other design shape mainsail optimums.

For all the mainsail design shapes, the optimum location parameter are presented in Tab. 3.3. The optimum region presents an ellipse shape defining two principals directions. The first one is less sensitive to the input conditions. In this direction small changes in the static trimming have few effects on the target function value (low gradient direction). Along this direction L_{car} and L_{sheet} evolution are opposite. If the traveller is trimmed up on windward side, the mainsail sheet must be eased. If the traveller is eased down on leeward side, the mainsail sheet must be trimmed in. On the contrary if a change is made in the other direction (high gradient direction), easing or trimming the car traveller and mainsail sheet at the same time, the target function evolution is more significant. This kind of change is in agreement with sailors knowledge. The trends of principal and secondary directions are the same for the different design shapes and different AWA.

Fig. 3.10 associated to the maximum camber mainsail indicates that the sheet load coefficient is significant at the optimum location. No bi directional pattern is observed here. The more you trim in, the higher the sheet load. The flat mainsail gives a higher sheet load coefficient in the space parameter for lower sheet length than the maximum camber one as illustrated on Fig. 3.11. Its cloth might be more rapidly stretched for a given trim due to the flatter design shape.

Mainsail type	L_{car} (mm)	L_{sheet} (mm)	C_{F_x} ([-])	C_{F_y} ([-])	$C_{F_{obj}}$ ([-])	$C_{F_{sheet}}$ ([-])
Standard	-16	140.1	0.28	-1.15	0.16	
Max camber	19	128.9	0.24	-9.72	0.15	1.87
Flat	0	160	0.2	-0.82	0.11	1.27

Table 3.3 – Optimum results for $\beta_{AW} = 25^\circ$. The sheet load coefficient is not measured for the standard mainsail.

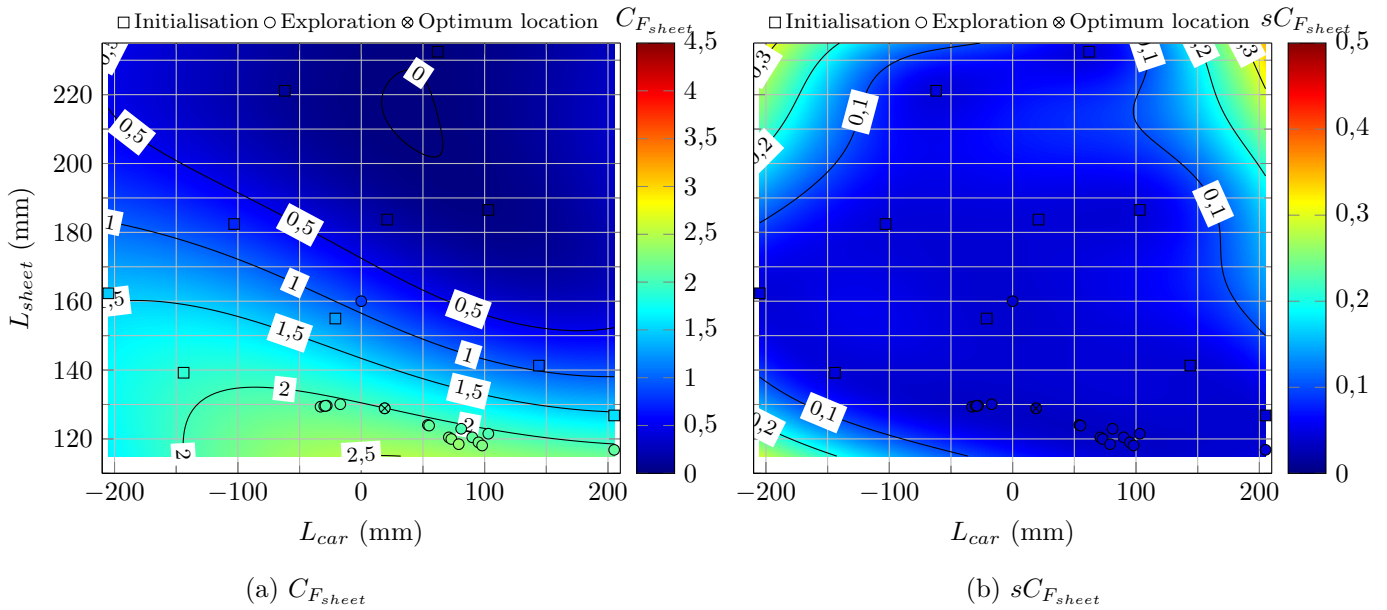


Figure 3.10 – Mainsail sheet load coefficient for the maximum camber mainsail $\beta_{AW} = 25^\circ$. \square : initialisation phase, \circ : exploration phase and \otimes : experimental optimum location.

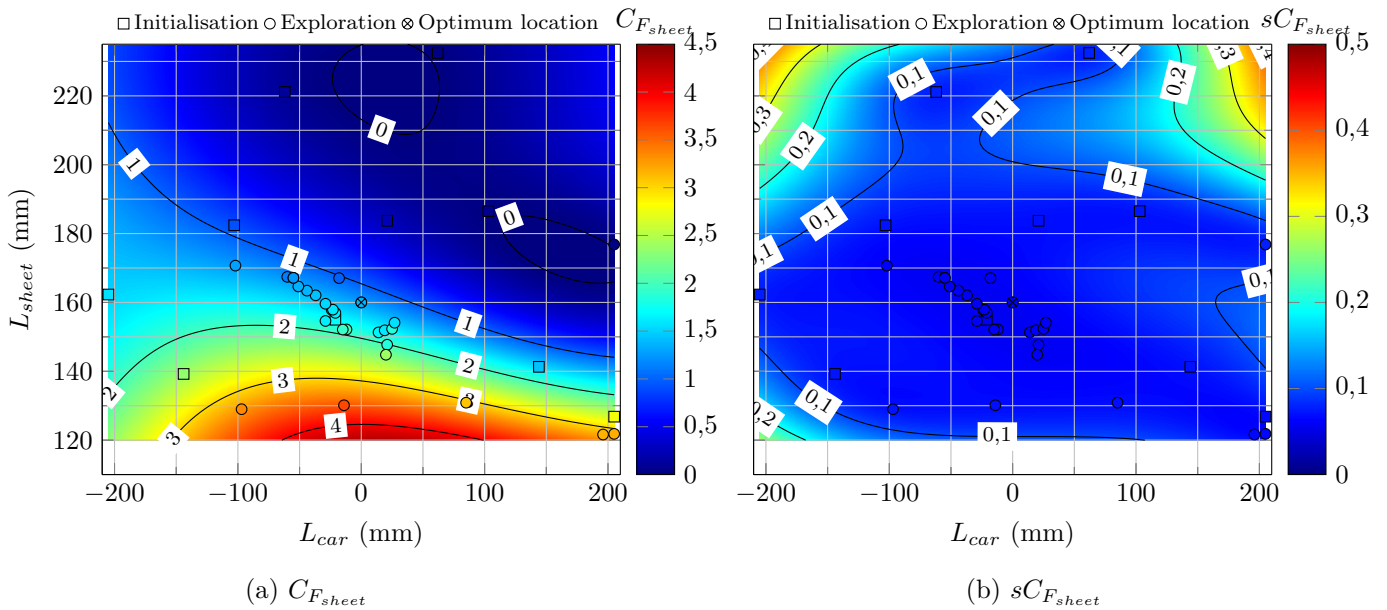


Figure 3.11 – Mainsail sheet load coefficient for the flat mainsail $\beta_{AW} = 25^\circ$. \square : initialisation phase, \circ : exploration phase and \otimes : experimental optimum location.

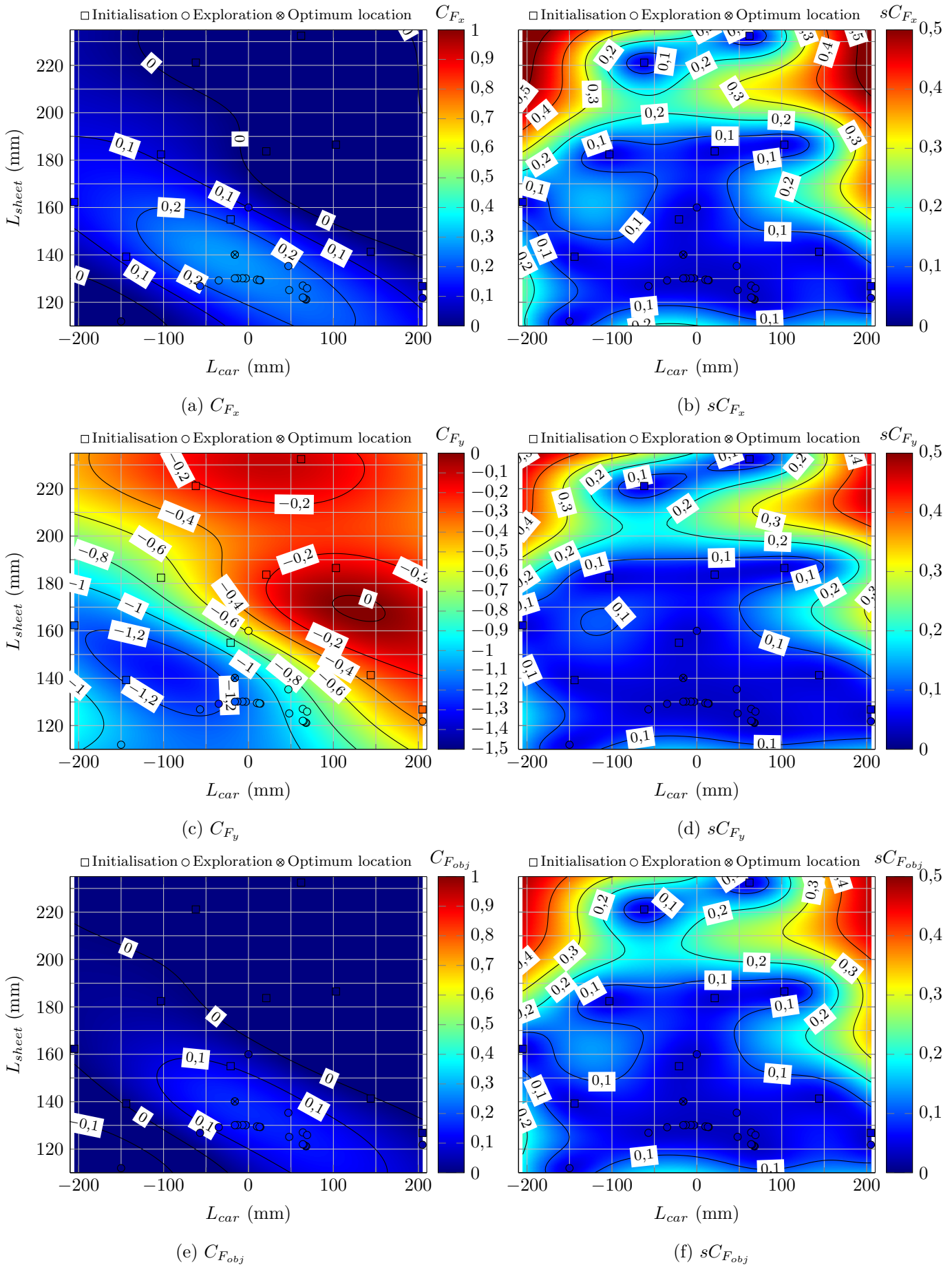


Figure 3.12 – Two-parameter optimisation for the standard mainsail $\beta_{AW} = 25^\circ$. \square : initialisation phase, \circ : exploration phase and \otimes : optimum location.

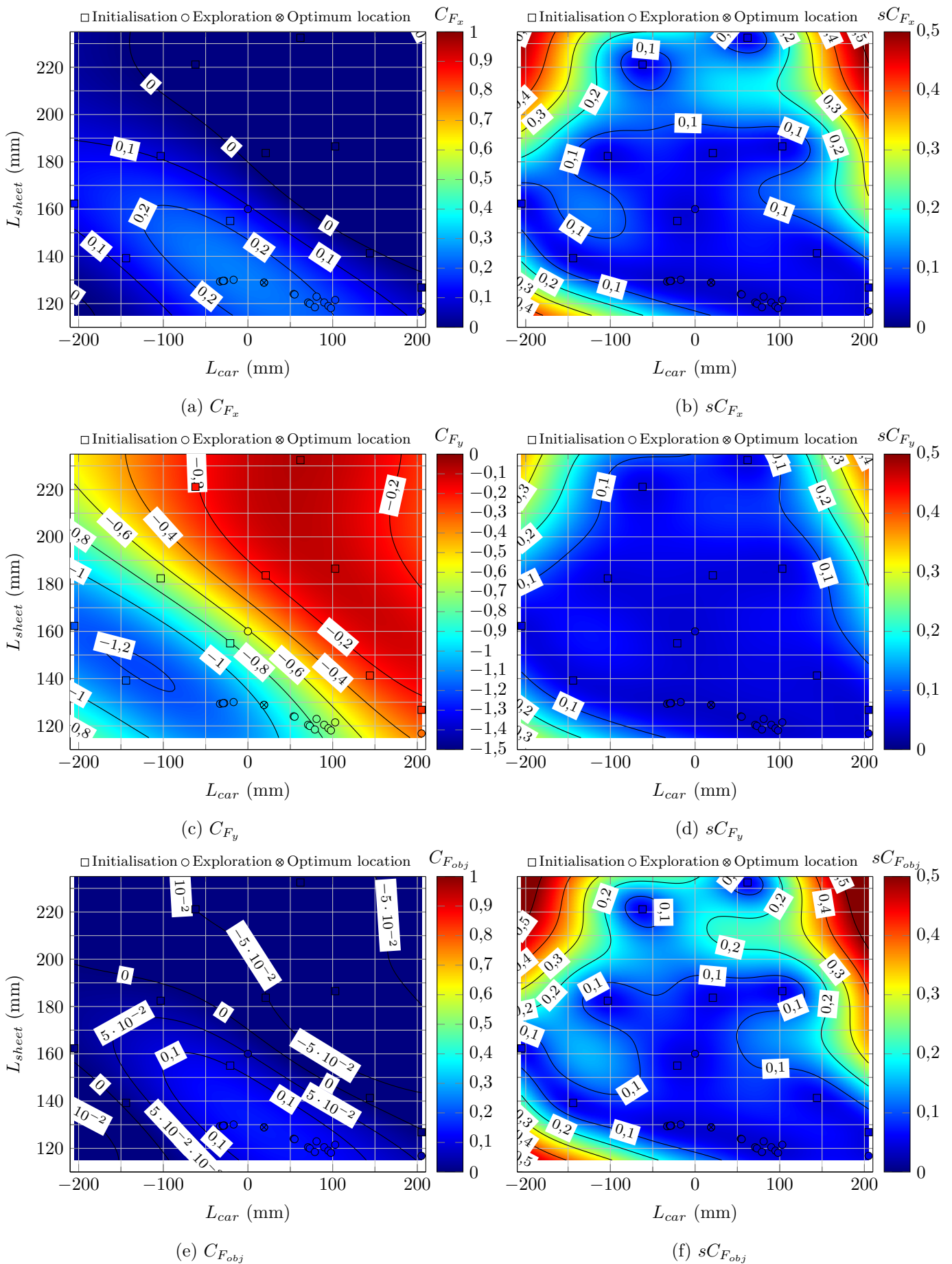


Figure 3.13 – Two-parameter optimisation for the maximum camber mainsail $\beta_{AW} = 25^\circ$. \square : initialisation phase, \circ : exploration phase and \otimes : optimum location.

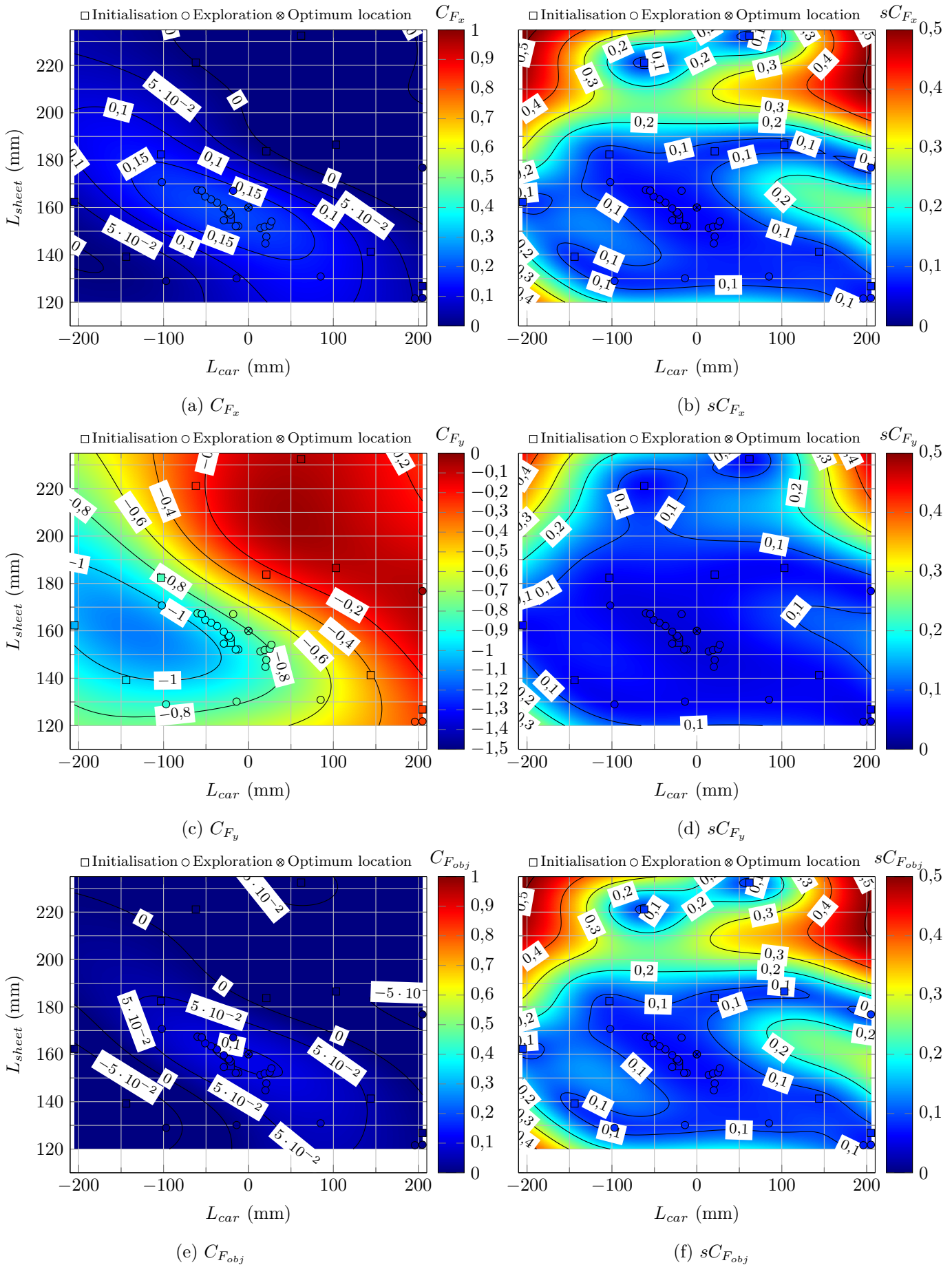


Figure 3.14 – Two-parameter optimisation for the flat mainsail $\beta_{AW} = 25^\circ$. \square : initialisation phase, \circ : exploration phase and \otimes : experimental optimum location.

3.2.4.2 Effect of design shape

Fig. 3.15 presents isolines of interpolation of the optimisation function focused on the optimum region for the different sails. Type line represents the type of sail and the colour is associated to the level indicated on the colour bar. This representation compares the interpolation of the target function between the different sails. One can notice that the standard mainsail shows the best optimum value, as indicated by the experimental measurements. For an identical level, the area enclosed by the standard mainsail isoline is larger than for the maximum camber mainsail. The standard mainsail is therefore considered as more tolerant to trim adjustment than the other sails in these conditions. A same trim modification around their respective optimum has less impact on the standard mainsail performance.

All the optimisation function presents an ellipse shape around their optimum location. However the main directions around the optimum are different between the standard and maximum camber mainsail. The slope of the main direction of the maximum camber mainsail is higher. It indicates that for a given change in the traveller position, the quantity of sheet length L_{sheet} to adjust is more important when the camber is more pronounced to stay closer to the optimum value.

Upwind sails are often designed for close hauled sailing corresponding to this AWA. This indicates here that the standard mainsail design and camber are appropriate.

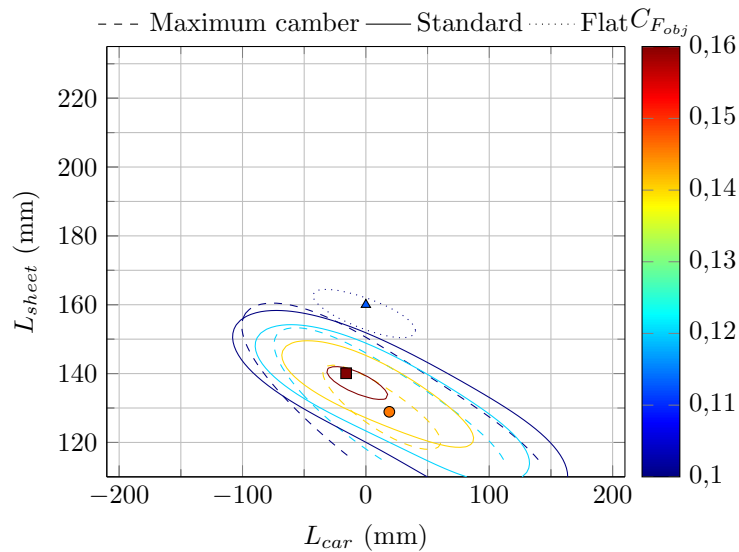


Figure 3.15 – Effect of design shape on the optimum at $\beta_{AW} = 25^\circ$. ● : maximum camber mainsail experimental optimum, ■ : standard mainsail experimental optimum, ▲ : flat mainsail experimental optimum.

3.2.5 Optimum location on a close reach $\beta_{AW} = 40^\circ$

Some of these results were presented in [Sacher et al., 2016] where numerical and experimental optimisation are compared. Matthieu Sacher PhD candidate has implemented the optimisation process developing its code, has participated to the wind tunnel experiments in 2015 and achieved the numerical simulations modelling the wind tunnel conditions. The mast was aligned here with the model centreline.

3.2.5.1 Respective optimum location

Here are presented the different results for the different design shapes at $\beta_{AW} = 40^\circ$.

Results for the standard mainsail are presented in Fig. 3.17. As expected the experimental optimum is located with a traveller on a leeward position compared to the previous AWA. The sail is more open when sailing on a deeper course. The two directions around the optimum still exist. As expected the optimisation target function reaches higher values than the previous AWA conditions as the aero force is directed more forward.

Results for the maximum camber mainsail are presented in Fig. 3.18. Results for the flat mainsail are presented in Fig. 3.19. They both present the same evolution than the standard mainsail case compared to the previous AWA with a more leeward optimum car position. The performance is more than doubled for all the sails due to an important increase in the drive force.

Fig. 3.16 indicates higher values of sheet load coefficient for this flat design at the lower limit of sheet length compared to the standard mainsail and maximum camber mainsail presented in the same figure.

Mainsail type	L_{car} (mm)	L_{sheet} (mm)	C_{F_x} ([-])	C_{F_y} ([-])	$C_{F_{obj}}$ ([-])	$C_{F_{sheet}}$ ([-])
Standard	127	137	0.52	-1.04	0.41	1.58
Max camber	144	126.3	0.53	-1.02	0.43	1.77
Flat	89	164.8	0.42	-0.89	0.33	1.27

Table 3.4 – Optimum results for $\beta_{AW} = 40^\circ$.

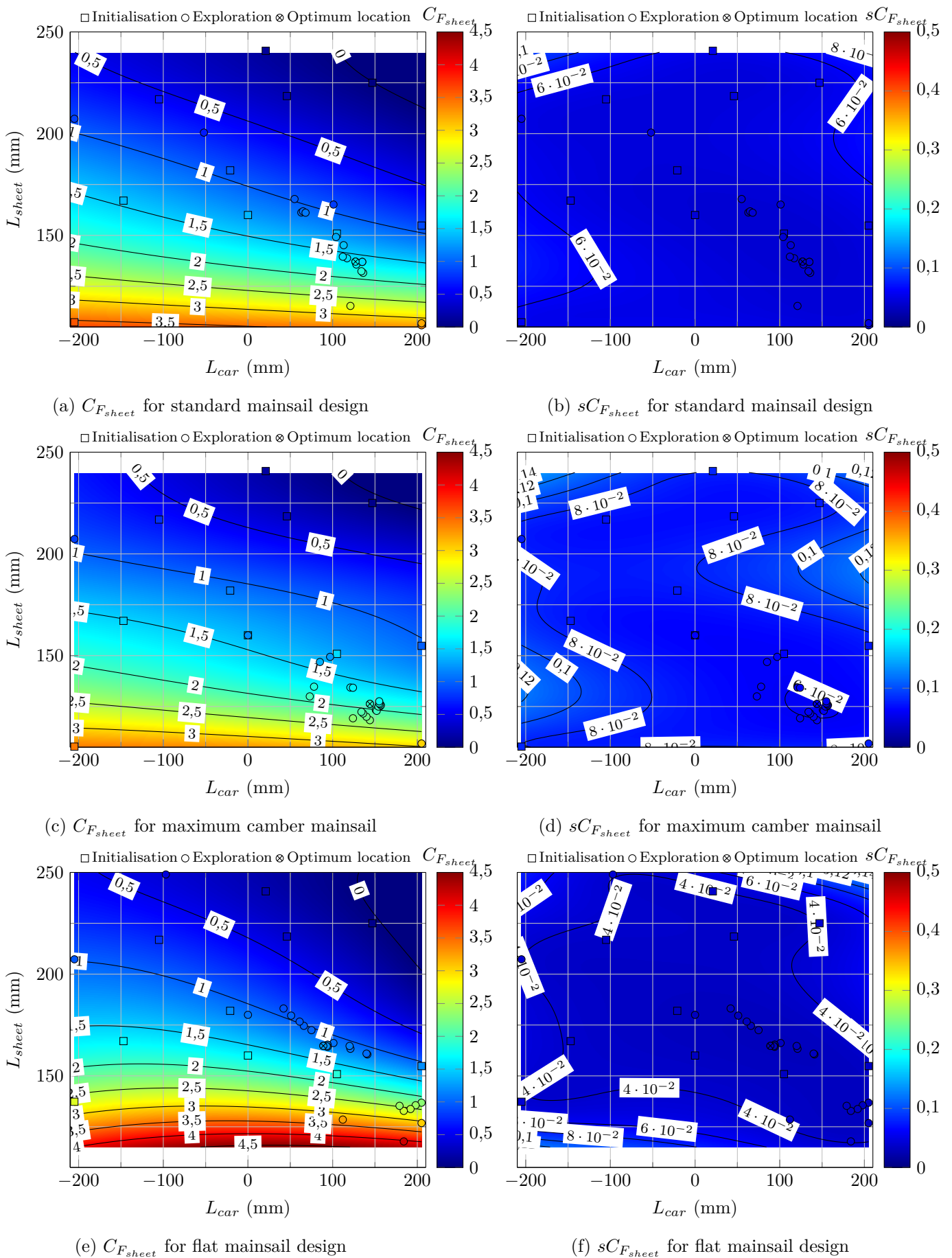


Figure 3.16 – Mainsail sheet load coefficient for the different design shapes $\beta_{AW} = 40^\circ$. \square : initialisation phase, \circ : exploration phase and \otimes : experimental optimum location.

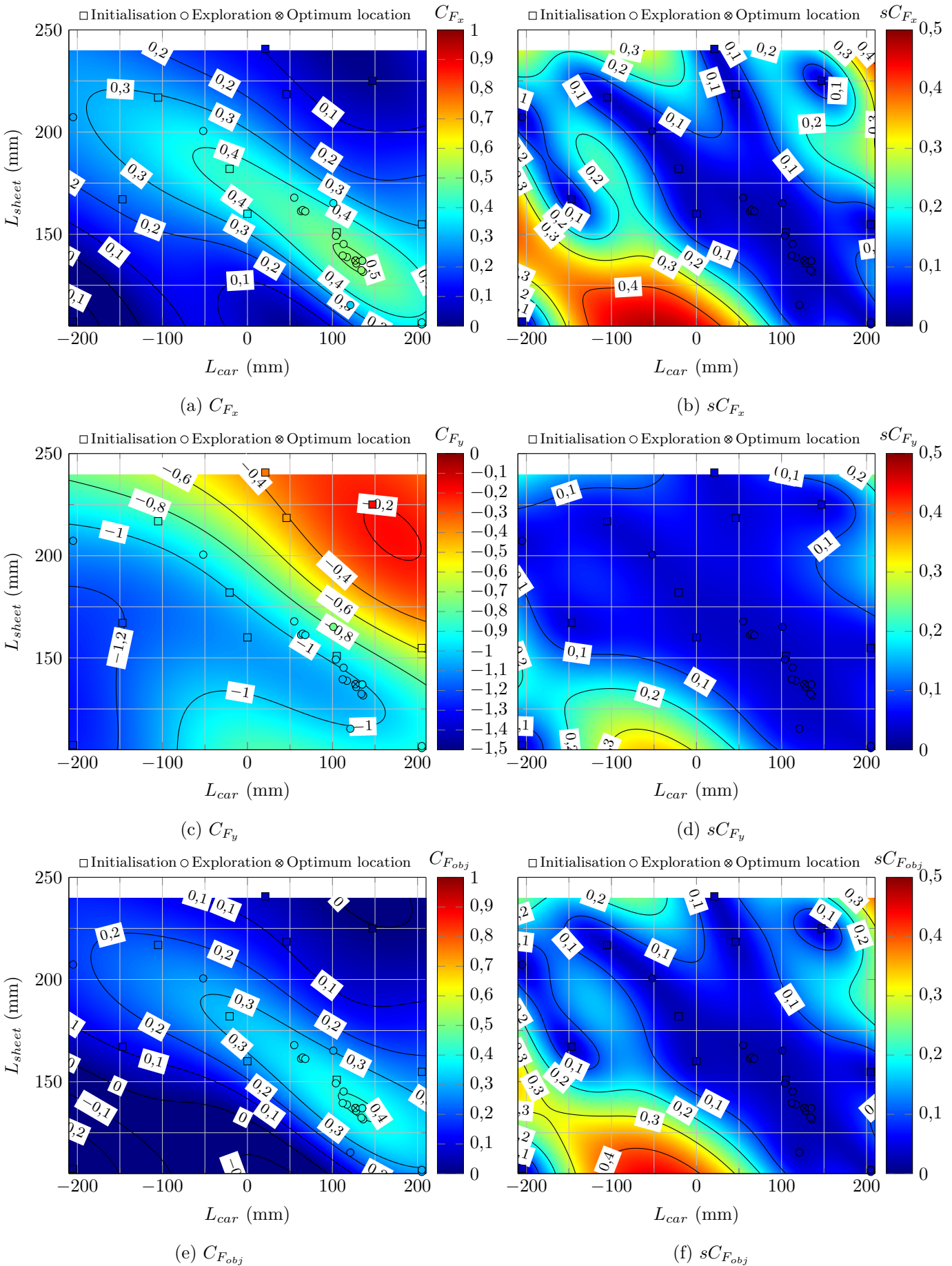


Figure 3.17 – Two-parameter optimisation for the flat mainsail $\beta_{AW} = 40^\circ$. □ : initialisation phase, ○ : exploration phase and ⊗ : experimental optimum location.

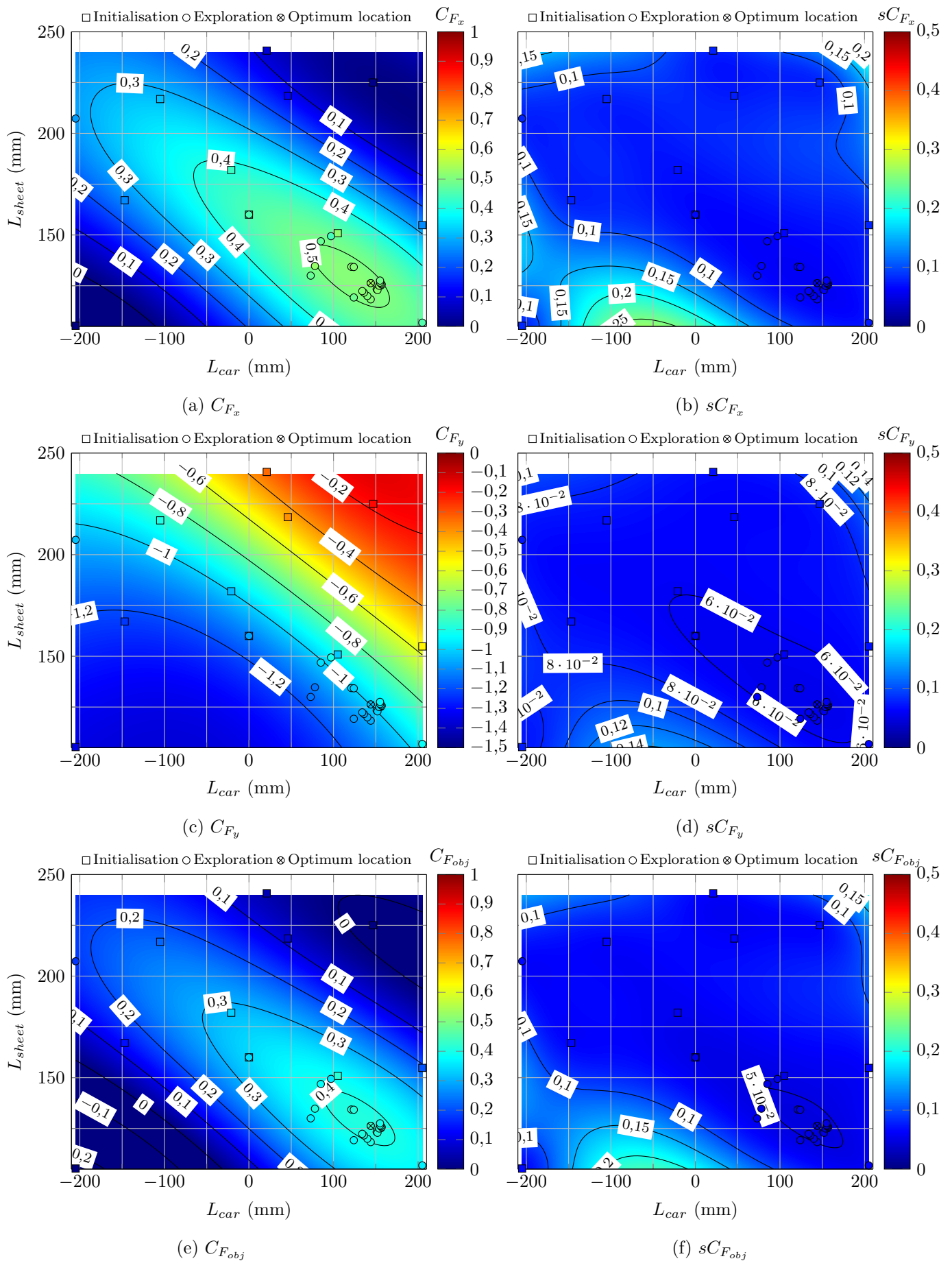


Figure 3.18 – Two-parameter optimisation for the maximum camber mainsail $\beta_{AW} = 40^\circ$. \square : the initialisation phase, \circ : exploration phase and \otimes : experimental optimum location.

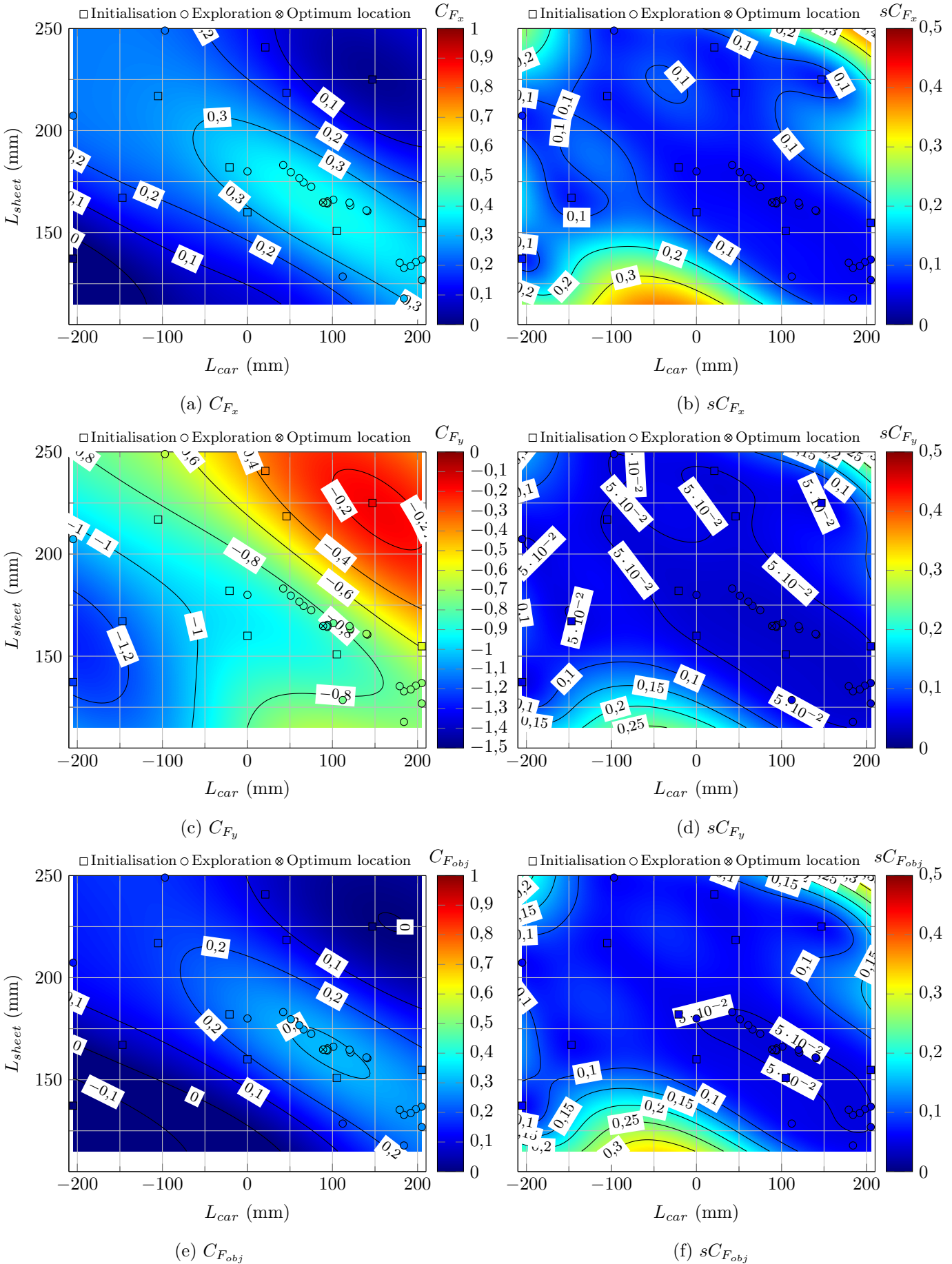


Figure 3.19 – Two-parameter optimisation for the flat mainsail $\beta_{AW} = 40^\circ$. \square : initialisation phase, \circ : exploration phase and \otimes : experimental optimum location.

3.2.5.2 Effect of design shape

Fig. 3.20 presents the comparison of the different design shapes at $\beta_{AW} = 40^\circ$. The maximum camber mainsail presents a larger area enclosed by a given level. The maximum camber mainsail is considered as more tolerant to trim adjustment than the other sails.

In this configuration, the standard mainsail is no longer the optimal design. This result is in agreement with sailors knowledge who tends to increase the camber of the sail easing the clew line when bearing away from close hauled.

The look alike ellipse shape main directions around the optimum are also different between the standard and maximum camber mainsail and leads to the same conclusion as the previous AWA. The slope of the main direction of the maximum camber mainsail is higher. It indicates that for a given change in the traveller position, the quantity of sheet length L_{sheet} to adjust is more important when the camber is more pronounced to stay close to the optimum trim.

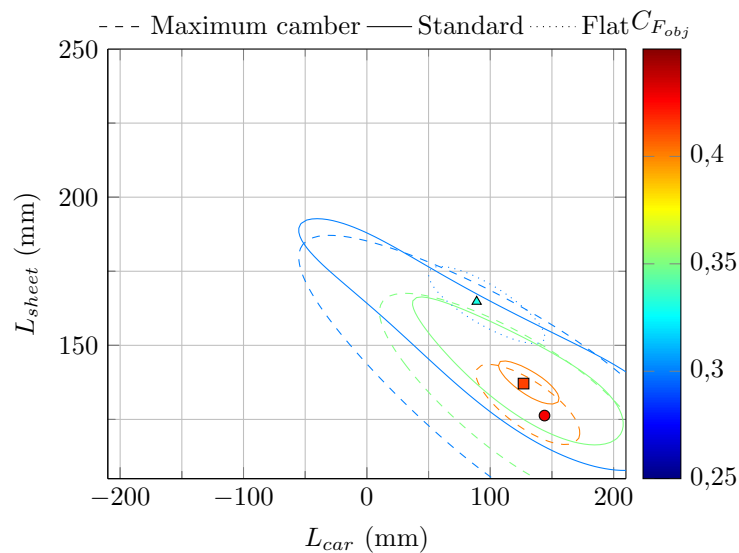


Figure 3.20 – Effect of design shape on the optimum at $\beta_{AW} = 40^\circ$. ● : maximum camber mainsail experimental optimum, ■ : standard mainsail experimental optimum, ▲ : flat mainsail experimental optimum.

3.2.5.3 Effect of mast alignment

On this AWA, an additional test was done to compare the effect of mast alignment presented in Fig. 3.21. The mast aligned with the wind tunnel flow direction (dashed curves) presents larger area for a given isoline level compared to the mast aligned with the boat centreline. This expected result confirms that rotating mast are more tolerant and perform better. The optimisation target function reaches 0.46 with the mast aligned with the TFWT main direction compared to 0.4 with the mast aligned with the boat centreline, representing a 15% improvement of the optimisation target function.

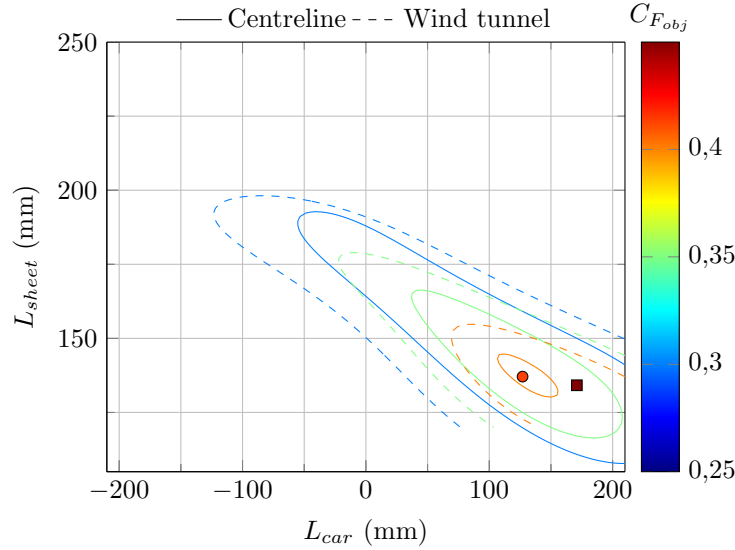


Figure 3.21 – Effect of mast alignment on the optimum for the standard mainsail at $\beta_{AW} = 40^\circ$. ● : centreline, ■ : wind tunnel.

For the next results presented at $\beta_{AW} = 60^\circ$, the mast was aligned with the TFWT flow direction.

3.2.6 Optimum location on a beam reach $\beta_{AW} = 60^\circ$

3.2.6.1 Respective optimum location

In this case, the mast was aligned with the wind tunnel main direction.

Results for the standard mainsail shown in Fig. 3.24 locate the optimum point at (205 mm, 168.8 mm). This position is on the leeward limit of the rail with the mainsail trimmed as much as possible according to live observations of the structural deformation. The experimental measurement at this optimum are described in Tab. 3.5. This optimum car position is located on a more leeward position than the two AWA previously presented. In this configuration, the optimum is located on the border of a forbidden area. The look alike ellipse shape and its two directions around the optimum still exist but the most tolerant direction (lower gradient) is limited on one side.

Results of the maximum camber mainsail shown in Fig. 3.25 locate the experimental optimum point at (205 mm, 167.8 mm). Again this optimum position is on the leeward limit of the rail. Results for the flat mainsail shown on Fig. 3.26 locate the experimental optimum point at (205 mm, 161.8 mm). The shape of the interpolation of the optimisation target function for the flat mainsail has a less pronounced ellipse shape compared to the other sail design patterns. When increasing the AWA, the optimisation process tends to test a point close to the optimum location rapidly because of the space parameter limitation due to the length of the rail. Then the exploration increases the time of the algorithm to determine the optimum location. This is probably due to the fact that when the AWA increases, the area where luffing occurs is smaller in the parameter space explored.

Mainsail type	L_{car} (mm)	L_{sheet} (mm)	C_{F_x} ([-])	C_{F_y} ([-])	$C_{F_{obj}}$ ([-])	$C_{F_{sheet}}$ ([-])
Standard	205	168.8	0.79	-0.90	0.69	
Max camber	205	167.8	0.79	-0.89	0.70	1.41
Flat	205	161.8	0.70	-0.85	0.62	1.45

Table 3.5 – Optimum results for $\beta_{AW} = 60^\circ$. The sheet load coefficient is not measured for the standard mainsail.

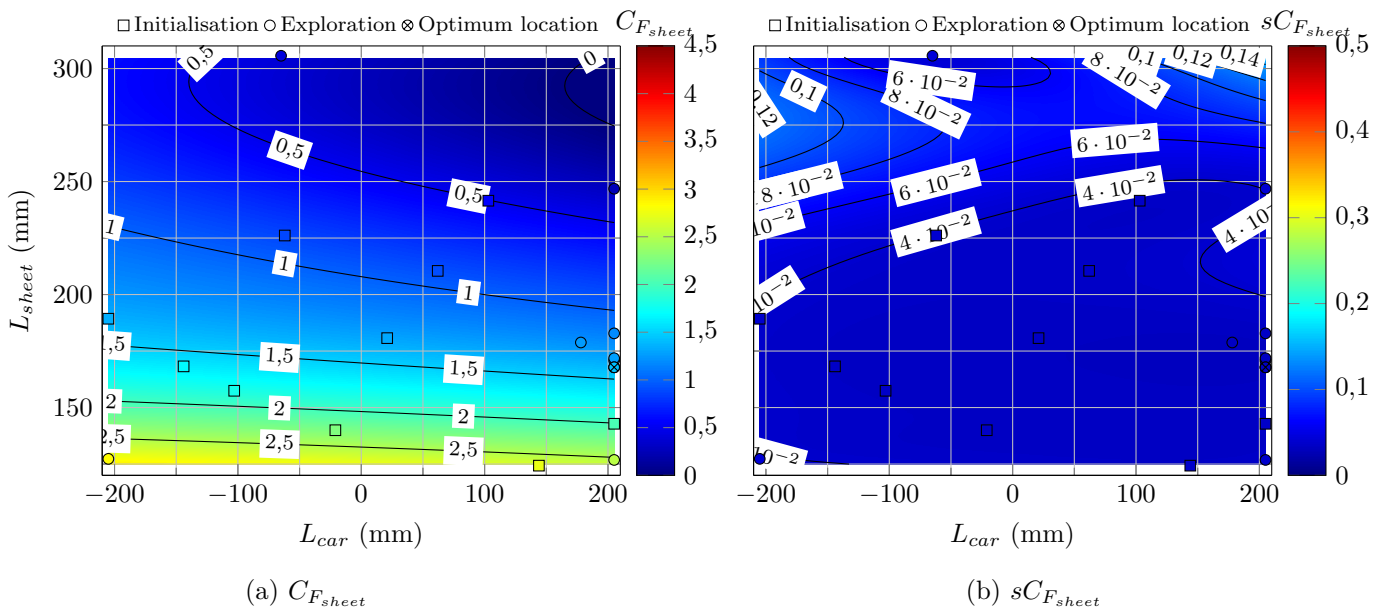


Figure 3.22 – Mainsail sheet load coefficient for the maximum camber mainsail $\beta_{AW} = 60^\circ$. \square : initialisation phase, \circ : exploration phase and \otimes : experimental optimum location.

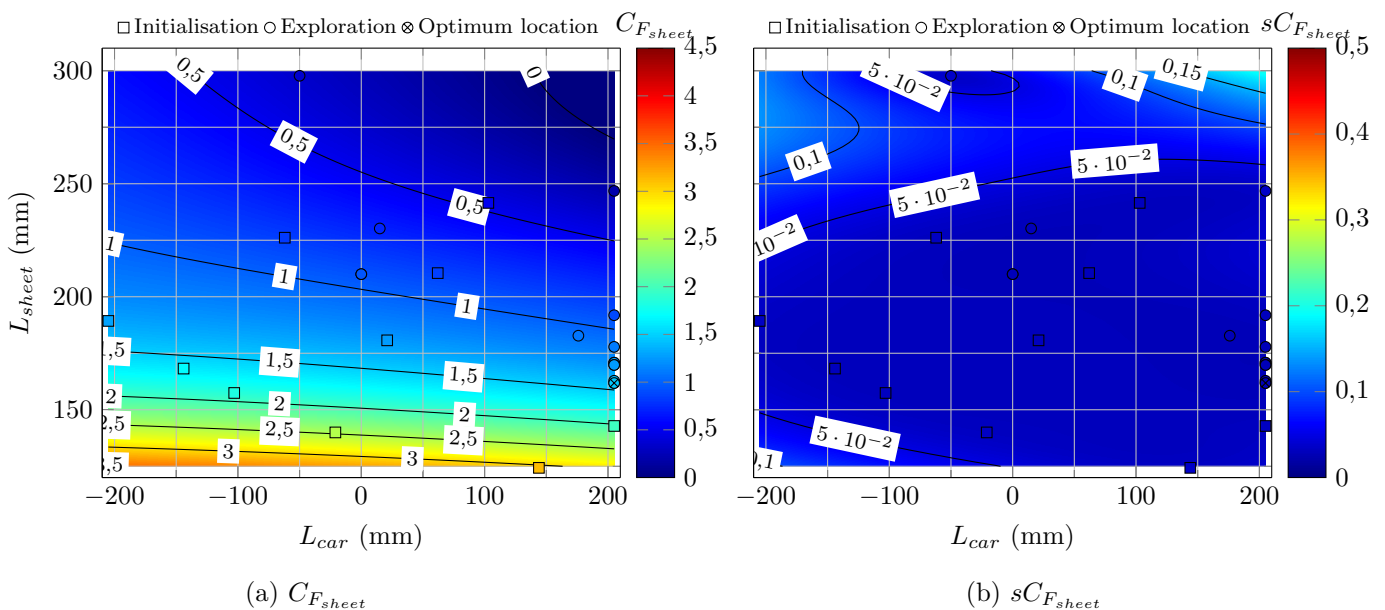


Figure 3.23 – Mainsail sheet load coefficient for the flat mainsail $\beta_{AW} = 60^\circ$. \square : initialisation phase, \circ : exploration phase and \otimes : optimum location.

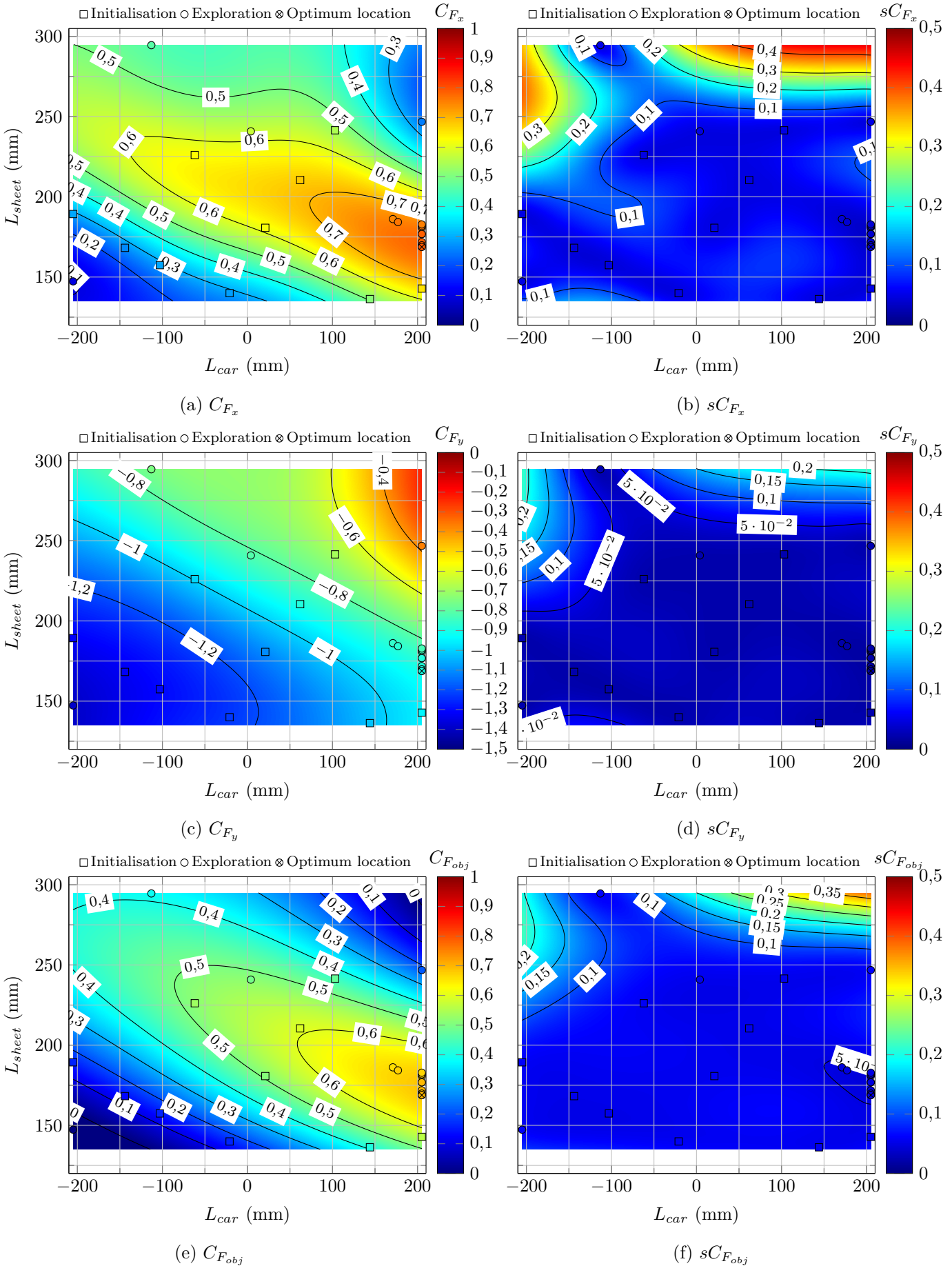


Figure 3.24 – Two-parameter optimisation for the standard mainsail $\beta_{AW} = 60^\circ$. \square : initialisation phase, \circ : exploration phase and \otimes : experimental optimum location.

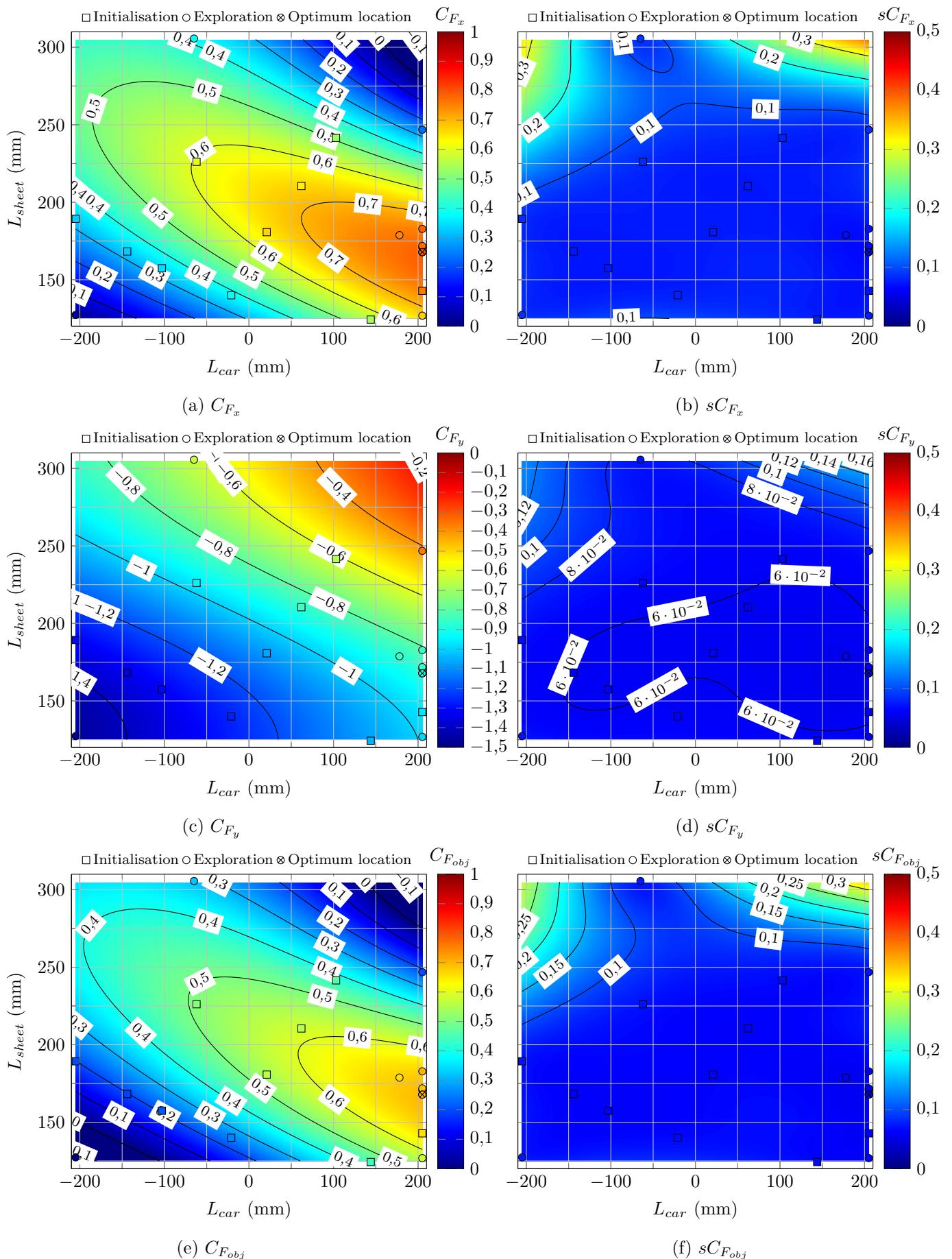


Figure 3.25 – Two-parameter optimisation for the maximum camber mainsail $\beta_{AW} = 60^\circ$. \square : initialisation phase, \circ : exploration phase and \otimes : experimental optimum location.

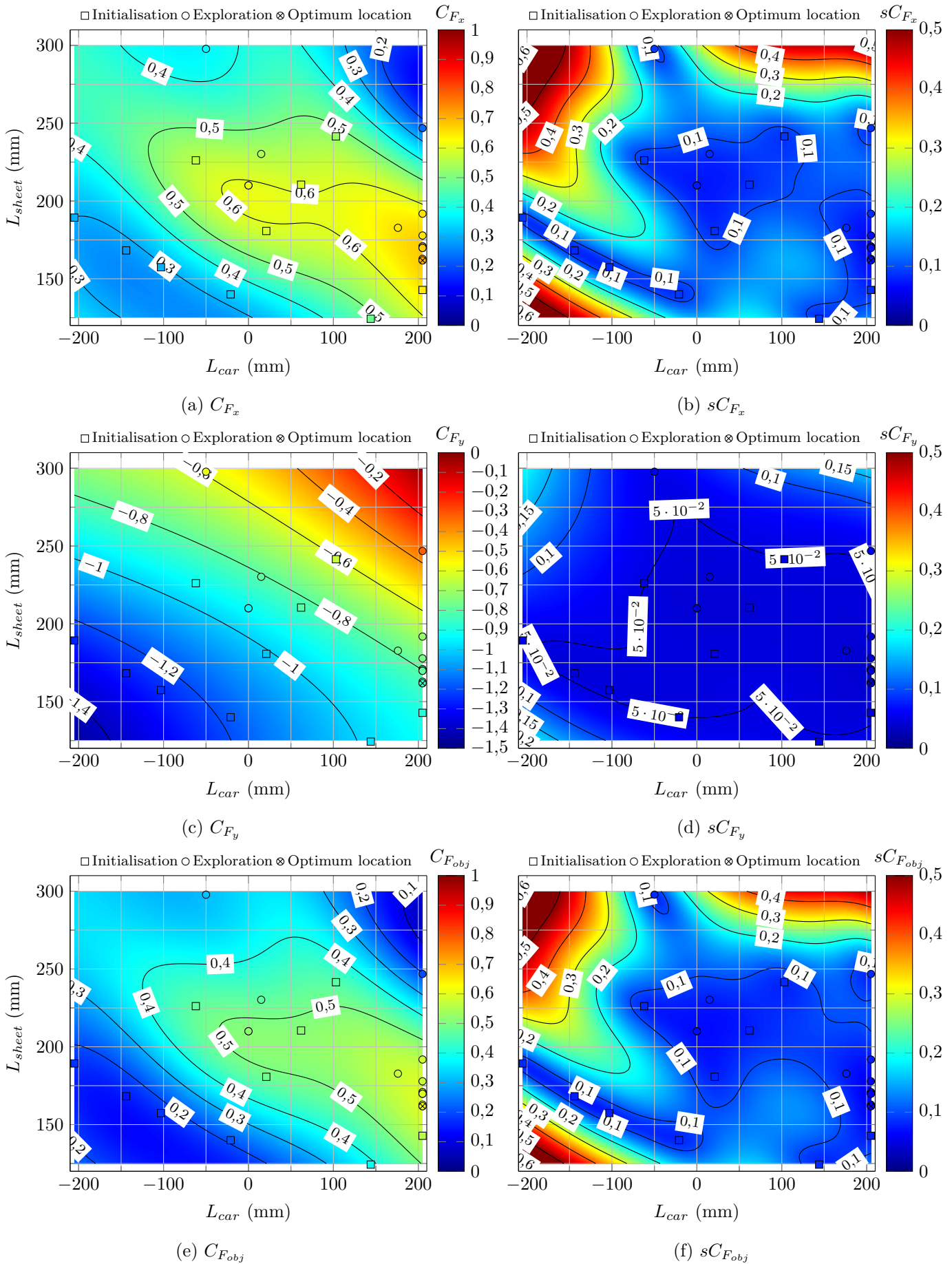


Figure 3.26 – Two-parameter optimisation for the flat mainsail $\beta_{AW} = 60^\circ$. \square : initialisation phase, \circ : exploration phase and \star : experimental optimum location.

3.2.6.2 Effect of design shape

Fig. 3.27 presents the comparison of the interpolation of the target function for the different design shape at $\beta_{AW} = 60^\circ$. The maximum camber mainsail presents a larger area enclosed by a given level. The maximum camber mainsail is therefore considered as more tolerant to trim adjustment than the other sails. Once again in this configuration, the standard mainsail is not the optimal design. Contrary to the two previous AWA tested, all the optimum are located here on the border of a forbidden area (maximum value of L_{car}).

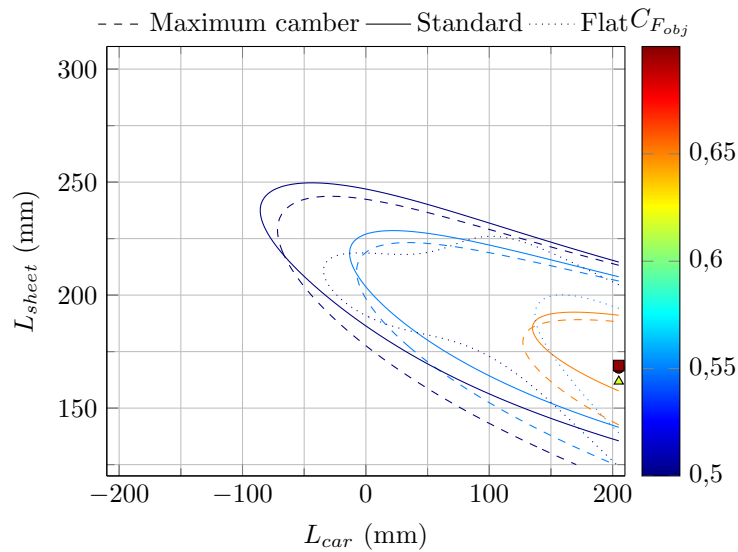


Figure 3.27 – Effect of design shape on the optimum at $\beta_{AW} = 60^\circ$. ● : maximum camber mainsail experimental optimum, ■ : standard mainsail experimental optimum, ▲ : flat mainsail experimental optimum.

3.2.7 Effect of AWA on the optimum and general conclusions

Static trim optimisation results show that:

1. the optimum sail design can change regarding the point of sail. The best design is the standard mainsail for close-hauled then the maximum camber mainsail achieves better performance for the two other AWA tested. The optimum target function increases when the AWA increases as the aerodynamic force is directed more forward.
2. the standard and maximum camber design shape are more tolerant to the trim adjustment around the optimum. The ellipse shape pattern of the $C_{F_{obj}}$ function in the parameter space (L_{car} , L_{sheet}) exists for all the AWA and design shapes tested with a main direction which slightly vary with the camber
3. mast alignment has an important effect on the sail performance as it change strongly the flow behaviour in the luff area. As expected, mast aligned with the incoming flow presents better performance.

Static optima have been located for different situations, dynamic study around these optima is presented in the next section.

3.3 Pumping: effect of dynamic trimming on respective optimum

The goal of this section is to investigate the unsteadiness of a sail aero-elastic system submitted to dynamic conditions in order to better understand the represented unsteady behaviour. One of the simplest action that can be modelled is a dynamic evolution on the sheet length L_{sheet} representing pumping. Therefore the unsteadiness was here achieved through a dynamic trimming device generating oscillation of the sheet length.

The question to address here as a second goal of this section is: does pumping effectively increase the aerodynamic propulsion compared to a static trim? Going further in the performance consideration, we may only focus on the dynamic behaviour around the static optimum. If so the complementary goal of this experiment is to quantify the potential gain or loss in the aerodynamic part with this dynamic action. Another key part of this study is to determine if there is an optimal frequency and amplitude of pumping. Using three different sails provides information about the effect of the design-shape on the dynamic results. The computation of the required energy provided by the trimming system to the sail and rig is also presented. This energy would correspond to the energy required by the crew to achieve this dynamic trimming. The evolution of this quantity gives information about the cost of the crew action compared to the benefits in the aerodynamic propulsion.

First the dynamic trimming system is introduced and pumping around the reference case is presented at $\beta_{AW} = 40^\circ$. Pumping at $\beta_{AW} = 60^\circ$ is then described for the different design shapes. The unsteadiness effect on mean values and time series evolution are shown. This higher value of AWA allows more important amplitude to be tested than close hauled where only small oscillation amplitudes are possible with few expected effect for an important trimming effort. A Lissajou representation is provided to present the dynamic evolution of force coefficients regarding the oscillation frequency. Then from the Lissajou representation of the load coefficient, required power to generate the oscillation can be computed.

Some discussions, conclusions, limitations and perspectives of this work end this section and chapter.

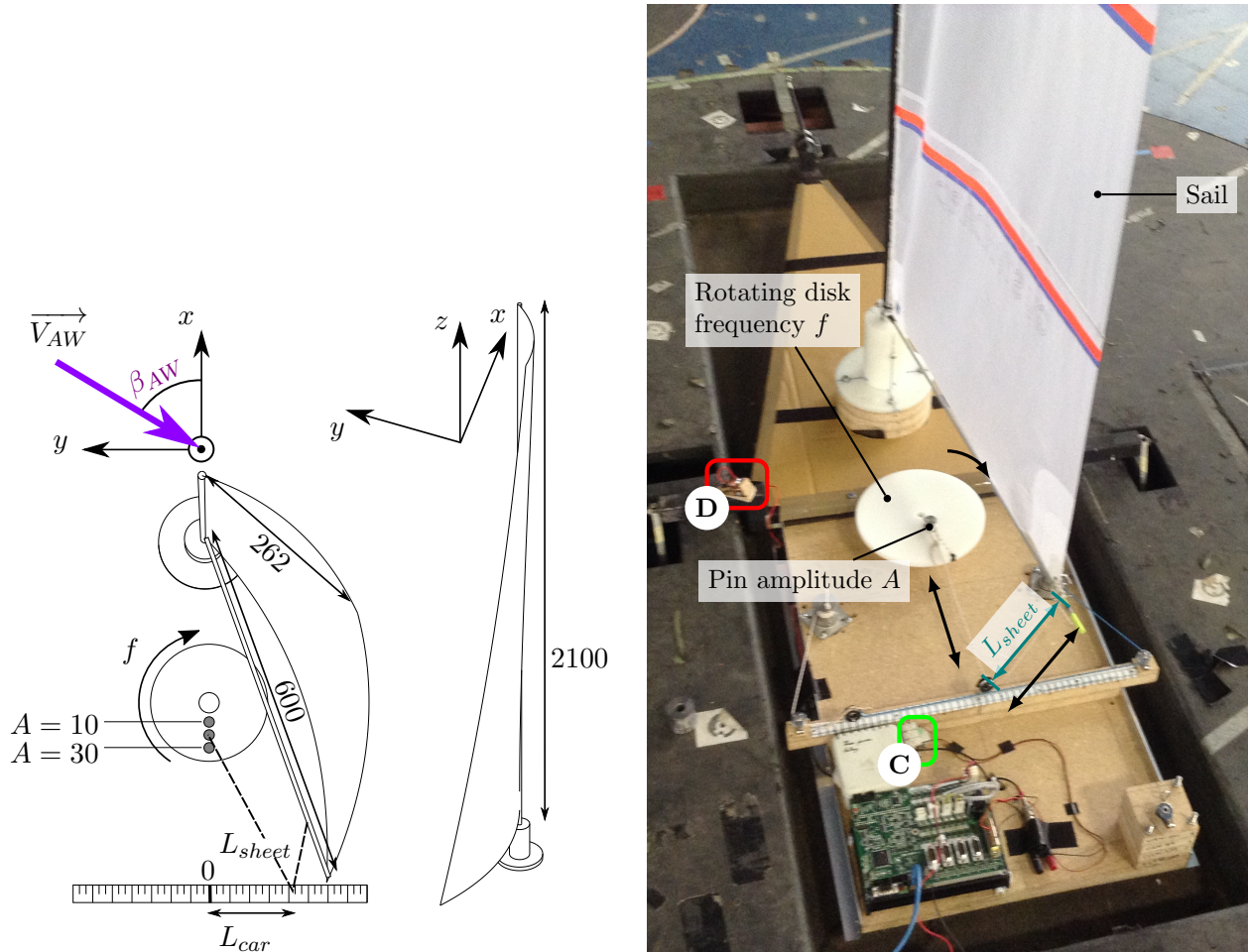
3.3.1 Dynamic trimming

3.3.1.1 Dynamic trimming presentation

The mainsail sheet was attached to an eccentric pin which position could radially be changed on the rotating disk as shown in Fig 3.28. This rotating disk was controlled by the same stepper motor than the mainsail sheet winch one in static trim configuration. Dynamic trimming is defined by several parameters:

- the reference static point corresponding to the static parameters (L_{car}, L_{sheet}) of each sail. It corresponds to the test with a rotating disk frequency $f = 0$ Hz.
- the pumping trimming frequency f defined by the rotation frequency of the rotating disk. It corresponds to the inverse of the rotation period T .

- the pumping amplitude A of the sheet oscillation defined by the radius of the eccentric location on the rotating disk. A could be chosen from 10 mm to 90 mm by 10 mm step. $A=10$ mm stands for an eccentric radially located at 10 mm of the disk centre *i.e.* a peak to peak amplitude of 20 mm on L_{sheet} . The associated sheeting angle variation requires extensive video post processing which had not been performed on all cases presented in this section.



(a) Dynamic trimming device in upwind configuration. Dimensions are in mm. Here only three possible eccentric positions are represented.

(b) Photograph taken without wind of upwind dynamic configuration. (C) synchronisation LED, (D) synchronisation laser.

Figure 3.28 – Dynamic trimming device in upwind configuration.

3.3.1.2 Dimensionless parameters of the study

f_r is defined as the reduced frequency $f_r = \frac{fc}{U_{Pitot}}$ with c the representative chord length defined by $c = \frac{S}{l_P} = 0.4748$ m with l_P the sail luff length and S the sail area, f the rotating plate frequency, and U_{Pitot} the reference wind speed provided by the Pitot tube. Here $U_{Pitot} = 3.5$ m s⁻¹. f_r is a dimensionless parameter defined as the ratio of the reference convection time over the oscillating motion period. If $f_r = 0$, there is no oscillation. The more f_r increases, the more dynamic the oscillating trim is, compared to the reference convecting time. In order to avoid reduced frequency differences between the different design shapes, all representative chords are based on the standard

mainsail design. The available maximum frequency is limited by the power supply card of the main stepper motor.

Some other studies may refer the reduced frequency as k like [Schutt and Williamson, 2016] or as a Strouhal number St like in [Taylor et al., 2003, Egan et al., 2016]. The reduced frequency notation f_r is chosen here to clearly associate the flapping action to a forced dynamic motion like in [Fossati and Muggiasca, 2012a] and not to a natural unsteady phenomena linked to the fluid behaviour where the Strouhal number was originally designed for [Williamson, 1988]. For instance in sailing engineering, Strouhal number is also associated to a characteristic fluctuation observed in measured pressure time series as given by [Bot et al., 2014]. Strouhal number in literature is sometime composed with other coefficients, like the wake width related to the motion amplitude ([Lua et al., 2016]) or based on the pulsation of motion as given by [Schouweiler et al., 2005].

f (Hz)	0	0.094	0.469	0.938	1.406	1.875	2.344	2.813	3.281	3.750	4.219
f_r (-)	0	0.013	0.064	0.127	0.191	0.254	0.318	0.381	0.445	0.509	0.572

Table 3.6 – Tested dynamic frequencies and the associated reduced frequencies.

The amplitude A is not taken into account in the previously defined reduced frequency for different reasons. A is not directly linearly representing a geometrical evolution of a parameter of the flying shape during dynamic trimming. A can only take discrete values and for really trimmed static situation the lowest amplitude value is more acting vertically on the boom than opening or closing the sheeting angle. It only affects the leech tension and mast bending. On the contrary with large amplitude value, the sheeting angle parameter changes largely. Including relevant geometric parameter about the motion amplitude different from A in the reduced frequency definition requires extensive video post processing. So far, no relevant and direct way to compute geometric parameter has been found. The sheeting angle might be a relevant parameter but still require further investigation. A parallel with bio-inspired work carried out on flapping wings could be established ([Shyy et al., 2013a, Shyy et al., 2013b]). However the main difference between most of those literature examples is the fact that the flapping wings in animal locomotions are most of the time created thanks to a structure close to the wing leading edge. In our case, the dynamic motion is created thanks the boom motion which can be compared to the foot of the lifting device.

Mean aerodynamic coefficients are averaged over an integer number of period of oscillations regardless of the reduced frequency. Results are presented up to the reduced frequency of 0.4 to be sure to study phenomenon under the first natural frequency of the mast as computed in App. H. The sail is attached at the tack and head points without extension of the luff length at rest and the luff can slide in the mainsail rear track. Therefore we assume that the mainsail luff tension is small compared to the mast stiffness and the attached sail does not lower down the natural frequency of the mast.

3.3.1.3 Dynamic sheet length computation

For the different frequency tested, L_{car} remains constant for a specific configuration (sail, mast orientation and AWA). Only L_{sheet} is changing according to a command law depending on the

initial sheet length, the initial angular position κ_0 and the actual angular position of the disk κ in Fig. E.3. The demonstration and notations are presented in App. E

$$L_{sheet}(\kappa_T) = L_m(\kappa_0) + L_{sheet}(\kappa_0) - L_m(\kappa_T) \quad (3.4)$$

using $\kappa_T = \kappa + \kappa_0$ and

$$L_m(\kappa_T) = \sqrt{(x_C + A \sin(\kappa_T) - x_{O_{disk}})^2 + (-L_{car} + A \cos(\kappa_T) - y_{O_{disk}})^2 + (z_C - z_{O_{disk}})^2} \quad (3.5)$$

$$\begin{aligned} L_{sheet}(\kappa_T) &= \sqrt{(x_C + A \sin(\kappa_0) - x_{O_{disk}})^2 + (-L_{car} + A \cos(\kappa_0) - y_{O_{disk}})^2 + (z_C - z_{O_{disk}})^2} + L_{sheet}(\kappa_0) \\ &\quad - \sqrt{(x_C + A \sin(\kappa_T) - x_{O_{disk}})^2 + (-L_{car} + A \cos(\kappa_T) - y_{O_{disk}})^2 + (z_C - z_{O_{disk}})^2} \quad (3.6) \end{aligned}$$

With the analytical definition it can be shown that the reference static case initial setup length is close but not equal to the mean value of the maximum and minimum value of the instantaneous sheet length. This explains why for dynamic curves presented in this section, when L_{sheet} is represented for a given amplitude, its value oscillates between $L_{sheet \ static} - A + \epsilon$ and $L_{sheet \ static} + A + \epsilon$ with ϵ a small real compared to the amplitude. For more details see App. E

3.3.1.4 Energy analysis

The mean value of the sheet load coefficient is an indication of the change of the dynamic aspect, however it does not provide any information about the energy required to trim the sail. The required work by the trimming system to make the sail oscillate can be evaluated using the load sensor, disk angular position and sheet length informations. Two methods could be used. The first one can compute the instantaneous torque applied on the disk by the sheet times the constant angular velocity. The second method uses the load sensor displacement and the load applied to it, regardless of the trimming device. Here this second method is presented because it can be compared to what a sailor might do, just adjusting the sheet tension and length without any rotating devices. It is a closer to actual power measurement while pumping suggested in [Ouahahi et al., 2014, Brummer, 2016]. The force measured by the load sensor is in the local sheet direction, *i.e.* from the sheeting point on the boom sb indicated in Fig. 3.2 to the low ring friction exit point indicated in Fig. E.2. The work exchanged between the trimming system and the sail can be computed using the instantaneous sheet load and the elementary displacement of the load sensor dL_{sheet} . A first approximation considering the elementary displacement mostly aligned with the sheet direction implies that this work is equal to the load times the sensor displacement $dW = \overrightarrow{F_{sheet}} \cdot \overrightarrow{dL_{sheet}} = F_{sheet} dL_{sheet}$

This property is interesting because it implies that the area contained in a $C_{F_{sheet}}$ vs L_{sheet} curve is proportional to the energy exchange between the trimming device and the sail and rig system during one oscillation cycle. The orientation of this curve also provides information about the exchange direction. This can be used to compute a power defined by:

$$P = \frac{\overline{q_{Pitot}(t)}S}{T} \oint_{one\ loop} C_{F_{sheet}}(L_{sheet})dL_{sheet} \quad (3.7)$$

Dynamic trimming is first presented around the reference case at $\beta_{AW} = 40^\circ$ then for a deeper AWA on different design shapes.

3.3.2 Pumping in the reference case $\beta_{AW} = 40^\circ$

Dynamic trimming was first tested around the optimum location of the static reference case. The car traveller was fixed on the model centreline and the standard mainsail reference sheet length was $L_{sheet\ 0} = 175$ mm. No load sensor was used for this test.

3.3.2.1 Effect of the reduced frequency f_r on mean values

Fig. 3.29 and Fig. 3.30 represent the mean drive and side force coefficients change for different trimming amplitudes. Square symbols represent the time series mean value, triangle pointing upward, the maximum value and triangle pointing downward the minimum value of the time series. In this representation $f_r = 0$ stands for the optimum static case. Several general comments can be done:

- the lower reduced frequency not equal to 0 presents a significant decrease in the drive and side force coefficient absolute value. Considering a quasi-static approach on this reduced frequency, the dynamic trimming will only change the trim value to positions which are not the static optimum. Moreover the change of sheet length is oriented in a direction close to the trim sensitive direction in the two-parameter space. Therefore a decrease in the performance optimisation target is due to the trim being not optimal most of the time and no actual dynamic effect is expected.
- the data are plotted until a reduced frequency of 0.4. For higher reduced frequency, the input frequencies is close to the first mode of the natural frequency of the mast as described in App. H. This strongly affects the results which are then not representative of the aerodynamic effect.
- the higher the amplitude of trimming tested, the higher maximum value and the lower the minimum value.
- for all the tested amplitudes, an optimum reduced frequency at $f_r \approx 0.25$ to $f_r \approx 0.3$ can be detected in Fig. 3.31 for the optimisation target function.
- the lowest amplitude presents few variations. In this case, the amplitude is small and does not tend to largely open the mainsail. The small motion at low amplitude trim or ease vertically the boom rather than opening the sheeting angle changing the AoA . The higher the amplitude, the higher the maximum and the smaller the minimum values. Results for larger amplitude $A = 40$ mm even present occasionally instantaneous values of F_x and F_y changing sign.

For all the tested amplitudes, dynamic trimming increases the drive force coefficient, up to 0.6 for the amplitudes $A = 30$ mm and $A = 40$ mm, for a reduced frequency of 0.25. It corresponds to a

20% increase of the static drive force coefficient. The dynamic part also produces higher mean drive force coefficient for reduced frequency above 0.125 compared to the static case. Similar comments can be done for the side force coefficient where the oscillations at the reduced frequency of 0.25 generates a 16% higher side force coefficient absolute value.

The optimisation target function indicates that the combined effect on drive and side forces also presents an optimum located at this reduced frequency around 0.25 with an increase around 10% for large amplitudes as shown in Fig. 3.31. The optimisation target function reach a higher mean value for a reduced frequency located between $f_r = 0.25$ and $f_r = 0.32$ depending on the amplitude.

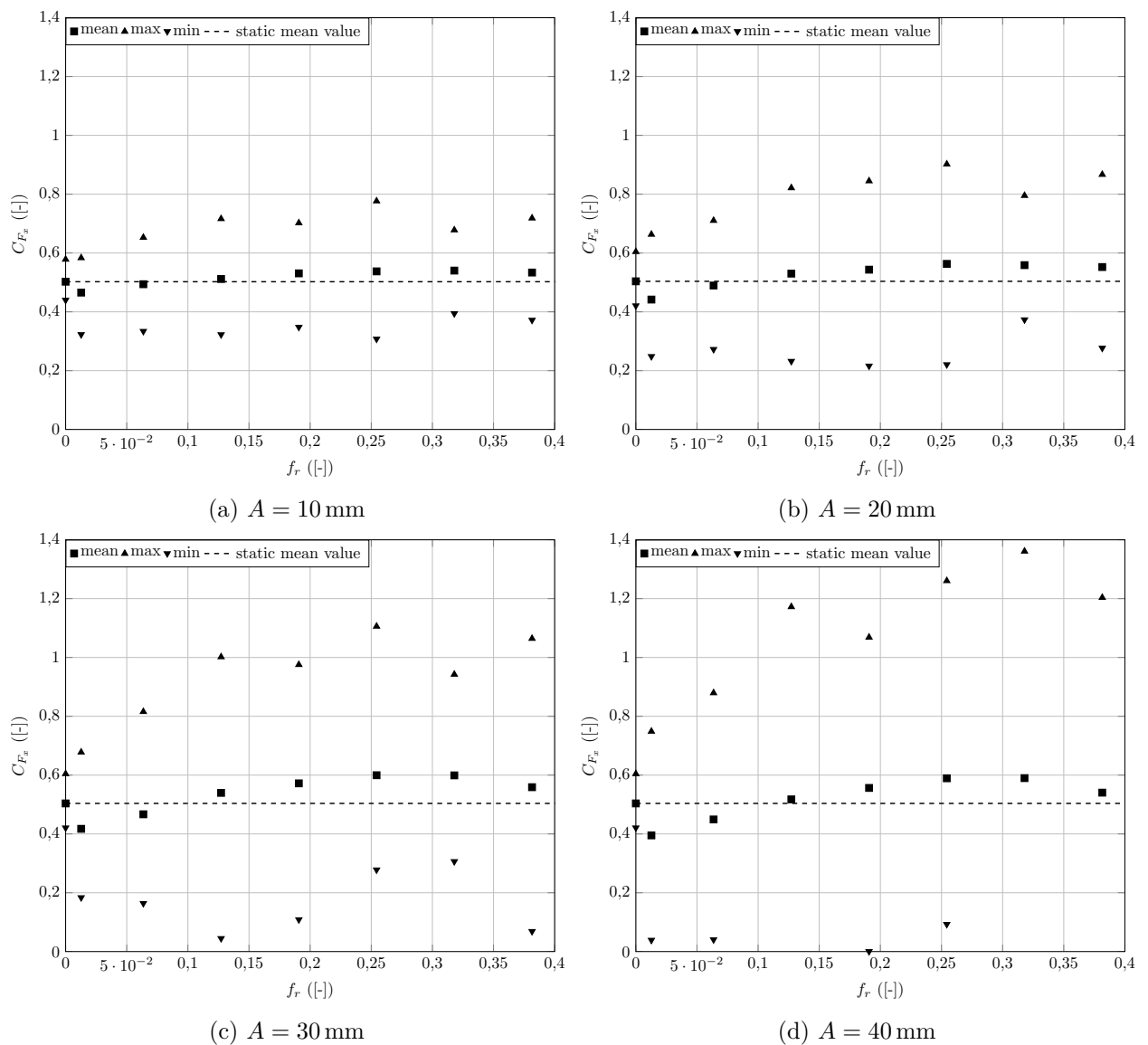


Figure 3.29 – Drive force coefficient with dynamic trimming for the reference case at $\beta_{AW} = 40^\circ$, standard mainsail.

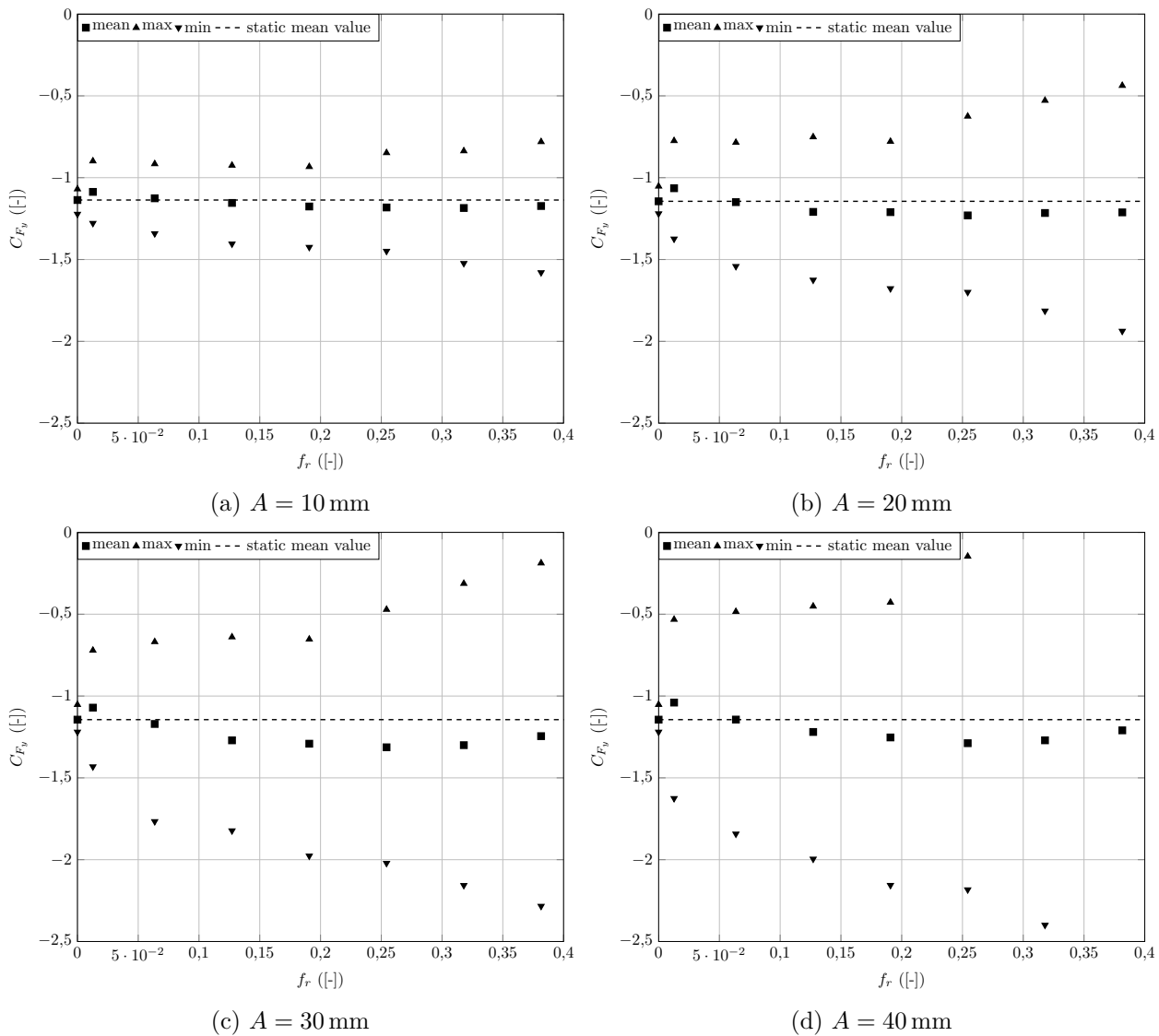


Figure 3.30 – Side force coefficient with dynamic trimming for the reference case at $\beta_{AW} = 40^\circ$, standard mainsail.

The maximum tested amplitude $A = 40$ mm gives a slightly lower maximum on the optimisation target function than the amplitude $A = 30$ mm. This difference is still in the uncertainty measurement but it could indicate that above a certain amplitude the sail is reaching a certain area where luffing may occur largely reducing the performance on the eased phase even with the dynamic trimming. These results indicate that there is an optimum couple of reduced frequency and amplitude values.

The maximum and minimum value of the drive force indicates that for the largest amplitude tested, some negative drive force occurs. This can be associated to the brief extreme phase where the sail is completely luffing and no longer generating propulsion. The lowest dynamic value tested even indicates drive force value close to 0, which is associated to a overeased sail luffing.

The side force presents positive values for the strong dynamic motions with the largest amplitude, probably due to the mast inertia going back in the windward direction transmitted on the oversheeted phase.

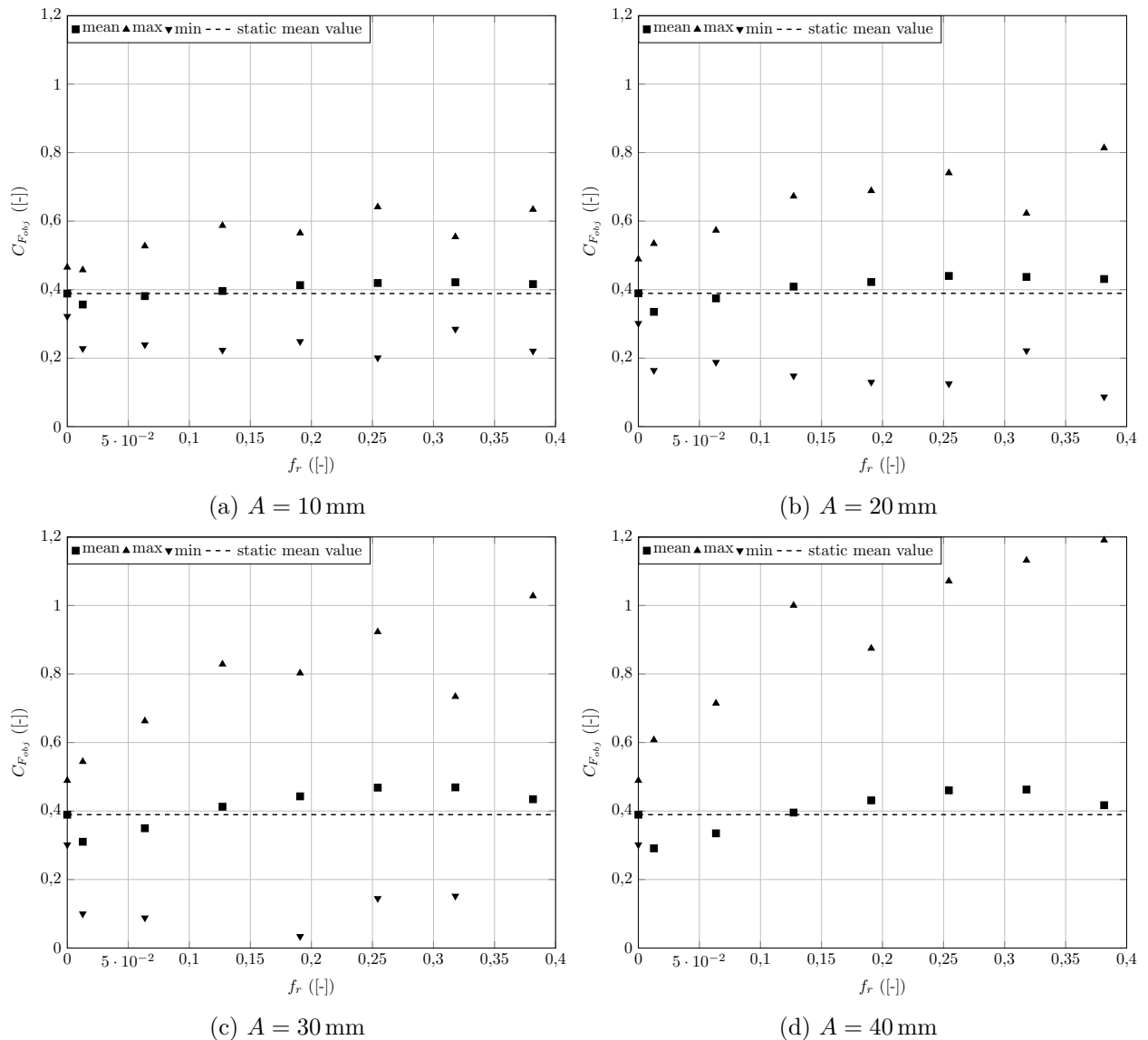


Figure 3.31 – Optimisation target function with dynamic trimming for the reference case at $\beta_{AW} = 40^\circ$, standard mainsail.

Dynamic trimming on the upwind reference case

This first dynamic trimming situation where the car traveller was fixed on the centreline already shown evolution of the mean value of the force coefficients depending on both the amplitude of motion and the reduced frequency. It has shown that the dynamic behaviour of the sail can improve the aerodynamic performance.

Next is presented the effect of dynamic trimming on different design shape for a deeper AWA which enable to test different sets of amplitudes around the static optimum. Dynamic effect on the time series coefficient will be investigated in the other case presented.

3.3.3 Pumping at beam reach $\beta_{AW} = 60^\circ$

The results in this situation are presented in [Aubin et al., 2016b]. Short conclusions of this work also benefited from a short popular scientific publication in [Larousserie, 2016]. For each sail, the car traveller position and initial reference sheet length corresponded to the optimum ones. The load sensor is used during this test providing dynamic information on sheet load. First are presented the dynamic effect on the mean value of force coefficient, then time series change is shown on one example which presents the general trends. The mast was aligned with the TFWT flow direction.

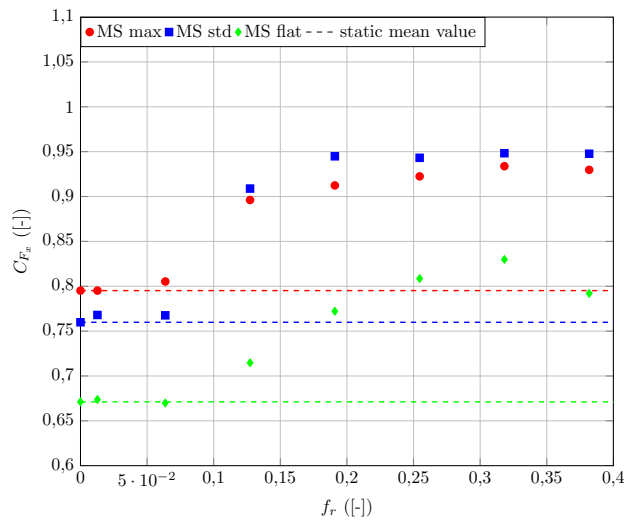
3.3.3.1 Effect of both the reduced frequency f_r and design shape on time averaged forces

Fig. 3.32 represents the evolution of the averaged drive and side force coefficient with the reduced frequency for the different design shapes. The trimming device being also changed between static to dynamic device, for $f_r = 0$ the difference observed with the static measured values presented in the previous section 3.2 remains in the uncertainty of measurement.

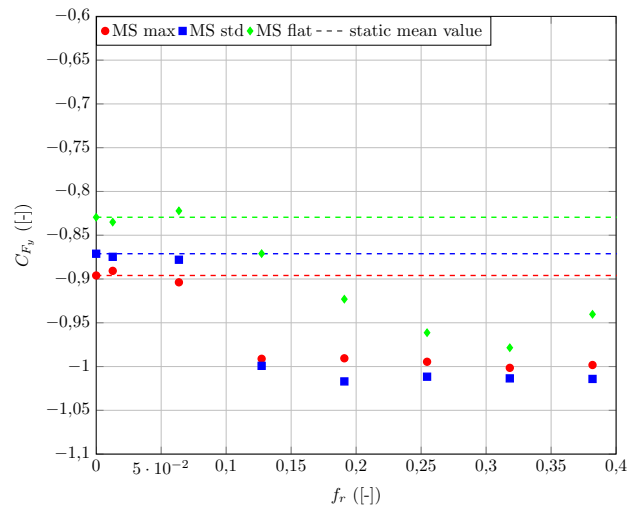
For the lowest amplitude tested $A = 10$ mm, the drive force coefficient does not seem to decrease for the reduced frequency $f_r = 0.013$ contrary to greater amplitudes. This can be explained by the small variations which are still contained on a fairly good location on the computed interpolation meta-model during the static optimisation process shown in Figs. 3.24, 3.25 and 3.26. For this configuration, a small vertical amplitude still remain close to the optimum static value. For the lowest amplitude, the quasi-static situation (0.013) has no effect and results are close to the static optimum. For an amplitude above 20 mm, the decrease compared to the optimum in static situation is significant and therefore observed in the dynamic lowest reduced frequency cases.

All amplitude and design shape configurations present a maximum drive force and minimum side force coefficient shown in Fig. 3.32 for a reduced frequency within 0.25 to 0.32. For the optimisation target function shown in Fig. 3.33, a maximum is observed for all situations. The flat mainsail benefits more from the dynamic behaviour than the other design shapes. The flat mainsail even reaches the same performances than the standard one. However the required mean sheet load is higher for the flat mainsail. Standard and maximum camber mainsails present similar performances except for the highest amplitude. For the lowest amplitude tested the standard mainsail have slightly better performance than the other ones for a reduced frequency above 0.1. The greater the amplitude, the better the maximum camber mainsail.

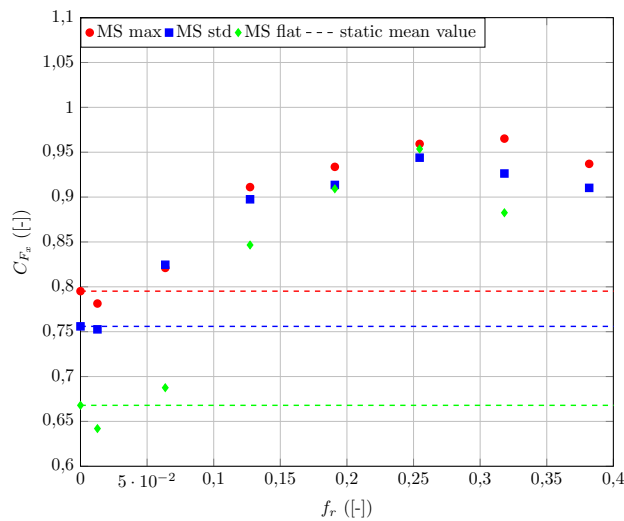
For a more complete analysis, the next section investigates the effect of dynamic trimming on the time series and Lissajou representation.



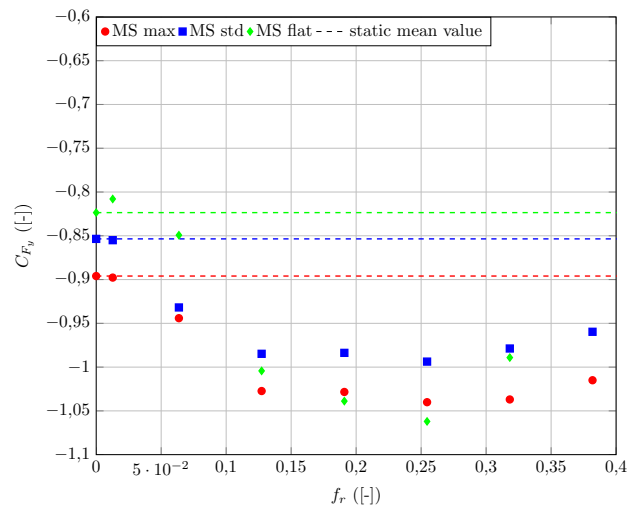
(a) C_{F_x} with $A = 10$ mm



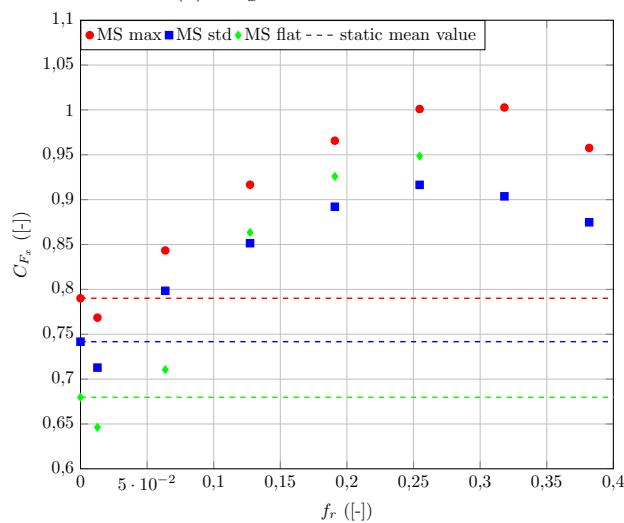
(b) C_{F_y} with $A = 10$ mm



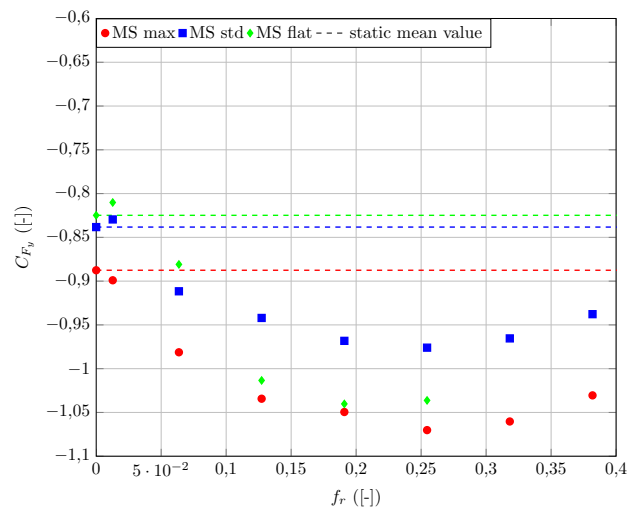
(c) C_{F_x} with $A = 20$ mm



(d) C_{F_y} with $A = 20$ mm



(e) C_{F_x} with $A = 30$ mm



(f) C_{F_y} with $A = 30$ mm

Figure 3.32 – Mean drive and side force coefficient with dynamic trimming for $\beta_{AW} = 60^\circ$.

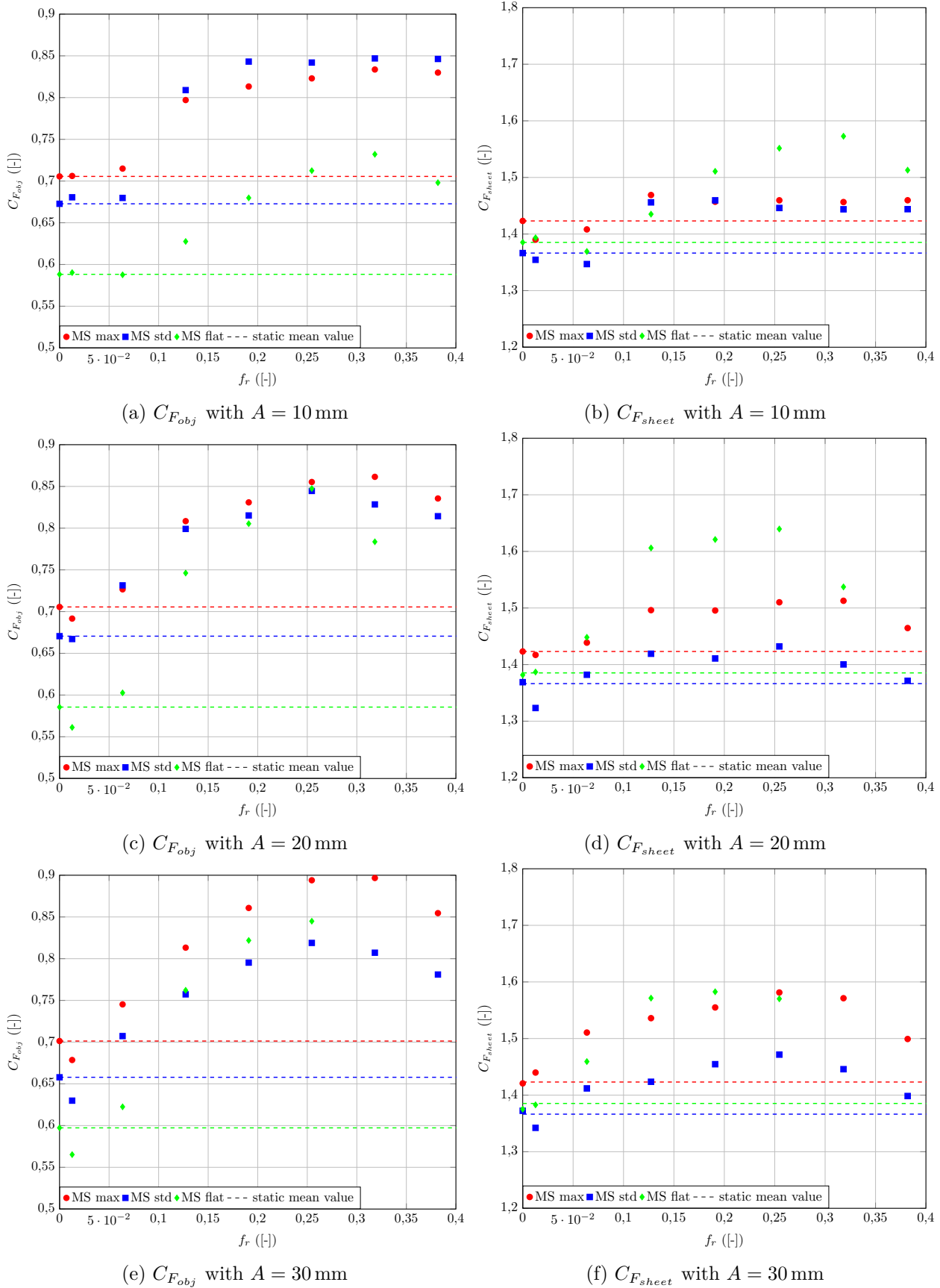


Figure 3.33 – Mean optimisation target function and sheet load coefficient with dynamic trimming for $\beta_{AW} = 60^\circ$.

3.3.3.2 Effect of the reduced frequency f_r on time series

Time series representing the coefficient evolution regarding a dimensionless time t/T (also often noted t^* in the literature) are presented in Figs. 3.35 and 3.36 for different reduced frequencies on the standard mainsail at amplitude $A = 20$ mm. The fluctuation $\Delta C_{F_i} = C_{F_i}(t) - C_{F_i,static}$ for the drive, side sheet load coefficients and optimisation target function are plotted over two representative oscillation periods. This way, the variation of the dynamic time series compared to the static initial situation is represented as used for full-scale situation in [Augier et al., 2012]. The relative instantaneous sheet length $\Delta L_{sheet} = L_{sheet} - L_{sheet,static}$ can be read on the right vertical axis. As shown in Fig. 3.34 when $\Delta L_{sheet} < 0$ the sheet is trimmed in compared to the static case and when $\Delta L_{sheet} > 0$ the sheet is eased compared to the static case. This kind of representation is quite usual for FSI situation where a periodic motion is studied ([Trizila et al., 2011, Gordnier et al., 2013]). The change due to dynamic trimming presented in this paragraph are identical regardless the design shape as shown in [Dhomé, 2016] therefore only the mainsail case is presented here.

Two representative periods are presented for each situations. A low pass filter defined as a Savitzky-Golay filter ([Schafer, 2011]) of order 1 and span 21 is used to filter the high frequencies component due to either quasi steady natural vibration at the lowest frequency or to possible higher component vibration of the recording system once the trimming frequency get closer to the natural frequency of the balance. This filtering step has very low effect on the mean value results.

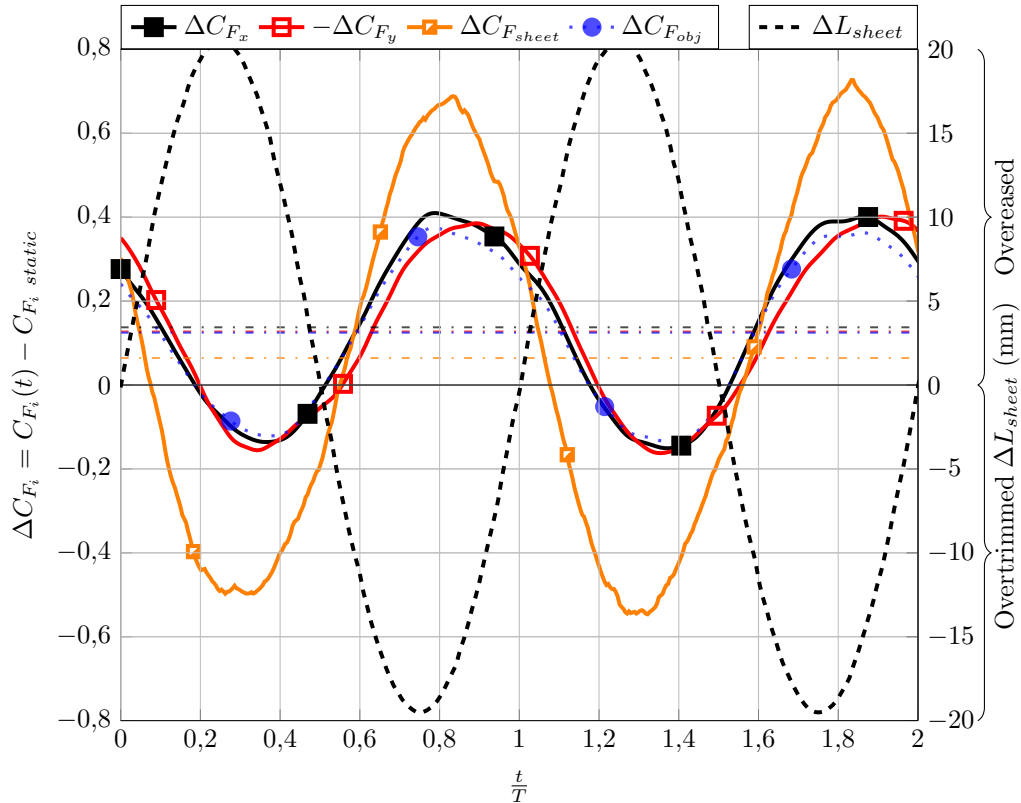


Figure 3.34 – Time series evolution representation for the standard mainsail with $A = 20$ mm at $f_r = 0.127$. Dashdotted horizontal lines represent the mean value of each force coefficient fluctuation signals.

Reader is referred to appendix E which explains why the minimum of ΔL_{sheet} is higher than $-A$ and the maximum of ΔL_{sheet} is higher than A and shows the geometric reason. On the different time series representation, the opposite of side force coefficient variation $-\Delta C_{F_y}$ is shown in order

to make a more direct comparison with the drive force coefficient evolution. Fig. 3.35a shows that the load sensor signal is affected by electronic noise which could not have been avoided during the recordings. Mean values of each force coefficient fluctuation signals are represented by horizontal lines which levels are associated to the evolution of the mean value presented in the previous part for the standard mainsail in Figs. 3.32c, 3.32d, 3.33d, 3.33c.

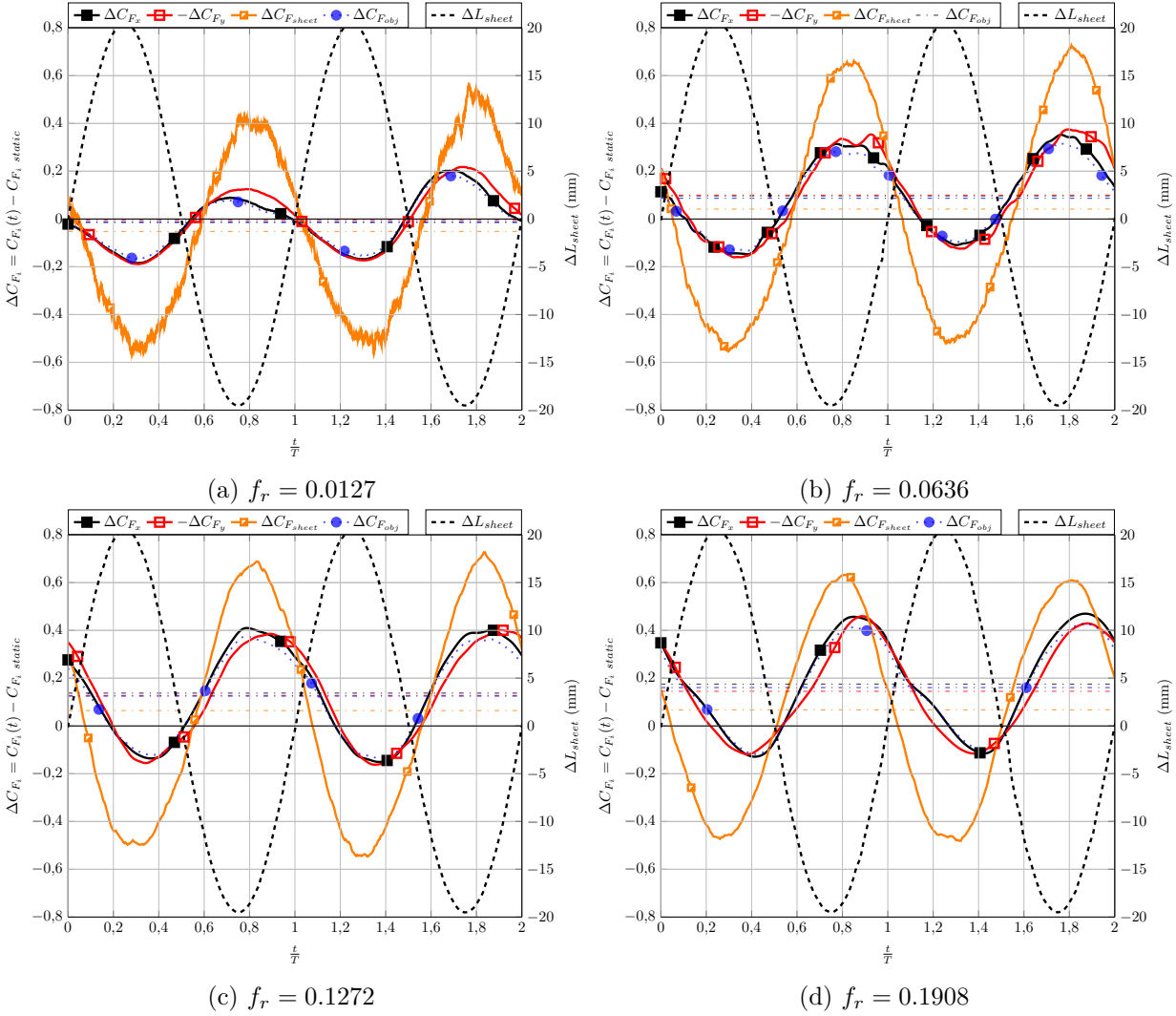
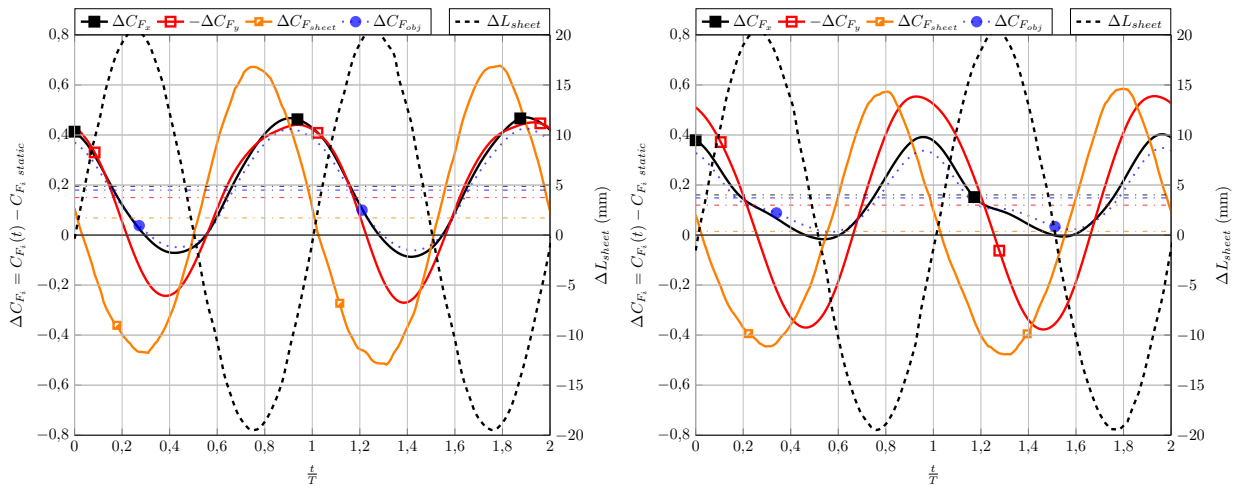


Figure 3.35 – Time series evolution for standard mainsail, $A = 20$ mm, $AWA = 60^\circ$, lower frequencies. Dashdotted horizontal lines represent the mean value of each force coefficient fluctuation signals.

For the lowest reduced frequency presented in Fig. 3.35a, the force coefficient signals contains a high frequency signal due to the vibration of the system in the quasi-static state explored. These vibrations also exist with the static trim which corresponds to a quasi-steady state and are due to the natural small vibration of the sail leech. In Fig. 3.35 corresponding to frequencies smaller than the optimal one, when the reduced frequency increases, the oscillations show that the averaged, maximum and minimum values of the time series of the drive force coefficients are increasing. On the contrary, the averaged, maximum and minimum value of side force coefficient decrease following the opposite trend of the drive force. The envelope of signals of drive and opposite side force fluctuation are superimposed. In other words, this regime corresponds to an exact opposite change in drive and side forces fluctuation until reaching the maximum mean value of the optimisation target function shown in Fig. 3.33c. For the sheet load coefficient, the signal does not significantly change with the

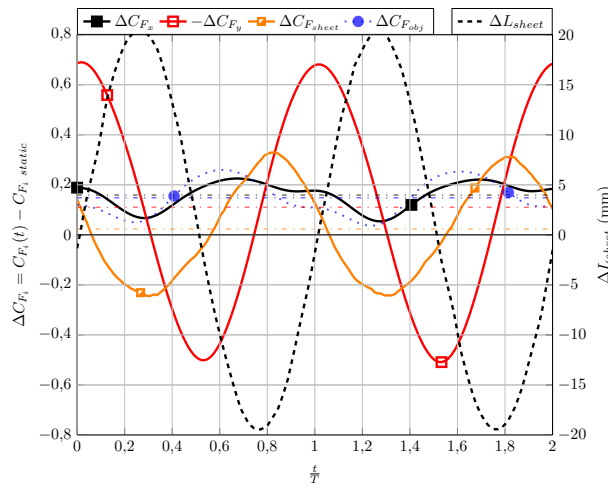
reduced frequency and has a mean value staying close to its initial value, the fluctuation signal envelope being kept almost identical. The load coefficient variation envelope shape is opposed to the sheet length fluctuation one.

In Fig. 3.36 for higher frequencies than the optimal one, a significant phase shift appears between the force coefficient main oscillation and the sheet length signal. The drive force stays mainly above the static value with smaller amplitude of fluctuations. The side force presents larger fluctuations. In this regime the envelop signals of drive and side force fluctuation are no longer exactly opposite. The mean value of the target optimisation function is mainly affected by the decrease in the mean drive force, the weight coefficient used on side force in the target function being quite small. The optimum mean value of the drive force coefficient and optimisation target function is obtained here for $f_r = 0.25$. The fluctuations of sheet load coefficient present smaller amplitude in the envelope signal above this optimum reduced frequency.



(a) $f_r = 0.2545$, where maximum mean drive force occurs

(b) $f_r = 0.3181$



(c) $f_r = 0.3817$

Figure 3.36 – Time series evolution for standard mainsail, $A = 20$ mm, $AWA = 60^\circ$, higher frequencies. Dashdotted horizontal lines represent the mean value of each force coefficient fluctuation signals.

The time series evolution can also be presented using the Lissajou representation as shown next.

Lissajou representation can also be used to represent the coefficient information according to the dynamic sheet length L_{sheet} . For instance Fig. 3.38 represents the evolution of the sheet load and drive force coefficients vs the dynamic sheet length evolution. On this representation, a low pass filter defined as a Savitzky-Golay filter ([Schafer, 2011]) of order 1 and span 21 is applied to clean high frequency components due to the quasi steady natural vibrations and only keep the main shape evolution due to the dynamic aspect.

The case presented on Figs. 3.38c and 3.38d already indicates that even for the lowest reduced frequency tested, the system behaviour already deviates from the quasi-static assumption. This behaviour can be explained by a reduced frequency already too high to respect the quasi-static assumption. Data presented here does not indicate that the hysteresis phenomenon, known when stalling occurs in quasi-steady conditions, is acting or not in this configuration. The orientation of C_{F_x} vs L_{sheet} changes with the reduced frequency. For the lowest reduced frequency, when we provide work to the system by trimming (decreasing L_{sheet}) the drive force coefficient increases. On the contrary, increasing L_{sheet} while easing, decreases the drive force coefficient. This orientation is changed for the reduced frequency $f_r = 0.25$ associated to the optimum reduced frequency

For the sheet load coefficient presented in Fig. 3.38, the orientation remains identical and while the sheet length decreases the load coefficient increases. Figs. 3.38c 3.38e 3.38g 3.38i are used to compute the mechanical power P as the area inside each loop is proportional to the work exchange during one trimming period, which divided by the oscillation period provides the averaged mechanical power associated to each situation . The computation of the required power to achieve dynamic trimming on the sail is therefore based on this Lissajou representation of the sheet load coefficient vs L_{sheet} as indicated by Eq. 3.8.

Fig. 3.37 represents the evolution of the sheet load power P computed for the different design shape at amplitude $A = 20$ mm. There is a maximum of energy exchange for a reduced frequency close to 0.25 associated to the value where the dynamic optimum occurs on this case. Above this value the required power to trim the sail drops down and the activation of the dynamic trimming seems facilitated when the trimming frequency get closer to the mast first natural frequency provided in App. H.

$$P = \frac{\overline{q(t)}S}{T} \oint_{one\ loop} C_{F_{sheet}}(L_{sheet})dL_{sheet} \quad (3.8)$$

The maximum energy exchanged corresponds to 0.8% of an incoming representative kinematic energy flow power $\frac{1}{2}\rho S U_{Pitot}^3 = 24.75$ W

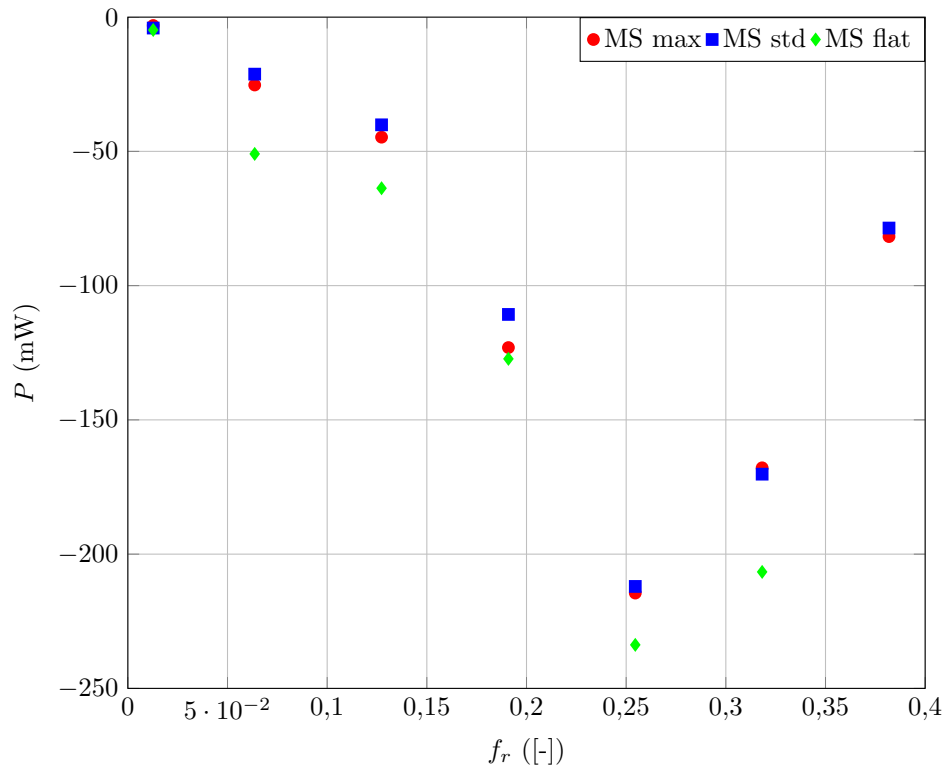


Figure 3.37 – Power calculation for the amplitude $A = 20$ mm, $\beta_{AW} = 60^\circ$. The sign indicates that this energy is given to aero-elastic system from the trimming device and corresponds to the energy required to achieve pumping.

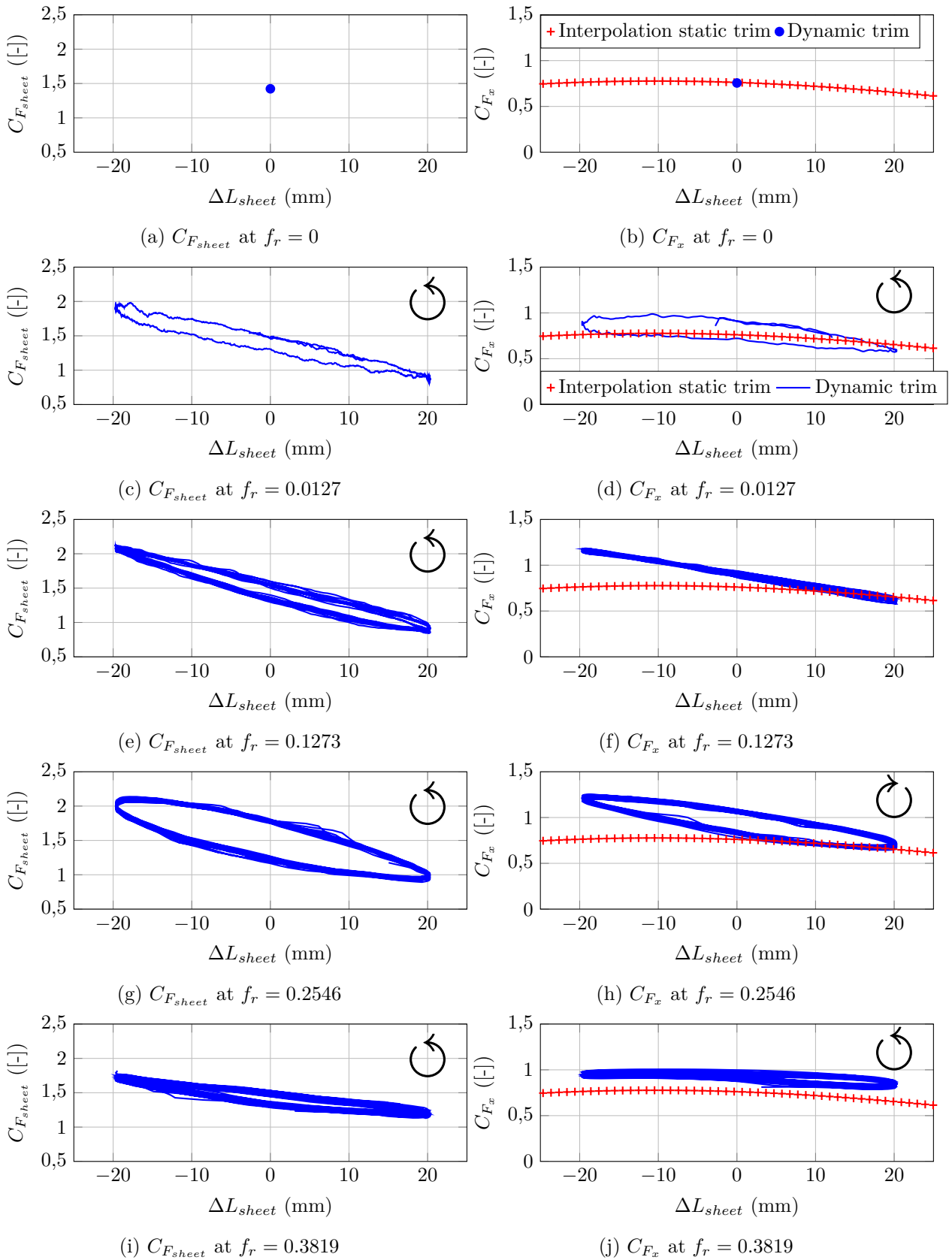


Figure 3.38 – Lissajou representation of drive and sheet load coefficients, standard mainsail $A = 20$ mm, $\beta_{AW} = 60^\circ$. The static value represented on the drive force coefficients corresponds to the static value interpolated from the meta-model interpolation. Circular arrow indicates the rotation direction. Signals are represented for 12s. The area contained in each loop of the sheet load coefficient curve is proportional to the energy exchanged during one oscillation period.

3.3.4 Results discussion

Dynamic trimming have been studied on different cases. First for the reference case at $\beta_{AW} = 40^\circ$ where those oscillations with a car position fixed on the model centreline already showed an evolution of the mean optimisation target function for the standard mainsail. For $\beta_{AW} = 60^\circ$, three different design shapes have been tested and present similar evolution trends. A maximum of the optimisation target function due to dynamic effect occurs for a reduced frequency located around 0.25 or 0.32.

The evolution of the force time series under dynamic trimming can be described in different phases:

1. for the lowest reduced frequency, the optimisation target function decreases compared to the static case. The trim in this quasi-static condition is no longer staying to the optimum trim. This kind of effect has already been noticed on thrust coefficient for a pitching airfoil by [Mackowski and Williamson, 2015] where thrust coefficient get lower than the static case for small Strouhal numbers.
2. then during a first phase from the lowest reduced frequency to $f_r \leq 0.25$, the drive and side force coefficient fluctuations present opposite behaviour. The mean value of drive force coefficient tends to increase when increasing the reduced frequency. The side force coefficient variations are opposed to the drive force coefficient ones. Drive force are almost in opposite phase with the evolution of the sheet length variations. As expected maximum drive force nearly corresponds to the minimum sheet length.
3. for frequencies above the one associated to the maximum optimisation target function, the forces signal start to show a phase shift compared to the sheet length signal. The evolution of the drive force coefficient tends to get flatter but the mean value remains higher than the static one. On the contrary the side force coefficient fluctuations tends to get larger peaks. The optimisation target function decreases.

The Lissajou representation is then used to plot the system output evolution compared to the evolution of the driving parameter here L_{sheet} .

First analysis of the flow measurement did not provide a relation between the observed optimum reduced frequency and any measured flow pattern frequency in our case. However dynamic pitching wings or foils have already been studied for solid bodies or for FSI situations. [Theodorsen, 1935, Theodorsen and Garrick, 1942] provided numerical functions to study an oscillating flap downstream of an airfoil. [Garrett, 1996] used NACA0012 air foil results to illustrate pumping effects showing that there is an optimum reduced frequency to generate a higher maximum lift coefficient. [Schouveiler et al., 2005] present the performance of a flapping foil propulsion. Energy analysis has been carried out on the power provided by the trimming device to the aero-elastic system. An efficiency can be defined like in [Egan et al., 2016] as the ratio of the required power to activate the motion of the structure over the thrust mechanical power generated. This definition would suit the wind tunnel situation considering a fixed object. However in the represented sailing boat case, the relevant elements to use to compute the output useful power would be the modelled boat speed combined to the measured drive force. The boat speed is here no longer aligned with

the upstream flow direction and is arbitrary. Moreover general studies are generally based on the angular position and amplitude of the wing motion which can only be obtained here by further video post processing to compute a representative angular position such as the sheeting angle. Some other studies also indicate that above a critical reduced frequency the thrust generation decreases. [Lua et al., 2016] shows this for a combined pitching and heaving foil motion. This study also indicates that the critical reduced frequency increases with the motion maximum angular position. Here only few sheeting amplitudes were tested resulting in probable low differences in the sheeting angle variation. The discretization of the reduced frequencies tested is not refined enough to get a clear trend about the evolution of the optimal reduced frequency with the amplitude of motion.

Here the wind tunnel situation is about $Re = 10^5$ which is one order of magnitude higher than usual literature results even if [Cleaver et al., 2009] suggest that the Reynolds number has low effect on the oscillating airfoil situation. The situation presented here has also an AoA not equal to 0° for the sail profile in its static position.

No flow visualisation has been carried out during this upwind experimental work however it is reasonable to think that the flow pattern is here affected by the trimming action. Many studies such as [Schnipper et al., 2009, Schouveiler et al., 2005, Lua et al., 2016] link the thrust generation of a pitching foil to an inversion in the Von-Karman pattern wake.

[Schutt and Williamson, 2016] carried out work on unsteady sails dynamic due to motion known as sail flicking. The gain of propulsion is investigated on a full-scale dinghy laser. Then two 3D-printed profiles, a solid and a flexible one, were tested in a water tank to model the aerodynamic effect of flicking. Their design shapes were based onto a sail flying shape stripe measured while sailing. Wake pattern inversion have been also noticed in this kind of representative sailing situation, but at lower Reynolds number ($Re = 10^4$ to $Re = 3.10^4$).

3.3.5 Conclusions, limitations and perspectives

This chapter dedicated to upwind pumping has shown that:

1. that dynamic trimming does improve the considered yacht performance compared to the optimum static one.
2. for the different design shapes tested there is an optimal pumping frequency. The associated reduced frequency is close to $f_r \approx 0.25$, $f_r \approx 0.32$. The flat mainsail design benefits more from the dynamic action than the two other designs compared to their respective static performance.
3. the input power needed to achieve the dynamic trimming can be estimated. It shows that the optimal pumping required a significant increase in the power provided by the trimming system compared to the lowest frequency tested.

The reference length when oscillating is set up to the corresponding sail optimum point, fixing the car traveller position and the initial sheet length to the values optimising the target function. This corresponds to a very trimmed in situation and the amplitude cannot be increased too much. Other investigation could be done with a more released averaged sheet length in order to be able to increase the amplitude. However this kind of situation might show fully luffing sail in the easing phase and may not present any benefit.

Keeping the heel angle to 0° in our case enables to focus on a given situation. An extension of this work would be to test the effect with different fixed heel angles, then to test with a dynamic heel model. These situations would require more developed experimental set up, probably using a proper yacht hull model attached to the heeling pole that can be remotely controlled in the TFWT. The rig could also be fully attached through backstay, forestay and shrouds in order to fully separate structural mast motion from aerodynamic part effect. However any miscalculation in the dynamic set up is likely to tear apart the fragile mainsails if the mast is not bending any more and the sail is overtrimmed. The IMOCA design has been selected for this experimental campaign for different reasons. The fully batten design with a squared top seemed more appropriate for pumping as it is less likely to have a top part strongly luffing and de powered once eased for a given twist. Moreover this choice was also made to provide experimental data for a sail of interest for the sailmaker as part of the collaboration work. As an extension of this work, different kind of mainsails could be investigated such as non squared mainsail to extend or modify for different sail geometry the conclusion presented here.

Dynamic trimming in this configuration corresponds to a change in L_{sheet} . Its representation on figures representing the static two-parameter space optimum location is a vertical line. We have seen previously that the isoline pattern close to the optimum static location presents an ellipse shape with two directions that can be identified in the interpolation of the optimisation target function. One direction makes the optimisation target function affected by a large loss when changing the input trim. This direction is closer to the vertical one representing the direction of change of L_{sheet} during dynamic trimming. It means that choosing a pure L_{sheet} dynamic change might not be the most appropriate way to dynamically increase the target function. Future investigation could focus

onto a combination of change in L_{sheet} and L_{car} which respects the appropriate direction shown on static test results. This may at least reduce the target function decrease observed at very low reduced frequency. Moreover this motion is more similar to what sailors might achieve on dinghies while pumping, taking directly the sheet part attached to the boom in order to act on the sail sheeting angle and no longer on the sheet length. It can be interesting to observe if a dynamic trim also changing the car position L_{car} would get a better dynamic optimum than the one with a pure L_{sheet} motion.

Flying shape measurement and rig tracking have been also performed using cameras but data still require further investigation especially to compute a relevant angular position parameter of the sail as the sheeting angle. The tracking of the mast head has been used to do trajectory comparison with numerical models. The boom end tracking is required to compute the sheeting angle. Video and data synchronisation procedure has been achieved through the triggered laser pulse during this work but this manual process requires a lot of time for post-processing. Those data could be used to ensure that the main effect of pumping is not simply due to a change in the local apparent flow velocity. At the centre of effort - even if the force coefficients being at an order of magnitude of the square of the flow velocity- the structural displacement velocity remains small compared to the main flow velocity for all frequency tested.

Time series data base of these experiments can also be used in order to implement rheologic model coefficient to characterize the pumping unsteady aero-elastic system. Such an analogy have been used by [Fossati and Muggiasca, 2010] but for a pitching yacht.

A last major improvement would be to reproduce a recorded trim motion from an expert dinghy sailor to establish a non symmetric command law or a more adapted one as suggested for example in [Orlowski and Girard, 2012]. Most of the time the trimming phase is shorter than the easing phase where the sail is let free to naturally open itself and only pushed away by the flow.

Upwind situations presented in this chapter are relatively close to usual lifting profile situation. Once the yacht reaches the upwind mark in a racing track, she has to go downwind. Next chapter topic is the downwind phase. Spinnaker sails present a natural unsteady behaviour known as curling or flapping. Once again we try to get a better understanding of this complex unsteady FSI phenomenon. We determine if usual sailor static trim recommendations on downwind phase effectively increase aerodynamic performance. Some data such as the curling frequency or the effect of curling on time series are eventually presented.

Downwind wind tunnel results

Contents

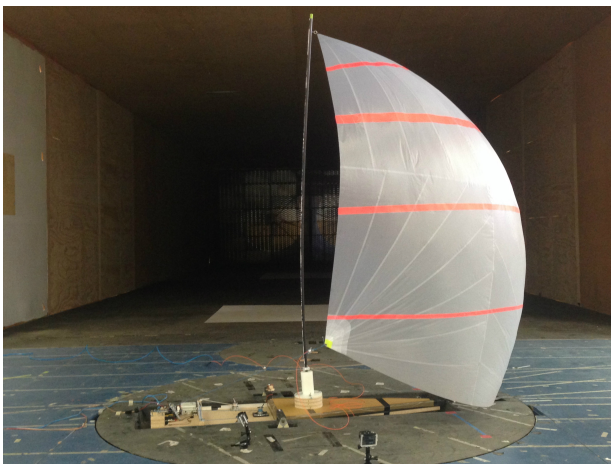
4.1	Downwind sail presentation	120
4.1.1	Spinnakers presentation	120
4.1.2	Curling phenomena presentation	121
4.2	Natural curling effect: free mast, partially-rigged mast and additional twisted flow	127
4.2.1	Free mast situation	127
4.2.2	Partially-rigged mast situation	139
4.2.3	Partially-rigged mast situation with twisted flow	144
4.2.4	Comparison of the different mast configurations	146
4.2.5	Unfolding dynamics of the folding hysteresis: usual recovering and extreme events	147
4.3	Natural curling effect: fully rigged mast	151
4.3.1	$\beta_{AW} = 80^\circ$	153
4.3.2	$\beta_{AW} = 100^\circ$	156
4.3.3	$\beta_{AW} = 120^\circ$	159
4.3.4	General conclusions about curling apparition	162
4.4	Curling frequency measurement and evolution	165
4.4.1	How to measure the curling frequency?	165
4.4.2	Curling frequency evolution	166
4.4.3	Why measuring the curling frequency?	171
4.5	Curling temporal evolution	172
4.6	Discussions, conclusions and perspectives	178

This chapter presents the results for the downwind configuration tests. First the downwind spinnakers and curling phenomenon are presented. Then the effect of curling is presented with a static trim in different configurations: free mast, half rigged mast, half rigged mast and twisted flow. Then fully rigged mast results are presented under static trim. The first goal of these two first sections is to bring complementary data in a more controlled environment compared to full-scale testing in order to get a better understanding of this FSI phenomenon. The second goal is the discussion of “on the verge of curling” recommendation trim used by sailors when racing. Some AWA configurations confirm that the apparition of curling can present a significant increase in the mean drive force coefficient with the rigged mast. The fourth section provides some frequencies characteristic about natural curling and the fifth section presents effect of curling on force time series. A discussions about the results will conclude this chapter.

4.1 Downwind sail presentation

4.1.1 Spinnakers presentation

Four different spinnakers were manufactured by Incidence sails with the same design shape but with different cuts and materials. Only two of them were used during the 2015 experimental campaign. At that time, stripes were stuck onto them to get information about the flying shape using stripes reconstructions post processing. The four of them were then used during the 2016 experimental campaign where photogrammetry method tracking stuck coded-targets was used to compute their flying shape. Those different spinnakers with the same design shape corresponding to the full-scale J80 spinnaker design shape are described in Tab. 4.1. The scale factor between the full-scale spinnaker and the model scale ones is 1 : 4.61. The AirX 500 material is the material also used for the mainsail models for the upwind tests of the 2015 experimental campaign. The full-scale J80 Incidence sail's triradial spinnaker is manufactured with a white nylon polyurethane 40 g m^{-2} Contender SuperKote 0.75 oz (SK75). For downwind tests the mast alignment was set up in the model centreline direction.



(a) Triradial manufactured in 2015: AirX 500



(b) Cross-cut manufactured in 2016: AirX 500



(c) Triradial manufactured in 2016: SuperKote 0.75



(d) Cross-cut manufactured in 2015: SuperKote 0.75

Figure 4.1 – Model spinnakers photographs. The 2015 experimental campaign mast was set up in different situation (cantilever only or partially rigged) and thicker than the 2016 experimental campaign one.

Spinnaker	Cut	Materials	Year of manufacturing	Presence of stripes	Mass during 2016 testing (g)
Spinnaker Tri 1	Triradial	AirX 500	2015	Orange stripes (stuck)	196
Spinnaker CC 1	Cross-cut	SuperKote 0.75(SK 75)	2015	Green stripes (painted)	170 (168 in 2015)
Spinnaker Tri 2	Triradial	SuperKote 0.75(SK 75)	2016	No stripe	199
Spinnaker CC 2	Cross-cut	AirX 500	2016	No stripe	140

Table 4.1 – Description of spinnaker models tested for the downwind 2015 and 2016 wind tunnel experimental campaigns. The design shape sail area is $S_{spinnaker} = 3.187 \text{ m}^2$ representing 12.6% of the testing section area.

The dimensionless numbers have been introduced in Tab. 5 and mainly show one order of magnitude difference in the Reynolds number between full-scale and wind tunnel. The relative stiffness information provided by the inverse of the Cauchy number indicates a higher relative stiffness in the wind tunnel case as the material used during those testing were identical to light ones which could have been used for real light downwind sails.

4.1.2 Curling phenomena presentation

Curling is a phenomenon already well known by sailors and can be defined by a fold appearing on the spinnaker shoulder (high part of luff edge). In this situation the flying spinnaker luff has an alternative folding-unfolding motion or a large fixed fold if the spinnaker is overeased. Photographs in Figs. 4.2 illustrate a typical curling period at full-scale on the J80. The different steps have been identified by [Motta, 2015, Deparday et al., 2014, Deparday, 2016] who correlate each instant with a measured full-scale pressure distribution. Footages in Figs.4.3 show the same phenomenon occurring in the TFWT during 2016 experimental campaign recorded with four HD triggered cameras.

[Deparday et al., 2014, Deparday, 2016] with full-scale results already provide some data about the curling effect (also called flapping). The dynamic evolution of the pressure distribution shows a strong suction peak at the luff in the recovering phase (instant D) which increases the instantaneous load values measured on the sail holding points compared to a non curling situation. On an entire curling period this dynamic evolution also increases the loads averaged value. [Motta, 2015] measures the sail flying shape and its pressure distribution which enables to compute aerodynamic forces using FEPV techniques and are compared to DLC measurements. Total aerodynamic forces such as drive or side forces have not been measured directly but computed in both cases. The use of wind tunnel experiments enables to directly measure these possible evolutions. Moreover, wind tunnel analysis provides data in a static environment where AWA and AWS are fixed.

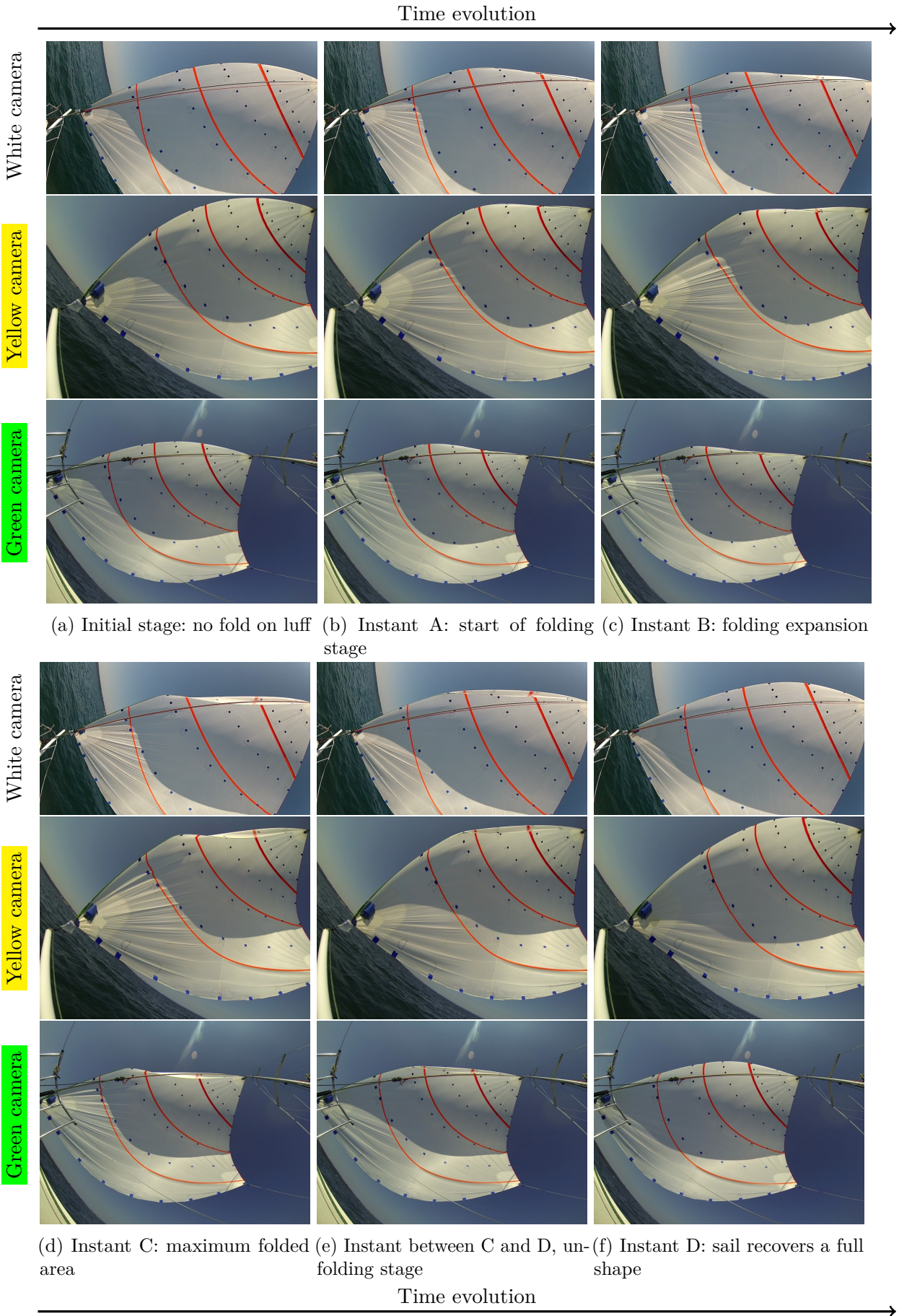


Figure 4.2 – Curling sequence at full-scale on J80 asymmetric spinnaker recorded by 3 cameras -one per line named after their identification colours- during 2014 full-scale test. Instant identification A, B, C, D correspond to [Deparday, 2016] convention. Fish eye effect has not been removed.

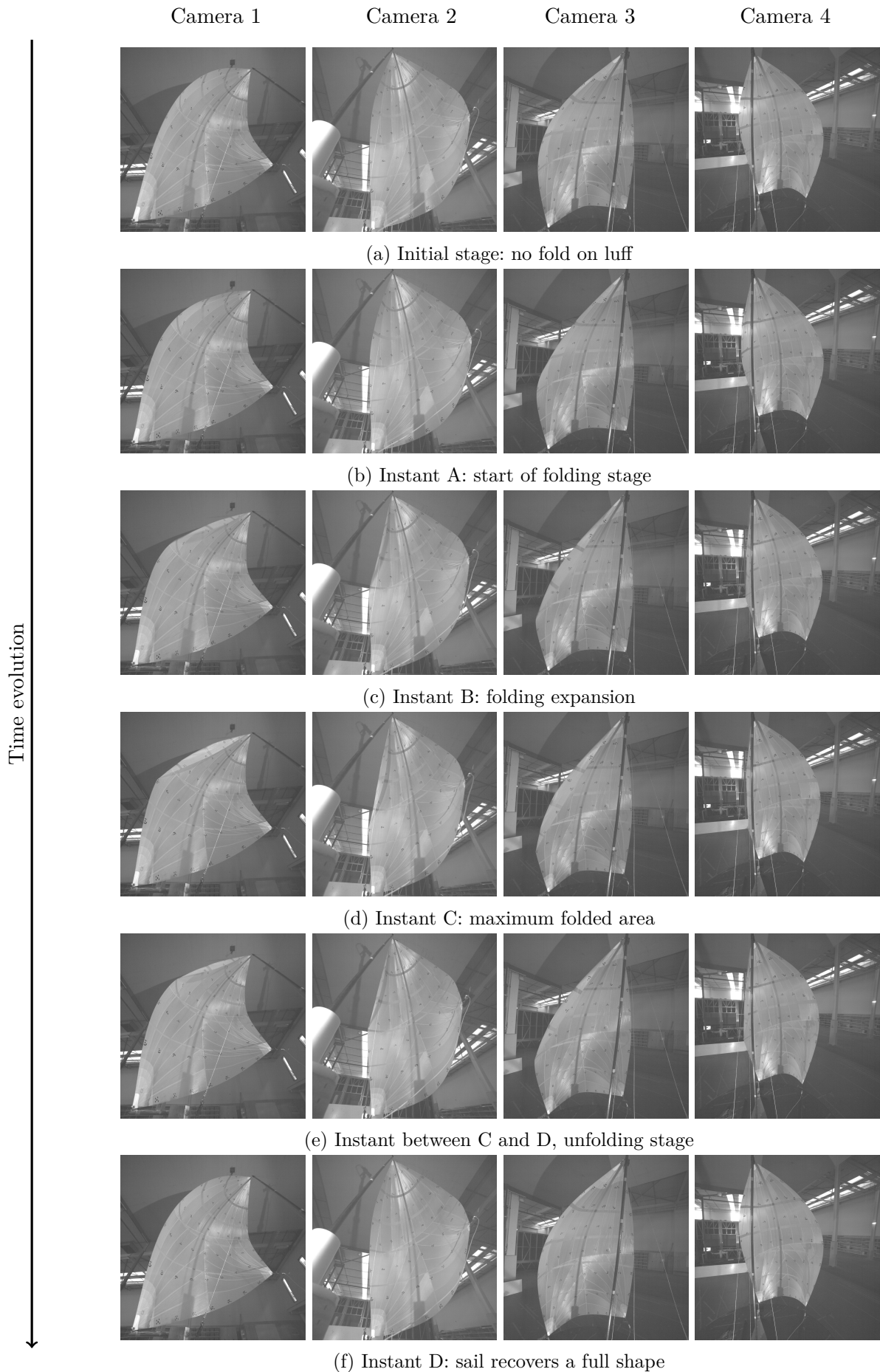


Figure 4.3 – Curling sequence in the wind tunnel recorded during 2016 experimental campaign. Instant identification A, B, C, D correspond to [Deparday, 2016] convention. Fish eye effect has not been removed. Camera point of view are ordered by cameras 1, 2, 3, 4. Their location can be seen in Fig. 4.4d.

Curling has already been characterized by [Deparday, 2016] as a strongly coupled FSI with a 3D membrane submitted to large displacements and rotations but small deformations, a reduced velocity close to 1 and a fluid inertia about 100 times higher than the inertia of the membrane creating an important added mass effect. Previous studies using numerical unsteady FSI models ([Durand, 2012, Durand et al., 2014]) were able to model the curling phenomenon but so far have not been performed on and compared with experimental cases for validation. The use of the wind tunnel and the results provided in this thesis might facilitate the numerical-experimental comparison for future projects compared to full-scale cases. Regarding those past studies, this chapter has several goals:

1. The main goal of this chapter is first to present results about curling in order to improve the understanding of this FSI phenomenon in a wind flow controlled environment such as wind tunnel conditions. Data about the effect on mean aerodynamic forces are presented. Natural curling frequencies for different AWA and AWS are also shown as well as the dynamic effect of curling on time-series.
2. The second goal of this chapter is to discuss the trim recommendations given by the sailing community about downwind sails which always involves curling but in different ways. For instance [Royal Yacht Association, 2017] advice to trim the spinnaker this way: “*ease the sheet and look for curling at the shoulder, when it starts to curl, sheet in until it stops*”. In this advice from a well acknowledged sailing institution, curling must disappear to get the good trim. Trimming advice also depends if you have a dedicated trimmer to the spinnaker sheet. Some people would advice to “*ease the sheet until the luff breaks, trim a bit... repeat the process as frequently as you can*”. This work focuses on the effect of the apparition of curling on the measured forces in order to get a better idea about the trim providing the more driving force. Dynamic trimming has been tested around curling but results are not presented here and require further investigation. Sailors do not indicate exactly an identical best trim location and they do not provide clear explanations about the origin of the curling benefit either. Only recent researches start to bring experimental elements and analysis about the origin and the benefits of curling. As part of the Sailing Fluids research collaboration [Motta, 2015, Deparday, 2016] works provide for the first time experimental results at full-scale on this phenomenon in different sailing conditions. This work resulted in the creation of a curling mechanical model.
3. Providing experimental data in wind tunnel conditions fulfils two remaining goals:
 - (a) The first one is related to sail engineering work and intends to distinguish the differences due to the cut or material of the tested spinnakers and eventually suggest a better spinnaker.
 - (b) The second one is to built an experimental data base for numerical experimental comparison, especially with the curling unsteadiness.

Results focus here on drive, side and sheet load coefficients change regarding the sheet length of the spinnaker. Relevant values are presented such as the mean value and the standard deviation of the time series. Error bars corresponding to uncertainty are not added onto these graphs to make them easier to read. However the reader is referred to Appendix C for drive and side force uncertainty

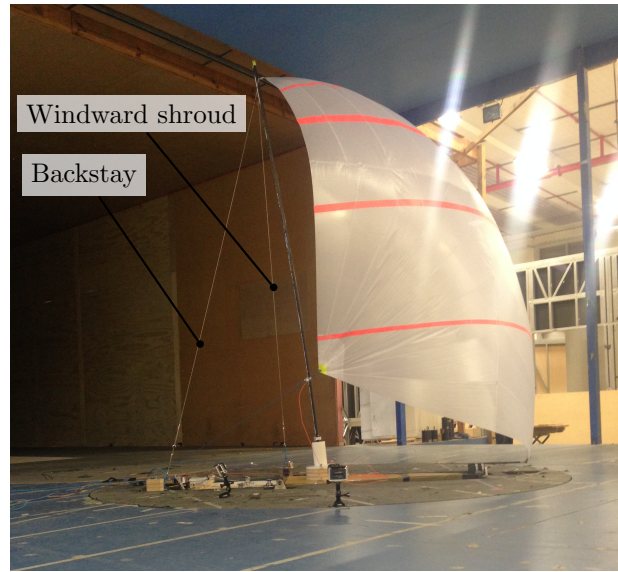
evaluation. This first approach provides a general idea about the spinnaker behaviour correlated with comments based on simple flying shape observations.

The next section shows different tests with the free (shown in Fig. 4.4a) or half rigged (shown in Fig. 4.4b) mast. The half rigged mast has been tested with (shown in Fig. 4.4c) or without twisted flow configurations. This first set of static trim results shows different kind of phenomena. Effect of curling is noticed and different hysteresis phenomena are presented. However these tests were carried out on the 2015 spinnakers which presented two differences: their cut and their materials. Their flying shapes were recorded using stripe recognition system which suffer of a large uncertainty for fuller downwind sails like the J80 spinnaker. Sail designers provide their design with stripes used as indicator of the flying shape. An indication is given when these stripes are horizontal for some of the tests to show how far the design shape can be from the optimum trim in wind tunnel conditions.

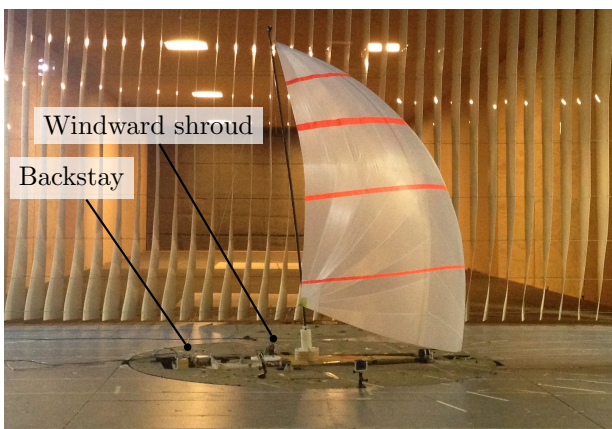
A second experimental campaign was carried out in 2016 with four different spinnakers in order to isolate cut and material effects on results. This is presented in the third section of this chapter. Experimental setup was improved for these tests and four triggered high definition cameras were used to record synchronized photographs for photogrammetry post-processing. The four HD cameras - which position is shown on Fig. 4.4d- could record 2046x2046 black and white photographs at 20 fps. The camera are remotely triggered by a common incoming signal generated by the instrumentation system and time stamped on the fly by the dedicated recording computer. Lights and laser signal visible from each cameras are also generated and recorded to ensure an accurate synchronisation between each camera and to verify the time stamping process. Recorded footage have been used to measure the dynamic steps involved in the curling phenomena as explained in the section 4.4 and used in the last section 4.5. Extensive future studies could use this recorded photogrammetric dynamic database to extensively gather dynamic flying shape evolutions. Bezier formalism as suggested in [Deparday, 2016] could be used to characterize such an evolution. Future numerical computation on the fluid parts could also be done using those flying shapes. Eventually unsteady FSI modelling involving viscous flow model could be validated thanks to these database. For this experimental campaign, the spinnaker was setup higher compared to previous configurations to make easier numerical modelling. Static results are presented in the same way than the 2015 results showing the curling effect on a more conventional rig with a mast held by shrouds, forestay and backstay as shown on 4.4.



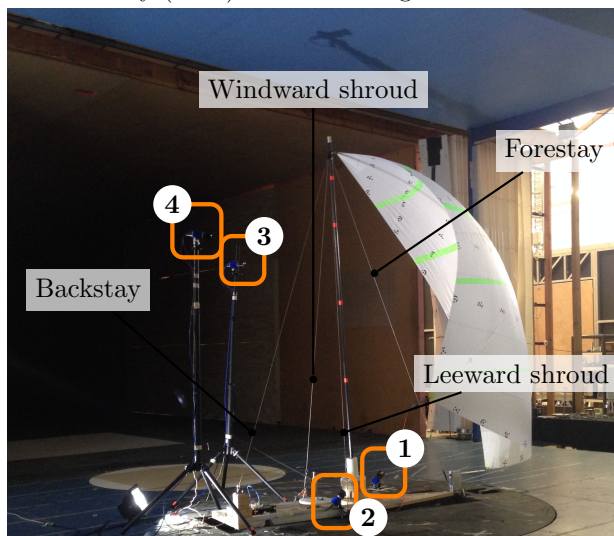
(a) Free mast configuration. The mast is cantilevered at the step and unstayed. Important mast bending can be observed (2015).



(b) Partially rigged mast configuration. The mast is cantilevered, hold by windward shroud and backstay (2015). Mast bending is limited.



(c) Partially mast configuration with twisted flow. The mast is cantilevered, hold by windward shroud and backstay (2015).



(d) Fully rigged mast configuration. The mast is cantilevered hold by lateral shrouds, backstay and forestay (2016). Circled numbers indicate the camera number.

Figure 4.4 – Rig downwind configuration, the experimental year is indicated into brackets.

4.2 Natural curling effect: free mast, partially-rigged mast and additional twisted flow

At first an unstayed configuration, where the mast was only cantilevered at step, was tested to get the simplest configuration easier to model. This configuration is called the free mast configuration. Because of excessive bending and mast movements observed in free mast configuration, we added windward shrouds and backstay as a half rigged configuration.

This section describes tests carried out in 2015 on free mast and partially rigged mast configurations to study their influence on two spinnakers with different cuts and materials. The carbon fibre mast diameter was 14mm. Twisted flow effect on measurement was eventually investigated on the half rigged mast. Some wind flow measurements are also presented here in a reference downwind case. Results about the effect of sheet length and the effect of curling on drive and side forces for different AWA are presented for each situation. For these results configuration, only stripes reconstruction was available to get information on the flying shape.

4.2.1 Free mast situation

In this situation the rig corresponds to a cantilevered mast without any backstay, forestay or shroud (unstayed). The fans frequency was set up to $f_{fans} = 20$ Hz corresponding to a Pitot wind speed close to 2.9 m s^{-1} .

4.2.1.1 $\beta_{AW} = 80^\circ$

Tab. 4.2 presents the sheet length where horizontal visualisation stripes (used by VSPARS) are estimated to be horizontal and the sheet length where curling appears for the free mast situation at $\beta_{AW} = 80^\circ$.

Spinnaker	Test	Date	Horizontal stripes(mm)	Curling apparition (mm)
			$L_{sheet H}$	$L_{sheet C}$
Spinnaker Tri 1	Test 0	31/03/2015	1065	1185
	Test 1	01/04/2015	1065	1185 \rightarrow ; 1180 \leftarrow
	Test 2	01/04/2015	1065	Curling not reach
	Test 3	20/04/2015	1065	1185
Spinnaker CC 1	Test 0	10/04/2015		1195 \rightarrow
	Test 1	10/04/2015		1175 \leftarrow
	Test 2	20/04/2015		1180 \rightarrow ; 1170 \leftarrow

Table 4.2 – Horizontal stripes and curling apparition for free mast at $\beta_{AW} = 80^\circ$. \rightarrow indicates an easing situation and \leftarrow indicates a trimming in situation. Empty cells indicate that no measurement of this configuration has been done.

The different limits presented in Tab. 4.2 can be placed onto a graph such as in Fig. 4.5. In this graph the drive force coefficient is represented as a function of the sheet length L_{sheet} . The

mean value is presented first then the standard deviation presented below.

The sheet length where VSPARS stripes are estimated to be horizontal by an external observer is indicated with a vertical line marked with a circled (H) on these graphs. These stripes are drawn on the numerical design shape during the design process by the sail maker. Then their respective reference mark are printed on the model sails panels. Final stripes were taped or painted following these reference lines. These stripes are used as a visual guideline when flying the spinnaker during navigation. This also helps the sail maker to have a flying shape information of his or her real sail flying shape compared to the design shape.

The sheet length where curling appears is indicated with a vertical line marked with a circled (C). The location of the limit of curling can depend of the direction of the test: easing when increasing the sheet length or trimming in when decreasing it. When a difference exists between the easing or trimming in case, an arrow is added on the corresponding vertical border with \rightarrow for easing curling limit, or \leftarrow for trimming in curling limit. The curling apparition may depends of the flow velocity. When curling appears for a different sheet length between several tests, each vertical limit is marked by the symbol and colour associated to the run.

(H) or (C) encircled letter are not repeated on standard deviation value graphs for clarity purpose. The reader should refer to the associated vertical alignment to get the legend letter on the mean value graph, every x axis scale and values being identical for all graphs.

Drive force coefficient C_{F_x} for the two 2015 spinnakers is presented in Figs. 4.5a and 4.5b. General trends are similar for the two spinnakers however several differences can be observed. The decrease in the mean drive force occurs just before reaching the curling limit for the triradial spinnaker contrary to the cross-cut spinnaker where the decrease occurs at the curling limit. For $1000 \text{ mm} < L_{sheet} < 1050 \text{ mm}$ the cross-cut spinnaker provides more drive force. The maximum drive force for the triradial spinnaker is located before reaching the curling part. The maximum drive force coefficient is provided by the cross-cut spinnaker and far from the curling limit around $L_{sheet} = 1020 \text{ mm}$. The horizontal stripes location corresponding to the design shape does not correspond to this maximum.

The curling limit can depend on the direction of the run. Generally when trimming in, going from large to smaller sheet length (right side to left side on the graphs), the curling limit is located for a smaller sheet length than for an easing action, going from small to larger sheet length (from left to right on the graphs). The curling phenomenon is more persistent due to the maintained oscillations mainly due to the free mast motion here once curling. The curling limit can clearly be identified with the sudden increase in the standard deviation of the drive force coefficient but does not correspond to the maximum drive force. Being overtrimmed with L_{sheet} close to 950 mm also shows high standard deviation. For this trim, sail oscillations can be observed probably related to a strong detached flow.

Side force coefficient C_{F_y} is presented in Figs. 4.5c and 4.5d. Contrary to the drive force coefficient, the side force coefficient does not seem to be much affected by the curling limit. The linear trend on the mean value seems kept quite identical and aligned with the non curling case,

however a significant step in the standard deviation of side force can be observed. This criterion is interesting to detect spinnaker curling apparition with side force coefficient. No important differences can be observed in the side force coefficient between the two different spinnakers.

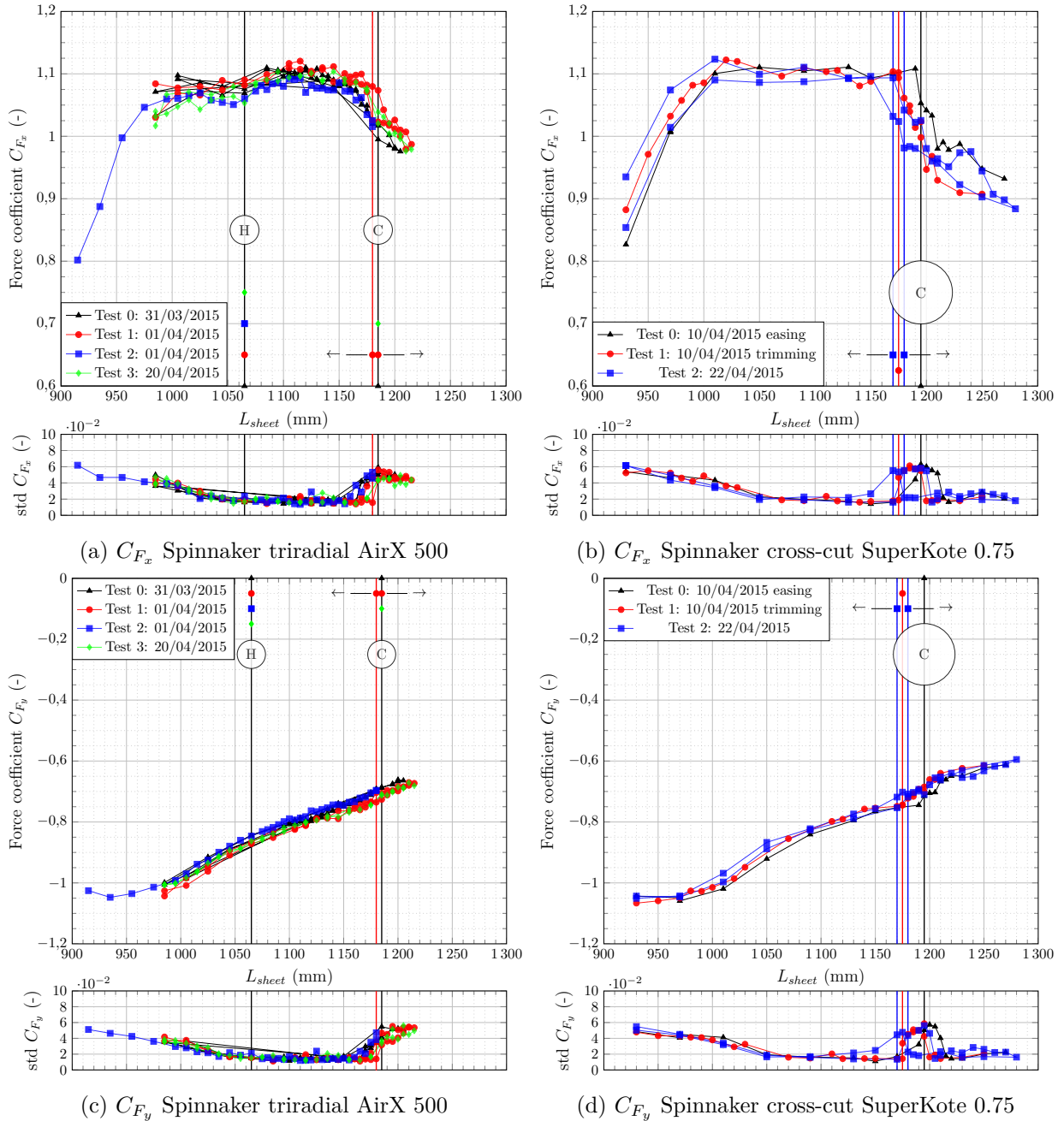
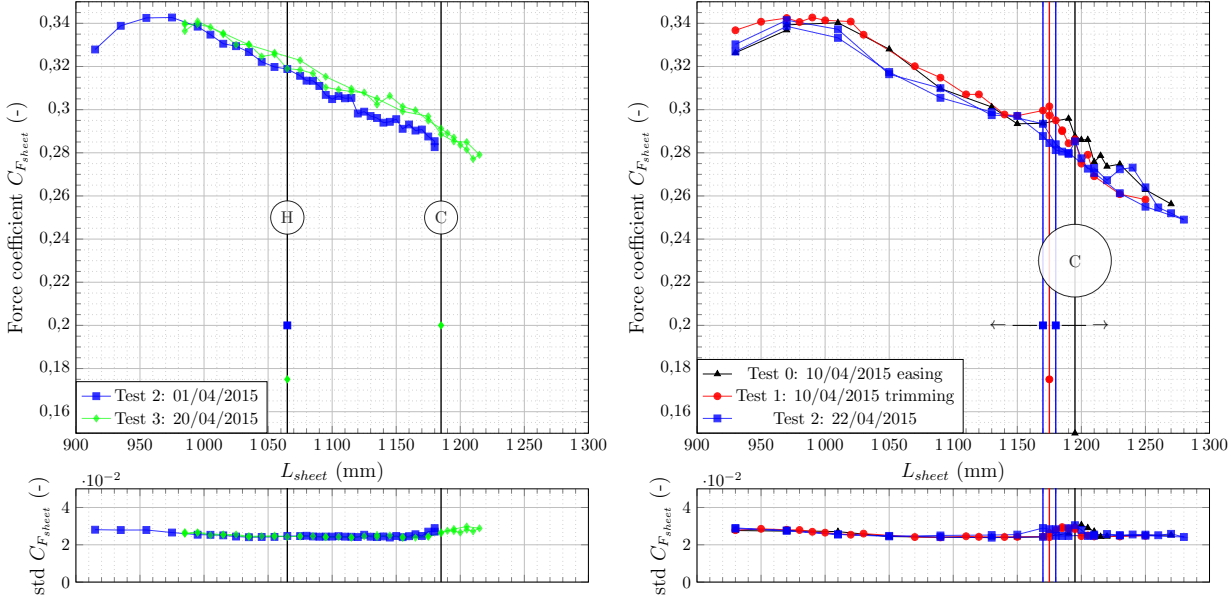


Figure 4.5 – Effect of curling with static trim on force coefficients with a free mast at $\beta_{AW} = 80^\circ$.

Sheet load coefficient $C_{F_{sheet}}$ is presented in Fig. 4.6. The maximum sheet load does not correspond to the curling phase but occurs in the trimmed phase where standard deviations of drive and side force increases. The sheet load coefficient seems to be less affected than the force coefficients when curling appears. This indicates that the major part of the aero-forces is not transmitted by the clew point but by the head and tack, the sheet load being about 30% of the drive force

along the drive force direction. This confirms the observation made at full-scale using DLC by [Motta, 2015, Deparday, 2016]. The curling apparition slightly affects the cross cut design, curling propagation from luff to clew point being maybe more damped in the triradial case due to seams. Level of load coefficient are quite similar for the two spinnakers.



(a) Spinnaker triradial AirX 500

(b) Spinnaker cross-cut SuperKote 0.75

Figure 4.6 – Effect of curling with static trim on sheet load coefficient at $\beta_{AW} = 80^\circ$.

4.2.1.2 Flow mapping for downwind reference case

The downwind flow mapping reference case is measured for an AWA of 80° using the triradial 2015 spinnaker (AirX 500) with a sheet length $L_{sheet} = 1065$ mm. This set up corresponds to the trim where stripes are estimated to be horizontal. The reference wind speed is about $U_{Pitot} = 2.9$ m s $^{-1}$.

The central velocity profile at the outlet ($Y_{WT} = 0$ on the wind tunnel frame) of the closed part is given in Fig. 4.7 and compared to the other velocity profiles on the same section which remain close to the central velocity profile standard deviation range. The downwind sail slightly slows down the reference velocity profile obtained for an empty wind tunnel represented by blue square dashed curve in Fig. 4.7. On the downstream part of the flow mapping in Fig. 4.8e the strong spinnaker wake effect can be observed with a high level of turbulence intensity and a strong decrease in the wind velocity on the lower and middle parts of the spinnaker. In Fig. 4.8e a flow acceleration area can also be noticed in the upper part of the spinnaker wake. The different section of measurement correspond to I, II and III locations indicated in Fig. 2.3a. Data is provided here for numerical simulation validation.

Flow velocity time series around the reference case, *i.e.* a non curling spinnaker, have been recorded but did not show any clear pattern which frequency could have been related to the curling phenomenon. Simultaneous recording on different point locations could maybe have brought a new insight about these measurements.

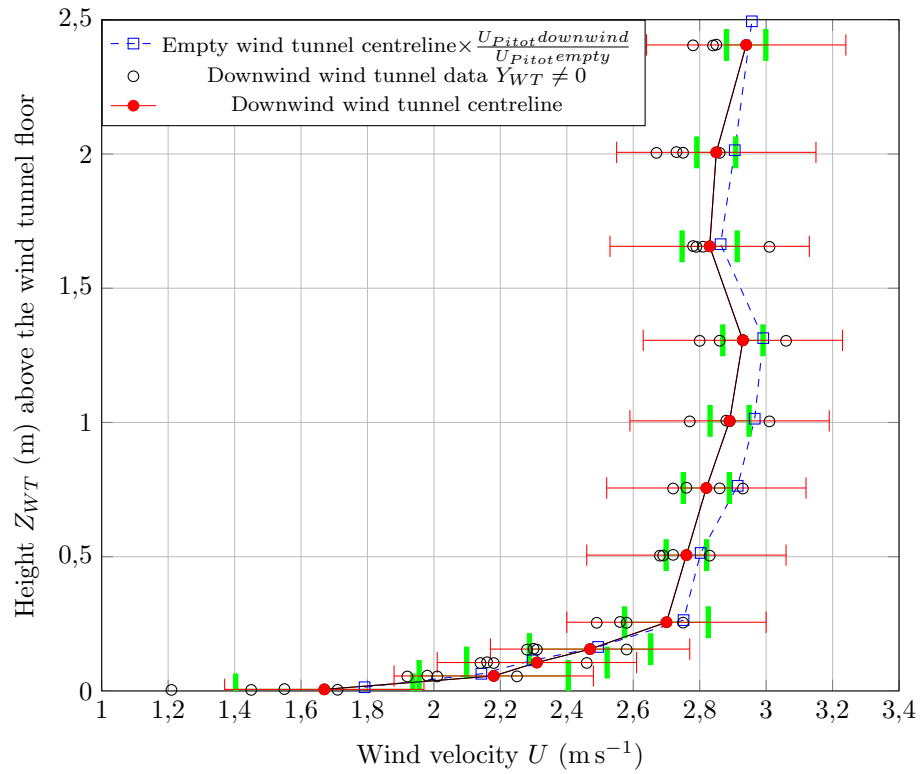
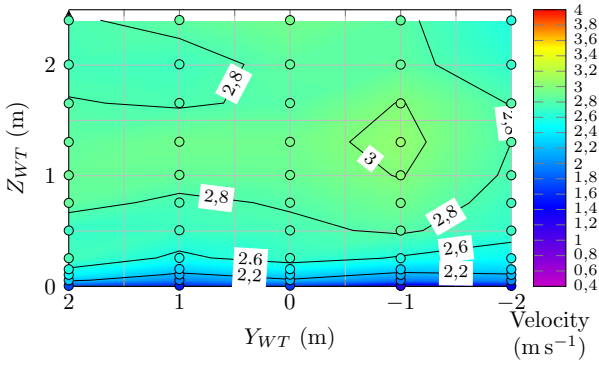
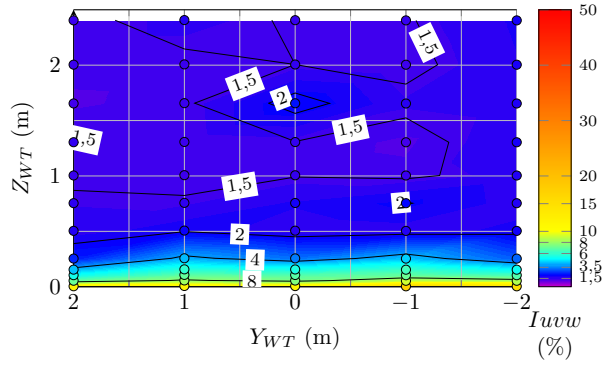


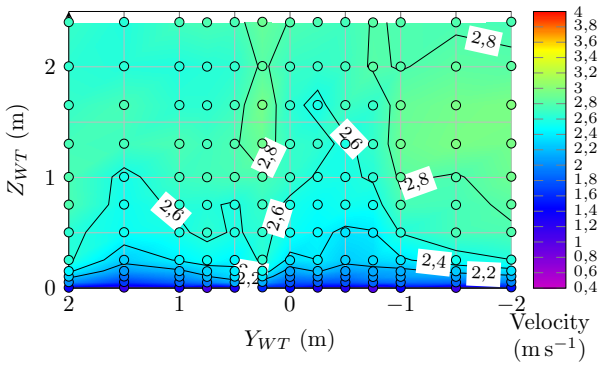
Figure 4.7 – Centreline wind profile compared to outlet section wind profile data at $f_{fans} = 20\text{ Hz}$ with downwind sails. Blue square dashed curve data corresponds to the empty wind tunnel configuration scaled to the downwind speed test. Red error bars represent the uncertainty provided by the instrument manufacturer. Green errors bars indicate the standard deviation measured on time series on the centreline wind tunnel profile.



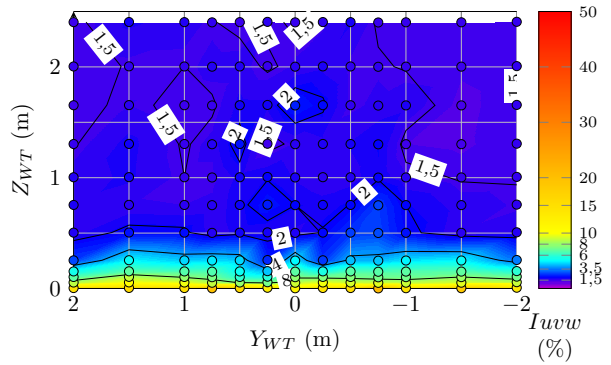
(a) Wind field, outlet of closed section (I).



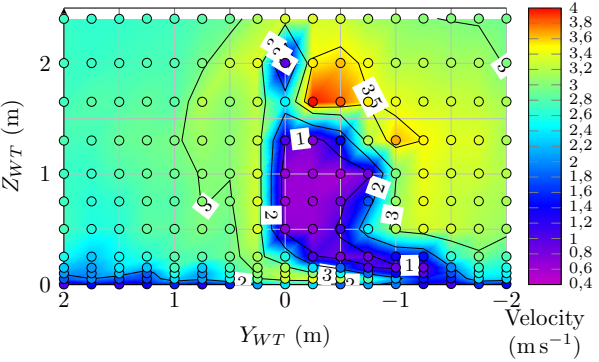
(b) Turbulence intensity, outlet of closed section (I).



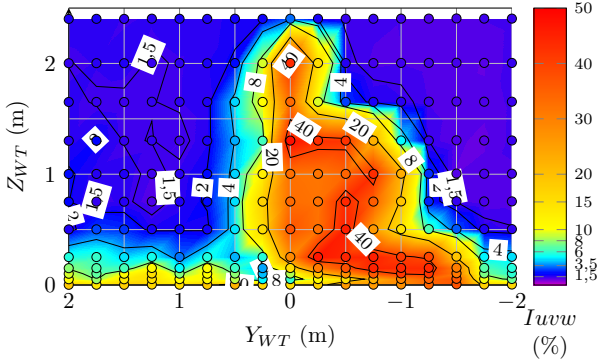
(c) Wind field, 1.59 m downstream from the outlet of the closed section. Upstream model side (II).



(d) Turbulence intensity, 1.59 m downstream from the outlet of the closed section. Upstream model side (II).



(e) Wind field, 4.04 m downstream from the outlet of the closed section. Downstream model side (III).



(f) Turbulence intensity, 4.04 m downstream from the outlet of the closed section. Downstream model side (III).

Figure 4.8 – Downwind configuration TFWT velocity field. \circ indicates location of measurement points. I, II, III sections are presented in Fig. 2.1.

4.2.1.3 $\beta_{AW} = 110^\circ$

Tab. 4.3 presents sheet length configuration where visualisation stripes are estimated to be horizontal and the sheet length where curling appears for the free mast situation at $\beta_{AW} = 110^\circ$. Repeatability between two tests recorded with a long time separation is here indicated for the triradial spinnaker. Trends remain identical between the two sets of data even if differences still exist. Several elements can explain these differences: change in the wind tunnel screen cleaning state between the two tests, fail to set up the rig on the exact same position, evolution of the testing environment in the wind tunnel hall.

Spinnaker	Test	Date	Horizontal stripes (mm)	Curling apparition (mm)
			$L_{sheet\ H}$	$L_{sheet\ C}$
Spinnaker Tri 1	Test 0	02/04/2015	1043	1403
	Test 1	20/04/2015		1410
Spinnaker CC 1	Test 0	21/04/2015	1170	1430

Table 4.3 – Horizontal stripes and curling apparition for free mast at $\beta_{AW} = 110^\circ$. Empty cells indicate that no measurement has been done.

Drive force coefficient C_{F_x} is presented in Fig. 4.10. The maximum is closely located on the curling limit. The cross-cut spinnaker presents a maximum located 5 mm after the curling limit. The maximum mean drive force coefficient for the cross-cut design shape is higher than the triradial one.

The loop presented for the triradial spinnaker is due to the phenomenon which occurs when a fold is maintained on the luff. This happens when sheet length is largely eased beyond the curling limit. In this case a fold appears and can be maintained on the luff even if the spinnaker is trimmed back before the curling apparition. The fold disappears by a transition to the normal situation either curling or not for a certain quantity of sheet length trimmed in back. This kind of loop is called in this study a folding hysteresis. Quasi-steady state illustration of the trimming in way back is presented in Fig. 4.9. This folding hysteresis by definition can be directly observed on the flying shape as indicated in Fig. 4.14. The performance of the maintained folded sail before recovering is about 60% of the full sail situation once recovered. To the author's knowledge no maintained folded sail presents more drive force than its normal curling or full situation. The maintained fold shape is expected to decrease the drive force as it changes the orientation of the luff part where normally the local aero dynamic forces are higher and more oriented in the yacht centreline. The folded hysteresis was not tested on the cross-cut design.

Another hysteresis in the measured data seems to exist for lower value of sheet length on both spinnakers. However direct observation of the flying shape did not provide any clue about this hysteresis existence. Side force coefficient presented below confirms these measurements.

Side force coefficient C_{F_y} is presented in Fig. 4.10. Here the curling apparition decreases the slope of the side force coefficient however it does not correspond to the maximum value of the standard deviation of the side force coefficient. The folding hysteresis can be observed on the side force coefficient. When the spinnaker stays folded, the side force coefficient absolute value is greater compared to the mean value while curling. The other hysteresis located for low sheet length value can be seen on both spinnakers more significantly than on the drive force coefficient.

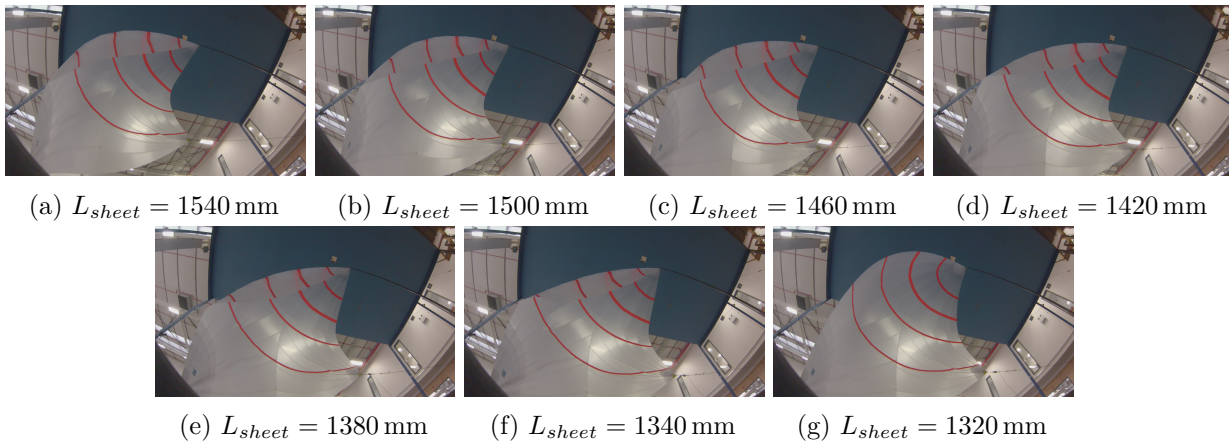


Figure 4.9 – Fold maintained while trimming in back on triradial spinnaker at $\beta_{AW} = 110^\circ$ with a free mast. Fish eye effect has not been removed.

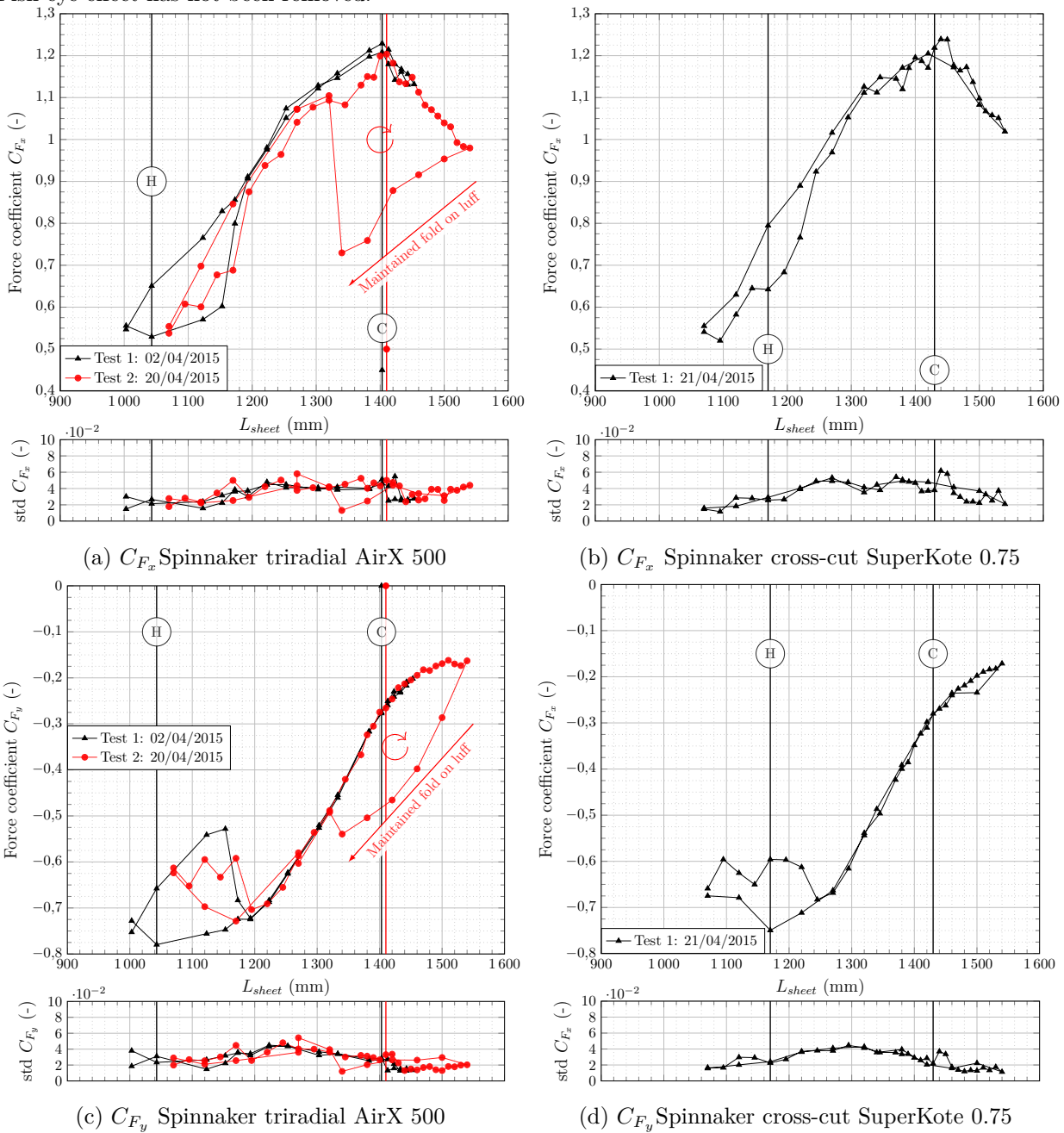


Figure 4.10 – Effect of curling with static trim on force coefficients with a free mast at $\beta_{AW} = 110^\circ$.

Sheet load coefficient $C_{F_{sheet}}$ is presented in Fig. 4.11. The two kinds of hysteresis loop previously noticed are also observed in the sheet load signal. Here the maximum sheet load coefficient occurs before the curling apparition.

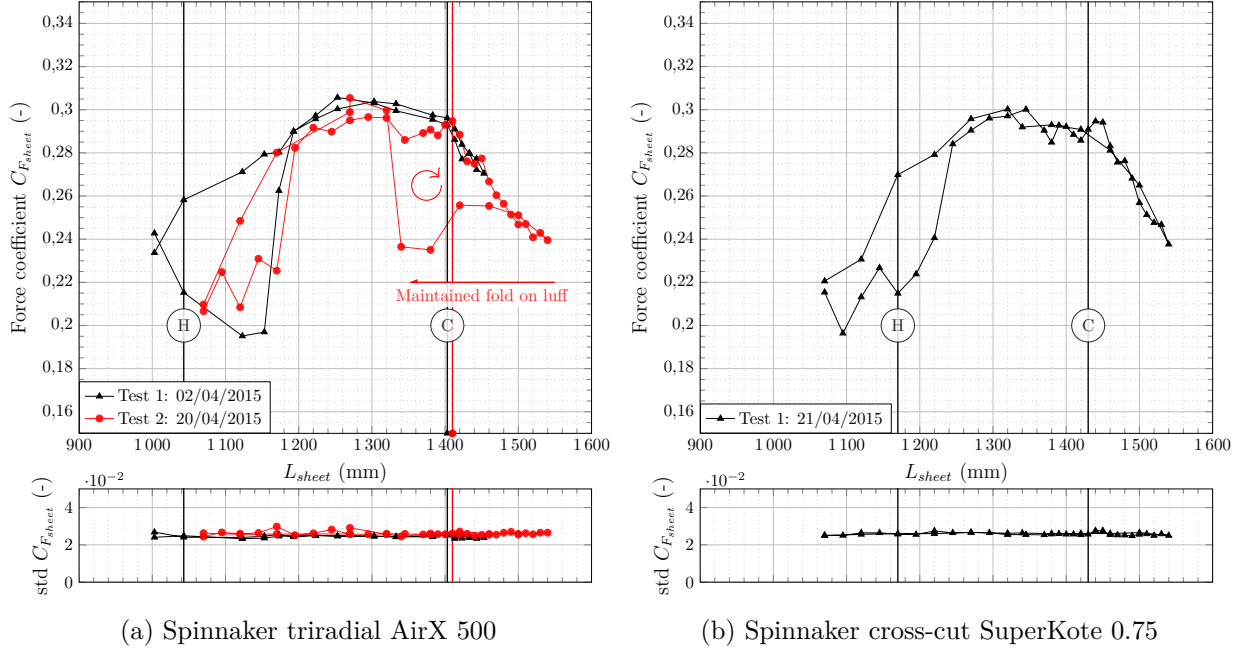


Figure 4.11 – Effect of curling with static trim on sheet load coefficient at $\beta_{AW} = 110^\circ$.

4.2.1.4 $\beta_{AW} = 140^\circ$

A deeper AWA is studied here. For the tested sheet length, visualisation stripes did not reach horizontal position.

Spinnaker	Test	Date	Curling apparition
			(mm) $L_{sheet} C$
Spinnaker Tri 1	Test 0	02/04/2015	
	Test 1	02/04/2015	1556
	Test 2	01/04/2015	1556
Spinnaker CC 1	Test 0	10/04/2015	
	Test 1	10/04/2015	1566

Table 4.4 – Curling apparition for free mast at $\beta_{AW} = 140^\circ$. Empty cell indicate that the configuration did not reach curling.

In this kind of situation the spinnakers present a strong oscillating motion along the crossflow direction, becoming more and more significant while easing the sheet and reaching the curling location. The spinnaker started to largely oscillate in the cross flow direction with a displacement at the order of magnitude of its size. From a FSI point of view this phenomenon is a movement induced excitation as classified by [Staubli et al., 2008].

This oscillating motion could also be related to what can be observed on kites where instabilities with strong oscillations can appear as described in [Du Pontavice, 2016]. In both case, the flying cloth is hold by several lines. The spinnaker has nevertheless a fuller 3D shape compared to the kite which shape is either modelled with a flat wing or with a flexible arch. Moreover two of the spinnaker holding lines - the halyard holding the head and the tack line holding the tack point- are also much smaller relatively to the spinnaker size compared to the length of the kite holding lines. Those two short lines maintain the cloth oscillation along an axis defined by the head-tack direction.

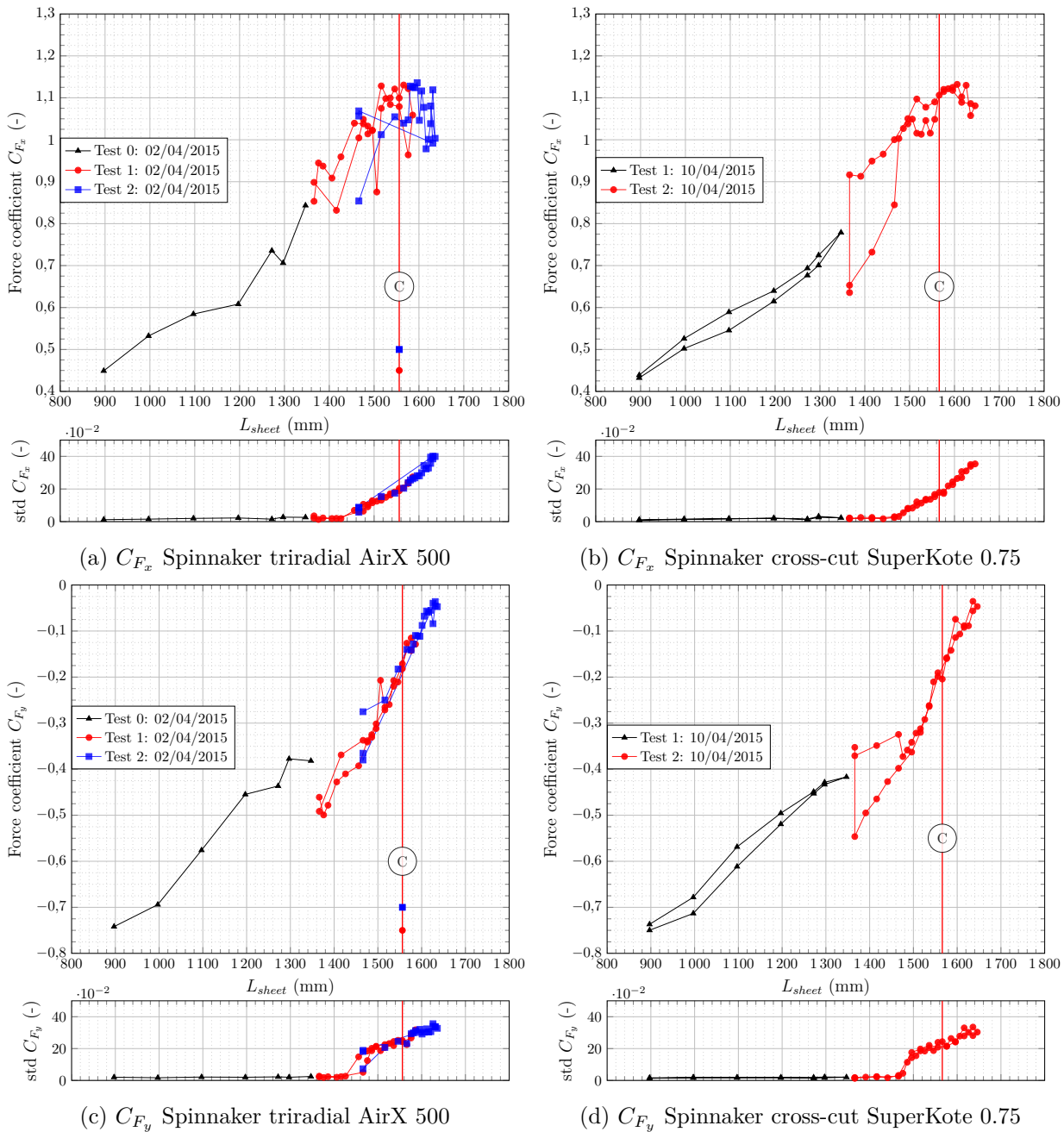


Figure 4.12 – Effect of curling with static trim on force coefficients with a free mast at $\beta_{AW} = 140^\circ$.

Strong oscillations start around $L_{sheet} = 1466$ mm for the triradial spinnaker. For both

spinnakers when curling appears, the maximum side force observed can be positive. Therefore on the curling limit the side force can either be oriented to windward or leeward side.

Drive force coefficient C_{F_x} is presented in Fig. 4.12, side force coefficient C_{F_y} in Fig. 4.12 and sheet load coefficient $C_{F_{sheet}}$ in Fig. 4.13. The repeatability here is affected by the strong displacement of the whole spinnaker but trends remain identical. The standard deviation of the time series of drive force, side force and sheet load coefficients close to the curling location is significantly higher than the two previous tested AWA. This could be used as a criterion to detect this kind of motion of the spinnaker. The standard deviation value does not decrease after passing the curling point, spinnaker motion being more and more important. The maximum drive force is located close to the curling apparition however this situation is really unstable and should be avoided while sailing.

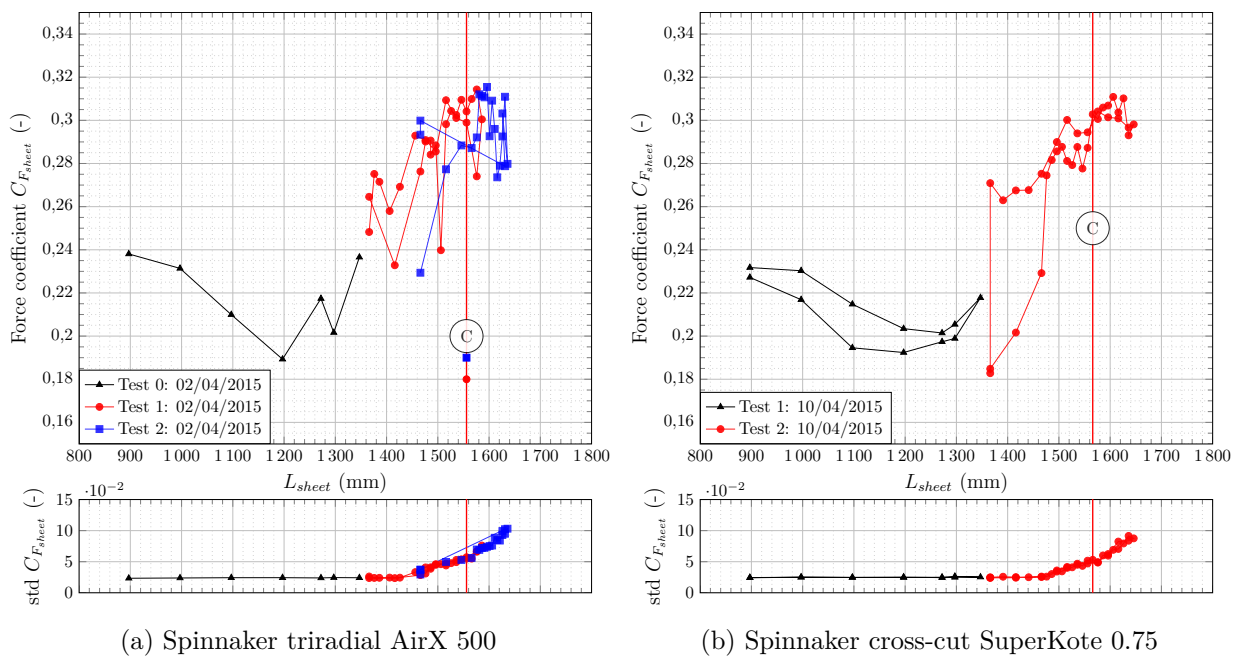


Figure 4.13 – Effect of curling with static trim on sheet load coefficient at $\beta_{AW} = 140^\circ$.

Conclusions on free mast configuration:

1. the relative position of the optimum sheet length providing the maximum drive force compared to the curling apparition depends of the AWA:
 - $\beta_{AW} = 80^\circ$, the maximum drive forces is located before the curling limit.
 - $\beta_{AW} = 110^\circ$, the curling limit is associated to the maximum drive force.
 - $\beta_{AW} = 140^\circ$, the maximum drive forces is located slightly after the curling limit but the spinnaker motions are important.
2. two hysteresis have been identified for an AWA of 110° :
 - the folding hysteresis appears after the curling limit as shown in Fig. 4.14. When easing the spinnaker from the full shape, the luff is full then flapping when it reaches

the curling limit then presents a permanent fold with a reduction of the drive force and an increase in the side force. When trimming in back, the fold is maintained until it recovers a previous state flying shape, either on the curling state or on the full shape state.

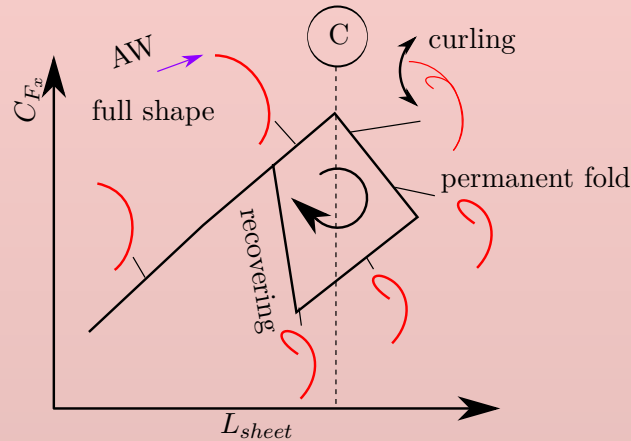


Figure 4.14 – Folding hysteresis description. Red sections represent the spinnaker section state (full, curling, folded). The apparent wind direction is indicated. The recovering phase can occur for shorter or longer sheet length than the curling apparition limit, depending how tall is the fold.

- the other hysteresis located for lower sheet length, *i.e.* before the curling limit, has not been clearly related to a flying shape change and can not be directly seen by an external observer.
3. when measured, the stripe horizontal alignment is not an appropriate indication to maximise boat performance and occurs before the optimum trim. For $\beta_{AW} = 110^\circ$, the drive force coefficient when stripes are estimated to be horizontal is about 50% of the maximum drive force for the triradial design and 58% for the cross cut one.
 4. most of the dynamic variations of aerodynamic forces are transferred by the head and tack points as suggested by the standard deviation of the sheet load less affected than the standard deviation of force coefficient when the curling appears. This conclusion is in agreement with full-scale measurements on J80 spinnaker in [Deparday, 2016]. An indicator of the oscillating behaviour might be a significant increase in the standard deviation of the different measured forces.

For the previous tested cases, the mast was free and therefore strong head mast motion can be observed. Next results present two different AWA where the mast has been partially rigged with a windward shroud and a backstay.

4.2.2 Partially-rigged mast situation

The fans frequency was set up to $f_{fans} = 20.5 \text{ Hz}$ ($U_{Pitot} \approx 3 \text{ m s}^{-1}$). The goal here is to investigate a half rigged mast with the two extreme previous AWA conditions tested. First each case is described in this part to focus on new observations. Comparisons with the previous free mast configuration are presented later.

4.2.2.1 $\beta_{AW} = 80^\circ$

Spinnaker	Test	Date	Curling apparition(mm)
			$L_{sheet} C$
Spinnaker Tri 1	Test 0	24/04/2015	935
Spinnaker CC 1	Test 0	22/04/2015	955

Table 4.5 – Curling apparition for partially-rigged mast at $\beta_{AW} = 80^\circ$.

Drive and side force coefficients are presented in Fig. 4.16 and sheet load coefficient in Fig. 4.15. The maximum mean drive force occurs to a position close to curling. The triradial design here presents a maximum mean drive force just before the apparition of curling. The maximum mean drive force coefficient is close to 1 for both spinnakers. Curling does not affect significantly the side force coefficient, the sheet load coefficient and the standard deviation of the drive force coefficient. The fact that the mast motion are drastically reduced restricts the general sail motion lowering the standard deviation levels. A folded hysteresis has been tested on the triradial design where the trimming in back branch presents a 10% lower drive force coefficient and more side force compared to the curling situation. The spinnaker recovers its flapping shape before being on the edge of curling.

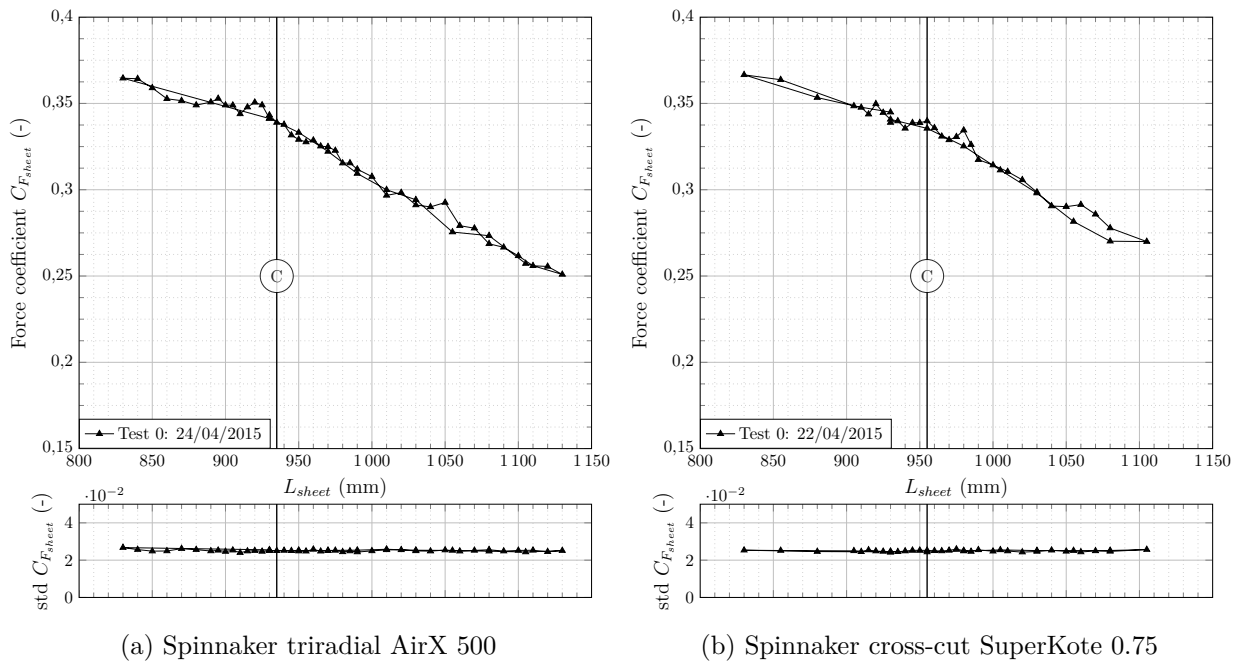


Figure 4.15 – Effect of curling with static trim on sheet load coefficient at $\beta_{AW} = 80^\circ$ with a partially-rigged mast.

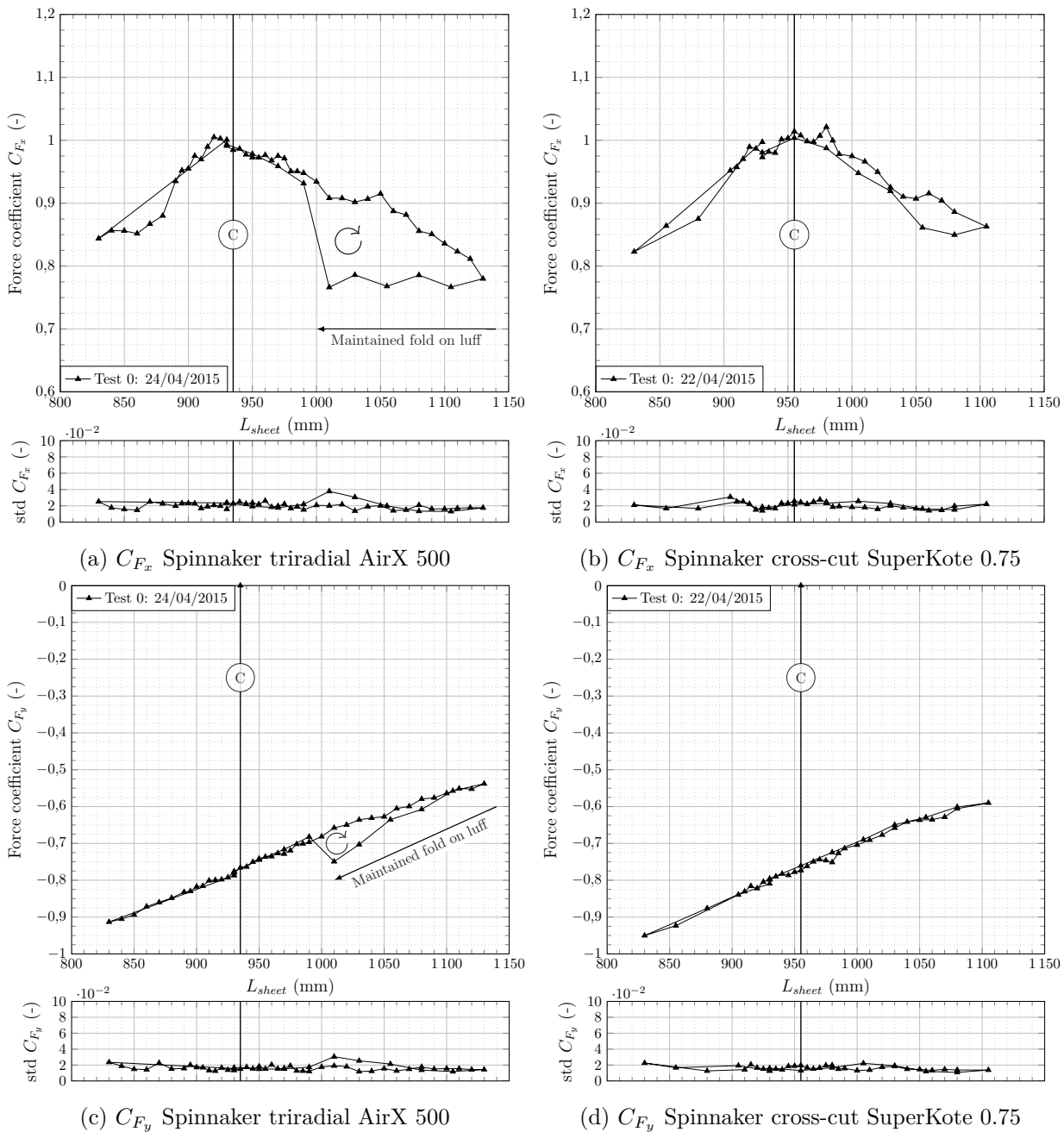


Figure 4.16 – Effect of curling with static trim on force coefficients at $\beta_{AW} = 80^\circ$ with a partially-rigged mast.

4.2.2.2 $\beta_{AW} = 140^\circ$: hysteresis phenomena occurring before curling

Several tests are carried out in this configuration to characterize a phenomenon which can occur on downwind sails. The curling apparition sheet length is presented in Tab. 4.6.

Drive and side force coefficients are presented in Fig. 4.18 and sheet load coefficient in Fig. 4.17. Here the standard deviations of the signals significantly increase when curling occurs. The drive and side force standard deviation are increasing also before the curling apparition.

Spinnaker	Test	Date	Curling apparition(mm)
			$L_{sheet} C$
Spinnaker Tri 1	Test 0	23/04/2015	
	Test 1	23/04/2015	1349
	Test 2	23/04/2015	1354
	Test 3	24/04/2015	
	Test 4	24/04/2015	
Spinnaker CC 1	Test 0	22/04/2015	
	Test 1	22/04/2015	
	Test 2	23/04/2015	1369

Table 4.6 – Horizontal stripes and curling apparition for partially-rigged mast at $\beta_{AW}=140^\circ$. Empty cells indicate that curling was not tested for this configuration.

An hysteresis loop is measured. It appears for shorter sheet length than the one associated to the curling limit. The mechanism here is not associated to a folding state of the spinnaker. Results show the existence of two possible states of the spinnaker in a region before curling. The higher branch (higher mean drive force coefficient when trimming in) is less stable than the lower branch occurring while easing. Being trimmed in this area will eventually end on the lower branch for long enough observation duration. However the transition from one state to another cannot be noticed by an external observer on the flying shape evolution. The higher branch on the drive force coefficient seems to be metastable: for a perturbation with enough amplitude, a transition occurs and leads to the lower branch with less drive force. Several tests have been carried out either with a static sheet length recording or with a quasi-static sheet length (test 3, 4 and 5) for the triradial design. The quasi-static trim is achieved with a low speed change in the sheet length.

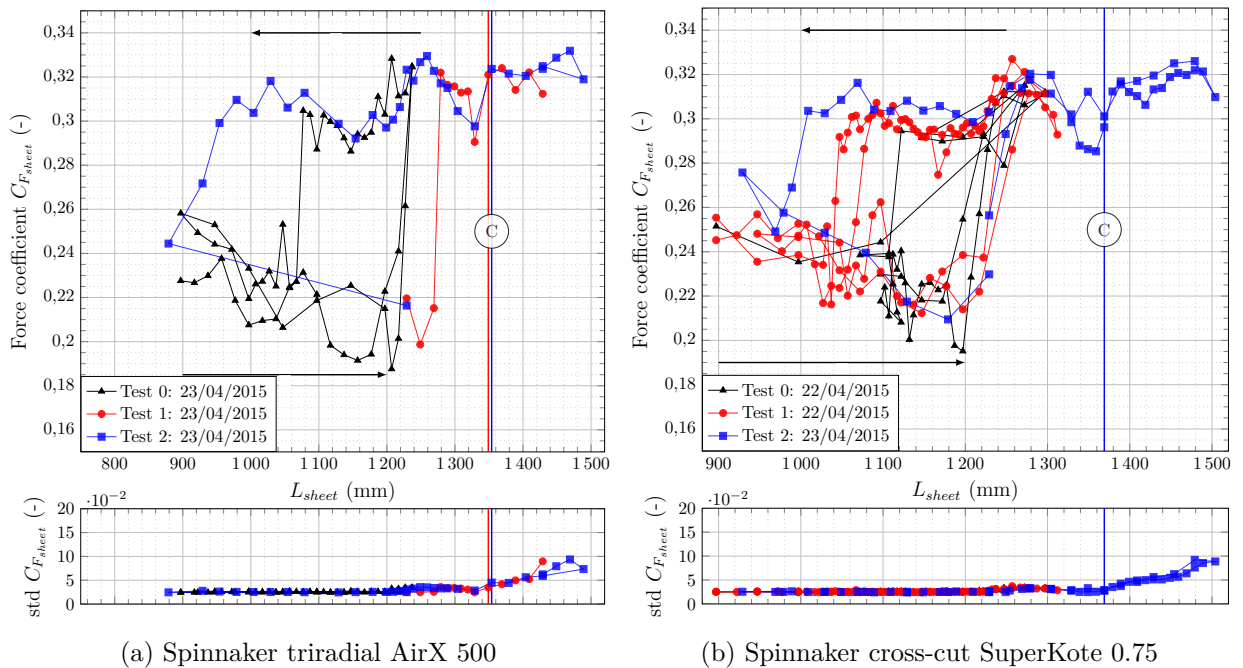


Figure 4.17 – Effect of curling with static trim on sheet load coefficient at $\beta_{AW}=140^\circ$ with a partially-rigged mast.

The more stable branch of the hysteresis loop presents higher absolute value of side force and lower value of drive force. The hysteresis phenomenon can also be observed on the sheet load signal where the unstable branch (trimming in direction) presents 50% more sheet load coefficient than the easing branch. No flow visualisation has been carried out during the experiment. However the results might indicate that this hysteresis is related to a detached attached and attached detached flow transition as shown in Fig. 4.19.

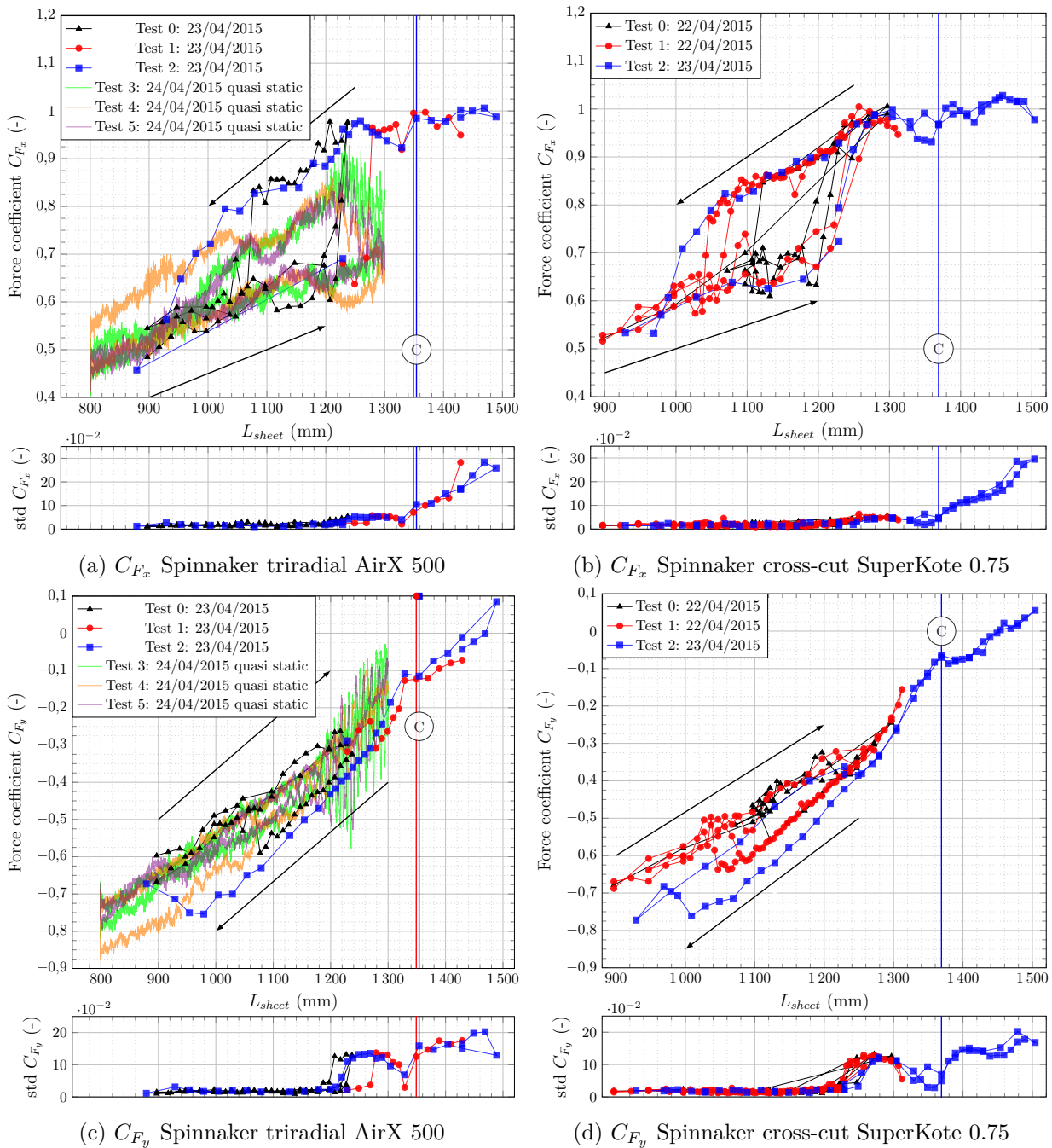


Figure 4.18 – Effect of curling with static trim on force coefficients at $\beta_{AW} = 140^\circ$ with a partially-rigged mast.

This hysteresis phenomenon occurs for the two different kinds of spinnaker, the cross-cut design keeping higher drive force coefficient in this area than the triradial design. Once the spinnaker is curling, the drive force coefficient stays close to 1 and the side force coefficient tends to decrease. The quasi-static tests show more pronounced oscillations of the spinnaker in the area before curling.

Conclusions on partially-rigged mast configuration:

1. the relative position of the optimum sheet length providing the maximum drive force compared to the curling apparition depends of the AWA:
 - $\beta_{AW} = 80^\circ$, the maximum drive forces is located close to the curling limit.
 - $\beta_{AW} = 140^\circ$, the maximum drive forces is located after the curling limit but the spinnaker motions are important.
2. two hysteresis have been identified:
 - the folding hysteresis has been observed on the triradial spinnaker at $\beta_{AW} = 80^\circ$.
 - the other hysteresis located for lower sheet length, *i.e.* before the curling apparition, is probably associated to an attached-detached flow transition as illustrated in Fig. 4.19.

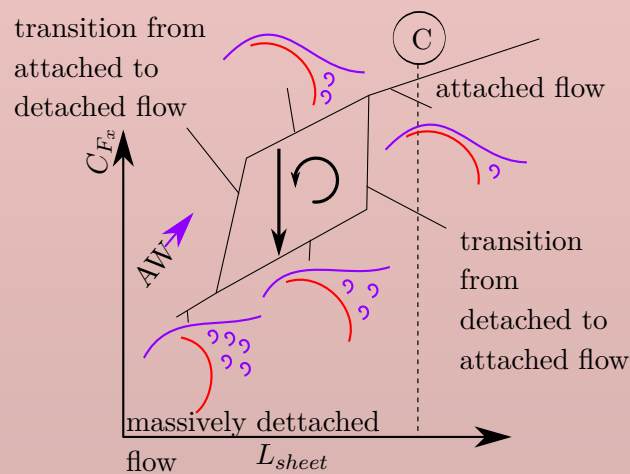


Figure 4.19 – Detached flow hysteresis description. Red sections represent the spinnaker section state (full in this case). The apparent wind direction is indicated relative to the section. A path line is associated to each section to indicate the attached or detached flow state.

No twist was used for the previous presented cases in order to facilitate the setup and make easier possible numerical-experimental comparison. Going one step further, the next subsection presents results adding twisted flow using vanes. Comparison between the different configurations to evaluate their effects is presented further.

4.2.3 Partially-rigged mast situation with twisted flow

The TFWT is known as the first wind tunnel to model the twist effect that a boat can encounter while sailing at sea. The twist is more important for downwind points of sail. Here is presented one situation with a partially-rigged mast and twisted flow in order to measure any possible difference with the no twist case. The fans frequency was set up to $f_{fans} = 20.5 \text{ Hz}$ ($U_{Pitot} \approx 3 \text{ m s}^{-1}$) with $\beta_{AW} = 80^\circ$.

Spinnaker	Test	Date	Curling apparition(mm)
			$L_{sheet} C$
Spinnaker Tri 1	Test 0	29/04/2015	920
Spinnaker CC 1	Test 0	30/04/2015	970
	Test 1	30/04/2015	

Table 4.7 – Curling apparition for partially-rigged mast at $\beta_{AW} = 80^\circ$ with twisted flow. Empty cells indicate that curling was not tested for this configuration.

The central twisted velocity profile is given on Fig. 4.20. It is associated to the realistic following condition extracted from the J80 polar diagram: $V_{BS} = 3 \text{ m s}^{-1} = 6 \text{ kn}$ at $\beta_{TW} = 131^\circ$ with $V_{TW} = 3.91 \text{ m s}^{-1} = 7.61 \text{ kn}$ at 10 m height for the real situation (associated to a reference height Z_{ref} of 2.17 m in the wind tunnel). This configuration corresponds to an apparent wind conditions of $\beta_{AW} = 80^\circ$ with $V_{AW} = 3 \text{ m s}^{-1} = 5.84 \text{ kn}$ at the reference altitude. As shown on Fig. 4.20 the twist angle or apparent velocity for the lower part do not match exactly the expected theoretical wind profile, the boat being fixed in the wind tunnel.

Drive and side force coefficients are presented in Fig. 4.22 and sheet load coefficient in Fig. 4.21. The maximum mean drive force coefficient occurs just before curling: 20 mm before it for the triradial spinnaker and 10 mm before it for the cross-cut spinnaker. A maintained fold configuration has been tested for the triradial cut and is observed on drive and side force and sheet load coefficients. The maximum mean drive force is slightly higher for the triradial cut. Folding hysteresis has been tested for the cross-cut design in the curling area but presents less clear trends than the other cut.

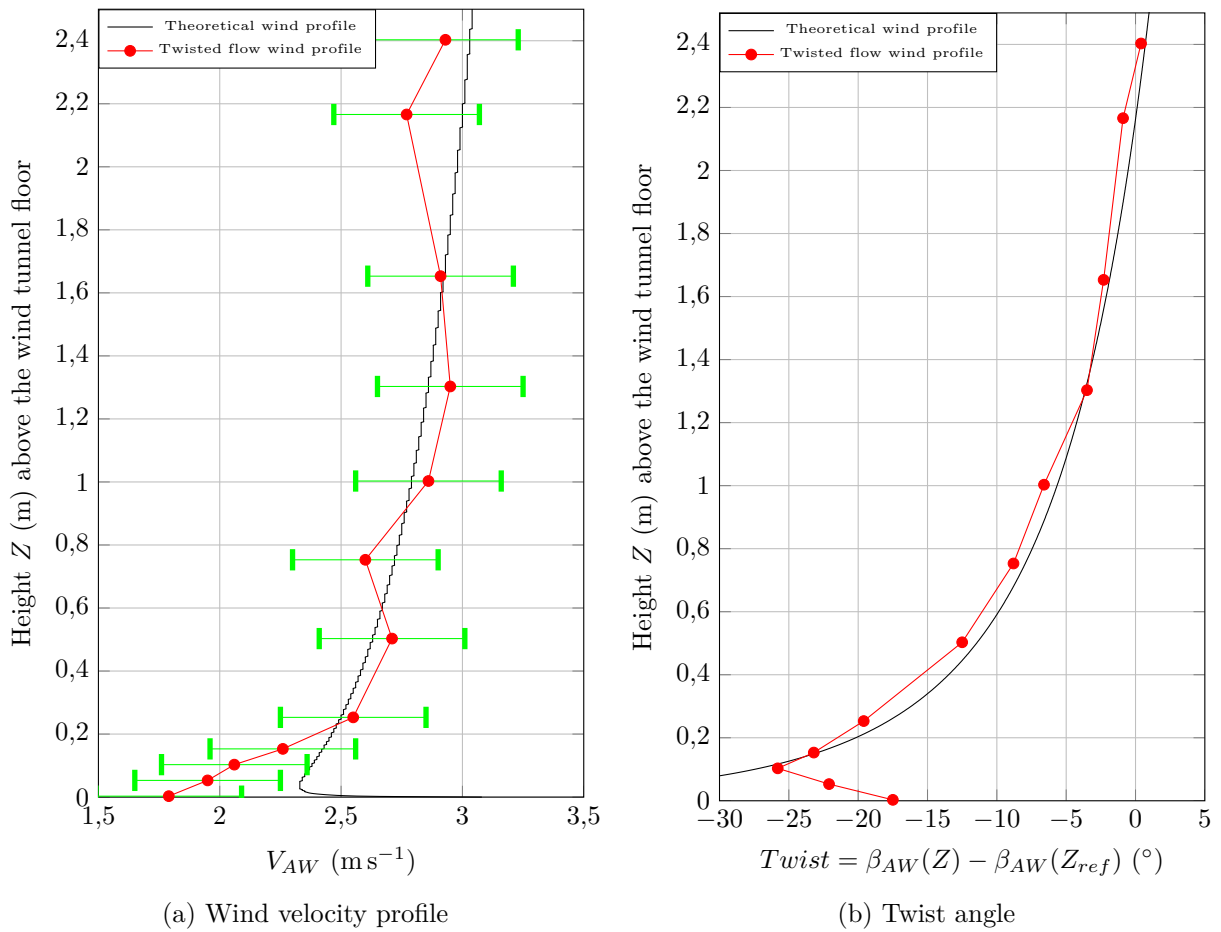


Figure 4.20 – Measured twisted flow wind profile vs the theoretical wind profile. Error bar for wind speed represents the maximum and minimum measured values.

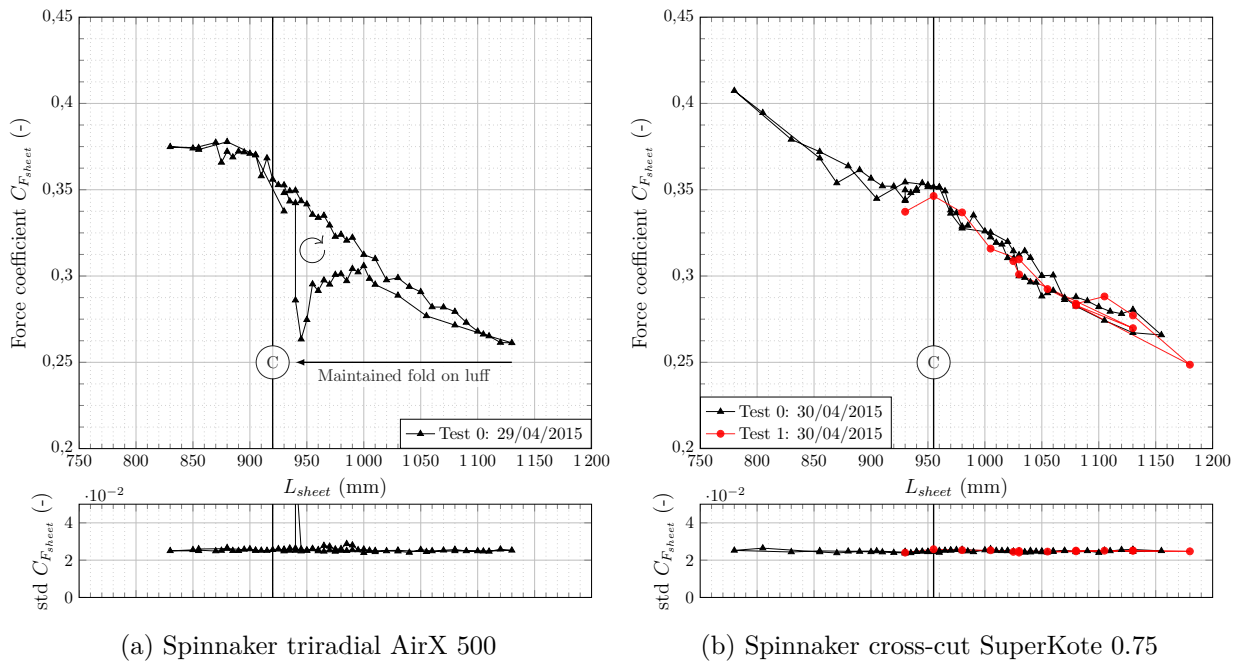


Figure 4.21 – Effect of curling with static trim on sheet load coefficient at $\beta_{AW} = 80^\circ$ with a partially-rigged mast and twisted flow.

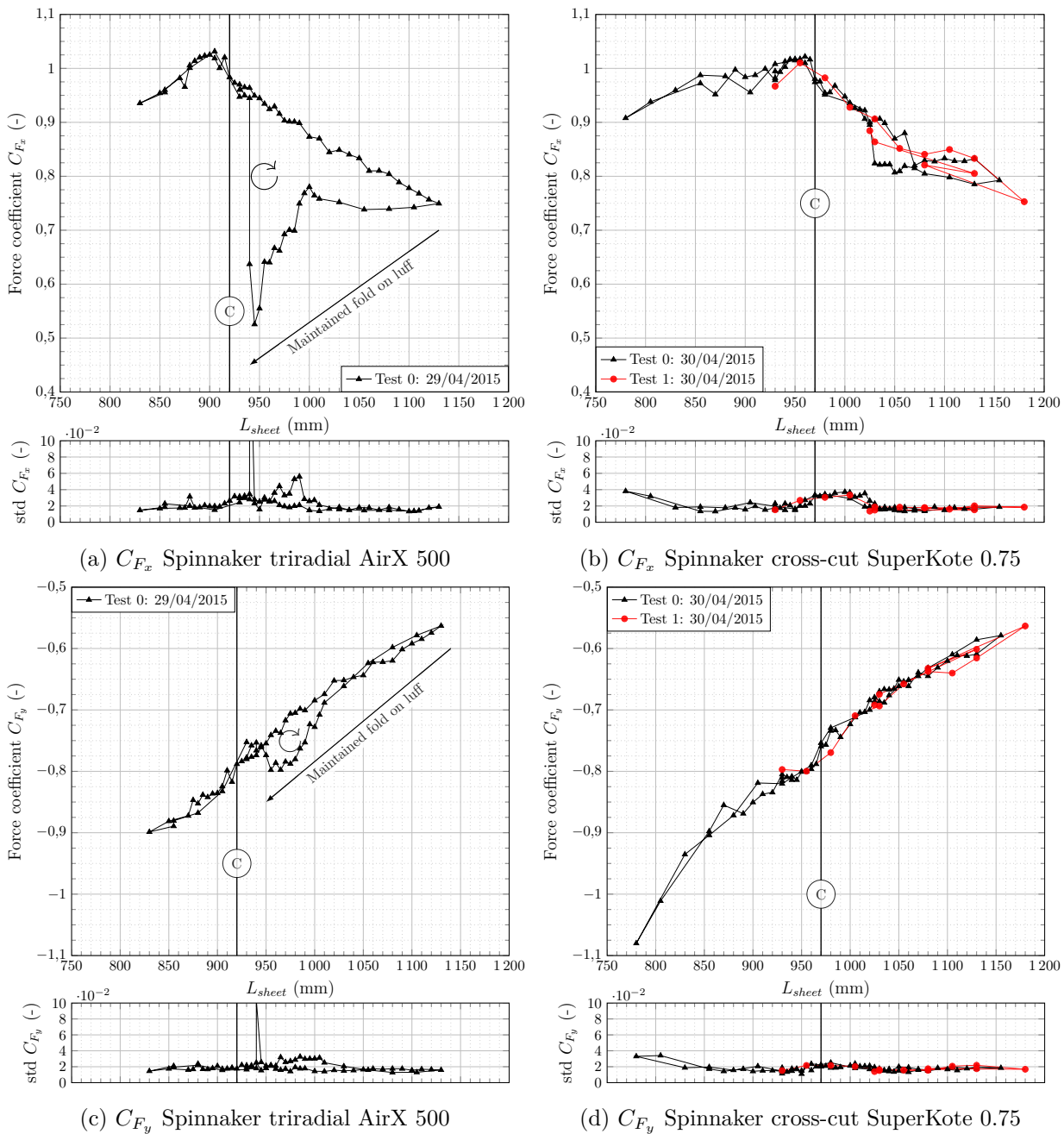


Figure 4.22 – Effect of curling with static trim on force coefficients at $\beta_{AW} = 80^\circ$ with a partially-rigged mast and twisted flow.

4.2.4 Comparison of the different mast configurations

Comparison discussions for the two spinnakers with several mast configurations, free mast, partially-rigged mast and partially-rigged with twisted flow, is presented here. Note that the fan frequency was set up to $f_{fans} = 20$ Hz for the mast without rig and to $f_{fans} = 20.5$ Hz for the partially rigged case mast where the averaged wind speed reference value was closer to 3 m s^{-1} .

Conclusions on difference on mast configuration:

1. free mast configuration has a curling limit located for a longer sheet length. The mast bending tends to delay the curling apparition certainly affecting the spinnaker flying shape which has in the free mast case a lower luff tension.
2. surprisingly free mast configuration generates higher mean drive force coefficient (about 10%), but increase the rig and spinnaker motion.
3. partially-rigged mast presents lower absolute value of side force coefficient than free mast.
4. for the sheet load coefficient, the trends depends on the AWA. For $\beta_{AW} = 80^\circ$, sheet load coefficient is higher for the free mast situation, and for $\beta_{AW} = 140^\circ$, the sheet coefficient is lower for the free mast situation compared to the partially-rigged mast.
5. the twisted flow effect on the curling limit depends of the type of sail. For the triradial cut, the twisted flow makes the curling appear for a shorter sheet length and the mean drive force is about 2% higher than without the twisted flow. For the cross-cut design, the curling appears for a longer sheet length than with a non twisted flow case.
6. the maximum mean drive force levels are quite identical between twisted and non twisted flow. The side force coefficient is not affected by the twist. The sheet load coefficient is slightly higher with twisted flow. The main difference is located on the trimmed in area compared to curling location, where the twisted flow configuration shows more mean drive force coefficient, especially for the cross-cut design.
7. twisted flow affects less the results than the mast configuration for the AWA of 80° .

Previous results show static configurations where several hysteresis phenomena have been observed. The observed hysteresis can be classified in two groups:

- the hysteresis occurring before the curling apparition, probably related to attached-detached flow transition, which require flow visualization to be confirmed. The transition from the metastable branch to the stable one occurs with a smooth transition which can be hardly perceived by an external observer.
- the folding hysteresis which occurs after the curling apparition. The fold on the luff which modifies the aerodynamic forces generated can be observed directly on the sail.

The different transition dynamics related to the folding hysteresis are presented next.

4.2.5 Unfolding dynamics of the folding hysteresis: usual recovering and extreme events

Two different processes can be observed for the unfolding stage with very different dynamics:

- the usual recovering corresponds to a smooth decrease of the folded area as shown on the recovering phase in Fig. 4.3 until the sail reaches the new equilibrium branch. This new state can be curling but the fold is no longer maintained. This kind of process looks similar to what happens during curling cycle when the luff part is unfolding.
- the second process is associated to an extreme event. The folded area increases first slowly then rapidly until the all spinnaker collapses violently before recovering its usual flying-shape. Such a case presents a very strong dynamic aspect and can look similar to a flag. This kind of situation should be avoided while sailing. The usual flying shape situation can take time to recover after the collapse of the spinnaker which implies that the boat is sailing with an inefficient sail during precious moments. Moreover strong loads are observed in the rig and felt by the trimmer in the spinnaker sheet during the collapse and recovery phase. This is a phenomenon where structural failure can appear either on the spinnaker (torn apart on weak seams), on the holding lines, on knots, or on the mast if weather conditions are strong. This kind of situation was also avoided during experimental test to preserve the recording devices and especially the load sensors.

Here is presented the peak loads associated to an unfolding extreme event run which was recorded by accident during the 2015 experimental campaign. It provides data to illustrate one of the strongest dynamic phenomenon that can be observed on downwind sails occurring with a constant sheet length. Drive force, side force and sheet load coefficients are shown in Fig. 4.23. The associated flying shapes corresponding to each step (indicated by vertical lines) are presented in Fig. 4.24. Some other extreme unfolding recorded in 2016 show the same dynamics and identical maximum and minimum order of magnitude.

Several things can be observed:

- the initial conditions corresponding to the folded case at t_0 has worst performance than the final situation at t_8 where the spinnaker is curling again (approximately 50% less of drive force than the final situation for a similar side force coefficient). This observation concur with the folding hysteresis loop direction observed on force coefficient vs L_{sheet} indicating that the fold case always has worst performance (less drive force and similar or more side force).
- the maximum instantaneous drive force coefficient is 2.2 times higher than the final value. The minimum instantaneous drive force coefficient becomes even negative reaching -44% of its final value. The negative drive force can be expected observing the video which indicates a reversed flying shape and camber during the collapse. The time duration between the minimum and maximum drive force is about 55 ms. Such a phenomenon is therefore strongly unsteady with high and fast variations measured in the forces.
- the minimum instantaneous side force coefficient is 2.7 times lower than the final value. The maximum instantaneous side force coefficient becomes even positive but close to zero.
- the maximum sheet load coefficient is 6.5 times higher than its final value and the minimum value is close to zero

This natural unsteady and non stationary situation illustrates the following principle: maximum and minimum forces and load applying on a sail boat measured during a strong unsteady case are not

identically proportional to their respective mean value during a quasi-steady situation. This implies that for structural failure prevention, a safety coefficient cannot be identical for all the different parts of the rig. This observation has already been underlined by [Augier et al., 2012] encouraging again refined experimental data analysis and justifying the need for accurate dynamic and unsteady models development.

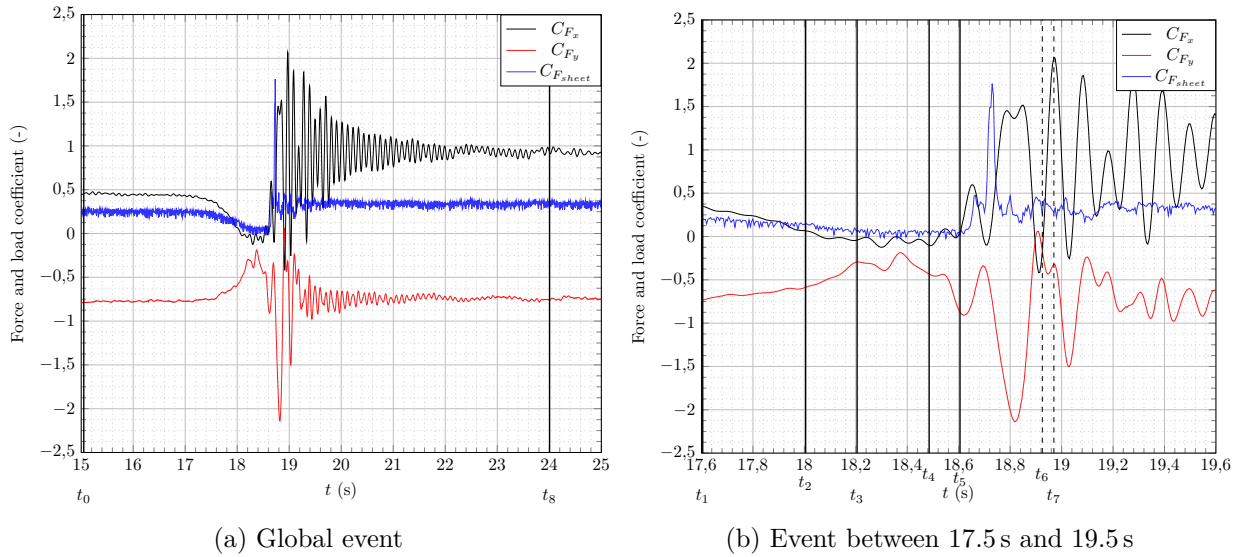


Figure 4.23 – Spinnaker extreme event while unfolding, with a constant sheet length, triradial spinnaker, partially rigged mast, $\beta_{AW} = 80^\circ$. Vertical lines indicate each state illustrated by Fig. 4.24 photographs.

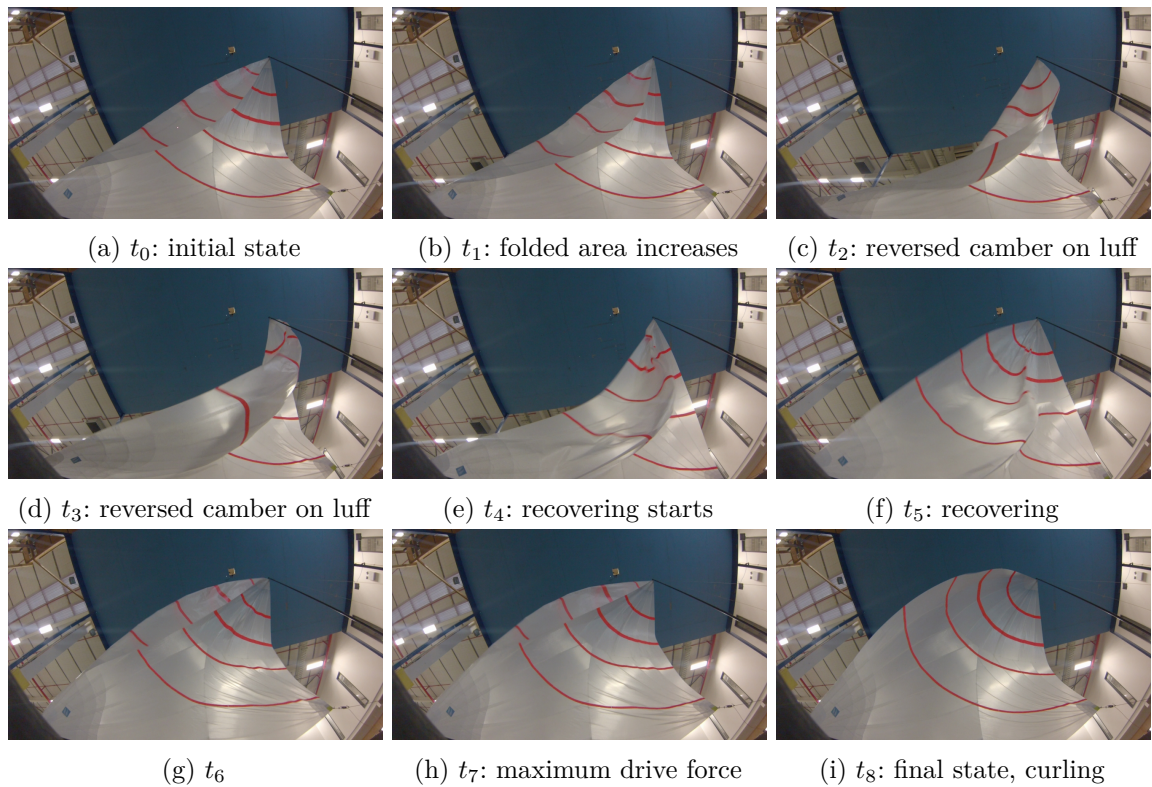


Figure 4.24 – Flying shape evolution during a spinnaker unfolding collapse, with a constant sheet length, triradial spinnaker, partially rigged mast, $\beta_{AW} = 80^\circ$. Fish eye effect has not been removed.

Conclusions on the different configuration tested:

The curling effect on drive, side and sheet load coefficients has been shown for different AWA in various situations tested in this section. The maximum drive force location can be different regarding the edge of curling limit and depends on the apparent wind angle and type of spinnaker:

- for a free mast configuration, the curling apparition does not correspond to the maximum mean drive force for $\beta_{AW} = 80^\circ$. A plateau is observed before this apparition for both spinnakers. For $\beta_{AW} = 110^\circ$ the curling apparition corresponds to a maximum drive force for the triradial cut. For the cross-cut spinnaker the maximum is reached for a 10 mm more eased trim than the apparition of curling. For $\beta_{AW} = 140^\circ$ the curling apparition corresponds to a good compromise between a maximum drive force and spinnaker stability.
- for a partially-rigged mast, at $\beta_{AW} = 80^\circ$ the curling apparition corresponds to the best trim with a maximum drive force. For a deeper AWA at $\beta_{AW} = 140^\circ$ the apparition of curling does not correspond to the maximum drive force but easing more makes the spinnaker really unstable with strong motion.
- adding twisted flow at $\beta_{AW} = 80^\circ$ changes slightly the position of the maximum drive force for both spinnakers which occurs just before curling. The maximum mean drive force also increase for the triradial spinnaker. The twisted flow affects the results but for this AWA, results still remain close to the partially-rigged mast compared to the free mast.

From a global consideration, optimum trim seems to be located close to the apparition of curling in the various situations. However some small differences have been measured in the wind tunnel conditions. For natural unsteady sailing conditions, it is reasonable to consider that the verge of curling trim is a relevant general recommendation. The trimmer constantly adapts the sheet length to get the curling following the wind variations.

The mast without rig presents a very strong dynamic behaviour and the mast head is submitted to large displacements. This simple cantilevered mast surprisingly has higher maximum drive force probably due to a different flying shape of the spinnaker in this situation. The additional dynamics aspects enabled by this free mast and larger sail displacement might also take part in the increase of drive force.

Dynamic trimming tests have been carried out on those situations but are not presented here. Moreover, for this section tests, only stripes recognition have been used to record the flying shape information. A first approach based on visual observation conclusion has firstly shown that the design shape targeted by the sail maker associated to the horizontal stripes trim, did not corresponds to the maximum drive force location. Moreover stripes recording using one camera is not really adapted for a full luff downwind sail shape like the J80 spinnaker. Another wind tunnel experimental campaign carried out in 2016 is presented in the next section. Improvements have been done such as a fully rigged mast and the use of photogrammetry techniques to measure the sail's flying shape.

4.3 Natural curling effect: fully rigged mast

This section describes tests carried out in 2016. The configuration of the spinnakers is slightly different than the 2015 configuration. The sail have been set up higher in order to get the sail foot further away from the wind tunnel floor which can explain differences between the two experimental campaigns. Two complementary sails have been manufactured for this experimental campaign in order to have a set of four different spinnakers with two parameters which can change: either the cloth material or the cut. The carbon fibre mast was fully rigged and had a diameter of 20 mm. This choices have been made to limit the mast motion as much as possible. Coded targets are stuck onto the spinnakers on identical positions and four triggered HD cameras have been used to record the flying shape.

Effects of reference wind speed is also studied during this experimental campaign. Some effects can be measured on the data mean value, probably due to a slight change in the flying shape due to different wind speeds and not to a change in the flow behaviour (such as a variation in Reynolds number). For the lowest wind velocity preliminary tested $f_{fans} = 15$ Hz, the effect of the spinnaker cloth weight combined with the effect of any extra weight such as the load sensor weight are more important on the flying shape itself and therefore on measured aerodynamic forces. Even for the 17.5 Hz frequency ($U_{Pitot} \approx 2.49$ m s⁻¹) some downwind results may indicate that the weight of the sail and the load sensor has a significant impact on the results. Wind speed also affects the curling dynamic such as its natural frequency.

Nevertheless, in our velocity range, the Reynolds number has a low impact on the attached detached flow type close to the luff of a spinnaker profile. For example in the thin air plate at shallow incidence, the thin airfoil bubble also nowadays called the leading edge separation bubble, has a reattachment length which is no longer Reynolds dependant for Reynolds number higher than 10^5 as indicated by [Crompton, 2001, Collie, 2006]. Moreover for downwind sails, [Viola and Flay, 2011b] has shown a good agreement for the pressure distribution on sails even in the trailing edge area, reflecting the attached or detached flow type close to the leech, between full-scale and wind tunnel tests.

Several flow velocities have been tested setting up the fans frequency to different levels and are given in Tab. 4.8. The corresponding value of flow speed are provided as an indication for a given fans frequency using the linear relation provided in Fig. 2.11. The measurement of the averaged flow speed velocity being actually different for every run *-i.e.* every plotted point on the figures of this section- these indications are used to classify the runs which were done with the same fans frequency.

f_{fans} (Hz)	17.5	20	22.5	25	27.5	30
U_{Pitot} (m s ⁻¹)	2.49	2.86	3.24	3.61	3.99	4.36
Re (10^5)	2.85	3.28	3.71	4.13	4.56	4.99

Table 4.8 – Flow velocity for the different fans frequencies for the 2016 experimental campaign. Value computed with the linear relation provided in Fig. 2.11. Re computation based on the representative length \sqrt{S} .

Results are presented the same way as in Fig. 4.1. For the four spinnakers, the influence of the

cut can be seen between the left graphs (triradial panelling) and right graphs (cross-cut panelling). The influence of the material can be seen between the top graphs (AirX 500) and the bottom graphs (SuperKote 0.75). In this section, drive, side and sheet load coefficients results are presented with their averaged and standard deviation value evolution. Standard deviation of the load sensor is not presented here as it is strongly affected by recording noise. The folding hysteresis is not investigated in this section, as it has previously be shown it always presents lower performance than full or curling shape.

Three different AWA have been tested and are presented in this section.

4.3.1 $\beta_{AW} = 80^\circ$

For $\beta_{AW} = 80^\circ$ the sheet length where curling appears is presented for the different spinnakers and flow velocities in Tab. 4.9. The trends of the apparition of curling sheet length compared to the wind flow velocity are different for the spinnakers. For the cross-cut spinnaker 2016, the faster the flow, the later the curling apparition. This trends is opposite to the trend of the triradial spinnaker 2015 made of the same material. No clear trend can be seen for the two other spinnakers.

Spinnaker	Spi Tri 2015 AirX 500	Spi CC 2016 AirX 500	Spi CC 2015 SuperKote 0.75	Spi Tri 2016 SuperKote 0.75
	$L_{sheet\ C}$ (mm)	$L_{sheet\ C}$ (mm)	$L_{sheet\ C}$ (mm)	$L_{sheet\ C}$ (mm)
$U_{Pitot} \approx 2.49\text{ m s}^{-1}$			1055	
$U_{Pitot} \approx 2.86\text{ m s}^{-1}$	1030	1030	1045	1040
$U_{Pitot} \approx 3.24\text{ m s}^{-1}$			1035	
$U_{Pitot} \approx 3.61\text{ m s}^{-1}$	1025	1035	1045	1035
$U_{Pitot} \approx 3.99\text{ m s}^{-1}$			1045	
$U_{Pitot} \approx 4.36\text{ m s}^{-1}$	1015	1040	1045	1040

Table 4.9 – Trim length when curling appears for $\beta_{AW} = 80^\circ$. The sheet length is indicated from the spinnaker clew point to the model ring. For these values the curling occurs during the entire duration of the associated run (and not only one or two curling sequence per run). Empty cells indicate that the associated configuration is not tested.

Results for the drive force coefficient C_{F_x} are presented in Fig. 4.25. The effect of curling apparition mainly depends of the cut. For a triradial spinnaker, the maximum drive force is located before curling. For a cross cut spinnaker, the drive force presents two local maxima including one located at the apparition of curling. For the AirX 500 cross-cut spinnaker, this maximum is the global maximum contrary to the one in SuperKote 0.75 where the maximum is about 80 mm more trimmed than the curling apparition. Being slightly overtrimmed does not penalize much the drive force coefficient for this AWA. Once curling the drive force coefficient decreases if the sheet length increases. Here sailors should not ease the sheet once curling. The cross-cut design seems to present slightly better performance in the curling area but is more sensitive to wind speed variation. For low wind speed, the cross-cut design generates more drive force coefficient than the triradial cut. The SuperKote 0.75 material seems to delay the apparition of curling regarding the sheet length and also seems to keep better performance in the overtrimmed area than the AirX 500. The SuperKote 0.75 material spinnakers curling appears for a longer sheet length compared to the AirX 500 material.

Results for the side force coefficient C_{F_y} are presented in Fig. 4.26. Curling apparition affects more the cross-cut design. Side force coefficient are quite close for the different type of spinnakers. If the sheet length increases after the curling point, the absolute value of side force coefficient decreases.

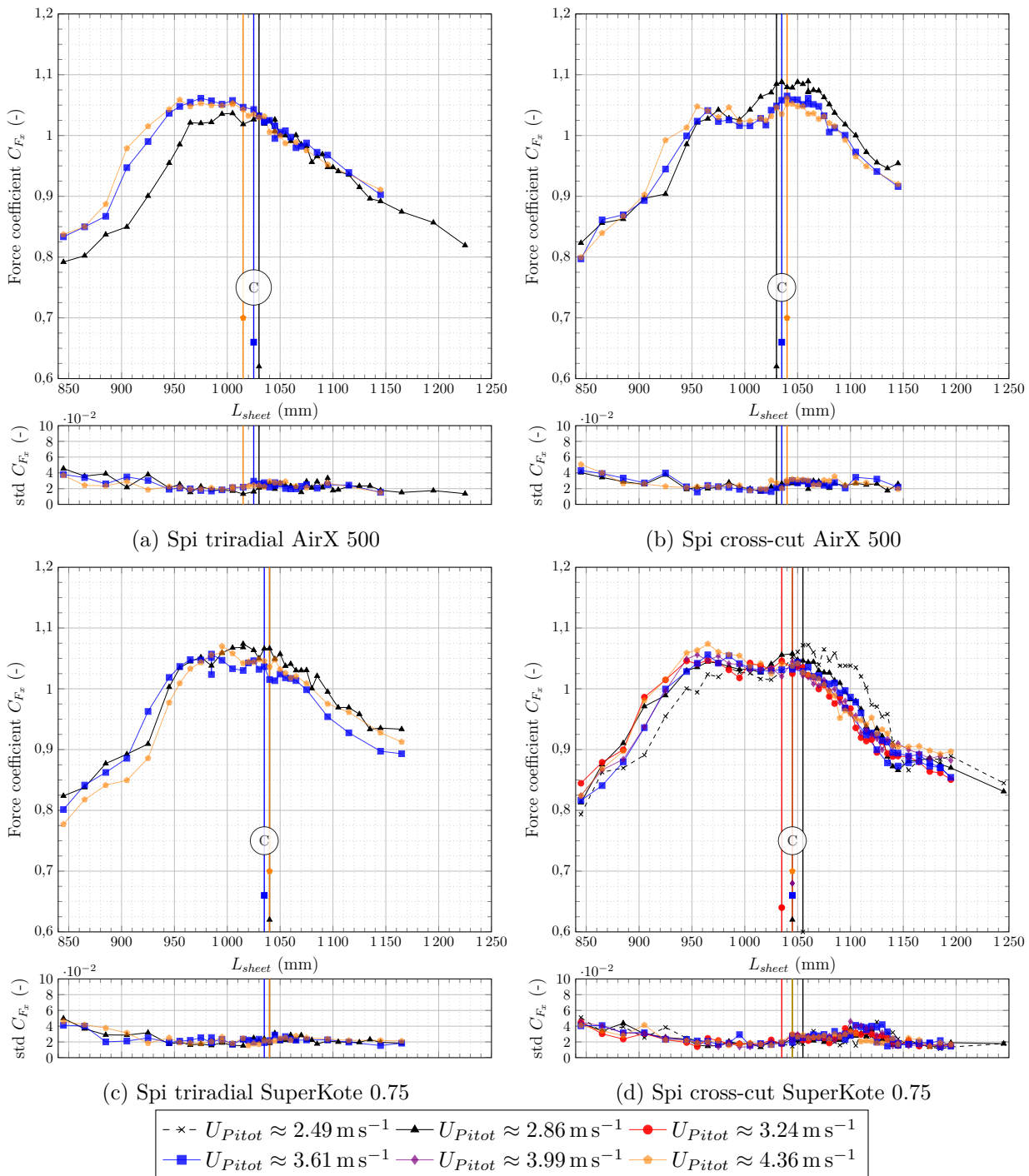


Figure 4.25 – Drive force coefficient C_{F_x} at $\beta_{AW} = 80^\circ$. Vertical lines represent the verge of curling limit. Mean and standard deviation values are presented for each case.

The standard deviation of force balance signals is higher in two areas. The first one corresponds to the area before the maximum drive force occurs. It is linked to oscillation of the sail that can be observed and probably related to flow detachment. The second area corresponds to well established curling situation.

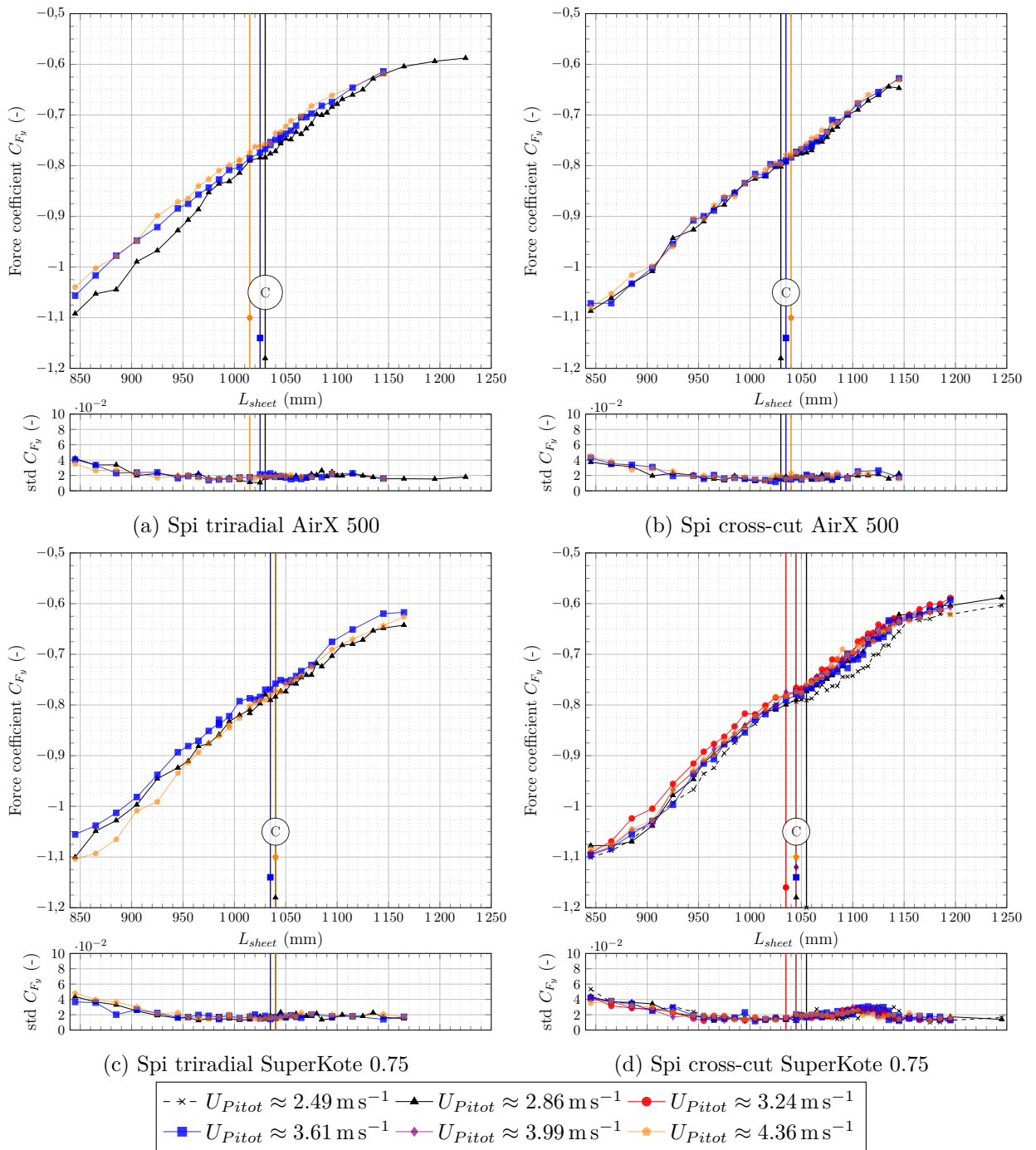


Figure 4.26 – Side force coefficient C_{F_y} at $\beta_{AW} = 80^\circ$. Vertical lines represent the verge of curling limit. Mean and standard deviation values are presented for each case.

Results for the sheet load coefficient $C_{F_{sheet}}$ are presented in Fig. 4.27. The apparition of curling has not an important effect on triradial cut for the sheet load coefficient. For the cross cut, a peak can be observed around the apparition of curling especially at low wind speed. Curling effect seems to be transmitted more easily on a cross-cut design. Triradial design may damp the propagation of the curling load peak in the section direction.

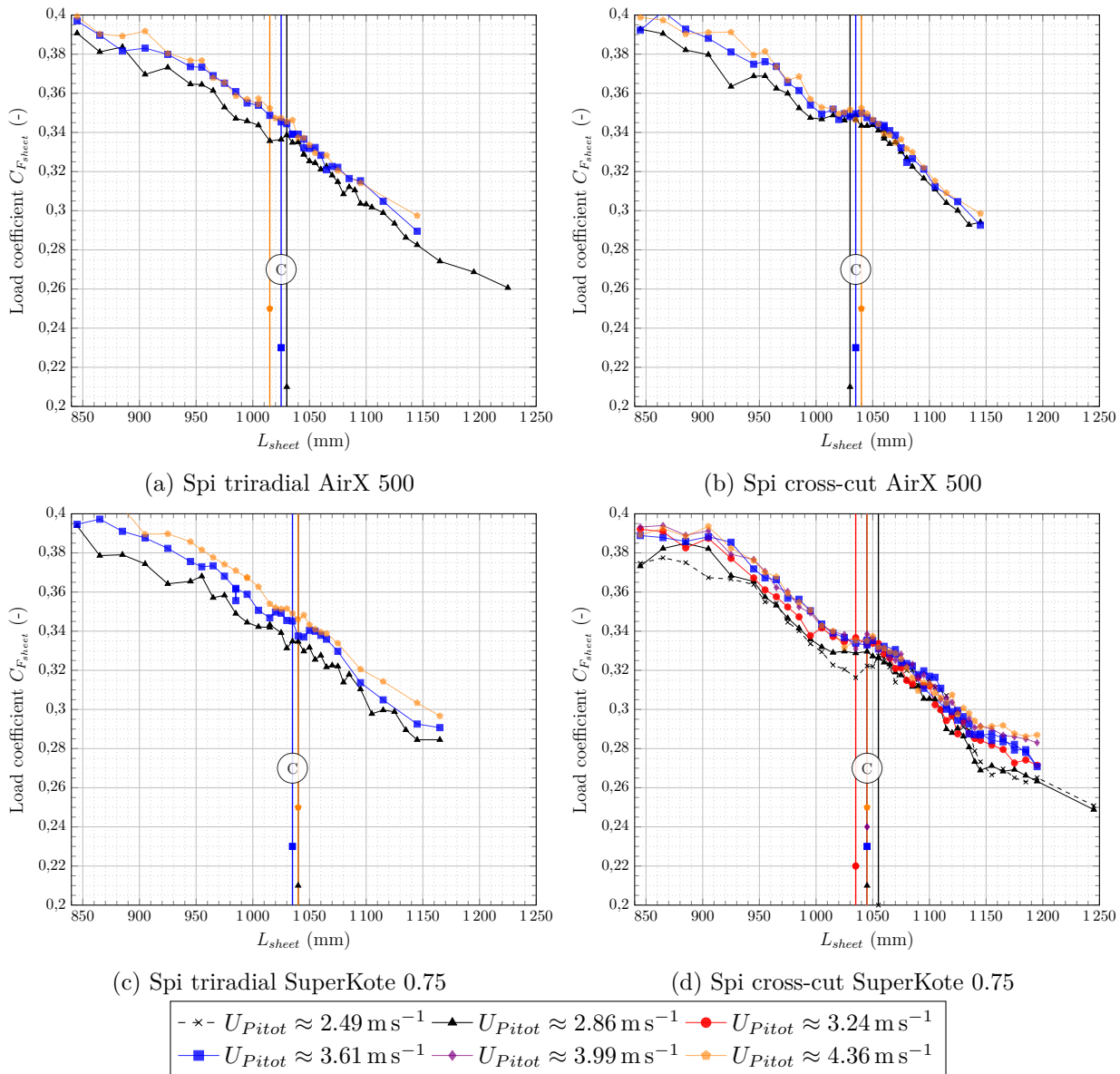


Figure 4.27 – $C_{F_{sheet}}$ at $\beta_{AW} = 80^\circ$. Vertical lines represent the verge of curling limit.

4.3.2 $\beta_{AW} = 100^\circ$

The sheet length where curling appears for $\beta_{AW} = 100^\circ$ are presented for the different spinnakers and flow velocities in Tab. 4.10.

Spinnaker	Spi Tri 2015 AirX 500	Spi CC 2016 AirX 500	Spi CC 2015 SuperKote 0.75	Spi Tri 2016 SuperKote 0.75
	$L_{sheet} C$ (mm)	$L_{sheet} C$ (mm)	$L_{sheet} C$ (mm)	$L_{sheet} C$ (mm)
$U_{Pitot} \approx 2.86 \text{ m s}^{-1}$	1175	1190	1205	1190
$U_{Pitot} \approx 3.24 \text{ m s}^{-1}$	1165	1190	1200	1185
$U_{Pitot} \approx 3.61 \text{ m s}^{-1}$	1165	1185	1195	1180
$U_{Pitot} \approx 4.36 \text{ m s}^{-1}$	1165	1185	1195	1175

Table 4.10 – Trim length when curling appears for $\beta_{AW} = 100^\circ$. The sheet length is indicated from the spinnaker clew point to the model ring. For these values the curling occurs during the entire duration of the associated run (and not only one or two curling sequence per run).

Results of the drive force coefficient C_{F_x} are presented in Fig. 4.28. For all spinnakers, the apparition of curling is related to a significant and sudden increase in the drive force up to 10% of the mean drive force before curling. These observations correspond to the highest improving effect of curling among the measured data.

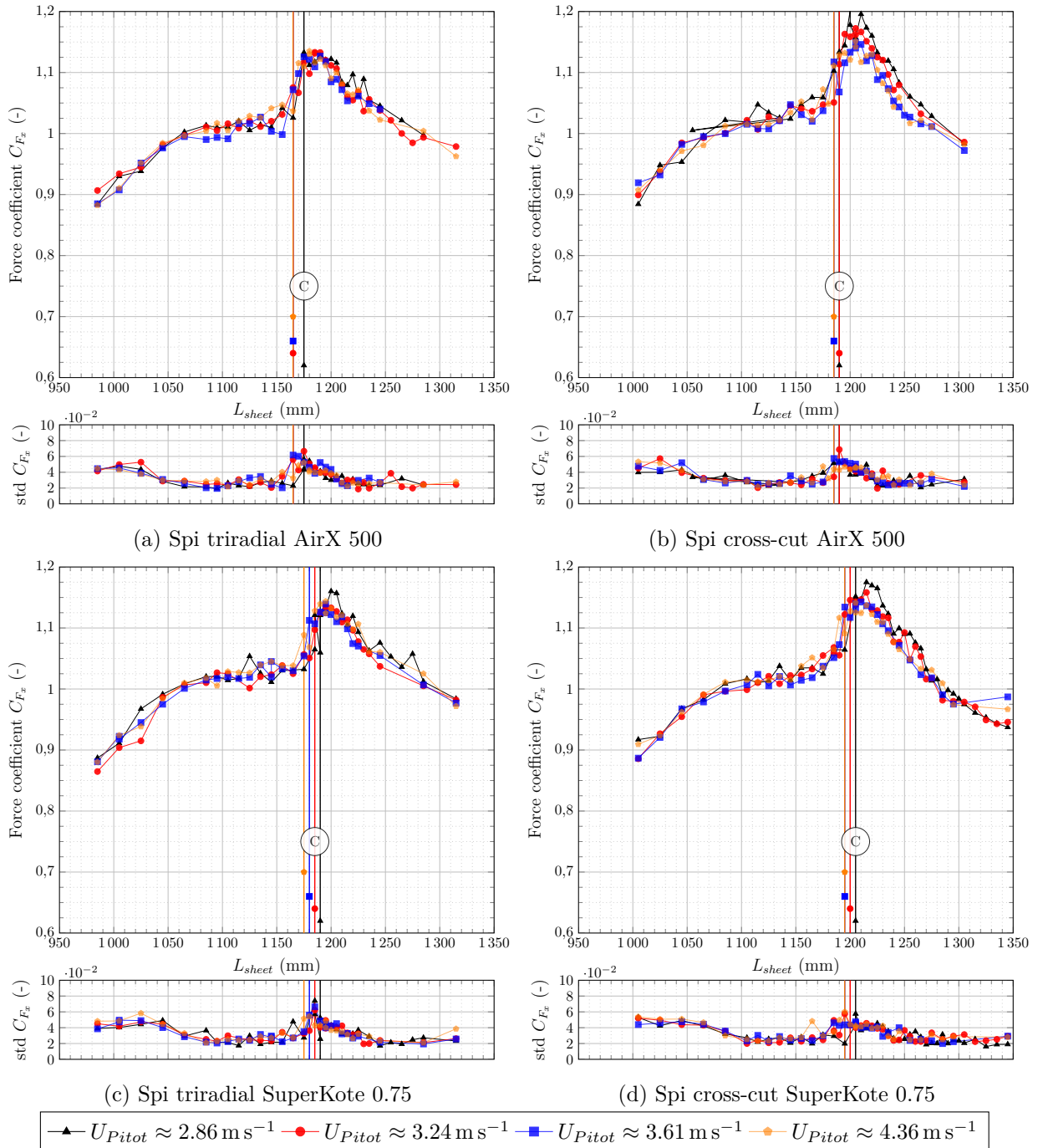


Figure 4.28 – Drive force coefficient C_{F_x} at $\beta_{AW} = 100^\circ$. Vertical lines represent the verge of curling limit. Mean and standard deviation values are presented for each case.

The cross cut design reaches higher mean values of drive force coefficient. Here the curling state gets the highest mean drive force for the four different types of spinnaker. Again the SuperKote 0.75 material spinnakers curling appears for a longer sheet length compared to the AirX 500 material.

For a given material, the triradial design is submitted to curling for a shorter sheet length compared to the cross-cut design.

Results of the side force coefficient C_{F_y} are presented in Fig. 4.29. When curling appears, the standard deviation of side force slightly increases and the mean value is slightly affected with a lower local slope. The trends and values are quite similar between the different spinnaker types. Easing the sheet decreases the absolute value of side force.

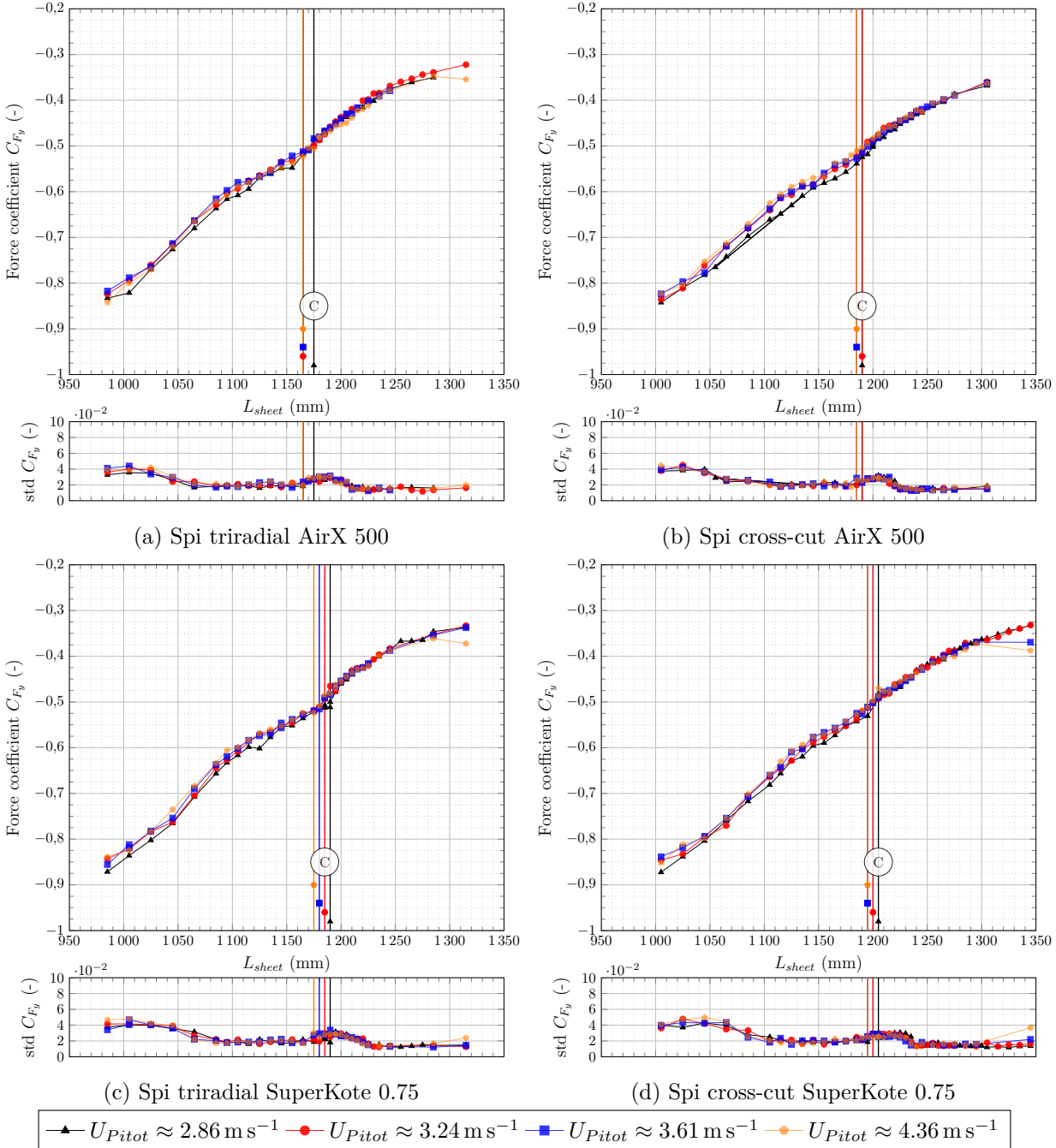


Figure 4.29 – Side force coefficient $\beta_{AW} = 100^\circ$. Vertical lines represent the verge of curling limit. Mean and standard deviation values are presented for each case.

Results for the sheet load coefficient $C_{F_{sheet}}$ are presented in Fig. 4.30. The apparition of curling increases the mean value of sheet load coefficient for the different spinnakers by 3% of its value before curling.

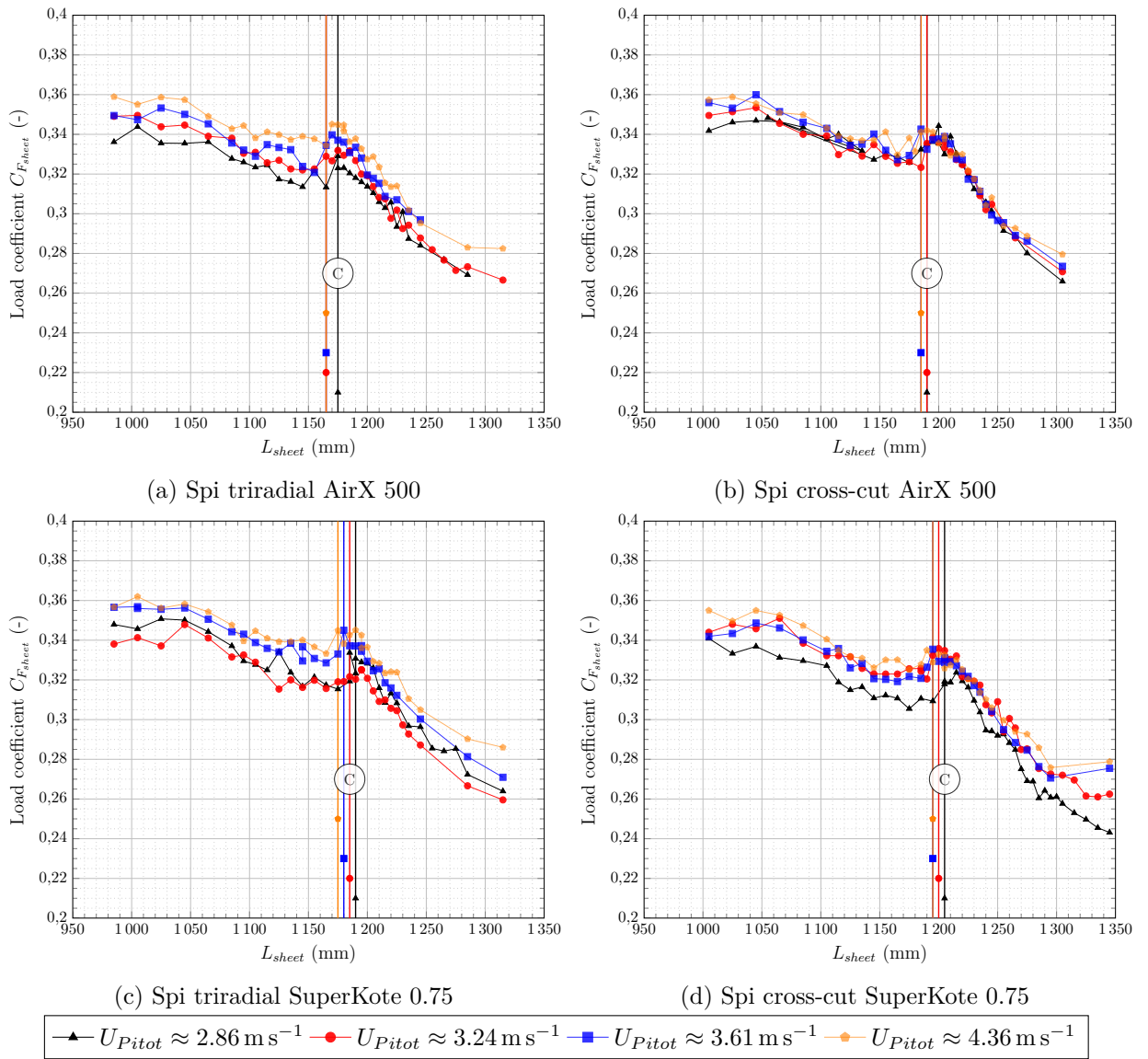


Figure 4.30 – $C_{F_{sheet}}$ at $\beta_{AW} = 100^\circ$. Vertical lines represent the verge of curling limit.

4.3.3 $\beta_{AW} = 120^\circ$

The sheet length where curling appears for $\beta_{AW} = 120^\circ$ is presented for the different spinnakers and flow velocities in Tab. 4.11. For this AWA, the faster the flow, the earlier the curling for all the spinnakers.

Spinnaker	Spi Tri 2015 AirX 500	Spi CC 2016 AirX 500	Spi CC 2015 SuperKote 0.75	Spi Tri 2016 SuperKote 0.75
	$L_{sheet C}$ (mm)	$L_{sheet C}$ (mm)	$L_{sheet C}$ (mm)	$L_{sheet C}$ (mm)
$U_{Pitot} \approx 2.86 \text{ m s}^{-1}$	1315	1325	1335	1335
$U_{Pitot} \approx 3.61 \text{ m s}^{-1}$	1305	1315	1325	1320
$U_{Pitot} \approx 4.36 \text{ m s}^{-1}$	1295	1315	1315	1305

Table 4.11 – Trim length when curling appears for $\beta_{AW} = 120^\circ$. The sheet length is indicated from the spinnaker clew point to the model ring. For these values the curling occurs during the entire duration of the associated run (and not only one or two curling sequence per run).

Results of the drive force coefficient C_{F_x} are presented in Fig. 4.31. The increase of drive force coefficient with the apparition of curling is about 10% of its value before curling. The maximum mean value occurs a bit after the curling apparition. Again for an identical material, the triradial design curling appears for a shorter sheet length than the cross cut design. The AirX 500 material has a curling apparition before the SuperKote 0.75 material. The standard deviation of the drive force becomes three times higher when curling appears. A local peak can be observed in the curling area. This peak is significant for the lowest flow velocity tested for the triradial cut contrary to the cross-cut design where this peak remains a local maximum.

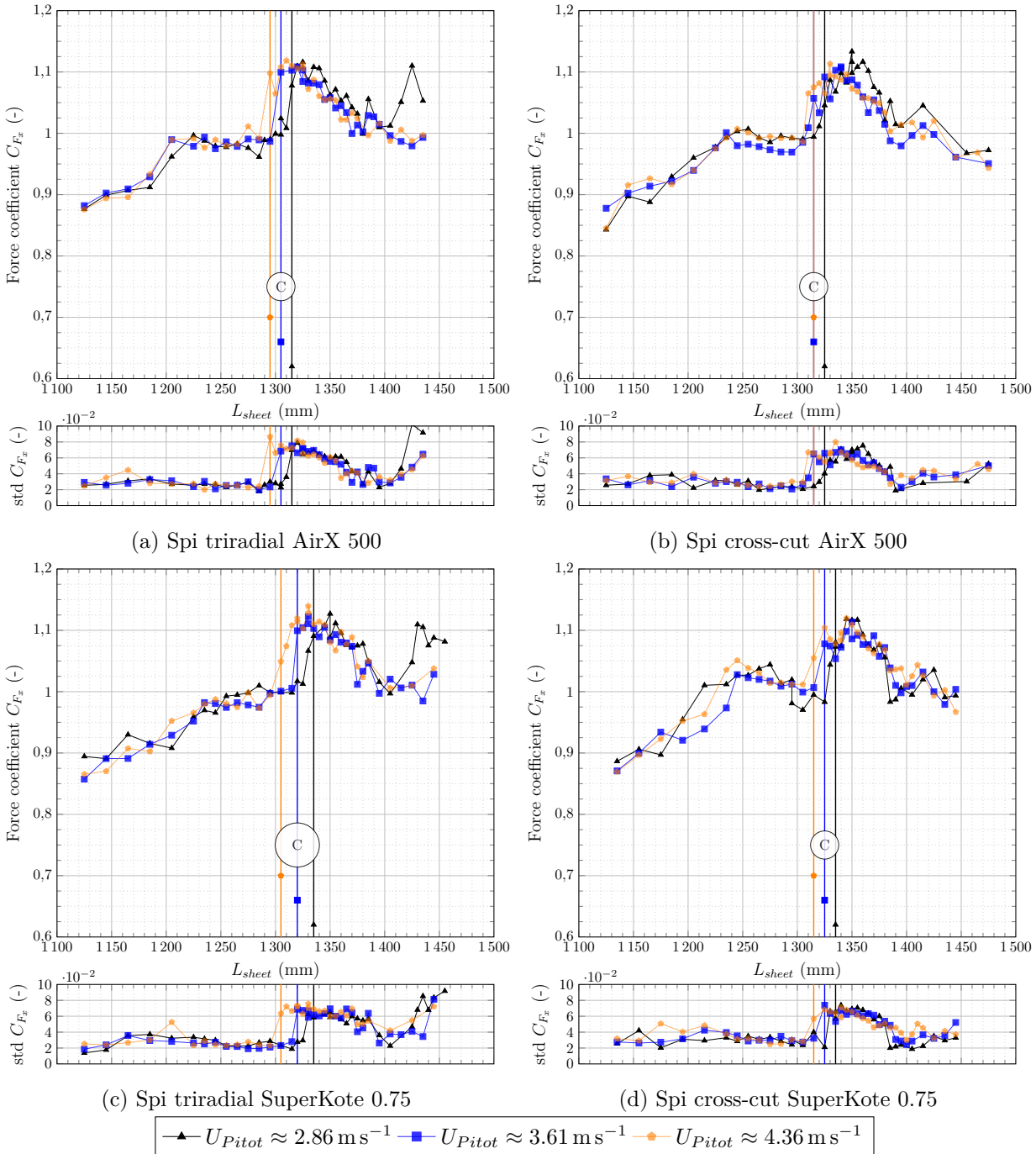


Figure 4.31 – Drive force coefficient C_{F_x} at $\beta_{AW} = 120^\circ$. Vertical lines represent the verge of curling limit. Mean and standard deviation values are presented for each case.

Results of the side force coefficient C_{F_x} are presented in Fig. 4.32. Again the side force presents a slight change in its local slope for the curling apparition. Trends and level of side force are quite similar for the different tested spinnakers.

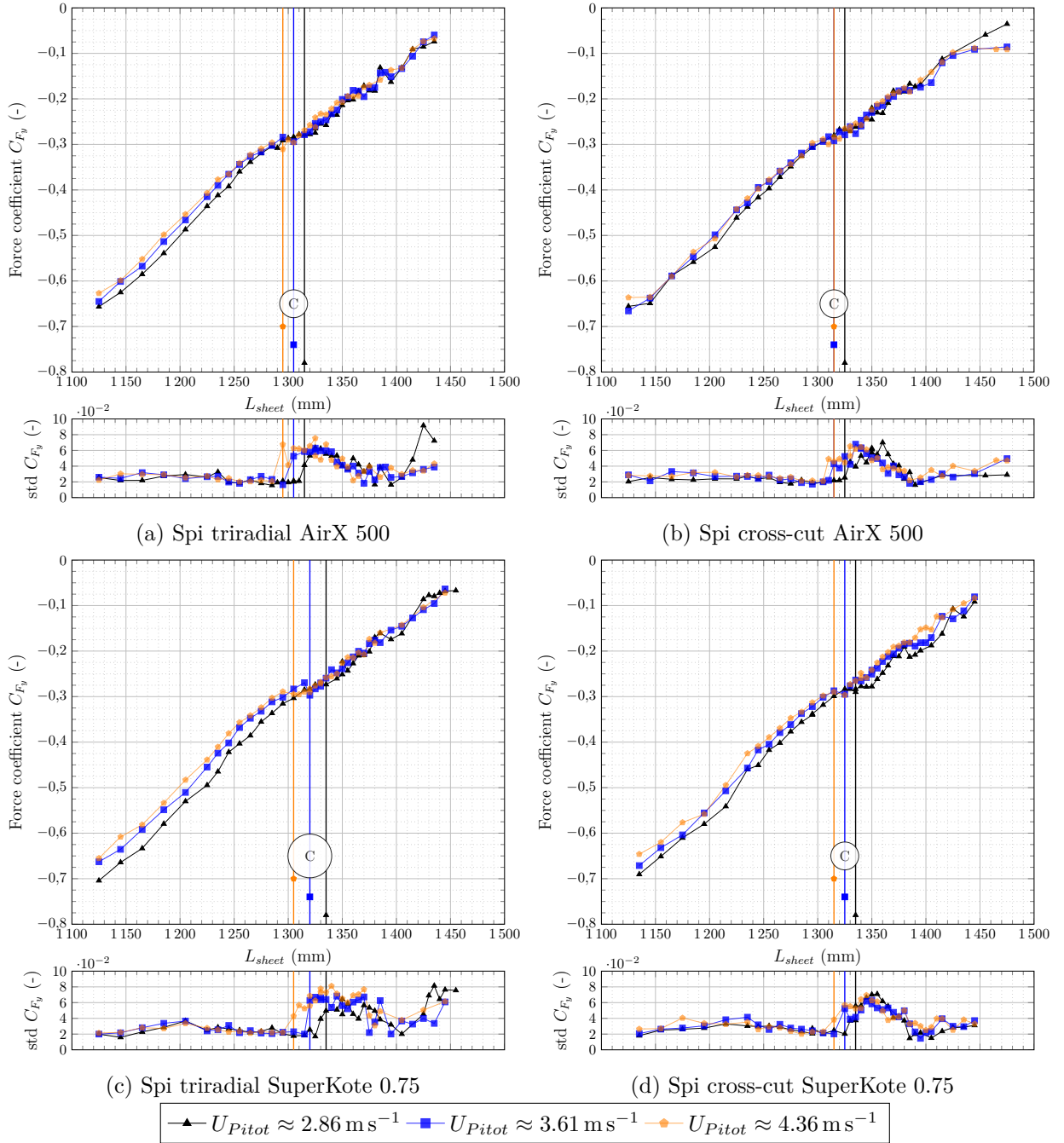


Figure 4.32 – Side force coefficient C_{F_y} at $\beta_{AW} = 120^\circ$. Vertical lines represent the verge of curling limit. Mean and standard deviation values are presented for each case.

Results of the sheet load coefficient $C_{F_{sheet}}$ are presented in Fig. 4.33. The apparition of curling increases the mean sheet load coefficient up to 10% of its value before curling.

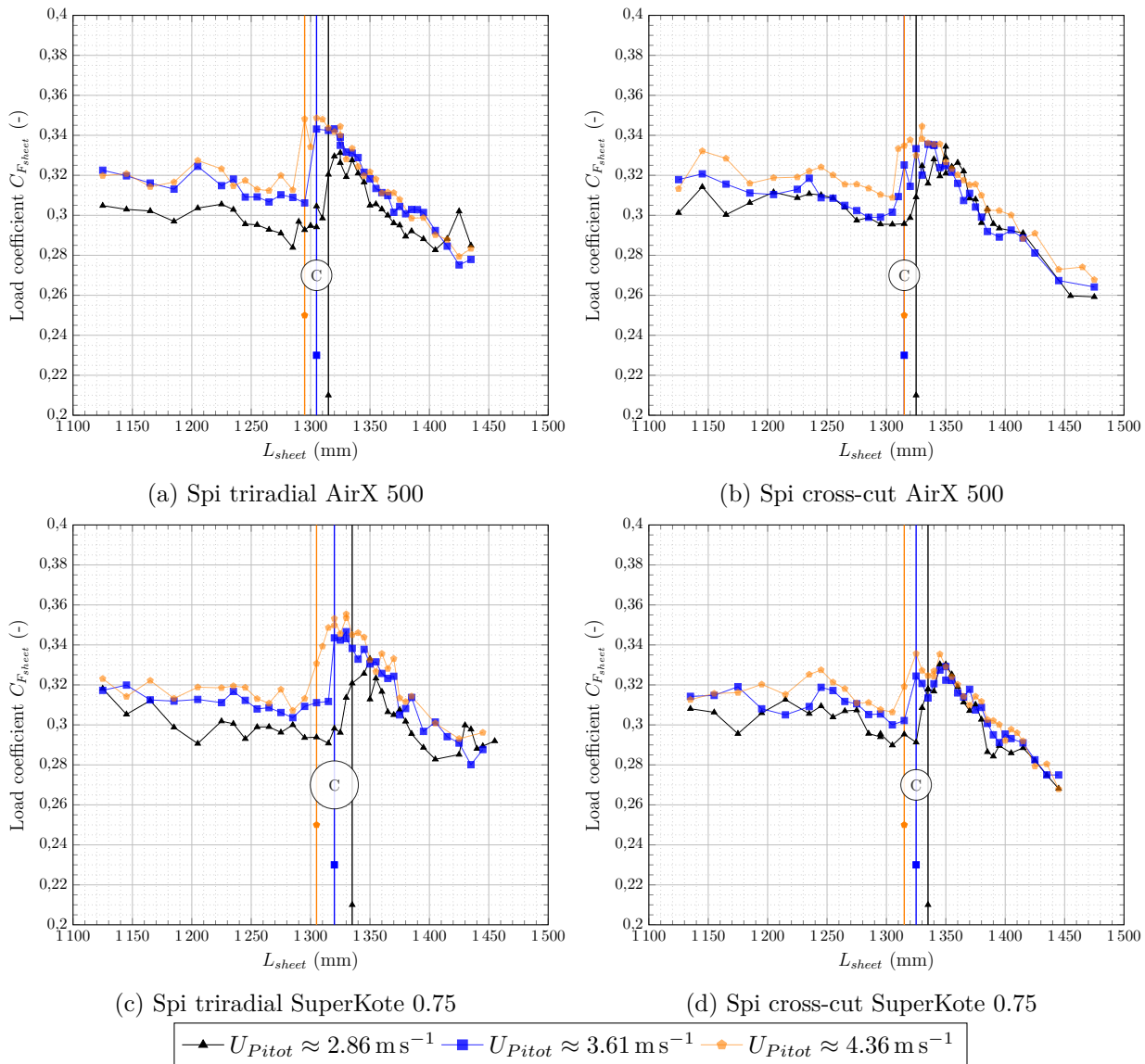
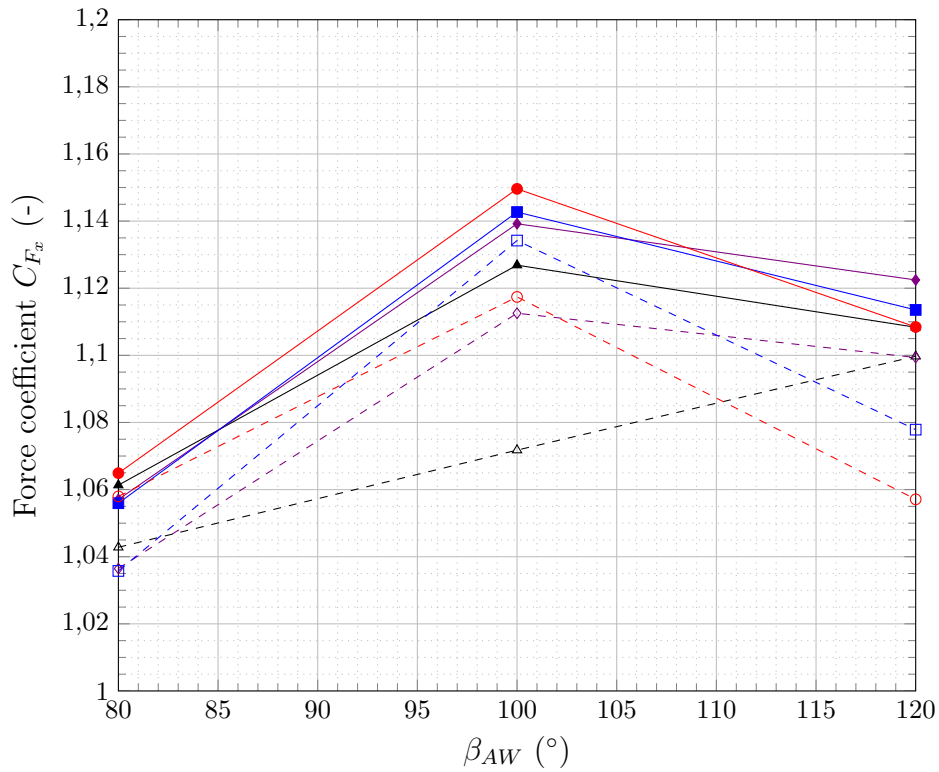


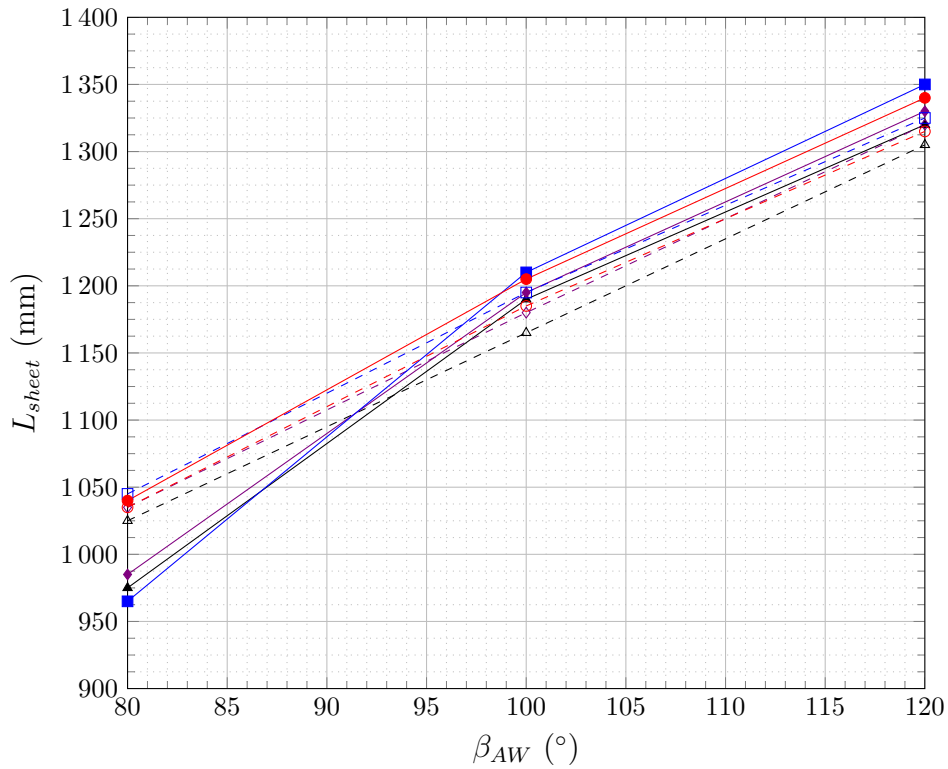
Figure 4.33 – $C_{F_{sheet}}$ at $\beta_{AW} = 120^\circ$. Vertical lines represent the verge of curling limit.

4.3.4 General conclusions about curling apparition

Fig. 4.34a shows the optimum drive force compared to the drive force at the edge of curling for the different AWA tested for a given flow speed ($U_{Pitot} \approx 3.61 \text{ m s}^{-1}$). The AirX 500 cross-cut design has the best performance for $\beta_{AW} = 80^\circ$ and $\beta_{AW} = 100^\circ$ whereas the SuperKote 0.75 triradial design has the best performance for $\beta_{AW} = 120^\circ$. All designs seems to generate more optimum driving force for $\beta_{AW} = 100^\circ$. The curling driving force is less important than the optimum one. As given in Fig. 4.34b the sheet length where optimum occurs is located after the curling apparition for all design at $\beta_{AW} = 100^\circ$ and $\beta_{AW} = 120^\circ$. For $\beta_{AW} = 80^\circ$, the optimum occurs before curling except for the cross-cut AirX 500 spinnaker.



(a) Optimum and curling drive force coefficient evolution with the AWA for $U_{Pitot} \approx 3.61 \text{ m s}^{-1}$ ($f_{fans} = 25 \text{ Hz}$).



(b) Optimum and curling sheet length evolution with the AWA for $U_{Pitot} \approx 3.61 \text{ m s}^{-1}$ ($f_{fans} = 25 \text{ Hz}$).

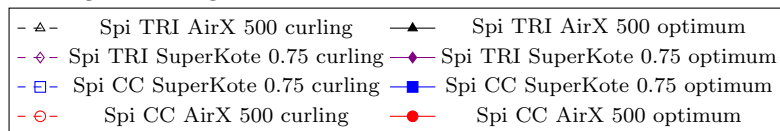


Figure 4.34 – Optimum and curling C_{F_x} and L_{sheet} evolution with the AWA for $U_{Pitot} \approx 3.61 \text{ m s}^{-1}$ ($f_{fans} = 25 \text{ Hz}$).

For the fully rigged mast

For the different AWA tested we can notice that:

1. curling appears on the triradial design for a shorter sheet length compared to the cross-cut design. The seams close to the luff seems to facilitate the initial folding for the triradial spinnaker.
2. curling appears on the AirX 500 material, which is the lighter material tested, for a shorter sheet length compared to the SuperKote 0.75 material. It is however unclear if this difference is due to the stiffness or the mass of the sails, or the combination of these two parameters. The AirX 500 material being lighter would tend to fly higher with a luff possibly in a more windward position triggering curling before the SuperKote 0.75 heavier material. The AirX 500 material being less stiff would also tend to facilitate the fold.
3. above $\beta_{AW} \geq 100^\circ$, the apparition of curling presents a significant increase in the drive force up to 10% of its value before curling. The sheet load coefficient is also affected on the apparition of curling. Side force coefficient is less affected when curling appears.
4. the standard deviation for $\beta_{AW} = 120^\circ$ are higher than the two other tested AWA. This is due to the whole spinnaker motion observed for this deep point of sail.
5. the side force coefficient levels are quite similar for the different types of tested spinnakers. The drive force coefficient levels can present noticeable differences between the different spinnakers. Surprisingly cross-cut type presents similar or slightly better performances than the triradial one. The cross-cut design is not used among the J80 racing spinnakers although it might require less manufacturing operations (less seams than the triradial one) and would potentially be cheaper.

As presented in this section the apparition of curling can have a significant impact on drive force and sheet load. These observations tend to confirm some of the sailor's recommendation or previous section studies results. The differences between the spinnakers remain small compared to the accuracy of the measurement system, however some trends have been indicated. The curling effect seems to be important at the wind tunnel scale. Further studies needs however to extend these results at full-scale highlighting such an important increase in the mean aerodynamic forces. So far, unsteady full-scale testing still remain challenging due to the non controlled environment. Theses studies such as [Deparday, 2016] have indicated that curling affects strongly the dynamic pressure distribution on the spinnaker in a way it would benefit the sail efficiency. However the studies were not able to conclude clearly about the benefit of curling on the boat performance. The curling phenomenon might required to be accurately modelled and validated first at the wind tunnel scale then to be extended at full-scale. Some mechanism part of this model such as added mass effect might then take an identical or less important part into the curling effect at full-scale, changing the conclusion regarding the trim recommendation. Therefore in order to better understand the curling phenomenon first in the wind tunnel and the involved FSI mechanism, the curling frequency information are provided on the next section.

4.4 Curling frequency measurement and evolution

This section presents some results about the measured curling frequency in the wind tunnel configuration. Contrary to full-scale tests, the effect of the AWA and AWS can be investigated separately.

4.4.1 How to measure the curling frequency?

The curling phenomenon is first of all defined by an observation. Measurement of the curling frequency can be done by visual observations post-processing of the recorded photographs timing. This method is quite manual and time consuming but efficient. Another method would use the flying shape post-processing which still remains time consuming but maybe less based on human observation criteria.

The curling apparition affects the mean forces and load coefficient, it is therefore possible to analyse the time series to measure the curling frequency. Methods like the following ones have been applied:

- usual spectral power density decomposition can reveal peaks in the expected curling frequency region. However curling is not exactly periodic then the peak remain difficult to detect.
- use of Empirical Mode Decomposition (EMD) ([Huang et al., 1998, Komaty et al., 2014, Komaty, 2014]) have been investigated however the unpredictable mode numbers and the randomness of order of the mode associated to curling can be applied on a single case but did not give any clear trends over the whole study.

Therefore results presented here are mostly obtained by post-processing the time stamped photographs of the HD cameras used during the 2016 campaign. The recorded frequency is about 20fps, for a resolution of 2046×2046 pixels.

Several temporal parameters of curling can be evaluated:

- the curling period T_c and the curling frequency f_c defined by $f_c = \frac{1}{T_c}$
- the ratio of the folded duration over the total period call $t_{c2} = \frac{T_{c2}}{T_c}$ where T_{c2} is the dimensional duration of the spinnaker curled phase. $t_{c1} = \frac{T_{c1}}{T_c}$ with T_{c1} is the duration where the spinnaker has its full flying shape. In this case $t_{c1} + t_{c2} = 1$ for each curling period. t_{c1} and t_{c2} are dimensionless parameters.
- the duration of the folding (from the start of the fold to the maximum fold) and unfolding steps (from the maximum fold to the end of the fold) can also be investigated to give more indication about the curling dynamics.
- the area of the fold. This can be computed using the flying shape analysis.

Dimensionless curling frequency f_{rc} can be defined as $f_{rc} = \frac{f_c \sqrt{S}}{U_{Pitot}}$ like in [Deparday, 2016] with S the sail area, and U_{Pitot} the reference velocity at the Pitot tube location.

The uncertainty computation of the frequency f_c shown in Eq. 4.1 is based onto the combination of two uncertainties. The first one is associated to the evaluation of the time stamping error which will affect the mean value δT_c . After verification, we assume here that no drift affects the time stamping process. Therefore the time stamping error is considered as random and the frame time stamped at the date T records an event within the dates $T - \frac{1}{2(fps-1)}$ and $T + \frac{1}{2(fps-1)}$ which generates at the first order an uncertainty ΔT_c about $\frac{1}{(fps-1)}$. The second part of the uncertainty is due to the partial derivative presented in Eq. 4.1 which indicates that the faster the flow, the lower the curling frequency and the higher the uncertainty Δf_c for a constant fps.

$$\Delta f_c = \left| \frac{\partial f_c}{\partial T_c} \right| \Delta T_c = \frac{1}{T_c^2} \Delta T_c \quad (4.1)$$

4.4.2 Curling frequency evolution

Here are presented some results about the dimensional and dimensionless curling frequency. Folded duration ratio t_{c2} is also presented. Measurements are done close to the trimming where the curling appears (only 5 mm to 10 mm eased compared to the spinnakers respective verge of curling limit).

4.4.2.1 Spinnaker type effect

The folded duration ratio is shown in Fig. 4.35 with a value about 0.5 for the two smallest AWA presented here. During one curling cycle the folded duration is quite identical to the duration where the spinnaker has its full shape. However for $\beta_{AW} = 120^\circ$, the folded duration ratio becomes smaller than 0.5 and close to 0.4. The folded stage corresponds to 40% of the curling period.

Fig. 4.36 represents the curling frequency and reduced frequency for the different AWA tested comparing the different spinnaker types. The cross-cut AirX 500 spinnaker has a higher curling frequency compared to the other spinnaker types. Curling behaviour is less erratic for $\beta_{AW} = 120^\circ$ where the trend of the curling frequency for all spinnakers seems to be linear which implies a constant reduced curling frequency close to 0.4, about half of the one observed at full-scale [Deparday, 2016].

The different curling frequency behaviour might indicate that a more relevant dimensionless number could be defined. However it is at a first order reasonable to admit that a full-scale measured reduced frequency could be higher than the wind tunnel one as the non controlled environment tends to add dynamic effects -such as boat pitching or wind gust- and therefore triggers additional curling cycles compared to a more steady wind conditions as achieved in the wind tunnel. The curling frequency results might also be sensitive to the luff tension depending of the halyard and tack line adjustment and might also depends on the relative stiffness, inverse of the Cauchy number as defined in Tab. 5.

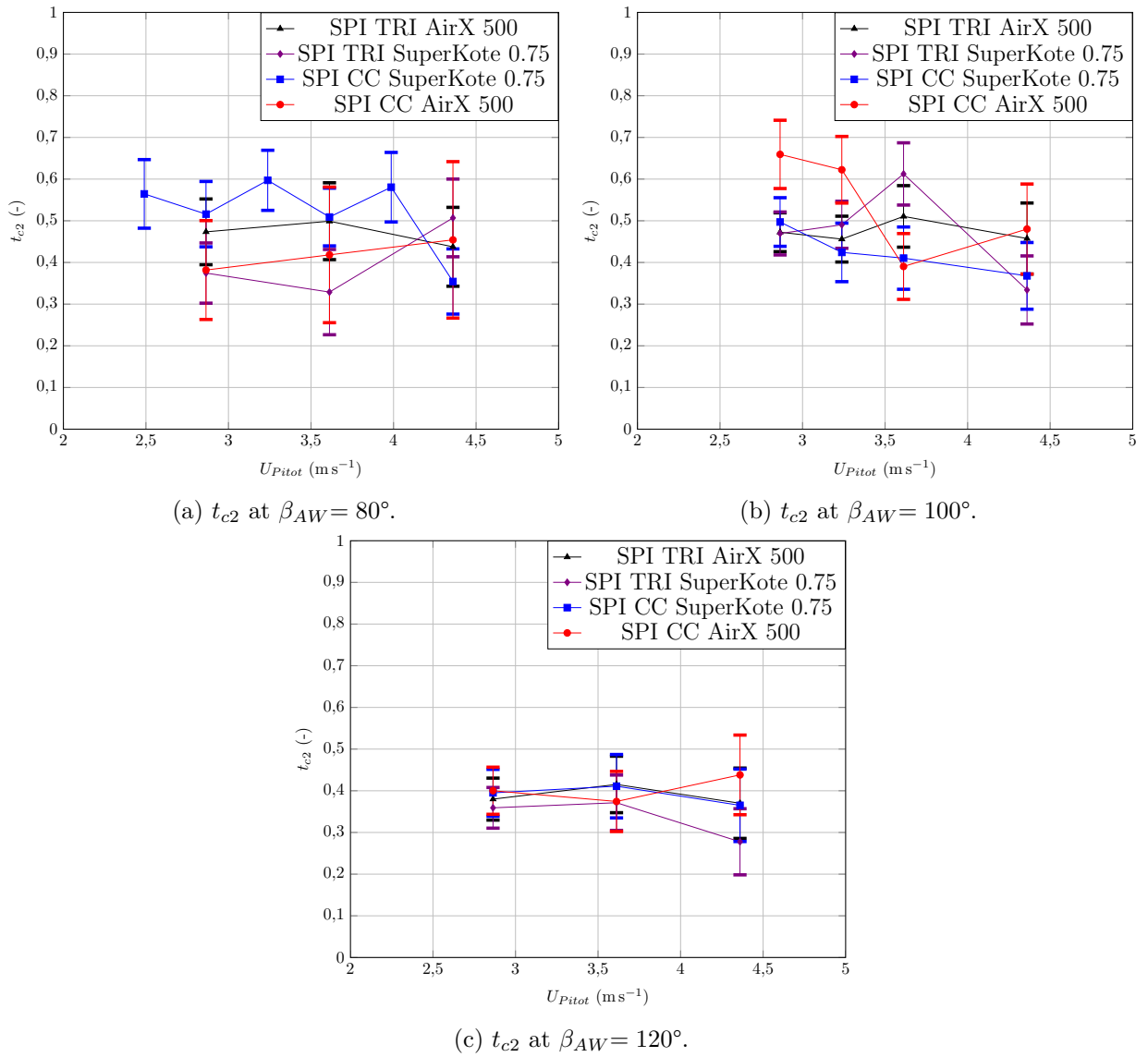
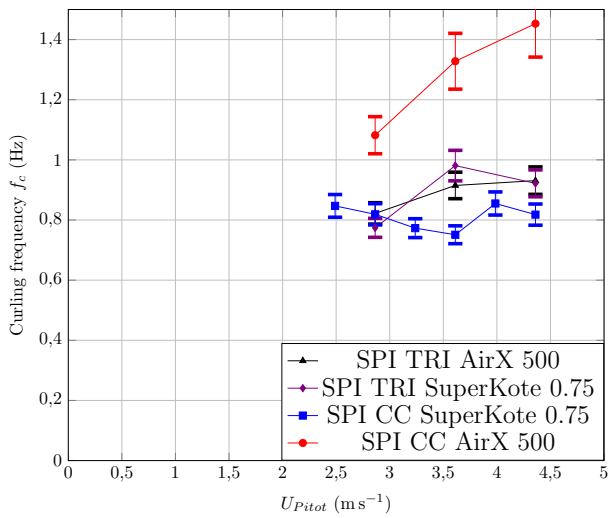
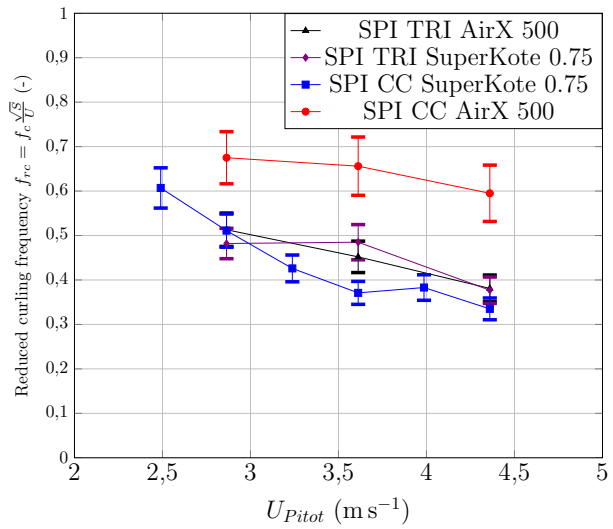


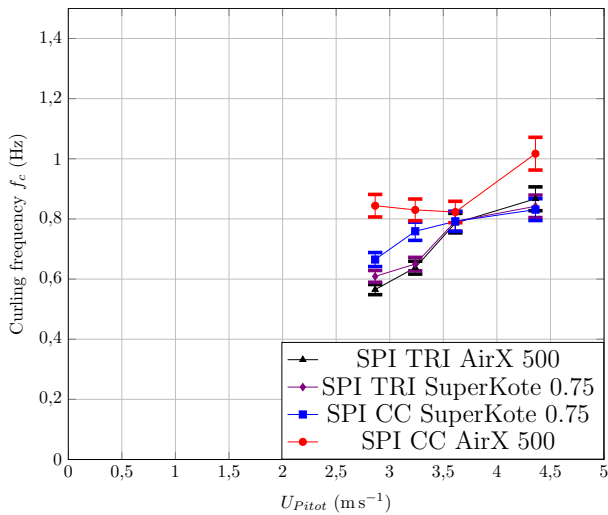
Figure 4.35 – Time folded fraction for different AWA. Error bars represent the uncertainty due to video post-processing.



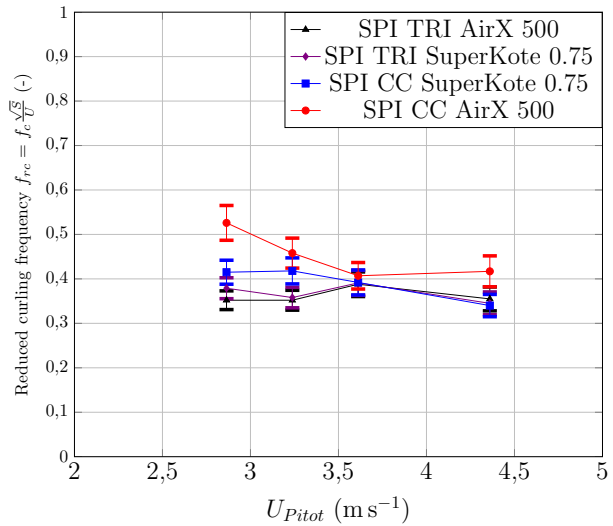
(a) f_c at $\beta_{AW} = 80^\circ$.



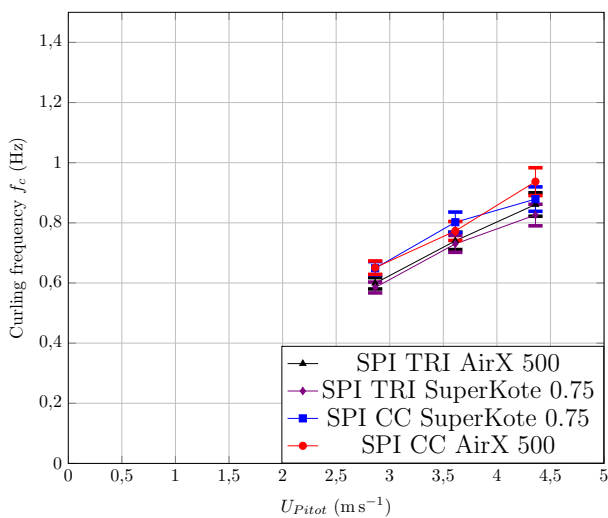
(b) f_{rc} at $\beta_{AW} = 80^\circ$.



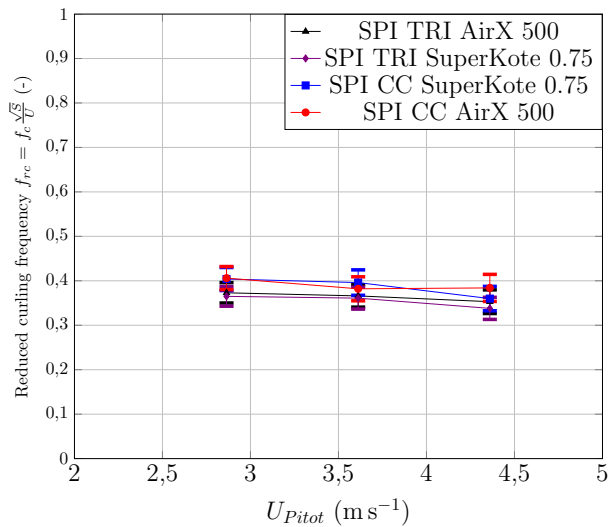
(c) f_c at $\beta_{AW} = 100^\circ$.



(d) f_{rc} at $\beta_{AW} = 100^\circ$.



(e) f_c at $\beta_{AW} = 120^\circ$.



(f) f_{rc} at $\beta_{AW} = 120^\circ$.

Figure 4.36 – Curling frequency and reduced frequency for the different AWA tested. Error bars represent the uncertainty due to video post-processing for the curling frequency and due to video post-processing, error on sail area and flow velocity measurement for the reduced frequency.

4.4.2.2 AWA effect

Fig. 4.37 represents the different curling frequencies for the different kinds of spinnaker. When the AWA increases, the trend becomes more linear for the largest AWA for the different spinnaker types and the curling frequency decreases. As observed at full-scale, the curling frequency is close to a linear trend regarding the flow velocity.

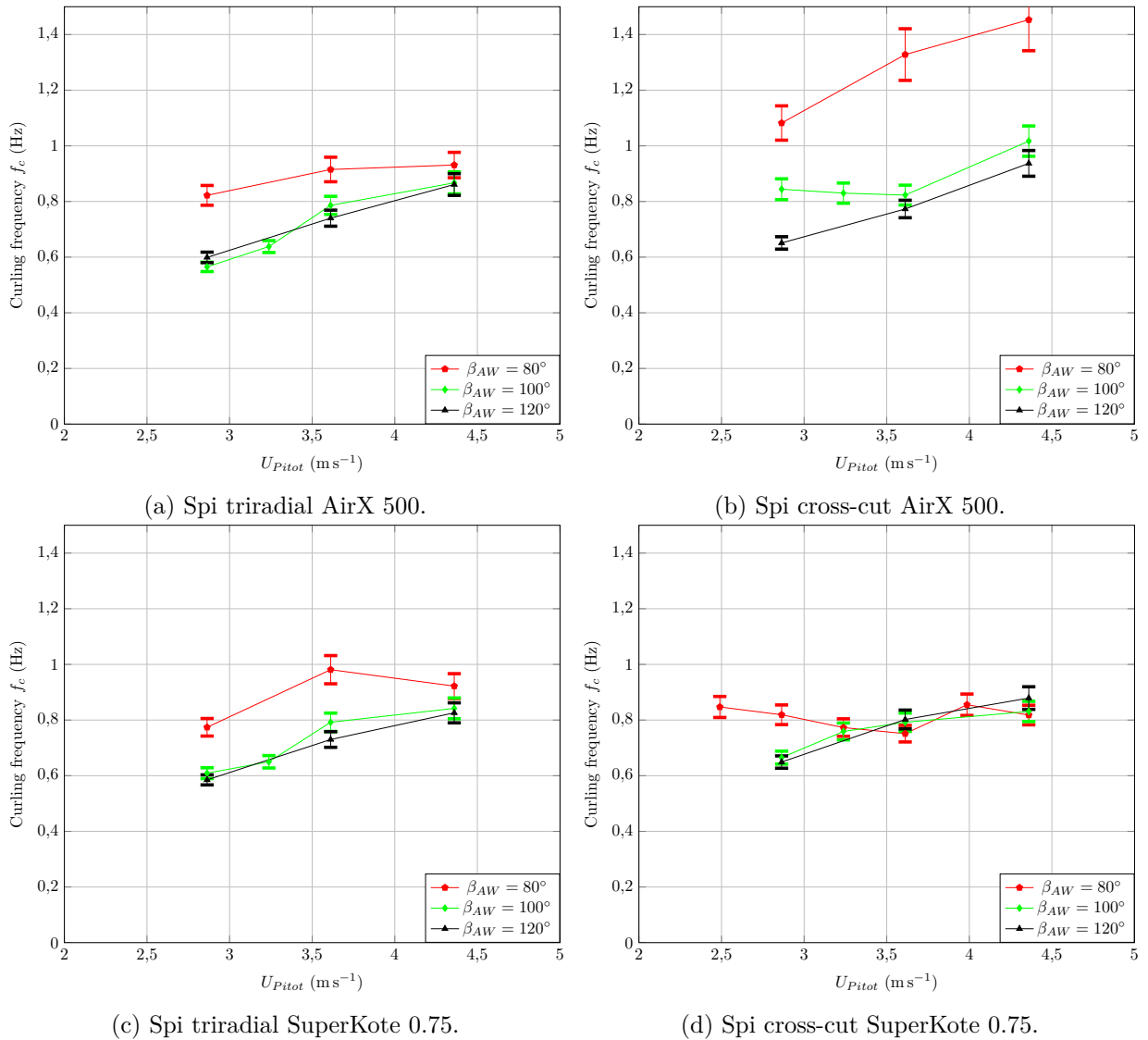


Figure 4.37 – Curling frequency for the different spinnaker with a variation of AWA. Error bars represent the uncertainty due to video post-processing.

Fig. 4.38 represents the different curling reduced frequencies for the different kinds of spinnaker. Linear trend of the curling frequencies implies a constant curling reduced frequency. For $\beta_{AW} = 120^\circ$ the reduced curling frequency is close or slightly lower than 0.4 for most of the flow velocity tested. This clear trend in the curling frequency is related to the whole spinnaker motion. This motion looks similar to vortex induced vibration and the constant reduced frequency may indicate a lock in phenomenon between the oscillation frequency and the vortex shedding in the wake.

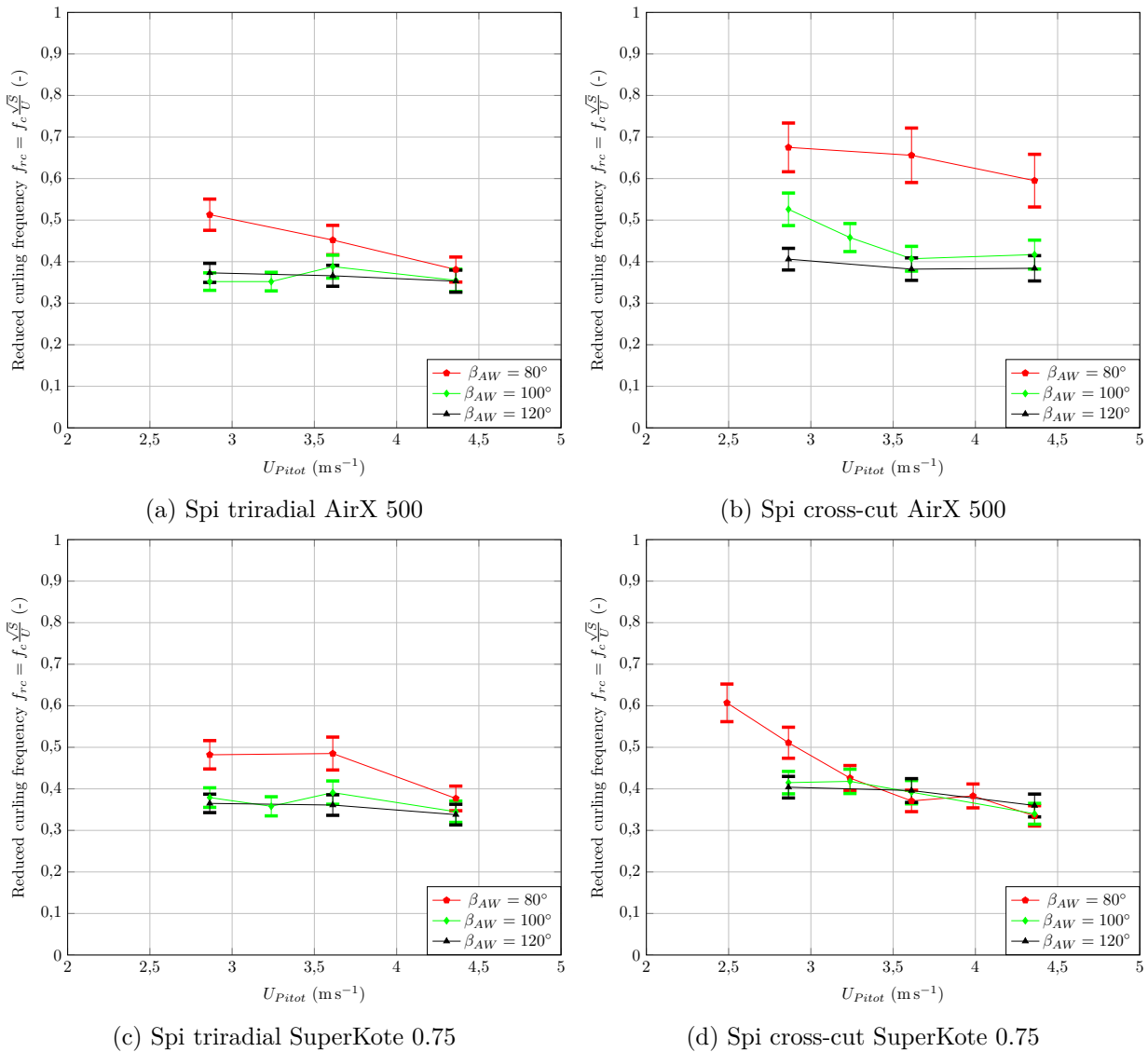


Figure 4.38 – Curling reduced frequency for the different spinnaker with a variation of AWA. Error bars represent the uncertainty due to video post-processing, error on sail area and flow velocity measurement.

4.4.2.3 General trends

Previous results show that the curling frequency is dependent of both the flow velocity and AWA. The curling frequency can be fitted by a linear curve with the flow velocity. The linearity improves when the AWA increases. The regular pattern is related to the whole sail displacement which might be locked in with a vortex shedding pattern associated to curling. This motions look similar to induced vortex vibration on a lock-in regime where the motion frequency is about 0.4 for the deepest AWA tested. Experimental data show that the value of the reduced frequency parameter depends of the cloth and cut properties and probably of the luff tension which has not been tuned as the tack and head attached points were fixed.

4.4.3 Why measuring the curling frequency?

Curling is a complex FSI phenomenon where the flow interacts with the sail and the curling origin is still investigated. Having more information about its natural frequency can be used to validate a model of this interaction. Measuring the natural frequency can give more indications confirming or not the kind of phenomenon involved in the process.

Results of the previous sections indicate that in some situations the maximum drive force is obtained with a curling spinnaker. Therefore to properly predict the performance that can be expected from one downwind sail, numerical tools should be able to model the dynamic behaviour of the spinnaker. The numerical curling frequency can then be compared to the experimental one in order to check if the dynamic behaviour matches the expected one for a given condition. The curling frequency is therefore a validation criterion when modelling curling. This curling frequency data can also be used to adapt the numerical time step to resolve the time scale corresponding the expected unsteady phenomenon.

Moreover a retro processing engineering analysis can use the curling frequency as an indicator of the flow speed seen by the sail and not measured by the wind sensor. If this information seems first less relevant than a proper measurement by a wind sensor of the flow velocity, the spinnaker reaction to the flow is maybe less affected by any upwash effect or less affected by any fast yacht motion. The fact that the sail itself has a significant dimension may smoothen the impact of the yacht motion on its possible curling frequency.

Measured curling frequency in the wind tunnel

The curling frequency has been measured using the camera system. It is affected by the AWA and the spinnaker type (cut and material). For the two deepest AWA tested here (100° and 120°), the reduced frequency in the wind tunnel conditions is about 0.4. Such a frequency match the frequency of the whole spinnaker motion which looks similar to vortex induced vibrations. The trend is less clear for $\beta_{AW}=80^\circ$.

The frequency of curling has been investigated in this section providing data which can be used for different applications (model validation, experimental-numerical validation). Next section discusses the effect of curling on the evolution of instantaneous aero-forces.

4.5 Curling temporal evolution

This section investigates the curling effect on the time series of the drive and side force coefficients. Here is presented the case of the cross-cut spinnaker SuperKote 0.75 (2015) for $\beta_{AW} = 120^\circ$ with $U_{Pitot} \approx 3.61 \text{ m s}^{-1}$ ($f_{f_{ans}} = 25 \text{ Hz}$) for which two characteristics have been previously established:

- the apparition of curling has a significant impact on the averaged value of forces (about 10% more drive force coefficient when curling)
- the curling frequency follows a clearer linear trend regarding the flow velocity compared to the other AWA tested

These two elements are suitable to make easier the observation of the effect of curling on the force time series. Fig. 4.39 shows time series of the fluctuations $C_{F_x}(t) - C_{F_x}$ for a not curling case ($L_{sheet} = 1295 \text{ mm}$) and a curling case ($L_{sheet} = 1345 \text{ mm}$) close to the maximum drive force location indicated in Fig. 4.31d. The curling situation presents a pattern with peaks higher and lower than the non curling case. Same trends can be observed for the side force coefficients. The mean value and standard deviation of the two cases are given in Tab. 4.12 showing an increase of 8.5% in the drive force for the curling case compared to the non curling case. The increase reaches even 10% for $L_{sheet} = 1350 \text{ mm}$ but no video recording has been performed for this run.

	Non curling	Curling
L_{sheet}	1295 mm	1345 mm
C_{F_x}	1.01	1.09
sC_{F_x}	2.9×10^{-2}	6.2×10^{-2}

Table 4.12 – Curling vs non curling case, comparison of mean value and standard deviation for the cross-cut spinnaker SuperKote 0.75 (2015) at $\beta_{AW} = 120^\circ$ with $U_{Pitot} \approx 3.61 \text{ m s}^{-1}$ ($f_{f_{ans}} = 25 \text{ Hz}$).

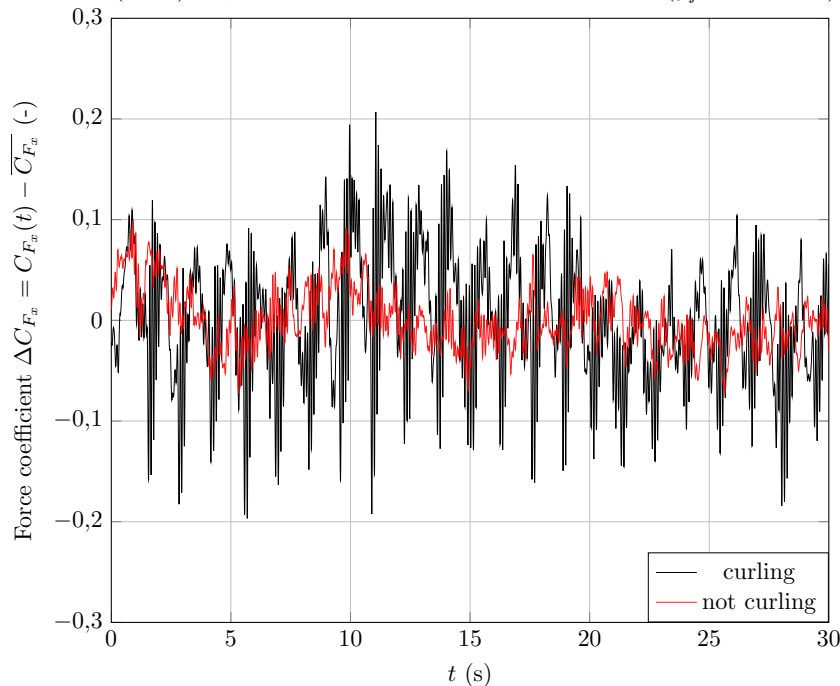


Figure 4.39 – Drive force coefficient fluctuations in a curling and a not curling cases. Cross-cut SuperKote 0.75 spinnaker at $\beta_{AW} = 120^\circ$ with $U_{Pitot} \approx 3.61 \text{ m s}^{-1}$ ($f_{f_{ans}} = 25 \text{ Hz}$) on a fully rigged mast.

Fig. 4.40 presents the forces time series for the curling case representing a 30 s test on the cross-cut SuperKote 0.75 spinnaker with a sheet length $L_{sheet} = 1345$ mm at $\beta_{AW} = 120^\circ$ with $U_{Pitot} \approx 3.61$ m s⁻¹ ($f_{fans} = 25$ Hz) on a fully rigged mast. Fig. 4.42 focuses the analysis on representative curling cycles between $t = 8$ s and $t = 12$ s on the run presented in Fig. 4.40 (not filtered). Fig. 4.43 presents the same focus but with filtered data with a Savitzky-Golay filter [Schafer, 2011] of order 2 with a span of 201 samples. Images associated to the different steps corresponding to the second cycle of curling (A, B, C, D) are presented in Fig. 4.44.

Fig. 4.41 represents the drive force versus the side force coefficients evolution along one curling cycle. The loop presented here is related to a direction indication about the resulting aero forces. As previously seen on the time series, some high frequency components exist in the raw signals and can correspond to a vibration mode of the balance or to natural fast oscillation of the sail which also presents high frequency motion (foot vibration). Filtering post processing enables a more refined analysis of forces variations and is applied further as suggested by [Egan et al., 2016]. The filtering used here is a Savitzky-Golay filter [Schafer, 2011] of order 2 with a span of 201 samples which cancels oscillations faster than the curling phenomena. Fig. 4.41 show the situation where both drive and side force coefficients are filtered. The filtering step has not a significant effect on the mean values computed on the previous sections and is only required in case of study of the temporal evolution of signals ([Dhomé, 2016]).

The curling cycle goes through the following steps:

- step A , luff fold appears on spinnaker shoulder, at this point the drive force is close to its maximum value
- step B , the fold area increases till reaching its maximum at C , the drive force slightly decreases and the side force nearly reaches its minimum absolute value
- from C to D , the fold area decreases as the drive force coefficient. The side force coefficient absolute value increases.
- from D to A , the spinnaker is no longer curled and the drive force increases again till the next fold starts

These different steps can be compared to the ones previously established by [Deparday, 2016] at full-scale. Significant differences can be noticed. In the wind tunnel configuration from A to D the drive force decreases, D corresponding to the location of its minimal value contrary to the full-scale experiments where D corresponds to the maximum drive force value. These differences rise interrogations about the mechanism of transmission of effort through the sail system and especially about a possible delay or phase shift in the transmission of effort in the membrane. In the two cases, full-scale and wind tunnel experiments, effort have been focused on the video and data synchronisation. Simple study cases were used to check and validate these synchronisations.

If force transmission is not instantaneous through the sail system, a measured force can correspond to an event observed previously on the sail. If such a delay exist, it is difficult to guess which situation would more be affected by this transmission delay. For the full-scale test, load and luff tension are important probably increasing the transmission speed of effort but dimensions

remain important. For the wind tunnel test dimensions are smaller, the sampling frequency of the measured force is higher, but load and effort are smaller. Moreover the relative stiffness of the material is more important than the full-scale one. In the two cases the cloth material is about the same but the cut is different. The cut difference between cross-cut and triradial design can also explain such a differences.

Therefore the study of one single curling cycle might give more indication about this phenomenon. Eased and trimmed tests were performed and recorded as part of forced dynamic curling study but still require further analysis.

An extension of this work using the video post-processing could study the evolution of the instantaneous force coefficients computed with the instantaneous flying shape area without the folded part *i.e.* $C_{F_i}(t) = \frac{F_i(t)}{q_{Pitot}S(t)}$ with $S(t)$ the flying shape area without the folded part close to the luff. The results would indicates if $C_{F_i}(t)$ and $S(t)$ are in phase. However during the unfolded phase from D to A the sail area remains constant and we observe the extrema values on these two steps with a maximum drive force in A when curling begins and a minimum drive force in D when the spinnaker recovers its full flying shape in the wind tunnel. This indicates clearly that the curling is not simply due to a change in the efficient *-i.e.* unfolded- sail area and involves complex FSI phenomena. Such a consideration would not make the loop C_{F_x} vs C_{F_y} shown in Fig. 4.41 to collapse.

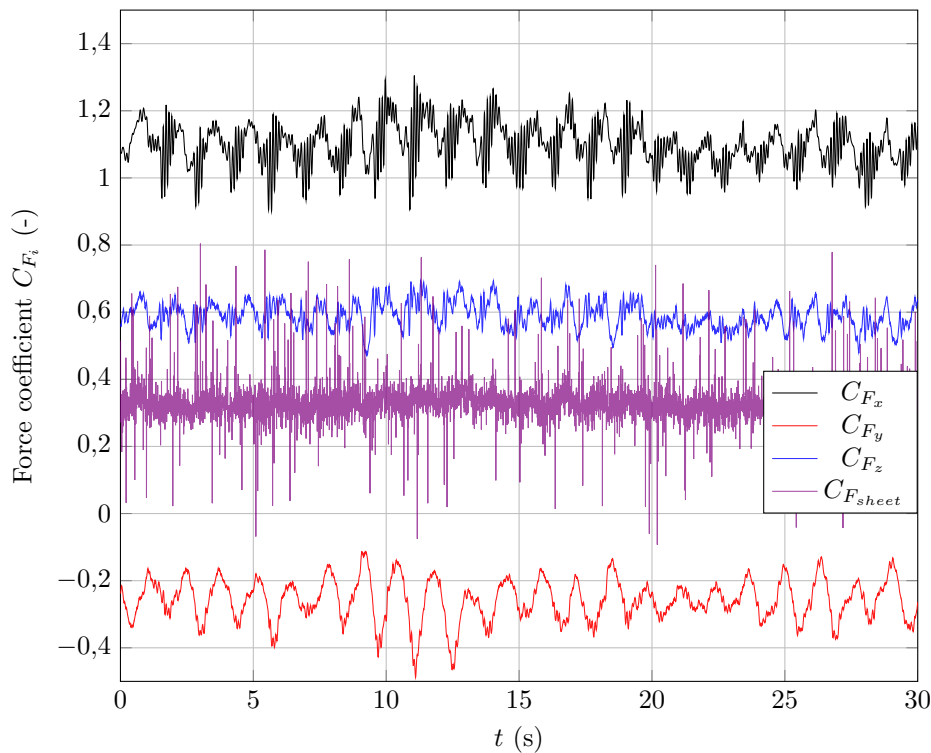


Figure 4.40 – Time series of force coefficients during a curling situation. Cross-cut SuperKote 0.75 spinnaker with a sheet length $L_{sheet} = 1345$ mm at $\beta_{AW} = 120^\circ$ with $U_{Pitot} \approx 3.61$ m s $^{-1}$ ($f_{fans} = 25$ Hz) on a fully rigged mast.

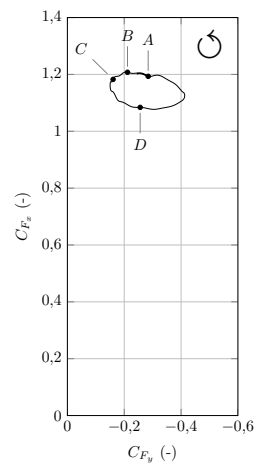


Figure 4.41 – Drive vs side force coefficient evolution during one curling cycle. Situations *A* (folding start), *B*, *C* (maximum folded area) and *D* (full flying shape recovering) correspond to photographs in Fig. 4.44. The origin location has been kept here in order to observe the change in the 2D direction of the total aero-forces. x axis has been reversed to respect the wind tunnel frame convention ($x > 0$ pointing to starboard side and $x < 0$ pointing to portside).

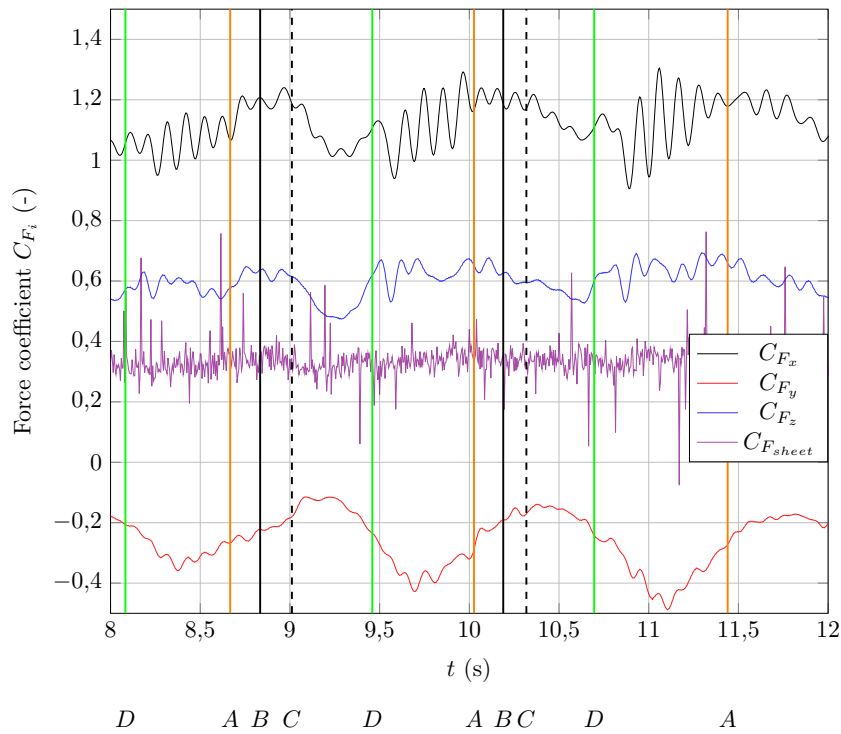


Figure 4.42 – Not filtered time series of force coefficients focused on two curling cycles. Cross-cut SuperKote 0.75 spinnaker with a sheet length $L_{sheet} = 1345$ mm at $\beta_{AW} = 120^\circ$ with $U_{Pitot} \approx 3.61$ m s^{-1} ($f_{fans} = 25$ Hz) on a fully rigged mast. Situations A (folding start), B, C (maximum folded area) and D (full flying shape recovering) are represented with vertical lines and correspond to photographs in Fig. 4.44.

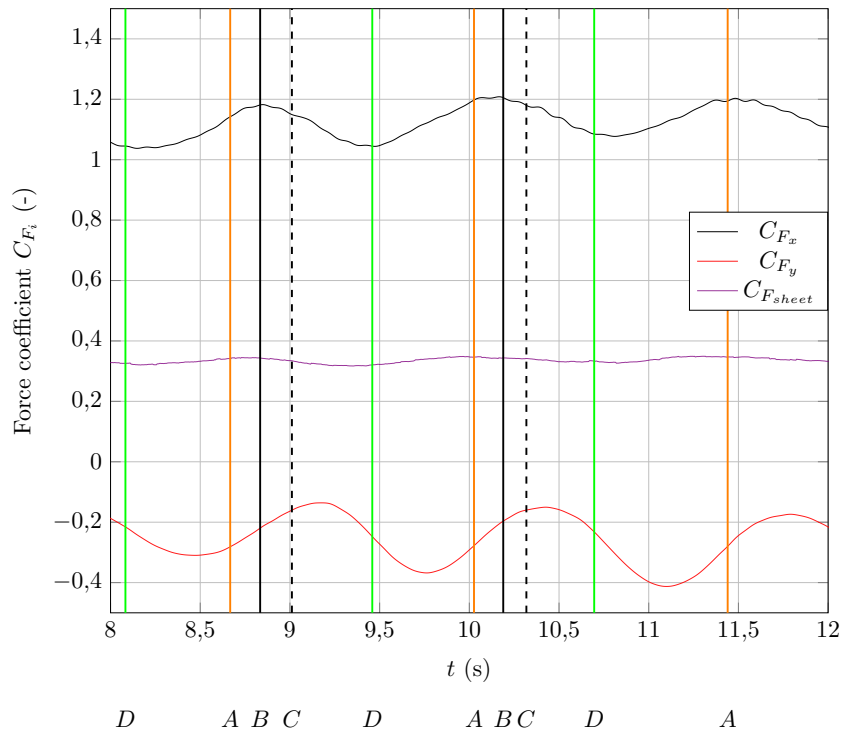


Figure 4.43 – Filtered time series of force coefficients focused on two curling cycles. Cross-cut SuperKote 0.75 spinnaker with a sheet length $L_{sheet} = 1345$ mm at $\beta_{AW} = 120^\circ$ with $U_{Pitot} \approx 3.61$ m s^{-1} ($f_{fans} = 25$ Hz) on a fully rigged mast. Situations A (folding start), B, C (maximum folded area) and D (full flying shape recovering) are represented with vertical lines and correspond to photographs in Fig. 4.44.

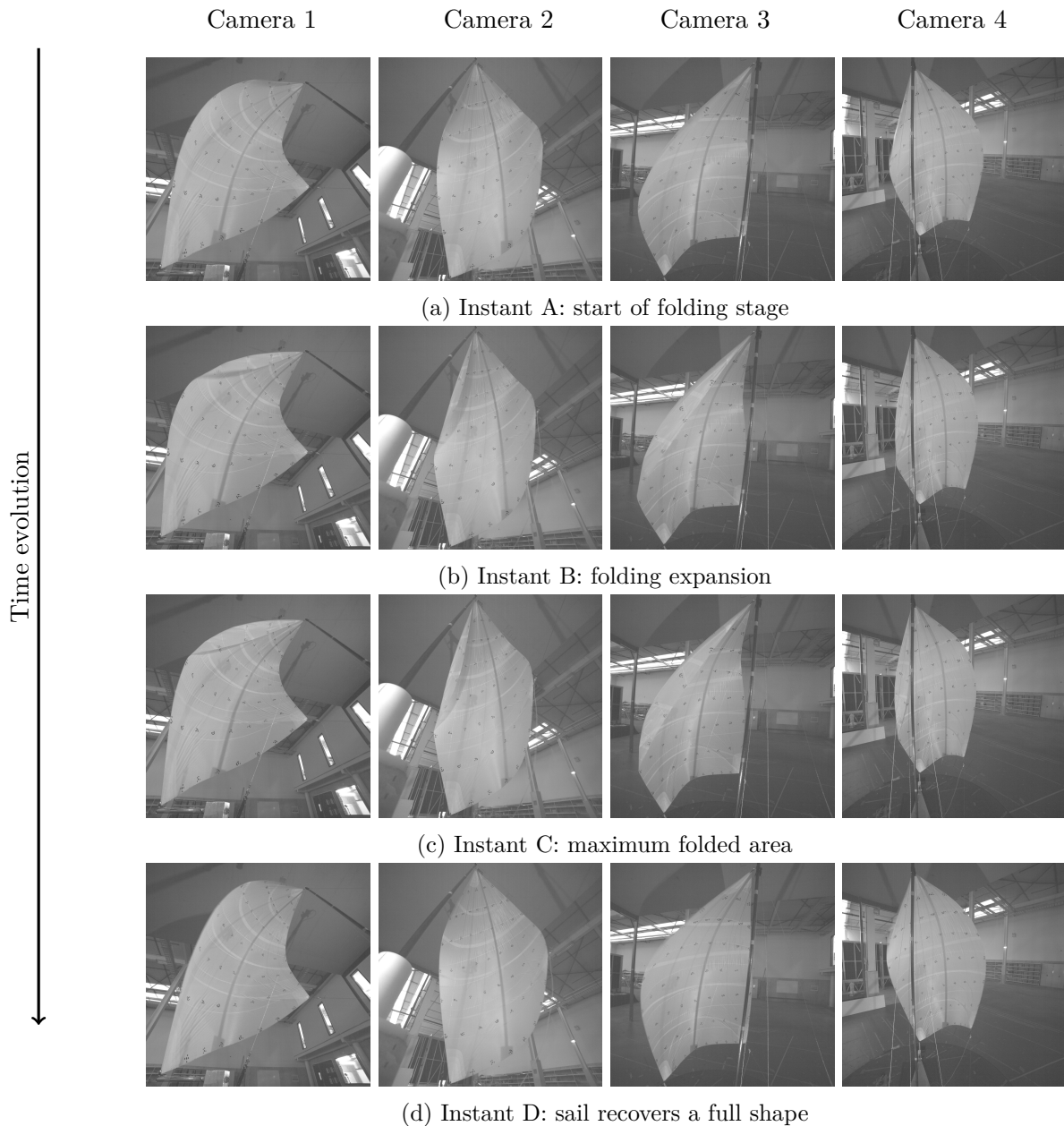


Figure 4.44 – Curling sequence in the wind tunnel recorded during 2016 experimental campaign with the cross-cut SuperKote 0.75 spinnaker with a sheet length $L_{sheet} = 1345$ mm at $\beta_{AW} = 120^\circ$ with $U_{Pitot} \approx 3.61$ m s⁻¹ ($f_{fans} = 25$ Hz) on a fully rigged mast. Instant identification A , B , C , D correspond to [Deparday, 2016] convention. Fish eye effect has not been removed.

The effect of natural curling on time series has been investigated in this section. Time series are affected by the curling phenomenon reaching more pronounced extrema than a non curling case. Video and data synchronisation is used to study the chronology of curling comparing the flying shape steps and the associated instantaneous aero forces. Differences in the step location are observed compared to the full-scale study in [Deparday, 2016]. Complementary analysis could give more indication on the origins of these differences. Smoke visualization tests have also been carried out trying to capture any possible flow pattern shed during curling without any convincing results.

4.6 Discussions, conclusions and perspectives

This chapter dedicated to curling study has presented several results:

1. This chapter presented the effect of curling for various situations providing wind tunnel experimental data. Results show that from a general consideration, the “verge of curling” recommendation is close to the trim associated to the maximum drive force location. This recommendation is therefore relevant for unsteady sailing conditions. For more steady conditions, the recommendation can be refined depending on the angle and the type of spinnaker used as the maximum drive force being slightly located before or after the verge of curling limit.
2. Differences were experimentally measured between the four types of spinnaker and the cross-cut design shows similar performances compared to the triradial cut design. Curling appears later for the cross-cut design for a given material and later for the SuperKote 0.75 material for a given panelling. For the two deepest apparent wind angles tested, the verge of curling limit presents a significant increase up to 10% in the drive force coefficient related to this phenomenon.
3. Measurements about the curling frequency are provided. Curling frequency follows a linear trend as a function of the flow velocity for $\beta_{AW} = 120^\circ$. This means that the reduced curling frequency is constant and close to 0.4 for this AWA.
4. Curling effect on time series has been shown on one representative case. Chronology of the different events occurring during one cycle is presented but does not match the one observed at full-scale. These differences might be explained by the load propagating time along the luff. The investigation of a single curling might provide clearer information in order to be sure that the aero forces measured are not related to the previous curling cycle.

The effect of wind must be investigated further. In the wind tunnel configuration the tested twisted flow situation make the curling appears for a shorter sheet length compared to straight flow which can be expected as the local AWA on the luff sail region is lower. It also tends to generate curling on different luff altitude and may affect the results for deeper AWA where twist is more important.

Experimental data gathered in this chapter can be also used for model validation or numerical-experimental comparison. An absolute nodal coordinate approach as presented in [Dmitrochenko, 2008] might be appropriate to model the large displacement of the sail structure in the curling case. Some improvements can be done to investigate further the curling phenomenon. Model heel angle might be adjusted to a realistic value and twisted flow used to get a more realistic configuration. The mainsail effect might play a role too in the general flow direction and therefore in the curling apparition.

A large investigation field would be to study more precisely pumping on downwind sails. The trimming system can be used to generate one curling cycle (with the ease and trim test achieved

at high speed). The dynamic trimming system can also be used to investigate repeated curling generated by an oscillating sheet length. Preliminary results did not show major improvement in the mean drive force coefficient when using the dynamic trim for the tested trimming frequency. Curling having a natural frequency, it would have been reasonable to test trimming frequencies close to its natural curling frequency -for configuration where curling shows better performance- hoping it would reinforce the natural dynamic effects.

Wind tunnel experimental results presented in this part are a complementary method to understand what can occur on a full-scale sailing boat. Hopefully, the experimental data gathered here could provide a better understanding of curling physical model and would facilitate numerical FSI unsteady simulations on downwind sails.

Conclusions

This PhD work taking part of the VOILENav project and the Sailing fluids collaboration has carried out several studies on FSI phenomena occurring on sails.

Chapter 1 in Part I presents some upwind full-scale results in quasi-static conditions. Several flying shape evolutions are given for different jib traveller and mainsail car position. The comparison with numerical simulation for two backstay adjustments gives a typical example of the inviscid flow limitation. A simple criterion with the boat righting moment is provided to ensure that a free heel numerical model gives coherent results.

Part II presents the different studies carried out in the Twisted Flow Wind Tunnel (TFWT). Chapter 2 introduces the general aspects of the wind tunnel equipments and wind flow measurement in empty configuration.

Chapter 3 presents results on an IMOCA model mainsail in steady configuration. A reference case where the traveller position is set up on the model yacht centreline is first investigated. In the optimum configuration, wind flow mapping is done. An optimisation algorithm is then used to determine the best two-parameter configuration with static trim for different AWA for three different design shapes. From this optimum static situation, pumping is studied using the dynamic trimming device. Several reduced frequencies and amplitudes are tested. Results indicate that an optimum reduced frequency exists around $f_r \approx 0.25$ to $f_r \approx 0.32$. The Lissajou representation with the sheet load coefficient provides the energy required to activate this dynamic trimming and show a peak close to the reduced frequency associated to the maximum optimisation function location. The dynamic evolution of drive and side force coefficients is illustrated over two trimming periods and indicates a change in the behaviour once the optimum reduced frequency is reached. The design shape comparison also indicates that the flat design shape benefits relatively more of the dynamic trimming compared to the other designs, due to its poor initial performance in static conditions.

Chapter 4 presents the downwind static trim for different mast configurations and spinnakers. The free mast configuration shows first a higher mean drive force once the spinnaker is curling than a partially rigged situation. The effect of twisted flow seems to slightly increase the maximum drive force for a shorter sheet length. Several hysteresis phenomena have been identified. If the luff fold is maintained in an over eased case, the performances are lower than the curling case. For the fully rigged configuration, several wind velocities and spinnakers have been studied. For the lowest AWA tested $\beta_{AW} = 80^\circ$ the curling apparition can either be the optimal trim or not, essentially depending on the cut. The triradial design has a maximum occuring before curling. For $\beta_{AW} = 100^\circ$ the maximum mean drive force is obtained just after the curling apparition. For $\beta_{AW} = 120^\circ$ the

maximum also occurs after the curling apparition. The cross-cut design shows close results or better performance than the triradial one in all configurations. The material effect shows that AirX 500 material *i.e.* the lighter makes the curling appears for shorter sheet length. The dynamic aspect of curling is presented with a reduced natural frequency about 0.4 for the different spinnakers at $\beta_{AW} = 120^\circ$.

Perspectives and future work

The work presented here has provided elements to discuss the unsteady aero-elastic behaviour of sails but many configurations can still be improved to get closer to an even more realistic sailing situation.

The upwind experimental campaign has provided both static and dynamic results. The model is set up in upright position. Further investigation can be achieved studying the effect of a static heel on the model. A dynamic heel synchronised with the pumping trimming would even be more relevant to fully represent the sailor actions on Finn boat for example. Moreover the mast is set up unstayed in this study. The effect of the rig on the mast can be another parameter to investigate. The trimming motion can probably be improved, combining a change in the car traveller position and the sheet length, in order to make the sheet length oscillation along the most benefit direction observed during the static optimisation. A change in the command law of the dynamic trimming with a more realistic one can also be suggested because the trimming in phase is usually shorter than the easing phase where sailors only let the sail pushed away by the flow.

The energy analysis has been introduced showing for instance that the optimum reduced frequency is close to the reduced frequency where there is a peak of required power to activate the dynamic trimming. An efficiency ratio can be defined for future investigation however the useful power generated by pumping is still under discussion for the author. Comparison with flapping foil can be done but here in the wind tunnel situation, the useful increase component might be defined as the product of the driving force times the represented boat speed. Flow visualization may also have been a major improvement of the upwind experiment to confirm the suspected reversed von-Karman street configuration at the drive force peak.

The downwind tests have also shown a clear trend in the forces generated by the sail at the curling apparition. It already indicates that with a static trim, the performance of the sail is better for a sheet slightly eased after the curling apparition for β_{AW} higher than 90° . Here the effects of twisted flow and heel angle still require further investigation. The natural curling frequency in wind tunnel measurement also provides more indication to establish or confirm curling model.

The experimental photogrammetry database on spinnaker can also be used to study the cut and material effect on the sail flying shape. Bezier curves formalism applied to downwind sails as shown in [Deparday, 2016] would be relevant to analyse such an amount of flying shape and their dynamic evolution. Dynamic trimming effect on downwind sails has been investigated but not presented here as preliminary results did not show such improvement as observable in upwind configuration.

Once each sail has been tested individually, a model with both sails could be used especially to observe if the mainsail can affect the curling behaviour (the curling natural frequency, the sheet length where it appears, the amount of extra drive force provided once curling).

After providing a better outlook about all these FSI phenomena occurring on sails, the experimental data can also be used for numerical-experimental comparison and numerical validation. Chapter 1 shows some comparisons at full-scale and insist on the benefit of the free heel model. The pitching simulation like in [Augier et al., 2014] but with a free heel model would be again a large improvement in the boat behaviour model.

Numerical-experimental comparison were initially done on full-scale cases, but the unsteadiness was not controlled and therefore justified the use of more controlled experiments to facilitate future steady and unsteady numerical models validation. This thesis wind tunnel results can be used and compared to CFD, without or with FSI, simulation. Some comparisons on the optimisation step have been published in [Sacher et al., 2017]. The wind flow measurements provided here are required to use accurate numerical inflow conditions. Flow computations can be achieved on rigid body which shape corresponds to a measured spinnaker flying shape in order to estimate the pressure distribution in quasi steady state (non curling spinnaker). Then aero-forces can be compared and pressure distribution acting on the rigid body can be applied in the FEM code ARA to compare the experimental measured flying shape to the computed one from ARA.

Numerical simulation of curling in the wind tunnel situation would also provide a reference unsteady case of comparison for the FSI tool ARA-FINETM/Marine. This case might be easier to investigate than the full-scale one where large uncertainty remains on the true wind information. Parallel work carried out by the PhD candidate Hugo Kerhascoët tends to improve the computation of the true wind information at full-scale to achieve the same work on full-scale spinnaker data. Other improvements of the full-scale inboard measuring system would be the development of an in house pressure measurement system combined with the photogrammetry at the same time. The use of synchronized camera lifted by drone to provide wider aerial flying shape point of view photographs may also be an innovative method for the full-scale flying shape recording.

Once the ARA-FINETM/Marine comparison achieved for downwind sails and validation obtained, optimisation process developed by Matthieu Sacher PhD project would be relevant for considering intensive sails FSI optimisation: numerical testing of sail trimming, new materials, design shape, panel assembling and eventually fibres layout orientation.

Appendices

A Yacht vocabulary

Some vocabulary about the yacht components as shown on Fig. A.1 are provided in this appendix. The luff of the sail corresponds to the leading edge (between tack and head points). The leech of the sail corresponds to the trailing edge (between clew and head point). The foot of the sail corresponds to the lower edge of the sail (between tack and clew points). Usually for modern downwind headsail, the spinnaker is a symmetric downwind sail and the gennaker is an asymmetric downwind sail. For the J80 boat which downwind headsail has an important curved full shoulder, the downwind headsail is called a spinnaker.

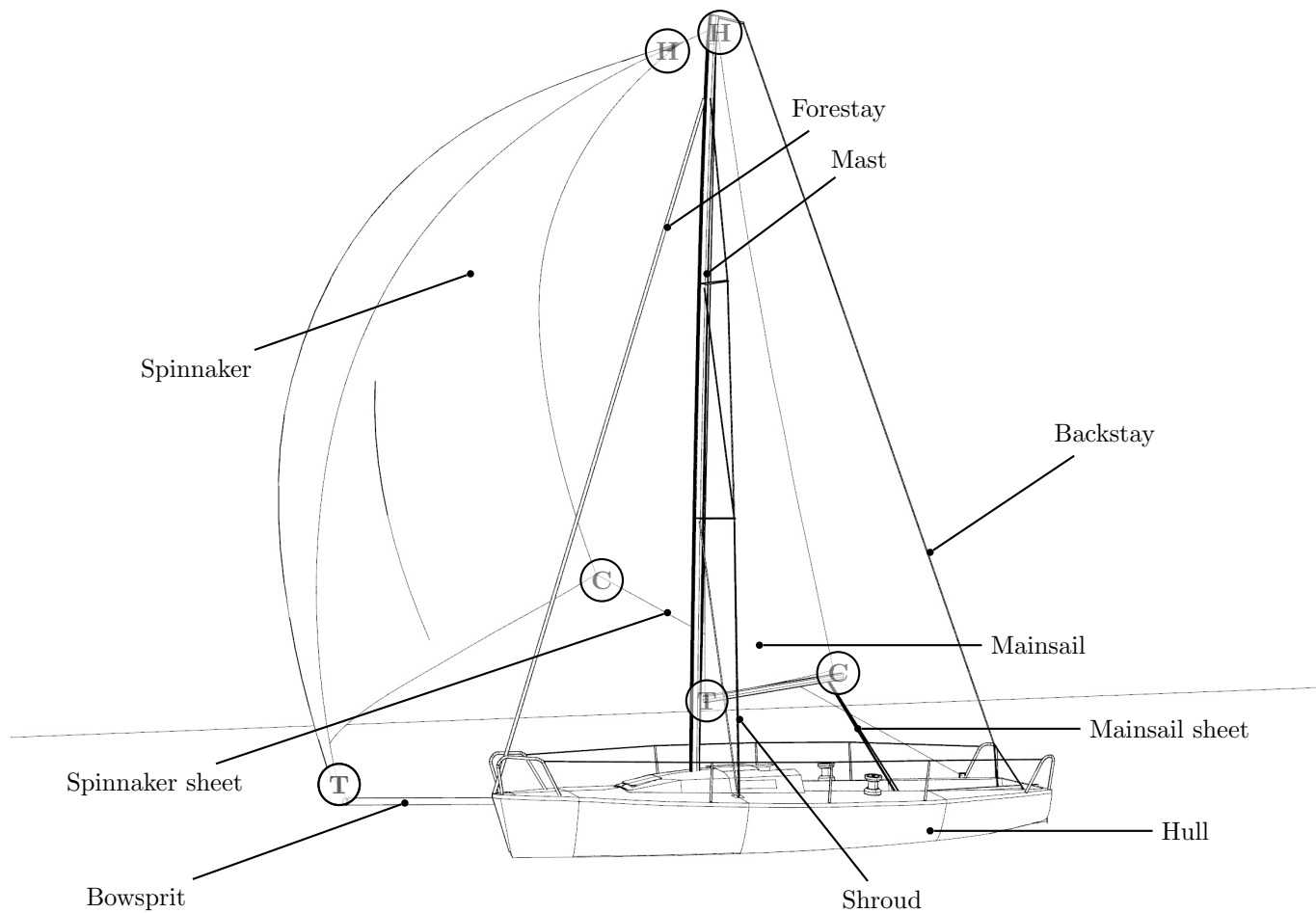


Figure A.1 – Yacht vocabulary inspired by [Deparday, 2016]. **T** for tack point, **C** for clew point, **H** for head point.

English	Definition	French translation	French definition
Adjustment	Tunning action of the rig or sheets.	Réglage	Modifications de longueur d'éléments du gréement ou des écoutes.
Backstay	Câble that can tune the mast rake, <i>i.e.</i> spanwise longitudinal shape.	Pataras	Cable permettant le réglage de la quète de mât en navigation, <i>i.e.</i> sa forme dans un plan longitudinal.
Cantilevered	Local holding condition where the local derivative of the object deformation and its local derivative (neutral fibre sloop) are assumed to be equal to 0.	Encastré	Condition de maintien où la déformation transversale locale et sa dérivée sont nulles.
Downwind	As defined in Fig. 1.1.	Portant	Allures représentées dans la Fig. 1.1.
Heel	Lateral angle associated to rolling.	Gîte	Angle latérale d'inclinaison.
Leech	Sail trailing edge.	Chute	Bord de fuite de la voile.
Luff	Sail leading edge.	Guindant	Bord d'attaque de la voile.
Seam	Join between sail panels.	Couture	Element liant par tissage les pannaux d'une voile.
To ease	Increase the sheet length (releasing the sheet).	Choquer	Augmenter la longueur d'une écoute.
To luff, luffing	The AoA is so small that the sail is acting like a flag.	Faseyer, faseyement	L'angle d'attaque est si faible que la voile bat de manière similaire à un drapeau.
To trim	Decrease the sheet length (pulling the sheet).	Border	Diminuer la longueur d'écoute.

Table A.1 – Sailing vocabulary.

B

Frames and coordinate system

Definition of some frames and points of interest in a general way as used in full scale studies in yacht engineering are presented in this appendix.

A coordinate system, also called frame is defined by a point of origin and a base vector. For numerical studies, it is important to know in which frame the calculation codes provides the results. For experimental studies, only a well defined motion frame enables to determine precisely formulae to get accurate results about boat attitude and wind information. In yacht study we can define different frames shown in Tab. B.1. All the frames are using direct orthogonal base vector defined by the vectorial or cross product. As shown in Fig. B.1, the angular orientation of the boat is defined using a yaw α , pitch θ , roll ϕ convention in the Eulerian angular convention.

All frames using the same directions, *i.e.* the same base vector, than the terrestrial and inertial frame will use capital letters for their own axes contrary to the other frames. Other frame such as the top of the mast frame or wind sensor frame can be defined in order to get accurate informations about the wind. We define here several important points useful for aerodynamic or hydrodynamic studies. These points can have a physical solid existence (defined as a point of a solid) or a physical definition existence (defined as a centre of effort for example). For experimental considerations we can define:

- H_{TF} as an arbitrary point of origin of the local terrestrial frame TF . It could be a given landmark. The locale terrestrial frame is oriented by the local geographic north, geographic west and upright vertical directions.
- $O_{frame\ name}$ is the origin of the corresponding frame. In our case we define the origin O at mast step at the neutral fibre of the mast. O , O_{IF} , O_{UBF} , O_{BF} are identical.
- point WS_i , point corresponding to the point of the wind sensor n° i where wind measurements is done. When the wind sensor is not specified, it becomes simply WS point.
- point of interest PoI used in equation in order to keep a general notation without choosing a specific point (centre of aero forces or wind sensor measurements point).
- point GPS where the GPS antenna sensor is inboard

The different frames are described in table B.1. [Hansen, 2006] provides detailed frame for the wind tunnel testing. In the work presented here, only the balance frame is required.

Name	Symbol	(Origin, Base) and Description	Relation with other frame
Terrestrial frame	TF	H_{TF} a no moving harbour point in the terrestrial frame X horizontal axis oriented to the geographic North Y horizontal axis oriented to the geographic West Z local vertical axis pointing upwards	Asbsolute coordinate system
Local ocean frame	LOF	OSS a point at average local sea surface, moving with the current tide X horizontal axis oriented to the geographic North Y horizontal axis oriented to the geographic West Z local vertical axis pointing upwards	Translation between TF and LOF
Inertial frame	IF	O_{IF} at the mast step X horizontal axis oriented to the geographic North Y horizontal axis oriented to the geographic West Z vertical axis pointing upwards	Translation between TF and IF
Upright boat frame	UBF	O_{UBF} at the mast step x_{UBF} horizontal axis aligned with centerline of yacht pointing forward (upright) y_{UBF} horizontal axis athwartships pointing portside (upright) z_{UBF} vertical axis pointing upwards	Rotation \mathcal{R}_α between IF and UBF
Leveled upright boat frame	$LUBF$	O_{LUBF} vertically aligned with the mast step but at the sea level plan $x_{LUBF} = x_{UBF}$ $y_{LUBF} = y_{UBF}$ $z_{LUBF} = z_{UBF}$	Rotation \mathcal{R}_α and translation between IF and $LUBF$
Boat frame	BF	O_{BF} at the mast step on neutral axes level of the mast beam x_{BF} or x axis aligned with centerline of heeled and pitched yacht direction pointing forward y_{BF} or y axis athwartships poiting portside (heeled and pitched yacht) z_{BF} or z axis along mast direction pointing upwards	Rotation \mathcal{R}_τ between IF and BF
Top of the mast frame	TOM	T_M defined at the neutral fibre at a given level on the top of the mast. For J80 case it wil be at the upper mast spar band defined in the international class rule (maximum 9144mm from the deck) x_{TOM} -axis is in the local forward direction perpendicular to the mast structural axes y_{TOM} -axis is in the local port direction z_{TOM} -axes is in the local direction given by the mast structural axes going out of the mast.	Rotation and translation between BF and TOM due to natural offset and mast distortion
Force balance frame	Ba	O_{Ba} x axis aligned with centreline of heeled and pitched yacht direction pointing forward y axis athwartships poiting portside (heeled and pitched) z axis along mast pointing upwards	Used during wind tunnel test

Table B.1 – Frames definition for full-scale, numerical experiments and wind tunnel testing.

C

Complementary information on the wind tunnel experimental campaign

This appendix provides general complementary informations about some aspects of the wind tunnel experimental campaign. Other appendices related to wind tunnel testing are dedicated for details referring to upwind or downwind aspects. Uncertainty evaluation is first presented here for some general output data measured. Some details about the recording architecture and its impact on the data are presented.

C.1 Uncertainty evaluation

Uncertainty evaluation is required to estimate if an observed evolution or a comparison between two cases is within the uncertainty range or is above the uncertainty range. Moreover the experimental uncertainty evaluation is required for numerical validation model.

C.1.1 Uncertainty on force coefficients

Uncertainty on aerodynamic coefficients depends on the uncertainties of the information provided by the force balance, the Pitot tube and the sail area evaluation. We can estimate the Pitot tube uncertainty about 1% of its measurement as a typical value, and the sail area about 4% of the total sail area given by the SailPack software. Sails panels are laser guided cut and extra care have been taken when assembling the sails panels. [Hansen, 2006] provides information about the force balance error: ± 0.09 N along x direction, ± 0.11 N along y direction and ± 0.27 N along z direction. The coefficient uncertainty can be computed using:

$$\Delta C_{F_i} = \left| \frac{\partial C_{F_i}}{\partial F_i} \right| \Delta F_i + \left| \frac{\partial C_{F_i}}{\partial q} \right| \Delta q + \left| \frac{\partial C_{F_i}}{\partial S} \right| \Delta S \quad (\text{C.1})$$

$$\Delta C_{F_i} = \frac{1}{qS} \Delta F_i + \left| \frac{F}{Sq^2} \right| \Delta q + \left| \frac{F}{qS^2} \right| \Delta S \quad (\text{C.2})$$

For typical parameter values measured during the experimental campaign, we get an uncertainty of ± 0.05 on C_{F_x} , ± 0.06 on C_{F_y} and ± 0.08 on C_{F_z} . On $C_{F_{obj}}$ the uncertainty is about ± 0.06 . The measuring range goes up to 200 N for the balance drive force direction.

A check operation has been done on the balance with the suggested calibration matrix which was considerate as accurate enough. A full calibration procedure is quite time consuming and requires the use of the dedicated pyramidal structure. If newest study is performed, one can still use the previous raw data either directly on the voltage signal, or applying the inverse of the previous calibration matrix to the forces signals then applying the new calibration matrix on the retro-processed signal data.

As indicated by [Hunt and Ferry, 1975], the local gravity acceleration might be taken equal to 9.8 m s^{-1} .

C.2 Recording architecture

The experiment records both time series and video informations. The challenging part of this study is to be able to synchronise those recording with the available hardware and software. Usually for wind tunnel testing at the YRU only static videos information for the flying shape using the VSPARS system are recorded. However, results presented in this thesis clearly show that some unsteady situations, especially on downwind situations with curling, present higher performance than steady cases.

C.2.1 Signal post-processing

Balance signals are transmitted to an Analog\Digital (A\D) card converter for the computer acquisition of the signals. This conversion can imply a time delay between the recorded force and the actual force signal. Several experiments were carried out to evaluate this possible time shift which has to be taken into account for accurate FSI time series studies, such as synchronisation between the sheet length, the load sheet and the forces signals.

Balance signals are recording with a sampling frequency of 200 Hz. The sheet load position is recorded with a non constant sampling frequency close to 90 Hz with an independent process. Moreover when using the dynamic trimming, the rotation frequency is considered as constant for each tested cases. The interpolation applied on angular position on the force time vector provides accurate information. This interpolation is then used to compute the sheet length signal.

With a model about 20 kg on the balance, there is a known natural frequency of the balance and model system around 10 Hz for usual model tested on the TFWT. It implies that above a certain frequency of the dynamic trimming system around $f_{ordered} = 4.5 \text{ Hz}$, the balance system is excited on its natural frequency and force signals are strongly affected. Therefore a hardware low

pass filter is applied on force balance signal which may generate a delay on the dynamic recording. This delay was evaluated with some dynamic calibration experiments.

C.3 Blockage effect on aero-forces coefficient measurements

In this thesis the reference dynamic pressure has been used to compute the force coefficients. The use of force coefficient prevent any flow fluctuation between different runs to significantly affect the results at the same ordered wind speed or to compare different runs when different wind speeds are selected or even compare sails with different area.

These dimensionless force coefficient can be computed using a representative flow velocity or directly a dynamic pressure. In [Fossati and Muggiasca, 2011] where pitching motion is studied, the model yacht is moving (pitching) and the chosen velocity to compute the aerodynamic coefficient takes into account the dynamic part of the model motion. In our unsteady situation with static or oscillating trim, the model scale frame is not moving. However the centre of effort position which can be considered as a reference point may change over time. Because such a motion cannot be predicted before measurement and because its computation can use hypothesis that can be discussed, only the dynamic pressure method to compute coefficient is selected here even for dynamic cases. This dynamic pressure is related to the flow velocity in a given fixed location.

Several choice can be done to select the reference pressure point:

- the reference point can be the upstream Pitot tube providing q_{Pitot} recorded directly during the experiment. This is the reference point used in this thesis. However this dynamic pressure might not be directly the one seen by the model scale, especially if the model scale is large enough to produce blockage effect on the wind tunnel.
- the reference point can be an upstream point at a given location providing q_{ref} . Most of the time its height corresponds to a reference height Z_{ref} . This height can be fixed arbitrary or associated to the centre of effort location or to the sail area centre. Because of the different possible configuration (upwind or downwind, steady or unsteady trim) only a fixed height can be used to reasonably compare runs results between each others.

As described in [Hansen, 2006], most of the time in the TFWT the measured dynamic pressure is q_{Pitot} and can be used to get the q_{ref} on a desired location point using a pressure factor c_q . This pressure factor is the ratio $c_q = \frac{q_{ref}}{q_{Pitot}}$. This reference point location is usually on the turning table. The pressure factor is affected by several elements:

- the height difference between the reference point and the Pitot tube altitude, which can provide different wind speed due to the boundary layer wind profile as shown in Eq. C.3. In this equation the wind velocity is not supposed to affect the theoretical value of c_q using a logarithmic boundary layer with a constant z_0 .
- the distance between the reference point and the model scale. Usually the reference point is chosen not too close to the model scale in order no to be affected by its free stream velocity change

- the size and trim of the model scale which can create an additional change in the wind speed due to blockage effect. This occurs essentially for large downwind model sails and evolves for the different configuration (AWA and AWS).

In this thesis results, the force coefficient is computed using the Pitot tube information. In order to achieve numerical-experimental comparison, Tab. C.1 provides some data that can be used to correct the computed coefficients using the pressure factor. Most of the time, due to small sail area and low bluff body aspect of upwind sails, the pressure factor is considered close to 1 for same altitude points in upwind configuration. Therefore the value of the pressure factor in upwind configuration is mainly due to the height difference between the Pitot tube and reference point in the boundary layer. For downwind configuration, the pressure factor can be affected by the bluff body aspect and blockage effect.

To compute the theoretical pressure factor in upwind configuration (no measurement was done), the logarithmic law wind profile is used to evaluate the effect of altitude difference between measuring points, with $Z_{ref} = 1500$ mm:

$$c_q = \frac{\ln^2\left(\frac{Z_{ref}}{z_0}\right)}{\ln^2\left(\frac{Z_{ref} - Z_{Pitot}}{z_0}\right)} \approx 0.8913 \quad (C.3)$$

A run measuring simultaneously q_{Pitot} and the reference pressure q_{ref} (using the Cobra probe) is done to measure any possible bluff body or blockage effect with a spinnaker. The location of the reference point is 1500 mm height, 795 mm upstream of the turning table windward limit on the centreline of the wind tunnel. A spinnaker is set up on the turning table under static trim before curling configuration at $AWA = 80^\circ$ with $f_{fans} = 20.5$ Hz (associated to a wind velocity of 3 m s^{-1} at the Pitot tube location).

Configuration	c_q	$\frac{S}{TFWT \text{ cross section area}}$ (%)
Upwind	0.8913	3.8 for the standard mainsail
Downwind	0.8629	12.6

Table C.1 – Pressure factor correction table between the Pitot tube location and a reference point at 1500 mm height, 795 mm upstream of the turning table windward limit on the centreline of the wind tunnel.

The comparison of numerical-experimental force coefficients is only relevant between definition using the same location for the dynamic pressure. For future experimental-numerical simulation, as the Pitot tube information is not presented in this thesis, the user first computes the expected numerical dynamic pressure at the reference point location. To get the corrected force coefficient, the user computes this thesis force coefficients divided by the pressure factor *i.e.* $\frac{C_{F_i}}{c_q}$. c_q being defined as the ratio of the numerical reference point dynamic pressure over the Pitot point location dynamic pressure.

D

Complementary information on the load sensor

Different elements about the load sensor used to measure the sheet load are provided in this appendix.

D.1 Load sensor calibration

Calibration of the load sensor was performed three times in 2015 and four times in 2016 as illustrated by Fig. D.1. Tables D.1 and D.2 show the different parameters from the calibration. The manufacturer Garos indicates a measured sensitivity of $S_e = 0.036\ 602\ \text{mV/V/N}$ which is relatively close to the measured values where connection settings and environment are different. The different types of measurement error are described in [Augier, 2012, Deparday, 2016] and are presented as percentage of the measurement range of the load sensor % Measuring Range (MR). Each calibration corresponds to one increasing phase where several loads were successively added and one decreasing phase where the loads were successively removed therefore no precision error can be computed for each calibration. The calibrations were performed with the fans turned off which may lower the noise level compared to the real testing conditions. The accuracy precision is 0.2% of the MR which implies a precision of $\pm 0.1\ \text{N}$ on the sensor itself.

In order to make the post processing simpler, only the averaged value of *Coef*f during each experimental campaign is considered to compute the sheet load then sheet load coefficient. In 2015, the averaged value is $5359.9\ \text{N V}^{-1}$. This value compared to each individual calibration value of *Coef*f gives a maximum relative error of 0.31%. Therefore if the averaged value is used, an uncertainty of the measured load value is $\pm 0.31\%$.

In 2016, the voltage power supply has been changed between the different part of the experimental campaign. For the first preliminary part the raw value of *Coef*f $5639.7\ \text{N V}^{-1}$ is chosen. For the other part, the averaged value is $5393.6\ \text{N V}^{-1}$. This value compared to each individual calibration value of *Coef*f gives a maximum relative error of 0.36%. Therefore using the averaged value makes the uncertainty of the measured load value about $\pm 0.36\%$.

The use of the averaged value of *Coef*f of calibrations for each experimental campaign increases the uncertainty up to $\pm 0.36\%$ of the measured load.

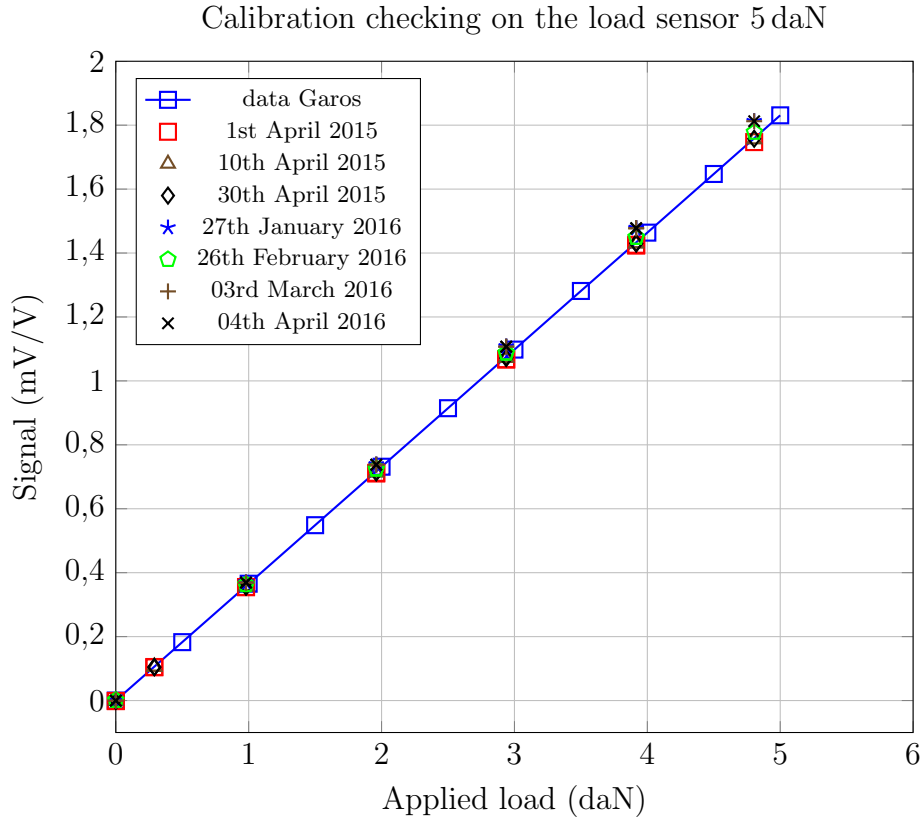


Figure D.1 – Comparison of load sensor calibration.

Calibration date		2015/04/01 (start)	2015/04/10 (end)	2015/04/30 (end)
S_e	$\text{mV V}^{-1} \text{N}^{-1}$	0.03640	0.03655	0.03658
S_0	mV V^{-1}	-0.00159	-0.00114	-0.00154
E_{hys}	%MR	0.05	0.01	0.03
E_{tru}	%MR	0.07	0.10	0.11
E_{acc}	%MR	0.20	0.10	0.15
V_{input}	V	5.11	5.11	5.11
<i>Coef</i> f	N V^{-1}	5376.3	5354.1	5349.2

Table D.1 – Calibration of Garos load sensor for 2015.

Calibration date		2016/01/27 (start)	2016/02/26 (start)	2016/03/03 (end)	2016/04/04 (start)
S_e	$\text{mV V}^{-1} \text{N}^{-1}$	0.03619	0.03699	0.03704	0.03721
S_0	mV V^{-1}	-0.00083	0.00030	-0.00068	0.00063
E_{hys}	%MR	0.02	0.03	0.01	0.02
E_{tru}	%MR	0.06	0.07	0.04	0.06
E_{acc}	%MR	0.07	0.13	0.07	0.11
V_{input}	V	4.9	5	5	5
$Coeff$	N V^{-1}	5639.7	5407.5	5399.0	5374.3

Table D.2 – Calibration of Garos load sensor for 2016.

D.2 Load sensor complementary information

The load sensor has an effect on the measurements therefore informations presented on this section improve experimental repeatability and are also required for relevant numerical-experimental comparison.

D.2.1 Zeroing of the load sensor

The load sensor zeroing is done before runs series without flow. For upwind configuration, the load sensor is hung at the point sb of Fig. 3.2 when zeroing therefore the weight of the load sensor is not measured while recording in the mainsail sheet load signal. For downwind configuration, the load sensor is laying when zeroing on the model without any tension through it. Therefore the weight of the load sensor is measured while recording as part of the spinnaker sheet load signal. Its very light weight (25 g) implies a change in the load signal about 0.245 N which is higher than the estimated error of accuracy.

D.2.2 Load sensor positioning

The load sensor position is important for two reasons: repeatability of the experimental test and accuracy of the numerical-experimental comparison. For upwind measurements, the load sensor is knotted to the boom where the clew line is attached (sb point on Fig. 3.2 in order to avoid bending moment applying on boom). Its position (65 mm from the boom to the load sensor holding point) remains identical across testing when the load sensor is used as illustrated by Fig. D.2b. The use of load sensor is indicated for each cases. The geometry of the load sensor is given on Fig. D.2a. For 2016 experimental campaign, the point of the load sensor attached to the sheet in the sail direction was positioned at 80 mm of the clew point of the spinnaker as defined on Fig. D.2b. For the 2015 downwind experimental campaign, this measure was not set up identically but close.

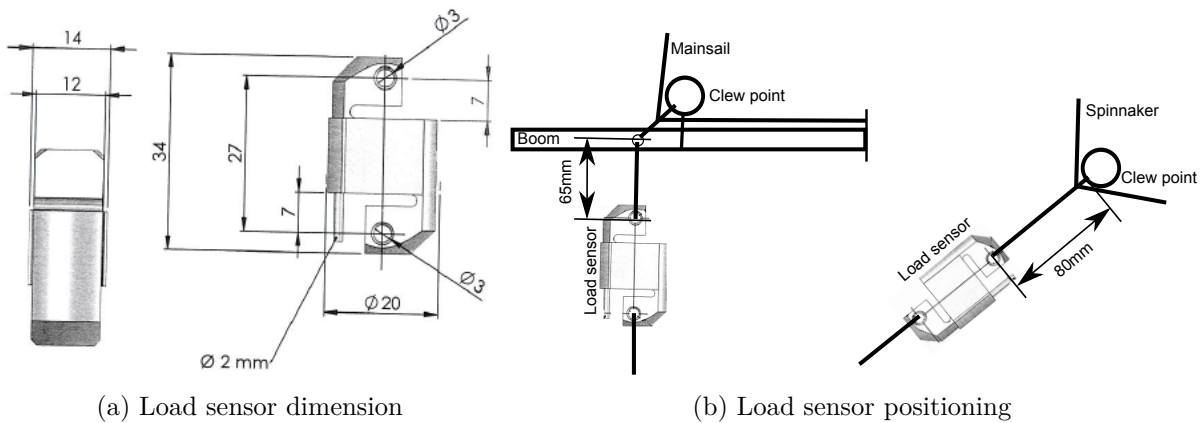


Figure D.2 – Load sensor dimensions and positioning.

For future numerical experimental-comparison, two strategies can be used to make accurate comparison on the sail sheet load :

- a first simple approached numerical model does not take into account the weight of the load sensor, and we may consider extra error of accuracy equal to ± 0.245 N for the load value on downwind conditions. This method does not take into account the possible effect of the load sensor weight on the experiment which can particularly strongly affect the spinnaker flying shape in low wind speed conditions
- a second approach takes into account the weight of the load sensor, but the position of this weight along the sheet on the numerical model has to be realistic, corresponding to the previous position described in Fig. D.2b. In that case an extra accuracy error equal to ± 0.245 N has to be added for upwind configuration where load sensor weight is not recorded in the load sensor signal.

The sheet length uncertainty is estimated to be about 2 mm as presented in the next appendix. The maximum force measured being about 12 N to 25 N with a 3 mm diameter dynema sheet which breaking load is about 9000 N, we are about 0,1% of the breaking load. We can fairly assume the elongation of being lower than the uncertainty of measurement. Therefore the sheet length can be considered as an input and the sheet load as an output of the simulation for numerical validation thanks to the experimental data.

E

Wind tunnel upwind configuration

This appendix provides informations (dimensions, mast alignment) about the model in upwind configuration. The static and dynamic command law are determined to compute the sheet length and an error evaluation is given.

E.1 Geometry of upwind configuration

Fig. 2.3a describes some environmental elements positions that can be seen on Fig. 1.4 and be used for refined numerical-experimental comparison. For conventional model yachts tested at the YRU, water is used to fill in the water tank in order to block the flow under the model hull reproducing natural flow behaviour over sea surface. In our experiments where multiple electronic devices are located onto and under the model itself, the turning table water tank under the model is not filled. The top section of the holding parts of the balance (red rectangle on Fig. 2.3b) is about 10 mm width for 30 mm large.

This first section gives geometric measurements of different elements in the upwind configuration.

E.1.1 Measured geometry of upwind elements

Tab. E.2 presents the measured value of geometric coordinates elements in the model frame. Because the origin of the model frame is not physically directly accessible (mast step location underneath the cantilever holding part) the measurement is done from another point location which model frame coordinates are known and described in Tab. E.1.

Reference points	Coordinates in model frame (mm)		
	x	y	z
$Ref_{South\ up}$	-80.72	0	9.30
Ref_{South}	-80.15	0	0
$Ref_{North\ up}$	79.98	0	19.06
Ref_{North}	80.15	0	0
$Ref_{West\ up}$	-0.87	80.15	14.18
Ref_{West}	0	80.15	0
$Ref_{East\ up}$	-0.87	-80.15	14.18
Ref_{East}	0	-80.15	0

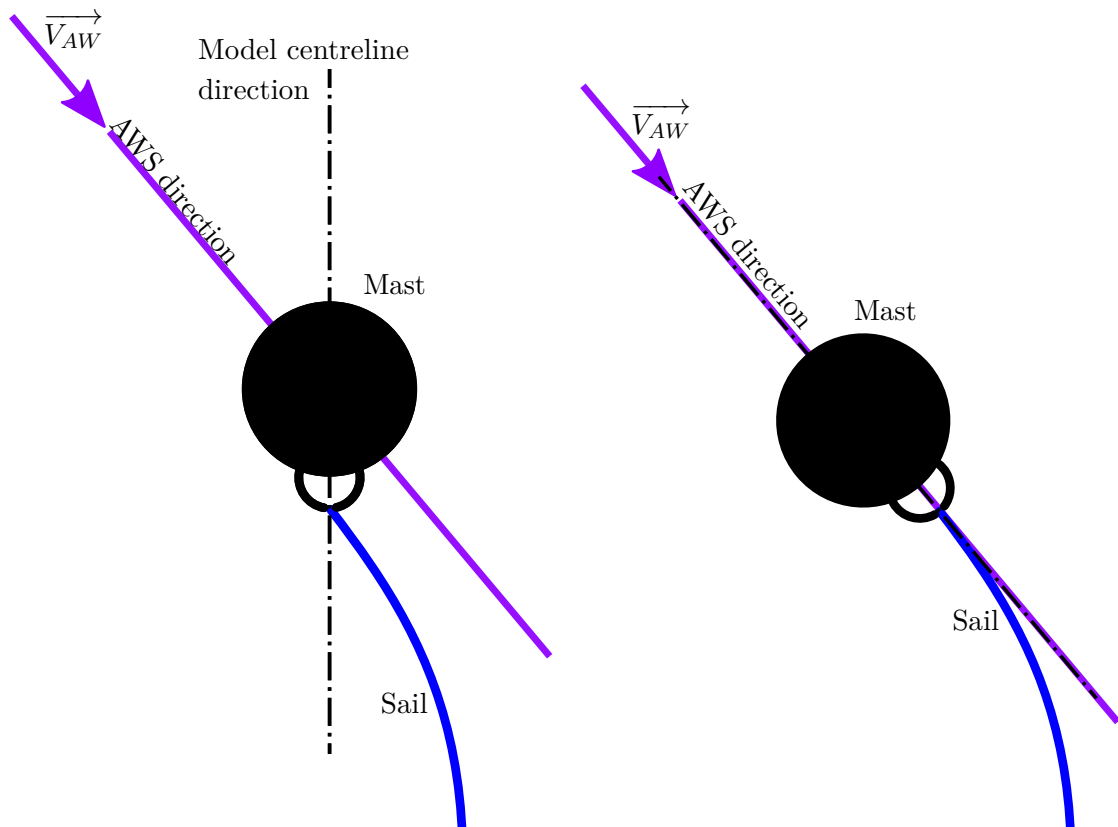
Table E.1 – Model reference points coordinates. Each cardinal points refers to its relative position from the model frame origin: North for front location, South for aft location, West for portside location, East for starboard side location. Up indicates that up location.

Element	Reference point	Measured coordinates (mm)			Coordinates in model frame (mm)		
		x	y	z	x	y	z
Axis stepper motor main sheet	Ref_{South}	-200	0	-52	-280.15	0	-52
Axis stepper motor portside car	Ref_{South}	-335	175	-57	-415.15	175	-57
Axis stepper motor starboardside car	Ref_{South}	-335	-175	-57	-415.15	-175	-57
Portside block axis	Ref_{South}	-527	242.5	-27	-607.15	242.5	-27
Starboard block axis	Ref_{South}	-527	-242.5	-27	-607.15	-242.5	-27
Portside block effective exit point	Ref_{South}	-534	242.5	-27	-614.15	242.5	-27
Starboard block effective exit point	Ref_{South}	-534	-242.5	-27	-614.15	-242.5	-27
Rail traveller upper outside low ring friction radius	Ref_{South}	-538	$\Delta y = \pm 230$	-27	-618.15	$\Delta y = \pm 230$	-27

Table E.2 – Measured upwind elements coordinates from a reference point and elements coordinates in the model frame. For the z coordinates, stepper motor axis points are considered at their highest altitude *i.e.* at the upper surface of the head winches. The coordinates in model frame are equal to the measured coordinates compared to the reference point added to the reference point coordinates.

E.2 Mast alignment

During the upwind experimental campaign, the mast could be oriented on several alignments (fixed angular orientation). It could be aligned with the centreline of the boat or aligned with the main direction of the TFWT corresponding to a rotation equal to the AWA from the yacht centreline. This choice is made for two reasons. The ability of the IMOCA 60 mast to rotate around their foot position corresponds to the first reason. The rotation in this case is done around the mast main axis (span wise direction). IMOCA 60 mast section shape is close to a wing profile and the rotation improves the flow behaviour close to the luff part of the sail and could even generate drive force without any hoisted sail. On the model, the mainsail is hoisted along a rail on the mast aft part. This open circular rails affect the mast general section shape, making it closer to a wing section. This has been observed in the windage measurement presented in section 2.1.3. The second reason for the different position of the mast is to make easier numerical simulation. Aligning the mast with the flow *i.e.* with the wind tunnel streamwise flow direction, tends to prevent any numerical mesh to collapse in the luff and luffrope (mast rail) area as shown on Fig. E.1. For $\beta_{AW} = 25^\circ$ and $\beta_{AW} = 40^\circ$ the mast is aligned with the boat centreline. Another test is done on the standard mainsail at $\beta_{AW} = 40^\circ$ where the mast is aligned with the TFWT flow direction *i.e.* the mast is rotated of 40° in order to study the effect of mast rotation on the optimum location and value. For $\beta_{AW} = 60^\circ$ the mast is aligned with the wind tunnel streamwise direction.



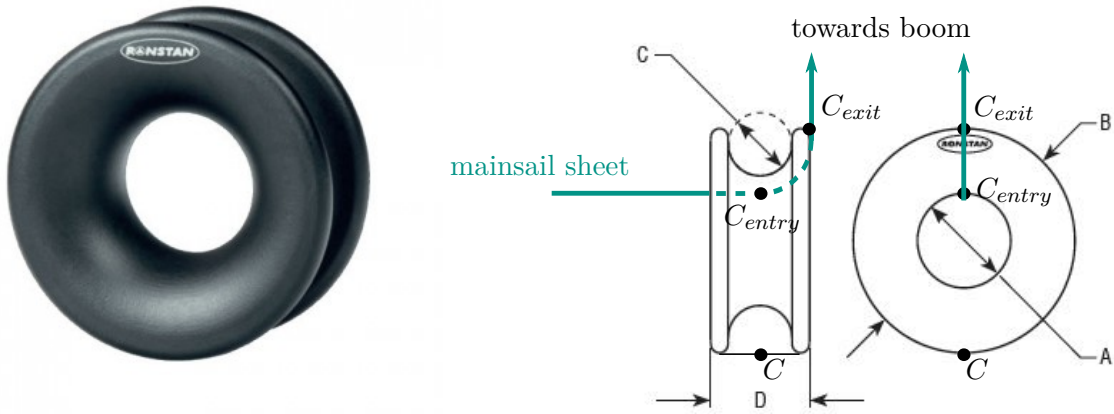
(a) Mast aligned with the model yacht centreline (b) Mast aligned with the apparent wind speed.

Figure E.1 – Mast alignment.

E.3 Upwind static command law: presentation of static trim

Here is presented the calculation of the mainsail sheet length L_{sheet} in static configuration according to two parameters: the ordered sheet length L_{ord} and ordered mainsail car traveller position L_{car} shown on Fig. 3.2. Because the traveller rail is not circular and centred on the mainsail sheet winch axis, the car traveller position L_{car} and the ordered sheet length L_{ord} have to be taken into account to compute the sheet length L_{sheet} . When the car traveller position is changing with L_{ord} remaining constant, L_{sheet} changes. To determine this relation several geometric points on the model are defined:

- the point w for the winch point where the sheet is ending its contact with the mainsail sheet winch cylinder part. It can be seen on Fig. 3.2. This point is first considered always on port side location of the cylinder. The mainsail is trimmed in when the winch is turning in clockwise direction seen from an above point of view. During the different tests, the sheet is supposed not to be rolled onto itself therefore only one sheet thickness has to be taken into account for the considered radius of the sheet rolled around the winch cylinder. However the altitude of this point w may change with the rolled sheet quantity. A first approximation where the altitude remains equal to the highest possible position on the winch external cylinder part is used.
- the point C for the car position at the rail altitude. The point C_{entry} corresponds to the central inner top point of the low friction ring with the same x and y coordinates of point C in the model frame as shown on Fig. E.2b (C_{entry} is the vertical translation of C of a length equivalent to the ring thickness plus the inner diameter of the low ring friction *i.e.* 15 mm). The point C_{exit} corresponds to the external aft top point of the low friction ring. C_{exit} is the translation of C decomposed in a translation of half thickness of the low friction ring backwards along the x direction and a translation of an external diameter upward in the z direction. These points position are presented on Fig. E.2b. The car position is controlled by the stepper motor #1 and #2 changing L_{car} . The quantity L_{car} corresponds to the oriented distance along the traveller rail from the centreline of the model to the car position. It is considered as negative on the portside part because it decreases the line length between the windward stepper motor and car position and positive on the starboard side part because it increases the line length between the windward stepper motor and car position. When $L_{car} = 0$, the car traveller is located on the model centreline.
- the point sb for the sheeting point on the boom. This position also corresponds to the position where the clew of the mainsail is attached to the boom.



(a) Photograph of low friction ring. (b) Geometry of low ring friction. $A=8$ mm, $B=22$ mm, $C=7$ mm, $D=11$ mm, weight=4 g. lfr is equal to $\frac{\pi}{2} \frac{D}{2} = \frac{\pi D}{4} \approx 8.64$ mm.

Figure E.2 – Low friction ring geometry.

Product No	A (mm)	B (mm)	C (mm)	D (mm)	M.W.L (kg)	Weight (g)
RF8090-08	8	22	7	11	1000	4

Table E.3 – Dimension for the RONSTAN low ring friction used for the upwind wind tunnel experiments.

The mainsail sheet from the winch to the sheeting point on the boom sb can be therefore decomposed into three parts using the previous defined points:

- the first part from the winch point w to the low ring friction entry C_{entry} . This part length can change according to the car traveller position depending on L_{car} .
- the second part from the low ring friction entry C_{entry} to the low ring friction exit C_{exit} can be considered as constant length in a first approximation and defined as lfr .
- the third part from the low ring friction exit C_{exit} to the sheeting point on the boom sb . Its length considered as L_{sheet} can change according to the change in L_{ord} and L_{car} .

All the static experiments started with the motor zeroing step. For this reference state, the initial sheet length $L_{sheet\ 0}$ corresponds to the distance between the point C_{exit} and the boom sheeting point sb . L_{tot} represents the total length from the winch point w to the sb passing trough the low ring friction. L_{ord} represents the ordered trim length from the reference state. In the following demonstration, the index 0 refers to the initial reference state when zeroing the motor and index 1 refers to an arbitrary state where the sheet length L_{sheet} has to be calculated from $L_{sheet\ 0}$, L_{ord} and L_{car} . The notation d_{AB} corresponds to the distance between point A and B .

$$L_{tot\ 0} = d_{wC_{entry}\ 0} + lfr + L_{sheet\ 0} \quad (E.1)$$

$$L_{tot\ 1} = L_{tot\ 0} + L_{ord} = d_{wC_{entry}\ 1} + lfr + L_{sheet\ 1} \quad (E.2)$$

$$\boxed{L_{sheet\ 1} = d_{wC_{entry\ 0}} - d_{wC_{entry\ 1}} + L_{sheet\ 0} + L_{ord}} \quad (E.3)$$

This formula can be used to compute the sheet length from a measured reference state which is usually done when zeroing the stepper motors. For all the static tests, the reference position for the car traveller remains on the centreline of the model scale $d_{wC_{entry\ 0}} = d_{wC_{entry\ ref}}$.

Element	Coordinates in model frame (mm)		
	x	y	z
w	-279.85	10	-55.25
C	-612.65	$-L_{car}$	-49
C_{entry}	-612.65	$-L_{car}$	-32.5
$C_{entry\ ref}$	-612.65	0	-32.5
C_{exit}	-619.35	$-L_{car}$	-27

Table E.4 – Element positioning on low friction ring for upwind elements, in the model scale frame, datum at mast step.

E.3.1 Experimental static sheet length application

The coordinates value in the model frame injected in the previous equation gives the formulation of L_{sheet} in mm:

$$\begin{aligned} L_{sheet} = & \sqrt{(x_{C_{entry\ ref}} - x_w)^2 + y_w^2 + (z_{C_{entry\ ref}} - z_w)^2} \\ & - \sqrt{(x_{C_{entry\ ref}} - x_w)^2 + (y_w - (-L_{car}))^2 + (z_{C_{entry\ ref}} - z_w)^2} \\ & + L_{sheet\ 0} + L_{ord} \quad (E.4) \end{aligned}$$

$$\begin{aligned} L_{sheet} = & \sqrt{(-612.65 + 279.85)^2 + 10^2 + (-32.5 + 55.25)^2} \\ & - \sqrt{(-612.65 + 279.85)^2 + (10 + L_{car})^2 + (-32.5 + 55.25)^2} \\ & + L_{sheet\ 0} + L_{ord} \quad (E.5) \end{aligned}$$

$$\boxed{L_{sheet} = 333.43 - \sqrt{111073.8125 + (10 + L_{car})^2} + L_{sheet\ 0} + L_{ord}} \quad (E.6)$$

The previous formula indicates that not taking into account the exact geometry of the trimming device with the moving traveller along the straight rail can largely overestimate the actual sheet length. For instance, the maximum difference is obtain when the traveller is at the leeward rail extremity $L_{car} = 210$ mm. The difference $\Delta L_{sheet} = L_{ord} + L_{sheet\ 0} - L_{sheet} = -333.43 + \sqrt{111073.8125 + (10 + L_{car})^2}$ can be computed. It represents the difference between the too simplified model where the car position has no effect on L_{sheet} and the model where the car position has an effect on L_{sheet} . The difference with the car located at the leeward rail extremity

gives $\Delta L_{sheet} = -333.43 + \sqrt{111073.8125 + (10 + 210)^2} = 65.9$ mm. This difference does not depend on the reference sheet length chosen. It shows that the simple model always overestimate L_{sheet} especially in situations where the car is close to the rail extremity. Optimum trimming often reach this kind of area with a traveller line largely eased for deeper AWA. In a classical case $L_{sheet 0}$ is about 160 mm and this error represents about 41% of the initial sheet length. Therefore such an important error make this first model inappropriate and the car position should be taken into account to compute the sheet length.

E.3.1.1 Model improvement

To increase precision of the previous formulation, we can take into account on the previous equations, the sheet line diameter $d = 3$ mm. In that case it only affects the coordinates along y and z direction of the point w , and the z coordinates of point C_{entry} :

$$L_{sheet} = \sqrt{(x_{C_{entry\ ref}} - x_w)^2 + (y_w + \frac{d}{2})^2 + (z_{C_{entry\ ref}} - \frac{d}{2} - (z_w - \frac{d}{2}))^2} - \sqrt{(x_{C_{entry\ ref}} - x_w)^2 + (y_w + \frac{d}{2} - (-L_{car}))^2 + (z_{C_{entry\ ref}} - \frac{d}{2} - (z_w - \frac{d}{2}))^2} + L_{sheet\ 0} + L_{ord} \quad (E.7)$$

$$L_{sheet} = \sqrt{(x_{C_{entry\ ref}} - x_w)^2 + (y_w + \frac{d}{2})^2 + (z_{C_{entry\ ref}} - z_w)^2} - \sqrt{(x_{C_{entry\ ref}} - x_w)^2 + (y_w + \frac{d}{2} - (-L_{car}))^2 + (z_{C_{entry\ ref}} - z_w)^2} + L_{sheet\ 0} + L_{ord} \quad (E.8)$$

$$L_{sheet} = \sqrt{(-612.65 + 279.85)^2 + (10 + 1.5)^2 + (-32.5 + 55.25)^2} - \sqrt{(-612.65 + 279.85)^2 + (10 + 1.5 + L_{car})^2 + (-32.5 + 55.25)^2} + L_{sheet\ 0} + L_{ord} \quad (E.9)$$

$$L_{sheet} = 333.48 - \sqrt{111073.8125 + (11.5 + L_{car})^2} + L_{sheet\ 0} + L_{ord} \quad (E.10)$$

The difference with the first model is about 0.8 mm when the $L_{car} = 210$ mm, $L_{sheet\ 0} = 160$ mm and $L_{ord} = 0$ mm. Next part describes other geometry considerations that can provide information about the uncertainty estimation of L_{sheet} .

E.3.2 Uncertainty estimation

The sheet length is one important input parameter of the experiments therefore it requires an uncertainty evaluation as precise as possible. The uncertainty on L_{sheet} is mainly due to several geometrical approximation. First are decomposed the different source of uncertainty depending of the geometrical approximations. The human error is lastly presented.

E.3.2.1 Command uncertainty: zeroing uncertainty $\epsilon_{r0} L_{sheet}$

This error is due to the zeroing stage of the angular position of the motor when powered on after zeroing. A stepper motor can be remotely positioned on a discrete number of positions, each separated by the angular step. When zeroing the stepper motor, the stepper motor reaches its closest reference static position. Therefore there might be an angular position uncertainty about half of the angular step (which is 1.8° for the main stepper motor). Using R the radius of the winch cylinder part (10 mm) and d the sheet line diameter (3 mm), this uncertainty is estimated by the following equation:

$$\frac{1.8}{2} \frac{\pi}{180} \left(R + \frac{d}{2}\right) \approx 0.2 \text{ mm} \quad (\text{E.11})$$

The zeroing error on traveller stepper motor is considered as neglected because the effect is much lower than the zeroing uncertainty on the initial sheet length.

E.3.2.2 Winch rolling-up error estimation: error on w position

Three kinds of uncertainty presented here can occur while rolling-up the mainsail sheet on the winch cylinder part.

First uncertainty: $\epsilon_{r1} L_{sheet}$. This first uncertainty corresponds to the sheet rolled up over itself and affect the actual radius to be considered *i.e.* an error in the y position of w . This error was avoided during testing however an estimation can be made on a simple case considering for instance two layers of rope around the winch cylinder compared to the reference case where there is only one rolled layer.

$$\epsilon_{r1} L_{sheet} = -\sqrt{(x_{C_{entry\ ref}} - x_w)^2 + \left(y_w + \frac{d}{2} - (-L_{car})\right)^2 + (z_{C_{entry\ ref}} - z_w)^2} + \sqrt{(x_{C_{entry\ ref}} - x_w)^2 + (y_w - (-L_{car}))^2 + (z_{C_{entry\ ref}} - z_w)^2} \quad (\text{E.12})$$

With $L_{car} = 210$ mm, $\epsilon_{r1} L_{sheet} \approx -1.7$ mm.

Second uncertainty: $\epsilon_{r2} L_{sheet}$. The second type of uncertainty is due to the altitude change of the point w when rolling up the sheet. This can be evaluated by the evolution of the altitude z of the point w . In the worst case scenario, this change in altitude occurs when the traveller is in the central position. The higher difference of position occurs when w is on one extremity of the winch

cylinder part when zeroing the motor and is located on the other extremity of the cylinder part for a given measurement. The difference of altitude between these two situations is equal to the height of the rolling part cylinder *i.e.* 18.71 mm. Taking into account the sheet length rolled around the winch cylinder, $L_{rolled\ 0}$

$$L_{tot\ 0} = L_{rolled\ 0} + d_{wC_{entry\ 0}} + lfr + L_{sheet\ 0} \quad (E.13)$$

$$L_{tot\ 1} = L_{rolled\ 1} + d_{wc\ 1} + lfr + L_{sheet\ 1} = L_{rolled\ 0} - L_{ord} + d_{wc\ 1} + lfr + L_{sheet\ 1} \quad (E.14)$$

The total quantity of the sheet length being constant $L_{tot\ 0} = L_{tot\ 1}$, we get the following equation where the altitude z_w changes between the reference (index 0) and an arbitrary state (index 1).

$$\begin{aligned} L_{sheet\ 1} = & \sqrt{(x_{C_{entry\ ref}} - x_w)^2 + y_w^2 + (z_{C_{entry\ ref}} - z_{w\ 0})^2} \\ & - \sqrt{(x_{C_{entry\ ref}} - x_w)^2 + (y_w - (-L_{car}))^2 + (z_{C_{entry\ ref}} - z_{w\ 1})^2} \\ & + L_{sheet\ 0} + L_{ord} \end{aligned} \quad (E.15)$$

The change of altitude is linked to the ordered sheet length change L_{ord} using the following formula: $z_{w\ 1} = z_{w\ 0} + \frac{L_{ord}}{\pi(D + \frac{d}{2})}d$ with D the diameter of the winch cylinder and d the sheet line diameter.

$$\begin{aligned} L_{sheet\ 1} = & \sqrt{(x_{C_{entry\ ref}} - x_w)^2 + y_w^2 + (z_{C_{entry\ ref}} - z_{w\ 0})^2} \\ & - \sqrt{(x_{C_{entry\ ref}} - x_w)^2 + (y_w - (-L_{car}))^2 + (z_{C_{entry\ ref}} - \left(z_{w\ 0} + \frac{L_{ord}}{\pi(D + \frac{d}{2})}d\right))^2} \\ & + L_{sheet\ 0} + L_{ord} \end{aligned} \quad (E.16)$$

The error between our model and the one taking into account the change in altitude due to the rolling sheet is:

$$\begin{aligned} \epsilon_{r2\ L_{sheet}} = & \sqrt{(x_{C_{entry\ ref}} - x_w)^2 + y_w^2 + (z_{C_{entry\ ref}} - z_w)^2} \\ & - \sqrt{(x_{C_{entry\ ref}} - x_w)^2 + y_w^2 + (z_{C_{entry\ ref}} - z_{w\ 0})^2} \\ & - \sqrt{(x_{C_{entry\ ref}} - x_w)^2 + (y_w - (-L_{car}))^2 + (z_{C_{entry\ ref}} - z_w)^2} \\ & + \sqrt{(x_{C_{entry\ ref}} - x_w)^2 + (y_w - (-L_{car}))^2 + (z_{C_{entry\ ref}} - \left(z_{w\ 0} + \frac{L_{ord}}{\pi(D + \frac{d}{2})}d\right))^2} \end{aligned} \quad (E.17)$$

To evaluate the maximum and minimum error possible we define:

- $f : \mathbb{R} \mapsto \mathbb{R}$ such as $f : x \mapsto \sqrt{(x_{C_{entry\ ref}} - x_w)^2 + y_w^2 + (z_{C_{entry\ ref}} - x)^2}$
- $g : \mathbb{R} \mapsto \mathbb{R}$ such as $g : x \mapsto -\sqrt{(x_{C_{entry\ ref}} - x_w)^2 + (y_w - (-L_{car}))^2 + (z_{C_{entry\ ref}} - x)^2}$

The previous equation is equivalent to: $\epsilon_{r2} L_{sheet} = f(z_w) - f(z_{w0}) + g(z_w) - g(z_{w1})$. The function f decreases until $z_{C_{entry\ ref}}$. The function g increases until $z_{C_{entry\ ref}}$. With $z_{w0} \leq z_w < z_{C_{entry\ ref}}$ and $z_{w1} \leq z_w < z_{C_{entry\ ref}}$ we get:

- $f(z_w) \leq f(z_{w0})$ *i.e.* $f(z_w) - f(z_{w0}) \leq 0$
- $g(z_{w1}) \leq g(z_w)$ *i.e.* $0 \leq g(z_w) - g(z_{w1})$

Therefore we can estimate the maximum and minimum value on this error:

$$f(z_w) - f(z_{w0}) \leq \epsilon_{r2} L_{sheet} \leq g(z_w) - g(z_{w1}) \quad (\text{E.18})$$

Using the limits given by the winch cylinder dimensions with $h = 18.71$ mm the height of the winch cylinder part:

$$f(z_w) - f(z_w - h) \leq \epsilon_{r2} L_{sheet} \leq g(z_w) - g(z_w - h) \quad (\text{E.19})$$

The upper limit is maximum when the car traveller is on the same coordinate of w point *i.e.* when $L_{car} = -y_w = -10$ mm. In this case we have:

$$-1.8 \text{ mm} \leq \epsilon_{r2} L_{sheet} \leq 1.8 \text{ mm} \quad (\text{E.20})$$

Third uncertainty: $\epsilon_{r3} L_{sheet}$. The third type of error is due to the approximation that considers that w is on the exact transversal portside location of the winch cylinder. When L_{car} is changing the contact point of the sheet on the winch changes its position along the winch cylinder circumference. This affect the sheet length L_{sheet} . In the worst case scenario, from the transversal to the aft position for w , the uncertainty is given by the following equation:

$$\epsilon_{r3} L_{sheet} = \sqrt{(x_{C_{entry\ ref}} - (x_w - \frac{D}{2}))^2 + (y_w - \frac{D}{2} - (-L_{car}))^2 + (z_{C_{entry\ ref}} - z_w)^2} + \frac{\pi D}{4} - \sqrt{(x_{C_{entry\ ref}} - x_w)^2 + (y_w - (-L_{car}))^2 + (z_{C_{entry\ ref}} - z_w)^2} \quad (\text{E.21})$$

With $L_{car} = 210$ mm, $\epsilon_{r3} L_{sheet} \approx -1.9$ mm.

E.3.2.3 Human error

It corresponds to the reading error on the initial value of L_{sheet} . It can be considered equal to 0.5 mm and therefore is lower than the uncertainty of the geometric configurations.

E.3.2.4 Total uncertainty

The combined uncertainty of the sheet length is about -5.4 mm to 6.6 mm in the upwind conditions.

Over a sheet length of 160 mm, it represents about 4% of the usual reference sheet length.

E.3.3 Numerical static sheet length equivalent

A numerical model is built using the experimental geometry. This model is used for numerical-experimental comparison in [Sacher et al., 2016] where the numerical reference is taken on the inside part of the low friction ring. Therefore $L_{num} = L_{sheet} + lfr$ with $lfr = 8.64$ mm the offset distance along the low friction ring inner radius. We can finally use the following relation for a computation of L_{num} in mm considering the numerical sheet starts from the inner part of the low ring friction.

$$L_{num} = 333.48 - \sqrt{111073.8125 + (11.5 + L_{car})^2} + L_{sheet\ 0} + L_{ord} + 8.64 \quad (\text{E.22})$$

For the distance between the upper part of the low friction ring and the sheeting point of the boom:

$$\boxed{L_{num} = 342.1 - \sqrt{116100 + (10 + c_{pos\ ord})^2} + L_0 + L_{ord}} \quad (\text{E.23})$$

For the low friction ring shown on Fig. E.2, some approximation have been done. In the numerical model the sheet is not following the curved part represented by lfr_{curved} . In the case of a curved part the length is:

$$lfr_{curved} = \frac{p}{4} = \frac{\pi D}{4} \quad (\text{E.24})$$

In the case the low friction ring is considered as a straight part:

$$lfr_{straight} = \frac{D}{\sqrt{2}} \quad (\text{E.25})$$

We can evaluate the error of this approximation:

$$\Delta lfrt = lfrt_{curved} - lfrt_{straight} = D\left(\frac{\pi}{4} - \frac{1}{\sqrt{2}}\right) \simeq 0.0783D \simeq 0.86 \text{ mm} \quad (\text{E.26})$$

For the numerical model, an difference about 0.9 mm can be assume to represent the sheet length uncertainty.

E.4 Dynamic command law

Here is presented the principle of calculation of the dynamic trimming command law in upwind configuration. The top view of the geometry trimming device design is shown on Fig. E.3.

The dynamic test is always done with a fixed given position of the mainsail car traveller, usually corresponding to the location of the optimal trimming. The instantaneous mainsail sheet length is defined by the rotation disk angle κ_T , the traveller car position L_{car} , the amplitude of the dynamic trimming A and the reference length $L_{sheet}(\kappa_0)$ chosen at the initial angular reference position κ_0 . The geometric angle $\kappa_T = \kappa_0 + \kappa$, is defined between the starboard side direction and the direction of the eccentric pin point P on the disk *i.e.* κ_T defines the geometric position of the pin P which coordinates in the model scale frame are describe by:

$$\text{Coordinate of } P: \begin{pmatrix} -A \sin(\kappa_T) + x_{O_{disk}} \\ -A \cos(\kappa_T) + y_{O_{disk}} \\ z_{O_{disk}} \end{pmatrix}_{\text{model frame}} \quad (\text{E.27})$$

κ_0 corresponds to the initial position when zeroing the reference of the stepper motor angular position, aligning the point P in the M_0 direction. κ corresponds to the angular value recorded by the remote control card and is written on the output .txt files. The rotating plate is turning always in the same direction (clockwise for an observer above the rotating plate) which corresponds to an initial increase in the recorded angle κ . Therefore the sign convention is:

- the angle κ_0 is negative if it is in the forward sector compared to $O_{disk}y$ direction and is positive if it is in the backward sector compared to the $O_{disk}y$ direction.
- the angle κ is set to 0° while zeroing the remote control card.
- the angle κ_T is negative if it is in the forward sector compared to $O_{disk}y$ direction and is positive if it is in the backward sector compared to the $O_{disk}y$ direction.

With this definition we got $\kappa_T = \kappa + \kappa_0$. Most of the time the two-parameter optimisation is get with a car traveller on the leeward side. This implies that the line perpendicular to the direction given by the disk axis of rotation to the car traveller is pointing forward. The direction between the disk rotation axis and the car traveller is used as a alignment reference. At the beginning of each dynamic run series, the reference position for the pin is perpendicular to this reference and on the leeward side *i.e.* $\kappa_0 < 0$. In dynamic cases, when zeroing the reference position:

$$L_m(\kappa_0) + L_{sheet}(\kappa_0) + lfr = L_{tot} \quad (\text{E.28})$$

Applying the conservation of the total length L_{tot} of the sheet along time, for any position of the rotating plate we have with the previous initial conditions:

$$L_m(\kappa_T) + L_{sheet}(\kappa_T) + lfr = L_{tot} \quad (\text{E.29})$$

Therefore the general formulae which give the instantaneous sheet length is described by:

$$\boxed{L_{sheet}(\kappa_T) = L_m(\kappa_0) + L_{sheet}(\kappa_0) - L_m(\kappa_T)} \quad (\text{E.30})$$

This equation can be written with distance definition, using d the diameter of the pin support part where the sheet is attached, and the instantaneous distance between the pin and the car position $L_m(\kappa_T) = PC(\kappa_T)$.

$$L_{sheet}(\kappa_T) = PC(\kappa_0) - \frac{d}{2} + L_{sheet}(\kappa_0) - (PC(\kappa_T) - \frac{d}{2}) \quad (\text{E.31})$$

$$\boxed{L_{sheet}(\kappa_T) = PC(\kappa_0) + L_{sheet}(\kappa_0) - PC(\kappa_T)} \quad (\text{E.32})$$

From now, we consider that $L_m(\kappa_T) = PC(\kappa_T)$ to be able to use directly the distance definition without using the $\frac{d}{2}$ constant.

$$\boxed{L_{sheet}(\kappa_T) = L_m(\kappa_0) + L_{sheet}(\kappa_0) - L_m(\kappa_T)} \quad (\text{E.33})$$

Analytical formulation of the dynamic trimming will provide a general formulation which can be used for different kind of situation. In a first step the general development of the function $L_{sheet}(\kappa_T)$ is presented then several properties of this function are verified. $L_{sheet}(\kappa_0)$ is usually known and measured before starting the dynamic run series. It corresponds to the optimal sheet length for the given sailing condition which also provide the car position. Therefore in the previous equation, $L_m(\kappa_T)$ is the only remaining part to be studied.

$L_m(\kappa_T)$ is studied using the distance definition in orthonormal coordinate system:

$$L_m(\kappa_T) = \sqrt{(x_C + A \sin(\kappa_T) - x_{O_{disk}})^2 + (y_C + A \cos(\kappa_T) - y_{O_{disk}})^2 + (z_C - z_{O_{disk}})^2} \quad (\text{E.34})$$

$$\boxed{L_m(\kappa_T) = \sqrt{(x_C + A \sin(\kappa_T) - x_{O_{disk}})^2 + (-L_{car} + A \cos(\kappa_T) - y_{O_{disk}})^2 + (z_C - z_{O_{disk}})^2}} \quad (\text{E.35})$$

The previous equation can be used to compute the sheet length where $x_{O_{disk}} = -280.15$ mm and $y_{O_{disk}} = 0$ mm and $z_{O_{disk}} = -34$ mm from Tab. E.2

Numerical study part of the dynamic trimming will provide the numerical formulation that can be used for the different geometric configurations.

For the altitude calculation we use the altitude in the model frame using the mast step O_{model} as the datum of the coordinate system. For the disk, a repeated dimension composed of two wooden part of 21 mm thickness used for the frame provide the altitude. For the point P , $z_P = -3 \times 21 - 31 + 2 \times 21 + 12 + 1 + 5.5 = -33.5$

$$\text{Coordinate of } P: \begin{pmatrix} -A \sin \kappa_T - 280.15 \\ -A \cos \kappa_T \\ -33.5 \end{pmatrix}_{model \ frame} \quad (\text{E.36})$$

$$\text{Coordinate of } C: \begin{pmatrix} -612.65 \\ -L_{car} \\ -32.5 \end{pmatrix}_{\text{model frame}} \quad (\text{E.37})$$

$$L_m(\kappa_T) = \sqrt{(A \sin \kappa_T - 332.5)^2 + (A \cos \kappa_T - L_{car})^2 + 1} \quad (\text{E.38})$$

$$L_{sheet}(\kappa_T) = \sqrt{(A \sin \kappa_0 - 332.5)^2 + (A \cos \kappa_0 - L_{car})^2 + 1} + L_{sheet}(\kappa_0) - \sqrt{(A \sin \kappa_T - 332.5)^2 + (A \cos \kappa_T - L_{car})^2 + 1} \quad (\text{E.39})$$

For some dynamic configuration, the low friction ring is screw onto the rail support 10 mm forward than the low friction ring position on the rail. In this case the formula that should be used is:

$$L_{sheet}(\kappa_T) = \sqrt{(A \sin \kappa_0 - 322.5)^2 + (A \cos \kappa_0 - L_{car})^2 + 1} + L_{sheet}(\kappa_0) - \sqrt{(A \sin \kappa_T - 322.5)^2 + (A \cos \kappa_T - L_{car})^2 + 1} \quad (\text{E.40})$$

The error estimation on this calculation due to error on the position measurement is estimate to be about ± 0.5 mm.

Cases	Measured angle (°)	κ_0 (°)
MS flat AWA 40°	78	-12
MS max AWA 40°	67	-23
MS std AWA 40°	65	-25
Spi	71	-19
MS AWA 60°	59	-31
Chariot 205 mm	56	-34
Isolated mark	53	-37

Table E.5 – Mark measurement for κ_0 calculation.

Upwind dynamic command law:

For upwind situation we got two formulas. The first one is used if the low friction ring stays on its static x position on the rail .

$$L_{sheet}(\kappa_T) = \sqrt{(A \sin \kappa_0 - 332.5)^2 + (A \cos \kappa_0 - L_{car})^2 + 1} + L_{sheet}(\kappa_0) - \sqrt{(A \sin \kappa_T - 332.5)^2 + (A \cos \kappa_T - L_{car})^2 + 1} \quad (\text{E.41})$$

The second one is used if the low friction ring is screwed in a forward position of the rail location in order to avoid the low friction ring motion during dynamic trimming.

$$L_{sheet}(\kappa_T) = \sqrt{(A \sin \kappa_0 - 322.5)^2 + (A \cos \kappa_0 - L_{car})^2 + 1} + L_{sheet}(\kappa_0) - \sqrt{(A \sin \kappa_T - 322.5)^2 + (A \cos \kappa_T - L_{car})^2 + 1} \quad (\text{E.42})$$

With the previous formulation we can compute the instantaneous sheet length from any initial situation used to set up the zero position of the stepper motor which is useful for numerical experimental comparison. Some analytical properties of L_{sheet} are studied next. However for FSI study, centering the oscillating value around its mean value can be useful therefore we are going to compute $L_{sheet}(\kappa_T) - \overline{L_{sheet}(\kappa_T)}$ after.

Analytical study of the dynamic trimming is done here. We study each part of the definition of the sheet length separately. We analytically study a bit further the analytical definition in equation E.35 in order to demonstrate some of the associated properties. For the x coordinates square difference part:

$$(x_C + A \sin(\kappa_T) - x_{O_{disk}})^2 = A^2 \sin^2(\kappa_T) + 2A(x_C - x_{O_{disk}}) \sin(\kappa_T) + (x_C - x_{O_{disk}})^2 \quad (\text{E.43})$$

For the y coordinates square difference part:

$$(-L_{car} + A \cos(\kappa_T) - y_{O_{disk}})^2 = A^2 \cos^2(\kappa_T) - 2A(L_{car} + y_{O_{disk}}) \cos(\kappa_T) + (L_{car} + y_{O_{disk}})^2 \quad (\text{E.44})$$

Regrouping the different elements:

$$L_m(\kappa_T) = \sqrt{2A(x_C - x_{O_{disk}}) \sin(\kappa_T) - 2A(L_{car} + y_{O_{disk}}) \cos(\kappa_T) + A^2 + (x_C - x_{O_{disk}})^2 + (L_{car} + y_{O_{disk}})^2 + (z_C - z_{O_{disk}})^2} \quad (\text{E.45})$$

Considering $x_C \neq x_{O_{disk}}$ we can use the notation:

$$L_m(\kappa_T) = \gamma_1 \sqrt{\sin(\kappa_T)} - \gamma_2 \cos(\kappa_T) + \gamma_3 \quad (\text{E.46})$$

where:

$$\begin{cases} \gamma_1 = \sqrt{2A(x_C - x_{O_{disk}})} \\ \gamma_2 = \frac{L_{car} + y_{O_{disk}}}{x_C - x_{O_{disk}}} \\ \gamma_3 = \frac{A^2 + (x_C - x_{O_{disk}})^2 + (L_{car} + y_{O_{disk}})^2 + (z_C - z_{O_{disk}})^2}{2A(x_C - x_{O_{disk}})} \end{cases} \quad (\text{E.47})$$

We can identify the term γ_2 to the opposite of the cotangent of the angle κ_a which corresponds to the situation where the sheet length is maximal (when L_m is minimal). This situation occurs when the pin P is aligned in the direction $M_{amax}C$ and belongs to the segment $[O_{disk}M_{amax}]$. In the experimental case $\tan(\kappa_a) \neq 0$ therefore we can identify $\gamma_2 = -\frac{1}{\tan(\kappa_a)}$.

$$L_m(\kappa_T) = \gamma_1 \sqrt{\sin(\kappa_T) + \frac{\cos(\kappa_a) \cos(\kappa_T)}{\sin(\kappa_a)}} + \gamma_3 \quad (\text{E.48})$$

$$L_m(\kappa_T) = \gamma_1 \sqrt{\frac{\sin(\kappa_T) \sin(\kappa_a) + \cos(\kappa_a) \cos(\kappa_T)}{\sin(\kappa_a)}} + \gamma_3 \quad (\text{E.49})$$

$$\boxed{L_m(\kappa_T) = \gamma_1 \sqrt{\frac{\cos(\kappa_T - \kappa_a)}{\sin(\kappa_a)}} + \gamma_3} \quad (\text{E.50})$$

Considering that $180^\circ > \kappa_a > 0^\circ$ we can rewrite this equation using:

$$L_m(\kappa_T) = \gamma_4 \sqrt{\cos(\kappa_T - \kappa_a) + \gamma_5} \quad (\text{E.51})$$

where:

$$\begin{cases} \gamma_4 = \frac{\gamma_1}{\sqrt{\sin(\kappa_a)}} \\ \gamma_5 = \sin(\kappa_a) \gamma_3 \end{cases} \quad (\text{E.52})$$

$$\begin{cases} \gamma_4 = \frac{\gamma_1}{\sqrt{\sin(\kappa_a)}} = \sqrt{\frac{2A(x_C - x_{O_{disk}})}{x_C - x_{O_{disk}}}} = \sqrt{2A \sqrt{(x_C - x_{O_{disk}})^2 + (-L_{car} + y_{O_{disk}})^2}} \\ \gamma_5 = \frac{A^2 + (x_C - x_{O_{disk}})^2 + (-L_{car} + y_{O_{disk}})^2 + (z_C - z_{O_{disk}})^2}{2A(x_C - x_{O_{disk}})} \frac{x_C - x_{O_{disk}}}{\sqrt{(x_C - x_{O_{disk}})^2 + (-L_{car} + y_{O_{disk}})^2}} \end{cases} \quad (\text{E.53})$$

So we can consider the analytical form as $L_m(\kappa_T) = \gamma_4 \sqrt{\cos(\kappa_T - \kappa_a) + \gamma_5}$ where

$$\begin{cases} \gamma_4 = \sqrt{2A \sqrt{(x_C - x_{O_{disk}})^2 + (-L_{car} + y_{O_{disk}})^2}} \\ \gamma_5 = \frac{A^2 + (x_C - x_{O_{disk}})^2 + (-L_{car} + y_{O_{disk}})^2 + (z_C - z_{O_{disk}})^2}{2A \sqrt{(x_C - x_{O_{disk}})^2 + (-L_{car} + y_{O_{disk}})^2}} \end{cases} \quad (\text{E.54})$$

Eventually we get $\boxed{L_m(\kappa_T) = \gamma_4 \sqrt{\cos(\kappa_T - \kappa_a) + \gamma_5}}$ with

$$\boxed{\begin{cases} \gamma_4 = \sqrt{2A \sqrt{(x_C - x_{O_{disk}})^2 + (-L_{car} + y_{O_{disk}})^2}} \\ \gamma_5 = \frac{A^2 + (x_C - x_{O_{disk}})^2 + (-L_{car} + y_{O_{disk}})^2 + (z_C - z_{O_{disk}})^2}{2A \sqrt{(x_C - x_{O_{disk}})^2 + (-L_{car} + y_{O_{disk}})^2}} \end{cases}} \quad (\text{E.55})$$

Contrary to what can be expected, this formulation shows that the sheet length is not directly a cosine function but corresponds to the square root applied onto the cosine function summed with a constant. This computation is different from a simple model which consider that the length is the sum of the initial length and the cosine function applied to the angle $L_m(\kappa_T) = L_m 0 + \cos(\kappa - 90)$. Fig. E.4 indicates the error between the cosine model and the model computed by $L_m(\kappa_T) = \gamma_4 \sqrt{\cos(\kappa_T - \kappa_a) + \gamma_5}$ for two configurations.

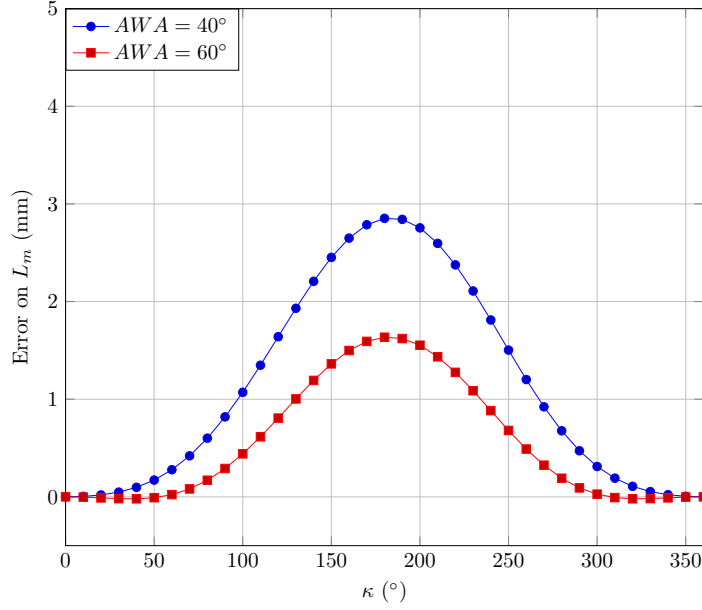


Figure E.4 – Error computation of dynamic sheet length model law. Results are tested for $A = 20$ mm with the standard mainsail.

The greater the L_{car} , the lower the maximum error. The maximum error can reach values up to 3 mm in the presented configuration. Therefore it is important to take into account the model computed in this part to minimize the error on the sheet length especially for numerical experimental comparison.

Let's check that $\gamma_5 \geq 1$ to ensure that the quantity under the square root is always positive.

$$\gamma_5 = \frac{A^2 + (x_C - x_{O_{disk}})^2 + (-L_{car} + y_{O_{disk}})^2 + (z_C - z_{O_{disk}})^2}{2A\sqrt{(x_C - x_{O_{disk}})^2 + (-L_{car} + y_{O_{disk}})^2}} \quad (\text{E.56})$$

Showing that $1 \leq \gamma_5 \Leftrightarrow 0 \leq \gamma_5 - 1$

$$\gamma_5 - 1 = \frac{A^2 + (x_C - x_{O_{disk}})^2 + (-L_{car} + y_{O_{disk}})^2 + (z_C - z_{O_{disk}})^2}{2A\sqrt{(x_C - x_{O_{disk}})^2 + (-L_{car} + y_{O_{disk}})^2}} - 1 \quad (\text{E.57})$$

$$\gamma_5 - 1 = \frac{A^2 + (x_C - x_{O_{disk}})^2 + (-L_{car} + y_{O_{disk}})^2 + (z_C - z_{O_{disk}})^2 - 2A\sqrt{(x_C - x_{O_{disk}})^2 + (-L_{car} + y_{O_{disk}})^2}}{2A\sqrt{(x_C - x_{O_{disk}})^2 + (-L_{car} + y_{O_{disk}})^2}} \quad (\text{E.58})$$

$$\gamma_5 - 1 = \frac{(A - \sqrt{(x_C - x_{O_{disk}})^2 + (-L_{car} + y_{O_{disk}})^2})^2 + (z_C - z_{O_{disk}})^2}{2A\sqrt{(x_C - x_{O_{disk}})^2 + (-L_{car} + y_{O_{disk}})^2}} \geq 0 \quad (\text{E.59})$$

$$\gamma_5 - 1 \geq 0 \quad (\text{E.60})$$

$$\gamma_5 \geq 1 \quad (\text{E.61})$$

Different properties of $L_m(\kappa_T)$ can be checked using this last analytical expression:

1. the extremum properties which may occurs for $\kappa_T = \kappa_a$ (where the sheet length L_{sheet} is maximal i.e. L_m is minimal) and $\kappa_T = \kappa_a + 180^\circ$ (where the sheet length L_{sheet} is minimal i.e. L_m is maximal).

$$\frac{dL_m(\kappa_T)}{d\kappa_T} = 0 \Leftrightarrow -\frac{\sin(\kappa_T - \kappa_a)\gamma_4}{2\sqrt{\cos(\kappa_T - \kappa_a) + \gamma_5}} = 0 \quad (\text{E.62})$$

$$\frac{dL_m(\kappa_T)}{d\kappa_T} = 0 \Leftrightarrow -\sin(\kappa_T - \kappa_a)\gamma_4 = 0 \quad (\text{E.63})$$

$$\frac{dL_m(\kappa_T)}{d\kappa_T} = 0 \Leftrightarrow \begin{cases} \sin(\kappa_T - \kappa_a) = 0 \\ \text{or} \\ \gamma_4 = 0 \end{cases} \quad (\text{E.64})$$

$$\frac{dL_m(\kappa_T)}{d\kappa_T} = 0 \Leftrightarrow \begin{cases} \kappa_T = \kappa_a \text{ or } \kappa_T = \kappa_a + 180^\circ \\ \text{or} \\ \gamma_4 = 0 \end{cases} \quad (\text{E.65})$$

Considering $\gamma_4 \neq 0$ this last equivalence verifies the expected property concerning the extrema positions which corresponds to $P \in [O_{disk}M_{amax}]$ or $P \in [O_{disk}M_{amin}]$.

2. the $L_m(\kappa_T - 2(\kappa_T - \kappa_a)) = L_m(\kappa_T)$ equation is associated to the symmetry property around the direction defined by the κ_a angle corresponding to the pin aligned on $[O_{disk}C]$ situation. Here we consider that the rotating plate is parallel to the $(0_{model\ frame}, x, y)$ plan.

$$L_m(\kappa_T - 2(\kappa_T - \kappa_a)) = L_m(2\kappa_a - \kappa_T) \quad (\text{E.66})$$

$$L_m(\kappa_T - 2(\kappa_T - \kappa_a)) = \gamma_4\sqrt{\cos(2\kappa_a - \kappa_T - \kappa_a) + \gamma_5} \quad (\text{E.67})$$

$$L_m(\kappa_T - 2(\kappa_T - \kappa_a)) = \gamma_4\sqrt{\cos(\kappa_a - \kappa_T) + \gamma_5} \quad (\text{E.68})$$

$$L_m(\kappa_T - 2(\kappa_T - \kappa_a)) = \gamma_4\sqrt{\cos(\kappa_T - \kappa_a) + \gamma_5} \quad (\text{E.69})$$

$$L_m(\kappa_T - 2(\kappa_T - \kappa_a)) = L_m(\kappa_T) \quad (\text{E.70})$$

The symmetry property is verified.

Mean sheet length expression of $L_{sheet}(\kappa_T)$ is one of the interesting parameter that can be used to plot some FSI graphs, especially when the X axis is centred around $L_{sheet}(\kappa_T) - \overline{L_{sheet}(\kappa_T)}$. This paragraph shows that the averaged definition chosen here is important. Three different definitions which can be used as the mean value definition of the sheet length $\overline{L_{sheet}(\kappa_T)}$ are going to be compared:

- the integral mean sheet length definition $\overline{L_{sheet}(\kappa_T)} = \frac{1}{2\pi} \int_0^{2\pi} L_{sheet}(\kappa_T) d\kappa_T$
- the mean sheet length definition using the average of the extreme value. Using this definition will make $L_{sheet}(\kappa_T) - \overline{L_{sheet}(\kappa_T)}$ evolves exactly between the value $\overline{L_{sheet}(\kappa_T)} - A$ and $\overline{L_{sheet}(\kappa_T)} + A$.
- the sheet length $L_{sheet}(\kappa_p)$ when the eccentric is in the perpendicular direction of the direction defined by $(O_{disk}C)$. This length was used to set up the configuration where the sheet length corresponds to the previously found two-parameter optimum. Even if it does not correspond to the mean value of the sheet length using the integral definition, this perpendicular position was chosen as the one where the optimum sheet length was set up. The motor has been zeroed in this position for the first frequency $f = 0$ Hz. This technique was quite fast, did not require computation, accurate to reproduce, and easy to use.

The integral mean sheet length definition is given by:

$$\overline{L_{sheet}(\kappa_T)} = \frac{1}{2\pi} \int_0^{2\pi} L_{sheet}(\kappa_T) d\kappa_T \quad (\text{E.71})$$

Using the sheet length definition in Eq. E.33:

$$\overline{L_{sheet}(\kappa_T)} = L_m(\kappa_0) + L_{sheet}(\kappa_0) - \frac{1}{2\pi} \int_0^{2\pi} L_m(\kappa_T) d\kappa_T \quad (\text{E.72})$$

Because the initial parameters remain constant for a given run, the only unknown part remaining is the integral:

$$\overline{L_m(\kappa_T)} = \frac{1}{2\pi} \int_0^{2\pi} \gamma_4 \sqrt{\cos(\kappa_T - \kappa_a) + \gamma_5} d\kappa_T \quad (\text{E.73})$$

$$\overline{L_m(\kappa_T)} = \frac{\gamma_4}{2\pi} \int_0^{2\pi} \sqrt{\cos(\kappa_T - \kappa_a) + \gamma_5} d\kappa_T \quad (\text{E.74})$$

This kind of integral might involve elliptic integral function. No analytical formulation has been found to be able to compute this quantity without any numerical approximation. The mean sheet length over one rotation given by the integral definition might not correspond to the perpendicular position situation where P belongs to $[M_{pw}M_{pl}]$ where $L_m(\kappa_0) = \gamma_4 \sqrt{\gamma_5}$. So far only a minimum and a maximum value of this quantity have been determined using the following notations presented on Fig. E.5.

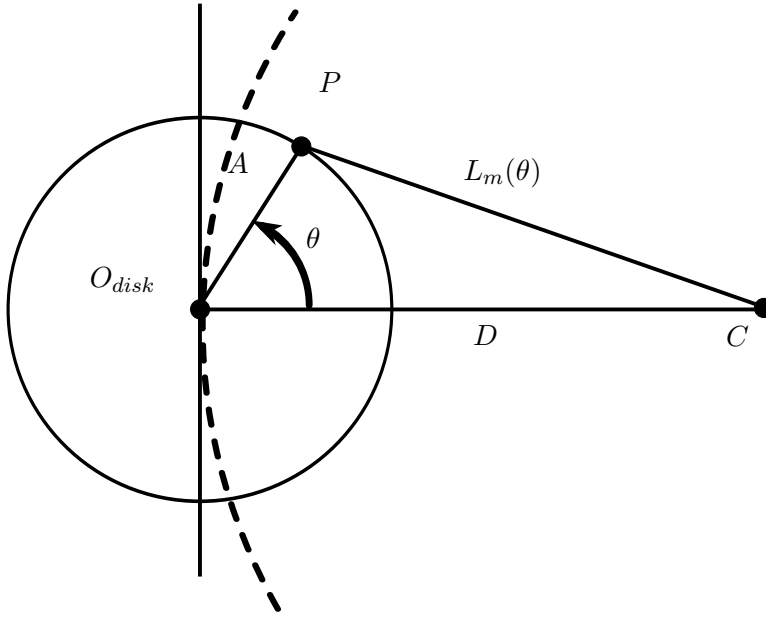


Figure E.5 – Reorientation of the dynamic trimming configuration.

Using implicit coordinates in the new geometry configuration, the length is now defined using the angle θ as:

$$L_m(\theta) = \sqrt{(A \cos \theta - D)^2 + (A \sin \theta)^2} \tag{E.75}$$

$$L_m(0^\circ) = D - A \tag{E.76}$$

$$L_m(90^\circ) = L_m(\kappa_0) = \sqrt{A^2 + D^2} \tag{E.77}$$

The average length is given by the following equation:

$$\overline{L_m(\theta)} = \frac{1}{2\pi} \int_0^{2\pi} \sqrt{(A \cos \theta - D)^2 + (A \sin \theta)^2} d\theta \tag{E.78}$$

We first determine a minimum value for the average length.

$$\frac{1}{2\pi} \int_0^{2\pi} \sqrt{(A \cos \theta - D)^2} d\theta \leq \overline{L_m(\theta)} \tag{E.79}$$

$$\frac{1}{2\pi} \int_0^{2\pi} |D - A \cos \theta| d\theta \leq \overline{L_m(\theta)} \tag{E.80}$$

In our case, $0 < A < D$

$$\frac{1}{2\pi} \int_0^{2\pi} (D - A \cos \theta) d\theta \leq \overline{L_m(\theta)} \tag{E.81}$$

$$D - \frac{A}{2\pi} [\sin \theta]_0^{2\pi} \leq \overline{L_m(\theta)} \tag{E.82}$$

$$\boxed{D \leq \overline{L_m(\theta)}} \tag{E.83}$$

The averaged value is longer than the distance between the disk center and the car traveller location. The associated angular position is therefore on the left side of the dashed limit indicating the

distance D on Fig. E.5. We now determine a maximum value for the averaged length:

$$\overline{L_m(\theta)} \leq \frac{1}{2\pi} \int_0^{2\pi} \sqrt{(A \cos \theta - D)^2} + \sqrt{(A \sin \theta)^2} d\theta \quad (\text{E.84})$$

$$\overline{L_m(\theta)} \leq \frac{1}{2\pi} \int_0^{2\pi} |D - A \cos \theta| d\theta + \frac{1}{2\pi} \int_0^{2\pi} |A \sin \theta| d\theta \quad (\text{E.85})$$

In our case, $0 < A < D$

$$\overline{L_m(\theta)} \leq \frac{1}{2\pi} \int_0^{2\pi} (D - A \cos \theta) d\theta + \frac{1}{2\pi} \int_0^{\pi} A \sin \theta d\theta + \frac{1}{2\pi} \int_{\pi}^{2\pi} -A \sin \theta d\theta \quad (\text{E.86})$$

$$\overline{L_m(\theta)} \leq D + \frac{1}{2\pi} [-A \sin \theta]_0^{\pi} + \frac{1}{2\pi} [A \cos \theta]_{\pi}^{2\pi} \quad (\text{E.87})$$

$$\overline{L_m(\theta)} \leq D + \frac{1}{2\pi} 2A + \frac{1}{2\pi} 2A \quad (\text{E.88})$$

$$\boxed{\overline{L_m(\theta)} \leq D + \frac{2A}{\pi}} \quad (\text{E.89})$$

The more restrained limit found so far are:

$$\boxed{D \leq \overline{L_m(\theta)} \leq D + \frac{2A}{\pi}} \quad (\text{E.90})$$

The extreme averaged mean sheet length definition is given by:

$$\overline{L_{sheet}(\kappa_T)} = \frac{\max(L_{sheet}) + \min(L_{sheet})}{2} \quad (\text{E.91})$$

This definition implies that:

$$\begin{cases} \overline{L_{sheet}(\kappa_T)} = \frac{\min(L_{sheet}) + 2A + \min(L_{sheet})}{2} = \min(L_{sheet}) + A \\ \overline{L_{sheet}(\kappa_T)} = \frac{\max(L_{sheet}) - 2A + \max(L_{sheet})}{2} = \max(L_{sheet}) - A \end{cases} \quad (\text{E.92})$$

As shown previously the extreme configuration occurs when $\kappa_T = \kappa_a$ or $\kappa_T = \kappa_a + 180^\circ$. Let's consider first that $\kappa_T = \kappa_a$:

$$L_{sheet}(\kappa_a) = L_m(\kappa_0) + L_{sheet}(\kappa_0) - L_m(\kappa_a) \quad (\text{E.93})$$

$$L_{sheet}(\kappa_a) = L_m(\kappa_0) + L_{sheet}(\kappa_0) - \gamma_4 \sqrt{1 + \gamma_5} \quad (\text{E.94})$$

Let's consider now that $\kappa_T = \kappa_a + 180^\circ$:

$$L_{sheet}(\kappa_a + 180^\circ) = L_m(\kappa_0) + L_{sheet}(\kappa_0) - \gamma_4 \sqrt{-1 + \gamma_5} \quad (\text{E.95})$$

Therefore for the definition of the averaged using the mean value of maximum and minimum value:

$$\boxed{\overline{L_{sheet}(\kappa_T)} = L_m(\kappa_0) + L_{sheet}(\kappa_0) - \gamma_4 \frac{\sqrt{1 + \gamma_5} + \sqrt{-1 + \gamma_5}}{2}} \quad (\text{E.96})$$

Integral mean sheet length vs the perpendicular situation comparison is important. We want to show now that the mean value defined as the averaged of the maximum and minimum values is different from the value of the sheet length when setting up the initial position in the perpendicular configuration, *i.e.* $\kappa_0 = \kappa_p = \kappa_a - 90^\circ$.

$$\overline{L_{sheet}(\kappa_T)} = L_m(\kappa_a - 90^\circ) + L_{sheet}(\kappa_0) - \gamma_4 \frac{\sqrt{1 + \gamma_5} + \sqrt{-1 + \gamma_5}}{2} \quad (\text{E.97})$$

$$\overline{L_{sheet}(\kappa_T)} = \gamma_4 \sqrt{\gamma_5} + L_{sheet}(\kappa_0) - \gamma_4 \frac{\sqrt{1 + \gamma_5} + \sqrt{-1 + \gamma_5}}{2} \quad (\text{E.98})$$

$$\overline{L_{sheet}(\kappa_T)} = L_{sheet}(\kappa_0) + \gamma_4 \left(\sqrt{\gamma_5} - \frac{\sqrt{1 + \gamma_5} + \sqrt{-1 + \gamma_5}}{2} \right) \quad (\text{E.99})$$

Due to the geometric configuration we have $\gamma_4 > 0$ so the sign of $v(\gamma_5) = \sqrt{\gamma_5} - \frac{\sqrt{1 + \gamma_5} + \sqrt{-1 + \gamma_5}}{2}$ has to be study for $\gamma_5 \in [1, +\infty[$. Let's demonstrate that: $\forall \gamma_5 \in [1, +\infty[, v(\gamma_5) > 0$

$$v(\gamma_5) = \sqrt{\gamma_5} \left(1 - \frac{\sqrt{1 + \gamma_5} + \sqrt{-1 + \gamma_5}}{2\sqrt{\gamma_5}} \right) \quad (\text{E.100})$$

$$v(\gamma_5) = \sqrt{\gamma_5} \left(1 - \frac{1}{2} \left(\sqrt{1 + \frac{1}{\gamma_5}} + \sqrt{1 - \frac{1}{\gamma_5}} \right) \right) \quad (\text{E.101})$$

Showing

$$\forall \gamma_5 \in [1, +\infty[, v(\gamma_5) > 0 \Leftrightarrow \forall \gamma_5 \in [1, +\infty[, \sqrt{1 + \frac{1}{\gamma_5}} + \sqrt{1 - \frac{1}{\gamma_5}} < 2 \quad (\text{E.102})$$

Replacing $x = \frac{1}{\gamma_5}$

$$\forall \gamma_5 \in [1, +\infty[, v(\gamma_5) > 0 \Leftrightarrow \forall x \in]0, 1], \sqrt{1 + x} + \sqrt{1 - x} < 2 \quad (\text{E.103})$$

Having $\forall x \in]0, 1], 0 < \sqrt{1 + x} + \sqrt{1 - x}$, we use the square power of previous results:

$$\forall \gamma_5 \in [1, +\infty[, v(\gamma_5) > 0 \Leftrightarrow \forall x \in]0, 1], 0 < (\sqrt{1 + x} + \sqrt{1 - x})^2 < 4 \quad (\text{E.104})$$

$$\forall \gamma_5 \in [1, +\infty[, v(\gamma_5) > 0 \Leftrightarrow \forall x \in]0, 1], 0 < (1 + x + 1 - x + 2\sqrt{1 + x}\sqrt{1 - x}) < 4 \quad (\text{E.105})$$

$$\forall \gamma_5 \in [1, +\infty[, v(\gamma_5) > 0 \Leftrightarrow \forall x \in]0, 1], 0 < 2(1 + \sqrt{1 + x}\sqrt{1 - x}) < 4 \quad (\text{E.106})$$

$$\forall \gamma_5 \in [1, +\infty[, v(\gamma_5) > 0 \Leftrightarrow \forall x \in]0, 1], 0 < 2(1 + \sqrt{1 - x^2}) < 4 \quad (\text{E.107})$$

$$\forall \gamma_5 \in [1, +\infty[, v(\gamma_5) > 0 \Leftrightarrow \forall x \in]0, 1], 0 < \sqrt{2}\sqrt{1 + \sqrt{1 - x^2}} < 2 \quad (\text{E.108})$$

$$\forall \gamma_5 \in [1, +\infty[, v(\gamma_5) > 0 \Leftrightarrow \forall x \in]0, 1], 0 < \sqrt{1 + \sqrt{1 - x^2}} < \sqrt{2} \quad (\text{E.109})$$

The square root function $x \mapsto \sqrt{x}$ being increasing on $[0, +\infty[$:

$$\forall \gamma_5 \in [1, \infty[, v(\gamma_5) > 0 \Leftrightarrow \forall x \in]0, 1], 0 < \sqrt{1 - x^2} < 1 \quad (\text{E.110})$$

The last condition being always verified, we can conclude that:

$$\overline{L_{sheet}(\kappa_T)} = L_{sheet}(\kappa_0) + \gamma_4 \left(\sqrt{\gamma_5} - \frac{\sqrt{1+\gamma_5} + \sqrt{-1+\gamma_5}}{2} \right) > L_{sheet}(\kappa_0) \quad (\text{E.111})$$

This section demonstrates that the mean value using the definition of the average of the maximum and minimum values is not equal to the value of the sheet length when the point P is in the perpendicular situation. Using the property from equation E.92, we get:

$$\begin{cases} \min(L_{sheet}) > L_{sheet}(\kappa_0) - A \\ \max(L_{sheet}) > L_{sheet}(\kappa_0) + A \end{cases} \quad (\text{E.112})$$

These equations explain the minimum and maximum location compared to $L_{sheet} - L_{sheet_0}$ on Fig. 3.34 or 3.38.

Conclusions about the dynamic trimming system:

An accurate modelling of the trimming system used for the sheet length computation is important. The sheet length cannot be modelled using a simple sinusoidal law. The geometric parameters, including the initial position at the static point associated to the static optimum for the car traveller have to be taken into account. The sheet length computation law is provided and has been used in this thesis to define the Lissajou representation. As a perspective, it could also be used for unsteady FSI simulation of the mainsail pumping. Several properties of the sheet length computation have been verified.

F

Wind tunnel downwind configuration

This appendix provides informations about the model in downwind configuration. Some geometrical aspects are presented. Tab. F.1 and Tab. F.2 give the geometry coordinates in the model frame of the different points. Some differences exist between the experimental campaigns due to a change in the geometry configuration.

mm	x	y	z
Head	-91	0	2100
Tack	1091	0	-1
Clew	-836	-180	3
Clew block exit	-874	-175	3
Clew block axis	-874	-168	3
Clew block entry	-874	-154	3
Motor axis	-280	0	-34

Table F.1 – Coordinate of points in the model frame for the 2015 experimental campaign. The model frame origin (mast step) is 67 mm height above the wind tunnel floor. The altitude for the motor axis is the one to use for the eccentric altitude to compute the dynamic sheet length.

mm	x	y	z
Head	-88.4	0	2100.5
Tack	1087.6	0	-32.5
Clew	-837.6	-178.5	34.5
Clew block exit	-860.6	-173.5	23.5
Clew block axis	-860.6	-166.5	23.5
Clew block entry	-860.6	-152.5	23.5
Motor axis	-230.2	0	-89

Table F.2 – Coordinate of points in the model frame for the 2016 experimental campaign. The model frame origin (mast step) is 180 mm height above the wind tunnel floor. The altitude for the motor axis is the one to use for the eccentric altitude to compute the dynamic sheet length.

To compute the dynamic sheet length (not presented in this thesis for downwind), the same methods described in App. E can be used with the numerical value provided in Tab. F.1 and Tab. F.2.

G Sail cloth properties

This appendix gives basic descriptions about sail cloth and provides the properties of the one used during this PhD project for the model sails. Two materials are used: AirX 500 for the mainsails and two spinnakers (sailcloth type from Bainbridge international shown on Fig. G.1b), and SuperKote 0.75 for two other spinnakers (sailcloth from Contender Sailcloth[®] shown on Fig. G.1c). A short description of sail cloth type is provided first, defining the sail cloth properties and vocabulary. Eventually the properties of the sail cloths used in this PhD project are provided.

Sail cloths have benefit from many developments in the past decades, essentially supported by the need of sails that were able to maintain their shapes through time in different wind and sea conditions. Reader is refer to [Taibi, 2001, Bohé, 2005, Augier, 2012, Durand, 2012, Voiles et Voiliers, 2014] for more details about general cloths and sail cloths technology and properties. Here the cloths used for the model sails are part of the simplest one that can be found in the sailing industry. Both are part of the woven type sails manufactured as illustrated in Fig. G.1a.

Basic sailcloth are woven on a loom and used to be fill-oriented weave. The warp yarns run vertical along the roll of the cloth and the fill yarns run horizontal. A fill oriented cloth has a straight fill yarn and a crimped warp yarn providing higher load resistance in the fill direction. Modern manufacturing techniques enable to produce warp oriented cloth. The cloth has therefore crimped fill yarns and straight warp yarns providing higher resistance in the warp direction as indicated for the cloths materials used for the model sails. It can be used to get longer panels where the loads are directed in their longest direction which is nowadays usually the case for triradial woven cloth design headsail.

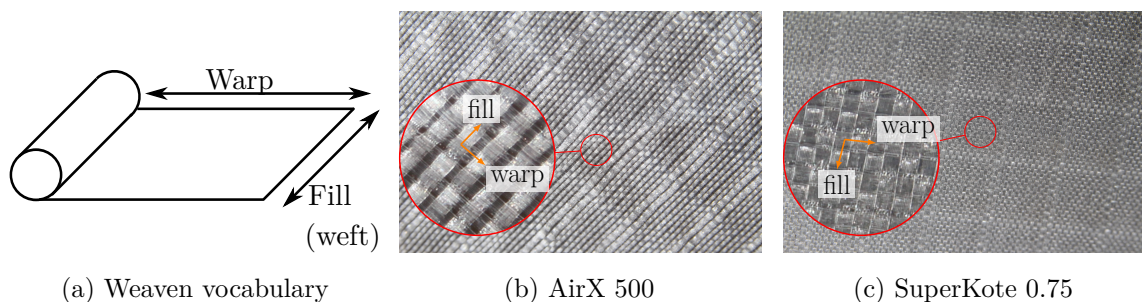


Figure G.1 – Weaven orientation and photographs of cloths. Photographs credit: Joseph Poupin. Magnification factor on photographs: 5.

Here is described how the cloths properties that can be used by the structural FEM code ARA are obtained from the raw data. More refined model could have been implemented following the method provided in [Bles et al., 2009] however the data available from standard tests do not provide information to establish such a model. Moreover, the use of these cloths in wind tunnel conditions may only require the linear behaviour part of the material. These raw data are usually provided by the sailcloth manufacturer and transmitted by the sail maker. Most of the time, the stretch properties are measured on standardized cloth sample of dimensions: 2 inch width and 16 inch long. The units provided in the sail cloth manufacturing field are usually in the imperial system units and transformed into the equivalent in the international system of units (1inch= 0.0254 m, 1lbs corresponds to a mass of 0.453 592 37 kg). Tabs G.1 and G.2 provides the raw properties of the materials.

The surface mass of the AirX 500 cloth is 35 g m^{-2} which is lighter than the SuperKote 0.75 cloth with 40 g m^{-2} . The two cloths are dedicated to spinnaker manufacturing. The SuperKote 0.75 cloth corresponds to a polyurethane coated nylon fibre. The data to compute the behaviour matrices of both materials must remains on the linear elastic part of the behaviour the cloth.

	Anglo saxon Units		SI Units	
	Load (lbs)		Loads (N)	
	20	40	88.99482	177.98965
Direction	Elongation (100 inch)		Elongation (m)	
Warp (0°)	17	44	0.00432	0.01118
Bias (45°)	21.9		0.00556	
Weft/Fill (90°)	47	90	0.01194	0.02286

Table G.1 – Data for AirX 500 cloth.

	Anglo saxon Units					SI Units				
	Load (lbs)				Elongation %	Load (N)				Elongation %
	5	10	15	20	1	20.81989	41.63978	62.45967	83.27956	1
Direction	Elongation (100 inch)				Load (lbs)	Elongation (m)				Load (N)
Warp (0°)	2.1	4.8	8	12.6	15	0.00053	0.00122	0.00203	0.00320	62.460
Bias (45°)	2.6	6	10.1	15.3	12.6	0.00066	0.00152	0.00257	0.00389	52.466
Weft/Fill (90°)	3.4	8.6	19.7	32.6	9.6	0.00086	0.00218	0.00500	0.00828	39.974

Table G.2 – Data for SuperKote 0.75 cloth.

From these data we want to determine the stiffness matrix (3×3) associated to the material in the linear behaviour part. Therefore for the SuperKote 0.75 we will consider only the data for a 1% strain of the sample. For the AirX 500 the lowest load available is used. We consider that the cloth corresponds to one network at 0° (warp direction), to another one at 90° (fill direction) combined with an homogeneous film with a Poisson coefficient $\nu = 0.3$. The behaviour matrix can be decomposed according the following equations:

$$[C] = a \begin{bmatrix} 1 & 0 & 0 \\ 0 & 1 & 0 \\ 0 & 0 & 1 \end{bmatrix} + b \begin{bmatrix} 1 & 0 & 0 \\ 0 & 1 & 0 \\ 0 & 0 & 1 \end{bmatrix} + c \begin{bmatrix} 1 & \nu & 0 \\ \nu & 1 & \frac{1-\nu}{2} \\ 0 & 0 & 1 \end{bmatrix} \quad (\text{G.1})$$

C_Y (-)	Lowest wind speed $U_{Pitot} = 2.1 \text{ m s}^{-1}$	Highest wind speed $U_{Pitot} = 4.4 \text{ m s}^{-1}$
AirX 500	3.10^{-9}	$1.2.10^{-8}$
SuperKote 0.75	$3.6.10^{-9}$	$1.5.10^{-8}$

Table G.3 – Cauchy number C_Y for the cloth in wind tunnel conditions, based on the order of magnitude of $[C]$.

a , b and c coefficients are determined using a Newton method using [Durand, 2012] work. The final stiffness matrices are:

$$[C]_{\text{AirX 500}} = \begin{bmatrix} 2.07428.10^5 & 5.64990.10^4 & 0 \\ 5.64990.10^4 & 7.50272.10^4 & 0 \\ 0 & 0 & 5.64990.10^4 \end{bmatrix} \quad (\text{G.2})$$

$$[C]_{\text{SuperKote 0.75}} = \begin{bmatrix} 1.50233.10^5 & 4.25657.10^4 & 0 \\ 4.25657.10^4 & 9.61507.10^4 & 0 \\ 0 & 0 & 4.25657.10^4 \end{bmatrix} \quad (\text{G.3})$$

The elastic modulus can be computed from the stiffness data using the sail thickness, considering a thickness about $th = 5.10 \times 10^{-5} \text{ m}$. For the spinnaker cases, the dimensionless Cauchy number evaluating the deformation due to fluid loading can be computed as $C_Y = \frac{\rho U_{Pitot}^2}{E}$ with E the elastic modulus defined as $E = \frac{C}{th}$ (C chosen as an order of magnitude of values in $[C]$). As indicated by G.3, the deformation of the sail cloths is expected to be small. The spinnaker FSI situation corresponds to a small deformation but important displacement of the sail, which justify the use of membrane model for numerical simulation.

H

Masts and battens properties

Mast properties used during the wind tunnel testing are determined in this appendix. Bending measurement have been carried out in the 14 mm diameter mast and battens sample (same material and diameter than the one used for the model mainsails). With the notation described on Fig. H.1a, the relative bending deformation (difference of bending b under the beam weight only and bending b under loading) is laser measured as a function of the local hooked mass acting as a local load F on the middle of the beam. In this configuration the bending $b = \frac{FL^3}{48EI}$ with E the Young modulus, and I the quadratic section moment in the associated directions. In our case, the mast has two main directions as defined in Fig. H.1b. The mast is considered as one material even being made of the main carbon part and its rear rail.

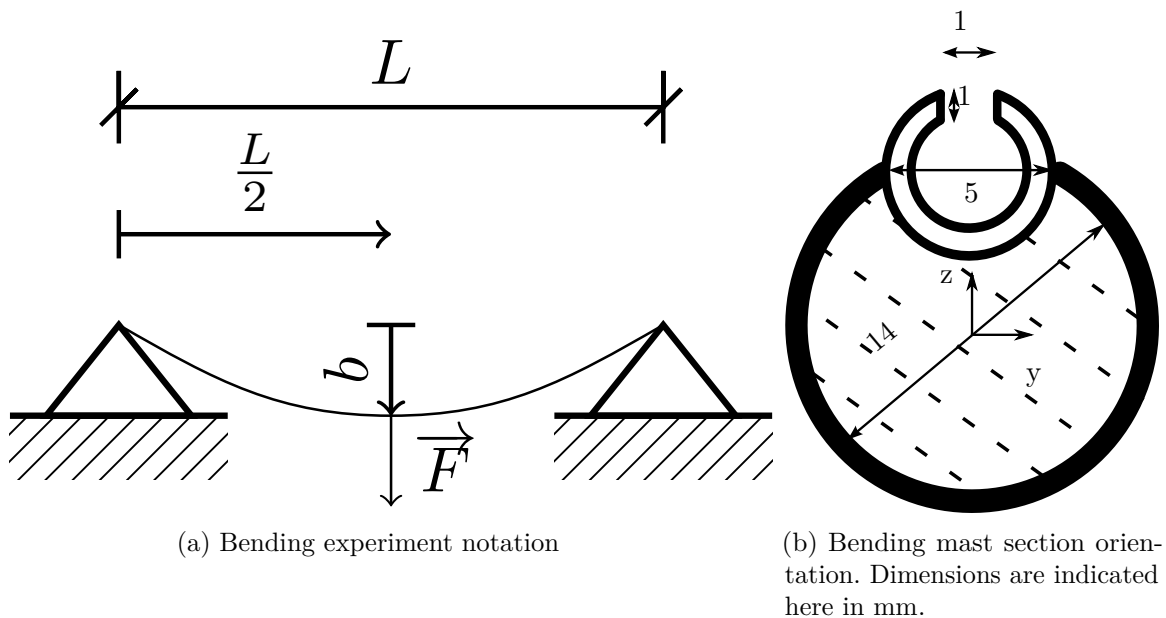


Figure H.1 – Bending experiments to measure the mechanical properties of structural parts of the model.

Measurement of bending b vs the loading F provides a linear curve which slope corresponds to $\frac{L^3}{48EI}$. The EI modulus results are then computed and presented in Tab. H.1. The boom and battens have a circular section which provides a quadratic moment of $\frac{\pi D^4}{64}$. For the mast with the rear rail,

the section shape considered is the one associated to the carbon material (the rail is not included *i.e.* corresponds to the dashed area on Fig. H.1b). A circular section in the mast case would have provide a quadratic moment about 1885.74 mm^4 . Battens have different length depending of their position on the sail.

Quantity	Units	14 mm diameter mast (carbon)	6 mm diameter boom	battens (carbon)
length	meter	2.304	0.6595	*
mass	kg	0.585	0.03	*
lineic mass ρ_l	kg m^{-1}	0.254	0.045	0.020
EI_{Gy}	N m^2	183.759	2.314	0.026
EI_{Gz}	N m^2	216.678	2.314	0.026
I_{Gy}	mm^4	1470	63.62	0.049
I_{Gz}	mm^4	1850	63.62	0.049
E_y	GPa	125	36.4	535
E_z	GPa	117	36.4	535
ES	N	$1.72 \cdot 10^7$	$1.03 \cdot 10^6$	$4.2 \cdot 10^5$

Table H.1 – Value of EI modulus and structural values for the different rig elements used in the wind tunnel experiments. The 20 mm mast used in 2016 was not tested. The full rig used in 2016 justifies small deformation assumption of the mast. * quantities depends of the batten number. High modulus carbon fibre can reach 825 GPa ([Dupupet, 2008]).

From the EI modulus, we can get the natural frequency of the mast corresponding to a free cantilevered circular beam ([Devalan, 2009, Dhomé, 2016]). The first natural frequency f_n is given by:

$$f_n = \frac{3.5}{2\pi} \sqrt{\frac{EI}{mL^3}} \quad (\text{H.1})$$

Considering $EI = 200 \text{ N m}^2$, $m = 0.585 \text{ kg}$ for the mass, $L = 2.1 \text{ m}$ for the free length, we get an estimation of the first natural frequency about $f_n = 3.4 \text{ Hz}$. In our case the section is close but not exactly circular. This may indicates that the resonance occurs for a reduced frequency close to $f_r = 0.46$ for the representative chord and wind speed used during upwind testing.

I

Directional Load Cells (DLC) applications

The DLC measure the forces direction of the spinnaker on the point where the DLC is attached to the sail and measure the force at that point at the same time. Here is suggested a method to evaluate the precision and draft of a DLC direction information. We consider two different time step, the initial one t_i and final one t_f . Between these two time step, the DLC is moved by a rotation of angle γ around the unspecified axes Δ . Using the rotation matrix notation $[R_T]$ applied on the DLC, we get equations I.1 and I.2 where $DLCframe)_{TF}^{t_i}$ is the orientation of the DLC frame expressed in the terrestrial frame at the time step t_i .

$$DLCframe)_{TF}^{t_i} = [R_T]^{t_i} Terrestrialframe)_{TF} = [R_T]^{t_i} [Id] = [R_T]^{t_i} \quad (I.1)$$

$$DLCframe)_{TF}^{t_f} = [R_T]^{t_f} \quad (I.2)$$

Because there is only a rotation \mathcal{R}_γ between the initial and final time step, equation I.3 is obtained. Without knowing anything about the Δ axes, we can get the rotation matrix $[R_\gamma]$ associated to the rotation \mathcal{R}_γ with equation I.4. Using the fact that $Tr([R_\gamma]_{TF}) = 1 + 2 \cos \gamma$ (Olinde-Rodrigue formulae for vectorial rotations), equation I.5 give the relation between two total rotation matrix given by yaw pitch roll data measured by a DLC at two time steps and the angle γ .

$$DLCframe)_{TF}^{t_f} = [R_\gamma]_{TF} DLCframe)_{TF}^{t_i} \quad (I.3)$$

$$[R_\gamma]_{TF} = [R_T]^{t_f} [R_T]^{t_i^{-1}} \quad (I.4)$$

$$\gamma = \arccos \frac{Tr \left([R_T]^{t_f} [R_T]^{t_i^{-1}} \right) - 1}{2} \quad (I.5)$$

With equation I.5, series of rotation tests can be done with the DLC attached to a turning axes in a random position with a random direction for the axes of rotation as long as the angle of rotation γ is measured. No calibration is required for setting the direction of rotation of the turning calibration device which make this method quite innovative. However this method will not give the precision in the real terrestrial frame TF but the precision in the calibration terrestrial frame seen by the DLC. Moreover, only a general information is provided here so if there is a draft or error on a specific angle, you do not know which angle is the origin of this draft.

J --- Résumé étendu en français

J.1 Introduction

J.1.1 Contexte

Au cours de ce dernier demi-siècle, la conception de voiles, notamment la phase de dessin, a bénéficié de l'évolution importante des moyens informatiques modernes. Les maîtres voiliers utilisent maintenant quotidiennement la conception assistée par ordinateurs et peuvent aussi disposer d'outils leur fournissant des résultats de simulations d'interaction fluide-structure sur les voiles et le gréement. Ces simulations permettent de prédire plus finement les efforts aérodynamiques générés afin d'optimiser le plan de voilure et d'alléger les structures à bord pour rendre les voiliers toujours plus performants. Ainsi ces simulations sont devenues complémentaires, voire ont pris le pas sur la connaissance empirique liée à la navigation et à un savoir faire ancestrale. Ces outils de simulation, souvent développés sous l'impulsion de la voile de compétition ou pour les besoins de voileries, ne permettent pas de modéliser à l'heure actuelle l'ensemble des configurations de navigations à une échelle de temps industrielle raisonnable. En particulier les écoulements fortement ou massivement détachés sur les voiles de portant nécessitent des moyens de simulations qui restent complexes et difficile à valider in situ dans des conditions instationnaires. L'instationnarité physique liée à l'environnement, aux mouvements du bateaux, aux réglages ou bien au comportement propre de la voile n'est alors pas encore couramment prise en compte lors des simulations.

Cependant la dynamique de certaines techniques utilisées en voile est souvent associée à des configurations plus performantes. C'est le cas par exemple du pumping de grand voile ou du repliement périodique du bord d'attaque d'un spinnaker. Les effets de ces techniques plébiscitées dans la communauté de navigants sont largement utilisés bien que pas complètement expliqués.

C'est pourquoi ces travaux de thèse du présent manuscrit se proposent d'apporter des mesures expérimentales inédites sur certains de ces phénomènes instationnaires observés sur les voiles. Ces travaux ont été réalisés dans le cadre du projet VOILENav commencé il y a 10 ans au sein du département de Mécanique et Energétique en Milieu Naval de l'Institut de recherche de l'Ecole Navale (IRENav). Ce projet a démarré avec le développement d'une instrumentation embarquée sur un voilier J80 par [Augier, 2012] qui a permis d'apporter des premières mesures quasi stationnaires ou instationnaires in situ pour des voiles de près. En parallèle [Durand, 2012], dans le cadre d'une collaboration entre la société K-Epsilon, l'Ecole Centrale de Nantes et l'IRENav, a développé des outils numériques instationnaires afin de modéliser ces situations. Le code structure éléments finis

ARA a été couplé au code AVANTI, utilisant la méthode fluide potentiel Vortex Lattice Method (VLM) adaptée aux écoulements attachés qui représentent la majorité des cas lors de navigation au près. Des simulations instationnaires en tangage ont été validées par les mesures expérimentales [Augier et al., 2013] et des simulations sur voiles de près rigides ont été validées par des mesures en soufflerie [Durand, 2012]. Le second outil d'interaction fluide structure couplant le code ARA et ISIS-CFD, développé par l'Ecole Centrale de Nantes (méthode Reynolds-Averaged Navier-Stokes (RANS) commercialisé sous le nom FINETM/Marine) est adapté aux conditions d'écoulement détaché. Les données expérimentales au portant restaient cependant nécessaire pour la validation de cet outil.

[Deparday, 2016] a permis d'étendre et d'adapter le système de mesure in situ aux voiles de portant dont la forme en navigation est plus complexe à mesurer. L'utilisation de techniques de photogrammétrie [Deparday, 2010] avec l'usage de cellules d'effort directionnel [Le Pelley et al., 2015] utilisées en collaboration avec [Motta et al., 2014, Motta, 2015] ont permis d'apporter des mesures dynamiques de l'évolution de la forme, des champs de pression et des efforts du spinnaker. L'étude du repliement périodique du guindant (bord d'attaque) de spinnaker a permis d'apporter une première explication de l'efficacité d'un tel réglage. [Durand et al., 2014] a pu réaliser des simulations sur ce phénomène afin de prédire la stabilité de spinnaker. A ce jour, aucune comparaison numérique expérimentale satisfaisante n'a pu être réalisée au cours de ce projet. La mesure du vent réel in situ à partir de l'instrumentation embarqué reste complexe bien que les travaux du doctorant Hugo Kerhascoët en collaboration avec la société NKE aient permis d'améliorer cette mesure ([Kerhascoët, 2017]). L'utilisation d'une soufflerie afin de mesurer des phénomènes d'interaction fluide structure instationnaire en milieu contrôlé était donc l'étape logique suivante.

Ces essais ont été possibles grâce au programme Sailing Fluids (<https://www.sailingfluids.org/>) qui développe les synergies dans le milieu de la recherche dans l'ingénierie des voiles entre l'Union Européenne et la Nouvelle-Zélande, regroupant l'IRENav à l'Ecole Navale, l'University de Newcastle et d'Edinburgh au Royaume-Uni et l'Université d'Auckland en Nouvelle-Zélande. Deux campagnes de trois mois ont pu être réalisées en 2015 et 2016 dans la très célèbre soufflerie Twisted Flow Wind Tunnel (TFWT) du Yacht Research Unit (YRU). Des essais sur le pumping de grand voile ou le repliement du guindant de spinnaker ont été menés sur des maquettes de voiles dessinées et réalisées par Incidence Sails. L'instationnarité observée fut alors générée par un réglage d'écoute dynamique dans le premier cas ou naturelle dans le second.

Ce projet a aussi bénéficié de nombreuses collaborations tel que le système Visualisation of Sail Position And Rig Shape (VSPARS) de [Le Pelley and Modral, 2008], certains instruments sur le voilier de la société NKE, du programme SailPack de la société BSG developments et du code d'interaction fluide structure ARAVANTI de la société k-Epsilon. Enfin la partie optimisation s'est appuyée sur les travaux du doctorant Matthieu Sacher ([Sacher et al., 2017]).

J.1.2 Méthodes et moyens pour l'étude de la physique des voiles

Les méthodes d'étude de l'interaction fluide structure et du comportement aéro-élastique des voiles peuvent être regroupées en trois groupes présentés dans cette section. On distingue souvent les essais au près des essais au portant car la nature de l'écoulement et le type de voiles utilisées peuvent être très différents. Enfin les études vont de l'approche statique simplifiée à l'approche

dynamique plus réaliste au vue des conditions normales de navigation. Un état de l'art est proposé dans les tableaux 3 and 4.

J.1.2.1 Les essais in situ

Cette méthode fût d'abord utilisée par les navigateurs de manière qualitative puis quantitative sur quelques données de navigation telles que la vitesse du bateau et du vent. La miniaturisation d'équipements électroniques et la diminution de leurs coûts ont rendu possible la mesure de bien d'autres données à bord en navigation. De nombreux projets ont permis d'instrumenter par exemple un dériveur [Williamson and Schutt, 2016], ou un quillard de sport [Augier, 2012]. Certaines campagnes d'essais se sont focalisées sur des données particulières telle que la mesure des champs de pression sur les voiles [Graves et al., 2008, Viola et al., 2010, Viola and Flay, 2010a] ou les efforts de gréements. Cependant pour mesurer les efforts aérodynamiques générés par les voiles, une balance doit être incorporée à la coque du bateau [Hochkirch and Brandt, 1999, Masuyama, 2014, Fossati et al., 2015a]. Ce type d'instrumentation reste onéreux et ne peut être monté que sur un bateau dédié à l'expérimentation. L'hypothèse de conditions statiques reste aussi difficile à obtenir lors d'essais. En J80, on peut en générale extraire 10 à 20 secondes de conditions stationnaires élargies sur le vent (tel que 10% de variation de vitesse et 4° de variation d'angle sur le vent apparent) proposée par [Deparday, 2016], sur plusieurs minutes d'enregistrement. La mesure du vent réel et de la dérive reste aussi complexe [Douguet, 2014].

J.1.2.2 Essais en soufflerie

La soufflerie peut fournir des conditions d'écoulement contrôlé facilitant l'approche statique. Le torseur d'effort aérodynamique est mesuré à l'aide d'une balance instrumentée qui couplée à la mesure de la pression dynamique permet l'obtention des coefficients aérodynamiques [Flay and Jackson, 1992, Flay, 1996, Hansen, 2006]. La vitesse du bateau sur la maquette immobile dans la veine est alors reproduite en modifiant le gradient de vent pour représenté le profil de vent apparent. Un twist doit être appliqué particulièrement pour les essais au portant. La soufflerie TFWT développée par [Flay and Vuletich, 1995, Flay, 1996] fût la première à réaliser ces conditions à l'aide de fanons. D'autres mesures peuvent être menées: la mesure de pression sur des voiles semi-rigides [McQuoid, 2010, Viola and Flay, 2011c, Bot et al., 2013] ou souples [Viola and Flay, 2015], la mesure d'effort, la mesure d'écoulement [Serres, 2004], la mesure de la forme de voile [Graf and Müller, 2009, Fossati et al., 2015b]. Des conditions dynamiques peuvent être simulées à l'aide de moteur ou vérin [Banks et al., 2010, Fossati and Muggiasca, 2011, Fossati and Muggiasca, 2012a, Aubin et al., 2016b]. L'utilisation de veine hydrodynamique est aussi possible pour utiliser des méthodes de visualisation d'écoulement en eaux sur des formes de voiles [Schutt and Williamson, 2016]. Cependant ces essais ont aussi des limitations: effet d'échelle due au non respect de nombre adimensionnel comme le Reynolds, ou des effets de blocage [Mompó Laborda, 2009].

J.1.2.3 Simulation numérique

L'évolution des méthodes potentiels 2D sur des formes rigides aux simulations 3D d'interaction fluide-structure fortement couplée sur des voiles déformables a été rendue possible grâce aux améliorations des capacités de calcul numérique. Les modèles utilisés dépendent principalement de la nature de l'écoulement. Au près avec écoulement attaché, les méthodes potentiels peuvent être appliquées sur une surface souple idéale [Le Maître et al., 1996, Le Maître, 1998, Le Maître et al., 1998, Le Maître et al., 1999]. Ces modèles sont bien plus rapides face à ceux qui peuvent modéliser le détachement au portant tel que le RANS-[Collie, 2006]-ou Detached Eddy Simulation [Viola et al., 2014]. Le couplage d'un solveur fluide et structure reste complexe dans le cas d'application des voiles qui subissent de forts déplacements et évolutions de pression [Mounoury et al., 2005b, Mounoury et al., 2005a, Michalski et al., 2015, Durand, 2012].

J.1.3 Interaction fluide-structure sur voiles de bateaux

L'analyse de la littérature des problèmes d'interaction fluide structure tel que proposée par [de Langre, 2009] a permis à [Deparday, 2016] de rappeler les principales caractéristiques liées aux écoulements sur les voiles déformables. Les nombres adimensionnels présentés dans Tab. J.1 soulignent que:

- la vitesse réduite, définie par le ratio des temps caractéristiques de déplacement de structure et de l'écoulement de fluide, est du même ordre de grandeur que le nombre de déplacement. L'hypothèse d'aéroélasticité quasi statique, où le problème dépend principalement de la position de la structure, ou d'aéroélasticité pseudo-statique, où le problème dépend principalement de la position et de la vitesse de la structure, ne peuvent être utilisées.
- le nombre de Cauchy définissant le rapport des forces d'inertie fluide sur la rigidité de la structure est relativement faible. La déformation en traction de la membrane est de l'ordre du 1% mais le déplacement de la surface peut être important.
- le nombre de Reynolds définit la nature de l'écoulement de laminaire à turbulent. Cependant cette nature est fortement affectée par la nature attachée ou détachée de l'écoulement et donc aux conditions de navigations.
- les effets de masses ajoutées sont importants comme le souligne [Durand, 2012].

Nombre adimensionnel	Signification	In-situ	Soufflerie
Vitesse réduite $U_R = \frac{T_s}{T_f}$	Comparaison de la dynamique du fluide et de la structure	0.6	0.4 to 0.7
Nombre de déplacement $D = \frac{\xi_0}{L}$	Comparaison de la déformation de la structure sur sa dimension caractéristique	0.125	0.112
Nombre de masse $M = \frac{\rho_f}{\rho_s}$	Rapport de la masse volumique du fluide sur la densité de la structure, utilisé comme première indicateur d'effet de masse ajoutée	1.2×10^{-3}	1.5×10^{-3} (SuperKote 0.75) 1.7×10^{-3} (AirX 500)
Cauchy $C_Y = \frac{\rho_f U^2}{E}$	Rapport des chargements fluides sur la rigidité de la structure, indiquant l'ordre de grandeur de la déformation due au chargement de l'écoulement	1.9×10^{-8}	3.1×10^{-9} à 1.5×10^{-8}
Reynolds $Re = \frac{\rho_f U L}{\nu}$	Rapport des effets d'inertie sur les effets visqueux au sein du fluide, indiquant un état laminaire ou turbulent de l'écoulement	2.7×10^6	3.0×10^5 à 6.5×10^5

Table J.1 – Nombres adimensionnels d'interaction fluide-structure pour l'étude des voiles. Les ordres de grandeurs sont donnés pour des voiles de portant dans les conditions in-situ ([Deparday, 2016]) ou en soufflerie tel que présenté dans le chapitre 4.

Motivations des axes de recherches de ces travaux de thèses:

Ces travaux cherchent à apporter des éléments de réponses complémentaires ou innovants quand à l'étude de certains phénomènes d'interaction fluide-structure sur les voiles de bateaux:

- étudier en écoulement contrôlé des phénomènes instationnaires fréquemment observés tels que:
 - les effets du réglage d'écoute dynamique, appelé pumping, sur grand voile. Est ce que cette pratique améliore les performances aérodynamiques et si c'est le cas, existent ils des conditions optimales en amplitude et fréquence réduite?
 - quels sont les effets du repliement périodique du guindant de voile de portant? En utilisant une approche dynamique, quelles sont les caractéristiques du curling et peut on rapprocher les résultats en soufflerie des essais in-situ et résultats numériques?
- améliorer l'utilisation d'une modélisation actuellement en place dans l'industrie: déterminer si il existe un critère simple permettant de détecter la limitation de l'approche fluide parfait à l'aide de comparaison numérique-expérimentale.

J.1.4 Objectifs

Ces travaux de thèse se sont donc focalisés sur différents aspects.

J.1.4.1 Evaluation de l'utilisation de l'hypothèse fluide parfait pour le dessin de voile: comparaison numérique-expérimentale.

Dans un premier temps, il était important de savoir si l'hypothèse sur laquelle se base les outils de dessin moderne reste vérifiée dans la plupart des conditions usuelles de navigations au près. En effet le modèle fluide parfait présente une limitation aux écoulements attachés. La première partie du manuscrit s'appuyant sur la publication [Aubin et al., 2016a] dans la section J.2 propose un critère simple d'équilibre du couple de chavirement et de redressement afin de s'assurer que les simulations ne surestiment pas les efforts aérodynamiques. Cette surestimation provient de la non modélisation du décollement de l'écoulement par le modèle par rapport au cas réel. Des mesures expérimentales in-situ sur J80 au cours d'une campagne réalisée en 2014 et des simulations numériques réalisées par le code ARAVANTI sont comparées. Deux cas de réglage de patara illustrent l'utilisation d'un tel critère.

J.1.4.2 Mesure du comportement aéroélastique sur des cas stationnaire et instationnaires.

L'étude in-situ de phénomènes instationnaires reste cependant difficile face à la complexité de certaines informations et notamment la mesure du vent réel. C'est pourquoi dans un deuxième temps, afin d'étendre la connaissance sur ces phénomènes instationnaires, nous nous sommes proposé de réaliser des expériences en écoulement contrôlé sur les phénomènes de réglage d'écoute dynamique sur grand voile et de repliement périodique de guidant de spinnaker. La seconde partie du manuscrit présente donc la soufflerie utilisée dans la section J.3, les essais en pumping dans la section J.4 et le phénomène de curling dans la section J.5.

J.1.4.3 Effet de la forme de dessin, de matériaux et de paramètre de navigation sur la performance.

Enfin au cours de ces différents tests, plusieurs voiles, de dessins différents au près, ou de coupes et matériaux différents au portant ont été testées sous plusieurs réglages. Ces éléments permettent de discuter les possibles choix de design de voiles ou les recommandations actuelles au sein de la communauté de navigants. Par ailleurs l'ensemble des données expérimentales recueillies permet d'espérer une possible validation des outils numériques d'interaction fluide-structure sous l'hypothèse fluide visqueux dans des conditions instationnaires.

J.2 Approche in situ et comparaison numérique-expérimentale

Cette partie s'intéresse aux limitations du modèle actuellement utilisé par des voileries à l'aide de comparaison numérique expérimentale. Quelques notions liées la physique du voilier sont d'abord rappelées ainsi que les différentes données qui peuvent être mesurées à bord. Enfin la comparaison s'appuie sur la publication [Aubin et al., 2016a] consultable dans la section 1.2 du chapitre 1.

J.2.1 Le vent et le voilier

J.2.1.1 Les allures

La direction de la ligne de foi du bateau par rapport à la direction du vent établi en mer, aussi appelé vent réel, définit les allures indiquées sur la Fig. J.1 allant du près où le bateau remonte le plus possible au vent aux allures de portant où le bateau descend sous le vent.

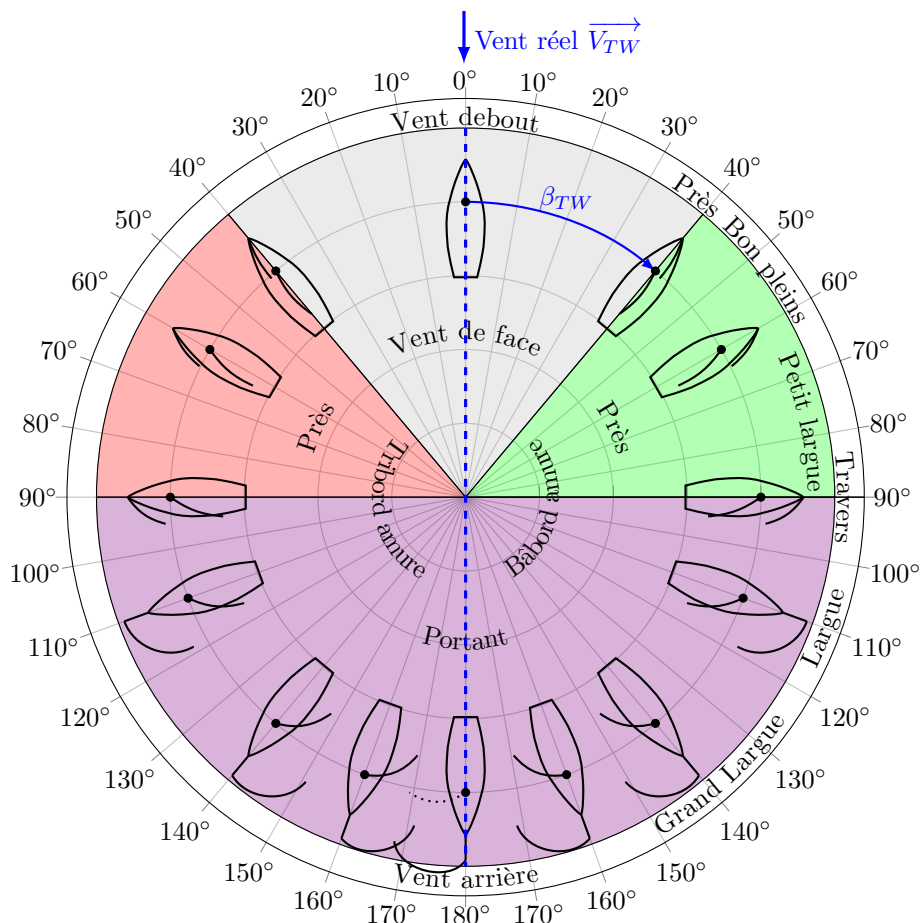


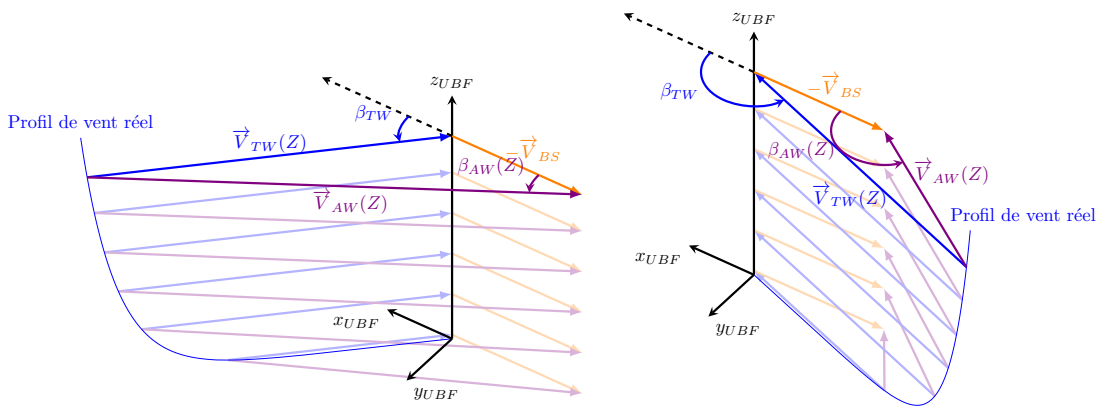
Figure J.1 – Allures de navigations pour un voilier.

J.2.1.2 Du vent réel au vent apparent

Le vent réel associé à l'écoulement naturel de l'air en milieu ouvert marin ou terrestre est décrit à l'aide d'un profil de vent représentant l'évolution de la vitesse en fonction de la hauteur par rapport au sol ou au niveau de la mer. Ce profil est associé au développement de la couche limite de l'atmosphère terrestre pour laquelle différents profils de vitesses peuvent être utilisés. Pour l'étude des voiliers, en se limitant au 100 m proche de la surface, on utilise souvent une loi logarithmique pour une couche limite dite établie c'est à dire pour laquelle le vent synoptique est prédominant en négligeant les effets thermiques locaux. Ainsi on pourra estimer la vitesse du vent réel U à la hauteur Z à partir d'une mesure V_{ref} faite à la hauteur Z_{ref} et du paramètre de rugosité aérodynamique z_0 approximé différemment dans [Cook, 1985, Hansen, 2006, Charnock, 1955, Chamberlain, 1983, Wiernga, 1993].

$$U(Z) = V_{ref} \frac{\ln(Z) - \ln(z_0)}{\ln(Z_{ref}) - \ln(z_0)} \quad (J.1)$$

Cependant, un voilier ayant une certaine vitesse d'avance va lui aussi générer un vent, dit vent vitesse, qui correspond à l'opposé du vecteur vitesse du voilier. La combinaison du vent réel et du vent vitesse va alors générer le vent apparent dont la vitesse et la direction varient avec la hauteur. Le profil de vent apparent présente alors un twist, variation de direction avec la hauteur, qui est plus prononcé pour les allures de portant comme illustré dans la figure J.2. D'autres phénomènes peuvent s'ajouter comme l'ajout d'un cisaillement lié au conditions de courant, d'état de mer ([Cathelain, 2017]), ou locaux, mais ne seront pas considérés dans ces travaux. Enfin l'information du vent réel ou apparent n'est pas obtenue directement mais doit être déterminée à l'aide d'un vent mesuré et d'autres informations mesurées à bord. Ces différentes informations ainsi que d'autres éléments sont présentés ci après.



(a) Vent apparent en navigation au près. Pour des conditions de vent réel de 16nœuds à $Z = 10$ m avec un angle de vent réel de $\beta_{TW} = 45^\circ$ le twist du vent apparent entre le niveau de la mer et la hauteur de référence est d'environ 5° en J80.

(b) Vent apparent en navigation au portant. Le twist est plus prononcé que dans la navigation au près. Pour des conditions de vent réel de 16nœuds à $Z = 10$ m avec un angle de vent réel de $\beta_{TW} = 135^\circ$ le twist du vent apparent entre le niveau de la mer et la hauteur de référence est d'environ 35° en J80.

Figure J.2 – Représentation du vent apparent. UBF est associé au repère du voilier à attitude nulle (gîte et assiette nulles).

J.2.2 Mesures à bord à des fins de comparaison

Dans le cadre de l'étude des interactions fluides-structures sur les voiles, de nombreuses données peuvent être utilisées.

- La mesure du vent et de l'écoulement à bord est en général issue d'un anémomètre et d'une girouette mécanique et ou par un capteur à ultrason. Cette information doit alors être traitée afin de pouvoir estimer le vent réel instantané en prenant en compte plusieurs effets. L'upwash associé à la déviation de l'écoulement par les voiles et le gréement influence grandement la mesure d'un instrument placé à proximité des voiles. Les mouvements du bateau et ses possibles déformations, surtout au niveau du mât, vont aussi ajouter des composantes dans le signal enregistré. Le calcul du vent réel reste donc complexe bien que des travaux de thèse menés en parallèle par [Kerhascoët, 2017] aient permis d'améliorer la qualité des mesures expérimentales. Le placement de centrale inertiel au plus près de l'instrument permet en grande partie de filtrer ces effets ([Gerster, 2016]) mais sa mise en place demeure plus onéreuse et complexe. Le vent réel et apparent sont pourtant des éléments fondamentaux de la navigation surtout dans le cadre de comparaison numérique expérimentale. L'évaluation du décollement de l'écoulement se fait traditionnellement de manière qualitative à l'aide de penons, bien qu'une version électronique moderne [Voisin et al., 2013] permet d'envisager une utilisation par des systèmes embarqués. Pour passer du vent apparent au vent réel il est aussi nécessaire de disposer d'information de navigation.
- Les informations de navigation comportent différents aspects. La vitesse surface du bateau est enregistrée à l'aide d'un loch mécanique (roue à aube) ou ultrasonique placé sous la coque. Ce dernier peut permettre d'avoir une première estimation de la dérive. La vitesse et route fond, sensible aux courants, peuvent être enregistrées par un GPS. Les attitudes du bateau en gîte, assiette et cap peuvent être fournies par une centrale inertiel, le cap pouvant être aussi fourni par un compas électronique.
- Les efforts dans les différentes parties du bateau présentent un intérêt important pour les fabricants. Des chargements mieux estimés en dynamique permettent d'ajuster les coefficients de sécurité afin d'alléger (gain de performance) ou de renforcer (gain en fiabilité) le gréement. Des manilles et ridoirs instrumentés développés par [Augier, 2012] permettent de fournir les efforts en dynamique lors de navigations dans le cas du J80. Une calibration du système est cependant nécessaire. Ces données de chargement peuvent servir à la fois d'éléments de comparaison numérique expérimental ou d'entrée du calcul numérique lorsque la longueur de l'élément concerné n'est pas disponible.
- Les efforts aérodynamiques restent un des objectifs principaux de mesures car ce sont notamment eux qui peuvent alimenter les Velocity Prediction Program (VPP). Cependant leur mesure directe n'est souvent pas possible à moins que le gréement ne soit monté sur une balance incorporée au bateau [Masuyama, 2014, Fossati et al., 2015a]. Un tel montage onéreux et complexe nécessite un bateau dédié à l'expérimentation. L'utilisation de Directional Load Cells (DLC) développées par [Le Pelley et al., 2015] permet la mesure pour les voiles de type spinnaker de l'effort et de sa direction aux différents points d'attaches de la voile ainsi de l'effort aérodynamique total généré par la voile. Une autre méthode telle que celle utilisée par [Motta et al., 2014] appelée

FEPV (Force Evaluation via Pressures and VSPARS) se base sur la mesure synchronisée de la forme de la voile et de la mesure de la distribution de pression sur la voile afin d'intégrer les efforts locaux et d'en déterminer l'effort total résultant.

- les distributions de pression sur les voiles peuvent être utilisées pour la validation des modèles d'écoulement utilisés en simulation numérique. En effet la forme des distributions de pression indique la présence d'éventuels détachements le long de profil de voile. Des capteurs différentiels placés sur la voile mesurent la différence de pression entre les deux côtés de la voile à l'aide de la déformation d'une membrane piézoélectrique à l'intérieur du capteur. Des résultats ont pu ainsi être comparés entre essais au réel et soufflerie ([Viola and Flay, 2009]). La pression absolue peut aussi être mesurée en soufflerie, sur des voiles rigides ou semi rigides, puis comparée à la pression dynamique de référence en amont de l'écoulement mesurée à l'aide d'un tube de Pitot ([Bot et al., 2014]). La mesure des champs de pression sur les voiles peut alors être directement injectée dans un solveur structure afin de prédire une première forme de voile sans réaliser aucun calcul à l'aide d'un solveur fluide.
- la forme des voiles en navigation appelée flying shape est un élément crucial car il est sans doute celui le plus utilisé par les navigateurs. Ainsi les navigateurs et les maîtres voiliers parleront souvent de valeur de creux, de sa position, et d'angle d'entrée sortie pour discuter d'une forme. Il existe des méthodes de mesures basées sur l'enregistrement vidéo de bande de visualisation tel que [Le Pelley and Modral, 2008] pour VSPARS, qui fût utilisé pour mesurer la forme des voiles de près du J80. Ainsi les navigateurs et maître voilier parlerons de valeur de creux, de sa position et d'angles d'entrée sortie pour décrire une section. Pour les voiles de portant [Deparday, 2016] a pu adapter l'analyse photogrammétrique en utilisant des pastilles codées collées sur le tissu afin de déterminer la forme 3D en navigation. Les nuages de points représentant la forme de la voile ont alors pu être traités en utilisant la représentation de Bézier qui allège le stockage et permet de dégager des tendances de forme en fonction de l'allure. Des méthodes par mesure de temps de vols type scanner laser ont pu aussi être mises en place par [Lindbom, 2006, Fossati et al., 2015b] pour obtenir un nuage de points. D'autres méthodes s'appuyant sur la mesure de contraintes utilisant de la fibre optique comme [Ferreira et al., 2017] permettent aussi d'obtenir la forme de section 2D.
- le suivi de position d'éléments du gréement tel que tête de mât ou bout de bôme peut fournir des informations complémentaires utiles pour évaluer la déformation et donc le chargement des structures.

L'analyse d'informations de différentes natures nécessite aussi de s'assurer de la synchronisation des données qui ont bien souvent aussi des fréquences d'échantillonnage différentes. Ces différentes techniques peuvent en général être utilisées ou adaptées en conditions réelles de navigation ou en soufflerie. Cependant la mise en place et l'analyse en soufflerie sont souvent facilitées de par un environnement moins hostile et un écoulement maîtrisé. La section suivante présente des comparaisons numériques expérimentales dans le cadre de navigation sur J80 au près.

J.2.3 Approche fluide parfait dans les phases de près

Les différents éléments de comparaison ainsi que les résultats sont présentés dans la section 1.2 de ce manuscrit. Les simulations permettent d'obtenir des résultats satisfaisants dans un temps de calcul raisonnable pour une approche industrielle dans la plupart des cas de navigations au près en terme d'effort de gréement et de forme de voile. Cependant ces données ont permis de mettre en avant un des effets de l'utilisation du modèle fluide parfait avec hypothèse de non décollement dans le cadre d'étude interaction fluide-structure sur des voiles de bateaux. Par exemple entre deux cas de régime d'écoulement différent, le modèle numérique va avoir tendance à surestimer les efforts numériques dans la configuration où l'écoulement est détaché au réel. Dans le cadre de l'étude, le réglage de pataras permet de définir un cas au réel sur la grand voile d'écoulement attaché (pataras repris) et détaché (pataras relâché). Le modèle gîte libre indique pour ce dernier réglage que la gîte obtenue va être très supérieure à la gîte cible lors de la simulation (7° supérieure). Ceci permet à l'utilisateur de détecter une probable surestimation des efforts liée à une situation d'écoulement détaché pour laquelle le maître voilier pourra au choix: changer le réglage en première approche, ou dans un avenir plus lointains envisager une simulation avec modèle fluide visqueux.

L'étude présentée précédemment correspondait à des phases stationnaires qui ont pu être isolée lors des enregistrements en navigation. Nous nous intéressons maintenant dans les prochaines parties à des phénomènes instationnaires qui sont cette fois ci étudiés en milieu contrôlé à l'aide d'une soufflerie.

J.3 Expérience en soufflerie: présentation de l'installation expérimentale

Face aux incertitudes de mesures des conditions expérimentales in-situ de vent qui rendent parfois l'interprétation de données délicates en phase instationnaire, ces travaux de thèse se sont donc intéressés à des instationnarités forcées ou naturelles ayant lieu sur des voiles dans un milieu contrôlé à savoir en soufflerie.

J.3.1 La soufflerie

Les essais expérimentaux ont eu lieu aux cours de deux campagnes expérimentales à la TFWT du YRU de l'University of Auckland (UoA). Cette soufflerie à veine ouverte, représentée en figure J.3 développée dans le cadre de la coupe de l'America par [Flay and Vuletich, 1995, Flay, 1996] fût la première à reproduire le twist du vent apparent à l'aide de fanons pour les essais des voiles de portant.

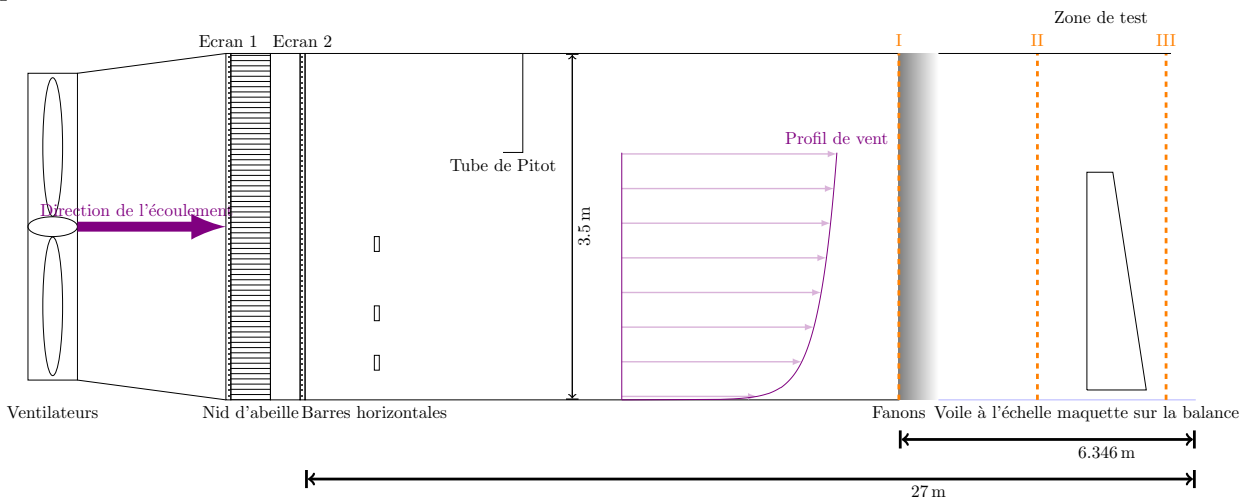
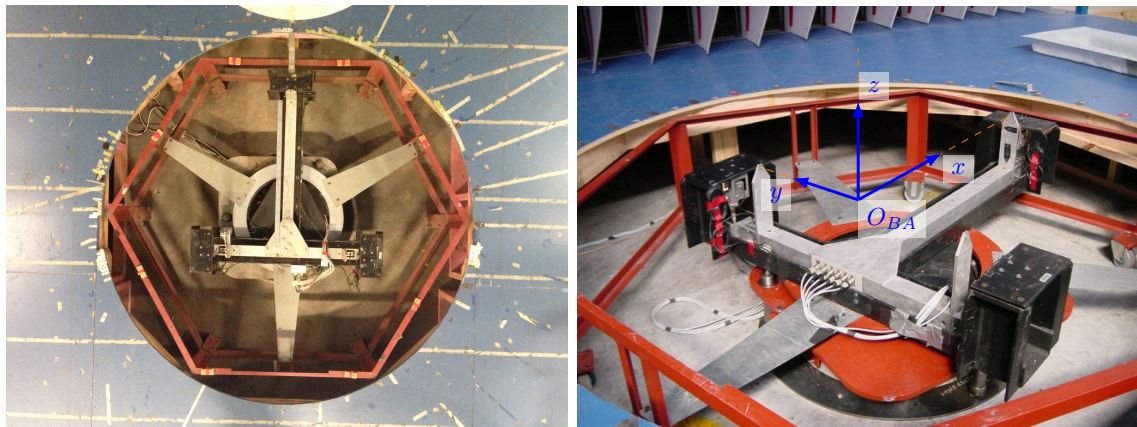


Figure J.3 – Illustration de profil de la soufflerie TFWT. les sections I, II et III indiquent les sections de mesures d'écoulement: I pour la sortie de la section fermée de la soufflerie, II pour l'écoulement proche amont, III pour l'écoulement proche aval (sillage) de la maquette. L'illustration n'est pas à l'échelle.

La maquette est placée sur une balance, photographiée en J.4, qui mesure à l'aide de six jauges extensiométriques toutes les composantes du torseur aérodynamique résultant, notamment l'effort propulsif F_x et l'effort de dérive F_y . Une vérification de la calibration de la balance fût nécessaire et est présentée en App. C. Un tube de Pitot visible sur J.3 en amont de l'écoulement mesure la pression dynamique q_{Pitot} . Un capteur d'effort fut attaché au grément afin de mesurer l'effort au point d'écoute F_{sheet} . A partir de chaque essai d'une durée de 30 s avec une fréquence d'échantillonnage de 200 Hz on définit les coefficients aérodynamique à l'aide de la formule J.2 où S est la surface de la voile et i peut être x (effort propulsif), y (effort de dérive), $sheet$ (effort dans l'écoute). Des caméras de différents types ont été utilisées dans la campagne au près (GoPro) et campagne voile de portant (caméra haute définition avec signal de déclenchement Basler avec lentille grand angle Kowa). Un signal laser et une LED visible sur les enregistrements vidéo permettent de vérifier la synchronisation. Le tableau J.2 donnent quelques dimensions caractéristiques des maquettes.



(a) Balance vue depuis le plafond sans la table tournante.

(b) Repère de la balance, photographie adaptée de [Hansen, 2006].

Figure J.4 – Balance d'effort de la soufflerie TFWT.

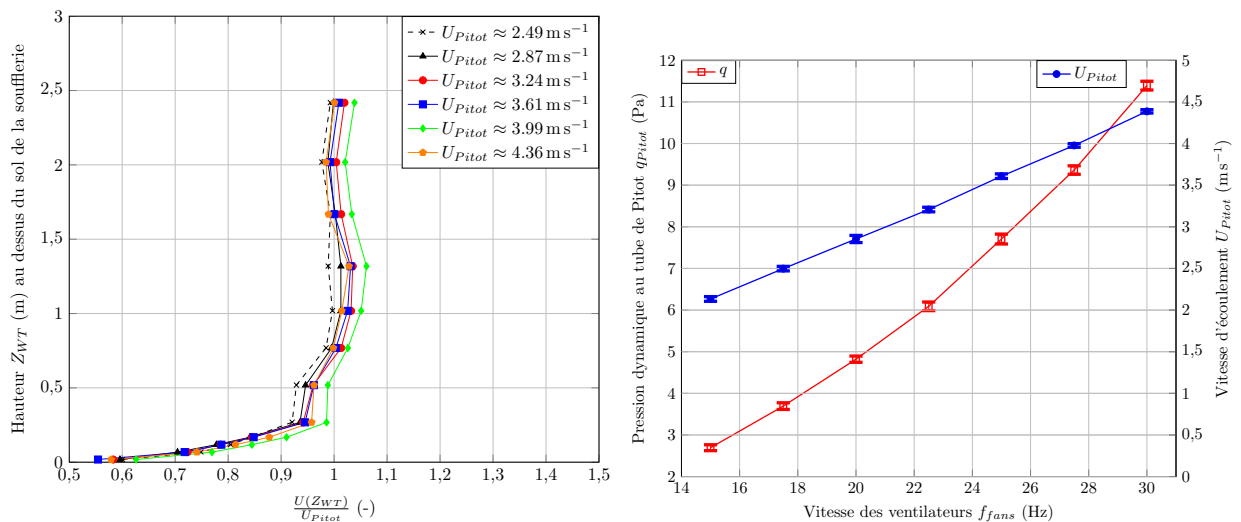
$$C_{F_i} = \overline{C_{F_i}(t)} = \frac{\overline{F_i(t)}}{q_{Pitot} S} \tag{J.2}$$

Voile	Echelle	Surface S (m ²)	Gamme de vitesse d'écoulement (m s ⁻¹)	Corde représentative (m)	Gamme de Reynolds (10 ⁵)
Grand-voile IMOCA	1:13	0.959	3.5	S/h: 0.475	1.07
Spinnaker J80	1:4.6	3.187	2.49 à 4.36	√S: 1.79	2.85 à 4.99

Table J.2 – Informations sur les voiles testées. Des informations sur les tissus utilisées sont données en App. G.

J.3.2 Profils de références mesurés

A l'aide d'une sonde Cobra l'écoulement a pu être mesuré en amont et aval de la voile maquette dans des certains cas. Ici sont présentées des courbes caractéristiques liées aux vitesses d'écoulement de référence utilisées au cours des campagnes expérimentales.



(a) Profil $\frac{U}{U_{Pitot}}$ pour différentes vitesses d'écoulement U_{Pitot} au centre de la sortie de la section fermée de la veine

(b) Vitesse d'écoulement en fonction de la fréquence ventilateurs pour la soufflerie TFWT, UoA. Les barres d'erreur représentent les écarts type des séries temporelles pour chaque mesure.

Figure J.5 – Profil de vitesse d'écoulement de la soufflerie.

J.4 Expérience en soufflerie: essais sur grand voile. De l'optimisation statique à l'étude du pumping

Cette première section présente des essais réalisés en soufflerie sur grand voile seule hissée sur un gréement non haubané encasté au pied de mât. Le phénomène auquel nous nous intéressons est le pumping, nom donné à l'action de pomper, défini dans [International sailing Federation, 2013] comme étant une *agitation répétée de toute voile, soit en bordant et choquant la voile, soit par mouvement du corps vertical ou perpendiculaire à l'axe du bateau*. Dans notre cas il s'agit d'un réglage d'écoute dynamique qui est admis comme étant plus efficace par les navigateurs, en particulier en dériveur. Cette technique souvent interdite peut parfois être admise en compétition officielle sur certaines classes sous certaines conditions de vent. Cependant cette technique est souvent couplée à une technique de roulis, qui peut améliorer là aussi la performance en navigation. C'est pourquoi dans notre approche nous nous proposons de déterminer d'un point de vue aérodynamique si le pumping améliore la performance d'un voilier et si oui, existent-ils des paramètres optimum en terme d'amplitude et de fréquence du réglage dynamique? Les voiles testées sont présentées dans une première section. Afin de noter une possible évolution de performance réaliste, une première phase d'optimisation de réglage statique sur deux réglages est présentée. Enfin les effets du pumping sur les coefficients moyens et dynamiques sont présentés en oscillant autour de cet optimum statique. Trois différents AWA (apparent wind angle) furent testé (25°, 40° et 60°) mais n'est présenté ici que le cas d'angle de vent apparent à 60° qui permet de plus larges oscillations lors du pumping.

J.4.1 Les grand-voiles

Pour cette expérience nous nous sommes proposés d'étudier trois grand-voiles de forme de dessin, appelée design shape, différentes. Ces voiles ont été dessinées et fabriquées par Incidences Sails. Bien que ces trois voiles soient inspirées d'un design International Monohull Open Class Association (IMOCA)60, elles présentent trois valeurs de creux différentes, illustrés en Fig. J.6 à savoir une voile plate dite MS flat, une voile standard dite MS std et une voile plus creusée dite MS Max. L'optimisation statique pour ces trois voiles a donc été réalisée, à la suite de laquelle l'étude du pumping autour de leur optimum respectif a pu être mené.

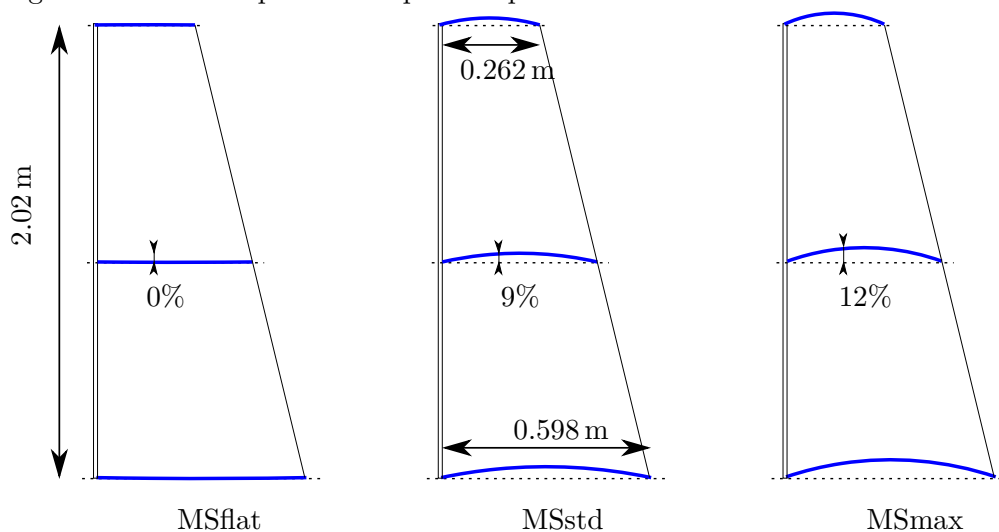


Figure J.6 – Illustration des creux de grand-voiles testées en soufflerie. Le creux est indiqué pour une même bande de visualisation.

J.4.2 Réglage statique et optimisation

Dans une première phase nous déterminons l'optimum pour des réglages statiques, c'est à dire pour lesquelles les longueurs sont fixes au cours des enregistrements. Deux réglages sont possibles: la position du chariot d'écoute de grand voile le long du rail d'écoute, notée L_{car} , et la longueur d'écoute depuis la position du chariot notée L_{sheet} . Ces deux grandeurs sont indiquées Fig. J.7 et Fig. J.8.

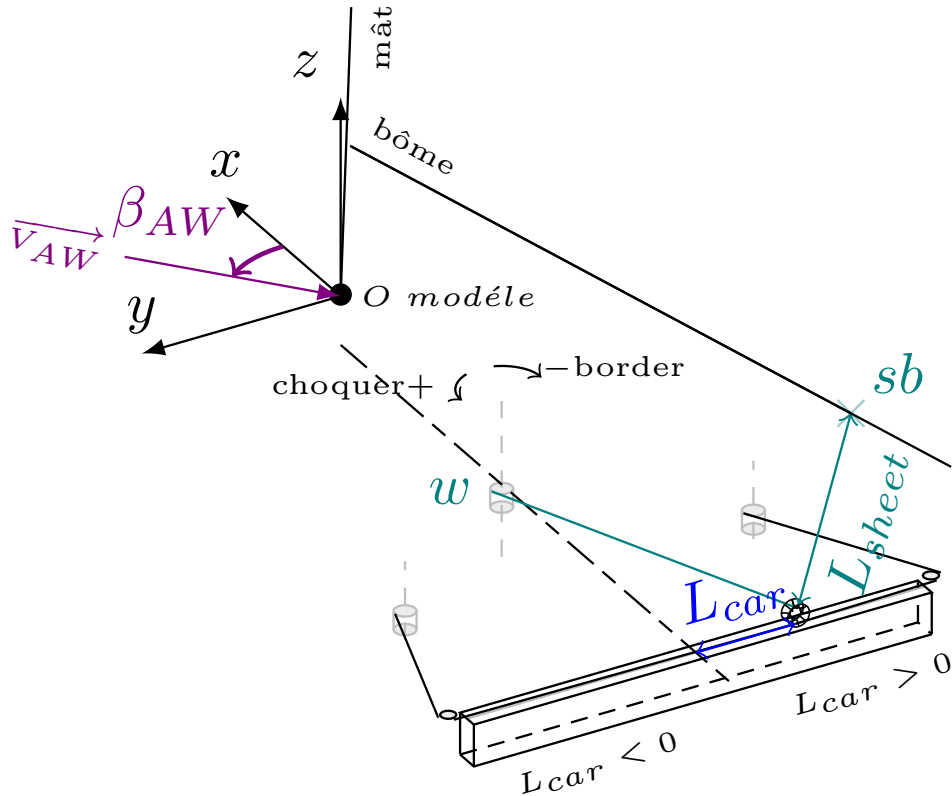


Figure J.7 – Géométrie du réglage à deux paramètres par moteur pas à pas pour les essais statique de grand voile.

Une méthode d'optimisation décrite dans [Sacher et al., 2017] est utilisée. Cette méthode est basée sur l'utilisation de méta-modèle qui cherche à déterminer l'optimum de la fonction objectif en minimisant le nombre d'évaluations de cette fonction. Cette méthode est particulièrement adaptée lorsque l'évaluation de la fonction objectif est coûteuse, comme cela peut être le cas en simulation numérique. Un processus Gaussien est utilisé pour déterminer la fonction objectif -qui représente la performance- ainsi qu'une évaluation de l'erreur et du bruit de cette fonction dans l'espace des paramètres. Une fonction de mérite est calculée afin de déterminer la localisation du prochain point à tester en prenant en compte la valeur de la fonction objectif et du bruit. Ainsi l'algorithme aura tendance à aller chercher des points où le gain en performance est plus probable et va éviter des zones pour lequel la fonction objectif est bien connue. La fonction objectif $C_{F_{obj}}$ est définie par:

$$C_{F_{obj}} = C_{F_x} + 0.1C_{F_y} \quad (J.3)$$

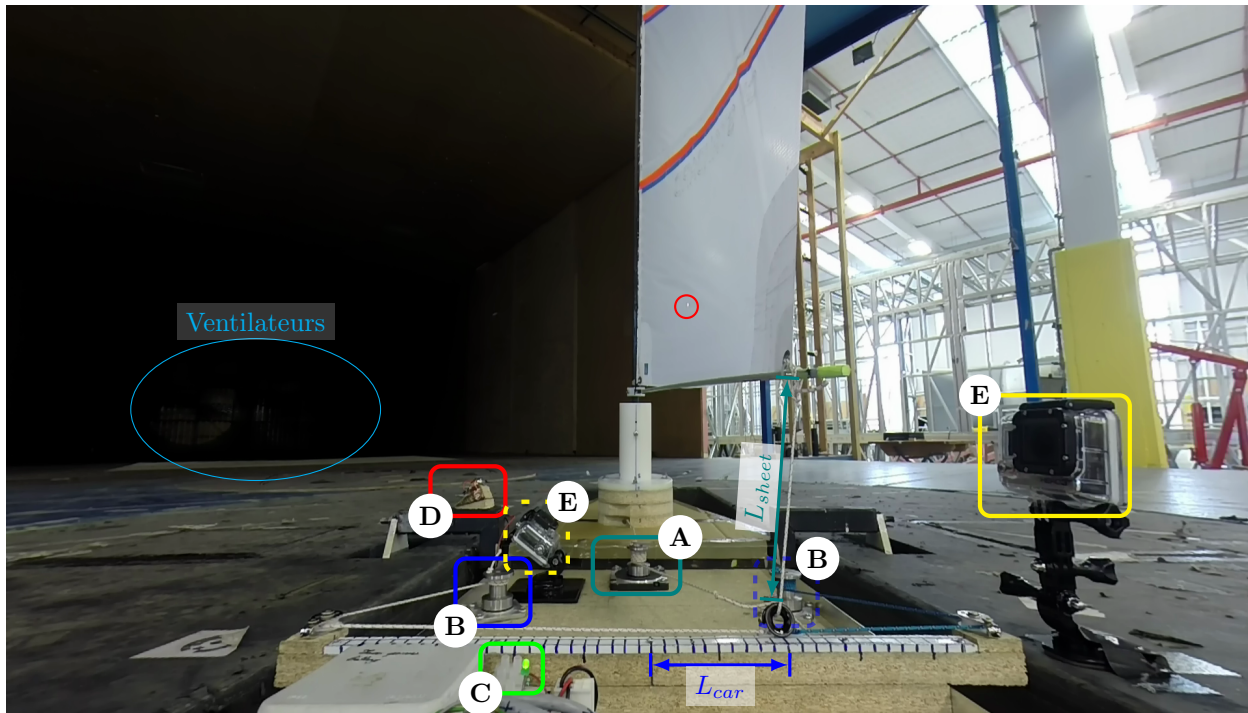


Figure J.8 – Réglage de grand voile vue par le cockpit. La distorsion de la lentille n'a pas été corrigée ici. (A) winch d'écoute, (B) winch de chariot, (C) diode de synchronisation, (D) laser de synchronisation (le cercle rouge représente la zone illuminée par le laser sur la voile), (E) caméras. Le capteur d'effort d'écoute n'est pas monté. La mâst est ici aligné avec la direction de l'écoulement de la soufflerie.

Cette fonction est une combinaison linéaire de l'effort de propulsion et de dérive (avec ici $C_{F_y} < 0$ au vue de l'orientation du repère de mesure, la maquette étant bâbord amure). Elle prend en compte la pénalisation d'une force de dérive qui va générer une gîte augmentant la traînée hydrodynamique. Le coefficient de pénalisation a été estimé en étudiant numériquement l'effet de la gîte et de dérive sur la vitesse à l'équilibre pour la partie hydrodynamique. Cette valeur reste proche de 0.1 pour différentes formes de coques dans des conditions de navigations au près. Lors de l'optimisation l'espace des paramètres (L_{car} , L_{sheet}) est délimité par des zones interdites associés à une trop forte tension dans la voile, déformation du mâst, ou une limite physique de déplacement comme par exemple les extrémités du chariot. La procédure d'optimisation se déroule ainsi:

- l'initialisation comporte dix points d'exploration de l'espace des paramètres, qui seront représentés par un carré dans l'espace des paramètres. Ces points sont identiques pour les trois voiles afin de disposer immédiatement de points de comparaisons à réglages identiques.
- phase d'exploration où l'algorithme va tester des points -représentés par des cercles dans l'espace des paramètres- en fonction de la fonction de mérite, explorant des zones inconnues qui peuvent présenter une performance plus importante (performance peu connue mais bruit important) ou bien affinant la connaissance de la fonction objectif dans la zone de meilleur performance (haute performance, faible bruit)
- l'exploration se fait jusqu'à convergence, à savoir ici que deux points testés successivement sont à une distance dans l'espace des paramètres inférieure à 1 mm. L'optimum, représenté par une

croix encadrée, peut alors être obtenue avant d'atteindre la convergence. En général environ 40 points sont nécessaires pour arriver à convergence.

Les résultats de l'optimisation se présentent donc sous forme de carte de contour des fonctions C_{F_i} et de leur incertitude sC_{F_i} - où i peut être x pour l'effort de propulsion, y pour l'effort de dérive, $sheet$ pour l'effort dans l'écoute ou obj pour la fonction objectif - dans l'espace des paramètres ayant L_{car} en abscisse et L_{sheet} en ordonnées. La grand-voile standard présente ainsi un optimum avec un chariot sous le vent comme indiqué par les résultats de l'optimisation en Fig. J.10. On voit sur ce type de graphe que l'algorithme va concentrer l'exploration sur la zone de plus haute performance après la phase d'initialisation. En réalisant l'optimisation pour les trois formes de dessin on peut alors comparer les optimums présenter dans Tab. J.3. La forme des réponses d'optimisation est aussi comparé dans Fig. J.9 montrant ici que la grand-voile avec un creux maximum présente de meilleures performances sur une zone de l'espace des paramètres plus étendue, cette voile sera dite plus tolérante. Ces mesures sont en accord avec la pratique des navigateurs qui va consister à creuser la voile en relâchant la bordure de grand-voile lors de phase de navigation plus abattue.

Après avoir déterminé le réglage optimum statique pour chaque grand-voile, la prochaine section s'intéresse à l'effet du pumping autour de ces optimums respectifs.

Mainsail type	L_{car} (mm)	L_{sheet} (mm)	C_{F_x} ([-])	C_{F_y} ([-])	$C_{F_{obj}}$ ([-])	$C_{F_{sheet}}$ ([-])
Standard	205	168.8	0.79	-0.90	0.69	
Max camber	205	167.8	0.79	-0.89	0.70	1.41
Flat	205	161.8	0.70	-0.85	0.62	1.45

Table J.3 – Résultats d'optimisation pour $\beta_{AW} = 60^\circ$. L'effort d'écoute ne fut pas mesuré pour la grand-voile standard.

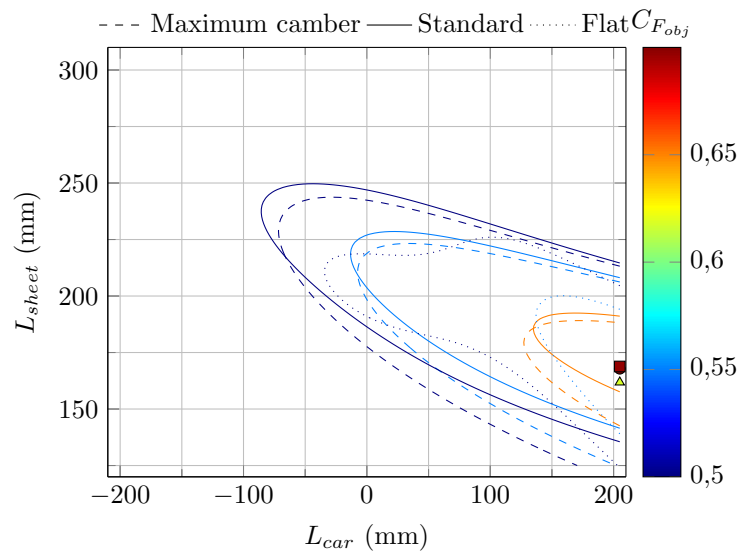


Figure J.9 – Effet de la forme de dessin sur l'optimum à $\beta_{AW} = 60^\circ$. ● : optimum expérimental de la grand-voile à creux maximum, ■ : optimum expérimental de la grand-voile à creux standard, ▲ : optimum expérimental de la grand-voile plate.

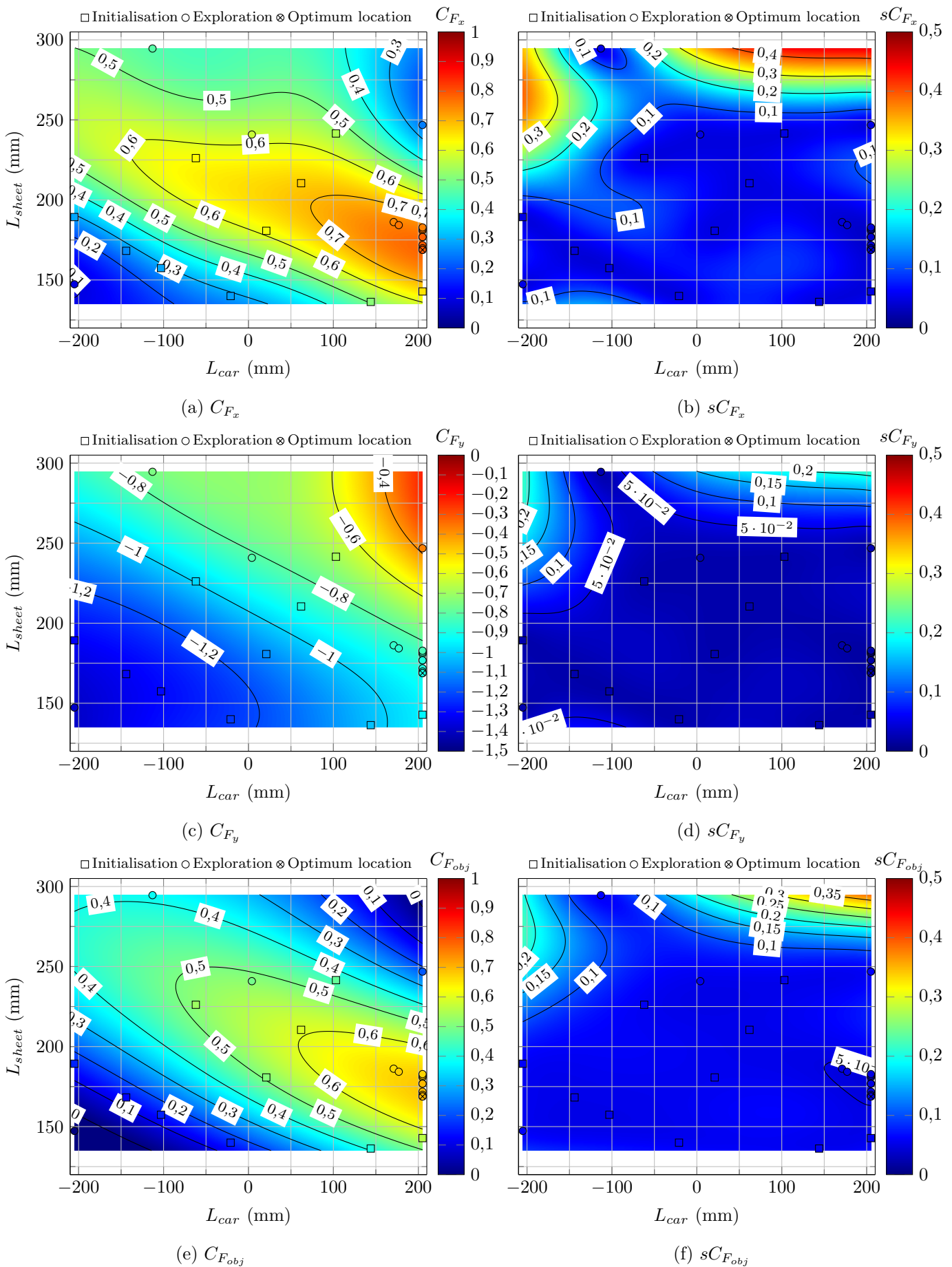


Figure J.10 – Optimisation à 2 paramètres pour la grand-voile standard à $\beta_{AW} = 60^\circ$. □ : phase d’initialisation, ○ : phase d’exploration et ⊗ : optimum expérimental.

J.4.3 Pomper au travers

Nous nous intéressons aux effets du pumping sur le cas $\beta_{AW} = 60^\circ$ -associé à une navigation au travers- qui permet de présenter des oscillations de plus grandes amplitudes en comparaison de cas de navigation plus près du vent où l'optimum statique est plus bordé avec un chariot plus au vent. Le réglage dynamique est généré à l'aide d'un plateau tournant sur lequel un pion peut être placé à différentes positions d'excentricité comme illustré en Fig. J.11a et Fig. J.11b. A partir de cette configuration géométrique on peut définir un paramètre adimensionnel représentant la dynamique du mouvement d'excitation par rapport à l'écoulement: la fréquence réduite f_r est donnée par $f_r = \frac{fc}{U_{Pitot}}$ avec c la corde représentative du profil, à savoir dans le cas de la grand-voile $c = \frac{S}{l_P} = 0.4748$ m avec l_P la longueur de guindant (bord d'attaque) et S la surface de la voile. Par souci d'unification la corde représentative est basée sur la forme de dessin de la voile standard afin d'avoir une même fréquence réduite pour une même fréquence d'oscillation pour les trois voiles. f est la fréquence de rotation du plateau, et U_{Pitot} la vitesse d'écoulement de référence fourni par le tube de Pitot. Si $f_r = 0$ il n'y a pas d'oscillation et il s'agit du cas statique optimum. Plus la fréquence réduite augmente, plus la dynamique d'oscillation est forte au regard du temps de convection. Un tel paramètre adimensionnel est parfois associé à k comme dans [Schutt and Williamson, 2016] ou à un nombre de Strouhal St comme dans [Taylor et al., 2003, Egan et al., 2016]. Le choix d'utilisation du terme fréquence réduite f_r a été fait pour associer ce mouvement à un mouvement de réglage dynamique forcé comme dans [Fossati and Muggiasca, 2012a] et non pas à un phénomène instationnaire naturel associé à une fluctuation de sillage par exemple. En effet le Strouhal est souvent associé à une fluctuation d'écoulement comme par exemple dans une série temporelle de mesure de pression dans [Bot et al., 2014]. Par ailleurs d'autres étude définissent le Strouhal en incorporant une amplitude caractéristique du mouvement ([Lua et al., 2016]) ou en se basant sur une pulsation ([Schouveiler et al., 2005]).

Ainsi les différentes fréquences réduites en fonction des fréquences de rotations du plateau tournant sont données dans Tab. J.4. Les résultats seront présentés pour des fréquences réduites inférieures à 0.4 afin de s'assurer de ne pas exciter les modes propres du mât.

f (Hz)	0	0.094	0.469	0.938	1.406	1.875	2.344	2.813	3.281	3.750	4.219
f_r (-)	0	0.013	0.064	0.127	0.191	0.254	0.318	0.381	0.445	0.509	0.572

Table J.4 – Fréquences dynamiques testées et fréquences réduites associées.

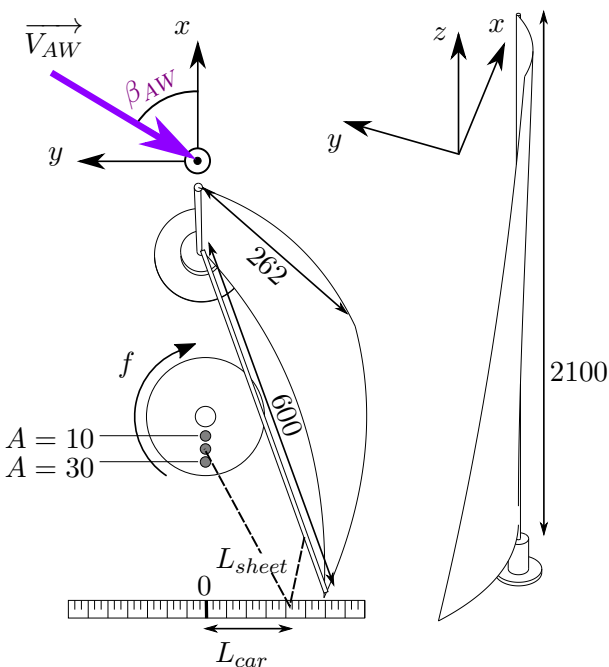
Fig. J.12 présente l'évolution des coefficients de propulsion et de dérive pour les trois grand-voiles et trois amplitudes pour différentes fréquences réduites testées. Fig. J.13 représente les évolutions de la fonction objectif et du coefficient d'effort dans l'écoute sous ces mêmes conditions. Les valeurs moyennes sont obtenues sur un nombre entier d'oscillation de réglage dynamique. On peut observer le comportement suivant:

- à fréquence réduite nulle, les résultats reflètent les optimum statiques précédemment déterminés
- lorsque la fréquence réduite augmente légèrement à 0.01 on observe une diminution du coefficient de propulsion moyen et de la fonction objectif. En effet dans ce cas de faible dynamique, en faisant une hypothèse quasi-statique, le réglage s'écarte donc la plupart du temps du réglage

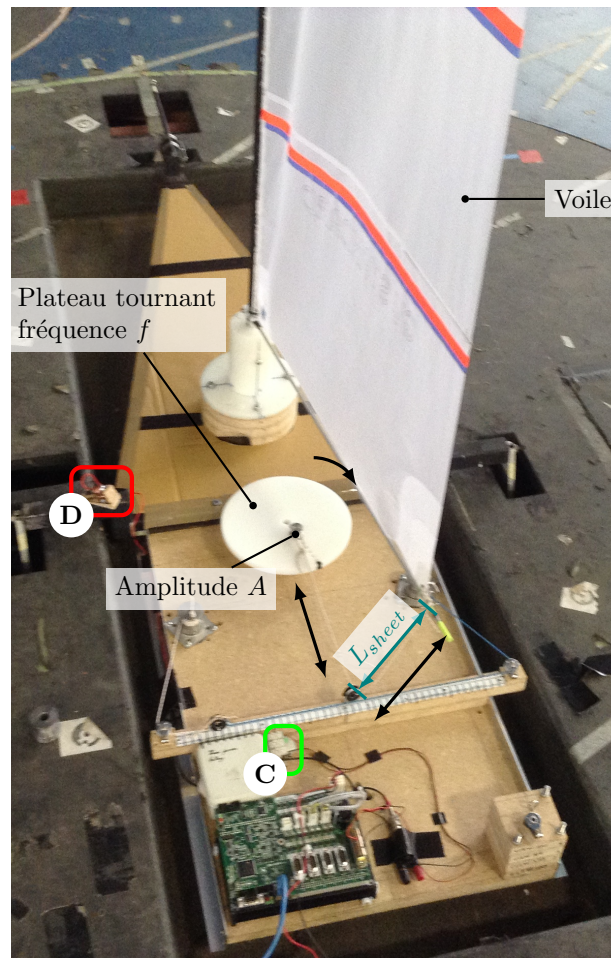
statique optimum. La dynamique de l'oscillation étant faible et modifiant peu la réponse du système, en moyenne la performance de la voile sur un cycle d'oscillation diminue.

- lorsque la fréquence réduite continue à augmenter, le coefficient de propulsion moyen et la fonction objectif augmentent jusqu'à atteindre un maxima dont la valeur peut être plus de 10% supérieure à leur valeur statique. L'effort de dérive présente lui aussi un maxima, mais la faible pénalisation permet d'obtenir une fonction objectif présentant de meilleure performance qu'en statique. La fréquence réduite présentant l'optimum se situe entre 0.25 et 0.3. De plus lorsque l'amplitude est suffisamment forte à partir de $A = 20$ mm, la voile plate présente des caractéristiques semblables aux autres voiles. En relatif cette dernière bénéficie donc plus des effets du réglage dynamique.

Le coefficient d'effort dans l'écoute moyen présente lui aussi un maxima localisé à la fréquence réduite optimum. Après avoir étudié l'effet du pumping sur les valeurs moyennes, nous nous intéressons aux évolutions dynamique au cours des cycles d'oscillations.

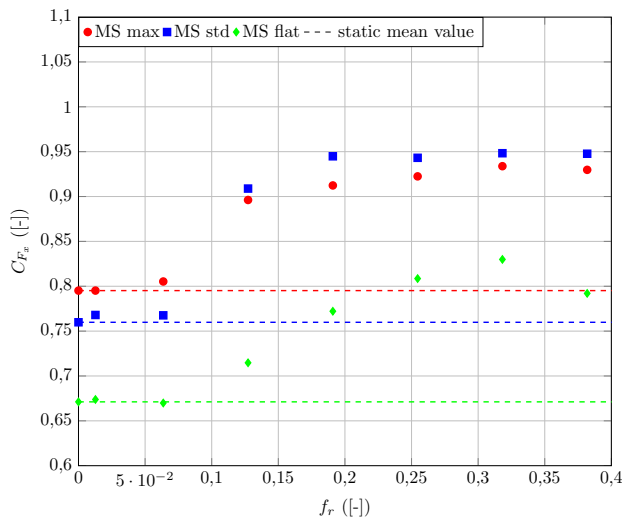


(a) Système de réglage dynamique. les dimensions sont en mm. Ici seulement trois position d'excentrique sont représentées.

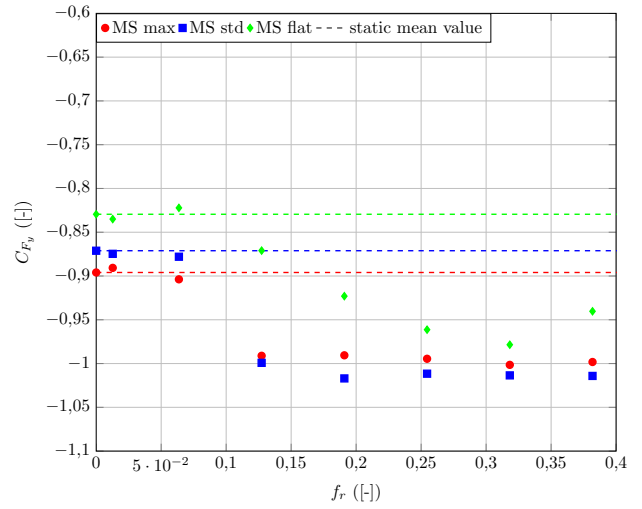


(b) Photographie sans écoulement du système de réglage dynamique. (C) diode de synchronisation, (D) laser de synchronisation.

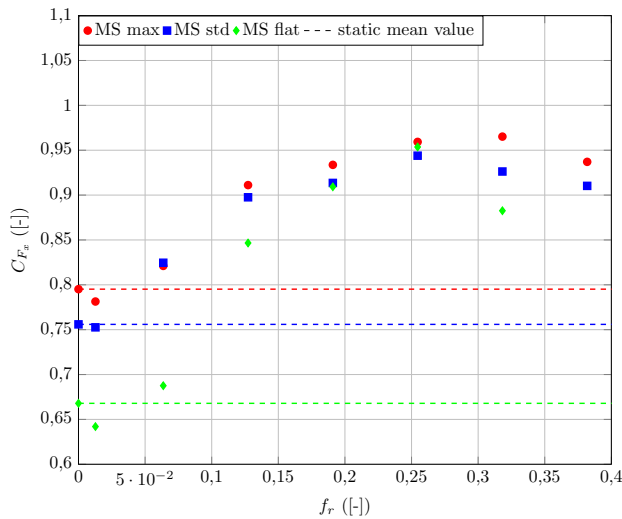
Figure J.11 – Système de réglage dynamique.



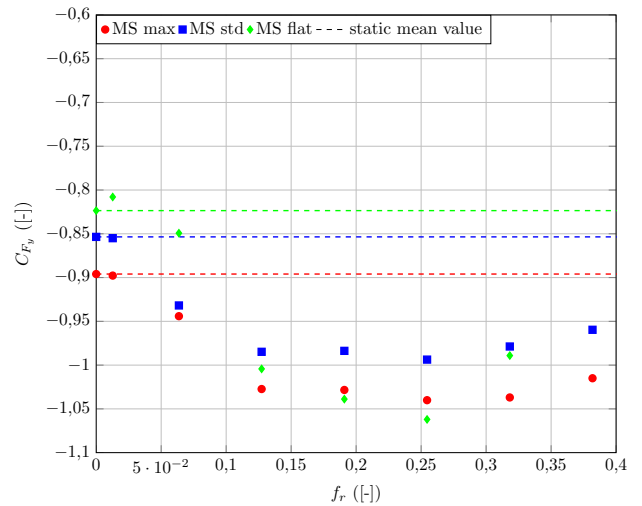
(a) C_{F_x} pour $A = 10$ mm



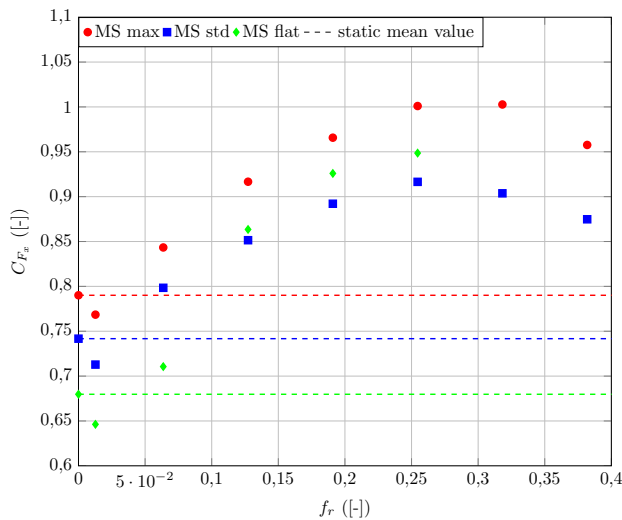
(b) C_{F_y} pour $A = 10$ mm



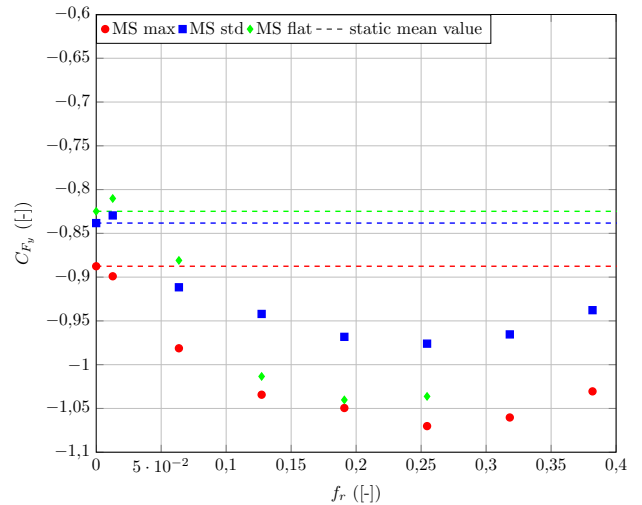
(c) C_{F_x} pour $A = 20$ mm



(d) C_{F_y} pour $A = 20$ mm

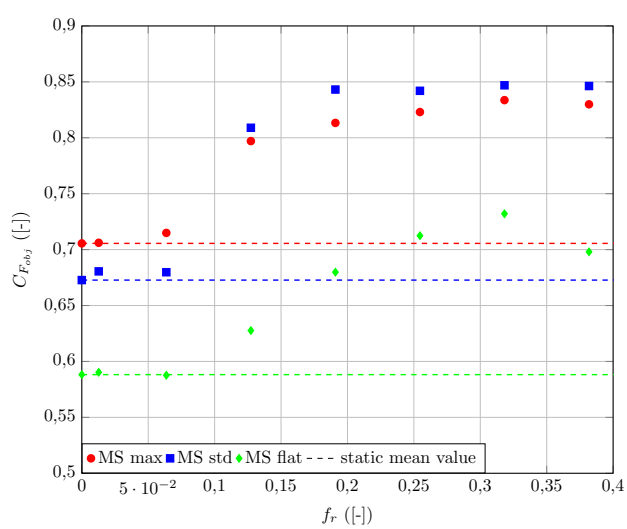


(e) C_{F_x} pour $A = 30$ mm

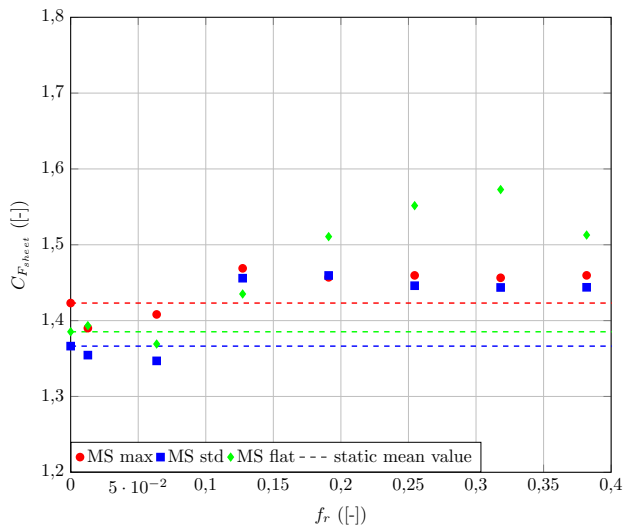


(f) C_{F_y} pour $A = 30$ mm

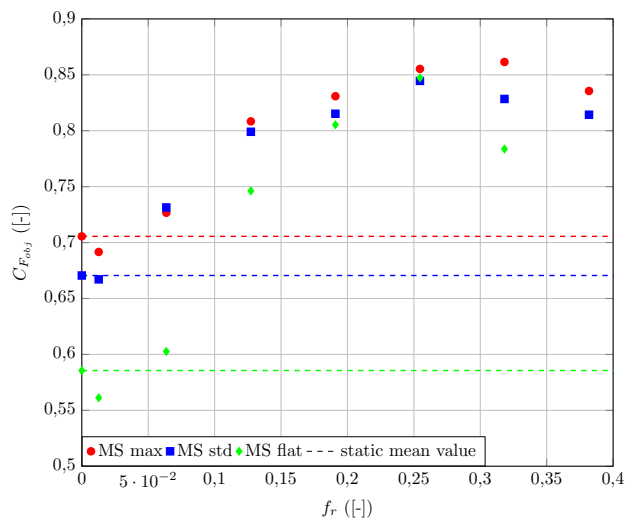
Figure J.12 – Coefficient d'effort de propulsion et de derivate moyen en réglage dynamique pour $\beta_{AW} = 60^\circ$.



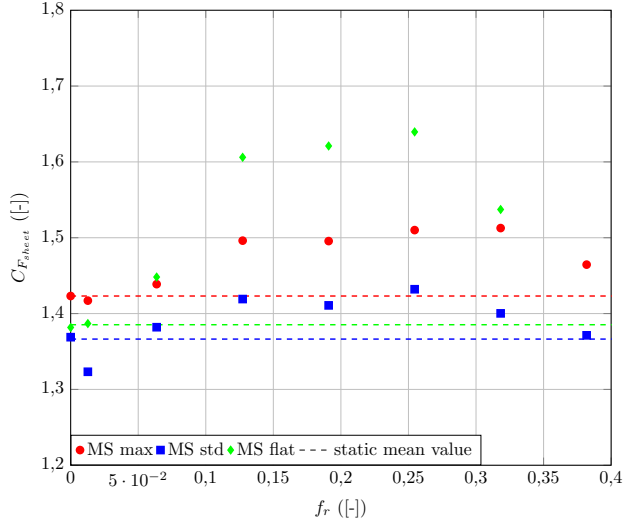
(a) $C_{F_{obj}}$ pour $A = 10$ mm



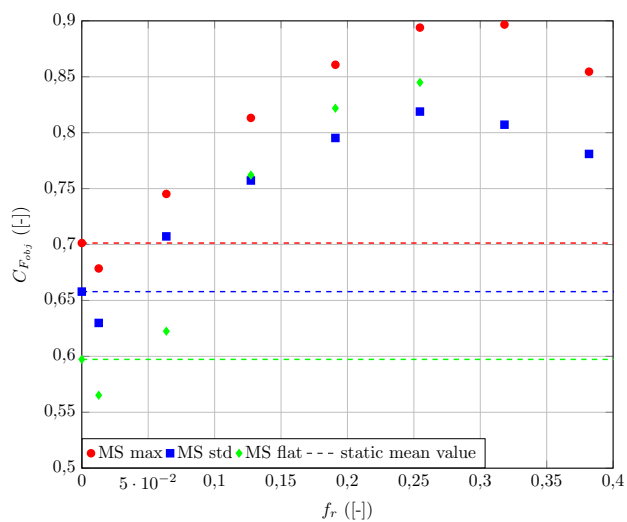
(b) $C_{F_{sheet}}$ pour $A = 10$ mm



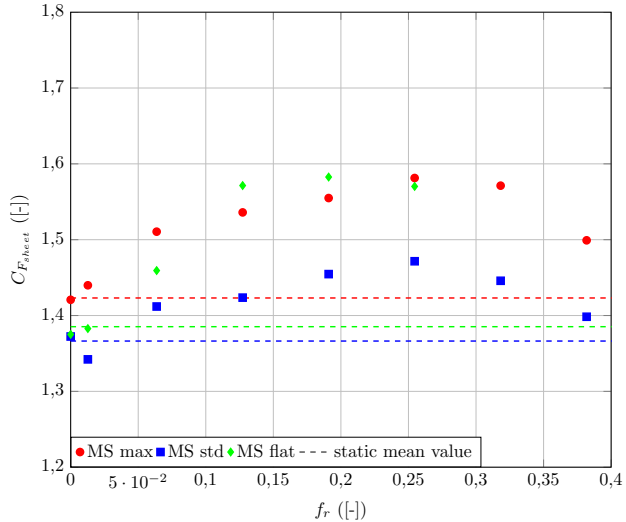
(c) $C_{F_{obj}}$ pour $A = 20$ mm



(d) $C_{F_{sheet}}$ pour $A = 20$ mm



(e) $C_{F_{obj}}$ pour $A = 30$ mm



(f) $C_{F_{sheet}}$ pour $A = 30$ mm

Figure J.13 – Fonction objectif et coefficient d’effort dans l’écoute moyen sous réglage dynamique pour $\beta_{AW} = 60^\circ$.

Les séries temporelles sont décrites sur deux périodes adimensionnelles représentatives comme illustrées sur la Fig. J.14. Les fluctuations des coefficients par rapport au cas statique sont représentées ainsi que les fluctuations de la longueur d'écoute par rapport au réglage optimum statique. Pour plus de clarté l'opposé des fluctuation de l'effort de dérive est tracé. Le comportement décrit ici est identique pour les différentes formes de dessins. On peut observer que de la plus faible fréquence réduite testée jusqu'à la fréquence réduite avant l'optimum, illustré en Fig. J.15, les fluctuation en propulsion et dérive sont en opposition de phase (l'opposé du coefficient de dérive étant représenté). L'effort de propulsion est en opposition de phase avec le signal de la longueur d'écoute. Les amplitudes des fluctuations en propulsion et dérive sont quasi identiques, cependant la valeur moyenne des signaux tend à augmenter une fois la plus basse fréquence réduite passée (décalage vertical des graphes vers le hauts). A la fréquence réduite optimale $f_r = 0.25$, on observe une divergence dans le comportement des fluctuations où l'effort de dérive tend à avoir une amplitude maintenant plus importante que celle de l'effort de propulsion et une légère avance de phase sur le signal de propulsion. Pour des fréquences réduites au delà de la fréquence réduite optimale, en Fig. J.16, l'amplitude des fluctuations de l'effort de propulsion tend à diminuer contrairement à celle des efforts de dérive qui augmente significativement. Le coefficient de la fonction objectif instantanée voit alors l'amplitude de ses fluctuations et sa valeur moyenne diminuer. Cette divergence dans le comportement des signaux semble donc associé à la localisation de l'optimum.

Une telle divergence dans les comportements des fluctuations, localisée à la fréquence réduite optimale, peut indiquer un changement de régime en terme de structure d'écoulement notamment avec la création d'un sillage de propulsion comme suggéré par [Schutt and Williamson, 2016] dans son étude du flicking sur un dériveur.

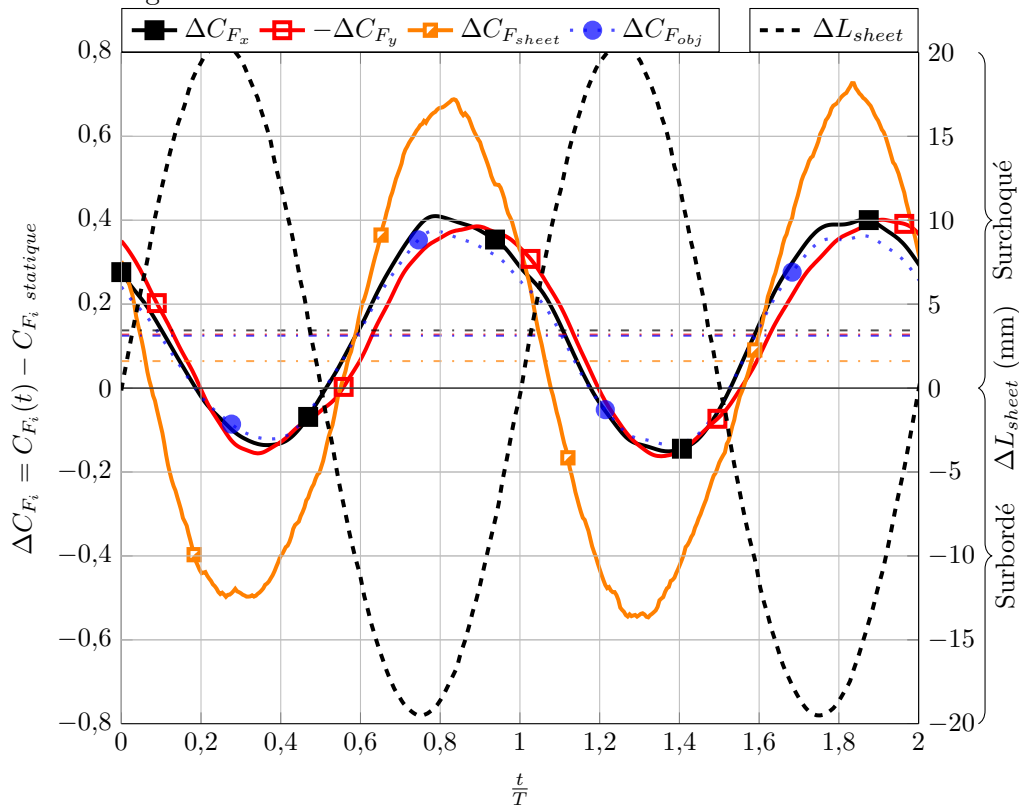


Figure J.14 – Evolution des séries temporelles de coefficient pour la grand-voile standard pour $A = 20$ mm à $f_r = 0.127$. Les lignes pointillées représentent les valeurs moyennes de chaque signaux.

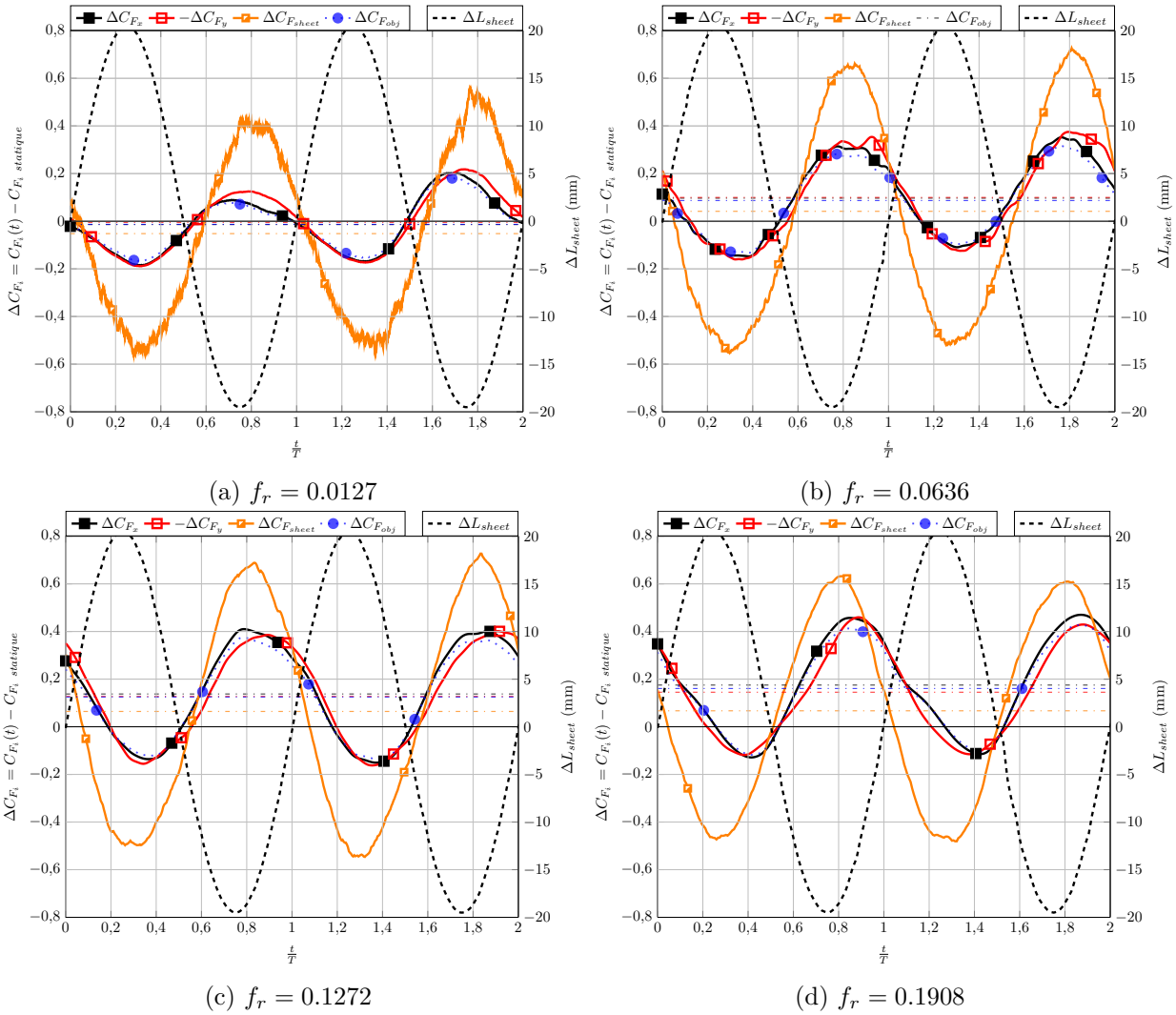


Figure J.15 – Evolution des séries temporelles de coefficient pour la grand-voile standard pour $A = 20$ mm à $AWA = 60^\circ$, pour les basses fréquences réduites. Les lignes pointillées représentent les valeurs moyennes de chaque signaux.

D'autres études [Schnipper et al., 2009, Schouveiler et al., 2005, Lua et al., 2016] dans des configurations proches associent la production de poussée par un foil oscillant à l'inversion du sillage de Von-Karman. Cependant au cours de la présente étude sur voile souple, aucune utilisation de technique de visualisation d'écoulement n'a été possible pour confirmer cette association entre fréquence optimale et inversion de sillage.

Une représentation de Lissajou traçant les différents coefficients en fonctions des fluctuations de la longueur d'écoute L_{sheet} peut aussi être utilisée. Le travail fourni par le moteur au cours d'un cycle et donc la puissance requise notamment pour l'activation du mouvement, peut être calculé à l'aide de la formule 3.8, si l'on s'intéresse à cette représentation avec le signal d'effort dans l'écoute. En traçant cette puissance en fonction de la fréquence réduite en Fig. 3.37, on peut noter que la puissance d'activation présente elle aussi un extremum associé à l'optimum. Un rendement pourrait sans doute être défini afin de déterminer si une fréquence réduite présenterait un meilleur rendement en terme de puissance dépensée vis à vis de l'amélioration de performance.

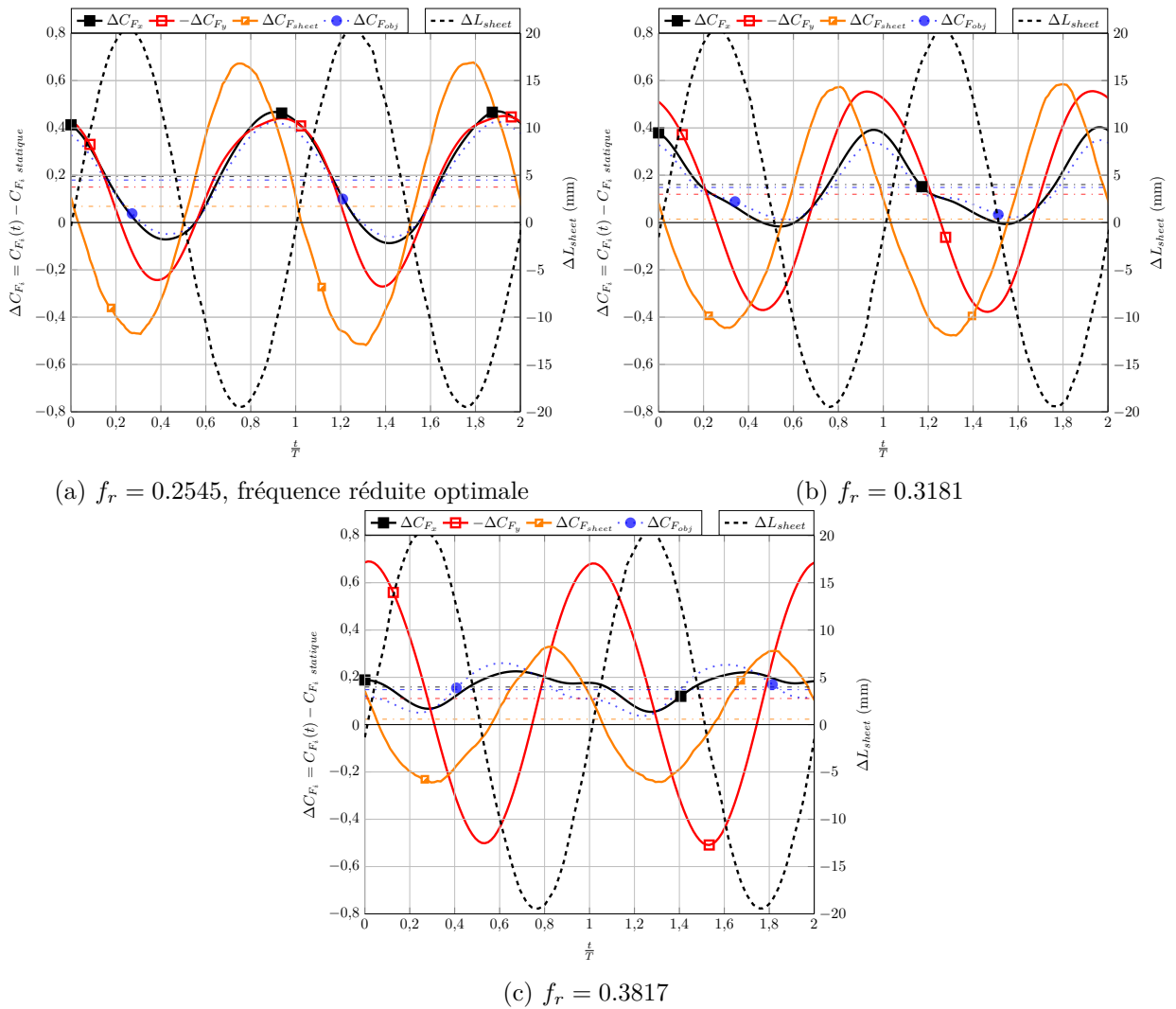


Figure J.16 – Evolution des séries temporelles de coefficient pour la grand-voile standard pour $A = 20$ mm à $AWA = 60^\circ$, pour les hautes fréquences réduites. Les lignes pointillées représentent les valeurs moyennes de chaque signaux.

Conclusion sur l'étude instationnaire du pumping en soufflerie:

Au cours de cette section:

- une méthode d'optimisation a pu être utilisée dans un cadre innovant ([Sacher et al., 2017]) afin de déterminer l'optimum statique à deux réglages pour trois voiles de forme de dessin différents: dans le cas de la navigation au travers, la voile la plus creuse présente de meilleure performance par rapport aux autres voiles.
- un réglage dynamique reproduisant le pumping a pu être réalisé avec plusieurs fréquences et amplitudes d'activations autour des optimums statiques. Les résultats montrent qu'il existe une fréquence réduite optimale $f_r \approx 0.25$, $f_r \approx 0.32$ pour laquelle la fonction objectif présente une valeur moyenne maximale. La voile sans creux bénéficie plus des effets dynamiques par rapports au cas statique respectifs des autres voiles.
- cette fréquence réduite optimale se caractérise en observant le comportement des séries

temporelles par une divergence dans les fluctuations des coefficients de propulsion et dérive. Plusieurs régimes sont ainsi observés lors de l'augmentation de la fréquence réduite:

1. pour la fréquence réduite la plus faible, la moyenne de la fonction objectif décroît par rapport au cas statique. Le réglage dans ces conditions quasi-statiques s'éloigne la plupart du temps du réglage optimum statique. Ce type d'effet a déjà pu être observé sur le coefficient de propulsion dans le cas d'une aile oscillante par [Mackowski and Williamson, 2015] qui observe une décroissance aux plus faibles nombre de Strouhal.
 2. puis pour $f_r \leq 0.25$, le coefficient de propulsion et de dérive présentent des fluctuations opposées. La valeur moyenne du coefficient de propulsion tend à augmenter avec la fréquence réduite. Le coefficient de propulsion est en opposition de phase avec le signal de longueur d'écoute.
 3. à la fréquence réduite optimale il y a apparition de divergence entre les fluctuations des coefficients de propulsion et de dérive.
 4. au delà de la fréquence réduite optimale, les signaux d'effort commencent à présenter un déphasage par rapport au signal de longueur d'écoute. Les amplitudes des fluctuations du coefficient de propulsion diminuent mais la valeur moyenne reste cependant supérieure au cas statique. L'amplitude des fluctuations de l'effort de dérive augmente. La valeur moyenne sur la fonction objectif diminue.
- la puissance d'activation présente un maxima à la fréquence réduite optimale

L'étude a été réalisée dans une certaine configuration afin d'établir des premiers résultats qui pourront avoir différentes applications: recommandations sur la technique du pumping en terme de fréquence optimale, validation numérique expérimentale de modèle d'interaction fluide-structure sur voiles, et enfin si une mécanisation d'un tel phénomène est envisagé, déterminer l'optimum énergétique en fonction de la puissance d'activation par rapport au gain de performance observé. Des modifications de certains paramètres expérimentaux permettraient d'étendre ces résultats:

- l'étude a été réalisée à gîte nulle. L'ajout d'une gîte fixe, voir d'une gîte variable au cours du mouvement, représentant l'équilibre apporterait sans doute un grand axe d'amélioration des conditions expérimentales. L'effet d'une voile d'avant devrait aussi être étudié.
- le mouvement d'oscillation est relativement simple et ne reproduit pas exactement ce qui se fait au niveau du réglage d'écoute en navigation sur dériveur. Généralement la phase de bordé est très rapide en opposition à la phase de choqué plus lente. Un réglage dynamique de la position du chariot rapprocherait le mouvement d'oscillation de ce qui peut se faire en dériveur. On peut envisager d'intégrer une loi d'oscillation qui suivrait le réglage d'un navigateur professionnel préalablement enregistré.
- les données concernant la mesure de la forme des voiles et du suivi de trajectoire de la tête de mât et du bout de bôme n'ont pas été présentés ici.

Nous avons donc vu que la technique de pompage, parmi les instationnarités forcées les plus utilisées lors de course à la voile lorsqu'elle est autorisée, est liée à une augmentation de la performance d'un point de vue aérodynamique. La prochaine section s'intéresse à une autre instationnarité, cette fois ci naturelle, que l'on peut observer sur le guindant de voile de portant.

J.5 Expérience en soufflerie: essais au portant. Etude de l'effet du curling: repliement périodique du guindant

Cette section porte sur l'étude en soufflerie du phénomène instationnaire naturelle appelé curling ou flapping illustré au réel en Fig. 4.2. Ce phénomène correspond au repliement périodique du guindant -bord d'attaque- d'une voile de portant. Les voiles testées ainsi que le phénomène de curling sont d'abord présentés. Puis les effets du curling sur les mesures des efforts moyens sont analysés en fonction du réglage pour trois angles de vent apparent (80° , 100° et 120°). Enfin la mesure de la fréquence réduite de curling et les évolutions dynamiques des efforts au cours de cycle de curling terminent cette section.

J.5.1 Les voiles de portant et le phénomène de curling

Quatre voiles de spinnaker de J80 à l'échelle 1 : 4.61 de design shape identiques ont été testées. Ces quatre voiles dessinées et fabriquées par Incidences Sails, décrites en Tab. J.6, présentent cependant deux coupes -méthodes d'assemblage de panneaux formant la voile- différentes: la coupe triradial montrée en Figs. J.17a J.17c et la coupe cross-cut montrée en Figs. J.17b J.17d. Le lot de spinnaker est aussi divisé en deux types de matériaux différents décrit en annexe G. Le matériaux AirX 500 présente une masse surfacique plus faible de 35 g m^{-2} en comparaison des 40 g m^{-2} du SuperKote 0.75. Ce dernier plus lourd est cependant en moyenne environ 40% plus raide en traction.

Les essais en soufflerie permettent aussi de découpler la relation vitesse et angle de vent apparent contrairement aux conditions de navigations réelles. Ainsi plusieurs vitesses d'écoulements ont pu être testées comme indiqué dans Tab. J.5. L'écoulement n'a cependant pas été twisté afin de diminuer les temps de mise en place, d'améliorer la répétabilité et de faciliter de futures comparaisons numériques expérimentales avec fluide visqueux. Des cas avec twist avaient été testés lors de la campagne expérimentale de 2015, ne montrant pas de différence significative quant à un même cas non twisté pour un angle de vent apparent de 80° . Lors de ces essais le mât en carbone d'un diamètre de 20 mm fut complètement haubané afin de diminuer ses possibles mouvements. Chaque spinnaker est testé sans autre voile afin de pouvoir faciliter les comparaisons avec des essais menés au réel sur J80 dans [Deparday, 2016] ou de faciliter de futures comparaisons numériques-expérimentales.

f_{fans} (Hz)	17.5	20	22.5	25	27.5	30
U_{Pitot} (m s^{-1})	2.49	2.86	3.24	3.61	3.99	4.36
Re (10^5)	2.85	3.28	3.71	4.13	4.56	4.99

Table J.5 – Vitesse d'écoulement en fonction des fréquences ventilateurs pour la campagne 2016. Les valeurs sont calculées à partir de la relation donnée en 2.11. Le calcul du Reynolds Re s'appuie sur la longueur caractéristique \sqrt{S} .

Lors de navigation au portant, le repliement périodique du guindant -bord d'attaque- est utilisé par les navigateurs comme un indicateur vis à vis du réglage à rechercher. Ce phénomène instationnaire naturel périodique non forcé peut être aussi observé en soufflerie comme illustré en Fig. J.18. Cependant le réglage à adopter par rapport à cette limite ne fait pas encore complètement

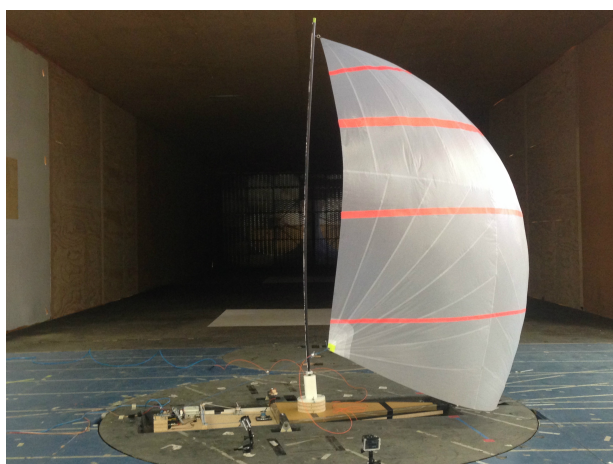
consensus dans la communauté de navigant. En effet, certains préconisent de se placer juste avant l'apparition du curling, avec une longueur d'écoute plus courte en bordant, quand d'autres recommandent d'être réglé à l'apparition du curling voir avec une longueur d'écoute plus longue, c'est à dire légèrement plus choqué. Par ailleurs l'origine de l'efficacité de ce réglage est aussi débattue. Plusieurs explications sont actuellement mises en avant: l'apparition du curling correspond à un flying shape global plus optimal, la dynamique naturelle du curling avec une longueur d'écoute fixe améliore les performances ou bien encore le fait d'ajuster en permanence la longueur d'écoute pour localiser cette limite de curling va améliorer les performances. Ici le critère de performance s'appuie principalement sur la force de propulsion pour les essais de voile de portant.

Des essais réalisés in-situ par [Deparday, 2016] et [Motta, 2015] ont pu apporter des premiers éléments de réponse innovants quant à l'efficacité du curling: des évolutions des champs de pression significatives -mesurées sur les voiles- créent périodiquement un pique de succion sur le bord d'attaque dans la direction d'avance. Ce pique se traduit alors par un effort instantané dans la phase de dépliement supérieure à une valeur obtenue sur un réglage sans curling. Le cycle de curling aura donc en général tendance à augmenter la valeur moyenne en effort de propulsion. [Deparday, 2016] a pu proposer un premier modèle de ce phénomène qui semble lié à des détachements périodique de structure convective dans l'écoulement lors du dépliement du guindant. Cependant jusqu'à présent aucune observation directe de l'écoulement sur ce phénomène n'a pu être réalisée bien que des travaux récents [Viola and Arredondo-Galeana, 2017] aient pu en bassin d'écoulement observer de telles structures convectives mais sur surface rigide, à échelle réduite et à des Reynolds différents de ceux au réel.

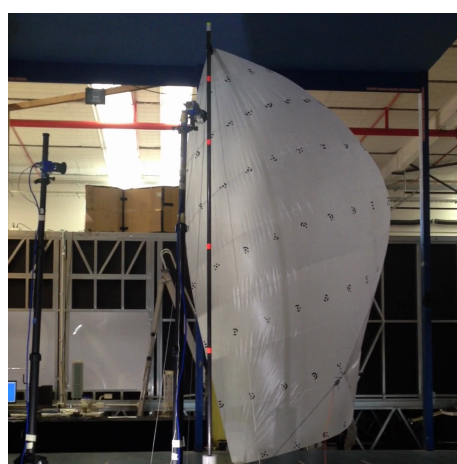
Les campagnes expérimentales en soufflerie sur ce phénomène ont donc eu plusieurs objectifs au regard des études passées:

1. étudier l'apparition du curling en tant que phénomène d'interaction fluide structure sur membrane souple. Quels sont les effets sur les efforts aérodynamiques moyens et dynamiques ainsi que les fréquences naturelles de curling? L'utilisation de la soufflerie permet une approche en milieu contrôlé, en découplant la vitesse et l'angle d'écoulement.
2. discuter les recommandations de réglages actuelles vis à vis de l'apparition du curling.
3. fournir des données expérimentales afin d'étudier les possibles effets de matériaux et de coupe par rapport à ce phénomène. Rappelons ici que les quatre spinnaker ont exactement la même forme de design shape.
4. construire une base de données expérimentales qui va pouvoir servir à la validation de modèle sur le curling mais aussi à des comparaisons numériques-expérimentales.

Les effets de l'apparition du curling sur les efforts en propulsion, dérive et effort d'écoute sont d'abord présentés pour différentes vitesses et angles d'écoulement. Puis des données sur la mesure des fréquences naturelles de curling pour les différents spinnakers sont fournies dans une deuxième partie. Enfin une dernière partie aborde des évolutions de séries temporelles d'efforts sur des cycles de curling.



(a) Triradial fabriqué en 2015: AirX 500



(b) Cross-cut fabriqué en 2016: AirX 500



(c) Triradial fabriqué en 2016: SuperKote 0.75



(d) Cross-cut fabriqué en 2015: SuperKote 0.75

Figure J.17 – Photographies des spinnakers. Les essais présentés ici correspondent à la configuration mâts haubanés visible en Fig. J.17c.

Spinnaker	Coupe	Tissu	Année de fabrication	Bandes de visualisation	Masse pendant les essais de 2016 (g)
Spinnaker Tri 1	Triradial	AirX 500	2015	Bandes orange collées	196
Spinnaker CC 1	Cross-cut	SuperKote 0.75(SK 75)	2015	Bande verte peintes	170 (168 en 2015)
Spinnaker Tri 2	Triradial	SuperKote 0.75(SK 75)	2016	Pas de bande	199
Spinnaker CC 2	Cross-cut	AirX 500	2016	Pas de bande	140

Table J.6 – Description des spinnakers utilisés pendant la campagne expérimentale en soufflerie. La surface de la voile est $S_{spinnaker} = 3.187 \text{ m}^2$ représentant 12.6% de la section de sortie de la partie de la veine fermée.

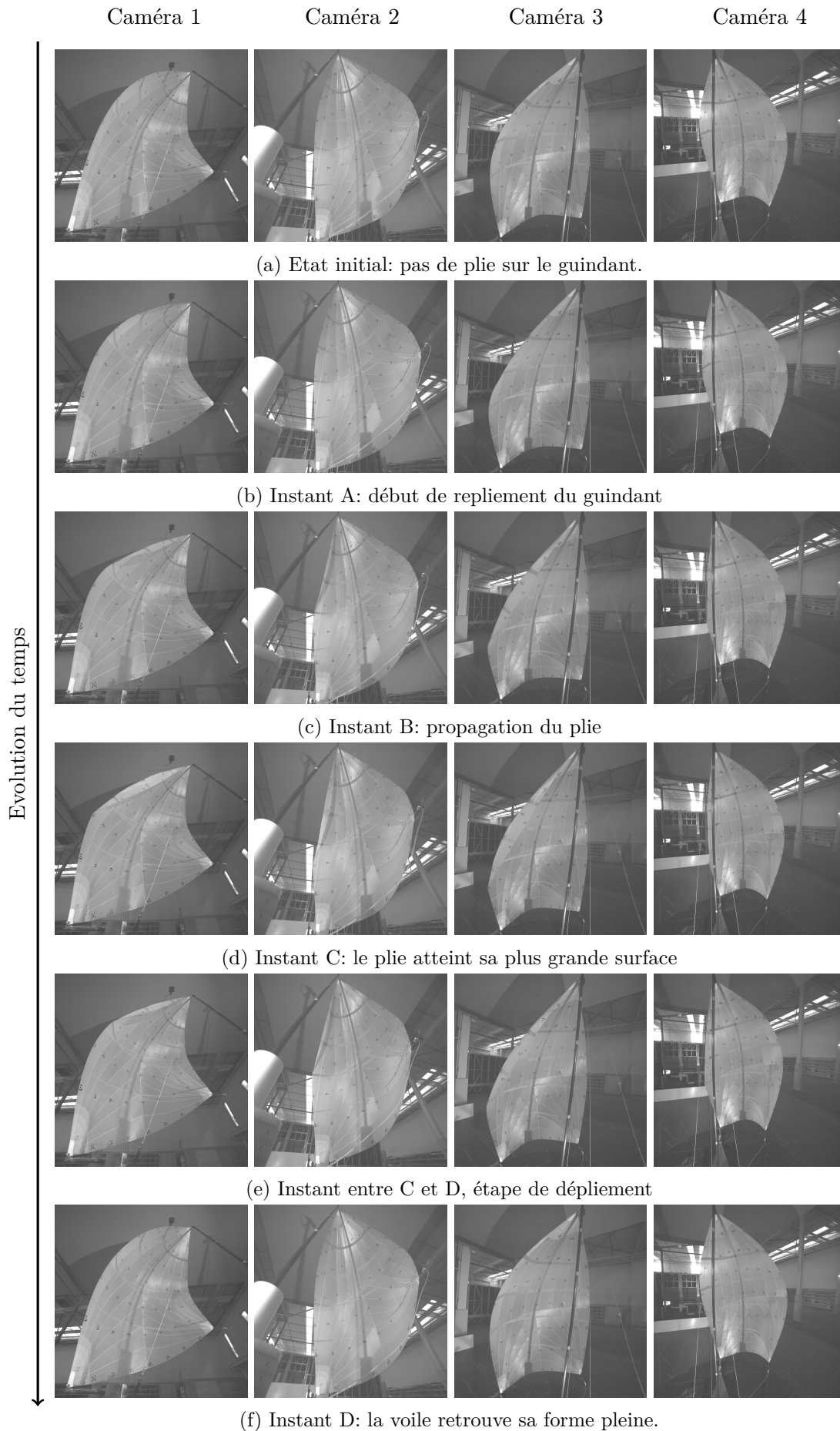


Figure J.18 – Séquence de repliement de guindant de spinnaker en soufflerie enregistré pendant la campagne expérimentale de 2016. Les instants A, B, C, D correspondent à la notation de [Deparday, 2016]. La distorsion liée aux lentilles n'a pas été corrigée ici. L'ordre des caméras 1, 2, 3, 4 est associé à leur positionnement indiqué dans la Fig. 4.4d.

J.5.2 Effet du repliement de guindant avec un gréement haubané

Dans cette section nous étudions l'effet de l'apparition du curling sur les efforts moyens. Les efforts seront tracés en fonction d'un paramètre d'entrée répétable à savoir la longueur d'écoute contrôlée L_{sheet} par un moteur pas à pas. L'apparition du curling est symbolisé par un \textcircled{C} attaché à un trait vertical correspondant à la longueur pour laquelle le curling apparaît. Cette longueur pouvant varier avec la vitesse d'écoulement, il peut avoir plusieurs barres verticales toute représentées en fonction de la vitesse d'écoulement associé. Dans chaque cas les résultats pour les quatre spinnaker sont donnés, avec les spinnakers en AirX 500, matériau léger en haut et spinnaker en SuperKote 0.75, matériau plus lourd et raide en bas. La coupe triradiale est donnée sur les figures de gauche et la coupe cross-cut sur les figures de droite.

La procédure pour les essais fût identique pour chaque voile et angle et vitesse d'écoulement: les mesures commencent avec une écoute surbordée, faible valeur de L_{sheet} , qui est progressivement choquée, augmentation de L_{sheet} . Lors de l'augmentation de L_{sheet} , le curling apparaît pour un certain réglage représenté par les barres verticales. l'écoute est choquée pour une longueur très au delà du curling périodique, longueur pour laquelle le pli peut être maintenu. Au cours de l'ensemble de la campagne expérimentale, lorsque le pli est maintenu la performance de la voile est moins importante que les maxima observés aux voisinage de l'apparition du curling, c'est pourquoi nous ne nous y sommes pas intéressés.

J.5.2.1 $\beta_{AW} = 80^\circ$

Dans le cas $\beta_{AW} = 80^\circ$, la longueur d'écoute pour laquelle le curling apparaît en fonction de la vitesse d'écoulement ne suit pas de tendance commune aux différents spinnakers.

Le coefficient de force propulsive est donné en Fig. J.19 sur laquelle nous pouvons observer deux types de comportements en fonction de la coupe du spinnaker. Les spinnakers de coupe triradial présentent un unique maximum local situé pour un réglage légèrement (environ 50 mm soit 23 cm à échelle réel) plus bordé que l'apparition du curling. Les coupes cross-cut présentent deux maxima locaux, un situé avant l'apparition du curling et un situé à l'apparition ou légèrement après. Pour le spinnaker en AirX 500 de coupe cross-cut en Fig. J.19b le maxima au voisinage du curling est plus performant. Pour le spinnaker en SuperKote 0.75 de coupe cross-cut en Fig. J.19d, le maxima au voisinage du curling est équivalent à celui 80 mm plus bordé (37 cm à l'échelle). Dans tout les cas de figure les cas extrêmement surbordés présentent des fluctuations d'effort plus important que les niveaux observés lors du curling. Ces fluctuations se traduisent par des mouvements d'oscillations globales de la membrane sans doute liés à un détachement massif pour un tel réglage.

Le coefficient de force de dérive donné en Fig. J.20 ne subit pas de changement brutal à l'apparition du curling pour les différents spinnakers. Les valeurs sont proches pour les différents spinnakers et plus l'écoute sera choquée, moins il y aura de force de dérive.

Le coefficient d'effort dans l'écoute présenté en Fig. J.21 montre une sensibilité plus importante pour la coupe cross-cut ou l'apparition du curling peut provoquer une augmentation locale du coefficient d'effort dans l'écoute, en particulier aux basses vitesses d'écoulement testées. La coupe triradial amortit la propagation d'effort dans le tissu entre le guindant et le point d'écoute car il y a plus d'interfaces liées aux coutures par comparaison à la coupe cross-cut.

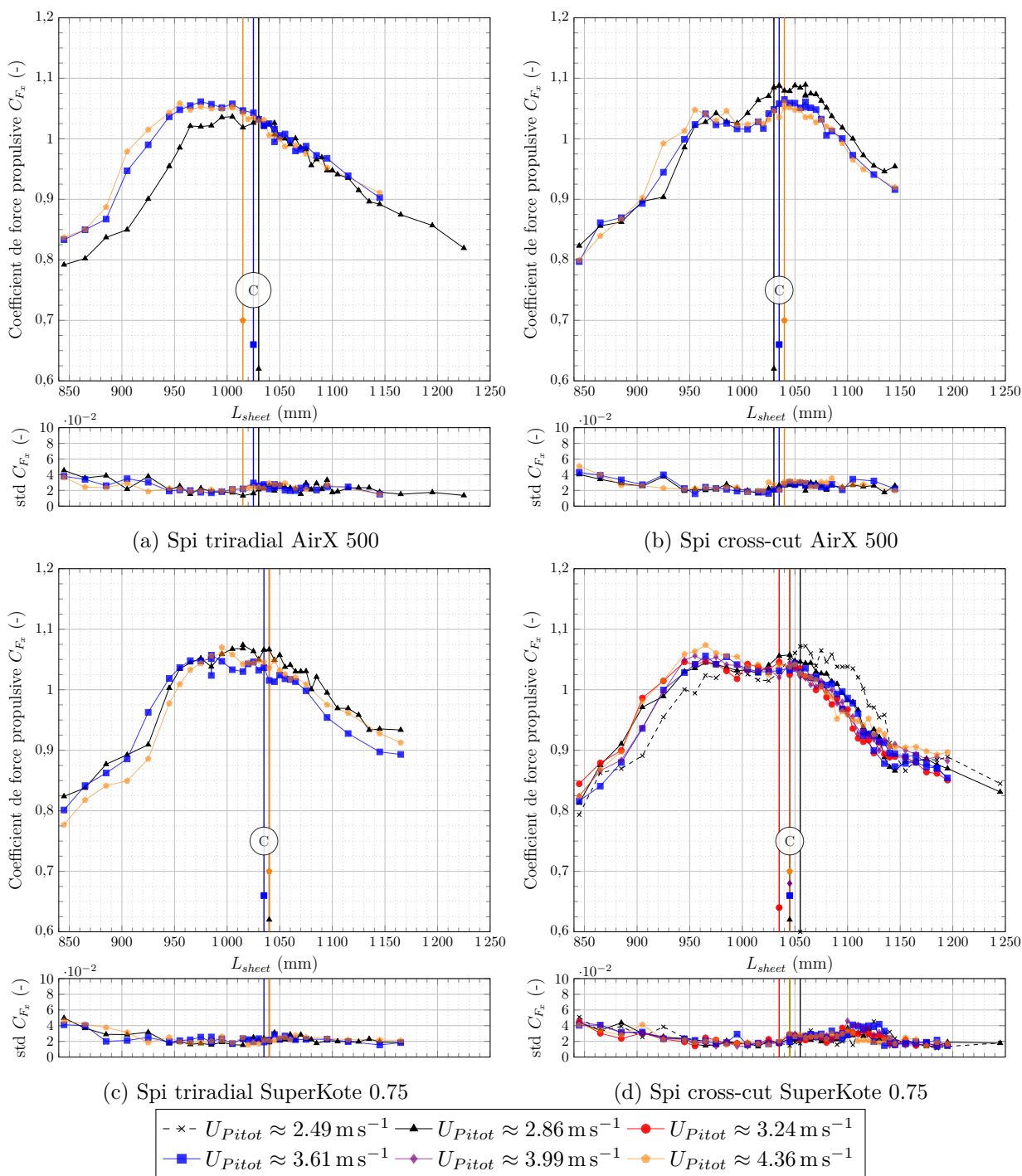


Figure J.19 – Coefficient de force propulsive C_{F_x} à $\beta_{AW} = 80^\circ$. Les limites verticales représentent l'apparition du curling. Les valeurs moyennes et écarts types (std) sont présentés pour chaque situation.

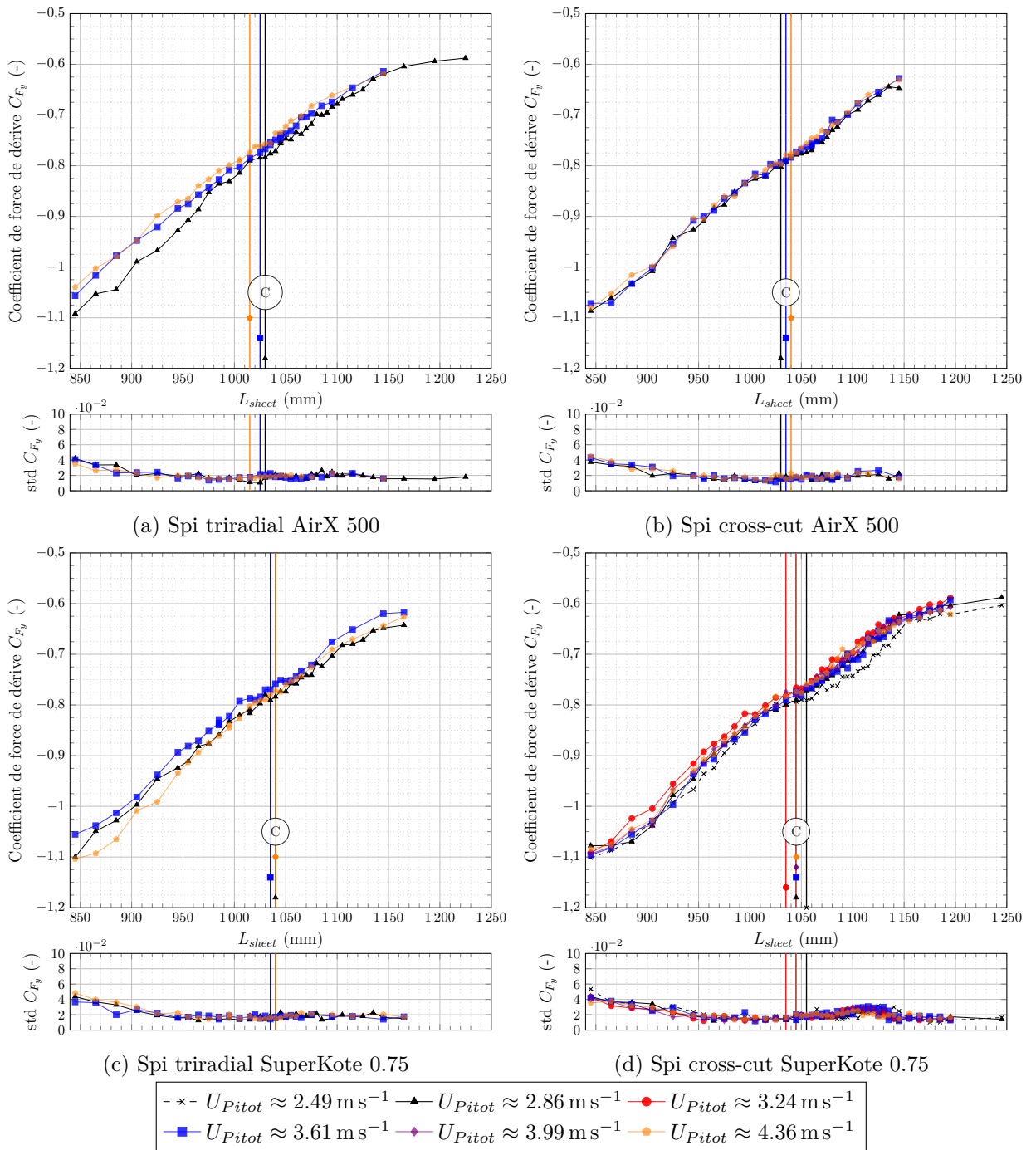


Figure J.20 – Coefficient de force de dérive C_{F_y} à $\beta_{AW} = 80^\circ$. Les limites verticales représentent l'apparition du curling. Les valeurs moyennes et écarts types (std) sont présentés pour chaque situation.

Pour $\beta_{AW} = 80^\circ$ il n'y a donc pas de recommandations communes pour le réglage à adopter, mais des tendances en fonction de la coupe et du matériau. En général être légèrement surbordé à cet angle par rapport au curling permet d'être proche de la performance maximale.

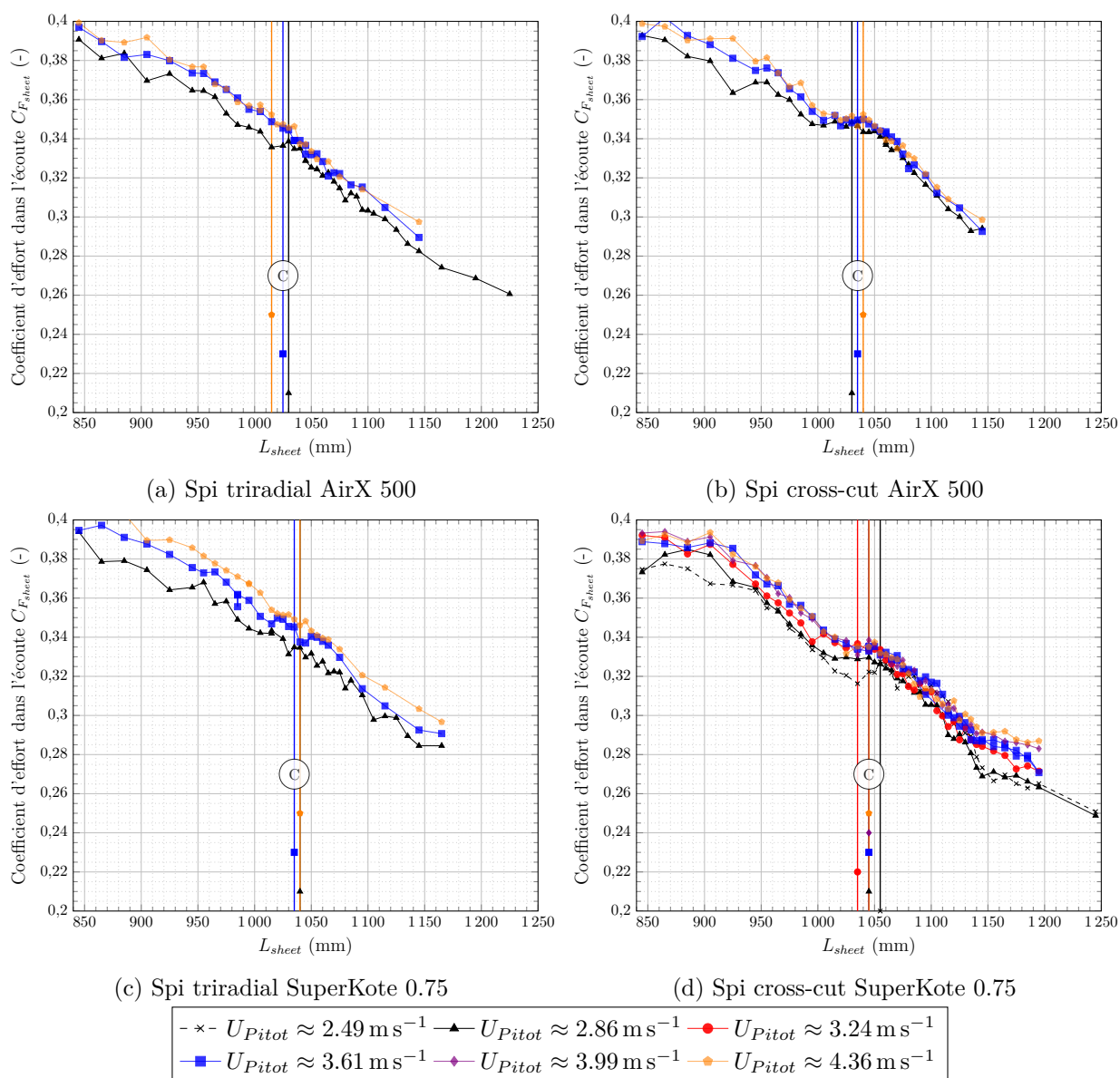


Figure J.21 – $C_{F_{sheet}}$ à $\beta_{AW} = 80^\circ$. Les limites verticales représentent l'apparition du curling.

J.5.2.2 $\beta_{AW} = 100^\circ$

Pour cet angle de vent apparent plus important, à matériau identique la coupe triradial déclenche le curling pour un réglage plus bordé par rapport à la coupe cross-cut. Le matériau plus léger, AirX 500 aura tendance à déclencher le curling pour une longueur d'écoute plus courte que le matériau plus lourd, sans doute du au décalage de la structure qui, plus légère aura tendance à se déplacer plus au vent.

Le coefficient d'effort propulsif présenté en Fig. J.22 indique maintenant un comportement identique pour l'ensemble des spinnakers. A l'apparition du curling il y a une augmentation significative du coefficient de force propulsive, représentant un bond de plus de 10% de la valeur avant l'apparition du curling. Cette nette augmentation est précédée d'une phase de plateau ou de faible augmentation avant curling. La rupture importante de comportement laisse penser ici que l'effet du curling n'est pas lié à une meilleure flying shape globale mais bien à l'apport de l'aspect dynamique du phénomène.

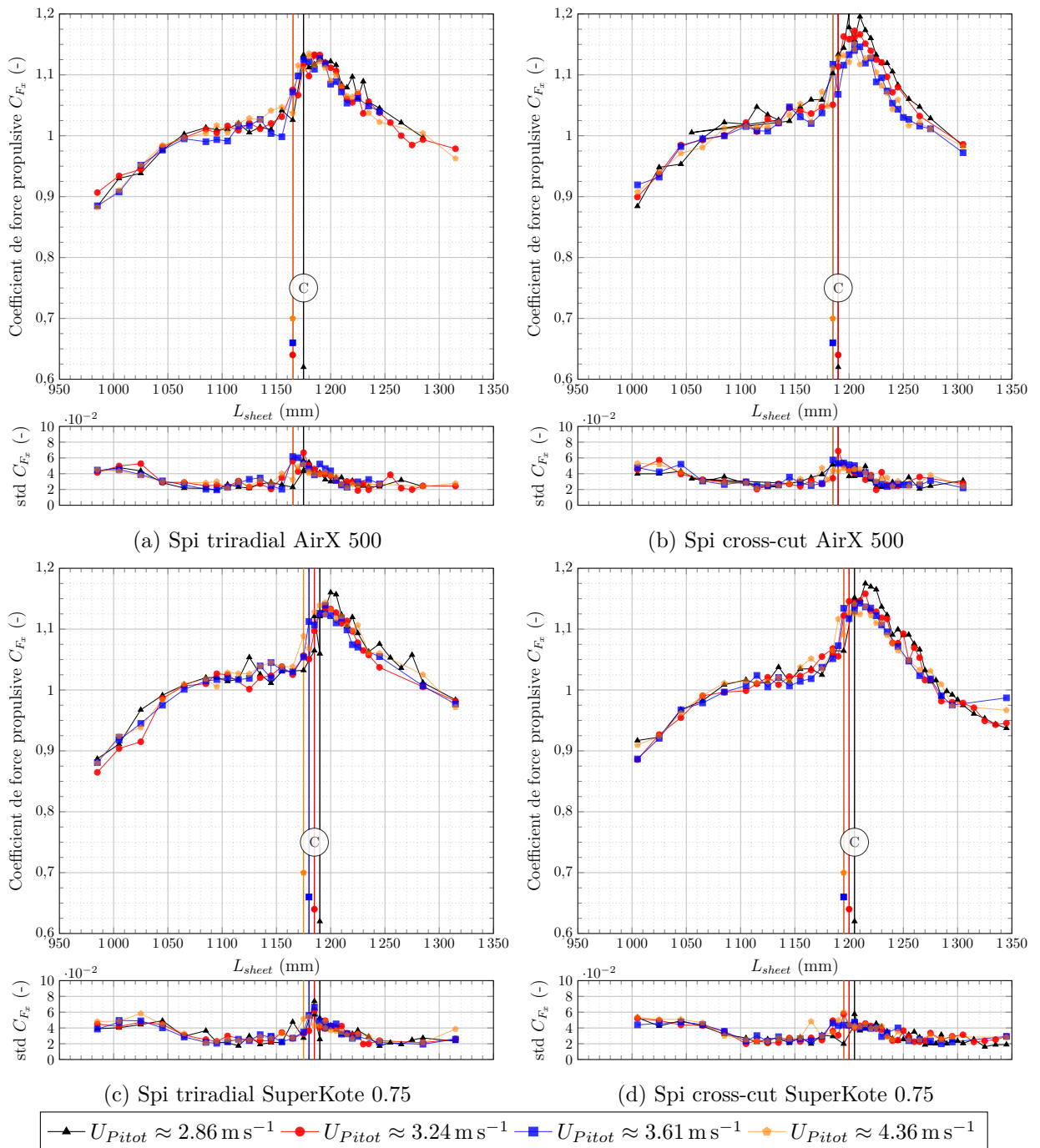


Figure J.22 – Coefficient de force propulsive C_{F_x} à $\beta_{AW} = 100^\circ$. Les limites verticales représentent l'apparition du curling. Les valeurs moyennes et écarts types (std) sont présentés pour chaque situation.

On notera que la coupe cross-cut présente aussi des niveaux de performances légèrement supérieures à la coupe triradial, ce qui est surprenant au vue des spinnakers utilisés sur le circuit de compétition de J80. La forme triradial en soufflerie présente cependant une forme en facettes suivant les coutures nettes en comparaison de sa forme qui peut être mesuré in-situ. Cela peut être du au fait que le tissu étant identique entre la maquette et le réel, va avoir tendance à moins subir de déformation à cause d'un chargement moindre en soufflerie, et en particulier aux niveaux des coutures qui sont en comparaison plus rigides à l'échelle maquette.

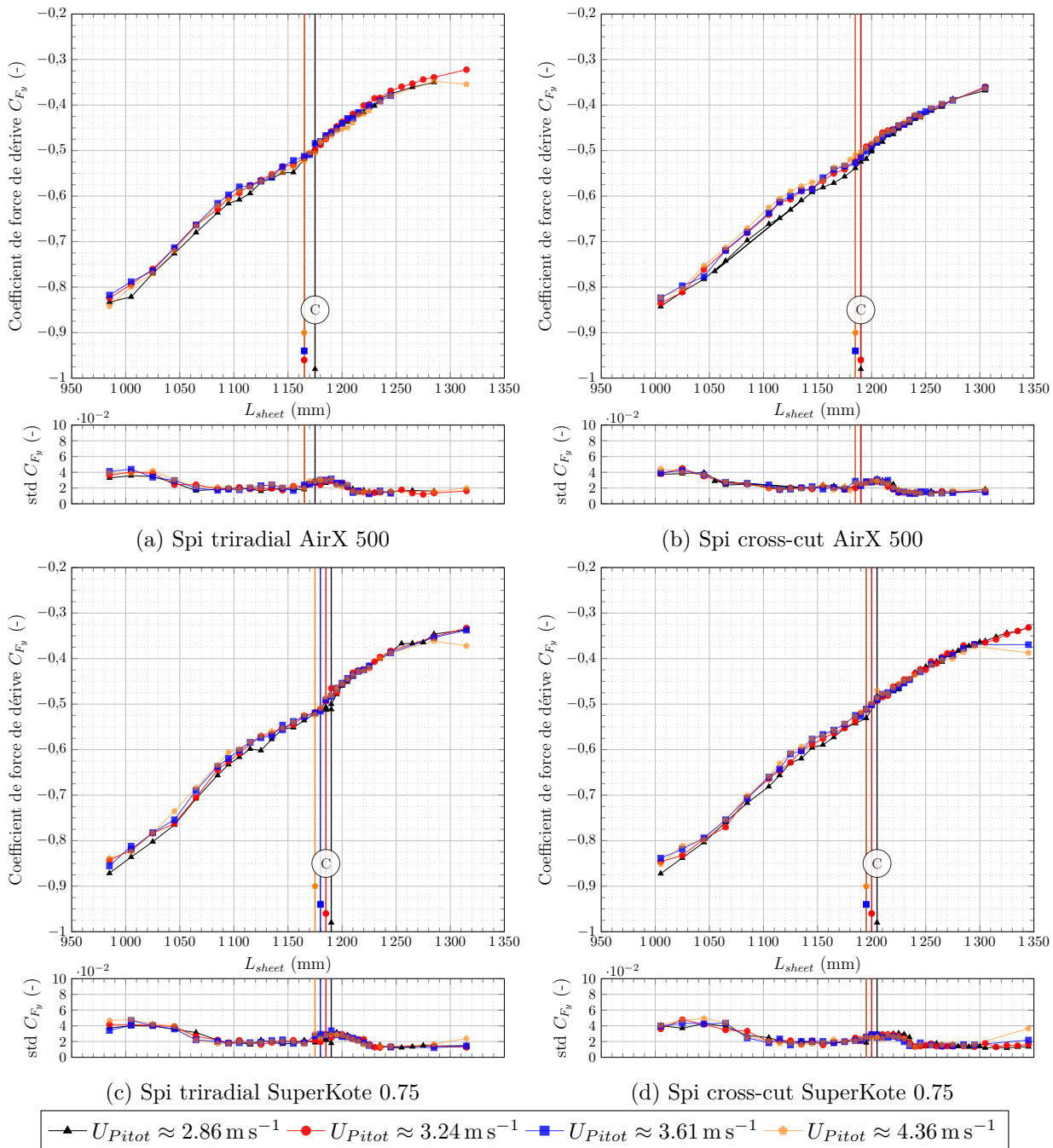


Figure J.23 – Coefficient de force de dérive à $\beta_{AW} = 100^\circ$. Les limites verticales représentent l'apparition du curling. Les valeurs moyennes et écarts types (std) sont présentés pour chaque situation.

Au niveau de l'apparition du curling, les fluctuations augmentent rapidement pour être du même ordre de grandeur que dans le cas surbordé, avant de diminuer à nouveau une fois le maximum de coefficient de force propulsive passé.

Le maximum dans tous les cas se situe légèrement plus choqué après l'apparition du curling, lorsque le phénomène est installé avec une surface de repliement périodique établie. La largeur de pique liée à ce maximum possède seulement une largeur d'environ 50 mm représentant environ 23 cm au réel.

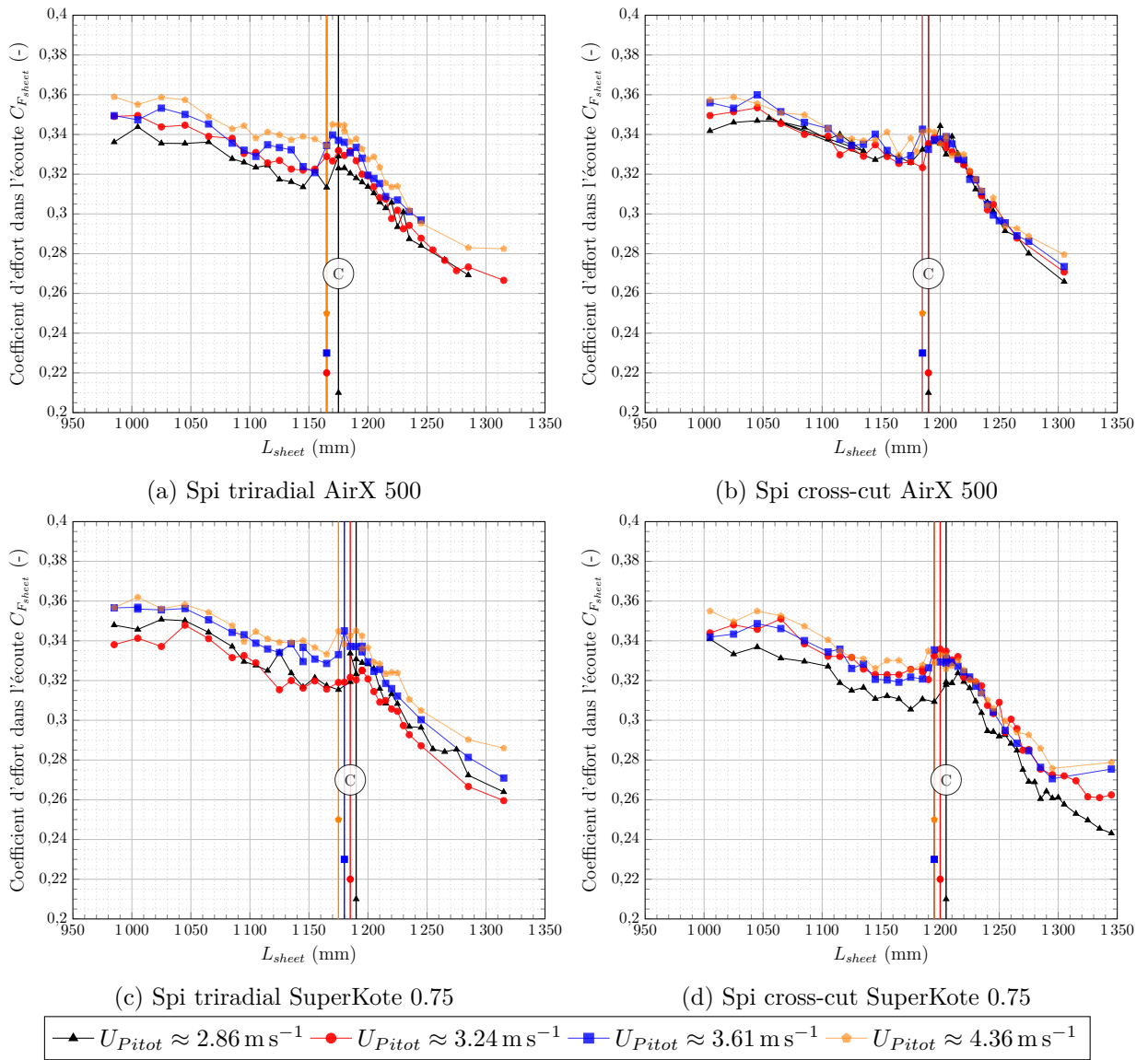


Figure J.24 – $C_{F_{sheet}}$ à $\beta_{AW} = 100^\circ$. Les limites verticales représentent l'apparition du curling.

Le coefficient d'effort de dérive présenté en Fig. J.23 montre peu d'évolution à l'apparition du curling contrairement aux fluctuations qui augmentent légèrement.

Le coefficient d'effort dans l'écoute présenté en Fig. J.24 comporte aussi un maximum légèrement après l'apparition du curling. L'augmentation, d'environ 3% de la valeur avant curling, n'est pas cependant aussi importante par rapport à l'effort propulsif, ce qui laisse à penser que la majorité de l'effort est transmis via le point d'amure et de tête du spinnaker. Ceci a été confirmé lors des mesures expérimentales in-situ sur J80 par [Deparday, 2016].

Les résultats pour $\beta_{AW} = 120^\circ$, similaires à $\beta_{AW} = 100^\circ$ en terme d'augmentation de l'effort propulsif lié au curling, sont visibles dans la section 4.3. Les fluctuations lors de l'apparition du curling sont cependant 30% plus importantes.

Ces résultats sur les efforts moyens indiquent que le mécanisme d'amélioration des performances (lorsqu'il y a augmentation de la force propulsive pour $\beta_{AW} \geq 100^\circ$) à l'apparition du curling semble lié au caractère in stationnaire du phénomène. En deçà de $\beta_{AW} = 100^\circ$, la recommandation quant au réglage dépend de la coupe et du matériau. Au delà de $\beta_{AW} = 100^\circ$, il y a un comportement net et commun à toute les configurations où le maximum se trouve légèrement après l'apparition du curling.

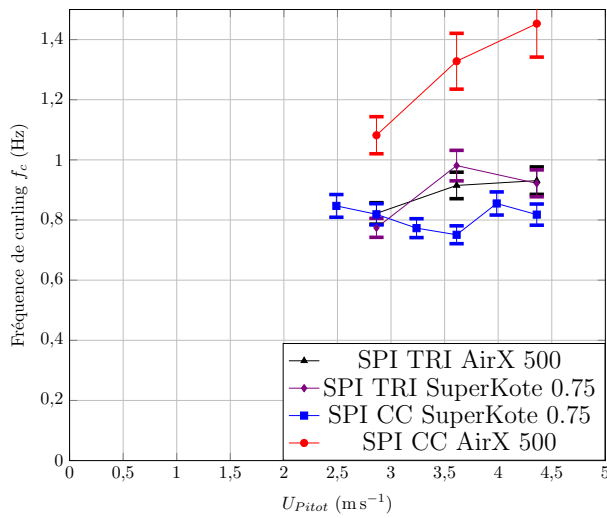
J.5.3 Mesure de la fréquence du repliement périodique de guindant

Afin de mieux caractériser le phénomène de curling, nous nous intéressons ici à sa fréquence caractéristique. Ici les effets d'angle et de vitesse d'écoulement peuvent être étudiés séparément contrairement aux expériences in-situ. Pour mesurer la fréquence de curling, plusieurs méthodes peuvent être utilisées:

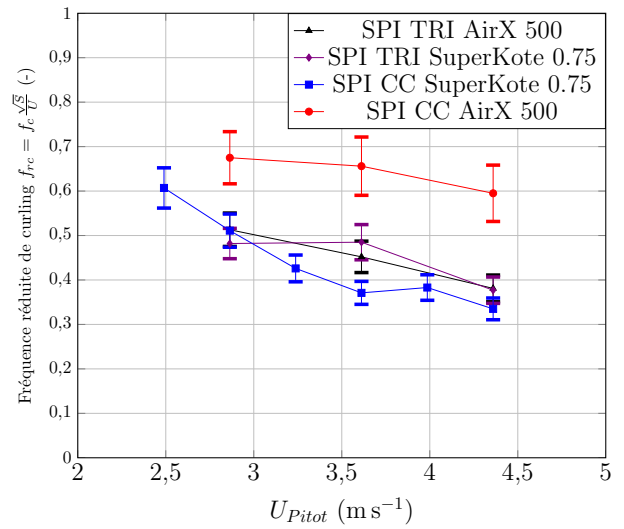
- analyse des données vidéos pour lesquelles chaque image est datée et synchronisée. Une première approche efficace mais longue a été réalisée par traitement manuel. D'autres approches de traitements automatisés basées sur l'analyse d'image ont pu être développées à la suite de ces travaux.
- analyse des signaux de forces. A l'aide de méthode d'analyse spectrale ou Empirical Mode Decomposition (EMD) ([Huang et al., 1998, Komaty et al., 2014, Komaty, 2014]) certaines fréquences peuvent être identifiées et associées à la fréquence de curling.

Ici la première méthode a été retenue afin de mesurer la fréquence de curling. Cette fréquence de curling f_c est définie comme étant l'inverse de la moyenne des périodes observées T_c entre deux événements identiques -deux repliements ou deux dépliements- aux cours d'un essai. Ainsi $f_c = \frac{1}{T_c}$. Une fréquence réduite de curling, adimensionnelle, f_{rc} est alors définie par $f_{rc} = \frac{f_c \sqrt{S}}{U_{Pitot}}$ ([Deparday, 2016]) avec S la surface de la voile et U_{Pitot} la vitesse de référence de l'écoulement. Fréquence et fréquence réduite de curling sont représentées en Fig. J.25.

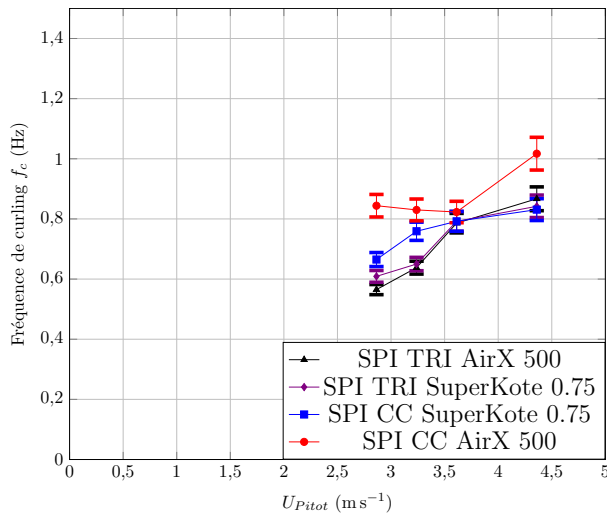
On peut alors observer qu'en fonction de l'angle de vent apparent, le comportement de la fréquence réduite est différent. Pour l'angle de vent apparent le plus faible, $\beta_{AW} = 80^\circ$, les valeurs varient en fonctions des types de spinnakers testés. Le phénomène de curling semble alors gouverné par la structure en terme d'assemblage de la voile et du matériau. Lorsque l'angle de vent apparent augmente, les fréquences tendent à se rapprocher pour les différents spi jusqu'à obtenir des valeurs proches de 0.4 à $\beta_{AW} = 120^\circ$. Dans ce dernier cas, la fréquence réduite de curling ne semble plus dépendre du matériau, mais seulement de l'écoulement, la fréquence dimensionnelle augmentant linéairement avec le vitesse d'écoulement. A la vue des oscillations de la voile dans ces conditions il est possible d'associer un tel mouvement et une telle régularité à un phénomène de lock-in entre la structure et un motif de convection de vortex dans l'écoulement. Cette valeur de 0.4 est cependant différente de la valeur observée au réel de 0.8 par [Deparday, 2016]. Cette différence semble indiquer qu'un nombre adimensionnelle plus approprié reste à définir. Ce nombre pourrait notamment prendre en compte la surface locale de repliement, le nombre de Cauchy pour représenter la rigidité de la structure par rapport aux chargements de l'écoulement et la tension de guindant qui doit avoir un impact significatif sur la fréquence du phénomène. La mesure de la fréquence réduite permet donc de caractériser expérimentalement la dynamique de la fréquence de curling.



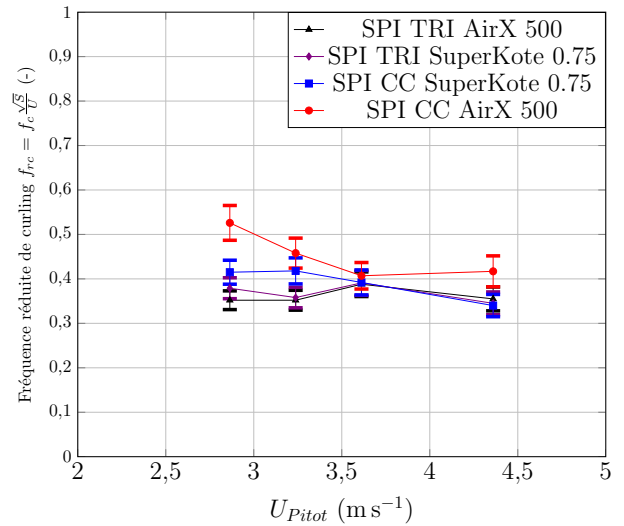
(a) f_c à $\beta_{AW} = 80^\circ$.



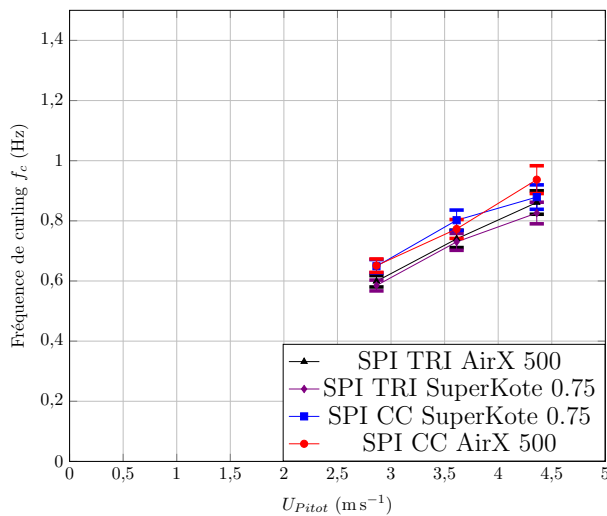
(b) f_{rc} à $\beta_{AW} = 80^\circ$.



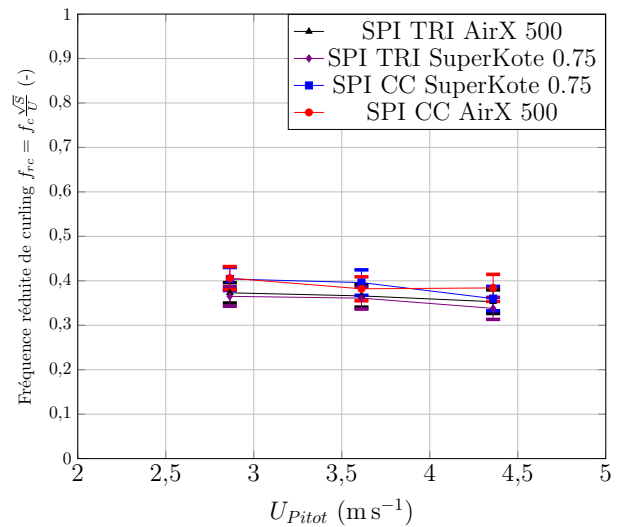
(c) f_c à $\beta_{AW} = 100^\circ$.



(d) f_{rc} à $\beta_{AW} = 100^\circ$.



(e) f_c à $\beta_{AW} = 120^\circ$.



(f) f_{rc} à $\beta_{AW} = 120^\circ$.

Figure J.25 – Fréquence et fréquence réduite de curling pour différents AWA. Les barres d'erreur pour la fréquence de curling représentent l'incertitude de mesure liée aux post-traitement vidéo. Les barres d'erreurs pour la fréquence réduite représentent la combinaison de l'incertitude de mesure liée aux post-traitement vidéo, de l'erreur de mesure de la surface de voile et sur la vitesse d'écoulement.

Une telle dynamique pourrait être alors comparée à de possibles future mesures d'écoulement sur des situations proches afin d'associer des structures observées à ce phénomène. Ces données expérimentales permettront aussi de valider un nombre adimensionnelle idoine caractérisant la dynamique du phénomène. On peut aussi envisager une application de mesure de vitesse et/ou d'angle d'écoulement à partir de l'observation du phénomène. La mesure de la fréquence réduite expérimentale permet par ailleurs d'envisager une validation de simulation numérique instationnaire d'interaction fluide-structure sur voile de portant.

J.5.4 Etude dynamique d'un cas de curling

Le spinnaker cross-cut en SuperKote 0.75 possède une fréquence réduite comparable aux différents angles de vent testé pour le milieu de la gamme de vitesse d'écoulement exploré. Nous nous proposons d'étudier des séries temporelles liées à un curling établi sur ce spinnaker à $\beta_{AW} = 120^\circ$ pour une vitesse d'écoulement de $U_{Pitot} \approx 3.61 \text{ m s}^{-1}$. Dans ce cas, il y a une nette augmentation du coefficient de force propulsive à l'apparition du curling. Deux cas sont d'abord comparés dans le Tab. J.7 où l'on peut voir que le curling présente des écarts types deux fois plus grands que le cas sans curling pour une valeur moyenne d'environ 8.5% plus importante. La différence d'amplitude des fluctuations entre ces deux cas est représentée en Fig. J.26 sur 30s d'enregistrement. Le cas avec curling présente des amplitudes de pique bien plus importantes que le cas sans curling. La même observation peut être faite sur le coefficient de force de dérive. La Fig. J.27 représente deux cycles de curling caractéristiques, pour lesquels nous avons filtré les signaux, à l'aide d'un filtre de Savitzky-Golay [Schafer, 2011] d'ordre 2 d'extension de 201 échantillons, afin de ne retenir que la composante principale lié au curling.

	Pas de curling	Curling
L_{sheet}	1295 mm	1345 mm
C_{F_x}	1.01	1.09
sC_{F_x}	2.9×10^{-2}	6.2×10^{-2}

Table J.7 – Cas avec et sans curling. Comparaison des valeurs moyennes et écarts types pour le spinnaker cross-cut SuperKote 0.75 (2015) à $\beta_{AW} = 120^\circ$ avec $U_{Pitot} \approx 3.61 \text{ m s}^{-1}$ ($f_{f_{ans}} = 25 \text{ Hz}$).

Pendant le cycle de curling:

- instant A: le guindant commence à se replier, à ce moment le coefficient de force propulsive est quasi maximale.
- instant B: le pli s'agrandit jusqu'à l'instant C, le coefficient de force propulsive diminue légèrement et le coefficient de force de dérive atteint son minimum d'intensité.
- de l'instant C à D: l'aire du pli diminue tout comme le coefficient de force propulsive. L'intensité du coefficient de force de dérive augmente à nouveau.
- de l'instant D à A: il n'y a plus de pli et le coefficient de force propulsive augmente jusqu'à son maxima.

Des différences significatives peuvent être notée en comparant la chronologie de ces différents instants aux mesures faites au réel par [Deparday, 2016], où l'effort maximale est mesuré au moment précis du dépliement. Dans ces différents travaux expérimentaux, des efforts importants afin de s'assurer de la synchronisation des données signaux/vidéo ont été réalisé. Des expériences de validation ont en parallèle été menées. Ces différences d'observations montrent que la dynamique de mécanisme de transmission d'effort au sein de la membrane peut subir un possible retard, ou déphasage, lié au

temps de propagation, qui peut être différent à l'échelle réelle et échelle maquette. Par ailleurs, il s'agit ici d'une coupe cross-cut contrairement à la coupe triradial testée au réel.

Cette partie consacrée au curling sur spinnaker a permis de montrer que:

1. l'apparition du curling pour $\beta_{AW} \geq 100^\circ$ présente une augmentation rapide et localisée du coefficient de force propulsive pour l'ensemble des spinnakers testés, jusqu'à 10% de la valeur avant curling. Pour tous les spinnakers, un réglage légèrement choqué par rapport à l'apparition du curling doit être recherché. Cette augmentation soudaine indique que l'origine de cette augmentation est liée à la dynamique du phénomène et non pas à une meilleur flying shape globale. Pour $\beta_{AW} = 80^\circ$, le curling apporte à la coupe cross-cut un maxima locale mais pas à la coupe triradial. Les recommandations quant aux réglages vont alors dépendre de la coupe et du matériau du spinnaker.
2. les mesures permettent d'observer des différences entre les coupes et matériaux utilisés pour les tests en soufflerie. La coupe cross-cut montre des tendances de performance similaire voir légèrement supérieure à la coupe triradial, cette dernière en soufflerie semblant souffrir d'une 'facettisation' importante. Le curling apparaît en général pour un réglage plus choqué pour la coupe cross-cut à matériau identique, et pour le matériau plus lourd SuperKote 0.75 pour une coupe identique.
3. une fréquence réduite de curling proche de 0.4 a pu être identifiée pour l'ensemble des spinnakers à $\beta_{AW} = 120^\circ$. La fréquence de curling à cet angle de vent apparent évolue linéairement avec la vitesse d'écoulement.
4. les séries temporelles d'un cas avec curling présentent des fluctuations dans les signaux de forces nettement supérieures au cas sans curling. Des différences de chronologie entre essais in-situ et au réel peuvent être expliquées par des temps de propagation des efforts dans la membrane différents.

Certaines pistes de recherches sont à envisager afin d'obtenir des résultats complémentaires:

- une campagne expérimentale avec l'ajout de twist pourrait faire apparaître des différences bien que des essais préliminaires avec ajout de twist n'aient pas indiqué de différence quant aux effets de l'apparition du curling avec ou sans twist. L'ajout d'une grand voile et de gîte permettraient de se rapprocher de conditions réelles de navigation.
- la détermination d'un nombre adimensionnel caractérisant la dynamique du curling, en se basant sur la fréquence réduite, le nombre de Cauchy et la tension de guindant pourrait être défini afin de mieux prédire le phénomène. La visualisation de l'écoulement permettrait aussi de confirmer le type de structure lié à ce phénomène et de confirmer les hypothèse faite à l'issue des essais in-situ.
- l'ajout d'un réglage dynamique, à l'image de celui présenté sur grand-voile dans la partie précédente, permettrait aussi de mesurer les effets d'un ajout d'une instationnarité forcée afin éventuellement d'augmenter les performances. On peut notamment se demander ce qu'il se passerait avec une fréquence de réglage proche de la fréquence naturelle de curling.
- enfin ces données expérimentales en milieu contrôlé permettent d'envisager la validation de simulation numérique instationnaire d'interaction fluide-structure sur voile de bateau, qui reste à l'heure actuelle toujours un verrou technologique sur le plan industriel.

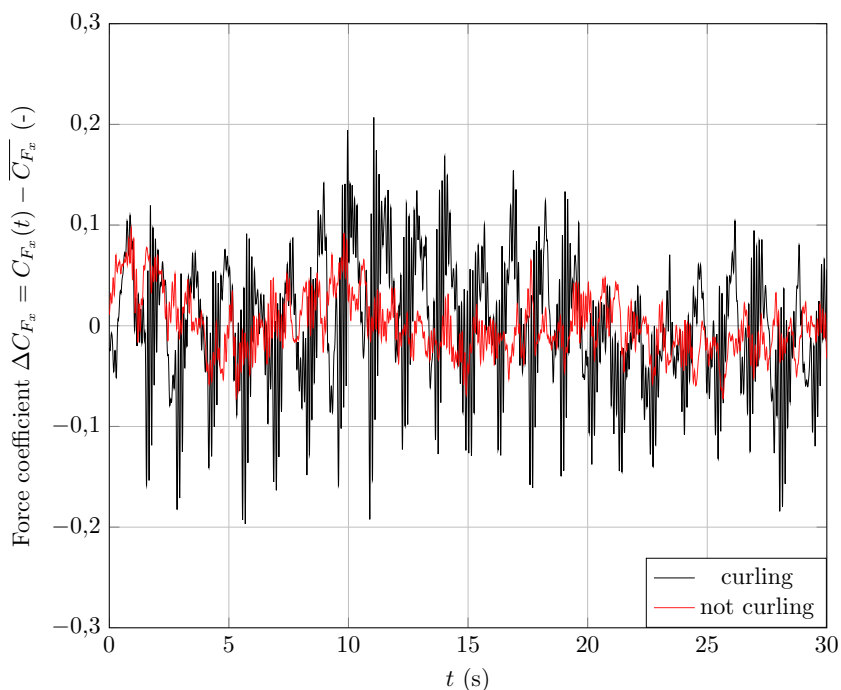


Figure J.26 – Fluctuations du coefficient de la force propulsive dans un cas avec et sans curling. Spinnaker cross-cut SuperKote 0.75 à $\beta_{AW} = 120^\circ$ avec $U_{Pitot} \approx 3.61 \text{ m s}^{-1}$ ($f_{fans} = 25 \text{ Hz}$) sur gréement haubané.

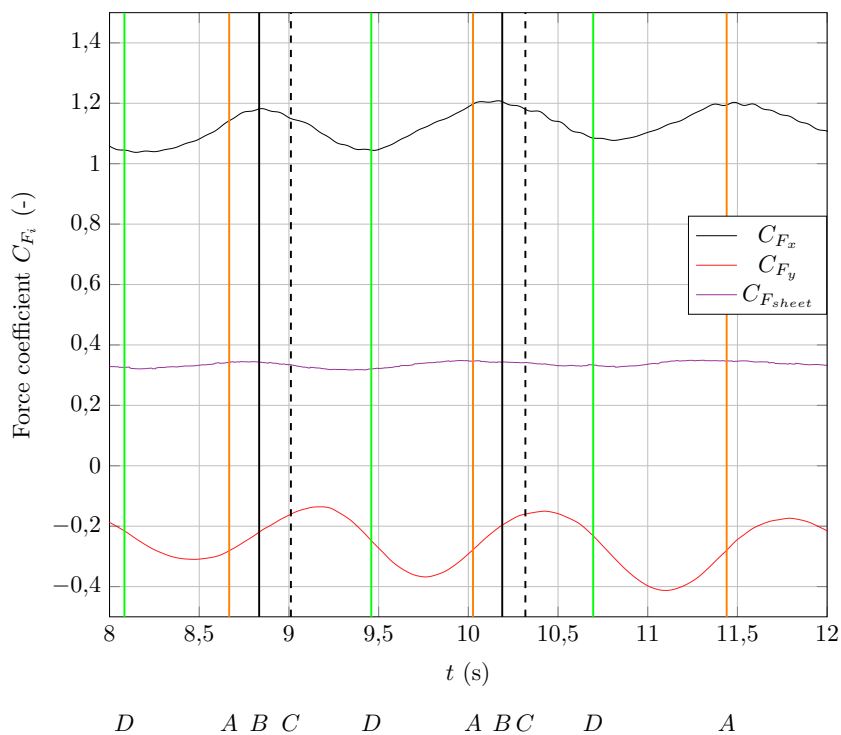


Figure J.27 – Séries temporelles filtrées sur un cas de curling sur deux cycles représentatifs. Spinnaker cross-cut SuperKote 0.75 avec $L_{sheet} = 1345 \text{ mm}$ à $\beta_{AW} = 120^\circ$ et $U_{Pitot} \approx 3.61 \text{ m s}^{-1}$ ($f_{fans} = 25 \text{ Hz}$). Les instants A (début du repliement), B, C (aire de pli maximale) et D (dépliement totale) sont indiqués à l'aide de ligne verticales et correspondent aux photographies de la Fig. 4.44.

J.6 Conclusion

Ce travail de thèse, dans le cadre du projet VOILENav et de la collaboration Sailing Fluids a permis de mener plusieurs études portant sur des phénomènes instationnaires d'interaction fluide-structure sur les voiles de bateaux.

La première partie au cours du chapitre 1 présente des résultats publiés in-situ au près dans des conditions quasi-statiques. L'évolution de la forme des voiles en fonction de réglage classique y est présentée puis comparée avec des simulations numériques. La comparaison de deux cas avec écoulement attaché ou détaché a permis d'illustrer une des limites du modèle fluide visqueux actuellement utilisé dans l'industrie nautique. Un critère simple d'équilibre sur le modèle à gîte libre permet alors d'identifier l'occurrence de telle situation afin de soit change le réglage, soit de prendre en compte une marge de sécurité plus importante quand aux résultats, ou enfin d'envisager des simulations avec modèle fluide visqueux qui restent cependant trop coûteuses en utilisation de design industriel. Face aux difficultés expérimentales in-situ pour l'analyse de phénomène instationnaire, l'étude s'est orientée vers l'utilisation d'une soufflerie.

La seconde partie présente différentes campagnes expérimentales réalisées à la soufflerie TFWT de l'Université d'Auckland. Le chapitre 2 présente les installations expérimentales utilisées.

Le chapitre 3 présente les résultats sur voile maquette d'IMOCA dans des conditions de réglage statique. Trois voiles de designs shape différents, allant d'un creux nul à un creux exagéré, sont testées. Un optimum sur deux réglages classiques est déterminé à l'aide d'une méthode d'optimisation. Pour l'angle de navigation abbatue de 60° , la voile de plus grand creux est plus performante. Un réglage dynamique est ensuite appliqué autour des optimum respectifs de chaque voile. A la plus faible fréquence réduite d'oscillation, le critère de performance diminue. Puis lorsque la fréquence réduite augmente, la performance augmente jusqu'à un maximum localisée pour une fréquence réduite autour de $f_r \approx 0.25$ à $f_r \approx 0.32$. La voile plate bénéficie en comparaison plus des effets dynamiques que les autres design. Une représentation de Lissajou est utilisée afin de calculer la puissance nécessaire à l'activation du réglage dynamique, montrant que la fréquence réduite optimale correspond aussi à un pique de puissance nécessaire. Des séries temporelles sur deux cycles d'oscillations montrent que la fréquence optimale marque le début de divergence entre les fluctuation des forces en propulsion et dérive.

Le chapitre 4 présente des essais en statique sur le repliement naturel et périodique du guindant -bord d'attaque- de spinnaker. Quatre spinnakers de J80 échelle maquette de même design shape mais de coupe et de matériaux différents sont testés sous trois angles de vent apparents et plusieurs vitesses d'écoulement. Pour $\beta_{AW} = 80^\circ$, le curling ne détermine pas une tendance claire en terme de maximum de performance et de recommandation de réglage. Pour $\beta_{AW} = 100^\circ$ et $\beta_{AW} = 120^\circ$, l'apparition du curling se traduit par une augmentation brutale du coefficient de l'effort de propulsion de l'ordre de 10% de la valeur avant curling. Le maximum se trouve alors localisé pour un réglage légèrement choqué par rapport à cette limite. Une fréquence réduite de curling proche de 0.4, commune à tous les spinnaker, est identifié à $\beta_{AW} = 120^\circ$. La chronologie des signaux temporels en soufflerie est présenté au cours de deux cycles de curling, montrant quelques différences avec les résultats observés in-situ [Deparday, 2016].

J.6.1 Perspectives

Les essais réalisés sur J80 ont permis d'améliorer les mesures in-situ grâce notamment aux travaux de [Kerhascoët, 2017], en particulier sur la mesure du vent. Le traitement de situation instationnaire en pleine échelle peut être envisagé. La généralisation de l'utilisation de modèle à gîte libre lors de simulation permet d'améliorer la détection de cas où le détachements n'est pas modélisé afin de prendre des mesures corrective en phase de design.

L'expérience sur le pumping pourrait être reproduite en y incluant les effets de gîte, à la fois statique ou dynamique comme l'on peut l'observer en dériveur. L'ajout d'une voile d'avant peut aussi être envisagé. Un grément haubané peut aussi être testé. La loi de commande du réglage d'écoute peut aussi être adaptée pour être plus réaliste vis à vis du pumping en navigation. La visualisation de l'écoulement permettrait par ailleurs de confirmer l'inversion de sillage à cette fréquence particulière comme suggéré par [Williamson and Schutt, 2016] dans le cas du flicking. L'analyse énergétique pourrait être étendue et ceux afin de pouvoir définir un rendement qui permettrait de déterminer quelle fréquence réduite semble améliorer la performance pour un coût énergétique restant acceptable. Lorsque cette techniques est autorisée, on pourrait alors suggérer deux fréquences adaptées à des phases de courses différentes. Une fréquence avec un mode endurance pour un effort sur la durée qui améliore un peu la performance mais consomme peu au regard d'un mode sprint améliorant grandement la performance mais nécessitant plus de puissance. De même des systèmes autonomes s'appuyant sur ce principe afin d'augmenter une vitesse de croisière d'un voilier robotisé peuvent être envisagés.

L'expérience sur le curling pourrait être étendue au cas avec gîte, twist de l'écoulement et avec la présence d'une grand-voile. L'analyse en courbe de Bézier permettrait de systématiser le traitement des images afin de produire des flying shape dynamiques au cours de curling. Les différences entre les flying shape par rapport aux coupes et matériaux pourraient alors être mieux identifiées. Des simulations numériques fluides sur certaines formes déjà obtenues sont réalisées dans le cadre de la continuation de ces travaux.

L'ensemble de ces travaux à donc montrer que les phénomènes aéro-elastique instationnaires apparaissant sur les voiles, de manière naturelle pour le curling ou forcée pour le pumping, sont en général liés à une augmentation de la performance du point de vue aérodynamique. En plus d'une meilleur caractérisation de ces phénomènes, les résultats expérimentaux en milieu contrôlé permettent d'espérer la validation de code d'interaction fluide-structure numérique in stationnaire pour des applications instationnaires. La simulation d'interaction fluide-structure d'écoulement détaché sur voile de portant reste un des verrous technologiques majeurs dans l'industrie nautique. Une fois ces outils de simulations validés et s'appuyant sur les méthodes développées par le doctorant Matthieu Sacher, de l'optimisation basée sur l'amélioration de performance en instationnaire pourra être envisagé afin de pouvoir tester de nouveaux réglages, nouveaux matériaux, design shape, coupe ou répartitions de fibre dans la voile.

Bibliography

- [Abbitt et al., 1996] Abbitt, J. D., Fuentes, C. A., and Carroll, B. F. (1996). Film-based pressure-sensitive-paint measurements. *Optics letters*, 21(22):1797–1799. pages 31
- [AC34th, 2017] AC34th (2017). 34th America’s Cup - LiveLine Data. <http://www.sailyachtresearch.org/resources/34th-americas-cup-liveline/> Last accessed on the 11th of June 2017. pages 9
- [Aubin et al., 2016a] Aubin, N., Augier, B., Bot, P., Hauville, F., and Floch, R. (2016a). Inviscid approach for upwind sails aerodynamics. How far can we go? *Journal of Wind Engineering and Industrial Aerodynamics*, 155:208–215. pages i, 13, 17, 21, 33, 242, 243
- [Aubin et al., 2016b] Aubin, N., Augier, B., Bot, P., Hauville, F., Sacher, M., and Flay, R. G. J. (2016b). Wind tunnel investigation of dynamic trimming on upwind sail aerodynamics. In *The 22nd Chesapeake sailing yacht symposium*, number March, pages 111–121, Annapolis, Maryland, USA. pages 10, 13, 106, 239
- [Augier, 2012] Augier, B. (2012). *Etudes expérimentales de l’interaction fluide-structure sur surface souple: application aux voiles de bateaux*. PhD thesis, Université de Bretagne Occidentale. pages 1, 9, 17, 30, 32, 197, 229, 237, 239, 245
- [Augier et al., 2012] Augier, B., Bot, P., Hauville, F., and Durand, M. (2012). Experimental validation of unsteady models for fluid structure interaction: Application to yacht sails and rigs. *Journal of Wind Engineering and Industrial Aerodynamics*, 101:53–66. pages 13, 29, 109, 149
- [Augier et al., 2013] Augier, B., Bot, P., Hauville, F., and Durand, M. (2013). Dynamic behaviour of a flexible yacht sail plan. *Ocean Engineering*, 66:32–43. pages 1, 13, 238
- [Augier et al., 2014] Augier, B., Hauville, F., Bot, P., Aubin, N., and Durand, M. (2014). Numerical study of a flexible sail plan submitted to pitching : Hysteresis phenomenon and effect of rig adjustments. *Ocean Engineering*, 90:119–128. pages 13, 27, 183
- [Banks et al., 2010] Banks, J., Webb, A., Spenkuch, T., and Turnock, S. R. (2010). Measurement of dynamic forces experienced by an asymmetric yacht during a gybe, for use within sail simulation software. In *The 8th Conference of the International Sports Engineering Association (ISEA)*, volume 2, pages 2511–2516. Elsevier. pages 6, 10, 14, 239
- [Bergsma et al., 2012] Bergsma, F., Motta, D., Le Pelley, D. J., Richards, P. J., and Flay, R. G. J. (2012). Investigation of shroud tension on sailing yacht aerodynamics using full-scale real-time

- pressure and sail shape measurements. In *The 22nd HISWA Symposium on Yacht Design and Yacht Construction*, number December, Amsterdam, The Netherlands. pages 13
- [Bles et al., 2009] Bles, G., Nowacki, W. K., and Tourabi, A. (2009). Experimental study of the cyclic visco-elasto-plastic behaviour of a polyamide fibre strap. *International Journal of Solids and Structures*, 46(13):2693–2705. pages 230
- [Bohé, 2005] Bohé, V. (2005). *Comportement mécanique des tissus à voile*. PhD thesis, Université Pierre et Marie Curie. pages 229
- [Bot et al., 2013] Bot, P., Viola, I. M., Flay, R. G. J., and Brett, J.-s. (2013). Wind-Tunnel pressure measurements on model-scale semi-rigid downwind sails. In *The Third International Conference on Innovation in High Performance Sailing Yachts (Innovsail)*, pages 119–127, Lorient, France. pages 10, 239
- [Bot et al., 2014] Bot, P., Viola, I. M., Flay, R. G. J., and Brett, J.-S. (2014). Wind-tunnel pressure measurements on model-scale rigid downwind sails. *Ocean Engineering*, 90:84–92. pages 14, 31, 100, 246, 255
- [Braun, 2016] Braun, J. B. (2016). Downwind Aero Moments & Forces. Technical report, Sailing Yacht Research Foundation. pages 12
- [Braun and Imas, 2008] Braun, J. B. and Imas, L. (2008). High fidelity CFD simulations in racing yacht aerodynamic analysis. In *3rd High Performance Yacht Design Conference*, pages 168–175, Auckland, New Zealand. pages 13
- [Brummer, 2012] Brummer, M. (2012). Finn mast dynamics. *FinnFare*, (April):24–25. pages 13
- [Brummer, 2016] Brummer, M. (2016). Free pumping: endurance, acrobatics and horsepower. *FinnFare*, (November):29–31. pages 7, 101
- [Campbell, 2014a] Campbell, I. M. C. (2014a). A comparison of downwind sail coefficients from tests in different wind tunnels. *Ocean Engineering*, 90:62–71. pages 14
- [Campbell, 2014b] Campbell, I. M. C. (2014b). Comparison of downwind sailing performance predicted from wind tunnel tests with full-scale trials from America’s Cup class yachts. In *The 23rd HISWA Symposium on Yacht Design and Yacht Construction*, pages 104–123, Amsterdam, The Netherlands. pages 14
- [Campbell and Claughton, 1994] Campbell, I. M. C. and Claughton, A. R. (1994). Wind tunnel testing of sailing yacht rigs. In *The 13th HISWA International Symposium on Yacht Design and Yacht Construction*, pages 86–106, Amsterdam. pages 13
- [Cathelain, 2017] Cathelain, M. (2017). *Development of a deterministic numerical model for the study of the coupling between an atmospheric flow and a sea state*. PhD thesis, Ecole Centrale de Nantes. pages 25, 244
- [Challis and Kitney, 1990] Challis, R. E. and Kitney, R. I. (1990). Biomedical signal processing (in four parts). Part 1. Time-domain methods. *Medical and Biological Engineering and Computing*, 28(6):509–524. pages 5

- [Chamberlain, 1983] Chamberlain, A. C. (1983). Roughness length of sea, sand, and snow. *Boundary-Layer Meteorology*, 25:405–409. pages 24, 244
- [Chapin et al., 2011] Chapin, V. G., de Carlan, N., and Heppel, P. (2011). A multidisciplinary computational framework for sailing yacht rig design & optimization through viscous FSI. In *The 20th Chesapeake Sailing Yacht Symposium*, number March, pages 1–18, Annapolis, Maryland, USA. pages 13
- [Charnock, 1955] Charnock, H. (1955). Wind stress on a water surface. *Quarterly Journal of the Royal Meteorological Society*, 81(350):639–640. pages 24, 244
- [Clauss and Heisen, 2005] Clauss, G. F. and Heisen, W. (2005). CFD analysis on the flying shape of modern yacht sails. In *The 12th International Congress of the International Maritime Association of the Mediterranean*, number September, pages 87–94, Lisbon, Portugal. pages 13
- [Cleaver et al., 2009] Cleaver, D., Wang, Z., and Gursul, I. (2009). Lift enhancement on oscillating airfoils. In *AIAA Fluid Dynamics Conference*, number June, pages 1–16, San Antonio, Texas, USA. pages 116
- [Collie, 2006] Collie, S. (2006). *Application of computational fluid dynamics to two-dimensional downwind sail flows*. PhD thesis, The University of Auckland. pages 151, 240
- [Combes and Daniel, 2001] Combes, S. a. and Daniel, T. L. (2001). Shape, flapping and flexion: wing and fin design for forward flight. *The Journal of experimental biology*, 204(Pt 12):2073–2085. pages 7
- [Cook, 1985] Cook, N. J. (1985). *The Designer’s Guide to Wind Loading of Building Structures, Part 1*. Butterworths, London. pages 24, 244
- [Crompton, 2001] Crompton, M. (2001). *The thin aerofoil leading edge bubble*. PhD thesis, University of Bristol. pages 151
- [de Langre, 2009] de Langre, E. (2009). *Fluides et Solides*. Les éditions de l’Ecole Polytechnique, Ellipse Diffusion, Palaiseau, France. pages 15, 240
- [Deparday, 2010] Deparday, J. (2010). Spinnaker flying shape determination: comparison of a spinnaker model in a Twisted Flow Wind Tunnel with a full-scale spinnaker using photogrammetric measurements. Technical report, ENSTA Bretagne (ENSIETA), Brest. pages 1, 238
- [Deparday, 2016] Deparday, J. (2016). *Experimental studies of Fluid-Structure Interaction on Downwind Sails*. PhD thesis, Université de Bretagne Occidentale, Brest. pages 1, 7, 8, 9, 13, 14, 15, 16, 29, 30, 31, 32, 121, 122, 123, 124, 125, 130, 138, 164, 166, 173, 177, 182, 187, 197, 238, 239, 240, 241, 246, 263, 264, 266, 273, 274, 276, 279
- [Deparday et al., 2016a] Deparday, J., Bot, P., Hauville, F., Augier, B., and Rabaud, M. (2016a). Full-scale flying shape measurement of offwind yacht sails with photogrammetry. *Ocean Engineering*, 127(October 2016):135–143. pages 14
- [Deparday et al., 2016b] Deparday, J., Bot, P., Hauville, F., Augier, B., Rabaud, M., Motta, D., and Le Pelley, D. (2016b). Modal Analysis of Pressures on a Full-Scale Spinnaker. *The 22nd Chesapeake Sailing Yacht Symposium*, (March):98–110. pages 14

- [Deparday et al., 2014] Deparday, J., Bot, P., Hauville, F., Motta, D., Le Pelley, D. J., and Flay, R. G. J. (2014). Dynamic measurements of pressures, sail shape and forces on a full-scale spinnaker. In *The 23rd HISWA Symposium on Yacht Design and Yacht Construction*, pages 61–73, Amsterdam, The Netherlands. pages 14, 121
- [Devalan, 2009] Devalan, P. (2009). Vibrations des structures - Systèmes discrets et poutres. Technical Report BM5023 V1. pages 234
- [Dhawan, 1991] Dhawan, S. (1991). Bird flight. *Sadhana*, 16(4):275–352. pages 7
- [Dhomé, 2016] Dhomé, U. (2016). Stage de recherche de 3ème année: Interaction fluide-structure sur surfaces souples : application aux voiles de bateau. Technical report, Ecole Polytechnique, Département de Mécanique. pages 109, 173, 234
- [Dmitrochenko, 2008] Dmitrochenko, O. (2008). Finite elements using absolute nodal coordinates for large-deformation flexible multibody dynamics. *Journal of Computational and Applied Mathematics*, 215(2):368 – 377. Proceedings of the Third International Conference on Advanced Computational Methods in Engineering (ACOMEN 2005). pages 178
- [Douguet, 2014] Douguet, R. (2014). *Optimisation de la mesure et de l'interprétation des performances dans le cadre de la course au large*. PhD thesis, Université de Bretagne sud. pages 9, 239
- [Drela, 1989] Drela, M. (1989). Xfoil: An analysis and design system for low Reynolds number airfoils. In *Low Reynolds number aerodynamics*, pages 1–12. Springer. pages 42
- [Du Pontavice, 2016] Du Pontavice, E. (2016). *Kite propulsion : rise and wander*. Theses, Université Paris-Saclay. pages 136
- [Dupupet, 2008] Dupupet, J. (2008). Fibres de carbone. *Techniques de l'ingénieur Report:AM5134 V1*, 33(0):19. pages 234
- [Durand, 2012] Durand, M. (2012). *Interaction fluide-structure souple et légère, applications aux voiliers*. PhD thesis, Ecole Centrale de Nantes. pages 1, 11, 12, 14, 15, 29, 32, 124, 229, 231, 237, 238, 240
- [Durand et al., 2013] Durand, M., Leroyer, A., Lothode, C., Hauville, F., Visonneau, M., Floch, R., and Guillaume, L. (2013). FSI investigation on stability of downwind sails with an automatic dynamic trimming. In *The Third International Conference on Innovation in High Performance Sailing Yachts*, Lorient, France. pages 14
- [Durand et al., 2014] Durand, M., Leroyer, A., Lothodé, C., Hauville, F., Visonneau, M., Floch, R., and Guillaume, L. (2014). FSI investigation on stability of downwind sails with an automatic dynamic trimming. *Ocean Engineering*, 90:129–139. pages 2, 10, 14, 124, 238
- [Egan et al., 2016] Egan, B. C., Brownell, C. J., and Murray, M. M. (2016). Experimental assessment of performance characteristics for pitching flexible propulsors. *Journal of Fluids and Structures*, 67:22–33. pages 7, 100, 115, 173, 255
- [Ferreira et al., 2017] Ferreira, P., Caetano, E., and Pinto, P. (2017). Real-time flying shape detection of yacht sails based on strain measurements. *Ocean Engineering*, 131:48–56. pages 31, 246

- [Flay, 1996] Flay, R. G. J. (1996). A twisted flow wind tunnel for testing yacht sails. *Journal of Wind Engineering and Industrial Aerodynamics*, 63(1-3):171–182. pages 10, 13, 49, 50, 51, 239, 248
- [Flay and Jackson, 1992] Flay, R. G. J. and Jackson, P. S. (1992). Flow simulations for wind-tunnel studies of sail aerodynamics. *Journal of Wind Engineering and Industrial Aerodynamics*, 44(1-3):2703–2714. pages 10, 25, 239
- [Flay and Millar, 2006] Flay, R. G. J. and Millar, S. (2006). Experimental considerations concerning pressure measurement on sails: wind tunnel and full-scale. In *The 2nd High Performance Yacht Design Conference*, volume 14, pages 123–130, Auckland, New Zealand. pages 13, 25, 26
- [Flay et al., 1982] Flay, R. G. J., Stevenson, D. C., and Lindley, D. (1982). Wind structure in a rural atmospheric boundary layer near the ground. *Journal of Wind Engineering and Industrial Aerodynamics*, 10(1):63–78. pages 25
- [Flay and Vuletich, 1995] Flay, R. G. J. and Vuletich, I. J. (1995). Development of a wind tunnel test facility for yacht aerodynamic studies. *Journal of Wind Engineering and Industrial Aerodynamics*, 58:231–258. pages 10, 25, 49, 50, 51, 239, 248
- [Fluck et al., 2010] Fluck, M., Gerhardt, F. C., Pilate, J., and J. Flay, R. G. (2010). Comparison of potential flow-based and measured pressure distributions over upwind sails. *Journal of Aircraft*, 47(6):2174–2177. pages 13
- [Fossati, 2009] Fossati, F. (2009). *Aero-hydrodynamics and the performance of sailing yachts*. International Marine / McGraw-Hill. pages 5
- [Fossati et al., 2015a] Fossati, F., Bayati, I., Orlandini, F., Muggiasca, S., Vandone, A., Mainetti, G., Sala, R., Bertorello, C., and Begovic, E. (2015a). A novel full scale laboratory for yacht engineering research. *Ocean Engineering*, 104:219–237. pages 9, 30, 239, 245
- [Fossati et al., 2015b] Fossati, F., Mainetti, G., Malandra, M., Sala, R., Schito, P., and Vandone, A. (2015b). Offwind sail flying shapes detection. In *The 5th High Performance Yacht Design Conference*, pages 48–59, Auckland, New Zealand. pages 10, 31, 239, 246
- [Fossati and Muggiasca, 2010] Fossati, F. and Muggiasca, S. (2010). Numerical modelling of sail aerodynamic behavior in dynamic conditions. In *The Second International Conference on Innovation in High Performance Sailing Yachts*, Lorient, France. pages 13, 27, 118
- [Fossati and Muggiasca, 2011] Fossati, F. and Muggiasca, S. (2011). Experimental investigation of sail aerodynamic behaviour in dynamic conditions. *Journal of Sailboat Technology*, (02):1–41. pages 5, 10, 13, 27, 191, 195, 239
- [Fossati and Muggiasca, 2012a] Fossati, F. and Muggiasca, S. (2012a). An experimental investigation of unsteady sail aerodynamics including sail flexibility. In *The 4th High Performance Yacht Design Conference*, pages 222–231, Auckland, New Zealand. pages 5, 10, 100, 239, 255
- [Fossati and Muggiasca, 2012b] Fossati, F. and Muggiasca, S. (2012b). Motions of a sailing yacht in large waves: an opening simple instationary modelling approach. In *The 22nd HISWA Symposium on Yacht Design and Yacht Construction*, Amsterdam, The Netherlands. pages 27

- [Fossati et al., 2008] Fossati, F., Muggiasca, S., Martina, F., Nazareth, A., Vallicelli, A., and Viola, I. I. M. (2008). Wind tunnel and CFD investigation of unconventional rigs. In *The Third High Performance Yacht Design Conference*, pages 91–100, Auckland, New Zealand. pages 60
- [Fossati et al., 2006] Fossati, F., Muggiasca, S., Viola, I. M., and Zasso, A. (2006). Wind tunnel techniques for investigation and optimization of sailing yachts aerodynamics. In *The 2nd High Performance Yacht Design Conference*, pages 105–113, Auckland, New Zealand. pages 13
- [Garrett, 1996] Garrett, R. (1996). *The symmetry of sailing: the physics of sailing for yachtsmen*. Sheridan House, Inc. pages 115
- [Gentry, 1971] Gentry, A. (1971). The Aerodynamics of Sail Interaction. In *Third AIAA Symposium of Aero/Hydrodynamics of Sailing*, Redondo Beach, California, USA. pages 10, 13
- [Gerhardt, 2010] Gerhardt, F. C. (2010). *Unsteady Aerodynamics of Upwind-Sailing and Tacking*. PhD thesis, The University of Auckland. pages 6, 13
- [Gerhardt et al., 2011] Gerhardt, F. C., Flay, R. G. J., and Richards, P. J. (2011). Unsteady aerodynamics of two interacting yacht sails in two-dimensional potential flow. *Journal of Fluid Mechanics*, 668:551–581. pages 13
- [Gerhardt et al., 2009] Gerhardt, F. C., Le Pelley, D. J., Flay, R. G. J., and Richards, P. J. (2009). Tacking in the Wind Tunnel. In *The 19th Chesapeake sailing yacht symposium*, pages 161–175, Annapolis, Maryland, USA. pages 13
- [Gerster, 2016] Gerster, Y. (2016). *Bestimmung der Windgeschwindigkeit gemessen von einem sich bewegendem Anemometer auf einem Masten. Determination of the wind speed measured by a moving anemometer at the mast head*. Master thesis, ETH Zürich. pages 27, 32, 245
- [Gordnier et al., 2013] Gordnier, R. E., Kumar Chimakurthi, S., Cesnik, C. E. S., and Attar, P. J. (2013). High-fidelity aeroelastic computations of a flapping wing with spanwise flexibility. *Journal of Fluids and Structures*, 40:86–104. pages 109
- [Graf and Müller, 2009] Graf, K. and Müller, O. (2009). Photogrammetric investigation of the flying shape of spinnakers in a Twisted Flow Wind Tunnel. In *The 19th Chesapeake sailing yacht symposium*, pages 97–108, Annapolis, Maryland, USA. pages 10, 14, 239
- [Graves et al., 2008] Graves, W., Barbera, T., and Braun, J. B. (2008). Measurement and Simulation of Pressure Distribution on Full Size Sails. In *The 3rd High Performance Yacht Design Conference*, pages 239–246, Auckland, New Zealand. pages 9, 239
- [Hansen, 2006] Hansen, H. (2006). *Enhanced wind tunnel techniques and aerodynamic force models for yacht sails*. PhD thesis, The University of Auckland. pages 10, 14, 24, 30, 50, 51, 53, 56, 189, 193, 195, 239, 244, 249
- [Hansen et al., 2002] Hansen, H., Jackson, P., and Hochkirch, K. (2002). Comparison of wind tunnel and full-scale aerodynamic sail force measurements. In *High Performance Yacht Design Conference*, page 9, Auckland, New Zealand. pages 14

- [Hansen et al., 2003] Hansen, H., Jackson, P. S., and Hochkirch, K. (2003). Real-Time Velocity Prediction Program for Wind Tunnel Testing of Sailing Yachts. In *The Modern Yacht Conference*, Southampton, UK. pages 10
- [Hansen et al., 2005] Hansen, H., Richards, P. J., and Hochkirch, K. (2005). Advances in the wind tunnel analysis of yacht sails. In *The 26th Symposium on Yacht Design and Construction*, Hamburg, Germany. pages 10
- [Hedges et al., 1996] Hedges, K. L., Richards, P. J., and Mallinson, G. D. (1996). Computer modelling of downwind sails. *Journal of Wind Engineering and Industrial Aerodynamics*, 63(1-3):95–110. pages 14
- [Hémon, 2006] Hémon, P. (2006). *Vibrations des structures couplées avec le vent*. Les éditions de l’Ecole Polytechnique, Palaiseau, France. pages 24
- [Herlédant, 2011] Herlédant, O. (2011). *Etude numérique et expérimentale de la micro-météorologie des sites de régates côtières appliquée à la baie de Quiberon*. PhD thesis, Ecole Centrale de Nantes (ECN). pages 25
- [Herman, 1989] Herman, J. S. J. (1989). *A sail force dynamometer: design, implementation and data handling*. Master thesis, Massachusetts Institute of Technology. pages 13
- [Hochkirch and Brandt, 1999] Hochkirch, K. and Brandt, H. (1999). Fullscale hydrodynamic force measurement on the Berlin sailing dynamometer. In *The 14th Chesapeake sailing yacht symposium*, pages 33–44, Annapolis, Maryland, USA. pages 9, 13, 239
- [Horel, 2011] Horel, B. (2011). *Measurement of full-scale wind turbulence on a moving yacht*. Master thesis, Ecole Centrale de Nantes et l’Université de Nantes. pages 26
- [Huang et al., 1998] Huang, N. E., Shen, Z., Long, S. R., Wu, M. C., Shih, H. H., Zheng, Q., Yen, N.-C., Tung, C. C., and Liu, H. H. (1998). The Empirical Mode Decomposition and the Hilbert spectrum for nonlinear and non-stationary time series analysis. *Proceedings of the Royal Society A*, 454(1971):903–962. pages 165, 274
- [Hubel et al., 2009] Hubel, T. Y., Hristov, N. I., Swartz, S. M., and Breuer, K. S. (2009). Time-resolved wake structure and kinematics of bat flight. *Experimental fluids*, pages 371–381. pages 7
- [Hunt and Ferry, 1975] Hunt, T. M. and Ferry, L. M. (1975). Gravity measurements at principal New Zealand Stations, 1973. *New Zealand Journal of Geology and Geophysics*, 18(5):713–720. pages 194
- [Incidence sails, 2017] Incidence sails (2017). Incidence sails. <http://www.incidence-sails.com/fr/incidence-technologies> Last accessed on the 11th of June 2017. pages 12
- [International sailing Federation, 2013] International sailing Federation (2013). *Racing rules of sailing*. pages 6, 250
- [Jackson et al., 1996] Jackson, P. S., Locke, N. J., and Flay, R. G. J. (1996). Lift and drag distributions of yacht sails using wake surveys. *Journal of Fluids Engineering*, 118(2):346. pages 76

- [Katzmayr, 1922] Katzmayr, R. (1922). Effect of periodic changes of angle of attack on behavior of airfoils. Technical report. pages 7
- [Kerhascoët, 2017] Kerhascoët, H. (2017). *De la mesure du vent au pilotage automatique d'un voilier : modélisation, optimisation & application du traitement du signal prédictif*. PhD thesis, Université de Bretagne sud, UFR, Sciences et Sciences de l'Ingénieur sous le sceau de l'Université Bretagne Loire Mention : STIC Ecole doctorale SICMA. pages 26, 238, 245, 280
- [Kerhascoët et al., 2016a] Kerhascoët, H., Laurent, J., Cerqueus, A., Sevaux, M., Senn, E., Hauville, F., and Coneau, R. (2016a). Methodology for optimal wind vane design. In *OCEANS 2016 - Shanghai*, pages 1–7, Shanghai. pages 2, 32
- [Kerhascoët et al., 2016b] Kerhascoët, H., Laurent, J., and Senn, E. (2016b). Speedometer Fault Detection and GNSS Fusion using Kalman Filters. In *Oceans'16 MTS/IEEE*, Monterey, California, USA. pages 2
- [Komaty, 2014] Komaty, A. (2014). *Traitement et analyse des processus stochastiques par EMD et ses extensions*. PhD thesis, Université de Bretagne Occidentale. pages 165, 274
- [Komaty et al., 2014] Komaty, A., Boudraa, A.-O., Augier, B., and Daré-Emzivat, D. (2014). EMD-Based filtering using similarity measure between probability density functions of IMFs. *IEEE Transactions on Instrumentation and Measurement*, 63(1):27–34. pages 165, 274
- [Kramer, 1932] Kramer, M. (1932). Increase in the maximum lift of an airfoil due to a sudden increase in its effective angle of attack resulting from a gust. Technical report, Washington. pages 7
- [Larousserie, 2016] Larousserie, D. (2016). Le sport, nouveau terrain de jeu des physiciens. *Le monde, science & médecine (Cahier du "Monde")*, 2237:4–5. pages 106
- [Larsson, 2005] Larsson, A. (2005). To measure full scale apparent wind velocities and turbulence profiles over the sea. Technical report, Chalmers university of technology, Göteborg, Sweden. pages 26
- [Lasher and Sonnenmeier, 2008] Lasher, W. C. and Sonnenmeier, J. R. (2008). An analysis of practical RANS simulations for spinnaker aerodynamics. *Journal of Wind Engineering and Industrial Aerodynamics*, 96(2):143–165. pages 14
- [Le Maître, 1998] Le Maître, O. (1998). *Contribution numérique à la résolution de problèmes d'interaction fluide-structure non linéaires*. PhD thesis, Université du Havre. pages 11, 240
- [Le Maître et al., 1998] Le Maître, O., De Cursi, J. S., and Huberson, S. (1998). Large displacement analysis for ideally flexible sails. *European Journal of Mechanics-A/Solids*, 17(4):619–636. pages 11, 240
- [Le Maître et al., 1996] Le Maître, O., Huberson, S., and De Cursi, J. S. (1996). Application of a non-convex model of fabric deformations to sail cut analysis. *Journal of wind engineering and industrial aerodynamics*, 63(1-3):77–93. pages 11, 240
- [Le Maître et al., 1999] Le Maître, O., Huberson, S., and Souza De Cursi, E. (1999). Unsteady Model of Sail and Flow Interaction. *Journal of Fluids and Structures*, 13:37–59. pages 11, 240

- [Le Pelley and Hansen, 2003] Le Pelley, D. J. and Hansen, H. (2003). An Investigation into the Effects of heel on Downwind Sails. In *The Modern Yacht*, pages 1–6, Southampton, UK. pages 10
- [Le Pelley and Modral, 2008] Le Pelley, D. J. and Modral, O. (2008). V-SPARS: a combined sail and rig shape recognition system using imaging techniques. In *The 3rd High Performance Yacht Design Conference*, pages 57–66, Auckland, New Zealand. pages 3, 31, 55, 238, 246
- [Le Pelley et al., 2015] Le Pelley, D. J., Richards, P. J., and Berthier, A. (2015). Development of a directional load cell to measure flying sail aerodynamic loads. In *The 5th High Performance Yacht Design Conference*, pages 66–75, Auckland, New Zealand. pages 1, 30, 238, 245
- [Lindbom, 2006] Lindbom, P. (2006). *Laser scanning of sails and shape fitting to scan data*. Master thesis, Chalmers University of Technology. pages 31, 246
- [Lombardi et al., 2012] Lombardi, M., Cremonesi, M., Giampieri, A., Parolini, N., and Quarteroni, A. (2012). A strongly coupled fluid-structure interaction model for wind-sail simulation. *The 4th High Performance Yacht Design*, pages 212–221. pages 14
- [Lozej et al., 2012] Lozej, M., Golob, D., and Bokal, D. (2012). Pressure distribution on sail surfaces in real sailing conditions. In *The 4th High Performance Yacht Design Conference*, pages 242–251, Auckland, New Zealand. pages 13
- [Lua et al., 2016] Lua, K. B., Dash, S. M., Lim, T. T., and Yeo, K. S. (2016). On the thrust performance of a flapping two-dimensional elliptic airfoil in a forward flight. *Journal of Fluids and Structures*, 66:91–109. pages 7, 100, 116, 255, 260
- [Mackowski and Williamson, 2015] Mackowski, A. W. and Williamson, C. H. K. (2015). Direct measurement of thrust and efficiency of an airfoil undergoing pure pitching. *Journal of Fluid Mechanics*, 765:524–543. pages 115, 262
- [Marchaj, 1964] Marchaj, C. A. (1964). *Sailing theory and practise (new and revised version)*. Dodd, Mead & Company, Inc. pages 7
- [Marchaj, 1991] Marchaj, C. A. (1991). *Aero-hydrodynamics of sailing*. Adlard col edition. pages 13
- [Marchaj, 1996] Marchaj, C. A. (1996). *Sail performance. Techniques to maximise sail power*. Adlard coles Nautical. pages 7
- [Masuyama, 2014] Masuyama, Y. (2014). The work achieved with the sail dynamometer boat "fujin", and the role of full scale tests as the bridge between model tests and CFD. *Ocean Engineering*, 90:72–83. pages 9, 13, 30, 239, 245
- [Masuyama and Fukasawa, 2011] Masuyama, Y. and Fukasawa, T. (2011). Tacking simulation of sailing yachts with new model of aerodynamic force variation during tacking maneuver. *Journal of Sailboat Technology*, pages 1–34. pages 13
- [Mausolf et al., 2011] Mausolf, J., Deparday, J., Graf, K., Renzsch, H., and Böhm, C. (2011). Photogrammetry Based Flying Shape Investigation of Downwind Sails in the Wind Tunnel and at Full Scale on a Sailing Yacht. In *The 20th Chesapeake Sailing Yacht Symposium*, number March, pages 33–43, Annapolis, Maryland, USA. pages 14

- [McQuoid, 2010] McQuoid, K. (2010). Development and construction of core flute sails for wind tunnel testing. Technical report, University of Auckland, Yacht Research Unit. pages 10, 239
- [Menotti et al., 2013] Menotti, W., Marine, M., Durand, M., Gross, D., Roux, Y., Glehen, D., and Dorez, L. (2013). An unsteady FSI investigation into the cause of the dismasting of the Volvo 70 Groupama 4. In *The Third International Conference on Innovation in High Performance Sailing Yachts*, pages 197–205, Lorient, France. pages 5
- [Michalski et al., 2015] Michalski, A., Gawenat, B., Gellenne, P., and Haug, E. (2015). Computational wind engineering of large umbrella structures. *Journal of Wind Engineering and Industrial Aerodynamics*, 144:96–107. pages 11, 240
- [Milgram and Frimm, 1993] Milgram, J. H. and Frimm, F. C. (1993). Elements of resistance of IACC Yachts. In *The 11th Chesapeake Sailing Yacht Symposium*, pages 223–229, Annapolis, Maryland, USA. pages 13
- [Mompó Laborda, 2009] Mompó Laborda, J. M. (2009). An investigation of wall interference blockage in the Twisted Flow Wind Tunnel at the University of Auckland. Technical report, Universidad politécnica de Valencia, Valencia. pages 10, 56, 239
- [Motta, 2015] Motta, D. (2015). *An experimental investigation of full-scale sail aerodynamics using pressures, shapes and forces*. PhD thesis, The University of Auckland. pages 2, 8, 14, 121, 124, 130, 238, 264
- [Motta et al., 2015] Motta, D., Flay, R. G. J., Richards, P. J., Le Pelley, D. J., Bot, P., and Deparday, J. (2015). An investigation of the dynamic behaviour of asymmetric spinnakers at full-scale. In *The 5th High Performance Yacht Design Conference*, pages 76–85, Auckland, New Zealand. pages 14
- [Motta et al., 2014] Motta, D., Flay, R. G. J., Richards, P. J., Le Pelley, D. J., Deparday, J., and Bot, P. (2014). Experimental investigation of asymmetric spinnaker aerodynamics using pressure and sail shape measurements. *Ocean Engineering*, 90:104–118. pages 2, 14, 31, 238, 245
- [Mounoury et al., 2005a] Mounoury, S., Hauville, F., Durand, M., and Astolfi, J.-A. (2005a). Aéroélasticité non linéaire appliquée à la déformation des voiles. In *7ème colloque national en calcul des structures*, Giens, France. pages 11, 240
- [Mounoury et al., 2005b] Mounoury, S., Hauville, F., Durand, M., Astolfi, J.-a., and Roux, Y. (2005b). Aéroélasticité non linéaire appliquée aux voiles. In *10èmes journées de l'hydrodynamique*, Nantes, France. pages 11, 240
- [Nakata and Liu, 2012] Nakata, T. and Liu, H. (2012). A fluid-structure interaction model of insect flight with flexible wings. *Journal of Computational Physics*, 231(4):1822–1847. pages 7
- [Nava et al., 2016] Nava, S., Cater, J., and Norris, S. (2016). A Comparison of RANS and LES for Upwind Sailing Aerodynamics. In *The 22nd Chesapeake Sailing Yacht Symposium*, pages 73–83, Annapolis, Maryland, USA. pages 13
- [NorthSails, 2017] NorthSails (2017). North design suite. <http://northsails.com/sailing/innovation/design-expertise/design-suite> Last accessed on the 11th of June 2017. pages 12

- [Orlowski and Girard, 2012] Orlowski, C. T. and Girard, A. R. (2012). Dynamics, stability, and control analyses of flapping wing micro-air vehicles. *Progress in Aerospace Sciences*, 51:18–30. pages 118
- [Ouadahi et al., 2014] Ouadahi, N., Ababou, A., Ababou, N., and Larbi, M. A. (2014). Windsurf ergometer for sail pumping analysis and mechanical power measurement. *Procedia Engineering*, 72:249–254. pages 101
- [Puddu et al., 2006] Puddu, P., Erriu, N., Nurzia, F., Pistidda, A., and Mura, A. (2006). Full-scale investigation of one-design class catamaran sails. In *The 2nd High Performance Yacht Design Conference*, pages 131–136, Auckland, New Zealand. pages 13
- [Ranzenbach and Armitage, 2013] Ranzenbach, R. and Armitage, D. (2013). Mainsail planform optimization for IRC 52 using fluid structure interaction. In *The 21st Chesapeake Sailing Yacht Symposium*, number March, Annapolis, Maryland, USA. pages 12, 13
- [Ranzenbach and Kleene, 2002] Ranzenbach, R. and Kleene, J. (2002). Utility of flying shapes in the development of offwind sail design database. In *High Performance Yacht Design Conference*, pages 4–6, Auckland, New Zealand. pages 14
- [Renzsch and Graf, 2010] Renzsch, H. and Graf, K. (2010). Fluid Structure Interaction Simulation of Spinnakers - Towards Simulation Driven Sail Design. In *the 21st Hiswa Symposium on yacht design and yacht construction*, Amsterdam, The Netherlands. pages 14
- [Renzsch and Graf, 2013] Renzsch, H. and Graf, K. (2013). An experimental validation case for fluid-structure-interaction simulations of downwind sails. In *The 21st Chesapeake Sailing Yacht Symposium*, number March, Annapolis, Maryland, USA. pages 14
- [Richards et al., 2001] Richards, P. J., Johnson, A., and Stanton, A. (2001). America’s Cup downwind sails - vertical wings or horizontal parachutes ? *Journal of Wind Engineering and Industrial Aerodynamics*, 89:1565–1577. pages 23
- [Richards et al., 2006] Richards, P. J., Le Pelley, D. J., Cazala, A., Mccarty, M., Hansen, H., and Moore, W. (2006). The use of independent supports and semi-rigid sails in wind tunnel studies. In *The 2nd High Performance Yacht Design Conference*, pages 14–16, Auckland, New Zealand. pages 10, 14
- [Rival et al., 2010] Rival, D., Prangemeier, T., and Tropea, C. (2010). The influence of airfoil kinematics on the formation of leading-edge vortices in bio-inspired flight. *Animal Locomotion*, (1994):261–271. pages 7
- [Royal Yacht Association, 2017] Royal Yacht Association (2017). Spinnakers: hoist, trim and drop. <http://www.rya.org.uk/knowledge-advice/cruising-tips/boat-handling-sail/Pages/spinnakers-hoist-trim-and-drop.aspx> Last accessed on the 11th of June 2017. pages 124
- [Sacher et al., 2015] Sacher, M., Hauville, F., Bot, P., and Durand, M. (2015). Sail trimming FSI simulation - comparison of viscous and inviscid flow models to optimise upwind sails trim. In *The 5th High Performance Yacht Design Conference*, pages 10–12, Auckland, New Zealand. pages 33, 77, 78, 79

- [Sacher et al., 2016] Sacher, M., Hauville, F., Duvigneau, R., Le Maître, O., Aubin, N., and Durand, M. (2016). Experimental and numerical trimming optimizations for a mainsail in upwind conditions. In *The 22nd Chesapeake sailing yacht symposium*, number March, pages 36–48, Annapolis, Maryland, USA. pages 3, 60, 77, 78, 86, 211
- [Sacher et al., 2017] Sacher, M., Hauville, F., Duvigneau, R., Le Maître, O., Aubin, N., and Durand, M. (2017). Efficient optimization procedure in non-linear fluid-structure interaction problem: Application to mainsail trimming in upwind conditions. *Journal of Fluids and Structures*, 69:209–231. pages 77, 78, 183, 238, 251, 261
- [Schafer, 2011] Schafer, R. W. (2011). What is a Savitzky-Golay filter? *IEEE Signal Processing Magazine*, 28(4):111–117. pages 109, 112, 173, 276
- [Schnipper et al., 2009] Schnipper, T., Andersen, A., and Bohr, T. (2009). Vortex wakes of a flapping foil. *Journal of Fluid Mechanics*, 633:411. pages 116, 260
- [Schoop and Bessert, 2001] Schoop, H. and Bessert, N. (2001). Instationary aeroelastic computation of yacht sails. *International Journal for Numerical Methods in Engineering*, 52(8):787–803. pages 13
- [Schouveiler et al., 2005] Schouveiler, L., Hover, F. S., and Triantafyllou, M. S. (2005). Performance of flapping foil propulsion. *Journal of Fluids and Structures*, 20(7 SPEC. ISS.):949–959. pages 7, 100, 115, 116, 255, 260
- [Schutt and Williamson, 2016] Schutt, R. R. and Williamson, C. H. K. (2016). Unsteady sail dynamics due to bodyweight motions. In *The 22nd Chesapeake sailing yacht symposium*, number March, pages 58–72, Annapolis, Maryland, USA. pages 6, 10, 13, 100, 116, 239, 255, 259
- [Serres, 2004] Serres, J. (2004). Development of a 2D-flow visualization tool. Technical report, INSA de Rouen, Rouen. pages 10, 239
- [Shyy et al., 2013a] Shyy, W., Aono, H., Kang, C.-k., and Hao, L. (2013a). *An Introduction to Flapping Wing Aerodynamics*. Cambridge University Press. pages 100
- [Shyy et al., 2013b] Shyy, W., Lian, Y., Tang, J., Vileru, D., and Liu, H. (2013b). *Aerodynamics of Low Reynolds Number Flyers*, volume 53. Cambridge University Press. pages 100
- [Sigrist, 2011] Sigrist, J.-F. (2011). Méthodes numériques de calculs fluide/structure. Cas du fluide s’écoulant : introduction. Technical report. pages 11
- [Sigrist, 2015] Sigrist, J.-F. (2015). *Fluid-structure interaction: an introduction to finite element coupling*. Wiley edition. pages 11
- [Spedding and Hedenström, 2010] Spedding, G. R. and Hedenström, A. (2010). PIV-based investigations of animal flight. *Animal Locomotion*, pages 187–201. pages 7
- [Staubli et al., 2008] Staubli, T., Waser, R., and Widmer, C. (2008). Airfoil in cross flow. In *International Conference on Flow-induced Vibration*, number 1985, Prague, Czech Republic. pages 135

- [Taibi, 2001] Taibi, E. H. (2001). *Caracterisation, modélisation et simulation du comportement d'un tissu textile*. PhD thesis, Université Mohamed V, Maroc et Université Bordeaux I, France. pages 229
- [Taylor et al., 2003] Taylor, G. K., Nudds, R. L., and Thomas, A. L. R. (2003). Flying and swimming animals cruise at a Strouhal number tuned for high power efficiency. *Nature*, 425:707–711. pages 100, 255
- [TFI, 2015] TFI (2015). Getting started series 100 Cobra Probe. Technical report, Turbulent Flow Instrumentation, Victoria, Australia. pages 25, 61
- [Theodorsen, 1935] Theodorsen, T. (1935). General theory of aerodynamic instability and the mechanism of flutter. Technical report, National Advisory Committee for Aeronautics. pages 115
- [Theodorsen and Garrick, 1942] Theodorsen, T. and Garrick, I. E. (1942). Nonstationary flow about a wing-aileron-tab combination including aerodynamic balance. Technical Report 736, National Advisory Committee for Aeronautics. pages 115
- [Trimarchi, 2012] Trimarchi, D. (2012). *Analysis of downwind sail structures using non-linear shell finite elements*. PhD thesis, University of Southampton, Faculty of Engineering and the Environment. pages 14
- [Trimarchi et al., 2009] Trimarchi, D., Turnock, S., Chapelle, D., and Taunton, D. (2009). Fluid-structure interactions of anisotropic thin composite materials for application to sail aerodynamics of a yacht in waves. *The 12th Numerical Towing Tank Symposium*, page 6. pages 14
- [Trimarchi et al., 2013] Trimarchi, D., Vidrascu, M., Taunton, D., Turnock, S. R., and Chapelle, D. (2013). Wrinkle development analysis in thin sail-like structures using MITC shell finite elements. *Finite Elements in Analysis and Design*, 64:48–64. pages 14
- [Trizila et al., 2011] Trizila, P., C-K, K., Anono, H., W, S., and Visbal, M. (2011). Low-Reynolds-number aerodynamics of a flapping rigid flat plate. *AIAA Journal*, 49(4):806–823. pages 109
- [Van Hemmen, 1986] Van Hemmen, R. F. (1986). Twelve meter design: state of the art in 1986. *Marine Technology*, 23(4):320–337. pages 13
- [Viieru et al., 2006] Viieru, D., Tang, J., Lian, Y., Liu, H., and Shyy, W. (2006). Flapping and flexible wing aerodynamics of low Reynolds number flight vehicles. *The 44th AIAA Aerospace Sciences Meeting and Exhibit*, (January):1–18. pages 7
- [Viola and Arredondo-Galeana, 2017] Viola, I. and Arredondo-Galeana, A. (2017). The leading-edge vortex of yacht sails. In *INNOVSAIL International Conference on Innovation in High Performance Sailing Yachts*, pages 115–126, Lorient, France. pages 264
- [Viola, 2009] Viola, I. M. (2009). Downwind sail aerodynamics: A CFD investigation with high grid resolution. *Ocean Engineering*, 36(12-13):974–984. pages 14
- [Viola et al., 2014] Viola, I. M., Bartesaghi, S., Van-Renterghem, T., and Ponzini, R. (2014). Detached Eddy Simulation of a sailing yacht. *Ocean Engineering*, 90:93–103. pages 11, 14, 240

- [Viola et al., 2013] Viola, I. M., Bot, P., and Riotte, M. (2013). Upwind sail aerodynamics : A RANS numerical investigation validated with wind tunnel pressure measurements. *International Journal of Heat and Fluid Flow*, 39:90–101. pages 13
- [Viola and Flay, 2009] Viola, I. M. and Flay, R. G. J. (2009). Force and pressure investigation of modern asymmetric spinnakers. *International Journal of Small Craft Technology*, 151. pages 14, 31, 246
- [Viola and Flay, 2010a] Viola, I. M. and Flay, R. G. J. (2010a). Full-scale pressure measurements on a Sparkman and Stephens 24-foot sailing yacht. *Journal of Wind Engineering and Industrial Aerodynamics*, 98(12):800–807. pages 9, 239
- [Viola and Flay, 2010b] Viola, I. M. and Flay, R. G. J. (2010b). On-water pressure measurements on a modern asymmetric spinnaker. In *The 21st International HISWA Symposium on Yacht Design and Yacht Construction*, Amsterdam, The Netherlands. pages 14
- [Viola and Flay, 2011a] Viola, I. M. and Flay, R. G. J. (2011a). Sail aerodynamics: Understanding pressure distributions on upwind sails. *Experimental Thermal and Fluid Science*, 35(8):1497–1504. pages 13
- [Viola and Flay, 2011b] Viola, I. M. and Flay, R. G. J. (2011b). Sail pressures from full-scale, wind-tunnel and numerical investigations. *Ocean Engineering*, 38(16):1733–1743. pages 14, 151
- [Viola and Flay, 2011c] Viola, I. M. and Flay, R. G. J. (2011c). Upwind sail aerodynamics. *International Journal of Small Craft Technology*, 153(1):47–58. pages 10, 239
- [Viola and Flay, 2015] Viola, I. M. and Flay, R. G. J. (2015). Pressure distributions on modern asymmetric spinnakers. *International Journal of Small Craft Technology*, 152(1):41–48. pages 10, 239
- [Viola et al., 2010] Viola, I. M., Gauvain, E., and Flay, R. G. J. (2010). Pressure measurements on full-scale and model-scale upwind sails. In *the 17th Australasian Fluid Mechanics Conference*, number December, pages 1–4, Auckland, New Zealand. pages 9, 239
- [Voiles et Voiliers, 2014] Voiles et Voiliers (2014). Tout savoir sur les voiles. *Voiles et voiliers hors-série*, 47. pages 229
- [Voisin et al., 2013] Voisin, D., Desjoyeaux, M., and Rive, C. (2013). Device and process for determining the flow regime and/or the direction of a fluid flow. US Patent 8,397,564. pages 32, 245
- [WB-sails, 2017] WB-sails (2017). WB sails simulations. <http://www.wb-sails.fi/en/sail-technology/technologies---videos> Last accessed on the 11th of June 2017. pages 12
- [Whitewright, 2011] Whitewright, J. (2011). The potential performance of ancient mediterranean sailing rigs. *International Journal of Nautical Archaeology*, 40(1):2–17. pages 22
- [Wiernga, 1993] Wiernga, J. (1993). Representative roughness parameters for homogeneous terrain. *Boundary-Layer Meteorology*, 63(4):323–363. pages 24, 244

-
- [Williamson, 1988] Williamson, C. H. K. (1988). Defining a universal and continuous Strouhal-Reynolds number relationship for the laminar vortex shedding of a circular cylinder. *Physics of Fluids*, 31(10):2742–2744. pages 100
- [Williamson and Schutt, 2016] Williamson, C. H. K. and Schutt, R. (2016). Unsteady sail dynamic in Olympic class sailboats. In *Division of Fluid dynamics 2016 meeting of the American physical Society*, Portland, Oregon, USA. pages 9, 239, 280

Interaction fluide-structure sur voiles de bateau : de l'approche in situ à l'étude instationnaire en soufflerie.

Résumé: Ce travail s'inscrit dans le projet VOILENav qui vise à améliorer la compréhension des phénomènes d'Interaction Fluide-Structure appliqués aux voiles. Des comparaisons numériques expérimentales sont réalisées sur des mesures « in situ » au près à l'aide d'un code fluide parfait. Un critère, fondé sur l'équilibre du couple aérodynamique avec le couple de redressement, est proposé, permettant de vérifier l'hypothèse d'un écoulement attaché. Les précédentes études sur un voilier instrumenté ont montré les limites d'une approche « in situ » de par l'instationnarité naturelle liée aux évolutions du vent et de l'état de mer. Les autres limites résident dans la mesure de ces dernières – et tout particulièrement la mesure du vent réel – ainsi que dans le spectre des conditions rencontrées au réel. Des essais en soufflerie sont ainsi réalisés dans le cadre de ces travaux pour répondre, par une approche systématique et contrôlée, aux interrogations soulevées par les mesures « in situ ». Deux campagnes expérimentales successives, soutenues par le programme d'échange Sailing Fluids ont été menées dans la soufflerie du Yacht Research Unit de l'Université d'Auckland se focalisant sur les essais de voiles au près puis au portant. Les essais au près sont réalisés sur trois modèles réduits de grand-voiles d'IMOCA60 dans des conditions de réglages statiques et dynamiques. Le meilleur réglage statique est obtenu grâce à l'utilisation d'un algorithme d'optimisation original puis l'influence de l'amplitude et de la fréquence du « pumping » sont étudiés. Les performances aérodynamiques du système soumis à un réglage dynamique sont supérieures à celles du réglage optimum statique et un maximum est observé autour d'une fréquence réduite de 0.25 à 0.3. Au portant, les effets de l'instationnarité naturelle du spinnaker connue sous le terme « curling » (repliement du bord d'attaque) sont étudiés. Quatre modèles de spinnakers de J80 de forme identique sont testés pour différents matériaux et différentes coupes. Les mesures en soufflerie montrent que, pour des angles de vent apparent supérieurs à 100°, l'apparition du « curling » conduit à une augmentation de la force propulsive pouvant atteindre 10%. Les effets de la vitesse et de l'angle de vent apparent sont également étudiés et permettent d'extraire une fréquence réduite de curling indépendante de la vitesse de l'écoulement de 0.4 pour un vent apparent de 120°. L'étendue de la gamme de mesures explorées et le soin particulier apporté aux données expérimentales font de ces travaux une base de données remarquable pour des comparaisons avec des simulations de l'Interaction Fluide-Structure.

Mots-clés: Interaction Fluide Structure, soufflerie, expérience in situ, voilier instrumenté, instationnaire, fluide parfait, comparaison numérique/expérience

Fluid-structure interaction on yacht sails: from full-scale approach to wind tunnel unsteady study.

Abstract: This work is part of the VOILENav project which aims to improve the understanding of Fluid-Structure Interaction applied to sails. Full-scale numerical experimental comparisons are achieved in upwind conditions with an inviscid flow code. A criterion using the equilibrium between the righting and heeling moment is suggested to check the attached flow hypothesis. Previous full-scale studies on instrumented boat are limited by the natural unsteadiness of wind and sea conditions and the measurement of these conditions. True wind computation and the wide range of encountered sailing conditions are still challenging. Complementary wind tunnel tests are carried out in this PhD project, using controlled conditions, to address some issues observed at full-scale. Thanks to the Sailing Fluids collaboration, two experimental campaigns in the Twisted Flow Wind Tunnel of the Yacht Research Unit of the University of Auckland have investigated upwind and downwind conditions. Upwind tests investigate static and dynamic trimming on three model IMOCA60 mainsails. The optimum static trim is determined thanks to an innovative optimization algorithm then the pumping amplitude and frequency are investigated. Aerodynamic performances under dynamic trimming are better than the optimum static trim with a maximum located for a reduced frequency about 0.25 to 0.3. For the downwind test, the natural unsteadiness known as curling (repeated folding-unfolding of leading edge) is studied. Four model J80 spinnakers with identical design shape are tested with different materials and cuts. Wind tunnel measurements show that for apparent wind angles higher than 100°, the curling apparition increases the drive force by up to 10%. Wind speed and wind angle effects are investigated and show a reduced curling frequency of 0.4 independent from the flow velocity for an apparent wind angle of 120°. The variety of the experimental conditions tested makes this work a precious database for Fluid Structure Interaction numerical-experimental comparison in the future.

Keywords : Fluid Structure Interaction, wind tunnel, full-scale experiment, instrumented sailing boat, unsteady, inviscid flow, numerical/experimental comparison